MicroVention®
TERUMO

Leading the Way in Neuroendovascular Therapy

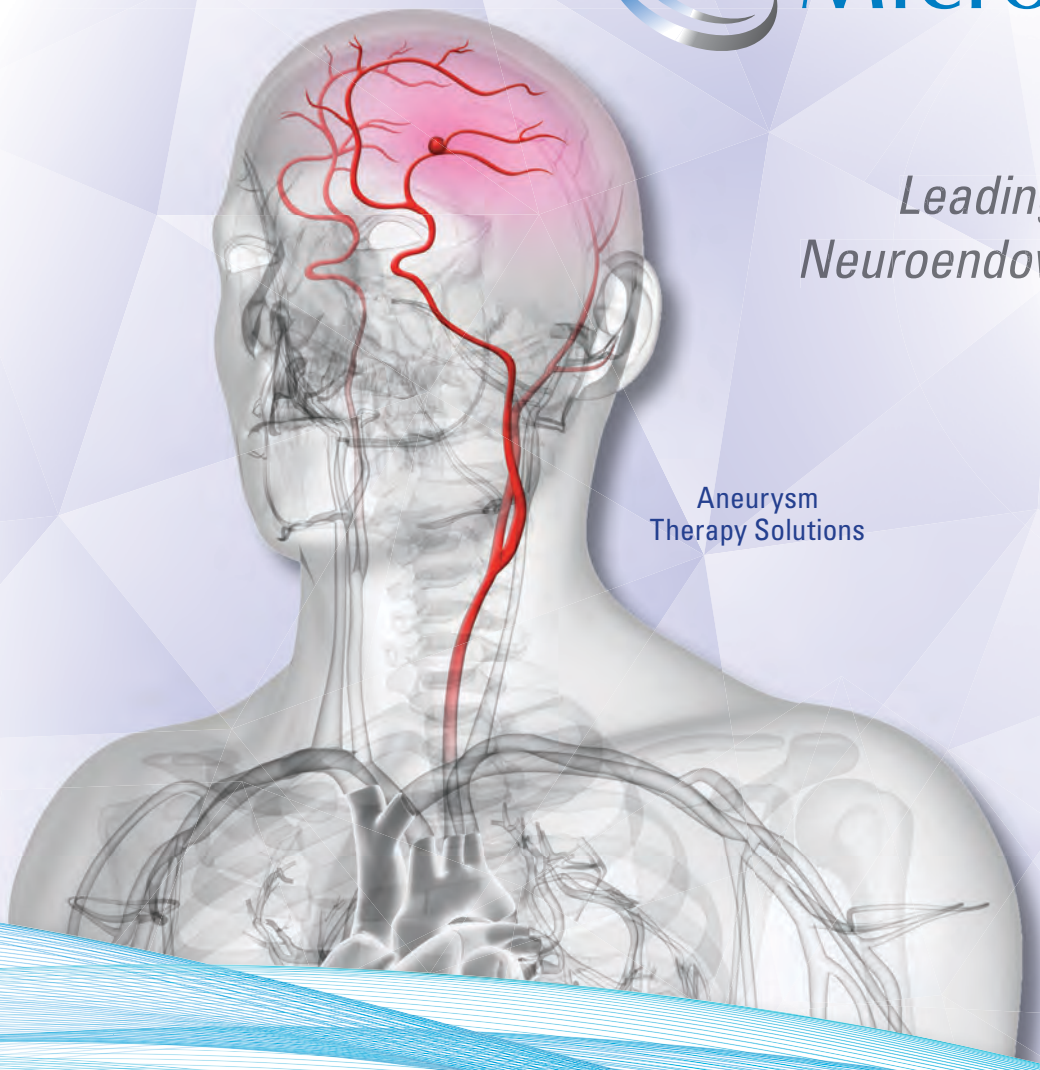

Aneurysm
Therapy Solutions

A 360-Degree Approach to Performance Based Solutions

microvention.com

stryker

NEW

Indication for Trevo® Retrievers

A New Standard of Care in Stroke

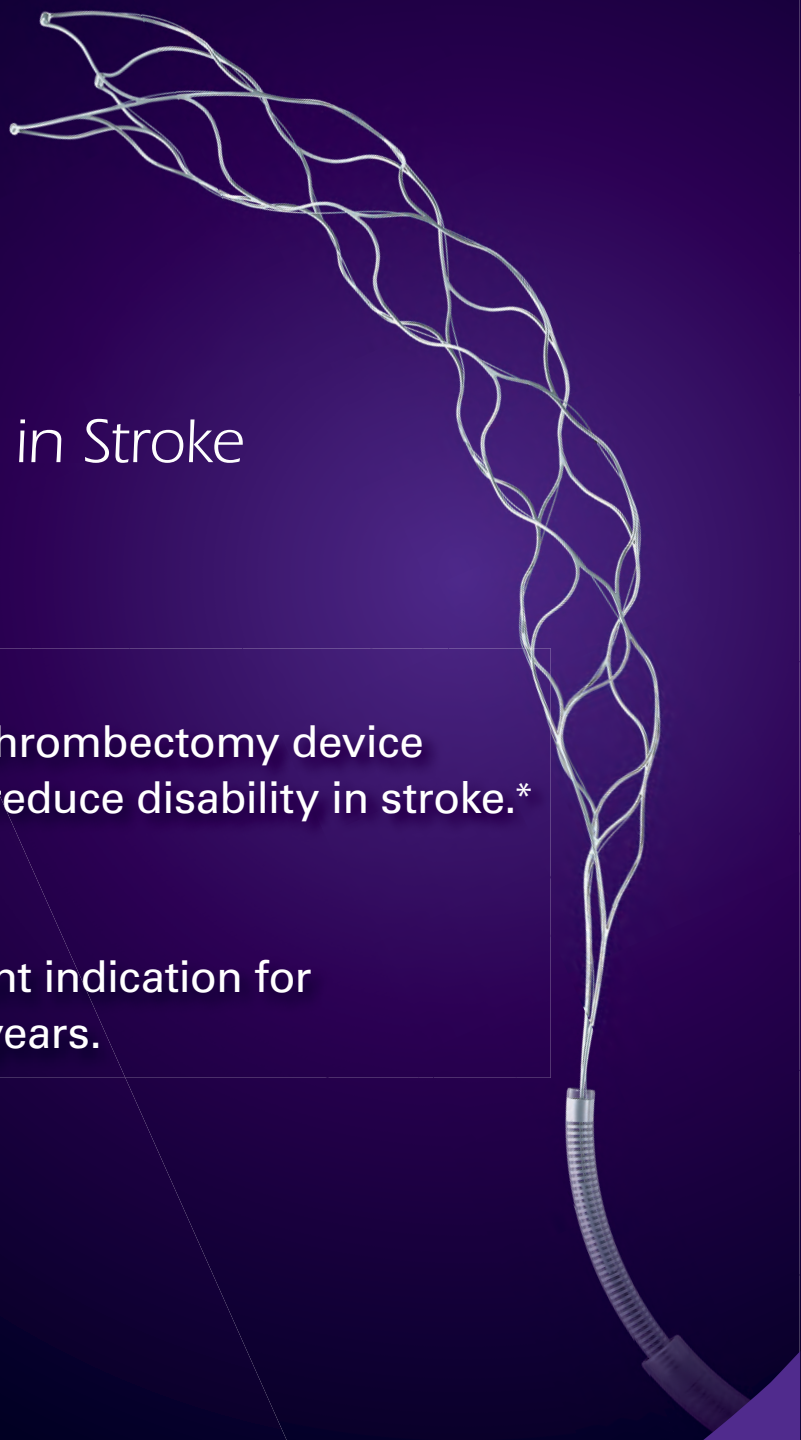

1st

FIRST
mechanical thrombectomy device indicated to reduce disability in stroke.*

FIRST
new treatment indication for stroke in 20 years.

Trevo XP
PROVUE RETRIEVER

Success accelerated.

*The Trevo Retriever is indicated for use to restore blood flow in the neurovasculature by removing thrombus for the treatment of acute ischemic stroke to reduce disability in patients with a persistent, proximal anterior circulation, large vessel occlusion, and smaller core infarcts who have first received intravenous tissue plasminogen activator (IV t-PA). Endovascular therapy with the device should start within 6 hours of symptom onset.

THE PROVEN LEADER

The STAR™ Tumor Ablation System is the proven leader in spine RF ablation with thousands of patients treated.

Dual thermocouples for active temperature monitoring on a single instrument

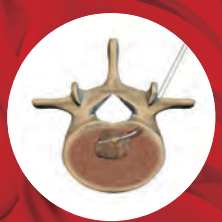

Steerable and navigational RF ablation instrument

SpineSTAR® delivers RF energy directly to the tumor

Tumor is debulked

STAR Clinical Studies Demonstrate[1-4]:

- Fast, durable pain relief
- Rapid improvement in mobility and quality of life
- Reduction or discontinuation of pain medication
- Site-specific ablation zones and real time temperature monitoring
- May be combined with radiation and/or chemotherapy

MERITMEDICAL®

Merit.com/star

Indications for Use: The STAR™ Tumor Ablation System is indicated for palliative treatment in spinal procedures by ablation of metastatic malignant lesions in a vertebral body. As with most surgical procedures, there are risks associated with the STAR procedure, including serious complications. For complete information regarding risks, contraindications, warnings, precautions, and adverse events please review the System's Instructions for Use.

References
1 Pain Physician 2014 Jul-Aug; 17(4):317-27 2 Radiology 2014 Oct; 273 (1): 261-7 3 J. Vasc Interv Radiol 2015; 18: 573-581 4 Pain Physician 2015; 18: 573-581

402549001/A ID 102016

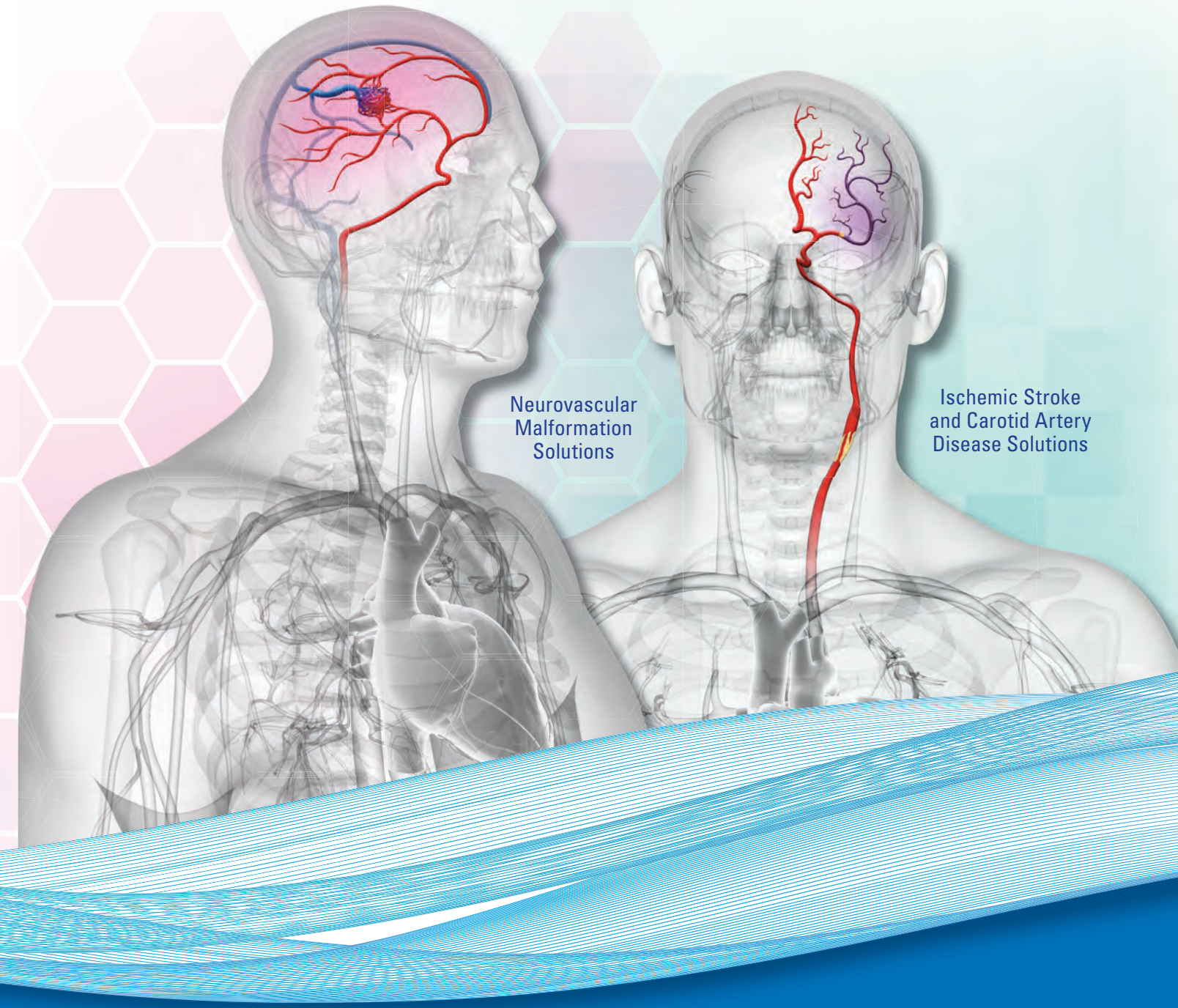

For more information or a product demonstration, contact your local MicroVention representative:

MicroVention®
TERUMO

MicroVention, Inc.
Worldwide Headquarters PH +1.714.247.8000
1311 Valencia Avenue
Tustin, CA 92780 USA
MicroVention UK Limited PH +44 (0) 191 258 6777
MicroVention Europe, S.A.R.L. PH +33 (1) 39 21 77 46
MicroVention Deutschland GmbH PH +49 211 210 798-0

stryker®
Neurovascular

Purposeful innovation in mind.

Smooth and stable.

Target Detachable Coils deliver consistently smooth deployment and exceptional microcatheter stability. Designed to work seamlessly together for framing, filling and finishing. Target Coils deliver the high performance you demand.

For more information, please visit www.strykerneurovascular.com/Target or contact your local Stryker Neurovascular sales representative.

Target®
DETACHABLE COILS

NV00018669.AA

BARRICADE™ COIL SYSTEM

COILS THAT
PERFORM

Cost Analysis of Cerebral Aneurysms Treated with the Barricade Coil System, A Retrospective Review

22 Patients Treated ◆ 114 Total Barricade Coils Used ◆ 8.2mm Mean Aneurysm Size

RIGHT PERICALLOSAL ANEURYSM

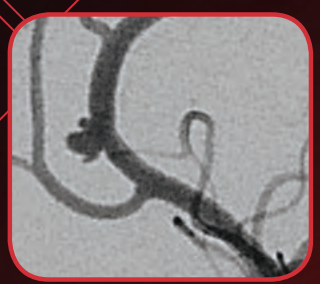

PRE-TREATMENT

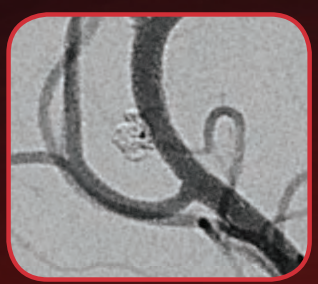

POST-TREATMENT

LEFT ICA TERMINUS ANEURYSM

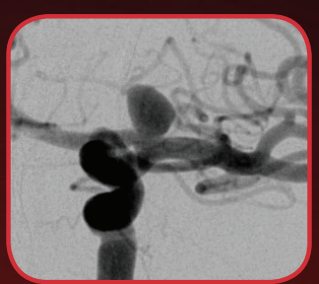

PRE-TREATMENT

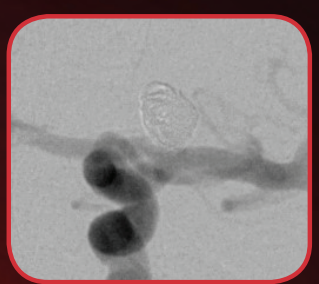

POST-TREATMENT

"I have successfully treated a wide range of aneurysms with the Barricade Coil System. I am impressed with the overall performance of the coils and the realized cost savings."

-Yince Loh, M.D.

COILS THAT
SAVE $

$110,000* SAVED

Images and data courtesy of Yince Loh, M.D., Seattle, WA

* Estimated savings in this case, data on file.

The Barricade Coil System is intended for the endovascular embolization of intracranial aneurysms and other neurovascular abnormalities such as arteriovenous malformations and arteriovenous fistulae. The System is also intended for vascular occlusion of blood vessels within the neurovascular system to permanently obstruct blood flow to an aneurysm or other vascular malformation and for arterial and venous embolizations in the peripheral vasculature. Refer to the instructions for use for complete product information.

18 TECHNOLOGY DRIVE #169, IRVINE CA 92618 | p: 949.788.1443 | f: 949.788.1444
WWW.BLOCKADEMEDICAL.COM

MKTG-050 Rev. A

BLOCKADE MEDICAL

The brain at your fingertips

Rapid Medical

www.rapid-medical.com > tigertriever

The Foundation of the ASNR Symposium 2017: *Discovery and Didactics* April 22-23, 2017

ASNR 55th Annual Meeting: *Diagnosis and Delivery* April 24-27, 2017

Register Now!
Visit 2017.asnr.org for more information.

Long Beach Convention & Entertainment Center

Jacqueline A. Bello, MD, FACR
ASNR 2017 Program Chair/President-Elect

Programming developed in cooperation with and appreciation of the…

American Society of Functional Neuroradiology (ASFNR)
Kirk M. Welker, MD

American Society of Head and Neck Radiology (ASHNR)
Rebecca S. Cornelius, MD, FACR

American Society of Pediatric Neuroradiology (ASPNR)
Susan Palasis, MD

American Society of Spine Radiology (ASSR)
Joshua A. Hirsch, MD, FACR, FSIR

Society of NeuroInterventional Surgery (SNIS)
Blaise W. Baxter, MD

American Society of Neuroradiology (ASNR) Health Policy Committee
Robert M. Barr, MD, FACR

Computer Sciences & Informatics (CSI) Committee
John L. Go, MD, FACR

Research Scientist Committee
Dikoma C. Shungu, PhD and Timothy, P.L. Roberts, PhD

The International Hydrocephalus Imaging Working Group (IHIWG)/CSF Flow Group
William G. Bradley, Jr., MD, PhD, Harold L. Rekate, MD and Bryn A. Martin, PhD

ASNR 55th Annual Meeting
c/o American Society of Neuroradiology
800 Enterprise Drive, Suite 205 • Oak Brook, Illinois 60523-4216
Phone: 630-574-0220 • Fax: 630 574-0661 • 2017.asnr.org

2017 ASNR Long Beach, California
Discovery Didactics Diagnosis Delivery

ASFNR ASHNR ASPNR ASSR SNIS
THE FOUNDATION OF THE ASNR

Come to the beach! Please join us in Long Beach, California, April 22-27, 2017, for the 55th Annual Meeting of the ASNR. Known for its 5.5 miles of Pacific Ocean waterfront, this southern California beach resort boasts a blend of city sophistication and seaside serenity. ASNR is delighted to provide a **"4D"** focus for this meeting, as depicted by our meeting logo: ***Discovery and Didactics*** for The Foundation of the ASNR Symposium 2017: ***Diagnosis and Delivery*** for the ensuing Annual Meeting Program.

Centered on Discovery and Didactics, the symposium will feature sessions on "What's New?" in the role neuroimaging plays defining CNS disease mechanisms and how to best prepare for "What's Next?" for our subspecialty in terms of training, teaching, and leading the process of lifelong learning. The annual meeting programming will address best practices in Diagnosis and Delivery, as we strive to provide value, promote quality in better health and care and consider cost. Our discussions will consider how to navigate the changing landscape of healthcare reform and reimbursement as subspecialists in a field that is changing at an equally "fast forward" pace!

Hyatt Regency Long Beach

Westin Long Beach

AJNR

CALL FOR AJNR EDITORIAL FELLOWSHIP CANDIDATES

ASNR and AJNR are pleased once again to join efforts with other imaging-related journals that have training programs on editorial aspects of publishing for trainees or junior staff (3–5 years after training), including Radiology (Olmsted fellowship), AJR (Figley and Rogers fellowships), JACR (Bruce J. Hillman fellowship), and Radiologia.

2017 Candidate Information and Requirements

GOALS

- Increase interest in "editorial" and publication-related activities in younger individuals.
- Increase understanding and participation in the AJNR review process.
- Incorporate into AJNR's Editorial Board younger individuals who have previous experience in the review and publication process.
- Fill a specific need in neuroradiology not offered by other similar fellowships.
- Increase the relationship between "new" generation of neuroradiologists and more established individuals.
- Increase visibility of AJNR among younger neuroradiologists.

ACTIVITIES OF THE FELLOWSHIP

- Serve as Editorial Fellow for one year. This individual will be listed on the masthead as such.
- Review at least one manuscript per month for 12 months. Evaluate all review articles submitted to AJNR.
- Learn how electronic manuscript review systems work.
- Be involved in the final decision of selected manuscripts together with the Editor-in-Chief.
- Participate in all monthly Senior Editor telephone conference calls.
- Participate in all meetings of the Editors and Publications Committee during the annual meetings of ASNR and RSNA as per candidate's availability. The Foundation of the ASNR will provide $2000 funding for this activity.
- Evaluate progress and adjust program to specific needs in annual meeting or telephone conference with the Editor-in-Chief.
- Embark on an editorial scientific or bibliometric project that will lead to the submission of an article to AJNR or another appropriate journal as determined by the Editor-in-Chief. This project will be presented by the Editorial Fellow at the ASNR annual meeting.
- Serve as liaison between AJNR and ASNR's Young Professionals Network and the 3 YPs appointed to AJNR as special consultants. Participate in meetings and telephone calls with this group. Design one electronic survey/year, polling the group regarding readership attitudes and wishes.
- Recruit trainees as reviewers as determined by the Editor-in-Chief.
- Participate in Web improvement projects.
- Serve as Guest Editor for an issue of AJNR's News Digest with a timely topic.

QUALIFICATIONS

- Be a fellow in neuroradiology from North America, including Canada (this may be extended to include other countries).
- Be a junior faculty neuroradiology member (< 3 years) in either an academic or private environment.
- Be an "in-training" or member of ASNR in any other category.

APPLICATION

- Include a short letter of intent with statement of goals and desired research project. CV must be included.
- Include a letter of recommendation from the Division Chief or fellowship program director. A statement of protected time to perform the functions outlined is desirable.
- Applications will be evaluated by AJNR's Senior Editors and the Chair of the Publications Committee prior to the ASNR meeting. The name of the selected individual will be announced at the meeting.
- Applications should be received by March 1, 2017 and sent to Ms. Karen Halm, AJNR Managing Editor, electronically at khalm@asnr.org.

ASHNR
American Society of
Head & Neck Radiology

51st Annual Meeting

American Society of

Head & Neck Radiology

Head and Neck Imaging in the City of Lights

Caesars Palace • Las Vegas, NV

September 16 – 20, 2017
(Saturday - Wednesday)

Please contact Educational Symposia at 813-806-1000 or ASHNR@edusymp.com or visit www.ASHNR.org for additional information.

INTRODUCING
FULLY AUTOMATED
STROKE APPLICATIONS

Olea Sphere 3.0

ZERO CLICK
Calculation of infarct penumbra & mismatch

AUTOMATED STROKE REPORT
(MRI & CT) by email

VENDOR-NEUTRAL
& easy integration into IT systems

Ask for a free trial
www.olea-medical.com

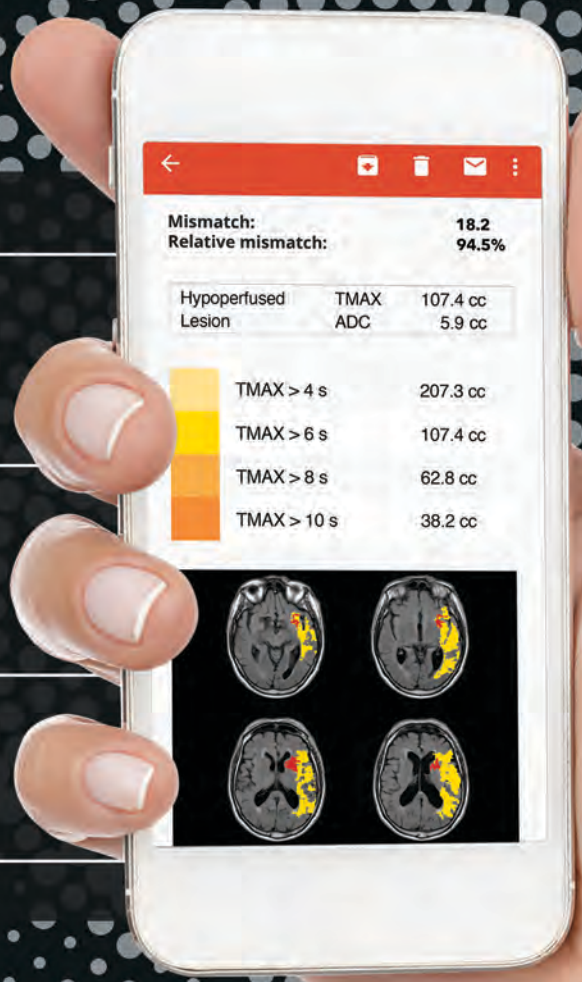

" **Innovation** is in our **DNA.** "

* FDA cleared

Olea MEDICAL

Improved diagnosis for life™

Strengthen ASNR's representation at the national level.

Your membership in the American Medical Association strengthens ASNR's representation in the AMA House of Delegates—the policymaking body of the AMA that brings forth the views and interests of all physicians to establish national policy on health, medical, professional and governance matters.

Please activate your 2017 AMA membership, visit ama-assn.org or call AMA Member Relations at (800) 262-3211. If you are currently a member, thank you.

AMA member benefits and resources include:

- Unlimited access to **The JAMA Network®** which brings together *JAMA* and all 11 specialty journals with CME.
  jamanetwork.com
- **STEPS Forward™**, the AMA's new practice transformation series designed to help physicians achieve the Quadruple Aim: better patient experience, better population health and lower overall costs with improved professional satisfaction.
  stepsforward.org
- Free 18-month trial of ***DynaMed Plus®***, an evidence-based, clinical support tool that features thousands of images and provides immediate answers to clinical questions.
  offers.jamanetwork.com

AMA AMERICAN MEDICAL ASSOCIATION

ASNR American Society of Neuroradiology

Trevo® XP ProVue Retrievers

See package insert for complete indications, complications, warnings, and instructions for use.

INDICATIONS FOR USE

1. The Trevo Retriever is indicated for use to restore blood flow in the neurovasculature by removing thrombus for the treatment of acute ischemic stroke to reduce disability in patients with a persistent, proximal anterior circulation, large vessel occlusion, and smaller core infarcts who have first received intravenous tissue plasminogen activator (IV t-PA). Endovascular therapy with the device should start within 6 hours of symptom onset.
2. The Trevo Retriever is intended to restore blood flow in the neurovasculature by removing thrombus in patients experiencing ischemic stroke within 8 hours of symptom onset. Patients who are ineligible for intravenous tissue plasminogen activator (IV t-PA) or who fail IV t-PA therapy are candidates for treatment.

COMPLICATIONS

Procedures requiring percutaneous catheter introduction should not be attempted by physicians unfamiliar with possible complications which may occur during or after the procedure. Possible complications include, but are not limited to, the following: air embolism; hematoma or hemorrhage at puncture site; infection; distal embolization; pain/headache; vessel spasm, thrombosis, dissection, or perforation; emboli; acute occlusion; ischemia; intracranial hemorrhage; false aneurysm formation; neurological deficits including stroke; and death.

COMPATIBILITY

3x20mm retrievers are compatible with Trevo® Pro 14 Microcatheters (REF 90231) and Trevo® Pro 18 Microcatheters (REF 90238). 4x20mm retrievers are compatible with Trevo® Pro 18 Microcatheters (REF 90238). 4x30mm retrievers are compatible with Excelsior® XT-27® Microcatheters (150cm x 6cm straight REF 275081) and Trevo® Pro 18 Microcatheters (REF 90238). 6x25mm Retrievers are compatible with Excelsior® XT-27® Microcatheters (150cm x 6cm straight REF 275081). Compatibility of the Retriever with other microcatheters has not been established. Performance of the Retriever device may be impacted if a different microcatheter is used.

Balloon Guide Catheters (such as Merci® Balloon Guide Catheter and FlowGate® Balloon Guide Catheter) are recommended for use during thrombus removal procedures.

Retrievers are compatible with the Abbott Vascular DOC® Guide Wire Extension (REF 22260).

Retrievers are compatible with Boston Scientific RHV (Ref 421242).

SPECIFIC WARNINGS FOR INDICATION 1

- The safety and effectiveness of the Trevo Retrievers in reducing disability has not been established in patients with large core infarcts (i.e., ASPECTS ≤ 7). There may be increased risks, such as intracerebral hemorrhage, in these patients.
- The safety and effectiveness of the Trevo Retrievers in reducing disability has not been established or evaluated in patients with occlusions in the posterior circulation (e.g., basilar or vertebral arteries) or for more distal occlusions in the anterior circulation.

WARNINGS APPLIED TO BOTH INDICATIONS

- Administration of IV t-PA should be within the FDA-approved window (within 3 hours of stroke symptom onset).
- Contents supplied STERILE, using an ethylene oxide (EO) process. Nonpyrogenic.
- To reduce risk of vessel damage, adhere to the following recommendations:
  - Take care to appropriately size Retriever to vessel diameter at intended site of deployment.
  - Do not perform more than six (6) retrieval attempts in same vessel using Retriever devices.
  - Maintain Retriever position in vessel when removing or exchanging Microcatheter.
- To reduce risk of kinking/fracture, adhere to the following recommendations:
  - Immediately after unsheathing Retriever, position Microcatheter tip marker just proximal to shaped section. Maintain Microcatheter tip marker just proximal to shaped section of Retriever during manipulation and withdrawal.
  - Do not rotate or torque Retriever.
  - Use caution when passing Retriever through stented arteries.
- Do not resterilize and reuse. Structural integrity and/or function may be impaired by reuse or cleaning.
- The Retriever is a delicate instrument and should be handled carefully. Before use and when possible during procedure, inspect device carefully for damage. Do not use a device that shows signs of damage. Damage may prevent device from functioning and may cause complications.
- Do not advance or withdraw Retriever against resistance or significant vasospasm. Moving or torquing device against resistance or significant vasospasm may result in damage to vessel or device. Assess cause of resistance using fluoroscopy and if needed resheath the device to withdraw.
- If Retriever is difficult to withdraw from the vessel, do not torque Retriever. Advance Microcatheter distally, gently pull Retriever back into Microcatheter, and remove Retriever and Microcatheter as a unit. If undue resistance is met when withdrawing the Retriever into the Microcatheter, consider extending the Retriever using the Abbott Vascular DOC guidewire extension (REF 22260) so that the Microcatheter can be exchanged for a larger diameter catheter such as a DAC® catheter. Gently withdraw the Retriever into the larger diameter catheter.
- Administer anti-coagulation and anti-platelet medications per standard institutional guidelines.

PRECAUTIONS

- Prescription only – device restricted to use by or on order of a physician.
- Store in cool, dry, dark place.
- Do not use open or damaged packages.
- Use by "Use By" date.
- Exposure to temperatures above 54°C (130°F) may damage device and accessories. Do not autoclave.
- Do not expose Retriever to solvents.
- Use Retriever in conjunction with fluoroscopic visualization and proper anti-coagulation agents.
- To prevent thrombus formation and contrast media crystal formation, maintain a constant infusion of appropriate flush solution between guide catheter and Microcatheter and between Microcatheter and Retriever or guidewire.
- Do not attach a torque device to the shaped proximal end of DOC® Compatible Retriever. Damage may occur, preventing ability to attach DOC® Guide Wire Extension.

Concentric Medical
301 East Evelyn Avenue
Mountain View, CA 94041

Stryker Neurovascular
47900 Bayside Parkway
Fremont, CA 94538

strykerneurovascular.com

Date of Release: SEP/2016

EX_EN_US

NV00018973.AB

Target® Detachable Coil

See package insert for complete indications, contraindications, warnings and instructions for use.

INTENDED USE / INDICATIONS FOR USE

Target Detachable Coils are intended to endovascularly obstruct or occlude blood flow in vascular abnormalities of the neurovascular and peripheral vessels.

Target Detachable Coils are indicated for endovascular embolization of:

- Intracranial aneurysms
- Other neurovascular abnormalities such as arteriovenous malformations and arteriovenous fistulae
- Arterial and venous embolizations in the peripheral vasculature

CONTRAINDICATIONS

None known.

POTENTIAL ADVERSE EVENTS

Potential complications include, but are not limited to: allergic reaction, aneurysm perforation and rupture, arrhythmia, death, edema, embolus, headache, hemorrhage, infection, ischemia, neurological/intracranial sequelae, post-embolization syndrome (fever, increased white blood cell count, discomfort), TIA/stroke, vasospasm, vessel occlusion or closure, vessel perforation, dissection, trauma or damage, vessel rupture, vessel thrombosis. Other procedural complications including but not limited to: anesthetic and contrast media risks, hypotension, hypertension, access site complications.

WARNINGS

- Contents supplied STERILE using an ethylene oxide (EO) process. Do not use if sterile barrier is damaged. If damage is found, call your Stryker Neurovascular representative.
- For single use only. Do not reuse, reprocess or resterilize. Reuse, reprocessing or resterilization may compromise the structural integrity of the device and/or lead to device failure which, in turn, may result in patient injury, illness or death. Reuse, reprocessing or resterilization may also create a risk of contamination of the device and/or cause patient infection or cross-infection, including, but not limited to, the transmission of infectious disease(s) from one patient to another. Contamination of the device may lead to injury, illness or death of the patient.
- After use, dispose of product and packaging in accordance with hospital, administrative and/or local government policy.
- **This device should only be used by physicians who have received appropriate training in interventional neuroradiology or interventional radiology and preclinical training on the use of this device as established by Stryker Neurovascular.**
- Patients with hypersensitivity to 316LVM stainless steel may suffer an allergic reaction to this implant.
- MR temperature testing was not conducted in peripheral vasculature, arteriovenous malformations or fistulae models.
- The safety and performance characteristics of the Target Detachable Coil System (Target Detachable Coils, InZone Detachment Systems, delivery systems and accessories) have not been demonstrated with other manufacturer's devices (whether coils, coil delivery devices, coil detachment systems, catheters, guidewires, and/or other accessories). Due to the potential incompatibility of non Stryker Neurovascular devices with the Target Detachable Coil System, the use of other manufacturer's device(s) with the Target Detachable Coil System is not recommended.
- To reduce risk of coil migration, the diameter of the first and second coil should never be less than the width of the ostium.
- In order to achieve optimal performance of the Target Detachable Coil System and to reduce the risk of thromboembolic complications, it is critical that a continuous infusion of appropriate flush solution be maintained between a) the femoral sheath and guiding catheter, b) the 2-tip microcatheter and guiding catheters, and c) the 2-tip microcatheter and Stryker Neurovascular guidewire and delivery wire. Continuous flush also reduces the potential for thrombus formation on, and crystallization of infusate around, the detachment zone of the Target Detachable Coil.
- Do not use the product after the "Use By" date specified on the package.
- Reuse of the flush port/dispenser coil or use with any coil other than the original coil may result in contamination of, or damage to, the coil.
- Utilization of damaged coils may affect coil delivery to, and stability inside, the vessel or aneurysm, possibly resulting in coil migration and/or stretching.
- The fluoro-saver marker is designed for use with a Rotating Hemostatic Valve (RHV). If used without an RHV, the distal end of the coil may be beyond the alignment marker when the fluoro-saver marker reaches the microcatheter hub.
- If the fluoro-saver marker is not visible, do not advance the coil without fluoroscopy.
- Do not rotate delivery wire during or after delivery of the coil. Rotating the Target Detachable Coil delivery wire may result in a stretched coil or premature detachment of the coil from the delivery wire, which could result in coil migration.
- Verify there is no coil loop protrusion into the parent vessel after coil placement and prior to coil detachment. Coil loop protrusion after coil placement may result in thromboembolic events if the coil is detached.
- Verify there is no movement of the coil after coil placement and prior to coil detachment. Movement of the coil after coil placement may indicate that the coil could migrate once it is detached.
- Failure to properly close the RHV compression fitting over the delivery wire before attaching the InZone® Detachment System could result in coil movement, aneurysm rupture or vessel perforation.
- Verify repeatedly that the distal shaft of the catheter is not under stress before detaching the Target Detachable Coil. Axial compression or tension forces could be stored in the 2-tip microcatheter causing the tip to move during coil delivery. Microcatheter tip movement could cause the aneurysm or vessel to rupture.
- Advancing the delivery wire beyond the microcatheter tip once the coil has been detached involves risk of aneurysm or vessel perforation.
- The long term effect of this product on extravascular tissues has not been established so care should be taken to retain this device in the intravascular space.

Damaged delivery wires may cause detachment failures, vessel injury or unpredictable distal tip response during coil deployment. If a delivery wire is damaged at any point during the procedure, do not attempt to straighten or otherwise repair it. Do not proceed with deployment or detachment. Remove the entire coil and replace with undamaged product.

- After use, dispose of product and packaging in accordance with hospital, administrative and/or local government policy.

CAUTIONS / PRECAUTIONS

- Federal Law (USA) restricts this device to sale by or on the order of a physician.
- Besides the number of InZone Detachment System units needed to complete the case, there must be an extra InZone Detachment System unit as back up.
- Removing the delivery wire without grasping the introducer sheath and delivery wire together may result in the detachable coil sliding out of the introducer sheath.
- Failure to remove the introducer sheath after inserting the delivery wire into the RHV of the microcatheter will interrupt normal infusion of flush solution and allow back flow of blood into the microcatheter.
- Some low level overhead light near or adjacent to the patient is required to visualize the fluoro-saver marker; monitor light alone will not allow sufficient visualization of the fluoro-saver marker.
- Advance and retract the Target Detachable Coil carefully and smoothly without excessive force. If unusual friction is noticed, slowly withdraw the Target Detachable Coil and examine for damage. If damage is present, remove and use a new Target Detachable Coil. If friction or resistance is still noted, carefully remove the Target Detachable Coil and microcatheter and examine the microcatheter for damage.
- If it is necessary to reposition the Target Detachable Coil, verify under fluoroscopy that the coil moves with a one-to-one motion. If the coil does not move with a one-to-one motion or movement is difficult, the coil may have stretched and could possibly migrate or break. Gently remove both the coil and microcatheter and replace with new devices.
- Increased detachment times may occur when:
  - Other embolic agents are present.
  - Delivery wire and microcatheter markers are not properly aligned.
  - Thrombus is present on the coil detachment zone.
- Do not use detachment systems other than the InZone Detachment System.
- Increased detachment times may occur when delivery wire and microcatheter markers are not properly aligned.
- Do not use detachment systems other than the InZone Detachment System.

Stryker Neurovascular
47900 Bayside Parkway
Fremont, CA 94538

strykerneurovascular.com

Date of Release: MAR/2016

EX_EN_US

NV00018669.AB

AJNR

AMERICAN JOURNAL OF NEURORADIOLOGY

FEBRUARY 2017
VOLUME 38
NUMBER 2
WWW.AJNR.ORG

THE JOURNAL OF DIAGNOSTIC AND INTERVENTIONAL NEURORADIOLOGY

Consensus recommendation vessel wall MRI
Synthetic MRI in multiple sclerosis
Quantifying intracranial plaque permeability

Official Journal ASNR • ASFNR • ASHNR • ASPNR • ASSR

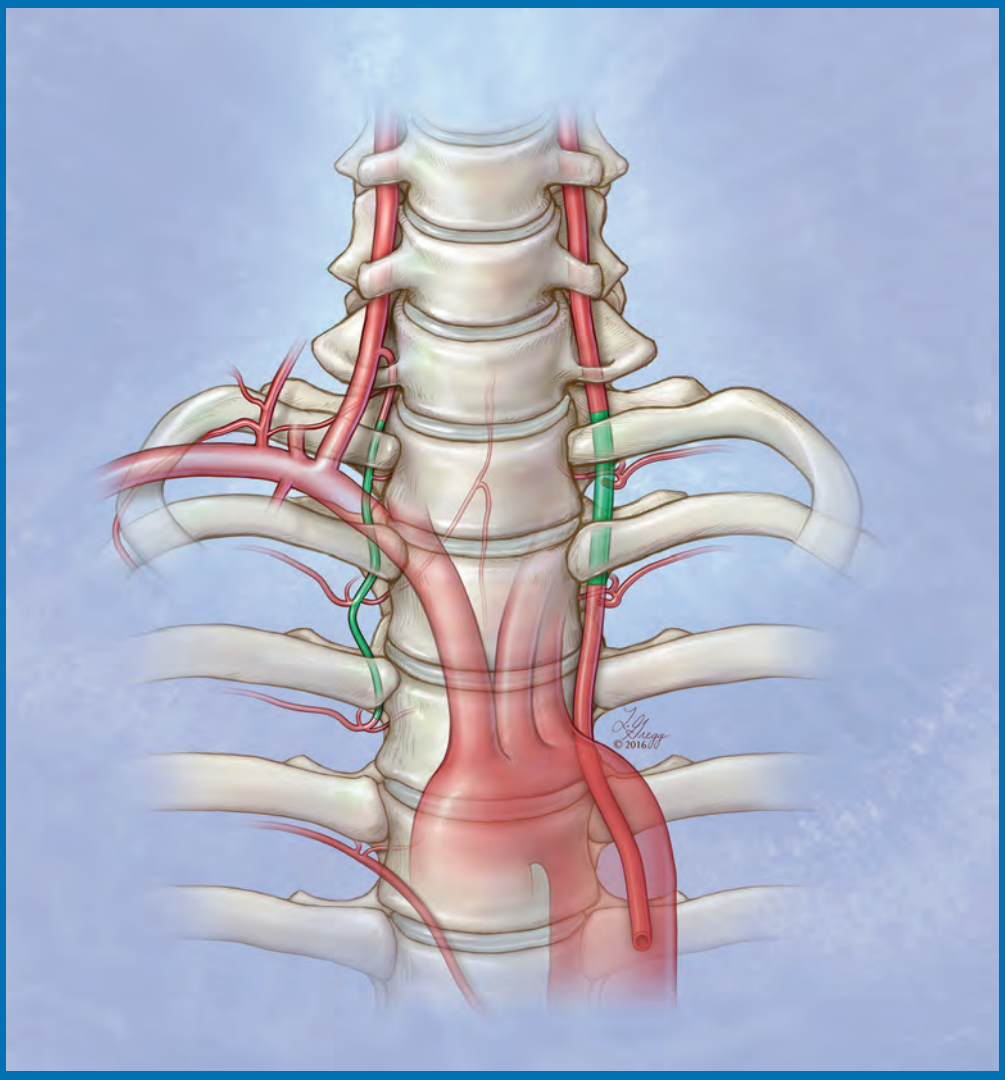

AJNR

AMERICAN JOURNAL OF NEURORADIOLOGY

Publication Preview at www.ajnr.org features articles released in advance of print. Visit www.ajnrblog.org to comment on AJNR content and chat with colleagues and AJNR's News Digest at http://ajnrdigest.org to read the stories behind the latest research in neuroimaging.

FEBRUARY 2017 • VOLUME 38 • NUMBER 2 • WWW.AJNR.ORG

Title: Lynx Rufus. Although not as rare as the Florida panther, Florida bobcats are still both elusive and beautiful. This one was eyeing a migrating merganser when I walked out the back door of my office in Bradenton, Florida! I barely had time to click a shutter before it was gone . . . vanished into the undergrowth. Lucky shot! Dedicated to Alisa Gean, MD, Catwoman.

John H. Rees, Chief, Neuroradiology, Partners Imaging Center, Bradenton, Florida

Intracranial Vessel Wall MRI: Principles and Expert Consensus Recommendations of the American Society of Neuroradiology

D.M. Mandell, M. Mossa-Basha, Y. Qiao, C.P. Hess, F. Hui, C. Matouk, M.H. Johnson, M.J.A.P. Daemen, A. Vossough, M. Edjlali, D. Saloner, S.A. Ansari, B.A. Wasserman, and D.J. Mikulis, on behalf of the Vessel Wall Imaging Study Group of the American Society of Neuroradiology

ABSTRACT

SUMMARY: Intracranial vessel wall MR imaging is an adjunct to conventional angiographic imaging with CTA, MRA, or DSA. The technique has multiple potential uses in the context of ischemic stroke and intracranial hemorrhage. There remain gaps in our understanding of intracranial vessel wall MR imaging findings and research is ongoing, but the technique is already used on a clinical basis at many centers. This article, on behalf of the Vessel Wall Imaging Study Group of the American Society of Neuroradiology, provides expert consensus recommendations for current clinical practice.

ABBREVIATIONS: RCVS = reversible cerebral vasoconstriction syndrome; VW-MR imaging = vessel wall MR imaging

Conventional techniques for imaging the intracranial arteries are CTA, MRA, and DSA. These techniques reveal abnormalities of the vessel lumen, but they can fail to fully characterize disease that resides within the vessel wall. There has been growing interest in direct visualization of the vessel wall with high-resolution intracranial vessel wall MR imaging (VW-MR imaging). This technique is now used on a clinical basis at many centers.

In 2012, the American Society of Neuroradiology formed a multidisciplinary study group to support the development and clinical implementation of VW-MR imaging. This article, on behalf of the study group, reviews the principles of intracranial VW-MR imaging and provides consensus recommendations for clinical practice. We make these recommendations with the recognition that there remain considerable gaps in knowledge and that research is ongoing.

From the Division of Neuroradiology (D.M.M., D.J.M.), Department of Medical Imaging, University Health Network and the University of Toronto, Toronto, Ontario, Canada; Department of Radiology (M.M.-B.), University of Washington, Seattle, Washington; The Russell H. Morgan Department of Radiology and Radiological Sciences (Y.Q., F.H., B.A.W.), Johns Hopkins Hospital, Baltimore, Maryland; Department of Radiology and Biomedical Imaging (C.P.H., D.S.), University of California, San Francisco, San Francisco, California; Departments of Neurosurgery (C.M., M.H.J.), Radiology and Biomedical Imaging (C.M., M.H.J.), and Surgery (M.H.J.), Yale University School of Medicine, New Haven, Connecticut; Department of Pathology (M.J.A.P.D.), Academic Medical Center, Amsterdam, the Netherlands; Departments of Surgery (A.V.) and Radiology (A.V.), Children's Hospital of Philadelphia and Perelman School of Medicine at the University of Pennsylvania, Philadelphia, Pennsylvania; Department of Radiology (M.E.), Université Paris Descartes Sorbonne Paris Cité, Institut National de la Santé et de la Recherche Médicale S894, Centre Hospitalier Sainte-Anne, Paris, France; and Departments of Radiology (S.A.A.), Neurology (S.A.A.), and Neurological Surgery (S.A.A.), Northwestern University, Feinberg School of Medicine, Chicago, Illinois.

Please address correspondence to Daniel Mandell, MD, Toronto Western Hospital, 399 Bathurst St, 3MCL-426, Toronto, ON, Canada, M5T 2S8; e-mail: danny.mandell@uhn.ca

Indicates open access to non-subscribers at www.ajnr.org

http://dx.doi.org/10.3174/ajnr.A4893

TECHNICAL IMPLEMENTATION

The American Society of Neuroradiology Vessel Wall Imaging Study Group is working with MR imaging vendors to promote the development and dissemination of commercial pulse sequences that are optimized for intracranial VW-MR imaging. Until such sequences are widely available, it is possible to adjust the scan parameters of existing sequences and obtain vessel wall images of sufficient quality for clinical use. Selection of sequences and scan parameters for VW-MR imaging is highly dependent on the particular scanner hardware and software available at a center. The technical sections that follow provide general recommendations on the development of an intracranial VW-MR imaging protocol, and we are also launching a dynamic document (via the American Society of Neuroradiology Web site) through which experienced centers can describe their MR imaging systems and the specific pulse sequences and scan parameters that they have found useful.

The principal technical requirements for intracranial VW-MR imaging are the following: 1) high spatial resolution, 2) multiplanar 2D acquisitions or 3D acquisitions, 3) multiple tissue weightings, and 4) suppression of signal in luminal blood and CSF.

Spatial Resolution

The normal middle cerebral artery and basilar artery wall thickness is 0.2–0.3 mm, which is approximately one-tenth of the luminal diameter[1] and smaller than the VW-MR imaging voxel dimensions currently achievable. However, it is possible to image the intracranial arterial wall because the wall generates detectable MR imaging signal and one can suppress the MR imaging signal

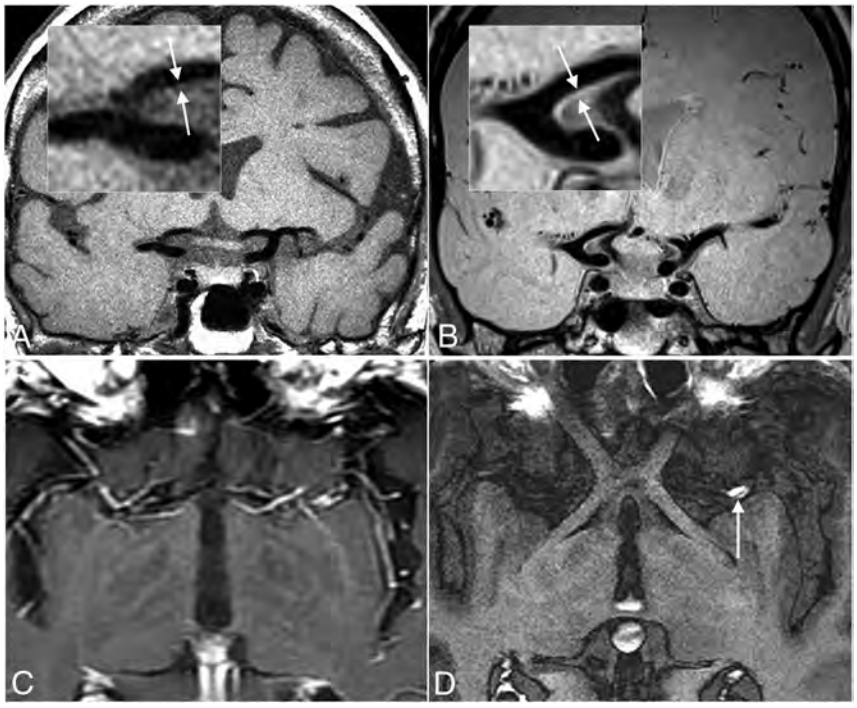

FIG 1. Technical implementation of VW-MR imaging. Comparison of a coronal 2D T1-weighted FLAIR VW-MR imaging sequence (*A*) and a 3D proton-density–weighted variable flip angle refocusing pulse, fast spin-echo VW-MR imaging sequence (*B*) in a healthy subject. Insets show magnified images of the carotid terminations with *arrows* pointing to the arterial wall. Comparison of a standard contrast-enhanced T1-weighted spin-echo sequence (*C*) and an optimized contrast-enhanced T1-weighted VW-MR imaging sequence (*D*) shows how blood suppression is needed to reveal an enhancing atherosclerotic plaque (*arrow*) in the left MCA M1 segment.

arising from neighboring blood and CSF within the voxel. In addition, vessel wall disease often results in wall thickening, which increases its conspicuity.

The higher signal-to-noise ratio at 3T than at 1.5T is advantageous for intracranial VW-MR imaging and, in many cases, necessary. At 3T with a 2D sequence, a voxel size of 2.0 × 0.4 × 0.4 mm provides a reasonable balance between spatial resolution and signal-to-noise ratio, with a scan duration of approximately 5–7 minutes for a 2- to 4-cm-thick section of tissue (Fig 1*A*). At 3T with a 3D sequence, a voxel size of 0.5 mm isotropic is a reasonable starting point (Fig 1*B*), and it is possible to cover the circle of Willis and second-/third-order branches in 7–10 minutes. Most experienced centers are using isotropic voxel dimensions in the 0.4- to 0.7-mm range for 3D acquisitions. Ongoing advances in MR imaging technology, including higher magnetic field strength,[2] may enable further increases in spatial resolution and image quality.[3]

Multiplanar 2D or 3D Acquisitions

Accurate interpretation of VW-MR imaging requires visualization of the vessel wall in both short- and long-axis planes. One option is to use 2D sequences multiple times in orthogonal planes, focusing on the particular vessels of interest. A limitation of this approach is that most intracranial arteries are curved rather than straight and vessel obliquity and curvature can result in partial volume averaging effects,[4] which confound the appearance of the arterial wall. Another option is to use a 3D (volumetric) sequence and then reformat the isotropic data for viewing in multiple 2D planes. The 3D approach reduces total scan time and provides more flexibility because any imaged vessel can be viewed in any reformatted plane. However, some groups have found that current 2D sequences provide better image quality when imaging is targeted to a particular vessel of interest. An optimal VW-MR imaging protocol may include both 2D and 3D sequences.

Multiple Tissue Weightings

Time-of-flight MRA is mainly used to characterize luminal abnormality and act as a localizer for subsequent vessel wall sequences. Low-velocity flow can cause intravascular signal loss on time-of-flight MRA, so in patients who have pronounced luminal narrowing or dilation, it is helpful to add a gadolinium-bolus MRA to accurately define the contour of the lumen (ie, the boundary between the lumen and wall). Most examinations require a T1-weighted vessel wall sequence before and after intravenous gadolinium contrast. It is possible to use a proton-density–weighted sequence instead of a T1-weighted sequence because the former provides higher SNR. The disadvantages of proton-density weighting are that contrast enhancement may be less conspicuous and CSF signal intensity can approach vessel wall intensity. A T2-weighted VW-MR imaging sequence is often helpful. Fat suppression is necessary for VW-MR imaging of the external carotid artery branches in the scalp (eg, in patients with suspected temporal arteritis) but is generally not needed for intracranial VW-MR imaging.

Suppression of MR Imaging Signal in Blood and CSF

MR imaging characterization of the vessel wall requires suppression of MR imaging signal arising from luminal blood and CSF (or brain parenchyma for a vessel residing adjacent to the brain) (Fig 1*C*, -*D*). Blood-suppression techniques usually exploit the condition of blood flowing and the vessel wall being stationary. Other techniques for blood suppression rely on the particular longitudinal relaxation time (T1) of blood, but these techniques usually have some dependence on flow as well. The most common methods of blood-signal suppression are the following:

Spin-Echo. Luminal spins that experience the section-selective 90° radiofrequency pulse but flow out of the imaging section before the section-selective 180° pulse do not yield signal, resulting in blood-signal suppression.[5]

Spatial Presaturation (Saturation Band). A spatially selective pulse tips a thick slab of spins on either side of the imaging section into the transverse plane, and then a spoiling gradient dephases this transverse magnetization.[5] The dephased spins flow into the imaging section, where they are exposed to an excitation pulse, but they

are not able to regain phase in the transverse plane until they have undergone longitudinal relaxation, so they do not yield signal.

Double Inversion Recovery Preparation. This technique exploits both the flow and T1 properties of blood to suppress its signal.[6] A 180° non-section-selective pulse inverts all spins. A section-selective 180° pulse, applied immediately after the first pulse, flips the imaging-section magnetization so it is realigned with the main magnetic field. There is then a time delay (TI), which allows inflowing inverted spins to relax to their null point; and at the expected null point for blood, another pulse is applied to generate an echo for readout. Only the stationary spins in the imaging section return signal. A disadvantage of the technique is that the time needed for spins to reach the null point lengthens the scan time, making it challenging to cover vessels of interest with sufficient spatial resolution for intracranial VW-MR imaging.

3D Sequences

The most commonly used 3D sequences for intracranial VW-MR imaging are the variable flip angle refocusing pulse, fast spin-echo sequences[7] with brand names such as VISTA (volume isotropic turbo spin-echo acquisition; Philips Healthcare, Best, the Netherlands), SPACE (sampling perfection with application-optimized contrasts by using different flip angle evolutions; Siemens, Erlangen, Germany), and Cube (GE Healthcare, Milwaukee, Wisconsin). These sequences have very long echo trains, a potential source of imaging blurring from decay of transverse magnetization between the start and end of the readout. These sequences minimize this blurring by varying the flip angle over the length of the echo train to maintain relatively stable signal.

Blood suppression techniques used with 2D sequences are generally less effective with 3D sequences. For example, spatial presaturation requires that spins in the imaging volume are replaced with inflowing suppressed spins, but this is unlikely to occur for the entirety of a large 3D imaging slab. However, other mechanisms can generate adequate blood suppression with 3D sequences. An important mechanism is intravoxel dephasing: Luminal blood contains spins traveling at varying velocities (eg, due to laminar flow). Between the time of excitation and readout, these spins move through the magnetic field gradients at different rates, resulting in intravoxel phase dispersion with signal loss.[8] One may further exploit the intravoxel dephasing effect by adding so-called diffusion-sensitizing gradient preparation to the 3D sequences.[9,10] This approach is similar to diffusion-weighted imaging, but the b-values are orders of magnitude lower, so the sequence suppresses bulk flow rather than molecular diffusion. Several centers have reported the details of how they optimized commercially available 3D sequences for intracranial VW-MR imaging.[11,12]

Peripheral Pulse Gating

Most centers are currently performing intracranial VW-MR imaging without peripheral pulse gating. Pulse gating is potentially useful for VW-MR imaging of dilated intracranial arteries or large aneurysms in which gating to the point of maximum flow in the vessel may reduce the artifacts associated with slow flow and improve blood suppression.

Monitored Versus Unmonitored

When using 2D sequences, some groups monitor the examination and select the sequences and scan planes that will optimally show the vessels of interest. When using 3D sequences, monitoring is less critical but still sometimes helpful to determine coverage and select sequences.

SITUATIONS IN WHICH INTRACRANIAL VW-MR IMAGING IS LIKELY A USEFUL ADJUNCT TO CONVENTIONAL IMAGING

To Differentiate between Intracranial Atherosclerotic Plaque, Vasculitis, Reversible Cerebral Vasoconstriction Syndrome, Arterial Dissection, and Other Causes of Intracranial Arterial Narrowing

Atherosclerotic Plaque. Atherosclerotic plaque is composed of lipids, thrombotic substances (platelets and fibrin), cellular material, and connective tissue matrix. Plaque progression is often associated with the development of a well-defined region of lipid accumulation ("lipid core") within the plaque, a fibromuscular layer ("fibrous cap") separating the lipid from the arterial lumen, and intraplaque hemorrhage.[13-15]

VW-MR imaging of intracranial atherosclerotic plaque typically demonstrates arterial wall thickening, which eccentrically (nonuniformly) involves the circumference of the arterial wall. The component of the plaque adjacent to the lumen is often hyperintense on T2-weighted images, and it may enhance (as discussed below), whereas the adjacent component is often hypointense on T2-weighted images and nonenhancing (Fig 2*F*).[16-22] There is sometimes a third thin layer in the periphery of the plaque that enhances. This layered appearance of intracranial atherosclerotic plaque correlates with the VW-MR imaging appearance of carotid atherosclerotic plaque, and carotid endarterectomy specimens have shown that the enhancing layer adjacent to the lumen represents fibrous cap, the nonenhancing layer adjacent to this represents lipid core, and the peripheral thin rim of enhancement is due to increased vasa vasorum in the adventitia of the artery.[23-25] Not every intracranial atherosclerotic plaque demonstrates all of these components on VW-MR imaging; for example, some plaques simply have the appearance of an eccentric homogeneously enhancing "lump" in the arterial wall. In addition, as we will discuss, not every intracranial plaque enhances.

The hypointensity-isointensity on T1- and T2-weighted images in the lipid core of atherosclerotic plaque differs from the MR imaging appearance of lipids in other tissues, such as subcutaneous fat, which is hyperintense on T1-weighted and T2-weighted fast spin-echo sequences. Two main factors likely account for this difference. First, even in relatively lipid-rich atherosclerotic plaque, the main contributor to MR signal is water protons and not lipid.[23] Second, the lipid in atherosclerotic plaque is mainly cholesterol and cholesteryl esters, which do not result in the same T1 shortening as extravascular lipid, which is composed mainly of triglycerides.[26]

Vasculitis. Visualization of the wall of the smaller intracranial vessels is beyond the spatial resolution and SNR limits of current VW-MR imaging. However, CNS vasculitis often involves larger intracranial arteries that are amenable to wall imaging.

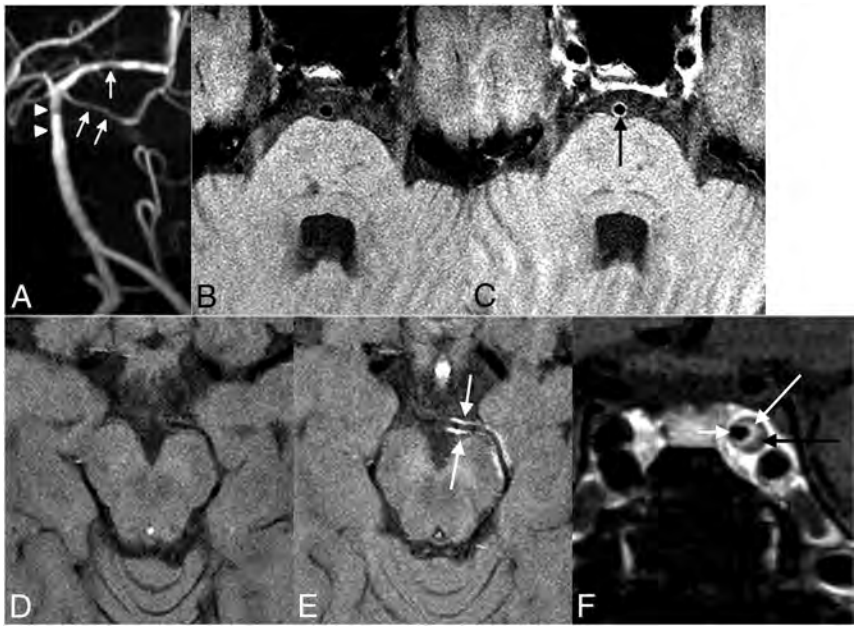

FIG 2. VW-MR imaging to differentiate among causes of intracranial arterial stenosis when angiography findings are inconclusive. This patient had multiple recent infarcts in the pons. MR angiogram (*A*) demonstrates short segments of mild narrowing of the distal basilar artery (*arrowheads*) and left superior cerebellar and posterior cerebral arteries (*arrows*). Axial T1-weighted VW-MR imaging before (*B*) and after (*C*) intravenous contrast injection shows smooth concentric enhancement of the basilar artery wall (*arrow*). VW-MR imaging before (*D*) and after (*E*) contrast injection shows similar enhancement of the left posterior cerebral artery wall (*arrow*). The vessel wall appearance is consistent with the final diagnosis, which was primary CNS vasculitis. For comparison, coronal contrast-enhanced T1-weighted VW-MR imaging (*F*) in a different patient shows characteristic features of an atherosclerotic plaque: eccentric arterial wall thickening with a contrast-enhancing fibrous cap (*long white arrow*) and peripheral non-enhancing plaque (*black arrow*). A *short white arrow* points to the arterial lumen.

VW-MR imaging often demonstrates smooth, homogeneous, concentric arterial wall thickening and enhancement in patients with CNS vasculitis (Fig 2*A*–*E*), in comparison with the typical nonconcentric (and often heterogeneous) wall abnormality of atherosclerotic plaque (Fig 2*F*).[19,27,28] However, subsequent experience has shown that vasculitis sometimes also results in eccentric wall abnormality.[29] The additional vessel wall features of atherosclerotic plaque on T1-, T2-, and enhanced sequences can be helpful for distinguishing between vasculitis and plaque.

Presumably, arterial wall enhancement in patients with CNS vasculitis is due to increased permeability of the endothelium with contrast leakage from the lumen into the arterial wall. Vasa vasorum–related contrast leakage is a potential alternative mechanism of wall enhancement, and dilated neovessels have been demonstrated within the extracranial arterial wall of patients with Takayasu arteritis.[30,31]

Reversible Cerebral Vasoconstriction Syndrome. Early discrimination between reversible cerebral vasoconstriction syndrome (RCVS) and its principal differential, vasculitis, is important: RCVS is treated with observation or calcium channel blockers, whereas vasculitis is treated with steroids and immunosuppressive drugs.

VW-MR imaging may enable prospective differentiation between vasculitis and vasoconstriction.[32] Both disorders result in arterial wall thickening, but the vessel wall in RCVS is typically nonenhancing (or mildly enhancing) compared with the typical intense wall enhancement in active vasculitis.[29,32,33] Arterial wall thickening with a lack of wall enhancement is consistent with the pathology of transient vasoconstriction. In vasospastic arteries, smooth-muscle cells shorten in length with increased overlap among cells, resulting in nearly a 500% increase in wall thickness for a 60% luminal narrowing.[32,34] Lack of arterial wall enhancement is concordant with the limited histopathologic data in RCVS, showing an absence of arterial wall inflammation.[32,35,36] We have seen some individual cases that appear to be RCVS with more than minimal wall enhancement, so we recommend caution in relying strongly on VW-MR imaging discrimination between RCVS and vasculitis until this approach is validated in a larger study. Some study group members have also observed a crenelated appearance of arterial wall thickening in RCVS.

Moyamoya Disease. Initial VW-MR imaging studies of small numbers of patients with Moyamoya disease found a lack of arterial wall thickening and enhancement[19,37]; and a study found a smaller outer diameter of the vessel wall, less eccentricity of wall thickening, and less wall enhancement in patients with Moyamoya disease compared with atherosclerotic plaque.[38] Atherosclerotic plaque may undergo negative remodeling with reduction of the outer diameter of the vessel, but this seems to differ from Moyamoya disease, in which the MCA trunk is not visible at all in some cases, the so-called "vanishing MCA."[39] These VW-MR imaging findings are consistent with histopathologic studies showing thinning of the arterial media and a paucity of inflammatory cells in the vessel wall of patients with Moyamoya disease.[40] However, a subsequent study[41] found a considerably higher frequency of concentric internal carotid and middle cerebral artery wall enhancement in patients diagnosed with Moyamoya disease and, perhaps surprisingly, no difference in vessel wall enhancement between early and late angiographic stages of the disease. Further research is needed to resolve the discordance among studies. It will remain important to accurately differentiate between Moyamoya disease and the multitude of other causes of narrowing at the carotid terminus.

Radiation-Induced Arteriopathy. There is limited experience with the VW-MR imaging appearance of radiation-induced intracranial arteriopathy. A study[37] of 5 patients with radiation-induced narrowing of the intracranial internal carotid arteries found circumferential arterial wall thickening and enhancement in all cases. Follow-up MR imaging 2 years later demonstrated persistence of the enhancement.

Arterial Dissection. Intracranial arterial dissection most often occurs as an extension of cervical vertebral artery dissection. How-

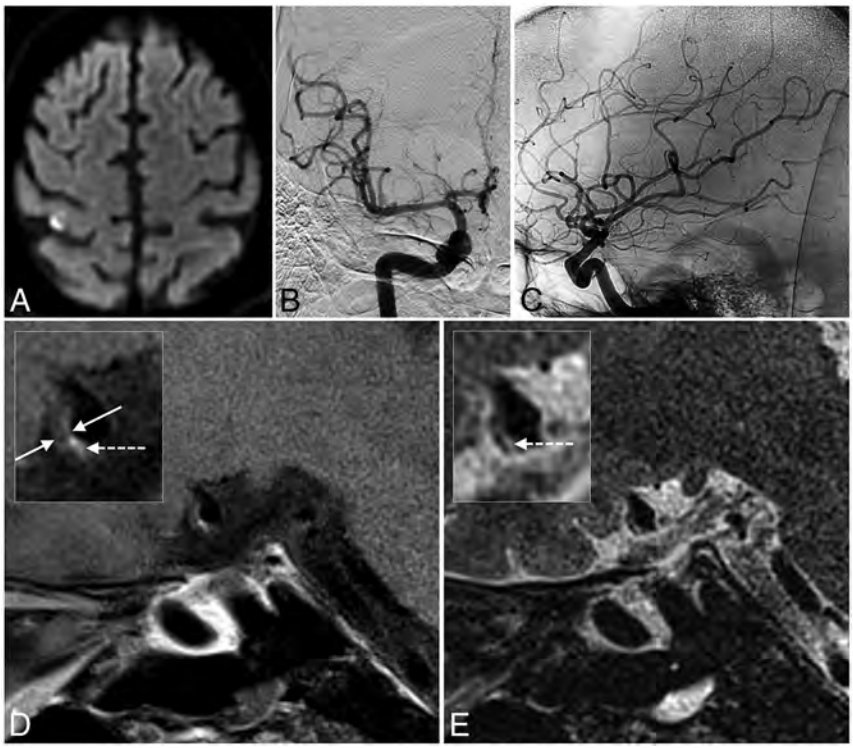

FIG 3. VW-MR imaging to identify symptomatic, nonstenotic intracranial atherosclerotic plaque. A 52-year-old man with a previous transient ischemic attack attributable to the right middle cerebral artery territory presented with an acute infarct (*A*) in the same vascular territory. Cardiac work-up, CT angiography of the head and neck and DSA (*B* and *C*) and cervical carotid VW-MR imaging failed to identify a cause of the stroke. Sagittal-oblique contrast-enhanced T1-weighted VW-MR imaging of the supraclinoid segment of the right ICA (*D*) shows eccentric arterial wall thickening (*arrows*) with enhancement (*dotted arrow*) in the more luminal aspect of the thickening, consistent with the fibrous cap of a recently symptomatic plaque. Sagittal-oblique T2-weighted VW-MR imaging (*E*) shows T2 prolongation (*arrow*) in the more luminal aspect of the thickening and T2 shortening peripherally, consistent with the fibrous cap and lipid core of atherosclerotic plaque, respectively. The arterial wall thickening without luminal narrowing is so-called positive remodeling of the vessel wall.

ever, it can also occur as an extension of cervical internal carotid artery dissection or as an isolated intracranial abnormality.

VW-MR imaging features of intracranial arterial dissection include a curvilinear hyperintensity on T2-weighted images (intimal flap) separating the true lumen from the false lumen and eccentric arterial wall thickening with the signal characteristics of blood (intramural hematoma) (Fig 3).[42] A VW-MR imaging study[43] of 67 patients with intracranial arterial dissection suspected on CTA, MRA, or DSA found an intimal flap on luminal imaging in 16% of patients and on VW-MR imaging in 42%. VW-MR imaging demonstrated intramural hematoma in 61% of patients, with 83% of the visible hematomas evident on T1-weighted images and 59% evident on T2-weighted images. The vessel wall abnormality had a layered appearance on contrast-enhanced T1-weighted images, with enhancement along the luminal and peripheral margins of the artery wall in 51% of patients.

Intramural hematoma is often diagnosed on the basis of hyperintensity on T1-weighted images, but similar to other kinds of intracranial hemorrhage, the signal characteristics of intramural blood evolve with time.[44,45] Among 7 patients with intracranial vertebral-basilar dissection, no patient had vessel wall hyperintensity on T1-weighted VW-MR imaging within a week of symptom onset, but 5 patients had hyperintensity in a subsequent week.[46] T2*-weighted or susceptibility-weighted MR imaging is also sometimes useful for the diagnosis of dissection. The deoxygenation of blood that makes it conspicuous on these sequences occurs earlier than the conversion from deoxyhemoglobin to methemoglobin required for intramural hematoma to become hyperintense on a T1-weighted sequence.[47]

The evolution of blood products is also complicated by the dynamic nature of dissection itself, which can be stable, progressive, or resolving. Intracranial arterial dissection with VW-MR imaging evidence of intramural hematoma is more likely to progress than dissection without hematoma.[48]

To Identify Symptomatic, Nonstenotic Disease of the Intracranial Arteries

In 15 patients with an acute lacunar infarct, normal angiography findings, and no other apparent cause of stroke, VW-MR imaging demonstrated enhancing atherosclerotic plaque in the supplying (middle cerebral or basilar) artery in 9 (60%) patients.[49] Similar studies have shown VW-MR imaging evidence of atherosclerotic plaque in the supplying artery of 52% of patients with MCA territory lacunar infarcts and 42% of patients with pontine infarcts, but normal MRA findings.[50,51] A VW-MR imaging study[52] that assessed the prevalence of MCA plaque both ipsilateral and contralateral to lenticulostriate territory infarcts in patients who had normal MRA findings found a similar prevalence (46% and 45%, respectively) bilaterally. This latter study did not report whether there was a difference in contrast enhancement between the plaques ipsilateral versus contralateral to the infarction. Figure 3 demonstrates VW-MR imaging identification of a culprit plaque when angiographic findings are normal. Study group members have also found that VW-MR imaging can help diagnose cases of CNS vasculitis and arterial dissection with minimal arterial luminal abnormality. Figure 4 demonstrates VW-MR imaging diagnosis of symptomatic intracranial arterial dissection in the context of a CTA considered equivocal for luminal narrowing.

SITUATIONS IN WHICH INTRACRANIAL VW-MR IMAGING IS POSSIBLY A USEFUL ADJUNCT TO CONVENTIONAL IMAGING

To Determine the Location of Atherosclerotic Plaque Relative to Branch Artery Ostia, to Diagnose Stroke Etiology, and to Assess Risk of Angioplasty

In the coronary circulation, atherosclerotic plaque most often develops in the arterial wall opposite a branch artery ostium.[53] Similarly, intracranial VW-MR imaging has shown that MCA plaque

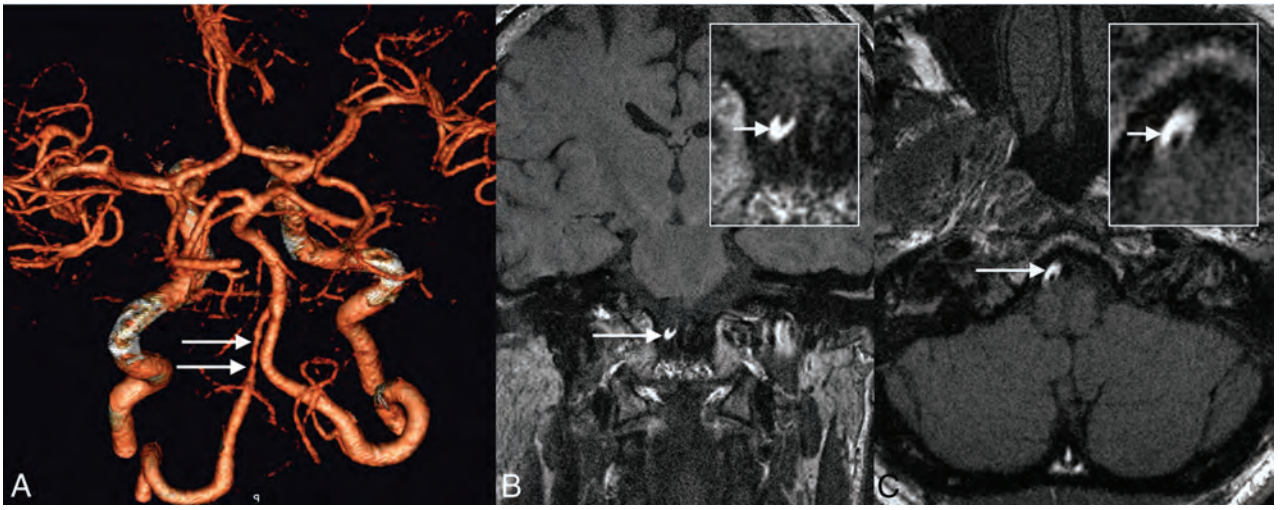

FIG 4. VW-MR imaging to diagnose intracranial arterial dissection with minimal luminal narrowing. A 57-year-old man presented to the emergency department with severe headache and neck pain for 1 week. 3D rendering of a CTA shows smooth narrowing of the intradural segment of the right vertebral artery (*A*, *arrows*). This angiographic appearance was considered most likely within the range of normal because the vertebral artery is commonly narrower beyond the posterior inferior cerebellar artery origin, but a bit equivocal. Coronal (*B*) and axial (*C*) nonenhanced T1-weighted VW-MR imaging shows eccentric intense hyperintensity (*B* and *C*, *arrows*) in the wall of the right vertebral artery, consistent with recent arterial dissection.

is more common in the ventral (45%) or inferior (32%) parts of the wall than in the superior (14%) or dorsal (9%) parts where branches arise,[54,55] and basilar artery plaque is more common in the ventral part of the wall, which is opposite the origins of the branches.[56] However, some atherosclerotic plaque does arise close to ostia, and VW-MR imaging has confirmed that indeed MCA plaque with associated infarction has more superior wall involvement than plaque without infarction (24% versus 7%).[54]

Angioplasty can generate a "snow plow" effect, in which atheromatous material is pushed from the treated artery into a branch. In the coronary circulation, location of atherosclerotic plaque close to a branch ostium increases the risk of branch occlusion following angioplasty and stent placement.[57] By determining the location of intracranial atherosclerotic plaque relative to branch ostia in individual patients, VW-MR imaging may be useful when estimating the risk of intracranial angioplasty.[58]

To Assess Atherosclerotic Plaque Activity

Higher risk intracranial atherosclerotic plaque shares pathologic features with higher risk carotid plaque.[59] Several imaging features may indicate higher-risk plaque.

Plaque Thickness and Surface Irregularity. Most VW-MR imaging studies[20,21] suggest that symptomatic intracranial plaque is thicker than asymptomatic plaque, though some[60] have found no significant relationship. A study of 14 patients with symptomatic MCA stenosis and 16 patients with asymptomatic stenosis found plaque surface irregularity (discontinuity of the plaque luminal surface margin) in 71% of symptomatic patients but in only 19% of asymptomatic patients ($P = .008$).[61]

Vessel Wall Remodeling. Atherosclerotic plaque often results in outward bulging of the outer surface of the artery.[62] This has been called compensatory enlargement ("adaptive remodeling" or "positive remodeling") because it can lessen the luminal narrowing caused by the plaque. In the coronary arteries, positive remodeling is more common in plaques that contain hemorrhage and inflammation[63]; this feature suggests that positive remodeling is an indicator of higher risk vessel wall pathology. Other plaques are associated with reduction of the outer diameter of the artery ("negative remodeling"),[64] and this may reflect a fibrotic healing response. Most VW-MR imaging studies[20,61] have found that MCA remodeling was (on average) outward in symptomatic plaques and inward in asymptomatic plaques, though some studies[16] have found no significant difference. Microembolic signals on transcranial Doppler sonography were more common in patients with MCA atherosclerotic plaque with VW-MR imaging evidence of positive remodeling,[65] consistent with the idea that positive remodeling is characteristic of the higher risk plaque that produces thromboembolism.

Intraplaque Hemorrhage. A postmortem study of MCA atherosclerosis found intraplaque hemorrhage in 30% of plaques associated with an infarct compared with 15% of plaques not associated with an infarct ($P = .07$).[66] A VW-MR imaging study of 107 adults with >70% MCA stenosis found that T1 shortening (thought to indicate intraplaque hemorrhage) was more common in symptomatic than in asymptomatic plaque (20% versus 2%, $P = .01$).[66] Another study reported a higher prevalence of intraplaque T1 shortening in symptomatic-versus-asymptomatic MCA plaques (27% versus 0%, $P = .002$).[60] In a research context, a signal intensity of >150% of the signal intensity of adjacent gray matter[60] or scalp muscle[66] on a T1-weighted sequence has been used as a criterion for defining intraplaque hemorrhage. Several study group members have observed a much lower prevalence of intracranial intraplaque hemorrhage than the values reported in the literature, possibly due to different patient populations or timing of the scans relative to symptom onset.

Plaque Enhancement. Contrast enhancement of carotid bulb atherosclerotic plaque occurs preferentially in the fibrous cap and

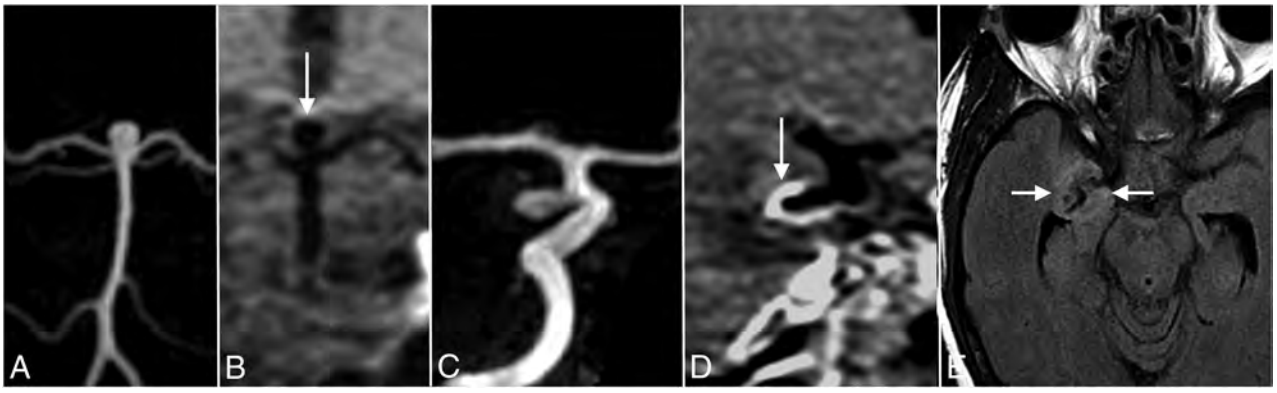

FIG 5. VW-MR imaging to evaluate vascular disease activity. MR angiogram demonstrates a saccular aneurysm at the tip of the basilar artery (*A*) and a saccular aneurysm at the right posterior communicating artery origin (*C*). Coronal contrast-enhanced T1-weighted VW-MR imaging shows no enhancement of the basilar artery aneurysm wall (*B, arrow*) but intense enhancement of the posterior communicating artery aneurysm wall (*D, arrow*). Axial T2-weighted FLAIR image (*E, arrow*) demonstrates a hematoma centered around the enhancing aneurysm, consistent with the preliminary research studies, suggesting that symptomatic and ruptured aneurysms have wall enhancement much more commonly than asymptomatic saccular aneurysms.

adventitia (though sometimes in the middle of the plaque) and is a marker of inflammation and neovascularization.[25,67-69] A postmortem study[59] found that neovascularity in MCA atherosclerotic plaque was associated with ipsilateral infarction. VW-MR imaging studies[19,70,71] have shown that intracranial plaque enhancement is associated with recent infarction in the territory of the plaque.

A study of the temporal characteristics of intracranial plaque enhancement found strong enhancement within 1 month of ischemic stroke and reduced enhancement several months later.[72] Another study[73] found no difference in enhancement when comparing patients with acute stroke versus those with stroke any time in the preceding 3 months, which is not inconsistent with the former study, which found that enhancement did not lessen until a few months after the acute event.

In some intracranial plaques, one can identify the enhancing fibrous cap and enhancing adventitia as distinct layers on either side of an intervening nonenhancing layer, but (possibly due to the limited spatial resolution of VW-MR imaging relative to the size of intracranial plaques) plaques often appear to enhance diffusely or not at all.

To Assess Vasculitis Activity

A small number of published cases[29] and the broader experience of the study group suggest that there may be a discordance between intracranial VW-MR imaging findings and the clinical impression of vasculitis disease activity. This is consistent with extracranial VW-MR imaging observations. An extracranial VW-MR imaging study of 24 patients with Takayasu arteritis found arterial wall edema (hyperintensity on T2-weighted images) in 94% of VW-MR imaging examinations performed in patients with clinically active disease and in 56% of examinations performed in those without clinically active disease.[74] There was also greater wall enhancement in those with clinically active disease. The high prevalence of wall edema in patients without clinically active disease may not be misleading though: In a different study, biopsy specimens revealed histopathologic evidence of active vasculitis in 44% of patients with Takayasu arteritis who had no clinical evidence of active disease.[75] Similarly, a study found new stenotic lesions on serial angiography in 61% of patients who were in clinical remission.[76]

The effects of treatment on inflammatory VW-MR imaging findings are potentially important. Intracranial VW-MR imaging data are lacking, but the sensitivity of extracranial VW-MR imaging for the diagnosis of temporal arteritis was lower in patients who were imaged >2 days after starting corticosteroid treatment.[77]

To Select an Intracranial Target for Biopsy in Suspected CNS Vasculitis

Extracranial VW-MR imaging has been used to identify an inflamed segment of the superficial temporal artery and guide arterial biopsy to diagnose giant cell arteritis.[78] There is a lack of high-quality data on the sensitivity and specificity of brain (or leptomeningeal) biopsy for the diagnosis of CNS vasculitis. However, CNS vasculitis can be spatially heterogeneous, and false-negative biopsies occur. Study group members have found that VW-MR imaging is a potential means of identifying a peripherally located inflamed vessel to target for biopsy.

To Determine Which Aneurysm Has Ruptured in Patients with Acute Subarachnoid Hemorrhage and Multiple Aneurysms

There has been more experience with intracranial VW-MR imaging in the context of ischemic stroke than subarachnoid hemorrhage. However, preliminary results suggest that VW-MR imaging may be a useful technique for evaluating patients with intracranial aneurysms. An initial study[79] used a 2D double inversion recovery VW-MR imaging sequence at 1.5T with a voxel size of $0.5 \times 0.6 \times 0.3$ mm to image the wall of saccular aneurysms, and there have been subsequent studies of the berry aneurysm wall at 3T and 7T.[80]

A VW-MR imaging study[81] of 5 patients with aneurysmal subarachnoid hemorrhage found that all ruptured aneurysms demonstrated thick peripheral enhancement. Three patients in this series had multiple aneurysms, and the unruptured aneurysms did not enhance. A subsequent study[82] confirmed these findings in a larger sample size: There was aneurysm wall enhancement in 16/17 ruptured aneurysms; enhancement in 5/5 unruptured aneurysms that had changed in morphology compared with a previous angiogram; and enhancement in 6/9 symptomatic unruptured aneurysms; but wall enhancement in only 22/77 unrup-

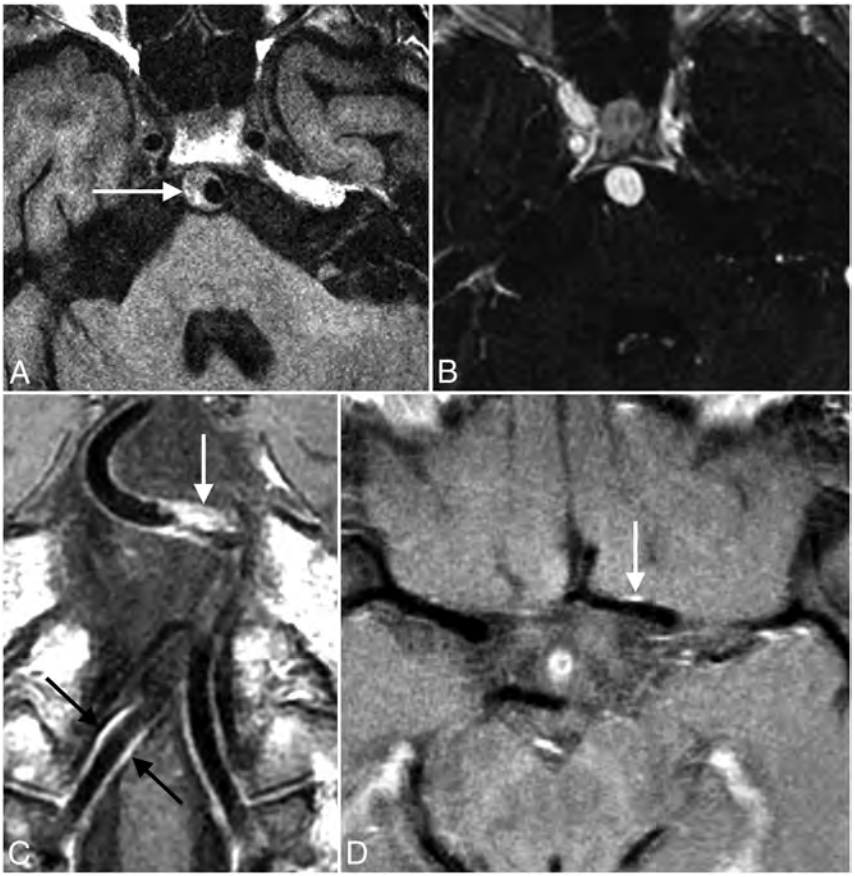

FIG 6. Common VW-MR imaging pitfalls. Case 1 (*A* and *B*) shows how slow flow can mimic arterial wall disease. Axial nonenhanced T1-weighted VW-MR imaging (*A*) demonstrates a crescent (*arrow*) of intermediate-to-hyperintense signal at the periphery of the basilar artery, suggestive of arterial wall thickening from dissection or atherosclerotic plaque. A corresponding image from a gadolinium-enhanced MRA (*B*) shows that the crescent of apparent arterial wall thickening fills with contrast and therefore represents a dilated basilar artery lumen rather than the arterial wall. Case 2 (*C*) shows how vasa vasorum can mimic vasculitis. Coronal contrast-enhanced T1-weighted VW-MR imaging shows a focal atherosclerotic plaque (*white arrow*) of the basilar artery, but also more diffuse smooth concentric enhancement of the vertebral (*black arrows*) and basilar artery walls, which has an appearance similar to that of vasculitis. The diffuse enhancement is consistent with increased intracranial vasa vasorum in this patient who has strong atherosclerotic risk factors. Case 3 (*D*) shows how a normal vein residing close to an artery can mimic arterial wall disease, such as enhancing atherosclerotic plaque. Axial contrast-enhanced T1-weighted VW-MR imaging shows a vein (*arrow*) adjacent to the left middle cerebral artery.

tured, asymptomatic, stable aneurysms. Another study[10] had similar results. Figure 5 provides an example of VW-MR imaging in a patient with 2 aneurysms, 1 unruptured and 1 ruptured.

There has also been interest in using VW-MR imaging to determine the source of hemorrhage in patients with angiogram-negative non-perimesencephalic subarachnoid hemorrhage,[83] but no evidence yet of utility.

SITUATIONS IN WHICH INTRACRANIAL VW-MR IMAGING IS CURRENTLY IN THE DOMAIN OF RESEARCH

To Predict Future Behavior of Unruptured Intracranial Saccular Aneurysms

A study of human aneurysm tissue found diffuse invasion of macrophages and leukocytes into the vessel wall of ruptured aneurysms but few inflammatory cells in the wall of unruptured aneurysms.[84,85] These inflammatory changes were already present shortly after the rupture and were not more pronounced when there was greater time between aneurysm rupture and surgical excision, suggesting that aneurysm wall inflammation might precede rupture rather than occur as a result of rupture.[84] If aneurysm wall inflammation is an important factor in aneurysm growth and rupture, then vessel wall enhancement may be a marker of rupture risk. However, prospective longitudinal studies are needed to prove that this is correct.

There is also interest in measuring aneurysm wall thickness to predict rupture risk. However, berry aneurysm wall thickness is approximately 0.02–0.5 mm,[86] leading to overestimation of wall thickness from the partial volume effects that will occur at the spatial resolutions currently achievable.[87] It is not yet possible to accurately measure berry aneurysm wall thickness by using VW-MR imaging.

IMPORTANT PITFALLS

Accurate diagnosis by using VW-MR imaging is critically dependent on both an adequate imaging technique and interpretive experience. When either of these is lacking, normal variations are easily misinterpreted as disease.

Slow Flow

Most VW-MR imaging techniques rely on blood flow to achieve blood-signal suppression. Blood flow is often laminar, with lower velocity closer to the vessel wall. Incomplete signal suppression in the periphery of the lumen can mimic vessel wall thickening and/or wall enhancement (Fig 6*A*, -*B*). Factors predisposing to these artifacts include recirculating or slow flow within an aneurysm, low velocity flow in a dilated artery, and retrograde filling of a branch artery via leptomeningeal collaterals when there is proximal arterial occlusion.[88]

Vasa Vasorum

The walls of major extracranial arteries receive blood supply through the vasa vasorum, a network of small vessels within the outer aspect of the vessel wall itself. Intracranial vessels in children lack a vasa vasorum.[89] However, with increasing age and with atherosclerotic risk factors, extracranial vasa vasorum can extend into the proximal intracranial segments of the internal carotid and vertebral arteries.[90] In patients with a variety of intracranial arterial diseases, a vasa vasorum can also develop distant from the extracranial vasa vasorum, with supply from nearby intracranial arteries.[91] A vasa vasorum can cause concentric arterial wall thickening and enhancement,[92] which mimic vasculitis (Fig 6*C*).

Veins

An enhancing vein located adjacent to an artery can mimic arterial wall enhancement (Fig 6*D*). It is usually possible to avoid this by careful examination of VW-MR imaging in multiple planes and comparison with MR angiography.

Effects of Thromboembolism and Thrombectomy on the Arterial Wall

Does thromboembolism itself injure the arterial wall and change the appearance of the wall? Does mechanical thrombectomy alter the appearance of the wall? These issues were explored in a VW-MR imaging study of 16 patients imaged within days of acute intracranial arterial occlusion.[93] The cause of stroke was an extracranial source of thromboembolism in most cases, and the intracranial arteries had fully recanalized at the time of VW-MR imaging in most cases. The study found that mechanical thrombectomy results in concentric intracranial arterial wall thickening and enhancement, potentially mimicking the VW-MR imaging appearance of primary arteritis. A similar arterial wall abnormality was observed in patients treated with medical therapy alone, but it was less common in this group.

RECOMMENDATIONS FOR CLINICAL PRACTICE

Intracranial VW-MR Imaging Is Likely a Useful Adjunct to Conventional Imaging

1) To differentiate among causes of intracranial arterial narrowing such as intracranial atherosclerotic plaque, vasculitis, reversible cerebral vasoconstriction syndrome, and arterial dissection.

2) To identify symptomatic, nonstenotic disease of the intracranial arteries.

Intracranial VW-MR Imaging Is Possibly a Useful Adjunct to Conventional Imaging

1) To determine the location of atherosclerotic plaque relative to branch artery ostia.

2) To assess atherosclerotic plaque activity.

3) To assess vasculitis activity.

4) To select an intracranial target for biopsy in suspected CNS vasculitis.

5) To determine which aneurysm has ruptured in patients with acute subarachnoid hemorrhage and multiple aneurysms.

Intracranial VW-MR Imaging Is Currently in the Domain of Research

1) To predict future behavior of unruptured intracranial saccular aneurysms.

Technical Implementation

1) Use pulse sequences that provide sufficient spatial resolution, black blood, and preferably black CSF.

2) Use 2D sequences in short- and long-axis planes through the vessels of interest, and/or 3D sequences with isotropic voxel dimensions and multiplanar reformatting.

3) Modify the VW-MR protocol in response to the particular clinical indication. Protocols will often include a time-of-flight MRA of the circle of Willis, T1-weighted (or proton-density–weighted) vessel wall sequences before and after intravenous administration of gadolinium, and T2-weighted sequences. Consider adding a gadolinium-bolus MRA, particularly if there is severe arterial narrowing or arterial dilation.

4) Recognize that the true performance capabilities of MR images are often unclear and important characteristics such as spatial resolution depend on multiple factors and not simply voxel size. Therefore, quantitative measurements (such as vessel wall thickness) should be validated against calibration standards by using phantom testing.

Interpretation

1) Interpret VW-MR imaging using the fundamental principles of radiologic interpretation used in other body tissues. Confirm vessel wall findings in multiple planes and preferably with multiple tissue weightings, and combine information from all available sequences to determine whether there is vessel wall thickening or enhancement. This assessment requires accurate determination of the inner and outer boundaries of the vessel wall by direct comparison of T1-, T2-, and contrast-enhanced T1-weighted images and MRA source images. For accurate interpretation, it is critical to harmonize observed abnormalities across all sequences.

2) Recognize common pitfalls such as age-related vasa vasorum enhancement in the large intracranial arteries near the skull base, slow flow mimicking arterial wall thickening or enhancement, normally enhancing veins that are commonly seen close to arteries, and the effects of therapy on the vessel wall.

3) Always seek knowledge of the broader clinical context of the VW-MR imaging.

4) Communicate VW-MR imaging results to referring physicians along with the appreciation that certain VW-MR imaging findings are well-studied but others (which may still be important) are not yet fully validated.

ACKNOWLEDGMENTS

The authors thank Dr. Max Wintermark and the Executive Committee of the ASNR for constructive feedback on our draft manuscript.

Disclosures: Christopher P. Hess—*UNRELATED*: *Expert Testimony*: various legal firms (medical-legal consulting); *Grants/Grants Pending*: National Institutes of Health,* Quest Diagnostics,* Cerebrotech Medical*; *Payment for Lectures (including service on Speakers Bureaus)*: Siemens,* *Comments*: travel and lodging to lecture on neuroimaging for internal research and development at Siemens Healthcare. David Saloner—*UNRELATED*: *Grants/Grants Pending*: National Institutes of Health.* Sameer A. Ansari—*UNRELATED*: *Grants/Grants Pending*: American Heart Association,* National Institutes of Health.* Bruce A. Wasserman—*Patents (planned, pending or issued)*: Dr Wasserman has a patent pending (No. 13/922,111) for a 3D black-blood MR imaging technique mentioned in this article; however, there have been no license agreements and he has not received any payments related to his patent application. *Money paid to the institution.

REFERENCES

1. Gutierrez J, Elkind MS, Petito C, et al. **The contribution of HIV infection to intracranial arterial remodeling: a pilot study.** *Neuropathology* 2013;33:256–63 CrossRef Medline
2. van der Kolk AG, Hendrikse J, Brundel M, et al. **Multi-sequence whole-brain intracranial vessel wall imaging at 7.0 Tesla.** *Eur Radiol* 2013;23:2996–3004 CrossRef Medline
3. Zhu C, Haraldsson H, Tian B, et al. **High resolution imaging of the**

intracranial vessel wall at 3 and 7 T using 3D fast spin echo MRI. *Magma* 2016;29:559–70 CrossRef Medline
4. Antiga L, Wasserman BA, Steinman DA. **On the overestimation of early wall thickening at the carotid bulb by black blood MRI, with implications for coronary and vulnerable plaque imaging.** *Magn Reson Med* 2008;60:1020–28 CrossRef Medline
5. Edelman RR, Mattle HP, Wallner B, et al. **Extracranial carotid arteries: evaluation with "black blood" MR angiography.** *Radiology* 1990;177:45–50 CrossRef Medline
6. Edelman RR, Chien D, Kim D. **Fast selective black blood MR imaging.** *Radiology* 1991;181:655–60 CrossRef Medline
7. Busse RF, Hariharan H, Vu A, et al. **Fast spin echo sequences with very long echo trains: design of variable refocusing flip angle schedules and generation of clinical T2 contrast.** *Magn Reson Med* 2006; 55:1030–37 CrossRef Medline
8. Alexander AL, Buswell HR, Sun Y, et al. **Intracranial black-blood MR angiography with high-resolution 3D fast spin echo.** *Magn Reson Med* 1998;40:298–310 CrossRef Medline
9. Fan Z, Zhang Z, Chung YC, et al. **Carotid arterial wall MRI at 3T using 3D variable-flip-angle turbo spin-echo (TSE) with flow-sensitive dephasing (FSD).** *J Magn Reson Imaging* 2010;31:645–54 CrossRef Medline
10. Nagahata S, Nagahata M, Obara M, et al. **Wall enhancement of the intracranial aneurysms revealed by magnetic resonance vessel wall imaging using three-dimensional turbo spin-echo sequence with motion-sensitized driven-equilibrium: a sign of ruptured aneurysm?** *Clin Neuroradiol* 2014 Oct 21. [Epub ahead of print] Medline
11. Qiao Y, Steinman DA, Qin Q, et al. **Intracranial arterial wall imaging using three-dimensional high isotropic resolution black blood MRI at 3.0 Tesla.** *J Magn Reson Imaging* 2011;34:22–30 CrossRef Medline
12. Zhang L, Zhang N, Wu J, et al. **High resolution three dimensional intracranial arterial wall imaging at 3T using T1 weighted SPACE.** *Magn Reson Imaging* 2015;33:1026–34 CrossRef Medline
13. Fuster V, Moreno PR, Fayad ZA, et al. **Atherothrombosis and high-risk plaque: part I, evolving concepts.** *J Am Coll Cardiol* 2005;46: 937–54 CrossRef Medline
14. Virmani R, Kolodgie FD, Burke AP, et al. **Lessons from sudden coronary death: a comprehensive morphological classification scheme for atherosclerotic lesions.** *Arterioscler Thromb Vasc Biol* 2000;20: 1262–75 CrossRef Medline
15. Stary HC, Chandler AB, Dinsmore RE, et al. **A definition of advanced types of atherosclerotic lesions and a histological classification of atherosclerosis: a report from the Committee on Vascular Lesions of the Council on Arteriosclerosis, American Heart Association.** *Arterioscler Thromb Vasc Biol* 1995;15:1512–31 CrossRef Medline
16. Lam WW, Wong KS, So NM, et al. **Plaque volume measurement by magnetic resonance imaging as an index of remodeling of middle cerebral artery: correlation with transcranial color Doppler and magnetic resonance angiography.** *Cerebrovasc Dis* 2004;17:166–69 Medline
17. Klein IF, Lavallée PC, Schouman-Claeys E, et al. **High-resolution MRI identifies basilar artery plaques in paramedian pontine infarct.** *Neurology* 2005;64:551–52 CrossRef Medline
18. Klein IF, Lavallée PC, Touboul PJ, et al. **In vivo middle cerebral artery plaque imaging by high-resolution MRI.** *Neurology* 2006;67: 327–29 CrossRef Medline
19. Swartz RH, Bhuta SS, Farb RI, et al. **Intracranial arterial wall imaging using high-resolution 3-Tesla contrast-enhanced MRI.** *Neurology* 2009;72:627–34 CrossRef Medline
20. Xu WH, Li ML, Gao S, et al. **In vivo high-resolution MR imaging of symptomatic and asymptomatic middle cerebral artery atherosclerotic stenosis.** *Atherosclerosis* 2010;212:507–11 CrossRef Medline
21. Ryu CW, Jahng GH, Kim EJ, et al. **High resolution wall and lumen MRI of the middle cerebral arteries at 3 Tesla.** *Cerebrovasc Dis* 2009; 27:433–42 CrossRef Medline
22. Li ML, Xu WH, Song L, et al. **Atherosclerosis of middle cerebral artery: evaluation with high-resolution MR imaging at 3T.** *Atherosclerosis* 2009;204:447–52 CrossRef Medline
23. Toussaint JF, LaMuraglia GM, Southern JF, et al. **Magnetic resonance images lipid, fibrous, calcified, hemorrhagic, and thrombotic components of human atherosclerosis in vivo.** *Circulation* 1996;94: 932–38 CrossRef Medline
24. Yuan C, Mitsumori LM, Ferguson MS, et al. **In vivo accuracy of multispectral magnetic resonance imaging for identifying lipid-rich necrotic cores and intraplaque hemorrhage in advanced human carotid plaques.** *Circulation* 2001;104:2051–56 CrossRef Medline
25. Wasserman BA, Smith WI, Trout HH 3rd, et al. **Carotid artery atherosclerosis: in vivo morphologic characterization with gadolinium-enhanced double-oblique MR imaging initial results.** *Radiology* 2002;223:566–73 CrossRef Medline
26. Yuan C, Petty C, O'Brien KD, et al. **In vitro and in situ magnetic resonance imaging signal features of atherosclerotic plaque-associated lipids.** *Arterioscler Thromb Vasc Biol* 1997;17:1496–503 CrossRef Medline
27. Han JS, Mandell DM, Poublanc J, et al. **BOLD-MRI cerebrovascular reactivity findings in cocaine-induced cerebral vasculitis.** *Nat Clin Pract Neurol* 2008;4:628–32 CrossRef Medline
28. Cheng-Ching E, Jones S, Hui FK, et al. **High-resolution MRI vessel wall imaging in varicella zoster virus vasculopathy.** *J Neurol Sci* 2015;351:168–73 CrossRef Medline
29. Obusez EC, Hui F, Hajj-Ali RA, et al. **High-resolution MRI vessel wall imaging: spatial and temporal patterns of reversible cerebral vasoconstriction syndrome and central nervous system vasculitis.** *AJNR Am J Neuroradiol* 2014;35:1527–32 CrossRef Medline
30. Choe YH, Kim DK, Koh EM, et al. **Takayasu arteritis: diagnosis with MR imaging and MR angiography in acute and chronic active stages.** *J Magn Reson Imaging* 1999;10:751–57 Medline
31. Choe YH, Han BK, Koh EM, et al. **Takayasu's arteritis: assessment of disease activity with contrast-enhanced MR imaging.** *AJR Am J Roentgenol* 2000;175:505–11 CrossRef Medline
32. Mandell DM, Matouk CC, Farb RI, et al. **Vessel wall MRI to differentiate between reversible cerebral vasoconstriction syndrome and central nervous system vasculitis: preliminary results.** *Stroke* 2012; 43:860–62 CrossRef Medline
33. Mossa-Basha M, Hwang WD, De Havenon A, et al. **Multicontrast high-resolution vessel wall magnetic resonance imaging and its value in differentiating intracranial vasculopathic processes.** *Stroke* 2015;46:1567–73 CrossRef Medline
34. Findlay JM, Weir BK, Kanamaru K, et al. **Arterial wall changes in cerebral vasospasm.** *Neurosurgery* 1989;25:736–45; discussion 745–46 CrossRef Medline
35. Serdaru M, Chiras J, Cujas M, et al. **Isolated benign cerebral vasculitis or migrainous vasospasm?** *J Neurol Neurosurg Psychiatry* 1984; 47:73–76 CrossRef Medline
36. Hajj-Ali RA, Furlan A, Abou-Chebel A, et al. **Benign angiopathy of the central nervous system: cohort of 16 patients with clinical course and long-term followup.** *Arthritis Rheum* 2002;47:662–69 CrossRef Medline
37. Aoki S, Hayashi N, Abe O, et al. **Radiation-induced arteritis: thickened wall with prominent enhancement on cranial MR images report of five cases and comparison with 18 cases of Moyamoya disease.** *Radiology* 2002;223:683–88 CrossRef Medline
38. Kim YJ, Lee DH, Kwon JY, et al. **High resolution MRI difference between Moyamoya disease and intracranial atherosclerosis.** *Eur J Neurol* 2013;20:1311–18 CrossRef Medline
39. Kim SM, Ryu CW, Jahng GH, et al. **Two different morphologies of chronic unilateral middle cerebral artery occlusion: evaluation using high-resolution MRI.** *J Neuroimaging* 2014;24:460–66 CrossRef Medline
40. Takagi Y, Kikuta K, Nozaki K, et al. **Histological features of middle cerebral arteries from patients treated for Moyamoya disease.** *Neurol Med Chir (Tokyo)* 2007;47:1–4 CrossRef Medline
41. Ryoo S, Cha J, Kim SJ, et al. **High-resolution magnetic resonance wall imaging findings of Moyamoya disease.** *Stroke* 2014;45: 2457–60 CrossRef Medline

42. Iwama T, Andoh T, Sakai N, et al. **Dissecting and fusiform aneurysms of vertebro-basilar systems. MR imaging.** *Neuroradiology* 1990;32:272–79 CrossRef Medline
43. Wang Y, Lou X, Li Y, et al. **Imaging investigation of intracranial arterial dissecting aneurysms by using 3 T high-resolution MRI and DSA: from the interventional neuroradiologists' view.** *Acta Neurochir (Wien)* 2014;156:515–25 CrossRef Medline
44. Habs M, Pfefferkorn T, Cyran CC, et al. **Age determination of vessel wall hematoma in spontaneous cervical artery dissection: a multisequence 3T cardiovascular magnetic resonance study.** *J Cardiovasc Magn Reson* 2011;13:76 CrossRef Medline
45. Kitanaka C, Tanaka J, Kuwahara M, et al. **Magnetic resonance imaging study of intracranial vertebrobasilar artery dissections.** *Stroke* 1994;25:571–75 CrossRef Medline
46. Hosoya T, Adachi M, Yamaguchi K, et al. **Clinical and neuroradiological features of intracranial vertebrobasilar artery dissection.** *Stroke* 1999;30:1083–90 CrossRef Medline
47. Kim TW, Choi HS, Koo J, et al. **Intramural hematoma detection by susceptibility-weighted imaging in intracranial vertebral artery dissection.** *Cerebrovasc Dis* 2013;36:292–98 CrossRef Medline
48. Ahn SS, Kim BM, Suh SH, et al. **Spontaneous symptomatic intracranial vertebrobasilar dissection: initial and follow-up imaging findings.** *Radiology* 2012;264:196–202 CrossRef Medline
49. Chung JW, Kim BJ, Sohn CH, et al. **Branch atheromatous plaque: a major cause of lacunar infarction (high-resolution MRI study).** *Cerebrovasc Dis Extra* 2012;2:36–44 CrossRef Medline
50. Yoon Y, Lee DH, Kang DW, et al. **Single subcortical infarction and atherosclerotic plaques in the middle cerebral artery: high-resolution magnetic resonance imaging findings.** *Stroke* 2013;44:2462–67 CrossRef Medline
51. Klein IF, Lavallée PC, Mazighi M, et al. **Basilar artery atherosclerotic plaques in paramedian and lacunar pontine infarctions: a high-resolution MRI study.** *Stroke* 2010;41:1405–09 CrossRef Medline
52. Xu WH, Li ML, Niu JW, et al. **Intracranial artery atherosclerosis and lumen dilation in cerebral small-vessel diseases: a high-resolution MRI study.** *CNS Neurosci Ther* 2014;20:364–67 CrossRef Medline
53. Watanabe H, Yoshida K, Akasaka T, et al. **Intravascular ultrasound assessment of plaque distribution in the ostium of the left anterior descending coronary artery.** *Am J Cardiol* 1996;78:827–29 CrossRef Medline
54. Xu WH, Li ML, Gao S, et al. **Plaque distribution of stenotic middle cerebral artery and its clinical relevance.** *Stroke* 2011;42:2957–59 CrossRef Medline
55. Zhu XJ, Du B, Lou X, et al. **Morphologic characteristics of atherosclerotic middle cerebral arteries on 3T high-resolution MRI.** *AJNR Am J Neuroradiol* 2013;34:1717–22 CrossRef Medline
56. Huang B, Yang WQ, Liu XT, et al. **Basilar artery atherosclerotic plaques distribution in symptomatic patients: a 3.0T high-resolution MRI study.** *Eur J Radiol* 2013;82:e199–203 CrossRef Medline
57. Aliabadi D, Tilli FV, Bowers TR, et al. **Incidence and angiographic predictors of side branch occlusion following high-pressure intracoronary stenting.** *Am J Cardiol* 1997;80:994–97 CrossRef Medline
58. Jiang WJ, Yu W, Ma N, et al. **High resolution MRI guided endovascular intervention of basilar artery disease.** *J Neurointerv Surg* 2011;3:375–78 CrossRef Medline
59. Chen XY, Wong KS, Lam WW, et al. **Middle cerebral artery atherosclerosis: histological comparison between plaques associated with and not associated with infarct in a postmortem study.** *Cerebrovasc Dis* 2008;25:74–80 Medline
60. Yang WQ, Huang B, Liu XT, et al. **Reproducibility of high-resolution MRI for the middle cerebral artery plaque at 3T.** *Eur J Radiol* 2014;83:e49–55 CrossRef Medline
61. Chung GH, Kwak HS, Hwang SB, et al. **High resolution MR imaging in patients with symptomatic middle cerebral artery stenosis.** *Eur J Radiol* 2012;81:4069–74 CrossRef Medline
62. Glagov S, Weisenberg E, Zarins CK, et al. **Compensatory enlargement of human atherosclerotic coronary arteries.** *N Engl J Med* 1987;316:1371–75 CrossRef Medline
63. Burke AP, Kolodgie FD, Farb A, et al. **Morphological predictors of arterial remodeling in coronary atherosclerosis.** *Circulation* 2002;105:297–303 CrossRef Medline
64. Pasterkamp G, Wensing PJ, Post MJ, et al. **Paradoxical arterial wall shrinkage may contribute to luminal narrowing of human atherosclerotic femoral arteries.** *Circulation* 1995;91:1444–49 CrossRef Medline
65. Shi MC, Wang SC, Zhou HW, et al. **Compensatory remodeling in symptomatic middle cerebral artery atherosclerotic stenosis: a high-resolution MRI and microemboli monitoring study.** *Neurol Res* 2012;34:153–58 CrossRef Medline
66. Xu WH, Li ML, Gao S, et al. **Middle cerebral artery intraplaque hemorrhage: prevalence and clinical relevance.** *Ann Neurol* 2012;71:195–98 CrossRef Medline
67. Kerwin WS, Oikawa M, Yuan C, et al. **MR imaging of adventitial vasa vasorum in carotid atherosclerosis.** *Magn Reson Med* 2008;59:507–14 CrossRef Medline
68. Yuan C, Kerwin WS, Ferguson MS, et al. **Contrast-enhanced high resolution MRI for atherosclerotic carotid artery tissue characterization.** *J Magn Reson Imaging* 2002;15:62–67 CrossRef Medline
69. Qiao Y, Etesami M, Astor BC, et al. **Carotid plaque neovascularization and hemorrhage detected by MR imaging are associated with recent cerebrovascular ischemic events.** *AJNR Am J Neuroradiol* 2012;33:755–60 CrossRef Medline
70. Vergouwen MD, Silver FL, Mandell DM, et al. **Eccentric narrowing and enhancement of symptomatic middle cerebral artery stenoses in patients with recent ischemic stroke.** *Arch Neurol* 2011;68:338–42 CrossRef Medline
71. Qiao Y, Zeiler SR, Mirbagheri S, et al. **Intracranial plaque enhancement in patients with cerebrovascular events on high-spatial-resolution MR images.** *Radiology* 2014;271:534–42 CrossRef Medline
72. Skarpathiotakis M, Mandell DM, Swartz RH, et al. **Intracranial atherosclerotic plaque enhancement in patients with ischemic stroke.** *AJNR Am J Neuroradiol* 2013;34:299–304 CrossRef Medline
73. Lou X, Ma N, Ma L, et al. **Contrast-enhanced 3T high-resolution MR imaging in symptomatic atherosclerotic basilar artery stenosis.** *AJNR Am J Neuroradiol* 2013;34:513–17 CrossRef Medline
74. Tso E, Flamm SD, White RD, et al. **Takayasu arteritis: utility and limitations of magnetic resonance imaging in diagnosis and treatment.** *Arthritis Rheum* 2002;46:1634–42 CrossRef Medline
75. Kerr GS, Hallahan CW, Giordano J, et al. **Takayasu arteritis.** *Ann Intern Med* 1994;120:919–29 CrossRef Medline
76. Hoffman GS. **Takayasu arteritis: lessons from the American National Institutes of Health experience.** *Int J Cardiol* 1996;54(suppl):S99–102 CrossRef Medline
77. Hauenstein C, Reinhard M, Geiger J, et al. **Effects of early corticosteroid treatment on magnetic resonance imaging and ultrasonography findings in giant cell arteritis.** *Rheumatology* 2012;51:1999–2003 CrossRef Medline
78. Bley TA, Wieben O, Uhl M, et al. **High-resolution MRI in giant cell arteritis: imaging of the wall of the superficial temporal artery.** *AJR Am J Roentgenol* 2005;184:283–87 CrossRef Medline
79. Park JK, Lee CS, Sim KB, et al. **Imaging of the walls of saccular cerebral aneurysms with double inversion recovery black-blood sequence.** *J Magn Reson Imaging* 2009;30:1179–83 CrossRef Medline
80. Kleinloog R, Korkmaz E, Zwanenburg JJ, et al. **Visualization of the aneurysm wall: a 7.0-Tesla magnetic resonance imaging study.** *Neurosurgery* 2014;75:614–22; discussion 622 CrossRef Medline
81. Matouk CC, Mandell DM, Günel M, et al. **Vessel wall magnetic resonance imaging identifies the site of rupture in patients with multiple intracranial aneurysms: proof of principle.** *Neurosurgery* 2013;72:492–96; discussion 496 CrossRef Medline
82. Edjlali M, Gentric JC, Régent-Rodriguez C, et al. **Does aneurysmal wall enhancement on vessel wall MRI help to distinguish stable from unstable intracranial aneurysms?** *Stroke* 2014;45:3704–06 CrossRef Medline
83. Coutinho JM, Sacho RH, Schaafsma JD, et al. **High-resolution vessel wall magnetic resonance imaging in angiogram-negative non-per-**

imesencephalic subarachnoid hemorrhage. *Clin Neuroradiol* 2015 Nov 25. [Epub ahead of print] Medline
84. Kataoka K, Taneda M, Asai T, et al. **Structural fragility and inflammatory response of ruptured cerebral aneurysms: a comparative study between ruptured and unruptured cerebral aneurysms.** *Stroke* 1999;30:1396–401 CrossRef Medline
85. Frösen J, Piippo A, Paetau A, et al. **Remodeling of saccular cerebral artery aneurysm wall is associated with rupture: histological analysis of 24 unruptured and 42 ruptured cases.** *Stroke* 2004;35:2287–93 CrossRef Medline
86. Suzuki J, Ohara H. **Clinicopathological study of cerebral aneurysms. Origin, rupture, repair, and growth.** *J Neurosurg* 1978;48:505–14 CrossRef Medline
87. Steinman DA, Antiga L, Wasserman BA. **Overestimation of cerebral aneurysm wall thickness by black blood MRI?** *J Magn Reson Imaging* 2010;31:766 CrossRef Medline
88. Hui FK, Zhu X, Jones SE, et al. **Early experience in high-resolution MRI for large vessel occlusions.** *J Neurointerv Surg* 2015;7:509–16 CrossRef Medline
89. Aydin F. **Do human intracranial arteries lack vasa vasorum? A comparative immunohistochemical study of intracranial and systemic arteries.** *Acta Neuropathol* 1998;96:22–28 CrossRef Medline
90. Takaba M, Endo S, Kurimoto M, et al. **Vasa vasorum of the intracranial arteries.** *Acta Neurochir (Wien)* 1998;140:411–16 CrossRef Medline
91. Portanova A, Hakakian N, Mikulis DJ, et al. **Intracranial vasa vasorum: insights and implications for imaging.** *Radiology* 2013;267:667–79 CrossRef Medline
92. Aoki S, Shirouzu I, Sasaki Y, et al. **Enhancement of the intracranial arterial wall at MR imaging: relationship to cerebral atherosclerosis.** *Radiology* 1995;194:477–81 CrossRef Medline
93. Power S, Matouk C, Casaubon LK, et al. **Vessel wall magnetic resonance imaging in acute ischemic stroke: effects of embolism and mechanical thrombectomy on the arterial wall.** *Stroke* 2014;45:2330–34 CrossRef Medline

Efficacy of Double-Blind Peer Review in an Imaging Subspecialty Journal

E.E. O'Connor, M. Cousar, J.A. Lentini, M. Castillo, K. Halm, and T.A. Zeffiro

ABSTRACT

BACKGROUND AND PURPOSE: Many scientific journals use double-blind peer review to minimize potential reviewer bias concerning publication recommendations. However, because neuroradiology is a relatively small subspecialty, this process may be limited by prior knowledge of the authors' work or associated institutions. We sought to investigate the efficacy of reviewer blinding and determine the impact that unblinding may have on manuscript acceptance.

MATERIALS AND METHODS: For manuscripts submitted to the *American Journal of Neuroradiology* (*AJNR*) from January through June 2015, reviewers completed a brief anonymous questionnaire after submitting their evaluations, assessing whether they were familiar with the research or had knowledge of the authors or institutions from which the work originated.

RESULTS: The response rate for 1079 questionnaires was 98.8%; 12.9% of reviewers knew or suspected that they knew authors, and 15.3% knew or suspected that they knew the associated institutions. Reviewers correctly identified the authors in 90.3% of cases and correctly stated the institutions in 86.8% of cases. Unblinding resulted from self-citation in 34.1% for both authorship and institutions. The acceptance rate when reviewers knew or suspected that they knew the authors was 57/137 (41.6%) and 262/929 (28.2%) when reviewers did not. The acceptance rate when reviewers knew or suspected that they knew the institutions was 60/163 (36.8%) and 259/903 (28.7%) when they did not. The Fisher exact test showed that author ($P < .038$) and institution ($P < .039$) familiarity was associated with greater manuscript acceptance.

CONCLUSIONS: While the *AJNR* process of double-blind peer review minimizes reviewer bias, perceived knowledge of the author and institution is associated with a higher rate of manuscript acceptance.

Although peer review has been characterized as the "centerpiece of the modern scientific review process"[1] and is a fundamental step in the publication of scientific research, the integrity of blinding in the peer review of neuroradiology manuscripts has not been studied. Critical appraisal and review by experts in one's chosen field of study is considered a rigorous form of recognition and is an important means of communication among scientific community members.[2,3] Peer-reviewed publication also serves as a measure of academic productivity that strongly influences academic career advancement.[4,5] Ideally, this process is based on scientific merit and research quality. However, several studies have revealed biases that may affect the integrity of the peer-review process related to author characteristics, such as nationality, language, prestige, and sex.[6-12]

Double-blind peer review, a system in which both reviewers' and authors' identities are hidden, is used by many medical journals to protect authors from potential reviewer bias concerning publication recommendations.[13] It has been argued that true blinding is difficult to accomplish,[14] with empiric studies demonstrating that reviewers can successfully identify authors as often as 25%–50% of the time in both biomedical and social science journals.[15-21] Although the *American Journal of Neuroradiology* (*AJNR*) uses a double-blind peer review system, its efficacy has not yet been examined. This issue is important because the subspecialty of neuroradiology consists of a relatively small number of physicians. The small size of this physician community and the limited number of neuroradiology professional scientific meetings in which preliminary research findings are discussed mean that reviewers may have knowledge of research findings described

Received June 12, 2016; accepted after revision September 26.

From the Department of Radiology (E.E.O., M.C., J.A.L.), Lewis Katz School of Medicine at Temple University, Philadelphia, Pennsylvania; Department of Radiology (M.C.), University of North Carolina School of Medicine, Chapel Hill, North Carolina; *American Journal of Neuroradiology* (K.H.), Oak Brook, Illinois; and Neurometrika (T.A.Z.), Potomac, Maryland.

Paper previously presented in part at: Annual Meeting of the American Society of Neuroradiology, May 21–26,2016; Washington, DC.

Please address correspondence to Erin E. O'Connor, MD, Department of Radiology, Lewis Katz School of Medicine at Temple University, 3401 N Broad St, Philadelphia, PA 19140; e-mail: erin.oconnor@umm.edu; @LanternLab

http://dx.doi.org/10.3174/ajnr.A5017

Table 1: *AJNR* reviewer questionnaire

Questionnaire
1) Can you identify the principal authors of manuscript reviewed?
A) I know I could.
B) I suspect I could.
C) I do not think I could.
2) Can you identify the institutions from which the reviewed work originates?
A) I know I could.
B) I suspect I could.
C) I do not think I could.
3) Can you identify either the authors or institutions?
A) I know I could.
B) I suspect I could.
C) I do not think I could.
4) If you answered A or B for the above question, please enter the suspected author, institution, or both.
5) Were you familiar with the research findings before review?
A) Yes
B) No
C) Not sure

in a manuscript assigned to them or knowledge of the manuscript authors. Peer reviewers' knowledge of author and/or institution identity may positively or negatively influence the content, quality, and final review recommendations. Thus, we sought to investigate the frequency with which perceived unblinding occurs and whether unblinding has an effect on manuscript acceptance. We hypothesized that perceived identification of the authors of a manuscript or related institutions would be associated with higher acceptance rates and that geographic residence of the reviewers or authors could independently affect the probability of manuscript acceptance.

MATERIALS AND METHODS

All manuscript reviewers submitting evaluations for *AJNR* from January 2015 to June 2015 were asked to answer a brief questionnaire using the electronic Manuscript Central system interface (Table 1). To evaluate the efficacy of blinding, the reviewers' questionnaire replicated items from a study by Jagsi et al.[21] Reviewers were asked whether they thought they could identify any of the principal authors or institutions from which the work originated. Possible responses for both of these questions included, "I know I could," "I suspect I could," or "I do not think I could identify any of the authors." Reviewers who thought or suspected that they knew the principal author of the manuscript and/or the institutions from which the manuscript originated were prompted to specify the suspected authors and/or institutions. Response accuracy was assessed by the *AJNR* editorial staff and then coded. Many reviewers who entered responses also provided some explanation of their knowledge of the authors and institutions of origin of a manuscript. Instances of self-citation were calculated from these explanations. The final question asked reviewers whether they were familiar with the research findings discussed in the manuscript before their review. Possible responses to this question included "yes," "no," or "not sure."

To assess potential geographic influences on manuscript disposition, we recorded ZIP/country codes of the corresponding authors and reviewers and coded them by using the following regions: Northeast United States, Southeast United States, Midwest United States, Mountain States United States, West Coast United States, North America (other than the United States), South America, Europe, Asia excluding China, China, Africa, and Australia. The regions of the corresponding authors and reviewers were treated as independent variables to investigate the effects of geography on the acceptance rate.

Table 2: Contingency table showing manuscript counts and percentages for the relationship between manuscript disposition and author or institution unblinding in cell percentages[a]

	Manuscript Accepted	
	No	Yes
Author unblinded		
No	635 (59.6%)	254 (23.9%)
Yes	112 (10.5%)	65 (6.10%)
Institution unblinded		
No	634 (59.5%)	254 (23.8%)
Yes	113 (10.6%)	65 (6.10%)

[a] Both author and institution unblinding are associated with a greater chance of manuscript acceptance.

Data Analysis

To determine the effect of author or institution perceived unblinding on manuscript disposition, we organized data as 2 × 2 contingency tables, with author unblinding (yes/no) and manuscript acceptance (yes/no) as factors. We used the Fisher exact test for count data to examine the relationship among the variables.

To determine the effect of author or reviewer location on manuscript disposition, we organized data as 12 × 2 contingency tables, with author or reviewer location and manuscript acceptance (yes/no) as factors. We used the Fisher exact test for count data to examine the relationship among the variables.

RESULTS

The response rate for the 1079 questionnaires offered to reviewers was 98.8%. Of the 1066 responses, 137 (12.9%) knew or suspected that they knew the principal author of the manuscript and 163 (15.3%) reviewers knew or suspected that they knew the institution from which the work originated. Of the 154 reviewers suspecting that they had knowledge of the manuscript authors, 139 (90.3%) correctly identified the authors of the submitted manuscripts. Of the 159 reviewers who stated that they knew the institution from which the work originated, 138 (86.8%) were correct. From the pool of reviewers who provided explanations for their suspected knowledge of authors and institutions of origin, unblinding resulted from self-citation in 34.1% of occurrences for both authorship and institutions.

The rate of acceptance when reviewers knew or suspected that they knew the authors was 57/137 (41.6%), and the rate of acceptance when reviewers did not identify the authors was 262/929 (28.2%). With a 2-sided Fisher exact test for count data, the null hypothesis that there was no association between perceived unblinding of the author and the rate of acceptance of the manuscript was rejected ($P = .038$; odds ratio = 1.45; 95% confidence interval, 1.016–2.059) (Table 2 and Fig 1*A*). An odds ratio of 1.45 measures the higher odds of the manuscript being accepted if perceived author unblinding occurs.

The rate of acceptance when reviewers knew or suspected that they knew the institutions from which the work originated was

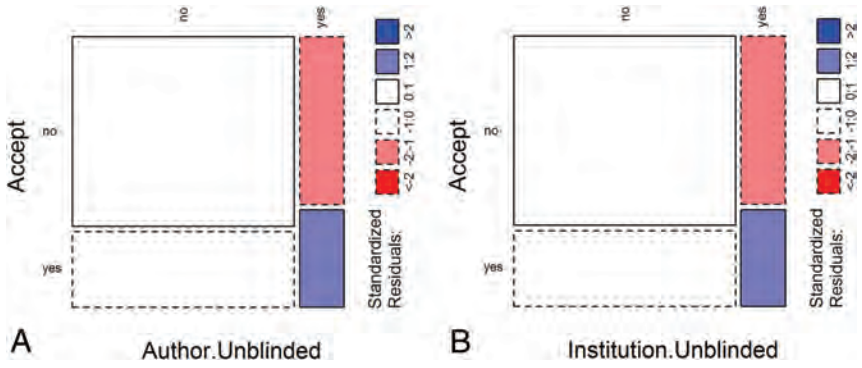

FIG 1. Mosaic plots graphically displaying data from 2 × 2 contingency tables. *A*, Unblinding of the author is associated with a higher rate of manuscript acceptance. *B*, Unblinding of the institution is associated with a higher rate of manuscript acceptance. There are 4 cells, and the area of each cell represents the frequency of each of the 4 unique combinations of variable levels. The "standardized residual" is the residual divided by its SD. Therefore, the standardized residual rating represents the degree to which the 2 categorical variables are independent of each other, in units of SD. Colors represent the deviation in each cell from those expected from the null hypothesis that the 2 variables are not associated, with the color intensity indicating the degree of "surprise" associated with rejection of the null hypothesis (http://www.r-tutor.com/elementary-statistics/simple-linear-regression/standardized-residual).

Table 3: Contingency table showing manuscript counts and percentages for the relationship between manuscript disposition and author or institution unblinding in row percentages[a]

	Manuscript Accepted		
	No	Yes	
Author unblinded			
No	635 (71.4%)	254 (28.6%)	100%
Yes	112 (63.3%)	65 (36.7%)	100%
Institution unblinded			
No	634 (71.4%)	254 (28.6%)	100%
Yes	113 (63.5%)	65 (36.5%)	100%

[a] Both author and institution unblinding are associated with a greater chance of manuscript acceptance.

60/163 (36.8%), and the rate of acceptance when reviewers did not believe they knew the institution from which the work originated was 259/903 (28.7%).

With a 2-sided Fisher exact test, the null hypothesis that there was no association between perceived unblinding of the institution and the manuscript acceptance rate was rejected ($P = .039$; odds ratio = 1.44; 95% confidence interval, 1.006–2.037) (Table 3 and Fig 1*B*).

With a 2-sided Fisher exact test, the null hypothesis that there was no association between perceived author unblinding and perceived institution unblinding was rejected ($P < .0001$, odds ratio = 6920).

To examine whether the manuscript acceptance rate was dependent on reviewers guessing correctly, we used a 2-sided Fisher exact test with the null hypothesis that there was no association between correctly guessing and manuscript acceptance. The resulting odds ratio was 0.46 ($P = .18$).

With a 2-sided Fisher exact test, the null hypothesis that there was no association between the corresponding author's geographic location and manuscript acceptance was rejected. Corresponding authors from the Southeast United States, Midwest United States, and West Coast United States were more likely to have a manuscript accepted, and corresponding authors from the Midwest United States were also less likely to have a manuscript rejected ($P < .0001$). Authors from Asia and China were less likely to have manuscripts accepted and were more likely to have manuscripts rejected (Fig 2*A*).

With a 2-sided Fisher exact test, the null hypothesis that there was no association between reviewer geographic location and manuscript acceptance was rejected. Reviewers from the Midwest were more likely to accept a manuscript, and reviewers from Asia were less likely to accept and more likely to reject a manuscript ($P = .0035$) (Fig 2*B*).

The rate of *AJNR* manuscript acceptance during the 6-month study period was 29.9%. This acceptance rate was consistent with journal acceptance rates during a longer period, including 2013 (21.3%), 2014 (23.6%), and 2015 (28.2%).

Across the United States, we observed strong geographic variation in reviewer and author density (Fig 3). Regional density was similar for authors and reviewers, with a strong association between the locations of authors and reviewers. These patterns appear to be related to the regional density of diagnostic radiologists reported by the Centers for Medicare and Medicaid Services (https://www.cms.gov/research-statistics-data-and-systems/statistics-trends-and-reports/medicare-provider-charge-data/physician-and-other-supplier.html).

DISCUSSION

Scientific progress depends on both the dissemination of ideas and their rigorous critique. Despite concerns about bias in the peer review process, most researchers still believe that double-blind peer review is essential for the appraisal of claims of new knowledge and effective communication with the scientific community,[22,23] motivating the research community to grapple with the question of how to improve the existing review processes.

In a single-blind review process, the reviewers' identities are concealed from the author, but author identity is revealed to reviewers. While this is a commonly used model for peer review in the scientific community, double-blind peer review is perceived as more objective and fair.[22] Its perceived benefits include protection of authors from potential reviewer bias and enabling reviewers to be forthright in their manuscript critiques without fear of interpersonal or political conflicts.[22,23] To test these assumptions, we examined the incidence of perceived manuscript unblinding, examining the relationship between reviewers' perceived knowledge of principal authors and institutions of manuscripts submitted to *AJNR* and their likelihood of acceptance.

Although the incidence of perceived unblinding in our study was relatively low compared with findings from studies evaluating its incidence in other journals,[15-21] when perceived author or institution unblinding occurred, there was higher likelihood of manuscript acceptance.

A number of possible mechanisms could explain our results. Reviewers could feel compelled to accept the work of a known and respected investigator. Alternatively, it may be difficult to blind

reviewers to authors with longer research histories and more publications or who may have a history of submitting higher quality manuscripts. Dissociating the effects of manuscript quality from author and institution name recognition could be difficult without amassing more observations than were available for this study because we would need to accrue enough instances of high manuscript quality and low author or institution recognition to allow accurate estimates of these effects. An explanation of the international author effects may be that investigators whose first language is not English or who have not spent time in Western countries may not have written English skills commensurate with the challenges inherent in scientific writing, leading to lower perceived quality of the associated work.

While *AJNR* maintains a policy of author anonymity, we found that authors either forgot or intentionally failed to eliminate mention of institutions, affiliations, or previous work in 34.1% of instances of perceived unblinding. Other studies have also cited self-referencing patterns as a frequent source of unblinding.[24] It may be possible to increase authors' compliance with the policy on author anonymity by having journal staff remove self-citations in the manuscript before sending it out for review. Instructions for authors should also emphasize avoiding the use of the first person in their writing. For example, phrases such as "we have shown that" should be replaced with "Jones et al have shown that."[25] It has been recommended that authors avoid the use of 3 or more references from the same individual and avoid citations that are "in press," because these typically reflect work by the same author or institution.[25] In the latter case, reviewers may not have access to these unpublished references. These tasks might increase the workload for journal administrative staff. However, such additional effort may decrease the authors' vulnerability to potential reviewer bias and may also improve the quality of the reviews.[26,27]

In some instances of unblinding, a reviewer may have previously reviewed the manuscript as a submission to a different journal before *AJNR* received it because there is a small pool of experts available for certain specialized topics. In a study evaluating factors that influence successful blinding, it was found that in 3 medical journals with a longstanding policy of blinding author identity, reviewers who spent more time in

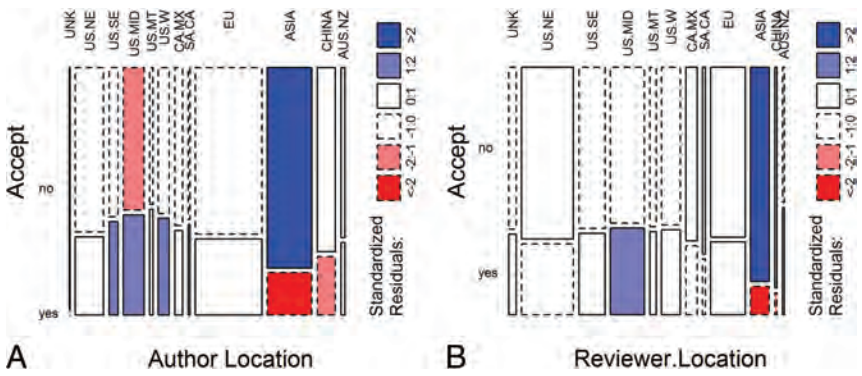

FIG 2. Mosaic plots graphically displaying data from 12 × 2 contingency tables. *A*, Author location is associated with a differential rate of manuscript acceptance. In the United States, with the exception of the northeast and mountain states, manuscripts are accepted at a higher rate. Manuscripts from Asia and China have a lower-than-expected acceptance rate. *B*, Reviewer location is associated with a differential rate of manuscript acceptance. Reviewers from the Midwest are more likely to accept a manuscript than would be expected, and reviewers from Asia are more likely to reject manuscripts. The area of each cell represents the frequency of each of the unique combinations of variable levels. The "standardized residual" is the residual divided by its SD. Therefore, the standardized residual rating represents the degree to which the 2 categoric variables are independent of each other, in units of SD (http://www.r-tutor.com/elementary-statistics/simple-linear-regression/standardized-residual).

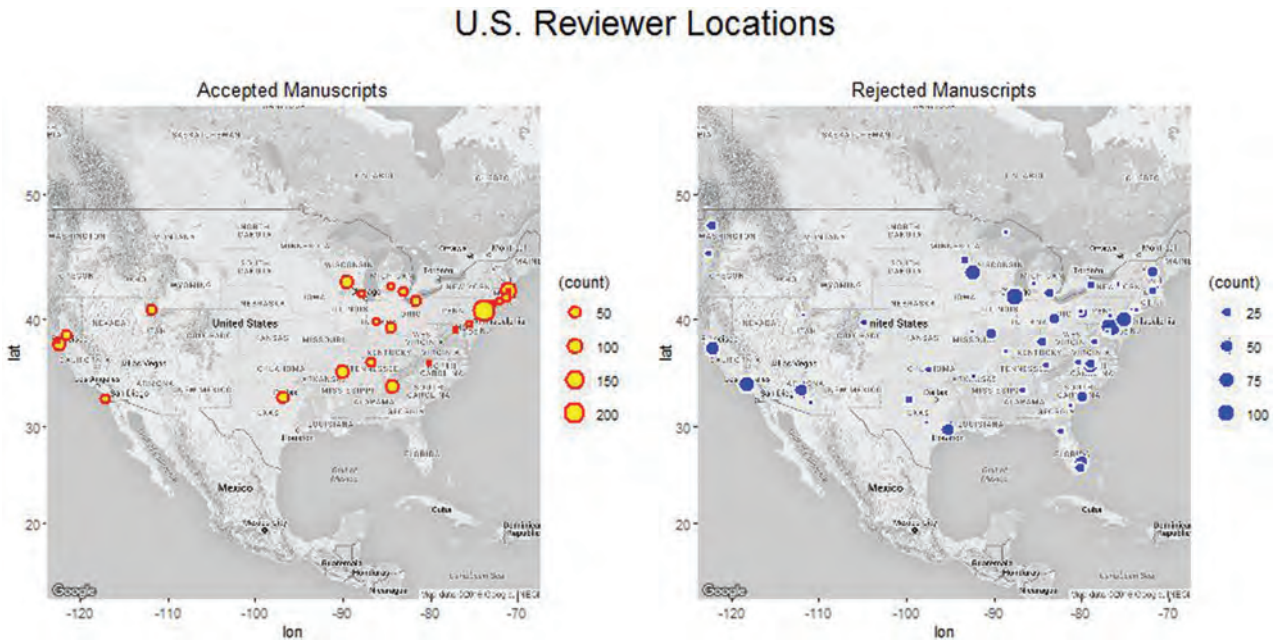

FIG 3. Reviewer locations for accepted and rejected manuscripts, while highly associated, are not distributed uniformly across the United States. This density distribution follows the distribution of diagnostic radiologists.

research were less likely to be successfully blinded.[28] While using reviewers with less research and reviewing experience increased the success of blinding by journals, it is uncertain how this strategy affects review quality. One study showed that younger age, lower academic rank, employment at a strong academic institution, knowledge of the editor, and previous referee experience are reviewer characteristics associated with higher quality reviews.[27,29] Higher review quality has also been shown to be associated with reviewers with training in epidemiology and statistics.[30] Another study has shown that younger and more experienced referees tend to provide stricter assessments of manuscript quality than more senior or less experienced colleagues.[31] It has also been shown that authors and editors perceived no difference in the quality of blinded and unblinded reviews.[16,20,32]

Peer review is intended to improve the publication process by helping editors select high-quality articles that are appropriate for the journal. It is also intended to improve the written presentation of the articles selected for publication.[33] Double-blind peer review is designed to protect both authors and reviewers. Our study shows that the double-blind peer review process used at *AJNR* effectively maintains double anonymity in most instances.

At a time when the millennial generation is joining the medical and scientific community, the possibility of an open or hybrid review system could be considered.[34] In an open system, scientists post their articles on dedicated Web sites to undergo a review process in which authors and reviewers are known to each other.[22,35] After nominated referees and other interested scientists post their comments regarding the work, the disposition for publication is determined. Proponents of this system argue that it increases transparency, incentivizes reviewers to be constructive in their critiques, and expedites the publication process.[22,35] *The British Journal of Psychiatry* conducted a randomized controlled trial of open peer review, in which referees were asked to sign their reviews. Not only did most referees agree to sign their reviews, but the signed review quality was higher and more courteous than anonymized reviews. Signed reviews also took longer to complete.[36]

When the *British Medical Journal* conducted a randomized trial of referees revealing their identity to authors in the peer review process, there were no effects on editors' ratings of the quality of the reviews provided or on manuscript disposition or the time taken to review. There was, however, a likelihood of referees declining to review.[32] Some journals that have tried an open review system have had less favorable results. For example, when *Nature* tried an open peer review system in 2006, only a small proportion of authors opted to participate in the open system, and of authors who did participate, few received technically substantive comments.[37] Currently, most journals are reluctant to adopt such a system because it can increase the time to final disposition, result in several article versions that may be confusing, may be associated with reviews of lesser quality than those from invited reviewers, and have fewer valuable reviews.[13]

A hybrid review system in which only selected articles undergo the open peer review process may provide the scientific community with exposure to this process before making a determination about its general viability. Nevertheless, whether an open or hybrid review system would be better for *AJNR* than the current double-blind peer review system is an open question because the current system is largely effective in minimizing potential biases against authors.

An editor takes responsibility for the quality of advice on the disposition of manuscripts. A judicious editor can prevent many of the abuses that a more open review system is intended to prevent, such as hostile comments, unsubstantiated criticisms, and delay of competitors' manuscripts.[38] We believe that scientific evaluation of the peer review process is of value to scientific journals because it will support them in maintaining the credibility of the publication process and demonstrating commitment to improving the process when needed. In addition, government agencies have taken interest in the peer review process during the past decade, emphasizing the importance of maintaining confidentiality,[39] improving the integrity of the prepublication process, and encouraging research groups to optimize their review systems.[34] Perhaps there could be more emphasis in the *AJNR* editorial process on the authors' responsibility to maintain anonymity. For example, instead of stating "our previous work," authors could be encouraged to say that "previous studies have shown."

Study Limitations

In this study, reviewers' experience with the manuscript blinding process was studied during a 6-month period. Sampling the review process for a longer time and allowing assessment of changing reviewer pool effects are needed for generalization of our findings. Also, some geographic regions had relatively few associated authors or reviewers; this feature limits the strength of the inferences that can be drawn from these data. Our study was observational rather than experimental in design, due to the need for *AJNR* to uphold its policy of anonymity to authors and reviewers. While a randomized experimental design would allow equal numbers of blinded and unblinded reviews, reviewers' knowledge of whether they had been placed in the unblinded or blinded groups could bias their assessment of the manuscripts and influence the acceptance rate in ways that would be difficult to determine. Highly cited or well-published authors are more likely to submit high-quality manuscripts with an associated high likelihood of acceptance, and manuscripts from these authors are more likely to be recognized. Our study did not attempt to assess the confounding effects of manuscript quality, a potentially important factor influencing manuscript acceptance. Although it is possible that perceived unblinding and manuscript quality both influenced acceptances rates, further studies will be needed to isolate these effects. Finally, although our results are derived from sampling manuscripts in the relatively small field of neuroradiology, larger studies may allow generalization to a broader range of biomedical research.

CONCLUSIONS

The process of double-blind peer review used by *AJNR* is largely effective in minimizing reviewer bias. However, perceived unblinding of authors or institutions is associated with a higher rate of manuscript acceptance. There is also an association between author or reviewer geographic location and manuscript acceptance. Our results should motivate further study of double-blind peer review with a larger sample for a longer period.

REFERENCES

1. Glantz SA, Bero LA. **Inappropriate and appropriate selection of 'peers' in grant review.** *JAMA* 1994;272:114–16 CrossRef Medline
2. Rowland F. **The peer-review process.** *Learned Publishing.* 2002;15: 247–58 CrossRef
3. Weller AC. *Editorial Peer Review: Its Strengths and Weaknesses.* Medford: Information Today, Inc; 2001
4. Choi M, Holliday EB, Jagsi R, et al. **Citation-based estimation of scholarly activity among domestic academic radiation oncologists: five-year update.** *J Radiat Oncol* 2014;3:115–22 CrossRef Medline
5. Jagsi R, Guancial EA, Worobey CC, et al. **The "gender gap" in authorship of academic medical literature: a 35-year perspective.** *N Engl J Med* 2006;355:281–87 CrossRef Medline
6. Budden AE, Tregenza T, Aarssen LW, et al. **Double-blind review favours increased representation of female authors.** *Trends Ecol Evol* 2008;23:4–6 CrossRef Medline
7. Wenneras C, Wold A. **Nepotism and sexism in peer-review.** *Nature* 1997;387:341–43 CrossRef Medline
8. Fisher M, Friedman SB, Strauss B. **The effects of blinding on acceptance of research papers by peer review.** *JAMA* 1994;272:143–46 CrossRef Medline
9. Ross JS, Gross CP, Desai MM, et al. **Effect of blinded peer review on abstract acceptance.** *JAMA* 2006;295:1675–80 CrossRef Medline
10. Link AM. **US and non-US submissions: an analysis of reviewer bias.** *JAMA* 1998;280:246–47 CrossRef Medline
11. Ernst E, Kienbacher T. **Chauvinism.** *Nature* 1991;352:560 CrossRef Medline
12. Peters DP, Ceci SJ. **Peer-review research: objections and obligations.** *Behavioral and Brain Sciences* 1982;5:246–55 CrossRef
13. Ware M. *Peer Review: Benefits, Perceptions and Alternatives.* London: Publishing Research Consortium; 2008:4
14. Brown RJ. **Double anonymity in peer review within the chemistry periodicals community.** *Learned Publishing* 2007;20:131–27 CrossRef
15. Baggs JG, Broome ME, Dougherty MC, et al. **Blinding in peer review: the preferences of reviewers for nursing journals.** *J Adv Nurs* 2008; 64:131–38 CrossRef Medline
16. Justice AC, Cho MK, Winker MA, et al. **Does masking author identity improve peer review quality? A randomized controlled trial.** *JAMA* 1998;280:240–42 CrossRef Medline
17. Ceci SJ, Peters D. **How blind is blind review?** *American Psychologist* 1984;39:1491 CrossRef
18. Yankauer A. **How blind is blind review?** *Am J Public Health* 1991;81: 843–45 CrossRef Medline
19. Blank RM. **The effects of double-blind versus single-blind reviewing: experimental evidence from the American Economic Review.** *The American Economic Review* 1991;81:1041–67
20. van Rooyen S, Godlee F, Evans S, et al. **Effect of blinding and unmasking on the quality of peer review: a randomized trial.** *JAMA* 1998;280:234–37 CrossRef Medline
21. Jagsi R, Bennett KE, Griffith KA, et al. **Attitudes toward blinding of peer review and perceptions of efficacy within a small biomedical specialty.** *Int J Radiat Oncol Biol Phys* 2014;89:940–46 CrossRef Medline
22. Lee CJ, Sugimoto CR, Zhang G, et al. **Bias in peer review.** *Journal of the American Society for Information Science and Technology* 2012;64: 2–17 CrossRef
23. Ware M. **Peer review in scholarly journals: perspective of the scholarly community—results from an international study.** *Information Services and Use* 2008;28:109–12
24. Katz DS, Proto AV, Olmsted WW. **Incidence and nature of unblinding by authors: our experience at two radiology journals with double-blinded peer review policies.** *AJR Am J Roentgenol* 2002;179: 1415–17 CrossRef Medline
25. Krinsky G. **How to avoid "unblinding" the peer review process.** *AJR Am J Roentgenol* 1999;172:1474 CrossRef Medline
26. McNutt RA, Evans AT, Fletcher RH, et al. **The effects of blinding on the quality of peer review: a randomized trial.** *JAMA* 1990;263: 1371–36 CrossRef Medline
27. Evans AT, McNutt RA, Fletcher SW, et al. **The characteristics of peer reviewers who produce good-quality reviews.** *J Gen Intern Med* 1993;8:422–28 Medline
28. Cho MK, Justice AC, Winker MA, et al. **Masking author identity in peer review: what factors influence masking success? PEER Investigators.** *JAMA* 1998;280:243–45 CrossRef Medline
29. Stossel TP. **Reviewer status and review quality: experience of the Journal of Clinical Investigation.** *N Engl J Med* 1985;312:658–59 CrossRef Medline
30. Black N, van Rooyen S, Godlee F, et al. **What makes a good reviewer and a good review for a general medical journal?** *JAMA* 1998;280: 231–33 CrossRef Medline
31. Nylenna M, Riis P, Karlsson Y. **Multiple blinded reviews of the same two manuscripts: effects of referee characteristics and publication language.** *JAMA* 1994;272:149–51 CrossRef Medline
32. Van Rooyen S, Godlee F, Evans S, et al. **Effect of open peer review on quality of reviews and on reviewers' recommendations: a randomised trial.** *BMJ* 1999;318:23–27 CrossRef Medline
33. Fletcher RH, Fletcher SW. **Evidence for the effectiveness of peer review.** *Science and Engineering Ethics* 1997;3:35–50 CrossRef
34. Castillo M. **Peer review: past, present, and future.** *AJNR Am J Neuroradiol* 2012;33:1833–35 CrossRef Medline
35. Cartlidge E. **Peer review steps out of the shadows.** *Physics World* 2007;20:29 CrossRef
36. Walsh E, Rooney M, Appleby L, et al. **Open peer review: a randomised controlled trial.** *Br J Psychiatry* 2000;176:47–51 CrossRef Medline
37. Greaves S, Scott J, Clarke M, et al. **Nature's trial of open peer review.** *Nature* 2006. doi:10.1038/nature05535 CrossRef
38. **Pros and cons of open peer review.** *Nat Neurosci* 1999;2:197–98 Medline
39. Berger E. **The JAMA and NEJM rulings and their impact on the sanctity of confidential peer review.** *Ann Emerg Med* 2008;51:737–39 CrossRef

Glass Half Full

In this issue, O'Connor and colleagues[1] report a study on the efficacy of double-blind peer review in the *American Journal of Neuroradiology* (*AJNR*). They found that 12.7% of reviewers thought or suspected that they knew the authors' identities. Most of the time when the reviewers thought they knew, they did—some 90% chose correctly. Several questions and interesting points are raised by this article:

1) Does this mean peer review doesn't work and that double-blind peer review is going away in *AJNR*? No.

Keep in mind that approximately 87% of the time, the blind held. Being a glass-half-full person, and knowing firsthand the incredible variety of manuscripts and writing styles that we encounter, that number seems a remarkably good data point. The literature attests to the overall high quality of the blinding process as it is applied in the *AJNR*, with previous publications reporting the blind can be broken 25%–46% of the time.[2,3] The *AJNR* currently has the lowest rate of unblinding in the literature.

2) When the blind is broken, does it harm the author's chance of having the manuscript accepted? Interestingly, this would seem to increase the chance of publication. There may be bias involved, but the bias helps the author. This effect has also been previously reported in that proportionally fewer manuscripts are published when there is no idea of the author's identity versus knowing the identity.[3,4] Perhaps the confounding aspect of the unblinding is that the well-known authors are well known for a very good reason, such as consistently producing good science.

3) As pointed out in the article, some of the onus is on us as the editors and staff to correctly modify the incoming articles to make them more neutral, where possible. Some of the onus, however, is on the author to write in a neutral style that does not include obvious self-citation or specific identifying information. You are proud of your previous work, and that work may have formed the basis for your current research, but keep the concept of double-blind review in your mind as the manuscript is written.

Sometimes, it is not possible to adequately blind the manuscript without gutting the manuscript of the necessary background information the reviewer will need to make an informed decision. The following are a few examples we have encountered in the past few months (scrubbed and sanitized to protect the innocent). How would you deal with these cases?

- Referencing a previously published patient cohort to either report a subset analysis or to reference the cohort demographics, inclusion criteria, outcome measures, etc.
- Use of prior publication conclusions to justify the current manuscript (eg, a recent study of X showed differences in Y, which we evaluated in this study of Z).
- Data from the previous intervention X have been reported.
- This study is part of the XYZ Foundation study into imaging of Q.
- Intervention X is the standard management of Q at our institution.
- We have used the XYZ sequence as previously performed by Q.
- A population-based study of XYZ imaging located in the Kingdom of Latveria. (Gold star if you recognize this location without a search engine.)

As O'Connor et al[1] concluded, "the double-blind peer review process used at *AJNR* effectively maintains double anonymity in most instances." We will continue to strive for better blinding on the editorial side, and with you on the author side, that is a realistic goal. To paraphrase Winston Churchill's democracy quote: Double-blind peer review is the worst form of review, except all the others that have been tried.

REFERENCES

1. O'Connor EE, Cousar M, Lentini JA, et al. **Efficacy of double-blind peer review in an imaging subspecialty journal.** *AJNR Am J Neuroradiol* 2016 Nov 17. [Epub ahead of print] CrossRef
2. Fisher M, Friedman SB, Strauss B. **The effects of blinding on acceptance of research papers by peer review.** *JAMA* 1994;272:143–46 CrossRef Medline
3. Isenberg SJ, Sanchez E, Zafran KC. **The effect of masking manuscripts for the peer-review process of an ophthalmic journal.** *Br J Ophthalmol* 2009;93:881–84 CrossRef Medline
4. Okike K, Hug KT, Kocher MS, et al. **Single-blind vs double-blind peer review in the setting of author prestige.** *JAMA* 2016;316:1315–16 CrossRef Medline

J.S. Ross
Editor-in-Chief

http://dx.doi.org/10.3174/ajnr.A5047

Utility of a Multiparametric Quantitative MRI Model That Assesses Myelin and Edema for Evaluating Plaques, Periplaque White Matter, and Normal-Appearing White Matter in Patients with Multiple Sclerosis: A Feasibility Study

A. Hagiwara, M. Hori, K. Yokoyama, M.Y. Takemura, C. Andica, K.K. Kumamaru, M. Nakazawa, N. Takano, H. Kawasaki, S. Sato, N. Hamasaki, A. Kunimatsu, and S. Aoki

ABSTRACT

BACKGROUND AND PURPOSE: T1 and T2 values and proton density can now be quantified on the basis of a single MR acquisition. The myelin and edema in a voxel can also be estimated from these values. The purpose of this study was to evaluate a multiparametric quantitative MR imaging model that assesses myelin and edema for characterizing plaques, periplaque white matter, and normal-appearing white matter in patients with MS.

MATERIALS AND METHODS: We examined 3T quantitative MR imaging data from 21 patients with MS. The myelin partial volume, excess parenchymal water partial volume, the inverse of T1 and transverse T2 relaxation times (R1, R2), and proton density were compared among plaques, periplaque white matter, and normal-appearing white matter.

RESULTS: All metrics differed significantly across the 3 groups ($P < .001$). Those in plaques differed most from those in normal-appearing white matter. The percentage changes of the metrics in plaques and periplaque white matter relative to normal-appearing white matter were significantly more different from zero for myelin partial volume (mean, $-61.59 \pm 20.28\%$ [plaque relative to normal-appearing white matter], and mean, $-10.51 \pm 11.41\%$ [periplaque white matter relative to normal-appearing white matter]), and excess parenchymal water partial volume ($13.82 \times 10^3 \pm 49.47 \times 10^3\%$ and $51.33 \times 10^2 \pm 155.31 \times 10^2\%$) than for R1 ($-35.23 \pm 13.93\%$ and $-6.08 \pm 8.66\%$), R2 ($-21.06 \pm 11.39\%$ and $-4.79 \pm 6.79\%$), and proton density ($23.37 \pm 10.30\%$ and $3.37 \pm 4.24\%$).

CONCLUSIONS: Multiparametric quantitative MR imaging captures white matter damage in MS. Myelin partial volume and excess parenchymal water partial volume are more sensitive to the MS disease process than R1, R2, and proton density.

ABBREVIATIONS: EDSS = Expanded Disability Status Scale; NAWM = normal-appearing white matter; PD = proton density; PWM = periplaque white matter; V_{CL} = cellular partial volume; V_{EPW} = excess parenchymal water partial volume; V_{FW} = free water partial volume; V_{MY} = myelin partial volume; $\%BPV_{EPW}$ = the percentage of excess parenchymal water volume in brain parenchyma; $\%BPV_{MY}$ = the percentage of myelin volume in brain parenchyma; QRAPMASTER = quantification of relaxation times and proton density by multiecho acquisition of a saturation-recovery using turbo spin-echo readout; R1 and R2 = inverse of T1 and transverse T2 relaxation times

MS is an inflammatory demyelinating disorder of the central nervous system, which mainly affects young adults. MR imaging plays a major role in the diagnosis and surveillance of patients with MS for initial and follow-up detection of focal cerebral lesions.[1] In addition to conventional MR imaging techniques including T2-weighted imaging, quantitative MR imaging techniques enable characterization of MS lesions and detection of otherwise hidden abnormalities in normal-appearing white matter (NAWM).[2,3] Moreover, diffusion tensor imaging and *q*-space imaging reveal abnormalities of white matter at the periphery of visible plaques on conventional MR images (periplaque white matter [PWM]) and NAWM[4,5]: The fractional anisotropy and apparent diffusion coefficient measured by diffusion tensor imaging and root mean square displacement measured by *q*-space imaging were worst in plaques, and in PWM, worse than in NAWM.

A recently developed MR imaging quantification pulse se-

Received June 13, 2016; accepted after revision August 29.

From the Department of Radiology (A.H., A.K.), Graduate School of Medicine, University of Tokyo, Tokyo, Japan; Departments of Radiology (A.H., M.H., M.Y.T., C.A., K.K.K., M.N., N.T., H.K., S.S., N.H., S.A.) and Neurology (K.Y.), Juntendo University School of Medicine, Tokyo, Japan; and Department of Radiological Sciences (M.N.), Graduate School of Human Health Sciences, Tokyo Metropolitan University, Tokyo, Japan.

This work was supported by: the Japan Society for the Promotion of Science, KAKENHI grant No. 16K19852; the program for Brain Mapping by Integrated Neurotechnologies for Disease Studies (Brain/MINDS) from Japan Agency for Medical Research and Development (AMED); and a Grant-in-Aid for Scientific Research on Innovative Areas (ABiS) from the Ministry of Education, Culture, Sports, Science and Technology of Japan. This work was funded by the Impulsing Paradigm Change through disruptive Technologies (ImPACT) Program of Council for Science, Technology and Innovation (Cabinet Office, Government of Japan).

Please address correspondence to Akifumi Hagiwara, MD, Department of Radiology, Graduate School of Medicine, University of Tokyo, 7-3-1, Hongo, Bunkyo-ku, Tokyo, Japan, 113-8655; e-mail: ahagiwara-tky@umin.ac.jp

http://dx.doi.org/10.3174/ajnr.A4977

quence, QRAPMASTER (quantification of relaxation times and proton density by multiecho acquisition of a saturation-recovery using turbo spin-echo readout), has made it possible to quantify longitudinal T1 and transverse T2 relaxation times, their inverses R1 and R2, and proton density (PD) in a single acquisition in a clinically acceptable time.[6] A phantom study has shown that these measurements are sufficiently accurate and reproducible for use in clinical practice.[7] Several studies have also shown the validity of this sequence in evaluating diseases such as metastatic brain tumors[8] and Sturge-Weber syndrome,[9,10] in addition to MS.[11] Even though the synthetic FLAIR image has lower image quality than the conventional FLAIR image, synthetic MR imaging overall has been shown to have comparable diagnostic power with conventional MR imaging for MS, while additionally offering fast and robust volumetry.[11] By using the QRAPMASTER pulse sequence, the R1, R2, and PD values of plaques, NAWM, and diffusely abnormal white matter of patients with MS were shown to be different from those of white matter in healthy controls.[12] Furthermore, the myelin partial volume (V_{MY}) and excess parenchymal water partial volume (V_{EPW}) can now be estimated from R1, R2, and PD,[13] to indicate the quantities of myelin and edema, respectively, in the brain. In the pathologic brain, a decrease in V_{MY} indicating myelin loss or an increase in V_{EPW} indicating edema will occur in this model. This model postulates 4 partial volume compartments: V_{MY}, the cellular partial volume (V_{CL}), the free water partial volume (V_{FW}), and V_{EPW}. The model assumes that each compartment has its own R1, R2, and PD values and that the relaxation behaviors of all 4 compartments contribute to the effective R1, R2, and PD values of an acquisition voxel. V_{MY} contains myelin water and myelin macromolecules. V_{CL} contains intracellular water, extracellular water, and nonmyelin macromolecules. Myelin water is trapped between myelin sheaths and has a much shorter T2 relaxation time than intracellular and extracellular water. The commonly calculated myelin water fraction corresponds to PD in the V_{MY}. The proportional relation between myelin water fraction and myelin content has been validated by histopathology.[14,15] V_{EPW}, or edema, adds water to the V_{CL}. Because no distinction can be made between excess water and the already present water in the V_{CL}, the magnetization exchange rate between V_{EPW} and V_{CL} is assumed to be infinitely high. V_{MY} and V_{EPW} may reflect the disease burden of patients with MS more specifically than R1, R2, and PD.

The aim of this study was to evaluate this multiparametric quantitative MR imaging model that assesses myelin and edema for characterizing plaques, PWM, and NAWM in patients with MS.

MATERIALS AND METHODS

Study Participants

The present study was approved by the institutional review board of Juntendo University Hospital, Japan. Given its retrospective nature, written informed consent was waived. All patient information was anonymized and de-identified before analysis. Data from 36 consecutive patients with MS who underwent quantitative MR imaging from April 2015 through November 2015 were retrospectively reviewed. These patients were diagnosed according to standard criteria.[1,16,17] Of the 36 patients, 15 had diffusely abnormal white matter[18] and were excluded from the study because it was difficult to adequately evaluate MS focal lesions in these patients. Therefore, 21 patients (4 males and 17 females; mean age, 38.3 years; age range, 16–61 years) were included in the analysis. Of these, 18 had relapsing-remitting MS and 3 had clinically isolated syndrome. The mean score on the Expanded Disability Status Scale (EDSS)[19] at image acquisition was 0.8 (range, 0–6.0), and the mean disease duration was 7.1 ± 4.8 years. With the exception of 1 plaque in 1 patient, no new lesion was detected on conventional MR imaging since the last ones obtained at least 4 months earlier. All patients were clinically stable for at least 6 months, except 1 who presumably had optic neuritis 2 months before MR imaging but showed no new lesion on conventional MR imaging.

MR Imaging

All MR imaging sequences were performed on a 3T scanner (Discovery MR750w; GE Healthcare, Milwaukee, Wisconsin) with a 12-channel head coil. All patients underwent quantitative axial MR imaging and conventional axial T1-weighted inversion recovery, T2-weighted, and FLAIR imaging.

Quantitative MR imaging was performed by using the 2D axial QRAPMASTER pulse sequence.[6] This pulse sequence is a multisection, multiecho, multisaturation delay method of saturation-recovery acquisition by a turbo spin-echo readout, with which images are obtained by different combinations of TE and saturation delay time. In this study, 2 sets of TE values and 4 sets of delay time values were used to generate 8 real images and 8 imaginary images in 1 section to quantify longitudinal T1 and transverse T2 relaxation times as well as the PD. The TE values used were 16.9 and 84.5 ms, and the delay time was set as defined by the manufacturer (SyntheticMR, Linköping, Sweden). The parameters used for quantitative MR imaging were as follows: FOV, 240 × 240 mm; matrix, 320 × 320; echo-train length, 10; bandwidth, 31.25 kHz; section thickness/gap, 4.0/1.0 mm; number of sections, 30.

On the basis of the assumption that R1, R2, and PD values of V_{MY}, V_{EPW}, V_{CL}, and V_{FW} all contribute to the effective R1, R2, and PD in a voxel, a model was created to estimate partial volumes of these 4 compartments by running Bloch equations and setting up a cost function in a spatially normalized and averaged brain from a group of 20 healthy controls described by Warntjes et al.[13] Using this model, we created V_{MY} and V_{EPW} maps from R1, R2, and PD maps. This procedure was automatically performed by SyMRI software (Version 8.0; SyntheticMR). The R1, R2, and PD maps were then used to create synthetic MR images. Conventional T1-weighted inversion recovery images were obtained by using the following parameters: TR, 3294 ms; TE, 18 ms; TI, 908 ms; FOV, 240 × 216 mm; matrix, 352 × 256; echo-train length, 8; section thickness/gap, 4.0/1.0 mm; number of sections, 30. T2-weighted images were obtained by using TR, 4500 ms; TE, 111 ms; FOV, 240 × 240 mm; matrix, 512 × 512; echo-train length, 24; section thickness/gap, 4.0/1.0 mm; number of sections, 30. FLAIR images were obtained by using TR, 9000 ms; TE, 124 ms; TI, 2472 ms; FOV, 240 × 240 mm; matrix, 320 × 224; echo-train length, 16; section thickness/gap, 4.0/1.0 mm; number of sections, 30. Conventional MR images were obtained at the same sections as the quantitative MR images.

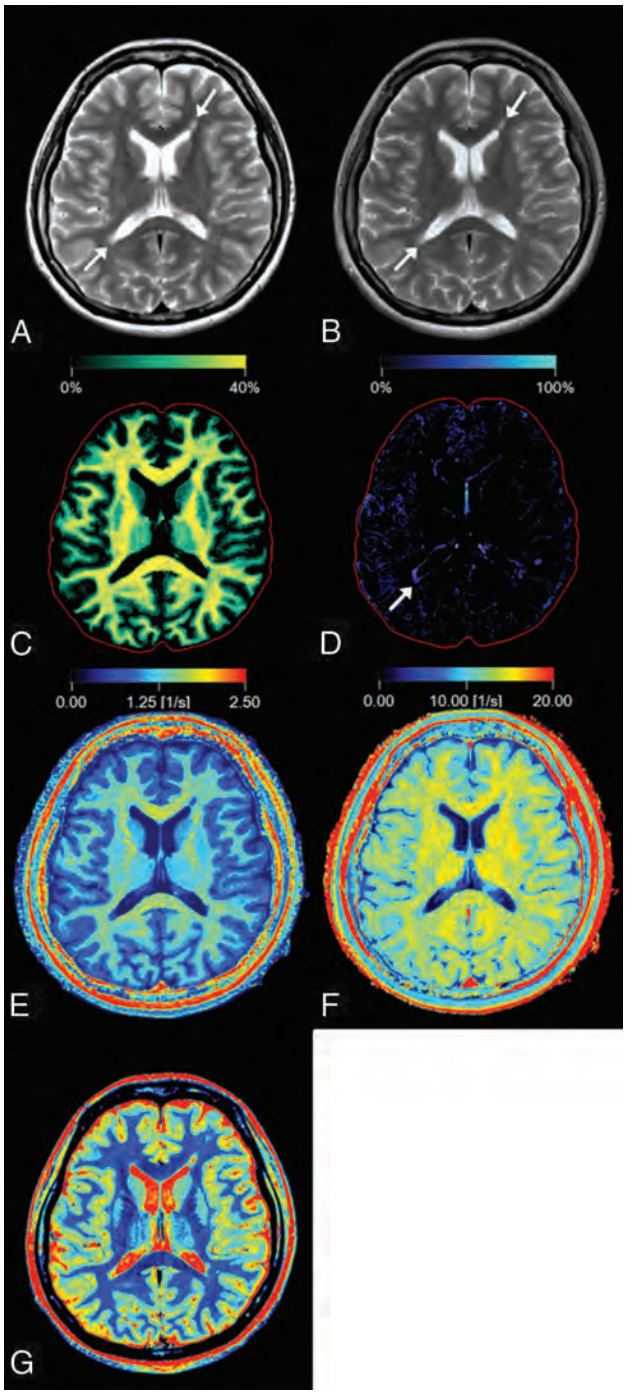

FIG 1. Representative images of a 27-year-old woman with multiple sclerosis. Panels show a synthetic T2-weighted image (*A*), a conventional T2-weighted image (*B*), and maps of myelin partial volume (*C*), excess parenchymal water partial volume (*D*), R1 (*E*), R2 (*F*), and PD (*G*). Two plaques are shown by *arrows* on the T2-weighted images (*A* and *B*). On the V_{EPW} map (*D*), the periphery of the plaque adjacent to the trigone of the right ventricle (*arrow*) is visible but the one adjacent to the anterior horn of the left ventricle is not. The V_{EPW} of this invisible plaque was very low but still higher than that of NAWM. The *red intracranial outline* is displayed for visual guidance in tissue images (*C* and *D*).

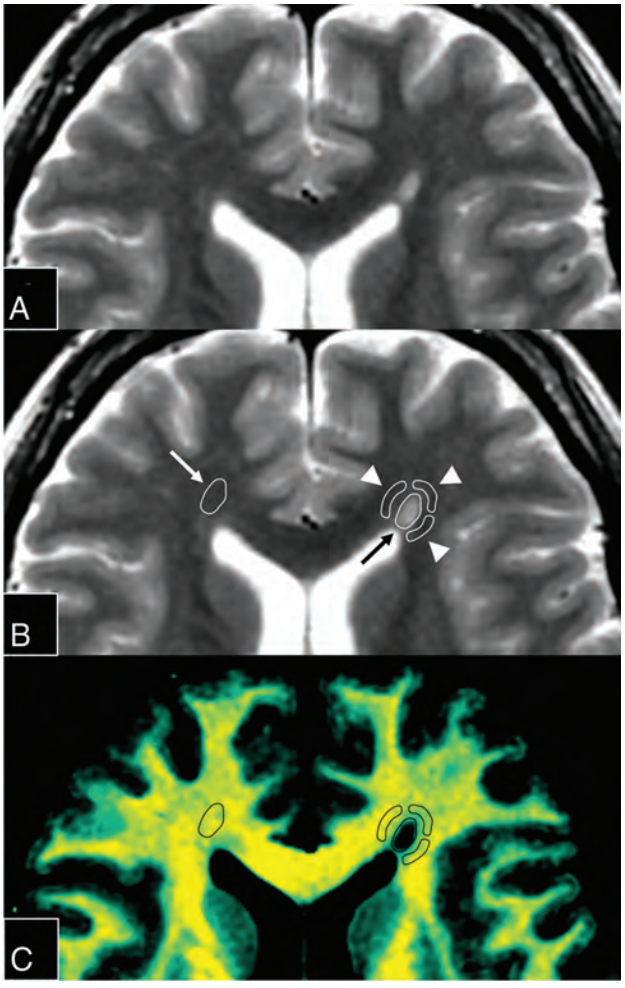

FIG 2. Magnified images of Fig 1*A*. The upper 2 panels show the same synthetic T2-weighted image without (*A*) or with (*B*) placement of ROIs. An ROI (*black arrow*) was drawn on a plaque adjacent to the left anterior horn, and 3 ROIs (*arrowheads*) were placed on periplaque white matter to encircle the plaque. The fourth ROI on PWM was discarded because it overlapped the CSF. The ROI of the plaque was copied and pasted onto the contralateral normal-appearing white matter (*white arrow*). These ROIs were then copied and pasted onto each quantification map. A map of the corresponding myelin partial volume (*C*) is shown as an example.

Image Analysis

Synthetic T2-weighted images and maps of V_{MY}, V_{EPW}, R1, R2, and PD were created from raw quantification data by the SyMRI software on a commercial personal computer and converted to DICOM files (Fig 1). Synthetic T2-weighted images were produced by using the following parameters: TR, 4500 ms; TE, 100 ms. These data were then analyzed by OsiriX Imaging Software, Version 7.0.3 (http:// www.osirix-viewer.com). ROIs were drawn on plaques, PWM, and NAWM on synthetic T2-weighted images. A plaque was defined as an area of abnormally high intensity, >5 mm, on a T2-weighted image; PWM was defined as a normal-intensity white-matter area closest to a plaque; and NAWM was defined as a normal-intensity area contralateral to a plaque.[4,5] An experienced neuroradiologist (A.H.) used conventional and synthetic images to confirm 135 plaques, which were then analyzed. A single investigator (M.N.), blinded to the clinical information, manually placed ROIs on T2-weighted images. A freehand ROI was drawn to encircle a plaque, after which up to 4 ROIs, approximately half the size of the initial ROI, were placed on the PWM of that plaque (Fig 2). The PWM ROIs were placed so that adjacent ROIs were approximately 90° apart to form a circle that sur-

rounded the plaque. A PWM ROI that overlapped CSF, gray matter, or other plaques was removed. Consequently, 128 PWM ROIs were discarded on this basis. The mean ROI size was 44.82 ± 29.12 mm^2 for a plaque and 21.19 ± 12.59 mm^2 for PWM. The ROI of a plaque was copied and pasted onto the contralateral NAWM. Finally, these ROIs were copied and pasted onto the maps of V_{MY}, V_{EPW}, R1, R2, and PD in the same patient, and the mean value of each ROI was recorded. The percentages of myelin and excess parenchymal water volume in brain parenchyma ($\%BPV_{MY}$ and $\%BPV_{EPW}$) were also calculated on SyMRI software and recorded.

Statistical Analysis

Statistical analysis was conducted with the software package R, Version 3.2.1 (http://www.R-project.org/). Not all data were normally distributed; therefore, we used the Steel-Dwass test, which is a nonparametric test for multiple comparisons, to compare the values of V_{MY}, V_{EPW}, R1, R2, and PD among plaques, PWM, and NAWM. The percentage change of plaques or PWM relative to NAWM was also calculated and compared among different metrics (ie, V_{MY}, V_{EPW}, R1, R2, and PD). The sign of this percentage change for V_{MY}, R1, and R2 was inverted for statistical analysis because overall, the values of these metrics were higher in NAWM than in plaques or PWM. EDSS and disease duration were correlated with $\%BPV_{MY}$ and $\%BPV_{EPW}$ by using the Spearman rank order correlation coefficient. A 2-sided P value $< .05$ was considered significant.

RESULTS

The results of ROI analysis and comparisons among plaques, PWM, and NAWM are shown in Table 1. All V_{MY}, V_{EPW}, R1, R2, and PD values differed significantly among plaques, PWM, and NAWM. V_{MY} was lower in plaques and PWM than in NAWM, with plaques showing the lowest value; V_{EPW} was higher in plaques and PWM than in NAWM, with plaques showing the highest value; R1 was lower in plaques and PWM than in NAWM, with plaques showing the lowest value; R2 was lower in plaques and PWM than in NAWM, with plaques showing the lowest value; and PD was higher in plaques and PWM than in NAWM, with plaques showing the highest value.

The percentage changes of V_{MY}, V_{EPW}, R1, R2, and PD in plaques and PWM relative to NAWM are shown in Table 2. Those of V_{EPW} in plaques and PWM relative to NAWM were significantly more different from zero than those of V_{MY}, R1, R2, and PD; those of V_{MY} in plaques and PWM relative to NAWM were significantly more different from zero than those of R1, R2, and PD.

To confirm the accuracy of the evaluation, the experienced neuroradiologist (A.H.) randomly selected 5 patients with 24 plaques and performed an ROI analysis for V_{MY} in the same manner. The interobserver reproducibility was measured between the 2 observers (M.N. and A.H.): interclass correlation coefficient for plaques, 0.86 (95% CI, 0.71–0.94); interclass correlation coefficient for PWM, 0.81 (95% CI, 0.62–0.91); interclass correlation coefficient for NAWM, 0.83 (95% CI, 0.64–0.92).

Significant correlations with EDSS and disease duration were not found with $\%BPV_{MY}$ and $\%BPV_{EPW}$ (EDSS versus $\%BPV_{MY}$, $P = .463$; EDSS versus $\%BPV_{EPW}$, $P = .758$; disease duration versus $\%BPV_{MY}$, $P = .99$; and disease duration versus $\%BPV_{EPW}$, $P = .488$).

DISCUSSION

The result of lower R1, lower R2, and higher PD in plaques than in NAWM is consistent with the results of a previous report.[12] Our report is the first to show that these measurements in PWM take values between plaques and NAWM. The finding that abnormal measurements extended beyond plaques agrees with previous studies of histology,[20,21] MR spectroscopy,[22] and MR diffusion metrics.[4,5] The MS disease process extends beyond the borders of visible plaques on conventional T2-weighted images.[4] Specifically, histologic studies have shown that Wallerian degeneration and retrograde degeneration of the cell body occur around demyelinating plaques.[23,24] The fact that axonal degeneration causes myelin degradation[25] suggests that demyelination in plaques leads to reduced V_{MY} in PWM. Another explanation for decreased V_{MY} in PWM can be found in the natural history of MS plaque evolution and regression. An MS plaque enlarges and regresses in a concentric manner around a small vein.[26] Therefore, partial remyelination without gliosis in PWM after regression of an MS plaque may lead to decreased V_{MY}, even after once hyperintense PWM on the T2-weighted image has already been normalized.

In this study, V_{EPW}, which reflects the amount of edema, was higher in plaques and PWM than in NAWM. It has been shown that the *aquaporin 4* gene is upregulated in PWM and even

Table 1: Descriptive values of plaques, periplaque white matter, and normal-appearing white matter[a]

	V_{MY} (%)	V_{EPW} (%)	R1 (s^{-1})	R2 (s^{-1})	PD (%)
Plaques	12.59 ± 6.66	5.82 ± 4.75	0.90 ± 0.20	10.88 ± 1.41	78.86 ± 6.35
PWM	29.29 ± 3.73	2.31 ± 2.38	1.31 ± 0.13	13.14 ± 0.77	68.09 ± 2.49
NAWM	32.88 ± 3.12	0.92 ± 1.90	1.40 ± 0.08	13.85 ± 0.97	63.97 ± 2.07

[a] Values are mean ± SD. $P < .001$ for all metrics among each tissue type.

Table 2: Percentage changes of V_{MY}, V_{EPW}, R1, R2, and PD in plaques and periplaque white matter relative to normal-appearing white matter[a]

	V_{MY} (%)	V_{EPW} (%)	R1 (%)	R2 (%)	PD (%)
Plaques	−61.59 ± 20.28[b]	$13.82 \times 10^3 \pm 49.47 \times 10^3$[b]	−35.23 ± 13.93[b]	−21.06 ± 11.39[b]	23.37 ± 10.30[b]
PWM	−10.51 ± 11.41[c]	$51.33 \times 10^2 \pm 155.31 \times 10^2$[c]	−6.08 ± 8.66[c]	−4.79 ± 6.79[c]	3.37 ± 4.24[b]

[a] Values are mean ± SD. Of the 135 ROIs, 39 were discarded after calculating the percentage change of V_{EPW} relative to NAWM because the V_{EPW} of these ROIs was equivalent to zero in NAWM.

[b] $P < .001$ in the percentage change for plaques relative to NAWM for comparison between each pair of metrics, except between R2 and PD ($P = .31$). Statistical analysis was performed for absolute values.

[c] $P < .001$ in the percentage change for PWM relative to NAWM between V_{EPW} and other metrics, and between V_{MY} and R2 or PD, $P < .05$ between V_{MY} and R1, and $P > .05$ between R2 and R1 (.31) or PD (.30). Statistical analysis was performed for absolute values.

more in plaques.[21] It is suggested that this upregulation is for protecting damaged tissue from disturbed water balance. Our result of elevated V_{EPW} in these regions supports this speculation. Because MR spectroscopy results suggest that acute lesions are more edematous than chronic lesions,[27] V_{EPW} in a plaque may predict the acute status of a lesion (ie, its enhancement). Visual inspection of Fig 1*D* (*arrow*) reminds us of a ring-pattern enhancement with the V_{EPW} for a plaque higher in its periphery than in its center. Given that blood-brain barrier disruption and edema formation are correlated phenomena,[28] a higher V_{EPW} may suggest the existence of blood-brain barrier disruption. Although R1, R2, and PD are good predictors of lesion enhancement,[29] the combination of V_{MY} and V_{EPW} may be a better predictor because it provides a more specific description of a lesion. This conjecture was not validated here because almost all lesions investigated were chronic and no contrast medium was used. In this study, V_{MY} and V_{EPW} were more sensitive in showing abnormalities in plaques and PWM than R1, R2, and PD. Therefore, V_{MY} and V_{EPW} are potentially more sensitive biomarkers of the disease process than R1, R2, and PD, especially in patients with MS.

Radiologic-pathologic correlations of plaques, diffusely abnormal white matter, and NAWM have been well-established, with axonal loss and decreased myelin density most severe in plaques and more severe in diffusely abnormal white matter than in NAWM.[18] Even though PWM has been investigated radiologically[4,5] and pathologically[21] so far, currently no study has correlated the normal-appearing PWM on T2-weighted images with histology. Alterations of astrocyte functions in PWM have been demonstrated, which are accompanied by low-grade inflammation and a progressive loss of myelin without sufficient remyelination.[21] Future study should investigate normal-appearing PWM on T2-weighted images histologically, which we investigated by multiparametric MR imaging in this study.

No significant correlations with EDSS and disease duration were found with $\%BPV_{MY}$ and $\%BPV_{EPW}$ in this study. The correlation between the myelin water fraction, which is the PD of V_{MY} investigated in this study, of NAWM and EDSS has been shown in primary-progressive MS[30] but not in relapsing-remitting MS so far.[31] These investigations suggest that the myelin content in the NAWM of the severe progressive form of MS (ie, primary-progressive MS) correlates more with EDSS than that of the less progressive form (ie, relapsing-remitting MS), which was investigated in this study. This conjecture should be validated in a larger study that includes both subtypes of patients with MS and uses a single method of measuring myelin water fraction or V_{MY}.

There are a number of potential limitations to our study. First, our study included a small number of patients and did not include healthy controls. Second, the age and disease burdens of the patients varied widely; consequently, the specific pathology of plaques, PWM, and NAWM may have been diverse. This problem could be resolved in the future by studying a large population stratified by age and disease burden. Third, the multiparametric model used in this study was trained only for healthy brains. It needs validation in several studies, including our current one, and further refinement for patients with brain diseases. Last, although the multiparametric quantitative MR imaging model used in this study represented the amount of myelin by V_{MY}, axonal status was not specifically investigated. The axonal volume fraction can now be estimated from neurite orientation dispersion and density imaging and the myelin volume fraction.[32,33] Therefore, the axonal volume fraction will be combined with the myelin partial volume to further clarify the MS disease process in a future study.

CONCLUSIONS

V_{MY}, V_{EPW}, R1, R2, and PD were more abnormal in plaques and PWM than in NAWM, with plaques showing the most abnormal values. V_{MY} and V_{EPW} were more sensitive to the MS disease process than R1, R2, and PD. V_{MY} and V_{EPW} are useful estimators of disease burden in patients with MS.

Disclosures: Akifumi Hagiwara—*RELATED*: *Grant*: Japan Society for the Promotion of Science; Nao Takano—*UNRELATED*: *Payment for Lectures including Service on Speakers Bureaus*: GE Healthcare Japan, *Comments*: The 42nd Japanese Society of Radiological Technology Autumn Scientific Congress, October 9–11, 2014, Sapporo, Hokkaido, Japan: luncheon seminar "Experience of MR Angiography (Silent MRA) using the SILENZ Sequence." Akira Kunimatsu—*UNRELATED*: *Payment for Lectures including Service on Speakers Bureaus*: Siemens Japan, Toshiba, Philips Electronics Japan, Terumo; *Payment for Manuscript Preparation*: Bayer Yakuhin, GE Healthcare Japan. Shigeki Aoki—*RELATED*: *Grant*: Impulsing Paradigm Change through Disruptive Technologies (ImPACT) program of Council for Science, Technology and Innovation (Cabinet Office, Government of Japan), program for Brain Mapping by Integrated Neurotechnologies for Disease Studies (Brain/MINDS) from Japan Agency for Medical Research and development (AMED), Grant-in-Aid for Scientific Research on Innovative Areas (ABiS) from the Ministry of Education, Culture, Sports, Science and Technology of Japan.* *Money paid to the institution.

REFERENCES

1. Polman CH, Reingold SC, Banwell B, et al. **Diagnostic criteria for multiple sclerosis: 2010 revisions to the McDonald criteria.** *Ann Neurol* 2011;69:292–302 CrossRef Medline
2. Filippi M, Rocca MA, De Stefano N, et al. **Magnetic resonance techniques in multiple sclerosis: the present and the future.** *Arch Neurol* 2011;68:1514–20 CrossRef Medline
3. Giorgio A, De Stefano N. **Advanced structural and functional brain MRI in multiple sclerosis.** *Semin Neurol* 2016;36:163–76 CrossRef Medline
4. Guo AC, MacFall JR, Provenzale JM. **Multiple sclerosis: diffusion tensor MR imaging for evaluation of normal-appearing white matter.** *Radiology* 2002;222:729–36 CrossRef Medline
5. Hori M, Yoshida M, Yokoyama K, et al. **Multiple sclerosis: benefits of q-space imaging in evaluation of normal-appearing and periplaque white matter.** *Magn Reson Imaging* 2014;32:625–29 CrossRef Medline
6. Warntjes JB, Leinhard OD, West J, et al. **Rapid magnetic resonance quantification on the brain: optimization for clinical usage.** *Magn Reson Med* 2008;60:320–29 CrossRef Medline
7. Krauss W, Gunnarsson M, Andersson T, et al. **Accuracy and reproducibility of a quantitative magnetic resonance imaging method for concurrent measurements of tissue relaxation times and proton density.** *Magn Reson Imaging* 2015;33:584–91 CrossRef Medline
8. Hagiwara A, Hori M, Suzuki M, et al. **Contrast-enhanced synthetic MRI for the detection of brain metastases.** *Acta Radiol Open* 2016;5:2058460115626757 CrossRef Medline
9. Hagiwara A, Nakazawa M, Andica C, et al. **Dural enhancement in a patient with Sturge-Weber syndrome revealed by double inversion recovery contrast using synthetic MRI.** *Magn Reson Med Sci* 2016;15:151–52 CrossRef Medline
10. Andica C, Hagiwara A, Nakazawa M, et al. **The advantage of synthetic MRI for the visualization of early white matter change in an infant with Sturge-Weber syndrome.** *Magn Reson Med Sci* 2016 Mar 21. [Epub ahead of print] Medline

11. Granberg T, Uppman M, Hashim F, et al. **Clinical feasibility of synthetic MRI in multiple sclerosis: a diagnostic and volumetric validation study.** *AJNR Am J Neuroradiol* 2016;37:1023–29 CrossRef Medline
12. West J, Aalto A, Tisell A, et al. **Normal appearing and diffusely abnormal white matter in patients with multiple sclerosis assessed with quantitative MR.** *PLoS One* 2014;9:e95161 CrossRef Medline
13. Warntjes M, Engström M, Tisell A, et al. **Modeling the presence of myelin and edema in the brain based on multi-parametric quantitative MRI.** *Front Neurol* 2016;7:16 CrossRef Medline
14. Bjarnason TA, Vavasour IM, Chia CL, et al. **Characterization of the NMR behavior of white matter in bovine brain.** *Magn Reson Med* 2005;54:1072–81 CrossRef Medline
15. Laule C, Leung E, Lis DK, et al. **Myelin water imaging in multiple sclerosis: quantitative correlations with histopathology.** *Mult Scler* 2006;12:747–53 CrossRef Medline
16. McDonald WI, Compston A, Edan G, et al. **Recommended diagnostic criteria for multiple sclerosis: guidelines from the International Panel on the Diagnosis of Multiple Sclerosis.** *Ann Neurol* 2001;50:121–27 CrossRef Medline
17. Polman CH, Reingold SC, Edan G, et al. **Diagnostic criteria for multiple sclerosis: 2005 revisions to the "McDonald Criteria."** *Ann Neurol* 2005;58:840–46 CrossRef Medline
18. Seewann A, Vrenken H, van der Valk P, et al. **Diffusely abnormal white matter in chronic multiple sclerosis: imaging and histopathologic analysis.** *Arch Neurol* 2009;66:601–09 Medline
19. Kurtzke JF. **A new scale for evaluating disability in multiple sclerosis.** *Neurology* 1955;5:580–83 CrossRef Medline
20. Nijeholt GJ, Bergers E, Kamphorst W, et al. **Post-mortem high-resolution MRI of the spinal cord in multiple sclerosis: a correlative study with conventional MRI, histopathology and clinical phenotype.** *Brain* 2001;124:154–66 CrossRef Medline
21. Lieury A, Chanal M, Androdias G, et al. **Tissue remodeling in periplaque regions of multiple sclerosis spinal cord lesions.** *Glia* 2014;62:1645–58 CrossRef Medline
22. Narayanan S, Fu L, Pioro E, et al. **Imaging of axonal damage in multiple sclerosis: spatial distribution of magnetic resonance imaging lesions.** *Ann Neurol* 1997;41:385–91 CrossRef Medline
23. Perry VH, Anthony DC. **Axon damage and repair in multiple sclerosis.** *Philos Trans R Soc Lond B Biol Sci* 1999;354:1641–47 CrossRef Medline
24. Dziedzic T, Metz I, Dallenga T, et al. **Wallerian degeneration: a major component of early axonal pathology in multiple sclerosis.** *Brain Pathol* 2010;20:976–85 CrossRef Medline
25. Simons M, Misgeld T, Kerschensteiner M. **A unified cell biological perspective on axon-myelin injury.** *J Cell Biol* 2014;206:335–45 CrossRef Medline
26. McDonald WI, Miller DH, Barnes D. **The pathological evolution of multiple sclerosis.** *Neuropathol Appl Neurobiol* 1992;18:319–34 CrossRef Medline
27. Helms G, Stawiarz L, Kivisakk P, et al. **Regression analysis of metabolite concentrations estimated from localized proton MR spectra of active and chronic multiple sclerosis lesions.** *Magn Reson Med* 2000;43:102–10 Medline
28. Brosnan CF, Raine CS. **The astrocyte in multiple sclerosis revisited.** *Glia* 2013;61:453–65 CrossRef Medline
29. Blystad I, Hakansson I, Tisell A, et al. **Quantitative MRI for analysis of active multiple sclerosis lesions without gadolinium-based contrast agent.** *AJNR Am J Neuroradiol* 2016;37:94–100 CrossRef Medline
30. Kolind S, Matthews L, Johansen-Berg H, et al. **Myelin water imaging reflects clinical variability in multiple sclerosis.** *Neuroimage* 2012;60:263–70 CrossRef Medline
31. Faizy TD, Thaler C, Kumar D, et al. **Heterogeneity of multiple sclerosis lesions in multislice myelin water imaging.** *PLoS One* 2016;11:e0151496 CrossRef Medline
32. Zhang H, Schneider T, Wheeler-Kingshott CA, et al. **NODDI: practical in vivo neurite orientation dispersion and density imaging of the human brain.** *Neuroimage* 2012;61:1000–16 CrossRef Medline
33. Stikov N, Campbell JS, Stroh T, et al. **In vivo histology of the myelin g-ratio with magnetic resonance imaging.** *Neuroimage* 2015;118:397–405 CrossRef Medline

Quantifying Intracranial Plaque Permeability with Dynamic Contrast-Enhanced MRI: A Pilot Study

P. Vakil, A.H. Elmokadem, F.H. Syed, C.G. Cantrell, F.H. Dehkordi, T.J. Carroll, and S.A. Ansari

ABSTRACT

BACKGROUND AND PURPOSE: Intracranial atherosclerotic disease plaque hyperintensity and/or gadolinium contrast enhancement have been studied as imaging biomarkers of acutely symptomatic ischemic presentations using single static MR imaging measurements. However, the value in modeling the dynamics of intracranial plaque permeability has yet to be evaluated. The purpose of this study was to use dynamic contrast-enhanced MR imaging to quantify the contrast permeability of intracranial atherosclerotic disease plaques in symptomatic patients and to compare these parameters against existing markers of plaque volatility using black-blood MR imaging pulse sequences.

MATERIALS AND METHODS: We performed a prospective study of contrast uptake dynamics in the major intracranial vessels proximal and immediately distal to the circle of Willis using dynamic contrast-enhanced MR imaging, specifically in patients with symptomatic intracranial atherosclerotic disease. Using the Modified Tofts model, we extracted the volume transfer constant (K^{trans}) and fractional plasma volume (V_p) parameters from plaque-enhancement curves. Using regression analyses, we compared these parameters against time from symptom onset as well as intraplaque hyperintensity and postcontrast enhancement derived from T1 SPACE, a black-blood MR vessel wall imaging sequence.

RESULTS: We completed analysis in 10 patients presenting with symptomatic intracranial atherosclerotic disease. K^{trans} and V_p measurements were higher in plaques versus healthy white matter and similar or less than values in the choroid plexus. Only K^{trans} correlated significantly with time from symptom onset ($P = .02$). Dynamic contrast-enhanced MR imaging parameters were not found to correlate significantly with intraplaque enhancement or intraplaque hyperintensity ($P = .4$ and $P = .17$, respectively).

CONCLUSIONS: Elevated K^{trans} and V_p values found in intracranial atherosclerotic disease plaques versus healthy white matter suggest that dynamic contrast-enhanced MR imaging is a feasible technique for studying vessel wall and plaque characteristics in the proximal intracranial vasculature. Significant correlations between K^{trans} and symptom onset, which were not observed on T1 SPACE–derived metrics, suggest that K^{trans} may be an independent imaging biomarker of acute and symptom-associated pathologic changes in intracranial atherosclerotic disease plaques.

ABBREVIATIONS: BBMRI = black-blood MRI; DCE = dynamic contrast-enhanced; GRE = gradient recalled-echo; ICAD = intracranial atherosclerotic disease; IPE = intraplaque enhancement; IPH = intraplaque hyperintensity; K^{trans} = volume transfer constant; NAWM = normal-appearing white matter; SPACE = sampling perfection with application-optimized contrasts by using different flip angle evolution; SI = signal intensity; V_L = extracellular extravascular space; V_p = fractional plasma volume

Stroke is the third leading cause of death in the United States, with an incidence of approximately 800,000 per year. Intracranial atherosclerotic disease (ICAD) is responsible for approximately 7%–10% of these patients; however, the risk of recurrent stroke in this population approaches nearly 12%–25% over 1–2 years, despite aggressive medical management including anti-

Received April 4, 2016; accepted after revision August 22.

From the College of Medicine (P.V.), University of Illinois, Chicago, Illinois; Departments of Radiology (P.V., A.H.E., F.S., C.G.C., T.J.C., S.A.A.), Biomedical Engineering (P.V., C.G.C., T.J.C.), and Neurology and Neurological Surgery (S.A.A.), Northwestern University, Chicago, Illinois; and Department of Economics and Decision Sciences (F.H.D.), Western Illinois University, Macomb, Illinois.

This work was supported by the following grants: American Heart Association 13GRNT17340018 and 14GRNT20380798 (Principal Investigators: S.A. Ansari and T.J. Carroll); PRE20380810 (Principal Investigator: C.G. Cantrell); National Institutes of Health 1R21HL130969 (Principal Investigator: S.A. Ansari); 1R01NS089926 and 1R21EB017928 (Principal Investigator: T.J. Carroll).

Paper previously presented in part at: Annual Meeting of the European Congress of Radiology, March 2–6, 2016; Vienna, Austria and Annual Meeting of the American Society of Neuroradiology, May 23–26, 2016; Washington, DC. The abstract was published in *Insights Imaging* 2016;7:162. doi:10.1007/s13244-016-0475-8

Please address correspondence to Sameer A. Ansari, MD, PhD, Departments of Radiology, Neurology, and Neurological Surgery, Northwestern University, Feinberg School of Medicine, 676 N St. Clair St, Suite 800, Chicago, IL 60611-2927; e-mail: s-ansari@northwestern.edu

http://dx.doi.org/10.3174/ajnr.A4998

platelet or antithrombotic medications.[1,2] ICAD risk assessment for ischemic complications based on a simple degree of luminal narrowing (percentage stenosis) is imprecise, with complex pathology at the level of the plaque and/or downstream vascular distribution. Several groups have proposed improving patient risk stratification and plaque characterization by using black-blood MR imaging (BBMRI) with high (submillimeter) spatial and contrast resolution to directly analyze the intracranial vessel wall and atherosclerotic plaque.[3-6] Swartz et al[3] initially reported contrast enhancement of symptomatic ICAD plaques with 3T high-resolution BBMRI; later in a small cohort, they demonstrated qualitatively decreasing enhancement of symptomatic plaques from acute/subacute-to-chronic phases, suggesting plaque inflammation and transient destabilization as an etiology for thromboembolic complications.[4]

While ICAD plaque enhancement has been shown to be highly associated with recent cerebrovascular ischemic events, its specificity remains uncertain. Using postcontrast BBMRI, Qiao et al[7] reported observing intracranial plaque enhancement in both culprit (the most stenotic lesion upstream from an ischemic event) and nonculprit lesions in patients with cerebrovascular events. Skarpathiotakis et al[4] reported "strong" ICAD plaque enhancement on postcontrast BBMRI, even 4 months after stroke presentation, and "mild" enhancement as much as 1 year later.

The concept of introducing additional quantitative MR imaging parameters by using dynamic contrast-enhanced (DCE) MR imaging to measure adventitial contrast uptake rates, represented by the volume transfer constant (K^{trans}), was first introduced by Kerwin et al[8] in patients with carotid atherosclerotic disease requiring surgical endarterectomy. These parameters were found to correlate with macrophage infiltration (inflammation) and neovasculature on subsequent histopathologic analysis.[8-10] In a separate cohort, Dong et al[11] demonstrated that intensive medical management with lipid therapy coincided with a significant decrease in the measured K^{trans} of carotid artery atherosclerosis. In fact, K^{trans} measurements decreased in intervals and responded to medical management with anticholesterolemic (statin) medications during 1 year of therapy, suggesting correlative reduction in neovascularization and/or inflammation, plaque stabilization, and even regression.[11]

These plaque perfusion parameters may provide information that is also correlated to intracranial plaque inflammation, indicative of both ischemic stroke risk and sensitivity to pharmacologic therapies. Chen et al[12] demonstrated neovascularization in MCA plaques in a postmortem study, suggesting applicability of DCE kinetic modeling to the intracranial vasculature; however, to date, no study has examined the dynamic characteristics of intracranial vessel walls or ICAD plaques using DCE-MR imaging. In this pilot study, we investigated the feasibility of modeling plaque perfusion parameters, fractional plasma volume (V_p), and K^{trans}, using DCE-MR imaging in patients with symptomatic ICAD. We hypothesized that kinetic modeling of the intracranial vessel wall and plaque provide quantitative biomarkers sensitive to time from symptom onset of ICAD, independent of relative T1 signal hyperintensity and post-gadolinium enhancement values as observed on BBMRI.

Table 1: Patient demographics[a]

Characteristics	Value
Age (mean) (yr)	58.9 ± 10
Sex	
Male	6
Female	4
Active smoker	3
Alcohol	2
Antiplatelets	9
Statins	8
Hypertension	5
Diabetes mellitus	6
Dyslipidemia	5
Atrial fibrillation	0
Coronary artery disease	1
Neurologic symptoms	10
Imaging data	
DWI+	9
Watershed	4
Perforator	4
Both	1
Vessel	
MCA	8
PCA	1
ICA	1

Note:—PCA indicates posterior cerebral artery.
[a] Data are numbers unless otherwise indicated.

MATERIALS AND METHODS

Patient Recruitment

Institutional review board approval was obtained for a prospective, Health Insurance Portability and Accountability Act–compliant study of symptomatic patients presenting with ischemic stroke or transient ischemic attack secondary to ICAD with >50% stenosis and plaques involving the internal carotid artery, A1-A2 anterior cerebral, M1-M2 middle cerebral, and P1-P2 posterior cerebral arteries, or basilar artery (Table 1). When attributable to the downstream vascular distribution of a single ICAD plaque, "ischemic stroke" was defined as hyperintensity findings on DWI and "TIA" was defined as neurologic deficits that resolved in <24 hours. Patients were identified and recruited for this study at Northwestern University from March 2013 to May 2015, after receiving a standard clinical head and neck MRI/MRA evaluation, including 3D TOF and DWI sequences. Patients provided consent based on a willingness to participate in a longitudinal study and the ability to undergo a research MR imaging examination within 30 days of the ischemic event.

Recruited patients underwent high-resolution, vessel wall imaging with 3T BBMRI of the intracranial vasculature. In addition, the ICAD stenosis was evaluated with DCE-MR imaging for the purpose of kinetic modeling of permeability (or contrast uptake) into the plaque. Major patient exclusion criteria included complete vessel occlusions, gross patient motion artifacts, susceptibility artifacts from implants, >50% stenosis of the cervical vasculature or tandem intracranial stenoses (via MRA/CTA or carotid Doppler sonography), cardioembolic risk profile including atrial fibrillation, and standard contraindications to MR imaging (pacemaker, claustrophobia, pregnancy, contrast allergy, or renal insufficiency). We further studied patient demographics, atherosclerotic risk factors, relevant medical management, and clinical presentations using Northwestern University's electronic medical records.

Imaging Protocol

All patients enrolled in our study were scanned on 3T (Magnetom Trio or Skyra; Siemens, Erlangen, Germany) MR imaging scanners. A 3D TOF MRA sequence was repeated to localize the ICAD plaque in the vessel of interest. The DCE-MR imaging volume was placed to cover the entire segment of the diseased intracranial vessel (Fig 1) with the axis of the vessel aligning with the through-plane direction and in-plane images containing perpendicular vessel cross-sections. Plaque permeability was measured with a standard DCE-MR imaging protocol using a multiphase 3D gradient recalled-echo (GRE)-based pulse sequence. Dynamic volumetric T1-weighted images were acquired approximately every 35 seconds following contrast injection for approximately 10 minutes with the following parameters: flip angle = 10°, TR/TE = 8.7/1.3 ms, matrix = 384 × 384, FOV = 190–220 mm, and 12 partitions placed to cover the plaque, resulting in voxel dimensions of 0.5 × 0.5 × 2.0 mm. A single dose (0.1 mmol/kg) of T1-shortening gadolinium contrast (gadopentetate dimeglumine, Magnevist; Bayer HealthCare Pharmaceuticals, Wayne, New Jersey) was injected at a rate of 4 mL/s during the DCE acquisition. Precontrast T1 values (T_{10}) of the tissue were determined using a multi-flip angle routine ($\alpha = 5°, 15°, 25°, 45°$) to fit the spoiled gradient-echo signal equation:[13,14]

$$1) \qquad S(\alpha) = A \sin\alpha \frac{1 - \exp(-TR/T_{10})}{1 - \cos\alpha \exp(-TR/T_{10})}.$$

3D isotropic, high-resolution BBMRI was performed with T1-weighted TSE sequences, acquired before and immediately after the DCE acquisition (ie, within 20 minutes of the gadolinium injection). A 3D variable flip angle TSE (T1 sampling perfection with application-optimized contrasts by using different flip angle evolution [SPACE]; Siemens) pulse sequence[5,15] was performed before and after contrast injection with the following parameters: FOV = 165 mm, TR/TE = 800/22 ms, integrated parallel acquisition technique factor = 2, 104 partitions, bandwidth = 372 Hz/pixel, turbo factor = 30, scan time ~ 8 minutes, voxel volume = 0.5 × 0.5 × 0.6 mm.

Permeability Modeling

The permeability-limited Modified Tofts Model[16] quantifies the kinetics of a tracer leaking through a semipermeable membrane with the following relationship:

$$2) \qquad C(t) = K^{trans} \int_0^t e^{-K_{ep}(t-\tau)} C_p(t)\, d\tau + V_p\, C_p(t),$$

with K^{trans} dictating the tracer transfer rate from the intravascular into the extracellular extravascular space (V_L) with units of minute^{-1}; $K_{ep} = K^{trans}/V_L$ in units of minute^{-1} describing the ratio of the transfer rate (K^{trans}) to the fractional volume of tracer in the V_L; $C_p(t)$, the intravascular tracer concentration; and V_p, the fractional plasma volume for each voxel. $C(t)$ is measured adjacent to the patent lumen of the stenotic vessel wall. A Levenberg-Marquardt algorithm was implemented in-house by using a commercially available software prototyping package (Matlab, Version 2014; MathWorks, Natick, Massachusetts) to find the K^{trans}, V_L, and V_p in Equation 2 that best fit the measured signal $C(t)$. Acquisition of the enhancement curve peak is required for an accurate measurement of V_L and may require imaging times greater than 10 minutes. While V_L may be related to plaque enhancement, it does not affect the wash-in phase of the enhancement curve[17]; thus, we restricted our analysis to K^{trans} and V_p values as in prior kinetic modeling analyses.[7,9]

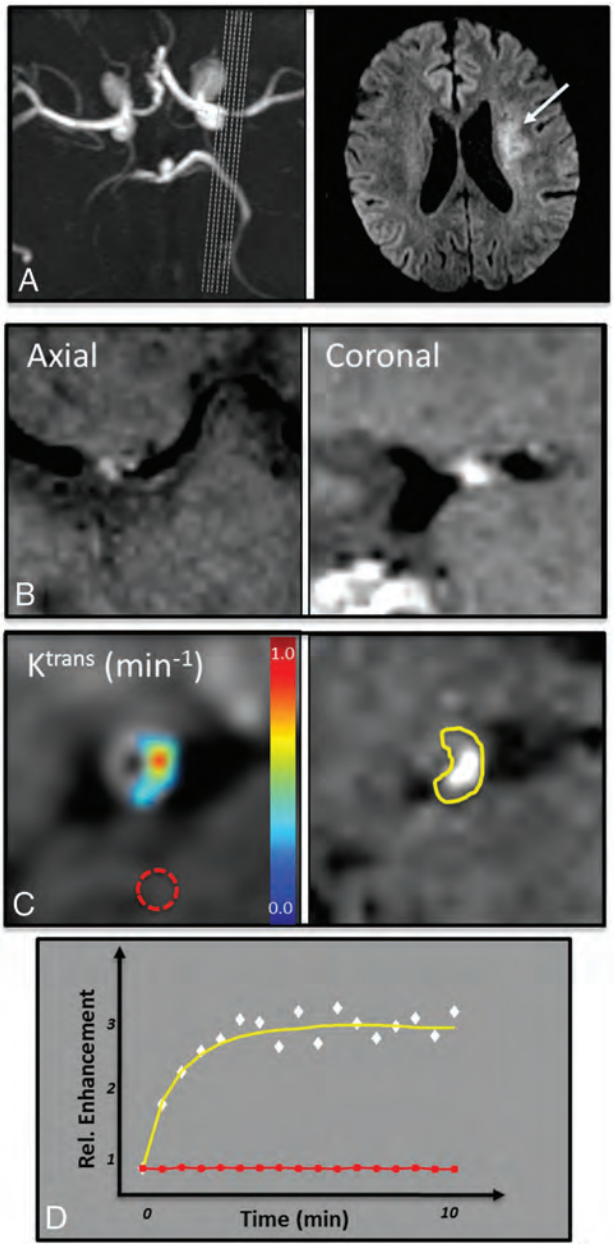

FIG 1. Vessel wall imaging data in a 63-year-old man with symptomatic severe left MCA stenosis resulting in perforator thromboembolic infarcts as seen on 3D TOF MRA MIP and DWI (*A*). 3D BBMRI with postcontrast T1 SPACE imaging demonstrates plaque enhancement in an axial and coronal cross-sections of the MCA (*B*). A manual ROI isolates the enhancing plaque on the postcontrast T1 SPACE image (*C*, right, *yellow ROI* on the plaque inset). Kinetic modeling of contrast uptake into the plaque was performed by using DCE-MR imaging in the coregistered plaque ROI, and K^{trans} values were calculated in each voxel (*C*, left). Normal control values were calculated in a region of normal white matter (*red dotted ROI* in *C*). The mean enhancement signal (*white diamonds*) and fitted Tofts curve (yellow) are shown from the plaque ROI (*D*). Note the difference in enhancement relative to healthy brain tissue (*D*, *red ROI* and *red curve/squares*).

Data Analysis and Imaging Evaluation

Both DCE and T1 SPACE images were evaluated as a postprocessing step by separate, independent operators who were blinded to both clinical history and the results of complementary image analysis.

T1 SPACE images were analyzed on a Leonardo workstation (Siemens) by a neuroradiologist with >10 years' experience (A.H.E). Measurements included relative postgadolinium plaque enhancement between pre- and postcontrast imaging, referred to as intraplaque enhancement (IPE), as well as the presence of precontrast signal intensity (SI), referred to as intraplaque hyperintensity (IPH). ROIs were drawn in one section at the site of maximal vessel stenosis, and the mean SI was recorded. ROIs were matched in size and location in the precontrast T1 SPACE dataset. IPE was calculated as $SI_{post} - SI_{pre} / SI_{pre.}$ Both SI_{post} and SI_{pre} were first normalized to the SI of normal-appearing white matter (NAWM). IPH was measured as the ratio of precontrast plaque SI to extraocular muscle SI.

DCE images were motion-corrected by using the Statistical Parametric Mapping (SPM8 (http://www.fil.ion.ucl.ac.uk/spm/software/spm12) software package in Matlab (R2014a). The ROI for contrast kinetic analysis was matched as closely as possible to the ROI used for IPE analysis by first coregistering the T1 SPACE postcontrast ROI volumes to DCE-MR imaging volumes and then applying pixel-by-pixel DCE modeling in the section containing maximal plaque enhancement on the coregistered T1 SPACE image. ROIs were drawn in Matlab by a trained operator with >10 years' experience (P.V.). We evaluated the permeability of the choroid plexus and NAWM[18-20] in the same patients to provide an internal reference for our plaque contrast kinetic parameters.

Table 2: Quantitative imaging findings

Subject	K^{trans} (min^{-1})	V_p (%)	IPE (%)	IPH (%)
1	0.53	20	230	84
2	0.12	24	131	58
3	0.11	5	181	8
4	0.24	20	159	38
5	0.20	9	215	46
6	0.39	11	123	80
7	0.28	16	99	89
8	0.33	40	294	25
9	0.45	12	226	32
10	0.41	26	175	82

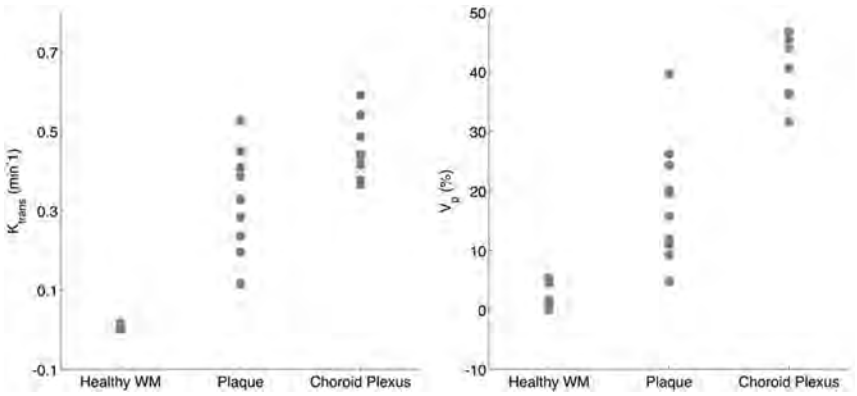

FIG 2. K^{trans} and V_p values are shown for ICAD plaques and compared against the paired choroid plexus and NAWM measured in the same subjects. Both mean plaque K^{trans} and V_p values were diverse and significantly different from choroid plexus and healthy white matter values (see text for relevant *P* values).

Statistical Analysis

We compared quantitative DCE-MR imaging parameters in plaques against the aforementioned independent controls (white matter and choroid plexus) and neuroanatomic structures with differential permeability characteristics.[18,19,21-23] Mean values were compared by using a Student *t* test with statistical significance defined at the 5% level ($P < .05$).

A linear regression analysis was preformed to compare DCE parameters (K^{trans} and V_p) as well as IPH and IPE ratios with the time from symptom onset (in days). Time from symptom onset was calculated as the number of days until DCE and T1 SPACE MR imaging studies were performed at our research institution. This analysis was conducted to evaluate the difference in associativity with time between the 2 imaging markers.

Finally, DCE parameters were compared with IPH and IPE ratios in all plaques by using linear regression to evaluate their interdependent relationships. All statistical analyses were conducted by using built-in statistical software in Matlab. Confidence intervals were set at 95%, and statistical significance was defined at the 5% level ($P < .05$).

RESULTS

We evaluated 10 consecutive symptomatic patients (6 men, 4 women; mean age, 58.9 years; range, 39–70 years) with ICAD plaques by using DCE and TI SPACE MR imaging. Patient demographics, comorbid atherosclerotic risk factors, relevant medical management, and clinical presentations are summarized in Table 1. In addition, 14 other patients were recruited for scanning but were excluded from this study: 2 with documented complete vessel occlusions in the plaque ROI, 3 with nondiagnostic imaging due to patient motion artifacts, and 9 with confounding tandem or distal plaques in the vessel of interest.

We found a broad-range of K^{trans} and V_p values in ICAD plaques (Table 2). In our cohort, mean plaque K^{trans} was 0.31 ± 0.14 $minutes^{-1}$, ranging from 0.11 to 0.53 $minutes^{-1}$. A Student *t* test found that plaque K^{trans} was significantly smaller than the uptake rates in the choroid plexus (mean, 0.47 $minutes^{-1}$; $P = .0037$) and larger than values measured in NAWM (mean, 0.0031 $minutes^{-1}$; $P = 2.3E-06$). Similarly, average plaque V_p was 18.3% ± 10.2%; range, 5%–40%, and it was significantly smaller than the mean values found in the choroid plexus (mean, 44%; $P = 6.8E-06$) and larger than mean values measured in NAWM (mean, 1.9%; $P = 9.4E-05$) (Fig 2).

Linear regression modeling of DCE plaque permeability parameters and T1 SPACE IPH and IPE ratios demonstrated that K^{trans} was most associated with time from symptom onset in days ($r^2 = 0.46$, $P = .03$), but vascular fraction V_p ($r^2 = 0.12$, $P = .3$), IPH ($r^2 = 0.07$, $P = .47$), and IPE ($r^2 = 0.005$, $P = .95$) ratios did not correlate significantly (Fig 3).

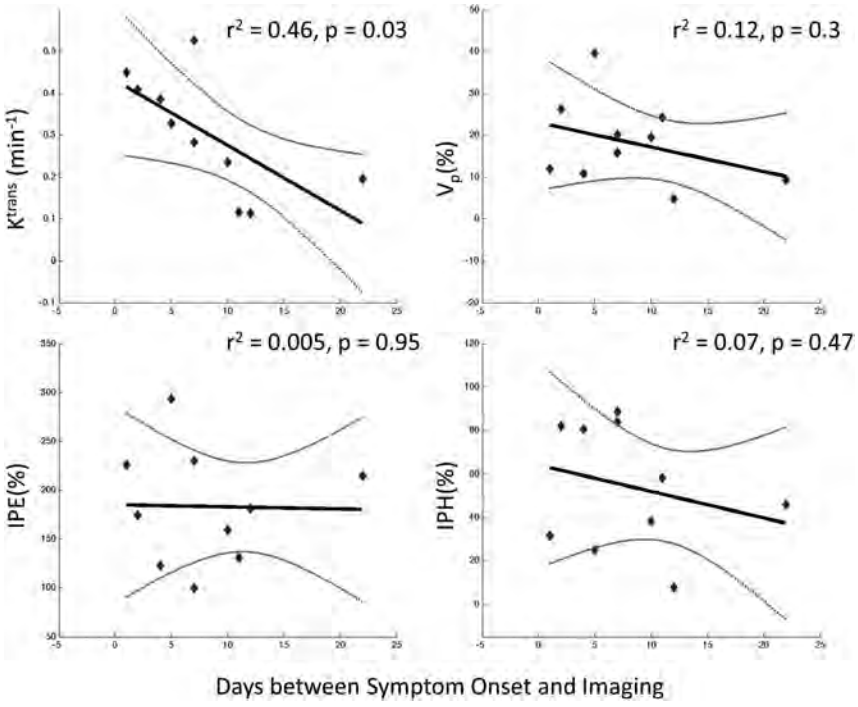

FIG 3. Linear regression analysis demonstrates that K^{trans} and V_p measured on DCE-MR imaging are more correlated (r^2 and *P* values) to time from symptom onset than intraplaque contrast enhancement and precontrast hyperintensity measured on T1 SPACE imaging. K^{trans} is the most associated and significant in its correlation ($r^2 = 0.46$ and $P = .03$).

DCE and T1 SPACE parameters did not correlate significantly with one another: K^{trans} versus IPE ($r^2 = 0.101$, $P = .4$); K^{trans} versus IPH ($r^2 = 0.221$, $P = .17$); V_p versus IPE ($r^2 = 0.16$, $P = .3$); and V_p versus IPH ($r^2 = 0.007$, $P = .818$). This finding is illustrated in Fig 4, which shows representative imaging in 2 patients, with 226% versus 122% IPE ratios. In contrast, despite this nearly 2-fold difference in IPE between the cases, K^{trans} levels remained consistently high at 0.39 minutes^{-1} and 0.45 minutes^{-1}, respectively.

DISCUSSION

In this pilot study, we demonstrated the feasibility of kinetic modeling of contrast uptake in ICAD plaques. Enhancement curve shapes and K^{trans}/V_p values were consistent with literature values reported in DCE studies on extracranial carotid plaques[8,10] and intermediate to values found in the healthy white matter (NAWM) and the choroid plexus. Furthermore, we found that DCE permeability parameters showed little correlation to IPE and IPH values derived from T1 SPACE imaging and demonstrated greater correlation with time from symptom onset. Our findings suggest that contrast kinetics modeled by DCE-MR imaging allows intracranial plaque characterization that differs from pre- and postcontrast plaque signal or enhancement seen with static vessel wall imaging protocols using BBMRI.

The strong relationship between K^{trans} and time from symptom onset may be evidence of the correlation of contrast kinetics to acute pathophysiologic changes occurring after the destabilization of intracranial plaques and thromboembolic conversion. Our data did not demonstrate similar temporal correlation with respect to IPE or IPH, consistent with recent intracranial vessel wall imaging studies that showed persistent and strong enhancement in ICAD plaques as much as 6 months after symptom onset. Additional studies that follow symptomatic and asymptomatic plaques longitudinally will be essential to establishing whether contrast uptake rates into the vessel wall provide a more specific and acute measure of plaque stability than static measures of pre- and postcontrast signal or enhancement.

Studies by Kerwin et al[8] have shown that DCE-MR imaging can provide a surrogate measure of plaque inflammation by visualizing the rate of intercompartmental exchange of contrast from the extracranial carotid vaso vasorum into the adjacent extracellular extravascular spaces within an atherosclerotic lesion. These rates, modeled as K^{trans}, correlated with macrophage infiltration and percentage neovascularization on histopathologic analysis. Increasing evidence indicates the role of neovascularization, ruptured thrombogenic lipid core, intraplaque hemorrhage, and recruitment of inflammatory cells (macrophages) in the progression and rupture of carotid atherosclerotic plaques, analogous to the coronary literature.[24-26] An analogous relationship of high intracranial plaque K^{trans} values to intracranial plaque destabilization and thromboembolic complications can be postulated. Although intracranial vessel wall pathology may have similar responses to progressing atherosclerotic disease, the nonpathologic absence of the vaso vasorum and an external elastic lamina in the intracranial vasculature may result in different pathophysiologic responses and hence contrast kinetics in symptomatic ICAD.

Despite inflammation leading to acute instability of an ICAD plaque, existing data on plaque K^{trans} values with associated neovascularization and macrophage infiltration are derived from carotid endarterectomy studies with histopathologic confirmation. Because these studies are not feasible in ICAD except in postmortem specimens, an alternative approach may be to correlate plaque K^{trans} values against GRE T2*- or T2 SPACE-weighted imaging of intracranial plaque following ferumoxytol infusion. Hasan et al[27] demonstrated early uptake (24 hours) of superparamagnetic iron oxide nanoparticles (ferumoxytol) as a marker of macrophage infiltration in the vessel walls of cerebral aneurysms. These studies demonstrated associations with early intracranial aneurysm rupture, increased inflammatory mediators (cyclooxygenase-2, microsomal prostaglandin E2 synthase-1), and macrophages on histopathologic immunostaining.

Because atherosclerosis is an inflammatory process, transient identification of acute inflammation/plaque enhancement, rate of contrast permeability, intraplaque hemorrhage, and macrophage infiltration (potentially early ferumoxytol uptake) may serve as

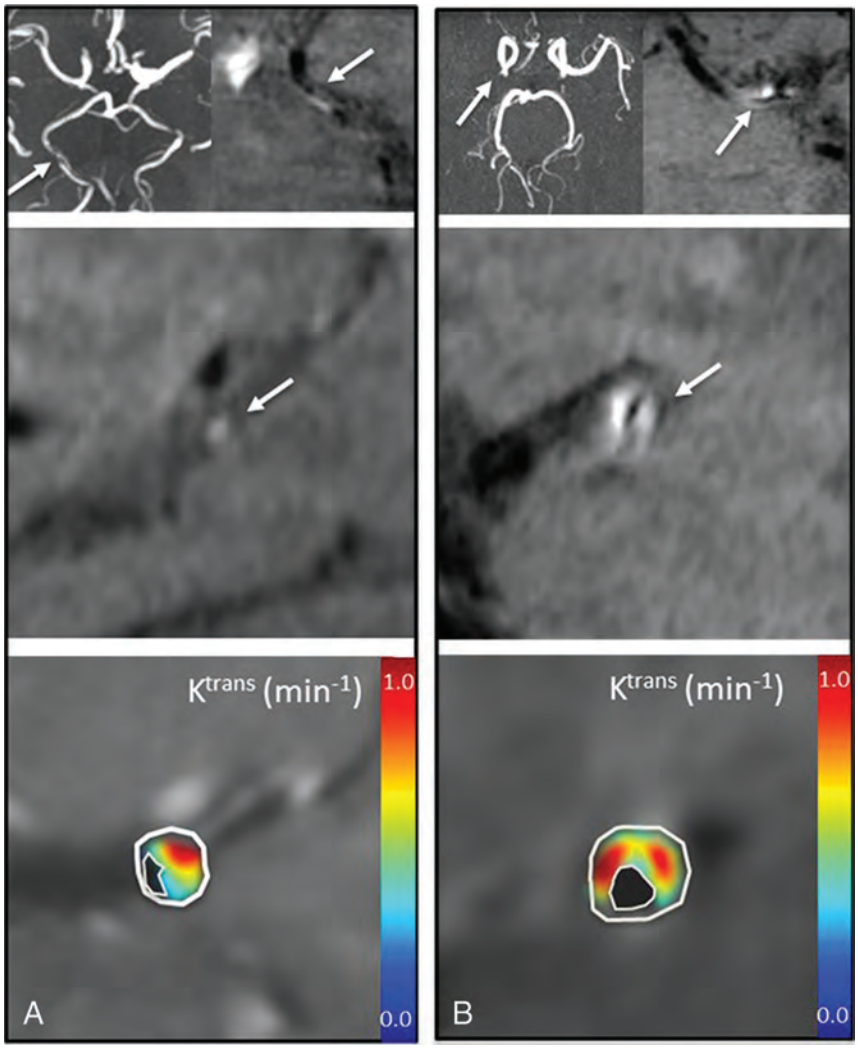

FIG 4. K^{trans} plaque permeability differs from relative signal enhancement in T1 SPACE imaging in 2 patients. Each panel shows axial TOF MRA (upper left), axial T1 SPACE (upper right), and sagittal T1 SPACE (middle) MR images confirming vessel patency with eccentric plaque, and K^{trans} (lower). *A*, A 69-year-old man with right posterior cerebral artery stenosis on TOF MRA and corresponding T1 SPACE plaque enhancement measured at 123%. K^{trans} measured at 0.39 minutes^{-1}, and V_p at 11%. *B*, A 54-year-old woman with right MCA stenosis and corresponding T1 SPACE plaque enhancement measured at 226%, K^{trans} measured at 0.45 minutes^{-1}, and V_p at 12%.

MR imaging markers to characterize and grade the acute vulnerability of these lesions to thromboembolic/perforator ischemic complications. Even chronic progressing intracranial stenoses may be exacerbated by episodes of plaque inflammation and, in a setting of poor collaterals, could also predispose to hypoperfusion-related ischemic complications irrespective of plaque instability. Differentiating these mechanisms of stroke in ICAD may modulate treatment of symptomatic ICAD in the future, whereby angioplasty/stent placement could be advocated, delayed, or contraindicated in favor of antiplatelets, anticoagulants, statins, or novel anti-inflammatory therapies.

Our study has several limitations. First, this pilot study included a relatively small sample size and no longitudinal follow-up, both of which should be addressed in subsequent studies. Additionally, the patient population was limited to subjects with symptomatic ICAD plaques with >50% stenosis. Examining asymptomatic plaques and less stenotic lesions, stenoses, which may not be easily characterized by K^{trans}, will be an important subject for future research. Furthermore, the inability to image the plateau and washout phase of plaque contrast prevents accurate estimation of V_L. However, this scenario does not preclude accurate measurement of K^{trans} from the wash-in phase of the curve because V_L does not affect it. Finally, our model of K^{trans} contrast permeability into the intracranial plaque from the intravascular space to the extracellular extravascular space may be prone to variable mechanisms. Although neovascularization in pathologic ICAD may be a primary mode for plaque permeability/enhancement, passive diffusion from the intraluminal space across a compromised fibrous cap cannot be excluded, and these processes may vary across a spectrum of intracranial plaques.

CONCLUSIONS

We present the results of a prospective pilot study examining the feasibility of kinetic modeling of contrast uptake in ICAD. We demonstrate elevated and variable permeability in symptomatic atherosclerotic plaques (K^{trans} and V_p) less than levels observed in the choroid plexus where an absence of the blood-brain barrier allows intercompartmental tracer exchange. We also found that plaque permeability is more associated with the time from symptom onset than IPE or IPH ratios as measured on BBMRI via T1 SPACE vessel wall imaging. Coupled with the fact that neither K^{trans} nor V_p strongly correlated with IPE or IPH, these findings suggest that permeability modeling of plaque contrast kinetics may provide a new imaging biomarker for ICAD plaque instability.

Disclosures: Charles G. Cantrell—*RELATED*: *Grant*: American Heart Association PRE20380810.* Timothy J. Carroll—*RELATED*: *Grant*: American Heart Association 14GRNT20380798*; National Institutes of Health 1R21EB017928* and 1R01NS089926*; Sameer A. Ansari—*RELATED*: *Grant*: American Heart Association 13GRNT17340018* and 14GRNT20380798*; National Institutes of Health 1R21HL130969.* *Money paid to the institution.

REFERENCES

1. Chimowitz MI, Lynn MJ, Howlett-Smith H, et al; Warfarin-Aspirin Symptomatic Intracranial Disease Trial Investigators. **Comparison of warfarin and aspirin for symptomatic intracranial arterial stenosis.** *N Engl J Med* 2005;352:1305–16 CrossRef Medline
2. Chimowitz MI, Lynn MJ, Derdeyn CP, et al; SAMMPRIS Trial Inves-

tigators. **Stenting versus aggressive medical therapy for intracranial arterial stenosis.** *N Engl J Med* 2011;365:993–1003 CrossRef Medline
3. Swartz RH, Bhuta SS, Farb RI, et al. **Intracranial arterial wall imaging using high-resolution 3-Tesla contrast-enhanced MRI.** *Neurology* 2009;72:627–34 CrossRef Medline
4. Skarpathiotakis M, Mandell DM, Swartz RH, et al. **Intracranial atherosclerotic plaque enhancement in patients with ischemic stroke.** *AJNR Am J Neuroradiol* 2013;34:299–304 CrossRef Medline
5. Qiao Y, Steinman DA, Qin Q, et al. **Intracranial arterial wall imaging using three-dimensional high isotropic resolution black blood MRI at 3.0 Tesla.** *J Magn Reson Imaging* 2011;34:22–30 CrossRef Medline
6. Xu WH, Li ML, Gao S, et al. **Plaque distribution of stenotic middle cerebral artery and its clinical relevance.** *Stroke* 2011;42:2957–59 CrossRef Medline
7. Qiao Y, Zeiler SR, Mirbagheri S, et al. **Intracranial plaque enhancement in patients with cerebrovascular events on high-spatial-resolution MR images.** *Radiology* 2014;271:534–42 CrossRef Medline
8. Kerwin W, Hooker A, Spilker M, et al. **Quantitative magnetic resonance imaging analysis of neovasculature volume in carotid atherosclerotic plaque.** *Circulation* 2003;107:851–56 CrossRef Medline
9. Espinosa-Heidmann DG, Reinoso MA, Pina Y, et al. **Quantitative enumeration of vascular smooth muscle cells and endothelial cells derived from bone marrow precursors in experimental choroidal neovascularization.** *Exp Eye Res* 2005;80:369–78 CrossRef Medline
10. Kerwin WS, Oikawa M, Yuan C, et al. **MR imaging of adventitial vasa vasorum in carotid atherosclerosis.** *Magn Reson Med* 2008;59:507–14 CrossRef Medline
11. Dong L, Kerwin WS, Chen H, et al. **Carotid artery atherosclerosis: effect of intensive lipid therapy on the vasa vasorum—evaluation by using dynamic contrast-enhanced MR imaging.** *Radiology* 2011;260:224–31 CrossRef Medline
12. Chen XY, Wong KS, Lam WW, et al. **Middle cerebral artery atherosclerosis: histological comparison between plaques associated with and not associated with infarct in a postmortem study.** *Cerebrovasc Dis* 2008;25:74–80 Medline
13. Fram EK, Herfkens RJ, Johnson GA, et al. **Rapid calculation of T1 using variable flip angle gradient refocused imaging.** *Magn Reson Imaging* 1987;5:201–08 CrossRef Medline
14. Deoni SC. **High-resolution T1 mapping of the brain at 3T with driven equilibrium single pulse observation of T1 with high-speed incorporation of RF field inhomogeneities (DESPOT1-HIFI).** *J Magn Reson Imaging* 2007;26:1106–11 CrossRef Medline
15. Fan Z, Zhang Z, Chung YC, et al. **Carotid arterial wall MRI at 3T using 3D variable-flip-angle turbo spin-echo (TSE) with flow-sensitive dephasing (FSD).** *J Magn Reson Imaging* 2010;31:645–54 CrossRef Medline
16. Tofts PS, Brix G, Buckley DL, et al. **Estimating kinetic parameters from dynamic contrast-enhanced T(1)-weighted MRI of a diffusable tracer: standardized quantities and symbols.** *J Magn Reson Imaging* 1999;10:223–32 Medline
17. Tofts PS, Kermode AG. **Measurement of the blood-brain barrier permeability and leakage space using dynamic MR imaging, 1: fundamental concepts.** *Magn Reson Med* 1991;17:357–67 CrossRef Medline
18. Provenzale JM, Wang GR, Brenner T, et al. **Comparison of permeability in high-grade and low-grade brain tumors using dynamic susceptibility contrast MR imaging.** *AJR Am J Roentgenol* 2002;178:711–16 CrossRef Medline
19. Jia Z, Geng D, Liu Y, et al. **Low-grade and anaplastic oligodendrogliomas: differences in tumour microvascular permeability evaluated with dynamic contrast-enhanced magnetic resonance imaging.** *J Clin Neurosci* 2013;20:1110–13 CrossRef Medline
20. Vakil P, Ansari SA, Cantrell CG, et al. **Quantifying intracranial aneurysm wall permeability for risk assessment using dynamic contrast-enhanced MRI: a pilot study.** *AJNR Am J Neuroradiol* 2015;36:953–59 CrossRef Medline
21. Cha S, Yang L, Johnson G, et al. **Comparison of microvascular permeability measurements, K(trans), determined with conventional steady-state T1-weighted and first-pass T2*-weighted MR imaging methods in gliomas and meningiomas.** *AJNR Am J Neuroradiol* 2006;27:409–17 Medline
22. Li KL, Zhu XP, Checkley DR, et al. **Simultaneous mapping of blood volume and endothelial permeability surface area product in gliomas using iterative analysis of first-pass dynamic contrast enhanced MRI data.** *Br J Radiol* 2003;76:39–50 CrossRef Medline
23. Kilgore DP, Breger RK, Daniels DL, et al. **Cranial tissues: normal MR appearance after intravenous injection of GD-DTPA.** *Radiology* 1986;160:757–61 CrossRef Medline
24. Moreno PR, Purushothaman KR, Sirol M, et al. **Neovascularization in human atherosclerosis.** *Circulation* 2006;113:2245–52 CrossRef Medline
25. Virmani R, Kolodgie FD, Burke AP, et al. **Atherosclerotic plaque progression and vulnerability to rupture: angiogenesis as a source of intraplaque hemorrhage.** *Arterioscler Thromb Vasc Biol* 2005;25:2054–61 CrossRef Medline
26. Kolodgie FD, Gold HK, Burke AP, et al. **Intraplaque hemorrhage and progression of coronary atheroma.** *N Engl J Med* 2003;349:2316–25 CrossRef Medline
27. Hasan D, Chalouhi N, Jabbour P, et al. **Early change in ferumoxytol-enhanced magnetic resonance imaging signal suggests unstable human cerebral aneurysm: a pilot study.** *Stroke* 2012;43:3258–65 CrossRef Medline

Measurement of Cortical Thickness and Volume of Subcortical Structures in Multiple Sclerosis: Agreement between 2D Spin-Echo and 3D MPRAGE T1-Weighted Images

A. Vidal-Jordana, D. Pareto, J. Sastre-Garriga, C. Auger, E. Ciampi, X. Montalban, and A. Rovira

ABSTRACT

BACKGROUND AND PURPOSE: Gray matter pathology is known to occur in multiple sclerosis and is related to disease outcomes. FreeSurfer and the FMRIB Integrated Registration and Segmentation Tool (FIRST) have been developed for measuring cortical and subcortical gray matter in 3D-gradient-echo T1-weighted images. Unfortunately, most historical MS cohorts do not have 3D-gradient-echo, but 2D-spin-echo images instead. We aimed to evaluate whether cortical thickness and the volume of subcortical structures measured with FreeSurfer and FIRST could be reliably measured in 2D-spin-echo images and to investigate the strength and direction of clinicoradiologic correlations.

MATERIALS AND METHODS: Thirty-eight patients with MS and 2D-spin-echo and 3D-gradient-echo T1-weighted images obtained at the same time were analyzed by using FreeSurfer and FIRST. The intraclass correlation coefficient between the estimates was obtained. Correlation coefficients were used to investigate clinicoradiologic associations.

RESULTS: Subcortical volumes obtained with both FreeSurfer and FIRST showed good agreement between 2D-spin-echo and 3D-gradient-echo images, with 68.8%–76.2% of the structures having either a substantial or almost perfect agreement. Nevertheless, with FIRST with 2D-spin-echo, 18% of patients had mis-segmentation. Cortical thickness had the lowest intraclass correlation coefficient values, with only 1 structure (1.4%) having substantial agreement. Disease duration and the Expanded Disability Status Scale showed a moderate correlation with most of the subcortical structures measured with 3D-gradient-echo images, but some correlations lost significance with 2D-spin-echo images, especially with FIRST.

CONCLUSIONS: Cortical thickness estimates with FreeSurfer on 2D-spin-echo images are inaccurate. Subcortical volume estimates obtained with FreeSurfer and FIRST on 2D-spin-echo images seem to be reliable, with acceptable clinicoradiologic correlations for FreeSurfer.

ABBREVIATIONS: 3D-GE = 3D gradient-echo; 2D-SE = 2D spin-echo; EDSS = Expanded Disability Status Scale; FIRST = FMRIB Integrated Registration and Segmentation Tool; ICC = intraclass correlation coefficient; TIV = total intracranial volume

Gray matter pathology in patients with multiple sclerosis is present from the very early stages of the disease and has been related to long-term disability.[1,2] Therefore, in recent years, research has focused on obtaining accurate markers of GM damage, and different software packages have been developed or optimized for measuring it in MS. FreeSurfer software (http://surfer.nmr.mgh.harvard.edu)[3,4] allows automatic calculation of cortical thickness and the volume of subcortical GM structures by using 3D T1-weighted images. Briefly, the image-processing pipeline includes Talairach transformation of the 3D T1-weighted images and segmentation of the subcortical white matter and deep GM structures, relying on the gray and white matter boundaries and pial surfaces. The FMRIB Integrated Registration and Segmentation Tool (FIRST; http://fsl.fmrib.ox.ac.uk/fsl/fslwiki/FIRST) software package[5] automatically segments subcortical GM structures also on the basis of 3D T1-weighted images. Briefly, FIRST is a model-based segmentation and registration program that uses shape and appearance models constructed from manually segmented images. On the basis of the learned models, FIRST searches through linear combinations of shape modes of variation for the most probable shape instance, given the observed intensities in the 3D T1-weighted input images. Both software packages have been shown to be accurate and reproducible.[6-11]

The study of cortical pathology in patients with MS by using

Received May 5, 2016; accepted after revision September 5.

From the Department of Neurology-Neuroimmunology and Multiple Sclerosis Centre of Catalonia (A.V.-J., J.S.-G., E.C., X.M.) and Magnetic Resonance Unit (D.P., C.A., A.R.), Radiology Department, Hospital Universitari Vall d'Hebron, Universitat Autònoma de Barcelona, Barcelona, Spain.

Paper previously presented, in part, at: Annual Meeting of the European Committee for Treatment and Research in Multiple Sclerosis–Americas Committee for Treatment and Research in Multiple Sclerosis, September 11–13, 2013; Boston, Massachusetts.

Please address correspondence to Deborah Pareto, MD, Radiology Department. Vall d'Hebron University Hospital, Psg Vall d'Hebron 119-129, Barcelona 08035, Spain; e-mail: deborah.pareto@idi.gencat.cat

http://dx.doi.org/10.3174/ajnr.A4999

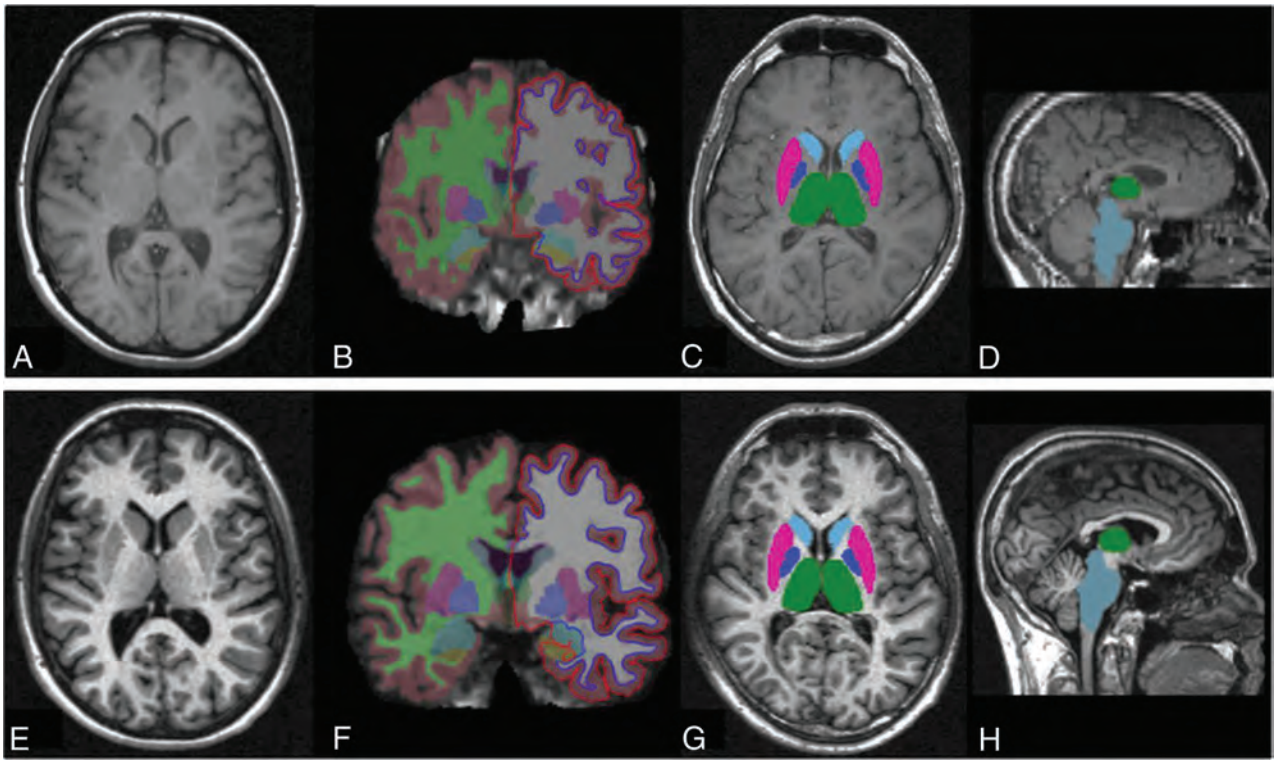

FIG 1. FreeSurfer and FIRST outputs from 3D-GE and 2D-SE T1-weighted images. The 2D-SE and 3D-GE T1-weighted image inputs for the same patient (*A* and *E*, respectively), the cortical parcellation and subcortical segmentation obtained with FreeSurfer for each input (*B* and *F*), and the subcortical segmentation overlaid onto the original T1-weighted images obtained with FIRST for each input (*C*, *D*, *G*, and *H*) are shown.

FreeSurfer has shown cortical thinning in patients with MS compared with healthy controls,[12,13] which has been related to lesion volume, disease duration, disability,[12] and cognitive impairment.[14] Also, cortical thinning of the superior frontal gyrus, thalamus, and cerebellum significantly predicted conversion to MS in patients presenting with clinically isolated syndromes,[15] and global cortical thinning for 6 years was significantly associated with a more aggressive disease evolution.[16] The volume of deep GM structures (measured with both FreeSurfer and FIRST) has also been shown to be lower in patients with MS compared with healthy controls,[17-19] and it has been related to different clinical disease outcomes such as fatigue,[20] cognitive impairment,[17-19,21] disability,[19] and walking function.[22]

Both FreeSurfer and FIRST have been optimized for 3D T1-weighted gradient-echo images that incorporate a magnetization-prepared inversion pulse that increases the T1-weighting.[23] Unfortunately, for most of the historical MS cohorts with long-term clinical and radiologic follow-up, only 2D spin-echo (2D-SE) T1-weighted images were acquired, a sequence that does not provide an optimal contrast between gray and white matter, particularly when acquired with high-field magnets.[24] The objectives of this work were the following: 1) to evaluate whether cortical thickness and subcortical volumes obtained with FreeSurfer could be reliably measured with 2D-SE T1-weighted images by using as the criterion standard the same measures obtained with 3D gradient-echo (3D-GE) T1-weighted sequences, 2) to investigate whether subcortical volumes obtained with FIRST could be reliably measured in 2D-SE T1-weighted images by using as the criterion standard the same measures obtained with 3D-GE T1-weighted images, and 3) to assess whether the correlations between clinical outcomes and subcortical normalized volumes obtained with 3D-GE and 2D-SE T1-weighted images had a similar strength and direction.

MATERIALS AND METHODS

Patients with relapsing-remitting MS with 2D-SE and 3D-GE T1-weighted images obtained at the same time were included in the analysis. Clinical and demographic data at the moment of MR imaging acquisition were recorded.

MR Imaging Acquisition and Analysis

All MR images were acquired on a 1.5T scanner (Magnetom Symphony; Siemens, Erlangen, Germany) with a standard head coil. The scanning protocol included 2 precontrast T1-weighted scans: a 3D magnetization-prepared rapid acquistion of gradient echo (TR/TE/TI, 2700/4.88/850 ms; voxel size, $1 \times 1 \times 1.2$ mm^3; matrix size, $224 \times 256 \times 144$; flip angle, 10°; receiver bandwidth, 130 Hz; averages, 1; acquisition time, 10 minutes) and a 2D-SE sequence (TR/TE, 450/17 ms; voxel size, $0.98 \times 0.98 \times 3$ mm^3; matrix size, $192 \times 256 \times 46$; section gap, 0; receiver bandwidth, 130 Hz; averages, 2; acquisition time, 2 minutes 52 seconds). Both sequences covered the whole brain. FreeSurfer software[3,4] (release Version 5.1.0) was used to obtain cortical thickness and volumes of subcortical structures in all 2D-SE and 3D-GE sequences (Fig 1). Ninety-one GM structures (70 cortical and 21 subcortical) were obtained and used for 2D-SE versus 3D-GE reliability assessment. Cortical parcellation was also grouped into a categoric variable by medial or lateral structures. The estimated total intracranial volume, a measure obtained with FreeSurfer, was used to

normalize the volume of subcortical structures as follows: raw subcortical structure volume/estimated total intracranial volume. FIRST software,[5] part of the FMRIB Software Library (FSL; http://www.fmrib.ox.ac.uk/fsl),[25] was used to obtain volumes of 15 subcortical structures in all 2D-SE and 3D-GE sequences (Fig 1). Because FIRST does not provide a measure of total intracranial volume (TIV), this was calculated by obtaining the matrix determinant of each scan (by using the avscale utility of the FMRIB Linear Image Registration Tool [FLIRT; http://www.fmrib.ox.ac.uk],[26,27] part of the FSL) and applying the following formula: (FIRST template volume/matrix determinant) × 1000. Normalized subcortical volume was then calculated as follows: raw subcortical structure volume/TIV.

Statistical Analysis

We used the SPSS program (IBM, Armonk, New York) to analyze clinical and demographic data. To assess reliability, we calculated the intraclass correlation coefficient (ICC) between the values obtained with 2D-SE and 3D-GE. ICC estimates of agreement were categorized as the following: slight (0.01–0.20), fair (0.21–0.40), moderate (0.41–0.60), substantial (0.61–0.80), and almost perfect agreement (0.81–1.0). Cortical thickness measures were grouped into lateral-versus-medial structures, and 2-tailed χ^2 tests were used for group comparison. Parametric and nonparametric correlation coefficients were used as appropriate to investigate associations between clinicodemographic data and normalized subcortical volume data. Because this was an exploratory study, correction for multiple comparisons was not performed. Statistical significance was set at $P < .05$.

RESULTS

Thirty-eight patients were included in the study. Twenty-three patients (60.5%) were women, with a mean age of 36.5 ± 8.8 years, a mean disease duration of 10.5 ± 7.2 years, and a median Expanded Disability Status Scale (EDSS) score of 4 (range, 1–6).

FreeSurfer Reliability Assessment

Cortical thickness measurements had the lowest ICC values, with 40% and 42.9% of the structures having a moderate or fair agreement, respectively. Only 1 structure (the right superior temporal gyrus) had a substantial agreement, and no structures had an almost perfect agreement (Table 1). Cortical thickness measurements of lateral structures had a higher proportion of moderate ICC estimates than medial structures (58.3% versus 15.6%, $P = .002$). For most cortical structures (except for some right and left frontal lobe structures: frontal pole, rostral middle frontal, medial orbitofrontal, and pars triangularis) thickness values were underestimated with 2D-SE sequences. Estimates of subcortical volumes showed a better agreement between 2D-SE and 3D-GE images, with 76.2% of the structures having either a substantial or almost perfect agreement compared with only 1.4% in the cortical structures ($P < .001$). The highest ICC values for subcortical volume estimates included relevant structures for MS pathology such as the thalamus, pallidum, caudate, brain stem, and putamen (Table 2). No clear pattern of over- or underestimation when using 2D-SE sequences was seen for subcortical structures.

Table 1: Intraclass correlation coefficients for 2D-SE and 3D-GE cortical thickness estimates using FreeSurfer[a]

Structure	ICC	Structure	ICC
None	≥0.81	L supramarginal	0.395
R superior temporal	0.663	R parahippocampal	0.393
R temporal pole	0.605	L inferior parietal	0.391
L superior temporal	0.59	L superior frontal	0.363
R inferior temporal	0.589	R lateral orbitofrontal	0.35
R superior parietal	0.58	R postcentral	0.343
L superior parietal	0.54	R isthmus cingulate	0.342
L inferior temporal	0.519	L precuneus	0.334
L fusiform	0.512	L precentral	0.329
R rostral middle frontal	0.508	R insula	0.328
R inferior parietal	0.503	L temporal pole	0.327
L lingual	0.501	L isthmus cingulate	0.325
L pars orbitalis	0.489	R entorhinal	0.324
R frontal pole	0.483	L parahippocampal	0.322
L middle temporal	0.481	R lateral occipital	0.319
R mean thickness	0.479	L transverse temporal	0.305
L caudal middle frontal	0.476	L lateral occipital	0.299
L pars triangularis	0.473	L entorhinal	0.293
L pars opercularis	0.465	R posterior cingulate	0.281
R pars opercularis	0.465	R caudal anterior cingulate	0.274
R caudal middle frontal	0.462	L pericalcarine	0.265
R fusiform	0.46	L posterior cingulate	0.251
R middle temporal	0.442	R medial orbitofrontal	0.248
R precuneus	0.439	L bankssts	0.223
L mean thickness	0.438	R pericalcarine	0.199
L rostral middle frontal	0.431	L paracentral	0.179
R supramarginal	0.431	L frontal pole	0.177
R pars orbitalis	0.429	R lingual	0.16
R precentral	0.428	R paracentral	0.159
L lateral orbitofrontal	0.418	R rostral anterior cingulate	0.156
L cuneus	0.409	L insula	0.128
R superior frontal	0.405	L rostral anterior cingulate	0.12
R pars triangularis	0.402	L medial orbitofrontal	0.103
L postcentral	0.401	R transverse temporal	0.04
R bankssts	0.399	L caudal anterior cingulate	0.016
R cuneus	0.399		

Note:—L indicates left; R, right; bankssts, banks of the superior temporal sulcus.
[a] ICCs for 2D-SE and 3D-GE cortical thickness estimates using FreeSurfer are shown. The ICC values are grouped in 5 categories. Zero percent of the structures had almost perfect agreement, 1.4% had substantial agreement, 40% had a moderate agreement, 42.9% had fair agreement, and 15.7% had slight agreement.

FIRST Reliability Assessment

With 2D-SE images, a registration error leading to a mis-segmentation occurred in 7 of 38 patients (18%) compared with none when 3D-GE images were used. Nevertheless, measurement of subcortical volumes from the studies that went through segmentation and registration showed a good agreement between 2D-SE and 3D-GE images, with 68.8% of the structures having either a substantial or almost perfect agreement (Table 2). Again, no clear pattern of over- or underestimation when using 2D-SE sequences was seen for subcortical structures.

Clinicoradiologic Correlations

Using normalized subcortical volume estimates obtained with FreeSurfer, we found the following: 1) Age did not correlate with any of the subcortical structures measured with both 3D-GE and 2D-SE images, and 2) disease duration and disability as measured with the Expanded Disability Status Scale showed a significant moderate correlation with most of the subcortical structures measured with both 3D-GE and 2D-SE images; however, when we used 2D-SE images, some correlations lost statistical significance (Table 3). Using normalized subcortical volume measures ob-

tained with FIRST, we found the following: 1) Age did not correlate with any of the subcortical structures measured with both 3D-GE and 2D-SE images, and 2) disease duration and EDSS scores showed a significant moderate correlation with most of the subcortical structures measured with 3D-GE images, while almost all correlations were nonsignificant if estimates from 2D-SE images were used (Table 4).

Table 2: Intraclass correlation coefficients for 2D-SE and 3D-GE subcortical volume estimates using FreeSurfer and FIRST[a]

FreeSurfer Software		FIRST Software	
Structure	ICC	Structure	ICC
Estimated TIV	0.942	R caudate	0.914
Subcortical gray volume	0.93	L caudate	0.899
R thalamus	0.903	L hippocampus	0.864
Brain stem	0.865	R thalamus	0.85
L putamen	0.861	L putamen	0.826
L caudate	0.833	R putamen	0.815
R putamen	0.82	R hippocampus	0.814
L ventral diencephalon	0.801	Brain stem	0.784
R ventral diencephalon	0.765	L pallidum	0.781
R pallidum	0.762	L thalamus	0.773
R caudate	0.743	R pallidum	0.605
L thalamus	0.737	R amygdala	0.456
L pallidum	0.71	L amygdala	0.406
R accumbens	0.694	L accumbens	0.25
R hippocampus	0.654	TIV[b]	0.175
R cerebellum cortex	0.616	R accumbens	0.009
L cerebellum cortex	0.579		
L hippocampus	0.568		
L accumbens	0.511		
R amygdala	0.397		
L amygdala	0.321		

Note:—L indicates left; R, right.

[a] The ICCs for 2D-SE and 3D-GE subcortical volume estimates using FreeSurfer and FIRST are shown. The ICC values are grouped in 5 categories: 33.3% and 43.8% of the structures with an almost perfect agreement using FreeSurfer and FIRST respectively, 42.9% and 25% of the structures with a substantial agreement using FreeSurfer and FIRST respectively, 14.3% and 12.5% of the structures with a moderate agreement using FreeSurfer and FIRST respectively, 9.5% and 6.25% of the structures with a fair agreement using FreeSurfer and FIRST respectively, and 0% and 12.5% of the structures with a slight agreement using FreeSurfer and FIRST respectively.

[b] FIRST total intracranial volume was calculated with the following formula: (FIRST template volume/matrix determinant) × 1000.

DISCUSSION

Brain volume loss, as measured with different postprocessing software packages, is known to occur in patients with MS, and it is clinically meaningful because it has been related to long-term motor and cognitive disability outcomes.[2,18,28] Historical MR imaging data from MS cohorts, with long-term follow-up that would provide relevant clinical information, do not include 3D heavily T1-weighted images (such as MPRAGE) but conventional 2D-SE T1-weighted images instead. Thus, reliability assessment of segmentation techniques in 2D-SE T1-weighted images may be of interest for these cohorts. As far as we are aware, this is the first time that FreeSurfer software has been evaluated by using 2D-SE T1-weighted images and that clinical correlations by using 3D-GE and 2D-SE images processed with FIRST and FreeSurfer have been compared.

Cortical thickness estimates by using FreeSurfer software have been previously evaluated and have been demonstrated to be a robust and reproducible measure, except when different field strengths were used.[6–8] All studies performed to date have used 3D T1-weighted sequences. In this study, we found that measurement of cortical thickness with 2D-SE images yields inaccurate and unreliable results, with ICC values below 0.6 for almost all structures; this finding was especially notable when medial structures were evaluated. Pulse sequence, voxel geometry, and parallel imaging do not seem to influence cortical thickness measurements.[6–8] Although FreeSurfer segmentation does not rely on voxel intensity histograms, the different gray-white matter contrast in 2D-SE compared with 3D-GE T1-weighted images (Fig 1) could partially explain this result. The contrast-to-noise ratio was calculated in a small subset sample ($n = 10$; data not shown). The mean contrast-to-noise ratio between gray and white matter was 10.1 in the 2D-SE sequence and 19.7 in the 3D-GE. There are fundamental differences between contrast behaviors of spin-echo and gradient-echo sequences, especially when this last sequence is obtained with a magnetization-prepared inversion pulse.[23] This magnetization-prepared inversion pulse produces a strong T1-weighting in the image, resulting in an excellent gray-white matter contrast compared with the standard 2D-SE

Table 3: Clinicoradiologic correlation using 3D-GE and 2D-SE normalized subcortical structure values obtained with FreeSurfer software

Subcortical Structure	FreeSurfer 3D-GE				FreeSurfer 2D-SE			
	Disease Duration		EDSS		Disease Duration		EDSS	
	r	*P*	*ρ*	*P*	*r*	*P*	*ρ*	*P*
Brain stem	−0.258	.123	−0.408[a]	.012[a]	−0.143	.400	−0.545[a]	<.001[a]
L thalamus	−0.249	.137	−0.268	.109	−0.301	.070	−0.313[b]	.059[b]
L caudate	−0.304[b]	.068[b]	−0.285[b]	.088[b]	−0.316[b]	.057[b]	−0.283	.090
L putamen	−0.443[a]	.006[a]	−0.494[a]	.002[a]	−0.466[a]	.004[a]	−0.510[a]	.001[a]
L pallidum	−0.489[a]	.002[a]	−0.409[a]	.012[a]	−0.315[b]	.057[b]	−0.404[a]	.013[a]
L hippocampus	−0.191	.256	−0.122	.472	−0.144	.397	−0.085	.615
L amygdala	−0.083	.627	−0.335[a]	.043[a]	0.001	.997	−0.141	.404
L accumbens	−0.332[a]	.045[a]	−0.418[a]	.010[a]	−0.358[a]	.030[a]	−0.096	.571
R thalamus	−0.409[a]	.012[a]	−0.402[a]	.014[a]	−0.386[a]	.018[a]	−0.376[a]	.022[a]
R caudate	−0.455[a]	.005[a]	−0.365[a]	.02[a]	−0.29[b]	.074[b]	−0.230	.171
R putamen	−0.505[a]	.001[a]	−0.490[a]	.002[a]	−0.472[a]	.003[a]	−0.494[a]	.002[a]
R pallidum	−0.459[a]	.004[a]	−0.395[a]	.016[a]	−0.220	.192	−0.28[b]	.093[b]
R hippocampus	−0.262	.118	−0.302[b]	.069[b]	−0.238	.157	−0.220	.190
R amygdala	−0.181	.285	−0.294[b]	.077[b]	−0.183	.279	−0.323[b]	.051[b]
R accumbens	−0.330[a]	.046[a]	−0.416[a]	.011[a]	−0.215	.202	−0.216	.199

Note:—*r* indicates the Pearson correlation coefficient; *ρ*, the Spearman correlation coefficient; L, left; R, right.

[a] Significant correlations.

[b] Trend toward a significant correlation.

Table 4: Clinicoradiologic correlation using 3D-GE and 2D-SE normalized subcortical structure values obtained with FIRST software

Subcortical Structure	FIRST 3D-GE				FIRST 2D-SE			
	Disease Duration		EDSS		Disease Duration		EDSS	
	r	*P*	*ρ*	*P*	*r*	*P*	*ρ*	*P*
Brain stem	−0.133	.433	−0.160	.345	0.079	.674	−0.150	.420
L thalamus	−0.424[a]	.009[a]	−0.226	.170	0.053	.777	0.080	.671
L caudate	−0.410[a]	.012[a]	−0.302[b]	.069[b]	−0.297	.105	−0.065	.728
L putamen	−0.383[a]	.019[a]	−0.364[a]	.027[a]	−0.056	.767	−0.262	.154
L pallidum	−0.308[b]	.063[b]	−0.430[a]	.008[a]	−0.073	.696	−0.002	.991
L hippocampus	−0.429[a]	.008[a]	−0.170	.313	−0.226	.222	−0.083	.658
L amygdala	−0.276[b]	.098[b]	−0.029	.864	0.195	.294	0.230	.213
L accumbens	−0.234	.164	−0.30[b]	.071[b]	0.384[a]	.033[a]	0.023	.901
R thalamus	−0.496[a]	.002[a]	−0.235	.162	−0.022	.905	−0.092	.621
R caudate	−0.501[a]	.002[a]	−0.270[a]	.106[a]	−0.419[a]	.019[a]	−0.188	.310
R putamen	−0.406[a]	.013[a]	−0.454[a]	.005[a]	−0.043	.817	−0.286	.119
R pallidum	−0.288[b]	.08[b]	−0.36[b]	.029[b]	−0.005	.980	0.013	.945
R hippocampus	−0.384[a]	.019[a]	−0.002	.988	−0.082	.662	−0.064	.731
R amygdala	−0.253	.131	0.046	.785	0.027	.887	0.331	.069
R accumbens	−0.316[b]	.057[b]	−0.322	.052	0.233	.208	−0.014	.941

Note:—L indicates left; R, right; *r*, the Pearson correlation coefficient; *ρ*, the Spearman correlation coefficient.

[a] Significant correlations.

[b] Trend toward a significant correlation.

images, facilitating morphologic evaluation and gray-white matter tissue segmentation.

The section thickness of the 2 sequences was quite different (1.2 mm^3 for the 3D-GE sequence versus 3 mm^3 for the 2D-SE sequence). This greater thickness in the 2D-SE sequences could probably have influenced the volumetric measures obtained with both software, since section thickness has already been demonstrated to play a role when estimating lesion volumes in patients with MS.[29] We are aware that visual inspection of intermediate outputs to exclude MR images with segmentation errors could have improved our reliability results[30]; however, this improvement would probably have been at the expense of introducing operator-derived biases. Furthermore, correcting cortical thickness segmentation errors (specially in 2D-SE T1-weighted images) would have been a very laborious and time-consuming task and very difficult to apply in future research involving a large number of patients. Thus, we decided to analyze the data obtained with FreeSurfer without adding control points to correct for topographic errors.

In this study, subcortical volume estimates of T1-weighted images by using both FreeSurfer and FIRST had a good 2D-SE versus 3D-GE reliability, with most of the ICC values being greater than 0.6. Subcortical GM volumes are estimated in both packages with a registration atlas–based technique (both by using the same atlas), a technique that is robust and insensitive to image contrast. We found that the amygdala and accumbens had the lowest ICC values, similar to descriptions in the literature for test-retest reliability assessment of 3D-GE subcortical segmentations by using FIRST software.[9,10,31] These structures are among the smallest; therefore, smaller volume differences may represent a higher percentage of error. The high ICC values obtained in our study for most of the subcortical structures using FIRST are in agreement with the only study performed to date that evaluated the performance of FIRST in 2D-SE T1-weighted images compared with 3D-GE T1-weighted images.[31] Also, we found segmentation errors in up to 18% of 2D-SE images, similar to what had been described in that work.[31] These mis-segmentations were not corrected because we did not focus on improving 2D-SE FIRST segmentation but on analyzing the performance of FIRST in these sequences in an automated fashion.

The main reason to study the performance of both packages in 2D-SE T1-weighted images was to test whether we could obtain measures that could be used to investigate clinical associations. Therefore, we assessed whether the subcortical normalized estimates obtained with 3D-GE and 2D-SE T1-weighted images by using the 2 packages were similarly associated with demographic and disease outcomes. Significant moderate correlations were obtained by using 3D-GE images, with relevant clinical outcomes such as disease duration and disability (measured with EDSS). However, by using 2D-SE scans, only normalized FreeSurfer estimates were significantly associated with clinical outcomes. This result could be partly explained because of the low ICC value of the TIV estimate between 2D-SE and 3D-GE T1-weighted images obtained by using FIRST (Table 2). Unlike FreeSurfer, FIRST does not provide a TIV estimate, and we calculated it by dividing the FIRST template volume (a fixed number of 1948.105) by the matrix determinant. Although both sequences covered the whole brain, the head coverage of the 2D-SE T1-weighted images is usually lower than the 3D template used in FSL, covering a lesser portion of the scalp and lower part of the brain stem (Fig 1). Thus, it is possible that the template volume used to calculate TIV does not match well enough for 2D-SE T1-weighted images.

We are aware that using FSL SIENAX software (http://fsl.fmrib.ox.ac.uk/fsl/fslwiki/SIENA)[25] to calculate TIV may have been a better approach. However, we wanted to evaluate whether robust volume measures could be obtained with 2D-SE T1-weighted images by using a single package and without using image-processing options in the volumetric analysis (ie, the adequate threshold) that could introduce biases. Nevertheless, to confirm our interpretation, we used SIENAX software to calculate the normalized brain volume from 2D-SE and 3D-GE sequences in a small subset sample ($n = 15$, data not shown). The ICC value of the normalized brain volume estimate between 2D-SE and 3D-GE T1-weighted images was 0.85 (almost perfect agreement), and most of the associations between subcortical normalized estimates and disease outcomes obtained by using 3D-GE se-

quences remained significant when using 2D-SE sequences. These results reinforce our hypothesis that the poor clinicoradiologic correlations seen with 2D-SE sequences are most probably due to a bad TIV estimation when using the avscale tool.

There are some limitations to our study. First, it was conducted with 2D-SE and 3D-GE T1-weighted images used in clinical practice with particular acquisition parameters. It is possible that a better optimized 2D-SE sequence obtained with a higher field scanner would have produced better segmentation results. Therefore, our results should be extrapolated with caution when using different 2D sequences. Second, a voxel-by-voxel comparison of the binary masks would have provided relevant information regarding whether the software included the same image points in both sequences. Unfortunately, 2D-SE and 3D-GE FIRST outputs have different resolutions; therefore, an accurate comparison of the binary masks could not be performed. Nevertheless, we believe this issue does not diminish the relevance of our results because a visual inspection of the outputs was performed to ensure that the FIRST software was correctly measuring subcortical structures in both sequences. Finally, a test-retest variability study with 2D-SE images would have provided more detailed information regarding reliability. Unfortunately, as stated before, the images used for this study were obtained in a clinical practice setting, with specific schedules, and test-retest studies are lacking.

CONCLUSIONS

We have demonstrated the following: 1) Measurement of cortical thickness with FreeSurfer with 2D-SE T1-weighted images is not accurate enough; 2) measurement of subcortical volumes with FreeSurfer and FIRST in 2D-SE images produces acceptable results; but 3) when we used normalized subcortical volumes of 2D-SE images for clinical correlations, FreeSurfer performed better than FIRST. Therefore, FreeSurfer should be preferred if normalized subcortical volume measures are to be used in transversal correlations with clinical and demographic variables but should not be used to measure cortical thickness in 2D-SE images.

Disclosures: Angela Vidal-Jordana—*UNRELATED*: *Payment for Lectures including Service on Speakers Bureaus*: Novartis, Roche, Sanofi, Biogen. Deborah Pareto—*UNRELATED*: *Payment for Lectures including Service on Speakers Bureaus*: Novartis, Genzyme. Jaume Sastre-Garriga—*UNRELATED*: *Consultancy*: Almirall; *Grants/Grants Pending*: Genzyme*; *Payment for Lectures including Service on Speakers Bureaus*: Novartis, Biogen, Almirall, Merck-Serono, Genzyme, Teva Pharmaceutical; *Payment for Development of Educational Presentations*: Novartis, TOPEC; *Travel/Accommodations/Meeting Expenses Unrelated to Activities Listed*: Merck, Novartis. Cristina Auger—*UNRELATED*: *Payment for Lectures including Service on Speakers Bureaus*: Novartis, Biogen, Sthendal. Ethel Ciampi—*RELATED*: *Other*: European Committee for Treatment and Research in Multiple Sclerosis, *Comments*: I received the European Committee for Treatment and Research in Multiple Sclerosis Clinical Training Fellowship Award 2013, which supported my stay in Barcelona for the period in which the study was performed but did not provide direct support of the study; *UNRELATED*: *Board Membership*: Biogen; *Employment*: School of Medicine UC; *Travel/Accommodations/Meeting Expenses Unrelated to Activities Listed*: Genzyme, Merck, Biogen. Xavier Montalban—*UNRELATED*: *Consultancy*: Actelion, Almirall, Biogen, Genzyme, Merck, Novartis, Receptos, Roche, Sanofi-Genzyme, Teva Pharmaceutical. Alex Rovira—*UNRELATED*: *Board Membership*: Novartis, Biogen, Genzyme, OLEA; *Consultancy*: Novartis, Biogen, Genzyme; *Payment for Lectures including Service on Speakers Bureaus*: Novartis, Biogen, Genzyme, OLEA, Bracco, Teva Pharmaceutical; *Payment for Development of Educational Presentations:* Novartis, Biogen, Genzyme, Teva Pharmaceutical. *Money paid to the institution.

REFERENCES

1. Pérez-Miralles FF, Sastre-Garriga J, Tintoré M, et al. **Clinical impact of early brain atrophy in clinically isolated syndromes.** *Mult Scler* 2013;19:1878–86 CrossRef Medline
2. Popescu V, Agosta F, Hulst HE, et al; MAGNIMS Study Group. **Brain atrophy and lesion load predict long term disability in multiple sclerosis.** *J Neurol Neurosurg Psychiatry* 2013;84:1082–91 CrossRef Medline
3. Fischl B. **FreeSurfer.** *Neuroimage* 2012;62:774–81 CrossRef Medline
4. Desikan RS, Ségonne F, Fischl B, et al. **An automated labeling system for subdividing the human cerebral cortex on MRI scans into gyral based regions of interest.** *Neuroimage* 2006;31:968–80 CrossRef Medline
5. Patenaude B, Smith SM, Kennedy DN, et al. **A Bayesian model of shape and appearance for subcortical brain segmentation.** *Neuroimage* 2011;56:907–22 CrossRef Medline
6. Han X, Jovicich J, Salat D, et al. **Reliability of MRI-derived measurements of human cerebral cortical thickness: the effects of field strength, scanner upgrade and manufacturer.** *Neuroimage* 2006;32:180–94 CrossRef Medline
7. Wonderlick J, Ziegler D, Hosseini-Varnamkhasti P, et al. **Reliability of MRI-derived cortical and subcortical morphometric measures: effects of pulse sequence, voxel geometry, and parallel imaging.** *Neuroimage* 2009;44:1324–33 CrossRef Medline
8. Govindarajan KA, Freeman L, Cai C, et al. **Effect of intrinsic and extrinsic factors on global and regional cortical thickness.** *PLoS One* 2014;9:e96429 CrossRef Medline
9. Morey RA, Selgrade ES, Wagner HR 2nd, et al. **Scan-rescan reliability of subcortical brain volumes derived from automated segmentation.** *Hum Brain Mapp* 2010;31:1751–62 CrossRef Medline
10. Nugent AC, Luckenbaugh DA, Wood SE, et al. **Automated subcortical segmentation using FIRST: test-retest reliability, interscanner reliability, and comparison to manual segmentation.** *Hum Brain Mapp* 2013;34:2313–29 CrossRef Medline
11. Derakhshan M, Caramanos Z, Giacomini PS, et al. **Evaluation of automated techniques for the quantification of grey matter atrophy in patients with multiple sclerosis.** *Neuroimage* 2010;52:1261–67 CrossRef Medline
12. Sailer M. **Focal thinning of the cerebral cortex in multiple sclerosis.** *Brain* 2003;126:1734–44 CrossRef Medline
13. Calabrese M, Atzori M, Bernardi V, et al. **Cortical atrophy is relevant in multiple sclerosis at clinical onset.** *J Neurol* 2007;254:1212–20 CrossRef Medline
14. Calabrese M, Rinaldi F, Mattisi I, et al. **Widespread cortical thinning characterizes patients with MS with mild cognitive impairment.** *Neurology* 2010;74:321–28 CrossRef Medline
15. Calabrese M, Rinaldi F, Mattisi I, et al. **The predictive value of gray matter atrophy in clinically isolated syndromes.** *Neurology* 2011;77:257–63 CrossRef Medline
16. Calabrese M, Favaretto A, Poretto V, et al. **Low degree of cortical pathology is associated with benign course of multiple sclerosis.** *Mult Scler* 2013;19:904–11 CrossRef Medline
17. Batista S, Zivadinov R, Hoogs M, et al. **Basal ganglia, thalamus and neocortical atrophy predicting slowed cognitive processing in multiple sclerosis.** *J Neurol* 2012;259:139–46 CrossRef Medline
18. Benedict RH, Ramasamy D, Munschauer F, et al. **Memory impairment in multiple sclerosis: correlation with deep grey matter and mesial temporal atrophy.** *J Neurol Neurosurg Psychiatry* 2009;80:201–06 CrossRef Medline
19. Datta S, Staewen TD, Cofield SS, et al; CombiRx Investigators Group. **Regional gray matter atrophy in relapsing remitting multiple sclerosis: baseline analysis of multi-center data.** *Mult Scler Relat Disord* 2015;4:124–36 CrossRef Medline
20. Calabrese M, Rinaldi F, Grossi P, et al. **Basal ganglia and frontal/parietal cortical atrophy is associated with fatigue in relapsing-remitting multiple sclerosis.** *Mult Scler* 2010;16:1220–28 CrossRef Medline
21. Bergsland N, Zivadinov R, Dwyer MG, et al. **Localized atrophy of the thalamus and slowed cognitive processing speed in MS patients.** *Mult Scler* 2016;22:1327–36 CrossRef Medline

22. Motl RW, Hubbard EA, Sreekumar N, et al. **Pallidal and caudate volumes correlate with walking function in multiple sclerosis.** *J Neurol Sci* 2015;354:33–36 CrossRef Medline
23. Mugler JP 3rd, Brookeman JR. **Three-dimensional magnetization-prepared rapid gradient-echo imaging (3D MP RAGE).** *Magn Reson Med* 1990;15:152–57 CrossRef Medline
24. Fischer HW, Rinck PA, Van Haverbeke Y, et al. **Nuclear relaxation of human brain gray and white matter: analysis of field dependence and implications for MRI.** *Magn Reson Med* 1990;16:317–34 CrossRef Medline
25. Smith SM, Zhang Y, Jenkinson M, et al. **Accurate, robust, and automated longitudinal and cross-sectional brain change analysis.** *Neuroimage* 2002;17:479–89 CrossRef Medline
26. Jenkinson M, Smith S. **A global optimisation method for robust affine registration of brain images.** *Med Image Anal* 2001;5:143–56 CrossRef Medline
27. Jenkinson M, Bannister P, Brady M, et al. **Improved optimization for the robust and accurate linear registration and motion correction of brain images.** *Neuroimage* 2002;17:825–41 CrossRef Medline
28. Lansley J, Mataix-Cols D, Grau M, et al. **Localized grey matter atrophy in multiple sclerosis: a meta-analysis of voxel-based morphometry studies and associations with functional disability.** *Neurosci Biobehav Rev* 2013;37:819–30 CrossRef Medline
29. Filippi M, Horsfield MA, Campi A, et al. **Resolution-dependent estimates of lesion volumes in magnetic resonance imaging studies of the brain in multiple sclerosis.** *Ann Neurol* 1995;38:749–54 CrossRef Medline
30. Iscan Z, Jin TB, Kendrick A, et al. **Test-retest reliability of Freesurfer measurements within and between sites: effects of visual approval process.** *Hum Brain Mapp* 2015;36:3472–85 CrossRef Medline
31. Amann M, Andělová M, Pfister A, et al. **Subcortical brain segmentation of two dimensional T1-weighted data sets with FMRIB's Integrated Registration and Segmentation Tool (FIRST).** *Neuroimage Clin* 2015;7:43–52 CrossRef Medline

Synthetic MRI in the Detection of Multiple Sclerosis Plaques

A. Hagiwara, M. Hori, K. Yokoyama, M.Y. Takemura, C. Andica, T. Tabata, K. Kamagata, M. Suzuki, K.K. Kumamaru, M. Nakazawa, N. Takano, H. Kawasaki, N. Hamasaki, A. Kunimatsu, and S. Aoki

ABSTRACT

BACKGROUND AND PURPOSE: Synthetic MR imaging enables the creation of various contrast-weighted images including double inversion recovery and phase-sensitive inversion recovery from a single MR imaging quantification scan. Here, we assessed whether synthetic MR imaging is suitable for detecting MS plaques.

MATERIALS AND METHODS: Quantitative and conventional MR imaging data on 12 patients with MS were retrospectively analyzed. Synthetic T2-weighted, FLAIR, double inversion recovery, and phase-sensitive inversion recovery images were produced after quantification of T1 and T2 values and proton density. Double inversion recovery images were optimized for each patient by adjusting the TI. The number of visible plaques was determined by a radiologist for a set of these 4 types of synthetic MR images and a set of conventional T1-weighted inversion recovery, T2-weighted, and FLAIR images. Conventional 3D double inversion recovery and other available images were used as the criterion standard. The total acquisition time of synthetic MR imaging was 7 minutes 12 seconds and that of conventional MR imaging was 6 minutes 29 seconds The lesion-to-WM contrast and lesion-to-WM contrast-to-noise ratio were calculated and compared between synthetic and conventional double inversion recovery images.

RESULTS: The total plaques detected by synthetic and conventional MR images were 157 and 139, respectively ($P = .014$). The lesion-to-WM contrast and contrast-to-noise ratio on synthetic double inversion recovery images were superior to those on conventional double inversion recovery images ($P = .001$ and < 0.001, respectively).

CONCLUSIONS: Synthetic MR imaging enabled detection of more MS plaques than conventional MR imaging in a comparable acquisition time. The contrast for MS plaques on synthetic double inversion recovery images was better than on conventional double inversion recovery images.

ABBREVIATIONS: CNR = contrast-to-noise ratio; DIR = double inversion recovery; PD = proton density; PSIR = phase-sensitive inversion recovery; QRAPMASTER = quantification of relaxation times and proton density by multiecho acquisition of saturation recovery with TSE readout; SI = signal intensity; TIIR = T1-weighted inversion recovery

MS is a CNS demyelination disorder that usually strikes young adults. MR imaging serves an important role in MS diagnosis and surveillance via the detection and follow-up of focal and diffuse CNS lesions. Monitoring new or enlarging MS plaques is suitable for following disease activity when evaluating treatment effects.[1] The number of lesions detected early in the disease process is associated with future relapse, disability accumulation, or cognitive deficits.[2] Several reports have shown the utility of double inversion recovery (DIR) and phase-sensitive inversion recovery (PSIR) images for detecting MS plaques, especially in intracortical or mixed WM-GM areas.[3–6] Relative to FLAIR and T2-weighted images, DIR suppresses WM and CSF signals, thereby increasing the conspicuity of lesions in both GM and WM.[7] PSIR is a T1-weighted inversion recovery (T1IR) sequence with phase-sensitive reconstruction that provides a greater dynamic range of signal intensity (SI) and higher tissue contrast than

Received June 27, 2016; accepted after revision September 20.

From the Departments of Radiology (A.H., M.H., M.Y.T., C.A., T.T., K.K., M.S., K.K.K., M.N., N.T., H.K., N.H., S.A.) and Neurology (K.Y.), Juntendo University School of Medicine, Tokyo, Japan; Department of Radiology (A.H., A.K.), Graduate School of Medicine, The University of Tokyo, Tokyo, Japan; and Department of Radiological Sciences (M.N.), Graduate School of Human Health Sciences, Tokyo Metropolitan University, Tokyo, Japan.

This work was supported by the Japan Society for the Promotion of Science KAKENHI, grant number 16K19852; and grants from the Ministry of Education, Culture, Sports, Science and Technology–Supported Program for the Strategic Research Foundation at Private Universities (2011–2015); and it was funded by the Impulsing Paradigm Change through disruptive Technologies (ImPACT) Program of the Council for Science, Technology and Innovation (Cabinet Office, Government of Japan).

Please address correspondence to Akifumi Hagiwara, MD, Department of Radiology, The University of Tokyo, 7-3-1, Hongo, Bunkyo-ku, Tokyo, Japan, 113-8655; e-mail: ahagiwara-tky@umin.ac.jp

Indicates open access to non-subscribers at www.ajnr.org

http://dx.doi.org/10.3174/ajnr.A5012

conventional T1IR sequences by additively combining positive and negative longitudinal magnetization.[8] However, the additional acquisition time required has hindered the clinical use of DIR and PSIR images.

Synthetic MR imaging enables the production of images with almost any contrast-weighting, including DIR and PSIR, by virtually adjusting the TR, TE, and TI after quantifying the longitudinal T1 and transverse T2 relaxation times and the proton density (PD).[9,10] Quantification of relaxation times and proton density by multiecho acquisition of saturation recovery with TSE readout (QRAPMASTER), an MR imaging quantification pulse sequence, was recently introduced into the clinical setting and has greatly shortened the time required for quantifying these parameters.[11] A recent phantom study revealed that T1, T2, and PD measurements made with the QRAPMASTER pulse sequence were sufficiently accurate and reproducible.[12] Synthetic MR imaging of the brain generates images inferior in quality but comparable in diagnostic power with those acquired by conventional MR imaging.[13] Synthetic MR imaging is reported to be useful in evaluating brain metastases[14] and Sturge-Weber syndrome.[15,16] Moreover, some reports have demonstrated the utility of synthetic MR imaging in evaluating patients with MS.[17-19] However, the added value of synthetic PSIR and DIR to detect MS plaques remains to be examined. The research described above suggests that generating PSIR and DIR images in addition to T2-weighted and FLAIR images may boost the detectability of MS plaques by MR imaging.

Here, we assessed the usefulness of synthetic MR imaging, which enables creation of any contrast-weighted images including PSIR and DIR, for detecting focal MS plaques by comparing images obtained from synthetic and conventional MR imaging.

MATERIALS AND METHODS

Study Participants

The study was approved by the institutional review board of Juntendo University Hospital, Tokyo, Japan. Given its retrospective nature, written informed consent was not required. Data from 22 consecutive patients with MS who had undergone quantitative and conventional MR imaging from August 2015 through November 2015 were retrospectively reviewed. These patients were diagnosed according to standard criteria.[20-22] Of the 22 patients, 10 had diffusely abnormal white matter[23] and were excluded from the study because the number of plaques was difficult to count accurately. Therefore, data from 12 patients (1 male and 11 females; mean age, 35.5 years; age range, 16–50 years) were evaluated. Of the 12 patients, 10 had relapsing-remitting MS and 2 had clinically isolated syndrome. The median score on the Expanded Disability Status Scale[24] at imaging was zero (range, 0–3.0), and the mean disease duration was 6.2 ± 5.1 years.

MR Imaging

For all patients, MR imaging was performed on a 3T scanner (Discovery MR750w; GE Healthcare, Milwaukee, Wisconsin) with a 12-channel head coil. All patients underwent quantitative 2D axial imaging and conventional 2D axial T1IR, T2-weighted, FLAIR, and 3D sagittal DIR imaging.

Quantitative MR imaging was performed by using the 2D axial QRAPMASTER pulse sequence.[11] This is a multisection, multiecho, multisaturation delay saturation-recovery turbo spin-echo acquisition method in which images are collected for different combinations of TEs and saturation delay times. At our institution, 2 TEs and 4 delay times were used to generate 8 real images and 8 imaginary ones, which were then used to quantify longitudinal T1 and transverse T2 relaxation times and the PD. The TEs used were 16.9 and 84.5 ms, and the delay time was set as defined by the manufacturer of SyMRI software (SyntheticMR, Linköping, Sweden). The parameters used for quantitative MR imaging were as follows: FOV, 240 × 240 mm; matrix, 320 × 320; echo-train length, 10; bandwidth, 31.25 kHz; section thickness/gap, 4.0 mm/1.0 mm; and sections, 30. The data acquired at each section were used to produce T1, T2, and PD maps, which were then used to calculate the synthetic MR images. Quantification map acquisition and raw data processing were performed with SyMRI software (Version 8.0; SyntheticMR).

The parameters used to produce synthetic T2-weighted images were TR, 4500 ms; and TE, 100 ms. Those used to generate FLAIR images were TR, 15,000 ms; TE, 100 ms; and TI, 2900 ms. Finally, those used to obtain PSIR images were TR, 6000 ms; TE, 15 ms; and TI, 500 ms. The parameters for DIR image synthesis, which were optimized for each patient, are shown in the following section.

The parameters used to obtain conventional T1IR images were the following: TR, 3294 ms; TE, 18 ms; TI, 908 ms; FOV, 240 × 216 mm; matrix, 352 × 256; echo-train length, 8; section thickness/gap, 4 mm/1 mm; and sections, 30. Those used to obtain T2-weighted images were the following: TR, 4500 ms; TE, 111 ms; FOV, 240 × 240 mm; matrix, 512 × 512; echo-train length, 24; section thickness/gap, 4 mm/1 mm; and sections, 30. Those used to obtain FLAIR images were the following: TR, 9000 ms; TE, 124 ms; FOV, 240 × 240 mm; matrix, 320 × 224; echo-train length, 16; section thickness/gap, 4 mm/1 mm; and sections, 30. Finally, those used to produce 3D sagittal DIR images were the following: TR, 7000 ms; TE, 90 ms; first TI, 2892 ms; second TI, 546 ms; FOV, 256 × 256 mm; matrix, 192 × 192; echo-train length, 160; section thickness, 1.0 mm; and sections, 160. The first TI was defined as the interval between the first 180° inversion pulse and the 90° excitation pulse. The second TI was defined as the interval between the second 180° inversion pulse and the 90° excitation pulse.

The acquisition time was 7 minutes 12 seconds for quantitative MR imaging, 1 minute 50 seconds for conventional T1IR, 2 minutes 6 seconds for conventional T2-weighted, 2 minutes 33 seconds for conventional FLAIR, and 6 minutes 15 seconds for conventional 3D DIR images. These images were saved as DICOM files and analyzed with OsiriX Imaging Software, Version 7.0 (http:// www.osirix-viewer.com) on a personal computer.

Synthetic DIR Optimization

The parameters for creating synthetic DIR images were optimized for each patient by adjusting the second TI to intensify the contrast between MS plaques and WM (Fig 1). All other parameters were the same for each patient, as follows: TR, 15,000 ms; TE, 100 ms; and first TI (*TI*1), 3750 ms. The second TI (*TI*2) was selected to suppress the WM and CSF signals while maximizing the GM

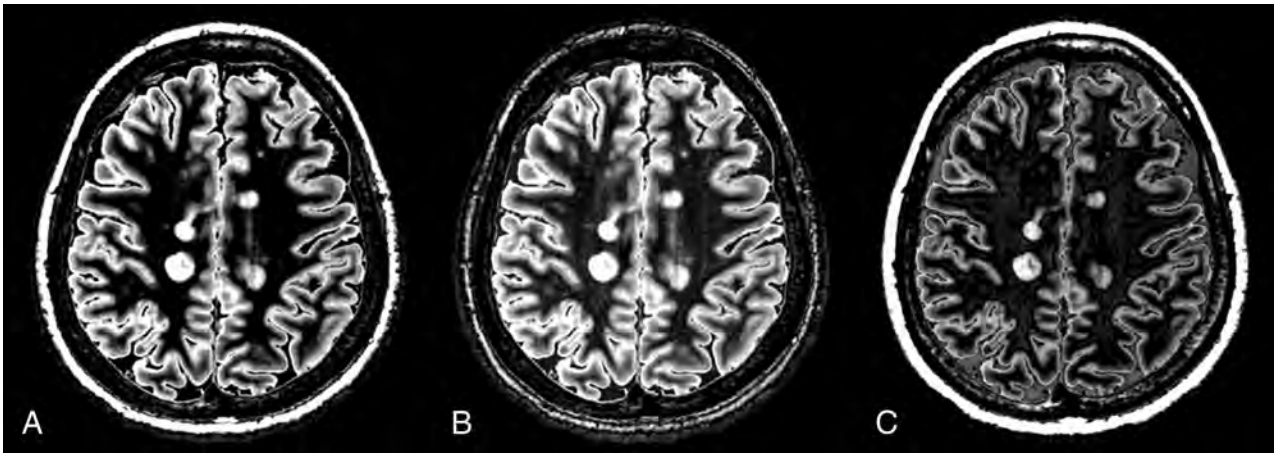

FIG 1. An example of DIR optimization. A DIR image with a second TI of 460 ms (*A*) (as determined according to the equations in the main text) shows better delineation of MS plaques than a DIR image with a second TI of 360 ms (*B*) or 560 ms (*C*).

signal, in accordance with the method of Gabr et al.[25] This procedure was accomplished by minimizing the following expression:

$$\frac{SI_{WM} + SI_{CSF}}{SI_{GM}},$$

where SI_{WM}, SI_{CSF}, and SI_{GM} denote the signal intensities (SIs) of WM, CSF, and GM, respectively. For each tissue type, we measured T1, T2, and PD on SyMRI software to estimate the SI by using the following expression, modified from the work of Redpath and Smith[26]:

$$SI = PD\{1 - 2exp(-TI2 / T1) + 2exp[-(TI1 + TI2) / T1] - exp(-TR / T1)[2exp(TE / 2T1) - 1]\}(exp(-TE / T2)).$$

Here, T1, T2, and PD of each tissue type were averaged from the following ROIs (3 × 3 voxels, corresponding to 2.25 × 2.25 mm^2): CSF, bilaterally in the anterior horns of the lateral ventricles; GM, bilaterally in the thalamus, occipital cortex, and frontal cortex; and WM, in the corpus callosum—one in the genu and another in the splenium—and bilaterally in the centrum semiovale. The second TI of each image fell in the range of 460–480 ms after optimization of the synthetic DIR images for each patient.

Image Analysis

Qualitative Analysis of Conventional and Synthetic Images. An experienced neuroradiologist (K.K.), blinded to the clinical information, individually counted the number of lesions in the synthetic and conventional image sets, which were shown in random order in 1 session. One synthetic image set included T2-weighted, FLAIR, DIR, and PSIR images for each patient (Fig 2). One conventional image set included T2-weighted, FLAIR, and T1IR images. Lesions at least 3 mm in diameter were counted. To confirm the accuracy of lesion counts, an experienced neuroradiologist (M.S.) also independently conducted MR imaging evaluations of the same imaging datasets. Conventional 3D DIR images and all other images were used as criterion standards by an experienced neuroradiologist (A.H.) to determine whether a counted lesion was a true- or false-positive and to classify the lesion according to its location as an infratentorial, deep GM, periventricular WM, deep WM, juxtacortical WM, or mixed WM-GM lesion. If a lesion was detected only on the conventional image set or the synthetic image set but not on conventional 3D DIR images, we defined it as a false-positive.

Quantitative Analysis of Conventional and Synthetic DIR Images. The lesion-to-WM contrast and the contrast-to-noise ratio (CNR) were among the indices used to quantify synthetic and conventional DIR images. To assess image quality, we also analyzed the GM-to-WM contrast, GM-to-CSF contrast, and CNR. To match the section thickness between synthetic and conventional DIR images, we reconstructed conventional 2D axial DIR images (thickness, 4 mm; gap, 1 mm) from conventional 3D DIR sagittal images.

ROI analyses were performed on synthetic and conventional DIR images by a single investigator (M.N.) blinded to the clinical information. For the quantitative analysis, the signal intensities of the MS lesions and corresponding WM were measured by ROI analyses and their mean values were recorded. A circular ROI that covered almost the entire lesion was placed on each MS plaque that measured ≥5 mm in diameter. The ROI was then copied and pasted on the corresponding WM (Fig 3). For a supratentorial lesion, the corresponding WM was defined as the normal-appearing WM contralateral to that lesion. For an infratentorial lesion, it was defined as the normal-appearing WM in the brain stem in the same section.

In synthetic MR imaging, the SI of the surrounding air is set to zero. Hence, the median SD of the SIs of the following 12 ROIs, all of which were 2.4 × 2.4 mm^2, was defined as the noise for each patient: ROIs in the CSF (bilaterally in the anterior horns of the lateral ventricles), in the GM (bilaterally in the thalamus, occipital cortex, and frontal cortex), and in the WM (in the corpus callosum—one in the genu and another in the splenium—and bilaterally in the centrum semiovale). This approach was a modified version of the method used by Blystad et al.[13]

To assess the effect of optimizing WM signal suppression on the image quality of DIR images, we compared the SI of GM (SI_{GM}) with the SIs of WM (SI_{WM}) and CSF (SI_{CSF}). SI_{GM}, SI_{WM}, and SI_{CSF} were obtained by averaging the values of the 6, 4, and 2 regions above, respectively, for each patient.

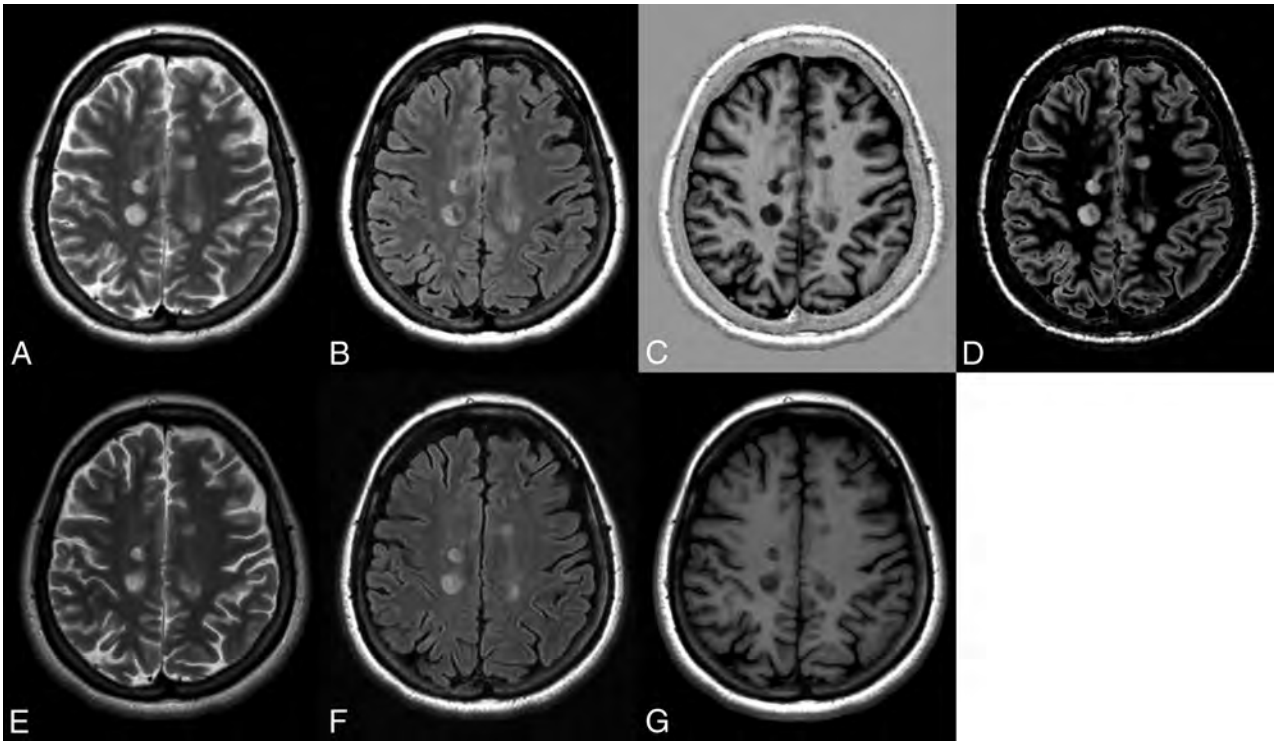

FIG 2. Representative sections of synthetic T2-weighted (*A*), FLAIR (*B*), PSIR (*C*), and DIR (*D*) images, along with conventional T2-weighted (*E*), FLAIR (*F*), and T1IR (*G*) images.

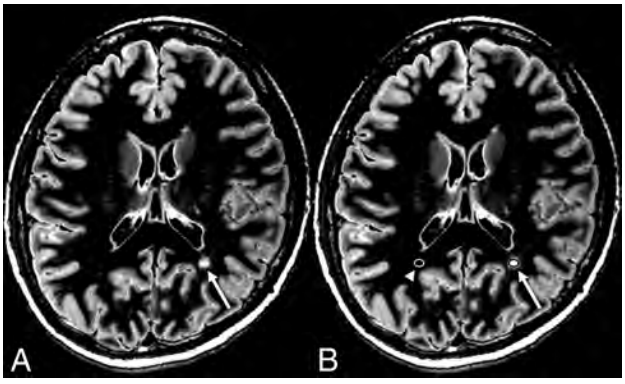

FIG 3. An example of ROI placement. A plaque (*arrow*) is shown on the synthetic DIR image (*A*). A circular ROI (*arrow*) that covers almost the entire lesion is placed in *B*. The ROI was copied and pasted on the contralateral normal-appearing WM (*arrowhead*).

The lesion-to-WM contrast was defined as the difference between the mean SI of a lesion and that of the corresponding WM divided by the SI of the corresponding WM. The lesion-to-WM CNR was defined as the difference between the SI of a lesion and that of the corresponding WM divided by the noise of each sequence. The GM-to-WM and GM-to-CSF contrasts and CNRs were calculated likewise.

Statistical Analysis

Statistics were computed by using the free software R, Version 3.2.1 (R statistical and computing software; http://www.r-project.org/). Because none of the datasets were normally distributed, we used the nonparametric Wilcoxon signed rank test to compare the number of lesions detected in the synthetic and conventional images as well as the contrasts and CNRs of synthetic and conventional DIR images. A 2-sided *P* value $< .05$ was considered significant.

Table 1: Multiple sclerosis plaques detected by a neuroradiologist on synthetic and conventional MR images

Region	Synthetic MRI (No.)	Conventional MRI (No.)	*P* Value
Infratentorial	2	2	1
Periventricular WM	31	28	.374
Deep WM	87	82	.198
Juxtacortical WM	25	20	.547
Mixed WM-GM	6	5	.773
Deep GM	6	2	.203
Total	157	139	.014
False-positives	3	1	.586

RESULTS

The total number of lesions detected by K.K. on synthetic images was significantly larger than that on conventional images (Table 1). However, no significant difference was detected in any individual region. Several lesions were easier to find on synthetic DIR or PSIR images than on conventional images and were detected only on the synthetic image set but not on the conventional image set by K.K. (Fig 4). All false-positives on synthetic images were located next to the CSF (Fig 5), because the surface of the brain tended to become hyperintense on synthetic FLAIR and DIR images.

The interobserver reproducibility between the 2 observers (K.K. and M.S.) for the total number of detected lesions was then measured. The interclass correlation coefficient of synthetic MR imaging was 0.858 (95% CI, 0.496–0.959). That of conventional MR imaging was 0.950 (95% CI, 0.824–0.986).

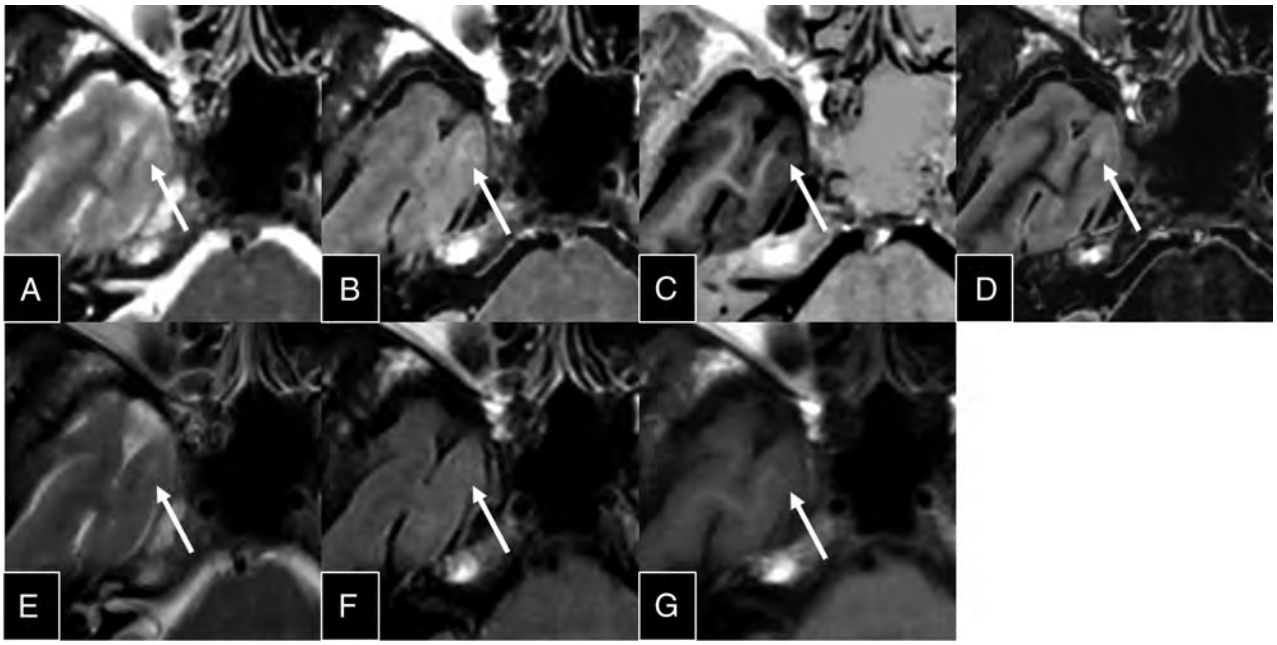

FIG 4. An MS plaque readily detected on PSIR and DIR images. This plaque (*arrows*) is difficult to identify on synthetic T2-weighted (*A*) and FLAIR (*B*) images and on conventional T2-weighted (*E*), FLAIR (*F*), and TIIR (*G*) images, but it is clearly delineated on synthetic PSIR (*C*) and DIR (*D*) images. The plaque was detected by a neuroradiologist (K.K.) on synthetic but not conventional MR images.

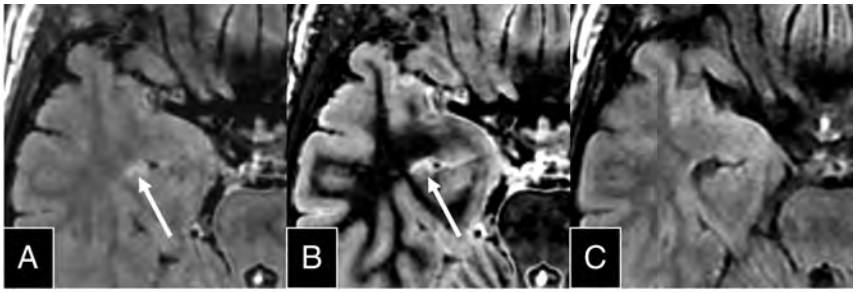

FIG 5. An example of a false-positive lesion. The surface of the brain tends to become hyperintense on synthetic FLAIR and DIR images. Note the hyperintense focus (*arrow*) in the inferior horn of the right lateral ventricle on synthetic FLAIR (*A*) and DIR (*B*) images; this focus was identified as an MS plaque by a neuroradiologist (K.K.). No hyperintense focus is seen in the same place on a conventional FLAIR image (*C*).

Table 2: Contrast and CNR among lesions, WM, GM, and CSF

	Synthetic DIR[a]	Conventional DIR[a]	*P* Value
Lesion-to-WM contrast	9.33 ± 5.92	6.74 ± 3.58	.001
Lesion-to-WM CNR	23.50 ± 7.90	20.20 ± 8.30	<.001
GM-to-WM contrast	5.21 ± 2.26	3.73 ± 1.18	.027
GM-to-WM CNR	13.07 ± 2.77	11.10 ± 3.89	.012
GM-to-CSF contrast	17.05 ± 20.30	3.98 ± 1.18	<.001
GM-to-CSF CNR	14.33 ± 2.68	11.17 ± 3.61	.009

[a] Values are means ± SD.

The lesion-to-WM, GM-to-WM, and GM-to-CSF contrasts and their corresponding CNRs of synthetic DIR images were significantly higher than those of conventional DIR images (Table 2 and Fig 6).

DISCUSSION

Synthetic MR imaging enabled us to detect more MS plaques than conventional MR imaging in a comparable acquisition time (7 minutes 12 seconds versus 6 minutes 29 seconds). Previous reports have shown that DIR and PSIR images are superior to T2-weighted and FLAIR images for detecting intracortical or mixed WM-GM lesions[3,4,6]; these reports were of MR images of ≤3-mm section thickness. However, the ability to detect mixed WM-GM plaques did not differ significantly between synthetic and conventional MR images in our study, which were obtained with a section thickness of 4 mm. In a study of DIR images with a section thickness of 5 mm, significantly more MS plaques were detected on DIR images than on FLAIR and T2-weighted images, but not in the case of mixed WM-GM lesions.[5] Likewise, our use of a section thickness of 4 mm and a small number of patients may have hindered the detection of more mixed WM-GM lesions on synthetic than on conventional MR imaging. Including more patients in our study may have enabled the detection of more intracortical or mixed WM-GM plaques on synthetic than on conventional MR imaging.

All the false-positives on synthetic images were located next to the CSF (Fig 5). In synthetic FLAIR and DIR images, the surface of the brain tends to become hyperintense, which is presumably caused by the partial volume effect. The surface of the brain is even brighter on synthetic DIR images than on synthetic FLAIR images (Fig 2). This feature may not be a problem if the existence of these artifacts is known in advance of reading synthetic MR images.

In this study, even though the interclass correlation coefficient of synthetic MR imaging between the 2 observers was excellent, it was lower and had a wider range than that of conventional MR imaging. One explanation is that these 2 readers had never been

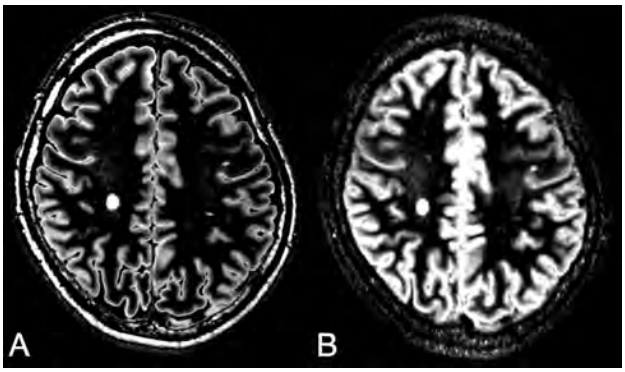

FIG 6. Sample sections of synthetic (*A*) and conventional (*B*) DIR images. Note the better suppression of WM on the synthetic DIR image.

exposed to synthetic MR imaging prior to this study. After the readers become accustomed to synthetic MR imaging, the agreement rate may be higher.

The quality of DIR images was better in synthetic MR imaging (which was optimized for each patient) than in conventional MR imaging. No previous report has evaluated the image quality of synthetic DIR. Synthetic T1-weighted and T2-weighted images were reported to have higher contrast and comparable CNR compared with conventional images.[13] Synthetic FLAIR images were reported to have lower contrast and lower CNR than conventional FLAIR images. In our study, we succeeded in creating synthetic DIR images with higher contrast and CNR than conventional DIR images by optimizing them for each patient. This result shows the potential advantage of synthetic MR imaging, which can be optimized for each patient after image acquisition. A recent report attempted to optimize the DIR image for each patient.[25] In this report, DIR images were acquired after obtaining T1 and T2 maps separately and then optimizing the acquisition parameters according to these maps. Because quantification and image creation can be completed in a single acquisition and on the same software, the method used in our study has the potential to reduce the time needed for DIR optimization.

Our study had a number of limitations. First, the sample size was small. Second, the section thickness of the MR images acquired was 4 mm with a 1-mm gap. This thickness was due to the technical problem of not being able to obtain synthetic MR images without a gap of at least 1 mm to reduce cross-talk between sections, even though current imaging guidelines for MS recommend a section thickness of ≤3 mm without a gap for 2D acquisition.[27,28] This problem should be addressed in future studies. Third, the resolution was not the same for all sequences. The retrospective nature of this study hindered the parameter adjustment.

CONCLUSIONS

Synthetic MR imaging enabled the detection of more MS plaques than conventional MR imaging in a comparable acquisition time, owing to the creation of useful contrast-weighted images (ie, DIR, PSIR) not acquired routinely on conventional MR imaging. The quality of DIR images in synthetic MR imaging optimized for each patient was superior to that in conventional MR imaging. Our results show that synthetic MR imaging has the potential to be useful for detecting MS plaques.

Disclosures: Akifumi Hagiwara—*RELATED*: *Grant*: Japan Society for the Promotion of Science; a Ministry of Education, Culture, Sports, Science and Technology–Supported Program; and the Impulsing Paradigm Change through disruptive Technologies (ImPACT) program, *Comments*: Japan Society for the Promotion of Science. KAKENHI, grant number 16K19852; a Ministry of Education, Culture, Sports, Science and Technology–Supported Program for the Strategic Research Foundation at Private Universities (2011–2015); ImPACT program of the Council for Science, Technology and Innovation. Nao Takano—*UNRELATED*: *Payment for Lectures including Service on Speakers Bureaus*: GE Healthcare Japan, *Comments*: The 42nd Japanese Society of Radiological Technology Autumn Scientific Congress, October 9–11, 2014, Sapporo, Hokkaido, Japan; luncheon seminar concerning experience in MR angiography (silent MRA) using the Silenz sequence. Akira Kunimatsu—*UNRELATED: Payment for Lectures including Service on Speakers Bureaus*: Siemens Healthcare K.K., Toshiba Medical Systems, Terumo, Philips Electronics Japan; *Payment for Manuscript Preparation:* Bayer Yakuhin, GE Healthcare Japan.

REFERENCES

1. Bonzano L, Roccatagliata L, Mancardi GL, et al. **Gadolinium-enhancing or active T2 magnetic resonance imaging lesions in multiple sclerosis clinical trials?** *Mult Scler* 2009;15:1043–47 CrossRef Medline
2. Lavery AM, Verhey LH, Waldman AT. **Outcome measures in relapsing-remitting multiple sclerosis: capturing disability and disease progression in clinical trials.** *Mult Scler Int* 2014;2014:262350 CrossRef Medline
3. Geurts JJ, Pouwels PJ, Uitdehaag BM, et al. **Intracortical lesions in multiple sclerosis: improved detection with 3D double inversion-recovery MR imaging.** *Radiology* 2005;236:254–60 Medline
4. Nelson F, Poonawalla AH, Hou P, et al. **Improved identification of intracortical lesions in multiple sclerosis with phase-sensitive inversion recovery in combination with fast double inversion recovery MR imaging.** *AJNR Am J Neuroradiol* 2007;28:1645–49 Medline
5. Wattjes MP, Lutterbey GG, Gieseke J, et al. **Double inversion recovery brain imaging at 3T: diagnostic value in the detection of multiple sclerosis lesions.** *AJNR Am J Neuroradiol* 2007;28:54–59 Medline
6. Sethi V, Yousry TA, Muhlert N, et al. **Improved detection of cortical MS lesions with phase-sensitive inversion recovery MRI.** *J Neurol Neurosurg Psychiatry* 2012;83:877–82 CrossRef Medline
7. Bedell BJ, Narayana PA. **Implementation and evaluation of a new pulse sequence for rapid acquisition of double inversion recovery images for simultaneous suppression of white matter and CSF.** *J Magn Reson Imaging* 1998;8:544–47 Medline
8. Hou P, Hasan KM, Sitton CW, et al. **Phase-sensitive T1 inversion recovery imaging: a time-efficient interleaved technique for improved tissue contrast in neuroimaging.** *AJNR Am J Neuroradiol* 2005;26:1432–38 Medline
9. Bobman SA, Riederer SJ, Lee JN, et al. **Cerebral magnetic resonance image synthesis.** *AJNR Am J Neuroradiol* 1985;6:265–69 Medline
10. Riederer SJ, Suddarth SA, Bobman SA, et al. **Automated MR image synthesis: feasibility studies.** *Radiology* 1984;153:203–06 Medline
11. Warntjes JB, Leinhard OD, West J, et al. **Rapid magnetic resonance quantification on the brain: optimization for clinical usage.** *Magn Reson Med* 2008;60:320–29 Medline
12. Krauss W, Gunnarsson M, Andersson T, et al. **Accuracy and reproducibility of a quantitative magnetic resonance imaging method for concurrent measurements of tissue relaxation times and proton density.** *Magn Reson Imaging* 2015;33:584–91 CrossRef Medline
13. Blystad I, Warntjes JB, Smedby O, et al. **Synthetic MRI of the brain in a clinical setting.** *Acta Radiol* 2012;53:1158–63 CrossRef Medline
14. Hagiwara A, Hori M, Suzuki M, et al. **Contrast-enhanced synthetic MRI for the detection of brain metastases.** *Acta Radiol Open* 2016;5:2058460115626757 CrossRef Medline
15. Hagiwara A, Nakazawa M, Andica C, et al. **Dural enhancement in a patient with Sturge-Weber syndrome revealed by double inversion recovery contrast using synthetic MRI.** *Magn Reson Med Sci* 2016;15:151–52 CrossRef Medline
16. Andica C, Hagiwara A, Nakazawa M, et al. **The advantage of synthetic MRI for the visualization of early white matter change in an infant with Sturge-Weber syndrome.** *Magn Reson Med Sci* 2016;15:347–48 CrossRef Medline

17. West J, Aalto A, Tisell A, et al. **Normal appearing and diffusely abnormal white matter in patients with multiple sclerosis assessed with quantitative MR.** *PLoS One* 2014;9:e95161 CrossRef Medline
18. Blystad I, Hakansson I, Tisell A, et al. **Quantitative MRI for analysis of active multiple sclerosis lesions without gadolinium-based contrast agent.** *AJNR Am J Neuroradiol* 2016;37:94–100 CrossRef Medline
19. Granberg T, Uppman M, Hashim F, et al. **Clinical feasibility of synthetic MRI in multiple sclerosis: a diagnostic and volumetric validation study.** *AJNR Am J Neuroradiol* 2016;37:1023–29 CrossRef Medline
20. McDonald WI, Compston A, Edan G, et al. **Recommended diagnostic criteria for multiple sclerosis: guidelines from the International Panel on the Diagnosis of Multiple Sclerosis.** *Ann Neurol* 2001;50:121–27 Medline
21. Polman CH, Reingold SC, Edan G, et al. **Diagnostic criteria for multiple sclerosis: 2005 revisions to the "McDonald Criteria."** *Ann Neurol* 2005;58:840–46 Medline
22. Polman CH, Reingold SC, Banwell B, et al. **Diagnostic criteria for multiple sclerosis: 2010 revisions to the McDonald criteria.** *Ann Neurol* 2011;69:292–302 CrossRef Medline
23. Seewann A, Vrenken H, van der Valk P, et al. **Diffusely abnormal white matter in chronic multiple sclerosis: imaging and histopathologic analysis.** *Arch Neurol* 2009;66:601–09 Medline
24. Kurtzke JF. **A new scale for evaluating disability in multiple sclerosis.** *Neurology* 1955;5:580–83 Medline
25. Gabr RE, Sun X, Pednekar AS, et al. **Automated patient-specific optimization of three-dimensional double-inversion recovery magnetic resonance imaging.** *Magn Reson Med* 2016;75:585–93 CrossRef Medline
26. Redpath TW, Smith FW. **Technical note: use of a double inversion recovery pulse sequence to image selectively grey or white brain matter.** *Br J Radiol* 1994;67:1258–63 Medline
27. Traboulsee A, Simon JH, Stone L, et al. **Revised recommendations of the Consortium of MS Centers Task Force for a standardized MRI protocol and clinical guidelines for the diagnosis and follow-up of multiple sclerosis.** *AJNR Am J Neuroradiol* 2016;37:394–401 CrossRef Medline
28. Wattjes MP, Rovira À, Miller D, et al; MAGNIMS study group. **Evidence-based guidelines: MAGNIMS consensus guidelines on the use of MRI in multiple sclerosis–establishing disease prognosis and monitoring patients.** *Nat Rev Neurol* 2015;11:597–606 CrossRef Medline

T1 Recovery Is Predominantly Found in Black Holes and Is Associated with Clinical Improvement in Patients with Multiple Sclerosis

C. Thaler, T.D. Faizy, J. Sedlacik, B. Holst, K. Stürner, C. Heesen, J.-P. Stellmann, J. Fiehler, and S. Siemonsen

ABSTRACT

BACKGROUND AND PURPOSE: Quantitative MR imaging parameters help to evaluate disease progression in multiple sclerosis and increase correlation with clinical disability. We therefore hypothesized that T1 values might be a marker for ongoing tissue damage or even remyelination and may help increase clinical correlation.

MATERIALS AND METHODS: MR imaging was performed in 17 patients with relapsing-remitting MS at baseline and after 12 months of starting immunotherapy with dimethyl fumarate. On baseline images, lesion segmentation was performed for normal-appearing white matter, T2 hyperintense (FLAIR lesions), T1 hypointense (black holes), and contrast-enhancing lesions, and T1 relaxation times were obtained at baseline and after 12 months. Changes in clinical status were assessed by using the Expanded Disability Status Scale and Symbol Digit Modalities Test at both dates (Expanded Disability Status Scale-difference/Symbol Digit Modalities Test-diff).

RESULTS: The highest T1 relaxation time at baseline was measured in black holes (1460.2 ± 209.46 ms) followed by FLAIR lesions (1400.38 ± 189.1 ms), pure FLAIR lesions (1327.5 ± 210.04 ms), contrast-enhancing lesions (1205.59 ± 199.95 ms), and normal-appearing white matter (851.34 ± 30.61 ms). After 12 months, T1 values had decreased significantly in black holes (1369.4 ± 267.81 ms), contrast-enhancing lesions (1079.57 ± 183.36 ms) (both $P < .001$), and normal-appearing white matter (841.98 ± 36.1 ms, $P = .006$). With the Jonckheere-Terpstra Test, better clinical scores were associated with decreasing T1 relaxation times in black holes ($P < .05$).

CONCLUSIONS: T1 relaxation time is a useful quantitative MR imaging technique, which helps detect changes in MS lesions with time. We assume that these changes are associated with the degree of myelination within the lesions themselves and are pronounced in black holes. Additionally, decreasing T1 values in black holes were associated with clinical improvement.

ABBREVIATIONS: BH = black hole; CE-L = contrast-enhancing lesion; EDSS = Expanded Disability Status Scale; NAWM = normal-appearing white matter; MP2RAGE = double inversion-contrast magnetization-prepared rapid acquistion of gradient echo; SDMT = Symbol Digit Modalities Test; T1-RT = T1 relaxation time

MR imaging is an established tool in diagnosing multiple sclerosis and in monitoring inflammatory disease progression. In clinical routine, T2 and T1 lesion load and the detection of contrast-enhancing lesions (CE-Ls) are commonly used for monitoring subclinical disease activity and evaluating the effectiveness of pharmaceutical treatments. While hyperintense lesions on T2-weighted images (FLAIR lesions) correspond to a wide spectrum of histopathologic changes, ranging from edema and mild demyelination to glial scars or liquid necrosis, nonenhancing T1 hypointense lesions, black holes (BHs), are reported to be more specific markers for demyelination, axonal loss, and tissue damage.[1-6] It was observed that for discriminating the different stages of cell damage, the degree of BH hypointensity seems to reflect the extent of axonal loss and might distinguish demyelinated and partially remyelinated lesions.[7,8] Consequently, T1 relaxation times (T1-RTs) are increased in edema, demyelination, and axonal loss.[9-11]

A recent study showed that the assessment of MS lesions by their T1 values helps to increase correlations with disability and might lead to a more differentiated lesion classification.[12] However, little is known about the potential of lesional T1 values as a clinical marker in disease progression. Only a small number of previous studies have applied T1 relaxometry in patients with MS and reported increased T1 values in normal-appearing white matter (NAWM).[13,14] Therefore, our study focuses on the longitudinal evaluation of T1 values in different MS lesion types, representing different grades of tissue destruction. With the recently introduced

Received June 16, 2016; accepted after revision September 8.

From the Departments of Diagnostic and Interventional Neuroradiology (C.T., T.D.F., J.S., B.H., J.F., S.S.) and Neurology (K.S., C.H., J.-P.S.) and Institute for Neuroimmunology and Clinical MS Research (K.S., C.H., J.-P.S., S.S.), University Medical Centre Hamburg-Eppendorf, Hamburg, Germany.

Please address correspondence to Christian Thaler, MD, University Medical Centre Hamburg-Eppendorf, Martinistr 52, 20246 Hamburg-Eppendorf, Germany; e-mail: c.thaler@uke.de

Indicates article with supplemental on-line tables.

http://dx.doi.org/10.3174/ajnr.A5004

Subject population

	Mean	SD	Range
Age (yr)	35.1	9.5	18–51
EDSS baseline	2.2	1.6	0–6.5
Disease duration (yr)	7.7	6.1	0.1–19
Sex	11 women, 6 men		
Disease course	17 RRMS		

Note:—RRMS indicates relapsing-remitting MS.

double inversion-contrast magnetization-prepared rapid acquisition of gradient echo (MP2RAGE) sequences, it is now possible to generate quantitative T1 maps with high reproducibility.[15]

The purpose of this study was to observe the evolution of T1 values in NAWM and in lesions in patients with MS for 1 year after starting immunotherapy with dimethyl fumarate. We hypothesized that longitudinal changes of lesional T1 values are associated with changes in clinical disability because T1 values might be a marker for ongoing tissue damage or even remyelination.

MATERIALS AND METHODS

MR imaging was performed in 17 patients with MS at baseline and after 12 months. Also, at both time points, the clinical status was assessed by experienced neurologists. For this study, all patients who decided to be treated with dimethyl fumarate were treated at the MS day hospital. The study was approved by the local Ethical Committee Hamburg (Ethik-Kommission der Ärztekammer Hamburg) following the guidelines of the Declaration of Helsinki, and patients provided written informed consent. At baseline, all patients were diagnosed with relapsing-remitting MS, of whom 1 transitioned to secondary-progressive MS at follow-up. Disease duration ranged from 1 month to 19 years. All patients started treatment with dimethyl fumarate after baseline scans. For further patient characteristics, see the Table.

MR Imaging Data Acquisition

All MR imaging at baseline and after 12 months was performed on a 3T scanner (Magnetom Skyra; Siemens, Erlangen, Germany). The MR imaging protocol included a sagittal 3D FLAIR sequence (TE = 390 ms, TR = 4700 ms, TI = 1800 ms, 192 sections, FOV = 256 mm, voxel size = 1.0 × 1.0 × 1.0 mm), a T1-weighted magnetization-prepared rapid acquisition of gradient echo sequence before and after gadolinium injection (TE = 2.43 ms, TR = 1900 ms, TI = 900 ms, 192 sections, FOV = 256 mm, voxel size = 1.0 × 1.0 × 1.0 mm, flip-angle = 9°), and a double inversion-contrast magnetization-prepared rapid acquisition of gradient echo sequence before contrast agent injection (TE = 2.98 ms, TR = 5000 ms, TI = 700 ms, 176 sections, FOV = 256 mm, voxel size = 1.0 × 1.0 × 1.0 mm, flip angle = 4°).

Image Analysis

For measuring T1-RT in NAWM, 6 ROIs were manually defined in the occipital, frontal, and parietal white matter on baseline and follow-up MP2RAGE images. Simultaneously, ROI placement was controlled in the corresponding FLAIR images to avoid partial volume errors from MS lesions.

In baseline scans, FLAIR lesions were semiautomatically segmented on FLAIR images by using an open-source lesion-segmentation software (Lesion Segmentation Tool for SPM; http://www.academia.edu/2729347/LST_A_Lesion_Segmentation_Tool_For_SPM).[16] For optimal lesion segmentation, the final threshold was set at $\kappa = 0.3$. If necessary, lesion outlines were corrected manually. FLAIR images were linearly registered to the MP2RAGE images on baseline and follow-up images, and the corresponding transformation was applied to the FLAIR lesion masks.

Additionally, BH lesion segmentation was performed by 2 independent raters with a minimum of 1-year specific training in MS image diagnostics and evaluation on T1-weighted MPRAGE images. "BHs" were defined as nonenhancing lesions that appear hypointense on T1WI with signal intensity below the cortex and are concordant with hyperintense lesions on a T2WI. Lesions were outlined by using the software Analyze 11.0 (AnalyzeDirect, Overland Park, Kansas). The BH lesion masks of both raters were binarized and multiplied patient-wise to obtain a consensus mask. Finally, the consensus masks were registered to MP2RAGE images at baseline and follow-up. We marked CE-Ls, applying the same algorithm as described for BH lesion outlining and registered them to nonenhanced MP2RAGE images.

Finally, we calculated a pure FLAIR lesion mask by subtracting the BH and CE-L mask from the corresponding FLAIR lesion mask, leaving only those lesions that were visible on FLAIR but did not correspond to a BH or CE-L.

An example of lesional ROI placement is shown in Fig 1. Due to the registration of the baseline and follow-up images, we understand that minor displacements of lesions ROIs might occur. To minimize this possible bias, we excluded lesions of <5 voxels and assessed lesion maps on follow-up images to exclude misplaced ROIs and correct them if necessary. For each patient, for FLAIR lesions, BHs, pure FLAIR lesions, and CE-L number, volumes were calculated, and lesion-wise, median T1 values were obtained at baseline and follow-up. New FLAIR lesions and CE-Ls were detected manually after 12 months and were listed separately.

Because larger lesions might have a greater impact on clinical disability, we adapted the changes in T1-RTs to the actual lesion size in which it was measured. To correct for lesion size, we calculated a weighted average of the lesional T1-RTs (ie, T1-RTs were multiplied by their lesion volume and afterward divided by the patient's total lesion volume).

Clinical Status

At baseline and follow-up, clinical status was assessed by experienced neurologists by using the Expanded Disability Status Scale (EDSS) according to published guidelines.[17] In addition, the oral Symbol Digit Modalities Test (SDMT) was assessed, and an SD for an age- and education-matched control cohort was calculated.[18]

Statistical Analysis

Statistical analysis was performed by using R 3.0.0 statistical and computing software (http://www.r-project.org/) and SPSS 21.0 (IBM, Armonk, New York). A paired *t* test was used to compare lesion T1-RTs at baseline and after 12 months within lesion groups. The Jonckheere-Terpstra Test (a rank-based nonparametric test) was used to test for changes in T1-RTs in patient groups classified by clinical changes.[19] Two-sided *P* values < .05 were statistically significant.

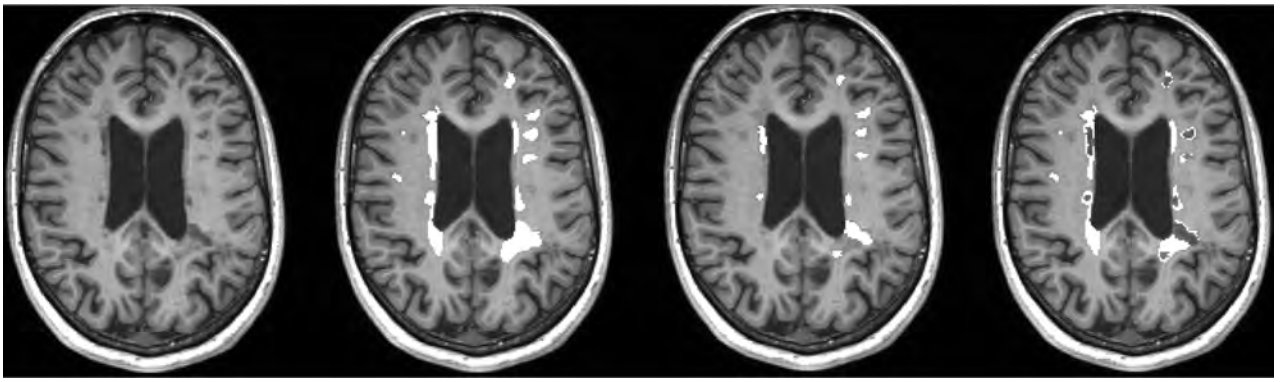

FIG 1. An example of ROI placement in T1WI MPRAGE at baseline. From left to right: 1) T1WI MPRAGE transversal without lesion ROIs, 2) ROIs indicating FLAIR-lesion masks, 3) ROIs indicating black hole lesion masks, and 4) ROIs indicating FLAIR-lesion masks without black holes (pure FLAIR lesion masks).

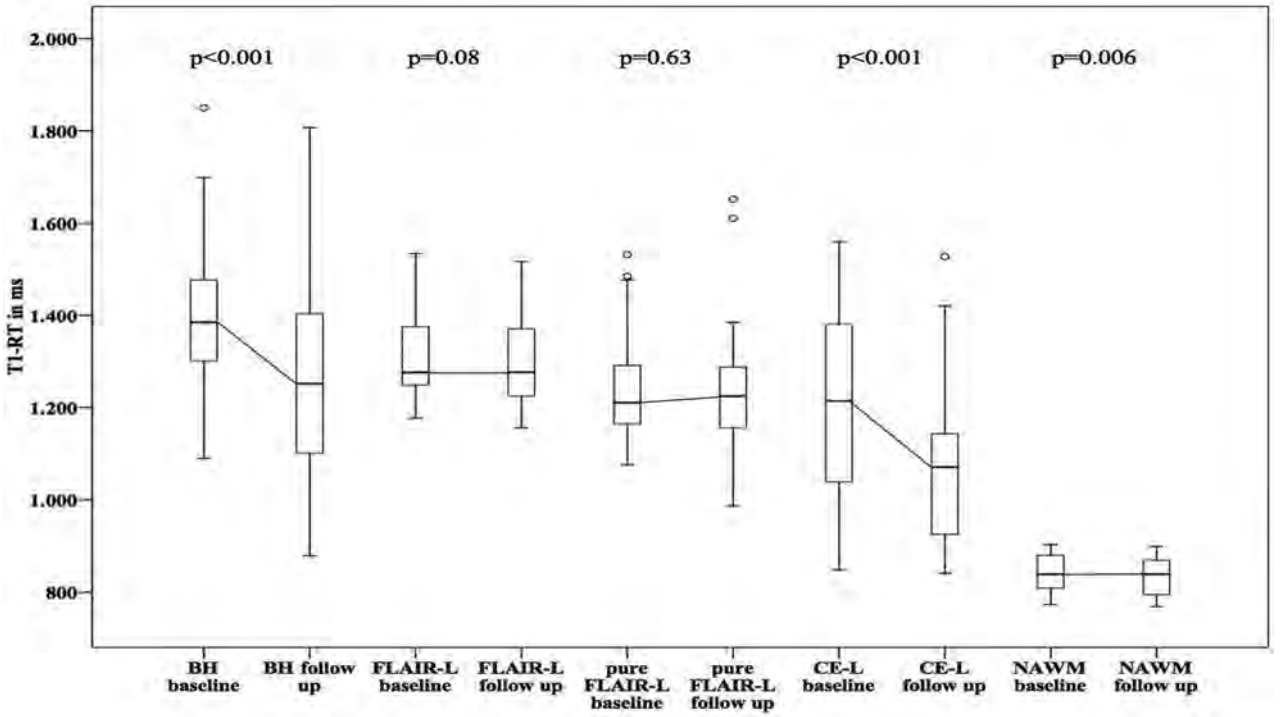

FIG 2. Boxplots showing T1 relaxation times at baseline and after 12-month follow-up for different lesion types. *P* values were calculated by using a paired *t* test.

RESULTS

MR Imaging Measurements

At baseline, at least 1 FLAIR lesion was detected in all patients, and BHs were detected in all except 1 patient. Overall, 380 FLAIR lesions, 504 BHs, and 362 pure FLAIR lesions were segmented on baseline scans. In 8 of 17 patients, 22 CE-Ls were detected at baseline. After 12 months, 1 patient demonstrated a new CE-L and 7 patients presented with new FLAIR lesions. Interrater reliability for the detection of black holes was high, with a Dice coefficient of 0.916.

T1 values in NAWM showed a significant decrease with T1-RTs at a baseline of 851.34 ± 30.61 ms to 841.98 ± 36.1 ms after 12 months ($P = .006$). In MS lesions, the highest T1-RT at baseline was measured in BHs (1460.21 ± 209.46 ms) followed by T1-RTs in FLAIR lesions (1400.38 ± 189.1 ms) and T1-RTs in pure FLAIR lesions (1327.5 ± 210.04 ms). In 8 of 17 patients, 22 CE-Ls were detected at baseline, with a mean T1-RT of 1205.59 ± 199.95 ms. After 12 months, T1 values decreased in all lesion types: BHs = 1369.4 ± 267.81 ms, FLAIR lesions = 1383.33 ± 274.53 ms, pure FLAIR lesions = 1322.64 ± 305.07 ms, CE-Ls = 1079.57 ± 183.36 ms. Changes in T1-RT were calculated for all lesion ROIs. Using paired *t* tests, we found significant differences only for T1-RTs measured in NAWM ($P = .006$), BHs, and CE-Ls (both $P < .001$) at baseline and after 12 months, but not for FLAIR lesions ($P = .08$) or pure FLAIR lesions ($P = .63$). A detailed overview of mean T1-RTs in FLAIR lesions, BHs, pure FLAIR lesions, and CE-Ls at baseline and follow-up is given in Fig 2 and On-line Tables 1 and 2.

There were no significant associations for changes in T1-RTs in BHs and NAWM or any other lesion type.

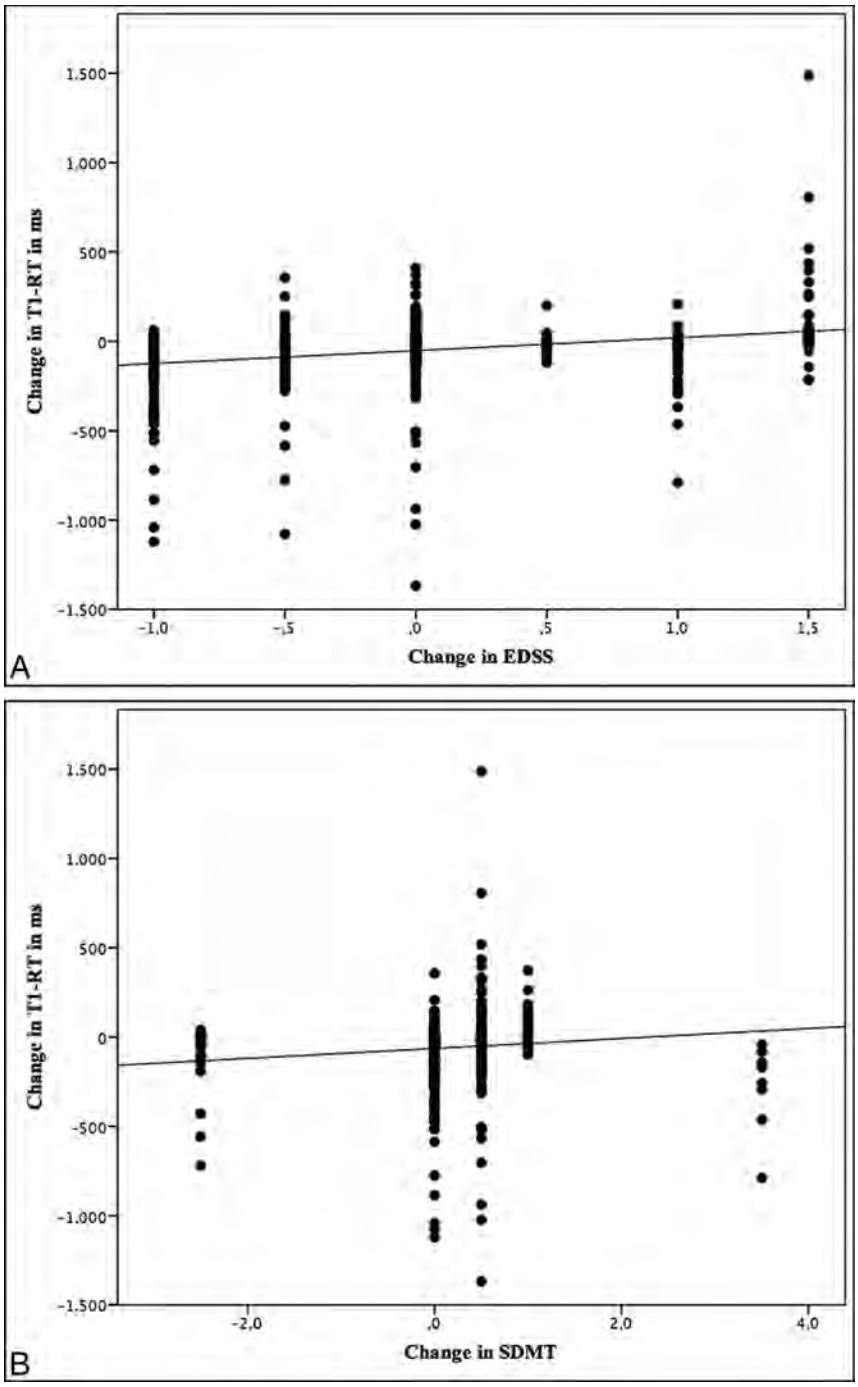

FIG 3. Scatterplots showing an association between lesional changes in T1 relaxation times and clinical scores.

Clinical Measurements

EDSS scores were obtained for all patients at baseline and follow-up. The mean EDSS score at baseline was 2.21 and changed only marginally to 2.18 after 12 months. In a subset of 14 patients, the SDMT was available. A mean SDMT-SD at baseline of −0.07 slightly increased to 0.21 after 12 months. With the Jonckheere-Terpstra Test, better clinical scores in EDSS and SDMT were associated with decreasing T1-RTs in BHs ($P < .001$) (Fig 3). However, there were no significant differences for changes in T1-RTs in NAWM, FLAIR lesions, pure FLAIR lesions, or CE-Ls.

DISCUSSION

For monitoring disease progression and the effectiveness of pharmaceutical treatment in MS, the number of T2, T1, and contrast-enhancing lesions presents a relevant diagnostic tool in clinical routine. However, with routinely used semiquantitative MS imaging biomarkers such as T1 and T2 lesion load or the number of FLAIR lesions and CE-Ls, clinical-radiologic correlations are still limited because MS lesions have histopathologic diversity.[20-22] Therefore, nonconventional MR imaging measures such as T1-RT have shown some promising results in cross-sectional and longitudinal studies to improve correlations with disability in patients with MS.[12,13,23,24] The purpose of this study was to present T1-RT changes in MS lesions for 12 months and, secondly, to show the association of T1-RT changes with clinical disability.

At baseline the highest lesional T1 values were detected in BHs, while the lowest values were measured in CE-Ls; this finding confirms the findings of Blystad et al (2016).[25] Due to severe tissue destruction, demyelination, and an increase in free water, T1-RTs are expected to be elevated in BHs. In contrast, CE-Ls represent an active inflammation process, associated with an accumulation of inflammatory cells, resulting in lower T1-RTs compared with FLAIR lesions or BHs.[26]

T1-RT alterations were observed in all lesion types and NAWM after 12 months compared with baseline. While T1-RTs in NAWM, BHs, and CE-Ls significantly decreased across time, FLAIR lesions and pure FLAIR lesions did not show meaningful changes of T1-RTs in 12-month follow-up. Our observations are in line with those in former studies, which reported increasing signal intensities of MS lesions in T1WI (comparable with decreasing T1-RTs) in up to 74% of initially T1WI hypointense lesions.[27-29] Although we did not evaluate the relative signal intensity, we observed decreasing T1-RTs in 66% of all BHs, in 82% of all CE-Ls, and in 54% of pure FLAIR lesions. However, little is known about decreasing T1-RTs in MS lesions. Bitsch et al (2001)[5] and Barkhof et al (2003)[7] demonstrated in histopathologic studies that the intensity of an MS lesion, and therefore its T1-RT, depends, to some extent, on the degree of its myelination. While the intensity of the lesion was decreased in demyelinated lesions, it showed an increase in remyelinated lesions. Remyelination is described as a frequent phenomenon in MS and can be

extensive in subsets of patients with MS.[7,30-33] We assume that decreasing T1-RTs in MS lesions depend, to some extent, on the level of remyelination in the lesion itself and might therefore indicate neuronal recovery.

Certainly, other pathologic processes such as resolution of edema, inflammation, or microstructural changes may influence T1-RT as well and might be the main reason for decreasing T1-RTs in CE-Ls. However, why overall T1-RTs are stable in pure FLAIR lesions but decrease in BHs remains unclear. One possible explanation could be that BHs represent a bygone, inactive inflammatory process with extensive tissue damage and prevailing neuronal recovery, whereas pure FLAIR lesions still have the potential for ongoing demyelination. This assumption is supported by histopathologic findings from Jonkman et al (2015),[34] who observed lower T1-RTs in preactive and active lesions than in chronic inactive lesions, classifying pure FLAIR lesions with smaller T1-RTs as active lesions with ongoing demyelination and BHs with higher T1-RTs as rather chronic inactive lesions.

In this study, we found a significant association between improving clinical status and decreasing T1 values in BHs. So far, studies focusing on changes of T1-RTs in MS lesions and their impact on clinical status are lacking. Manfredonia et al (2007)[14] observed T1 values in normal-appearing white and gray matter during a 2-year follow-up in patients with primary-progressive MS and found a significant correlation between increasing T1-RTs and clinical impairment. However, Manfredonia et al did not evaluate T1-RTs within MS lesions and included only patients with primary-progressive MS, which might explain the significant increase in T1-RTs, because progressive subtypes of MS are associated with greater damage to white matter. Also, all individuals in our study cohort were treated with dimethyl fumarate, which significantly reduces disease activity as measured by MR imaging in patients with relapsing-remitting MS[35,36] and might be a reasonable explanation for decreasing T1 values in NAWM and BHs in our study cohort.

As mentioned before, we hypothesized that changes in T1-RT at least partially represent some changes in the degree of myelination. In contrast to Manfredonia et al,[14] we predominantly observed decreasing T1 values in NAWM and BHs. However, it is still unclear whether remyelination leads to functional recovery in humans because there is no approved method to measure the degree of demyelination/remyelination in vivo. Yet, promising results were reported in experimental animal models, demonstrating an association between remyelination and functional recovery.[37-39] To support our findings and especially to confirm an association of lesion evolution and clinical status and to gain deeper insight into the underlying histopathologic process, additional longitudinal studies, including measurements of other quantitative MR imaging parameters such as diffusion tensor imaging, magnetization transfer ratio, and myelin water imaging, are needed.

There was no significant association between the appearance of new FLAIR lesions after 12 months and changes in clinical status. However, when one assesses new lesions in MS, their strategic location is an important feature when correlating with clinical changes.[13,40,41] It was not the purpose of this study to evaluate the influence of single lesion locations on clinical disability but rather to search for new strategies to assess lesion quality and evolution. Nevertheless, further investigations of the localization of lesions are needed for a better understanding of their clinical impact.

To generate T1 maps, we acquired MP2RAGE sequences, which create a homogeneous T1-weighted contrast with an intrinsic correction of B1 inhomogeneities and reduce residual proton density and T2* weighting. T1 values measured in MP2RAGE sequences are highly reproducible both across subjects and within the same subject by using different scanning parameters; this feature makes these sequences applicable to longitudinal studies.[15]

CONCLUSIONS

T1-RT is a useful quantitative MR imaging technique that helps detect changes in MS lesions with time. We assume that these changes are associated with remyelination in the lesions themselves and are predominantly found in BHs rather than in FLAIR lesions or pure FLAIR lesions. Supporting this hypothesis, changes in T1-RT were associated with clinical status, possibly indicating neuronal and even functional recovery. To confirm our findings, further emphasis should be on combining T1-RT with other nonconventional MR imaging techniques such as magnetization transfer ratio, DTI, and myelin water imaging to gain further knowledge of myelin measurement in vivo. Undoubtedly, histopathologic studies would provide the best evidence to verify these MR imaging techniques but are naturally limited.

Disclosures: Christian Thaler—*UNRELATED: Support for Travel to Meetings for the Study or Other Purposes*: Deutsche Gesellschaft für Neuroradiologie (German Society of Neuroradiology), *Comments*: travel grant to present study results at the Annual Meeting of the American Society of Neuroradiology in 2016 in Washington, DC. Christoph Heesen—*UNRELATED: Grant*: German Ministry of Education and Research, *Comments*: Analysis was part of a Phase II study on boswellic acids in MS.* Jan-Patrick Stellmann—*UNRELATED: Consultancy*: Genzyme; *Grants/Grants Pending*: Biogen, Genzyme*; *Payment for Lectures including Service on Speakers Bureaus*: Biogen, Genzyme; *Travel/Accommodations/Meeting Expenses Unrelated to Activities Listed*: Novartis. *Money paid to the institution.

REFERENCES

1. MacKay A, Laule C, Vavasour I, et al. **Insights into brain microstructure from the T2 distribution.** *Magn Reson Imaging* 2006;24:515–25 CrossRef Medline
2. Laule C, Leung E, Lis DK, et al. **Myelin water imaging in multiple sclerosis: quantitative correlations with histopathology.** *Mult Scler* 2006;12:747–53 CrossRef Medline
3. De Groot CJ, Bergers E, Kamphorst W, et al. **Post-mortem MRI-guided sampling of multiple sclerosis brain lesions: increased yield of active demyelinating and (p)reactive lesions.** *Brain* 2001;124:1635–45 CrossRef Medline
4. van Walderveen MA, Kamphorst W, Scheltens P. **Histopathologic correlate of hypointense lesions on T1-weighted spin-echo MRI in multiple sclerosis.** *Neurology* 1998;50:1282–88 CrossRef Medline
5. Bitsch A, Kuhlmann T, Stadelmann C, et al. **A longitudinal MRI study of histopathologically defined hypointense multiple sclerosis lesions.** *Ann Neurol* 2001;49:793–96 CrossRef Medline
6. Faizy TD, Thaler C, Kumar D, et al. **Heterogeneity of multiple sclerosis lesions in multislice myelin water imaging.** *PLoS One* 2016;11:e0151496 CrossRef Medline
7. Barkhof F, Bruck W, De Groot CJ, et al. **Remyelinated lesions in multiple sclerosis: magnetic resonance image appearance.** *Arch Neurol* 2003;60:1073–81 CrossRef Medline
8. Riva M, Ikonomidou VN, Ostuni JJ, et al. **Tissue-specific imaging is a robust methodology to differentiate in vivo T1 black holes with**

advanced multiple sclerosis-induced damage. *AJNR Am J Neuroradiol* 2009;30:1394–401 CrossRef Medline
9. Naruse S, Horikawa Y, Tanaka C, et al. **Proton nuclear magnetic resonance studies on brain edema.** *J Neurosurg* 1982;56:747–52 CrossRef Medline
10. Schmierer K, Scaravilli F, Altmann DR, et al. **Magnetization transfer ratio and myelin in postmortem multiple sclerosis brain.** *Ann Neurol* 2004;56:407–15 CrossRef Medline
11. Schmierer K, Tozer DJ, Scaravilli F, et al. **Quantitative magnetization transfer imaging in postmortem multiple sclerosis brain.** *J Magn Reson Imaging* 2007;26:41–51 CrossRef Medline
12. Thaler C, Faizy T, Sedlacik J, et al. **T1-thresholds in black holes increase clinical-radiological correlation in multiple sclerosis patients.** *PLoS One* 2015 10:e0144693 CrossRef Medline
13. Parry A, Clare S, Jenkinson M, et al. **MRI brain T1 relaxation time changes in MS patients increase over time in both the white matter and the cortex.** *J Neuroimaging* 2003;13:234–39 CrossRef Medline
14. Manfredonia F, Ciccarelli O, Khaleeli Z, et al. **Normal-appearing brain T1 relaxation time predicts disability in early primary progressive multiple sclerosis.** *Arch Neurol* 2007;64:411–15 CrossRef Medline
15. Marques JP, Kober T, Krueger G, et al. **MP2RAGE, a self bias-field corrected sequence for improved segmentation and T1-mapping at high field.** *Neuroimage* 2010;49:1271–81 CrossRef Medline
16. Schmidt P, Gaser C, Arsic M, et al. **An automated tool for detection of FLAIR-hyperintense white-matter lesions in multiple sclerosis.** *Neuroimage* 2012;59:3774–83 CrossRef Medline
17. Kappos L, Lechner-Scott J, Lienert C. Neurostatus. Neurostatus training and documentation DVD for a standardized neurological examination and assessment of Kurtzke's functional systems and expanded disability status scale for MS patients. 2002, 2007, Basel, Switzerland. http://neurostatus.net; 2015. Accessed January 6, 2015
18. Smith A. **The symbol-digit modalities test: a neuropsychologic test of learning and other cerebral disorders.** In Helmuth J, ed. *Learning Disorders*. Seattle: Special Child Publications; 1968;83–91
19. Jonckheere AR. **A distribution-free K-sample test against ordered alternatives.** *Biometrika* 1954;41:133–45 CrossRef
20. Miller DH, Altmann DR, Chard DT. **Advances in imaging to support the development of novel therapies for multiple sclerosis.** *Clin Pharmacol Ther* 2012;91:621–34 CrossRef Medline
21. Galego O, Gouveia A, Batista S, et al. **Brain atrophy and physical disability in primary progressive multiple sclerosis: a volumetric study.** *Neuroradiol J* 2015;28:354–58 CrossRef Medline
22. McFarland HF, Barkhof F, Antel J, et al. **The role of MRI as a surrogate outcome measure in multiple sclerosis.** *Mult Scler* 2002;8:40–51 CrossRef Medline
23. Steenwijk MD, Vrenken H, Jonkman LE, et al. **High-resolution T1-relaxation time mapping displays subtle, clinically relevant, gray matter damage in long-standing multiple sclerosis.** *Mult Scler* 2016;22:1279–88 CrossRef Medline
24. Simioni S, Amarù F, Bonnier G, et al. **MP2RAGE provides new clinically-compatible correlates of mild cognitive deficits in relapsing-remitting multiple sclerosis.** *J Neurol* 2014;261:1606–13 CrossRef Medline
25. Blystad I, Håkansson I, Tisell A, et al. **Quantitative MRI for analysis of active multiple sclerosis lesions without gadolinium-based contrast agent.** *AJNR Am J Neuroradiol* 2016;37:94–100 CrossRef Medline
26. Filippi M, Rocca MA, Barkhof F, et al; Attendees of the Correlation between Pathological MRI Findings in MS workshop. **Association between pathological and MRI findings in multiple sclerosis.** *Lancet Neurol* 2012;11:349–60 CrossRef Medline
27. Bagnato F, Jeffries N, Richert ND, et al. **Evolution of T1 black holes in patients with multiple sclerosis images monthly for 4 years.** *Brain* 2003;126:1782–89 CrossRef Medline
28. van Waesberghe JH, van Walderveen MA, Castelijns JA, et al. **Patterns of lesion development in multiple sclerosis: longitudinal observations with T1-weighted spin-echo and magnetization transfer MR.** *AJNR Am J Neuroradiol* 1998;19:675–83 Medline
29. Rovira A, Alonso J, Cucurella G, et al. **Evolution of multiple sclerosis lesions on serial contrast-enhanced T1-weighted and magnetization-transfer MR images.** *AJNR Am J Neuroradiol* 1999;20:1939–45 Medline
30. Raine CS, Wu E. **Mutlitple sclerosis: remyelination in acute lesions.** *J Neuropathol Exp Neurol* 1993;52:199–204 CrossRef Medline
31. Lassmann W, Brück W, Luchinetti C, et al. **Remyelination in multiple sclerosis.** *Mult Scler* 1997;3:133–36 CrossRef Medline
32. Patrikios P, Stadelmann C, Kutzelnigg A, et al. **Remyelination is extensive in a subset of multiple sclerosis patients.** *Brain* 2006;129:3165–72 CrossRef Medline
33. Fox RJ, Cronin T, Lin J, et al. **Measuring myelin repair and axonal loss with diffusion tensor imaging.** *AJNR Am J Neuroradiol* 2011;32:85–91 CrossRef Medline
34. Jonkman LE, Soriano AL, Amor S, et al. **Can MS lesion stages be distinguished with MRI? A postmortem MRI and histopathology study.** *J Neurol* 2015;262:1074–80 CrossRef Medline
35. Gold R, Kappos L, Arnold DL, et al; DEFINE Study Investigators. **Placebo-controlled phase 3 study of oral BG-12 for relapsing multiple sclerosis.** *N Engl J Med* 2012;367:1098–107 CrossRef Medline
36. Bar-Or A, Gold R, Kappos L, et al. **Clinical efficacy of BG-12 (dimethyl fumarate) in patients with relapsing-remitting multiple sclerosis: subgroup analyses of the DEFINE study.** *J Neurol* 2013;260:2297–305 CrossRef Medline
37. Duncan ID, Brower A, Kondo Y, et al. **Extensive remyelination of the CNS leads to functional recovery.** *Proc Natl Acad Sci U S A* 2009;106:6832–36 CrossRef Medline
38. Liebetanz D, Merkler D. **Effects of commissural de- and remyelination on motor skill behaviour in the cuprizone mouse model of multiple sclerosis.** *Exp Neurol* 2006;202:217–24 CrossRef Medline
39. Murray PD, McGavern DB, Sathornsumetee S, et al. **Spontaneous remyelination following extensive demyelination is associated with improved neurological function in a viral model of multiple sclerosis.** *Brain* 2001;124(pt 7):1403–16 CrossRef Medline
40. Roosendaal SD, Moraal B, Pouwels PJ, et al. **Accumulation of cortical lesions in MS: relation with cognitive impairment.** *Mult Scler* 2009;15:708–14 CrossRef Medline
41. Rovaris M, Filippi M, Minicucci L, et al. **Cortical/subcortical disease burden and cognitive impairment in patients with multiple sclerosis.** *AJNR Am J Neuroradiol* 2000;21:402–08 Medline

Impact of Pial Collaterals on Infarct Growth Rate in Experimental Acute Ischemic Stroke

G.A. Christoforidis, P. Vakil, S.A. Ansari, F.H. Dehkordi, and T.J. Carroll

ABSTRACT

BACKGROUND AND PURPOSE: Cerebral infarction evolves at different rates depending on available blood flow suggesting that treatment time windows vary depending on the degree of pial collateral recruitment. This work sought to mathematically model infarct growth and determine whether infarct volume growth can be predicted by angiographic assessment of pial collateral recruitment in an experimental MCA occlusion animal model.

MATERIALS AND METHODS: Pial collateral recruitment was quantified by using DSA, acquired 15 minutes following permanent MCA occlusion in 6 canines based on a scoring system (average pial collateral score) and arterial arrival time. MR imaging–based infarct volumes were measured 60, 90, 120, 180, 240 and 1440 minutes following MCA occlusion and were parameterized in terms of the growth rate index and final infarct volume (V_{Final}) as $V(t) = V_{Final}\,[1 - e^{(-G \times t)}]$ (t = time). Correlations of the growth rate index and final infarct volume to the average pial collateral score and arterial arrival time were assessed by linear bivariate analysis. Correlations were used to generate asymptotic models of infarct growth for average pial collateral score or arterial arrival time values. Average pial collateral score– and arterial arrival time–based models were assessed by *F* tests and residual errors.

RESULTS: Evaluation of pial collateral recruitment at 15 minutes postocclusion was strongly correlated with 24-hour infarct volumes (average pial collateral score: $r^2 = 0.96$, $P < .003$; arterial arrival time: $r^2 = 0.86$, $P < .008$). Infarct growth and the growth rate index had strong and moderate linear relationships to the average pial collateral score ($r^2 = 0.89$; $P < .0033$) and arterial arrival time ($r^2 = 0.69$; $P < .0419$), respectively. Final infarct volume and the growth rate index were algebraically replaced by angiographically based collateral assessments to model infarct growth. The *F* test demonstrated no statistical advantage to using the average pial collateral score– over arterial arrival time–based predictive models, despite lower residual errors in the average pial collateral score–based model ($P < .03$).

CONCLUSIONS: In an experimental permanent MCA occlusion model, assessment of pial collaterals correlates with the infarct growth rate index and has the potential to predict asymptotic infarct volume growth.

ABBREVIATIONS: AAT = arterial arrival time; G = growth rate index; MCAO = MCA occlusion; Pc = average pial collateral score; SSE = sum square of the error; V_{Final} = final infarct volume; V(t) = volume at a given time

Reperfusion treatment in acute ischemic stroke due to major vessel occlusion aims to rescue brain at risk for ischemic injury. Compromise in cellular function during the early phases of cerebral ischemia precedes but does not consistently predict irreversible dysfunction or infarction. On the basis of the premise that discrepancies exist between tissue with irreversible damage and tissue with reversible functional compromise, reversible functional compromise could be operationally defined as a component of the diffusion-perfusion mismatch profile derived from MR imaging.[1-3] Tissue infarction is known to depend on both the degree to which blood flow is compromised and the duration of the compromise (time from onset of ischemia).[4] In major vessel occlusion, blood flow via pial collateral vessels sustains tissue at risk, so an effective measure of the collaterals may approximate the tissue state as indicated by the perfusion-diffusion mismatch. Furthermore, given the identical cerebrovascular occlusion site,

Received May 18, 2016; accepted after revision September 6.

From the Department of Radiology (G.A.C., S.A.A., T.J.C.), University of Chicago, Chicago, Illinois; College of Medicine (P.V.), University of Illinois, Chicago, Illinois; Departments of Radiology, Neurology, and Neurological Surgery (S.A.A.), Northwestern University, Chicago, Illinois; and Department of Economics and Decision Sciences (F.H.D.), Western Illinois University, Macomb, Illinois.

This work was supported by the following grants: National Institutes of Health R21-EB017928, R01-NS093908, and American Heart Association GRNT-20380798.

Paper previously presented in part at: International Symposium on Cerebral Blood Flow, Metabolism and Function, June 27–30, 2015; Vancouver, British Columbia, Canada.

Please address correspondence to Gregory A. Christoforidis, MD, University of Chicago, Department of Radiology, 5841 South Maryland Ave, MC 2026, Chicago, IL 60637; e-mail: gchristoforidis@radiology.bsd.uchicago.edu

Indicates open access to non-subscribers at www.ajnr.org

http://dx.doi.org/10.3174/ajnr.A5003

patients with acute cerebrovascular occlusion with the same degree and time of reperfusion can vary in their final irreversible tissue damage or infarct volume.[5] Final infarct volumes in patients with prolonged occlusion of the middle cerebral artery, for example, vary depending on the degree of sustained pial collateral recruitment and on the degree to which the cerebral tissue type at risk is able to withstand permanent ischemic damage.[5,6] A better understanding of the infarct growth rate has the potential to lead to a more personalized treatment plan based on tissue rather than time selection alone and to improve the effectiveness of reperfusion therapy in the current era of precision medicine.

With respect to the mathematic modeling of cerebral infarct volume growth within the first 24 hours of ictus, growth rate decreases as infarct volume increases. This characteristic indicates that infarct volume evolves in a nonlinear fashion; thus, nonlinear growth models more accurately reflect true infarct volume growth relative to a linear model. Nonlinear models can be divided into asymptotic (those that level off with time) and nonasymptotic models (those that grow indefinitely). Because infarct volume does not enlarge indefinitely but rather approaches a point in time after which any growth is negligible or cannot be measured, an asymptotic model makes more sense. This work sought to mathematically model the infarct growth rate as a nonlinear asymptotic function of time and hypothesized that the infarct growth rate can be predicted by pial collateral recruitment in a setting of acute and permanent MCA occlusion (MCAO) in a canine model.

MATERIALS AND METHODS

Animal care guidelines of the University of Chicago were followed. Six mongrel dogs (20–30 kg) underwent 4-vessel cerebral angiography and permanent endovascular MCAO from its origin at the carotid terminus, to the M1 segment by using previously described endovascular techniques.[7,8] Briefly, following induction, animals were anesthetized (1.5%–2.0% isoflurane) and ventilated. Cardiac rhythm, end-tidal CO_2, glucose, body temperature, hematocrit, and arterial pressure were maintained within physiologic range. The MCA was accessed from the posterior circulation via the circle of Willis by using a microcatheter (Echelon 10; Covidien, Irvine, California) and was occluded by using embolic coils (Axium; Covidien).[7] DSA images were acquired (OEC 9800; GE Healthcare, Milwaukee, Wisconsin) to confirm occlusion and quantify pial collateral blood supply by selective injection of the contralateral internal carotid artery and the vertebral artery 15 minutes following MCAO.

MR Imaging Protocol

All MR images were acquired on a 3T human magnet (Achieva; Philips Healthcare, Best, the Netherlands). Animals were placed in the head-first, prone position within a 32-channel transmit-receive head coil. Diffusion-weighted MR imaging (FOV = 140 × 140 mm, matrix = 128 × 128, NEX = 1, TR/TE = 192–2131/71 ms, b-values = 0, 1000 s/mm^2, section thickness = 3 mm) was acquired 1, 1.5, 2, 3, and 4 hours post-MCAO; and T2-weighted fluid-attenuated inversion recovery MR imaging (FOV = 160 mm, matrix = 512 × 512, NEX = 1, TR/TE/TI = 11,000/125/2800 ms, section thickness = 3 mm, scan time ~ 8 minutes) was acquired at 24 hours to quantify final infarct volume. Susceptibility-weighted imaging (FOV = 160 mm, matrix = 148 × 148, NEX = 1, TR/TE = 14.89/21.00 ms, flip angle = 10°, section thickness = 0.5 mm) was acquired after the 1-, 2-, and 4-hour DWI scans and at 24 hours.

Quantification of Pial Collateral Arterial Recruitment

Two interventional neuroradiologists (G.A.C., S.A.A.) semiquantitatively assessed pial collateral recruitment (average pial collateral score [Pc]) by using a previously published scoring method.[7] The results of the 2 observers were averaged. Briefly, this 11-point scoring system compares postocclusion with preocclusion arteriographic images to assess the extent of reconstitution of the occluded MCA territory and transit time relative to jugular vein opacification. Extent is evaluated within each of 3 sections of the MCA territory (anterior, middle, and posterior). For each section, 1 point is assigned if only the medial parts of the MCA distal branches were reconstituted; and 2 points, if the lateral parts of the MCA branches were reconstituted within that section. Up to 2 additional points were added if there was reconstitution of the distal and proximal M2 segments within the operculum. Transit time was assigned up to 1 point for each section of the MCA territory (anterior, middle, and posterior) if contrast arrived in the MCA branches along the lateral aspect of each section before contrast arrived to the jugular bulb. The Bland-Altman statistic for this pial collateral scoring system between 2 observers has been reported at 22.6% (95% of scores within 1.3 points of each other) and the mean difference of 0.23 between observers.[7] Pial scores were averaged and treated as continuous variables in all statistical analyses. Agreement of Pc between the 2 observers in this study was assessed by using a Bland-Altman analysis.

Arterial Arrival Time

Pial collateral recruitment was also quantitatively assessed by arterial arrival time (AAT). Signal-versus-time curves were extracted from time-resolved angiograms by using a combination of Amira software (www.amira.com) and Matlab, Version 2012b (MathWorks, Natick, Massachusetts), which measured contrast density across time within ROIs. The AAT was defined as the time interval between contrast arrival at the normal M1 segment and contrast arrival at the reconstituted M3/4 junction on the hemisphere distal to the permanent MCAO (Fig 1).

Quantification of Infarct Volume

The evolution of the infarct was determined from parametric images of mean diffusivity and T2 FLAIR images independently by 2 trained observers. A previously described semiautomated infarct segmentation algorithm was used to quantify infarct volumes across time.[7] Briefly, infarct volumes by mean diffusivity maps and FLAIR MR imaging were estimated by using a quantitative voxelwise threshold by setting a threshold of 1.5 SDs relative to normal values based on an ROI drawn to cover the entire contralateral normal hemisphere inclusive of gray and white matter but exclusive of the ventricles on a section-by-section basis. "Total infarct volume" was defined as the number of voxels that were 1.5 SDs greater than the mean value of normal tissue multiplied by the voxel volume. Volumes were calculated by using ImageJ software (National Institutes of Health,

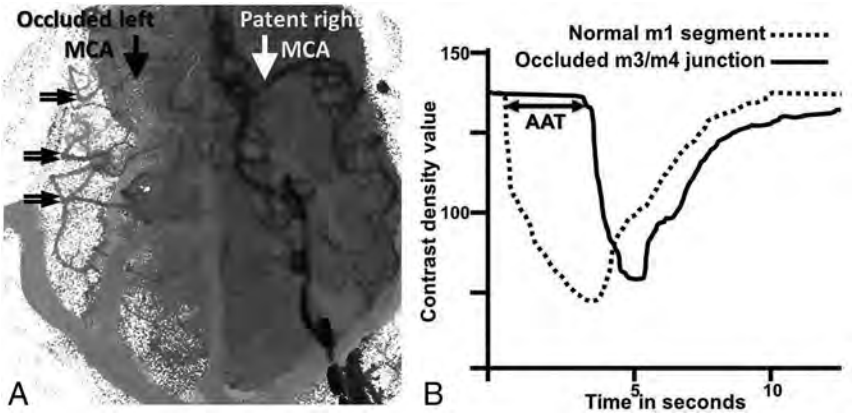

FIG 1. Arterial arrival times measured from angiographic time-density curves. ROIs within the normal MCA proximal M1 segment (*white arrow*, *A*) and from collateralized MCA branches (*double arrows*, *A*) are identified on composite angiographic images. ROIs were used to calculate time-density curves (*B*). "Average arterial time" (in seconds) was defined as the time interval between contrast arrival at the normal M1 segment (*interrupted curve*, *B*) and the average of 3 ROIs at the M3/4 junction of the MCA corresponding to the occluded MCA (*continuous curve*, *B*). AAT is graphically depicted by the *horizontal double arrow line*.

Table 1: Raw data

	Experiment No.					
	1	2	3	4	5	6
Pc	9.00	7.00	10.50	5.50	4.00	3.50
AAT (sec)	1.344	3.469	1.812	4.938	4.656	4.156
V (60 min) (mm^3)	3533	8960	3575	9842	14,947	15,074
V (90 min) (mm^3)	3976	9221	4009	10,310	15,428	16,464
V (120 min) (mm^3)	3922	9174	4430	14,493	16,805	18,134
V (180 min) (mm^3)	5492	13,043	5312	16,811	18,034	20,694
V (240 min) (mm^3)	5058	14,800	6461	17,419	19,257	22,197
V (24 hr) (mm^3)	9612	17,987	9668	20,946	24,479	25,419

Note:—V (time) indicates infarct volume at "time" evaluated with diffusion-weighted MRI; V (24 hour), final infarct volume from FLAIR MRI.

Bethesda, Maryland). Previous results by Bland-Altman statistics indicated that there is good reproducibility of infarct volume estimations by using the mean diffusivity maps (15.9%) acquired between 0 and 240 minutes post-MCAO and FLAIR images (13.3%) acquired at 24 hours.[7] Therefore, a combination of early (ie, 0–240 minutes) mean diffusivity measured infarct volume at a given time [V(t)] and 24-hour T2 FLAIR (V_{Final}) images was used to determine the evolution of the infarcted volume over time.

Predicting 24-Hour Infarct Volume from Angiography

Least-squares regression analysis was performed to test the hypothesis that angiographic assessment of pial collateral arterial reconstitution (ie, Pc and AAT) can predict final infarct volumes. Both Pc and AAT were compared by using a correlation analysis to determine the level of agreement between both Pc and AAT and V_{Final}. Cytotoxic, ionic, and vasogenic edema were not differentially accounted for when deriving this representative asymptotic function.

Modeling Infarct Growth

Asymptotic infarct growth was mathematically modeled by an asymptotic function. Infarct growth was parameterized as

$$1) \qquad V(t) = V_{Fit} \times [1 - e^{(-G \times \text{time})}],$$

where $V(t)$ was infarct volume at time t, with G and V_{Fit} being free parameters in the fit. For this analysis, infarct-across-time data collected during the acute phase of the stroke (t = 0, 240 minutes) were combined with 24-hour (t = 1440 minutes) infarct volume, V_{Final}. Levenberg-Marquardt fits were performed to extract G and V_{Fit} for each experiment separately. The goodness of fit was then reported as the coefficient of determination, r^2. Growth rates and V_{Fit} values resulting from the fits were then subject to a linear regression analysis to derive an expression that would allow the modeling of infarct growth rate as a function of pial collateral recruitment (Pc and AAT). The modeling of infarct growth by using Pc and AAT was compared. The slope intercept of the correlation plots and correlation coefficients of Pc and AAT were compared to determine which more closely followed a linear model.

Parameterizing Infarct Growth from Collateralization

Expressions for infarct volume and infarct growth rate were back-substituted into Equation 1 to yield infarct-versus-time curves as a function of Pc and AAT, (ie, angiographic measures acquired 15 minutes postocclusion). A 2-sided Wilcoxon signed rank test determined the difference (if any) between the measured and model-predicted volume of the lesion size at all time points. Because Pc- and AAT-derived models used a similar number of parameters, we applied an F test with the following formula for measuring the F statistic: $F = SSE_{AAT}/SSE_{Pc,}$ where SSE_{AAT} and SSE_{Pc} are the sum square of the errors (SSE) between the AAT- and Pc-modeled lesion volumes and the 24-hour postocclusion FLAIR-measured volumes. Subsequently, comparison of the F statistic with an F distribution was used to assess the Pc- and AAT-derived models for goodness of fit to the measured data. In addition, mean absolute errors of both models were compared at each time point by using a Wilcoxon signed rank test to determine whether the errors from each model were significantly different. Statistical significance was defined at the 5% level.

RESULTS

All experiments were successful, and all 6 dogs survived to the 24-hour time point. None of the animals showed evidence of hemorrhagic conversion or herniation on the 24-hour MR imaging examinations. The Bland-Altman statistic for Pc determination between the 2 observers in this investigation was 22.4% (95% of scores within 1.5 points of each other), and the mean difference was 0.17 between observers. This result is similar to previously described reproducibility.[7] Raw data for each experiment (infarct volumes by time, Pc, and AAT) are shown in Table 1.

Predicting 24-Hour Infarct Volume from Angiography

Strong linear relations were observed between baseline pial collateral score and final infarct volume ($V_{Final} = -1483.6 \times Pc + 20{,}578$; $r^2 = 0.96$, $P < .003$) as well as AAT and final infarct volume ($V_{Final} = 2596.3 \times AAT + 1994.4$; $r^2 = 0.86$; $P < .008$) (Fig 2*A*, -*B*, respectively). A secondary analysis showed that a strong correlation exists between the pial collateral score and average arterial time ($ATT = -0.4754 \times Pc + 6.52$; $r^2 = 0.78$, $P < .02$) as might be expected from simple physiologic arguments (ie, robust collaterals provide earlier contrast agent arrival distal to an occlusion). The pial collateral score is a semiquantitative assessment, whereas AAT is a continuous quantitative measure of pial collateral recruitment.

Modeling Infarct Growth

Representative images for early (Fig 3*A*, upper part) and final (24-hour, Fig 3*A*, lower part) infarcts are shown along with the results of the semiautomated infarct volume algorithm. In all cases, infarct volumes were observed to increase asymptotically with time until reaching a final infarct volume (Fig 3*B*). Levenberg-Marquardt fits to Equation 1 converged with r^2 values exceeding 0.92 in all cases (Table 2). The growth rate index (G) extracted from the fits of the full time course (combined mean diffusivity for 0–240 minutes and 24-hour FLAIR) exhibited a strong linear relation to Pc ($G = -0.0013 \times Pc + 0.0179$; $r^2 = 0.89$; $P < .003$) and a moderate linear relation with AAT ($G = 0.0022 \times AAT + 0.0017$; $r^2 = 0.69$; $P < .04$) (Fig 2*C*, -*D*, respectively).

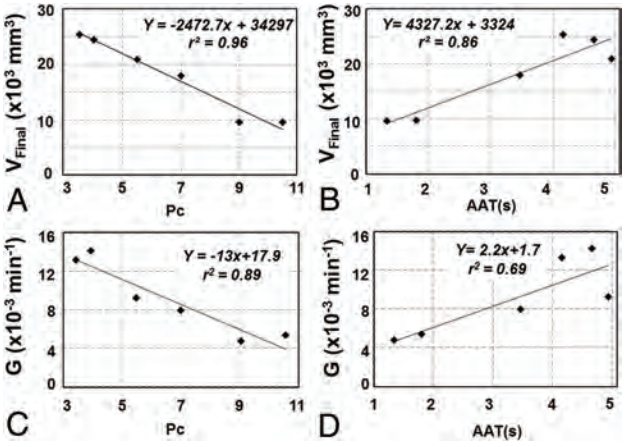

FIG 2. Final infarct volumes by T2 FLAIR images acquired 24 hours post-MCA occlusion are compared with baseline (ie, 15 minutes postocclusion) angiographic measures of pial collateral recruitment. *A*, Angiographic scoring of pial collateral score and arterial arrival time (*B*) strongly correlates with final infarct volume. Both pial collateral score (*C*) and AAT (*D*) are predictive the infarct growth rate index (derived from the fits shown in Fig 3*B*) on the basis of a linear function.

Parameterizing Infarct Growth from Collateralization

Because the experimental data indicated that both V_{Final} and G could be linearly approximated by each of Pc and AAT, a parameterization of infarct volume based solely on angiographic observables determined 15 minutes postocclusion was derived through simple algebraic back-substitution of V_{Fit} and G to obtain

$$2) \qquad V(t) = (A1 \times Pc + B1) \times [1 - e^{(C1 \times Pc + D1) \times t}],$$

with $A1 = -1483$, $B1 = 20{,}578$, $C1 = -0.0013$, and $D1 = 0.0179$). The equivalent expression for AAT was

$$3) \qquad V(t) = (A2 \times AAT + B2) \times [1 - e^{(C2 \times AAT + D2) \times t}],$$

with $A2 = 2596$, $B2 = 1994$, $C2 = 0.0022$, and $D2 = 0.0017$. The resulting curves are displayed on Fig 4 for a range of Pc and AAT values. The sum squares of the error of the AAT-based models were 3.99, 4.06, 1.93, 1.57, 1.31, and 3.98 times greater than the corresponding Pc-based model SSEs at the 60-, 90-, 120-, 180-, 240-minute and 24-hour time points. Congruently, the *F* test did not demonstrate a significant difference between the Pc- or AAT-based model of infarct volume growth at any time point with respective *P* values = .10, .10, .30, .30, .40, and .10. However, a comparison of the mean absolute error showed significantly better agreement between the Pc-based infarct growth modeling ($\varepsilon = -0.66 \pm 0.22$) compared with the AAT-based ($\varepsilon = 1.49 \pm 2.08$) modeling on a 2-sided Wilcoxon signed rank test ($P < .03$).

DISCUSSION

Our experimental results indicate that infarct growth in a permanent MCAO canine model can be mathematically modeled on the basis of an angiographic assessment of pial collateral recruitment. Reperfusion during the evolution of acute ischemia to cerebral infarction has the potential to either salvage brain at risk leading to improved clinical outcomes or cause reperfusion injury/hemorrhage leading to poorer clinical outcomes. Thus, the ability to assess salvageable ischemic tissue during the early phases of an acute ischemic stroke may impact treatment decisions.[1-3] Patients with acute ischemic stroke with large-vessel occlusion are potential candidates for embolectomy and undergo angiography before embolectomy. This circumstance lends itself to angiographic evaluation of pial collateral recruitment and may help in the assessment for embolectomy. Additionally, a clear understanding of the in-

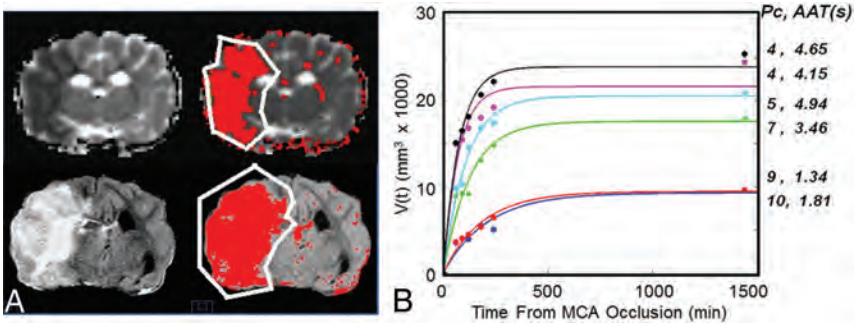

FIG 3. Single-section 120-minute mean diffusivity (upper part) and 24-hour FLAIR (lower part) images (*A*) were used to estimate and plot the growth of the infarct volume with time (*B*). A semiautomated algorithm was used to estimate the volume of the infarct on the basis of signal intensity within the affected hemisphere (red area), varying 1.5 times the SD from the mean of the signal in the contralateral normal-appearing hemisphere exclusive of spinal fluid. *B*, Infarct volume growth with time follows a predicable trend. Each curve corresponds to 1 experiment. The pial collateral scores and AAT measured immediately after occlusion (ie, at $t = 15$ minutes) for each curve are listed on the right.

farct volume growth rate as it relates to specific parameters can assist in estimating residual brain at risk and time available for intervention.

This work demonstrates that infarct growth after permanent occlusion of the MCA follows a predictable trend that can be mathematically modeled with respect to the degree of collateral blood supply distal to the occluded artery. During the early phases of cerebral ischemia after MCAO in mongrel canines, infarct volume measured by MR imaging diffusion restriction can be approximated by an asymptotic function of time. On the basis of this function, the infarct growth rate decreases with time and a growth rate index can be derived from this function. If the growth rate index is known, predictors of the final infarct volume can be used to define the evolution of cerebral infarction during MCAO. Final infarct volume and growth rate index can be linearly fitted to the pial collateral score on the basis of results derived in this study. Even if a linear relationship does not truly exist, an assessment of pial collateral recruitment can be used to estimate the final infarct volume as well as the infarct growth rate index. Ultimately in a controlled animal model with a specific occlusion site, such as the proximal middle cerebral artery, a set of estimated infarct growth curves can be generated for each pial collateral score and for various arterial arrival times (Fig 4). Using these curves, one may be able to estimate the salvageable brain tissue at risk. Given that the assessment of pial collaterals is reflective of the cerebral perfusion during acute ischemic infarction, cross-sectional perfusion imaging may also be predictive of the infarct growth index and final infarct volume.

Previous studies have assessed infarct growth with time and have determined that the growth of infarct volume changes in the early hours and reaches a maximum volume after which it decreases.[9-15] There is tremendous intraspecies and interspecies variation in the time course of cerebral infarct volume growth. Indeed, in humans, the mean time for maximal infarct volume for anterior circulation infarction appears to be around 70 hours.[9] If one compares Wistar rats with Sprague Dawley rats, the time it takes to reach maximum infarct volume appears to be 2 and 4 hours, respectively.[10] In Macaque monkeys, MCA infarction appears to reach a maximum at 24 or 48 hours.[11] Furthermore, the growth rate is suddenly altered if and when reperfusion occurs. Vasogenic edema appears to be more profound if reperfusion occurs later in the time course of infarction.[12] Finally, most studies that use MR imaging to assess infarct volume appear to suggest that a maximal infarct volume is reached on the basis of a logarithmic growth function.[11,13,14] After the maximal volume is reached, infarct volume decreases in size. On the basis of observations from this study as well as prior studies, given similar occlusion sites, the growth rate and the maximum infarct volume within each species vary to a large degree depending on the degree of pial collateral recruitment.[5,16] This feature assumes that less variability in the susceptibility of the cerebral tissues to ischemia exists within each species. The current study did not account for change in the MR imaging–based infarct growth rate as a result of reperfusion, which would represent an additive function likely depending on the degree of blood-brain barrier breakdown—that is, $V(t) = Vf\,[1 - e^{(-Gt)}] + B(t)$, where $B(t)$ represents this additive function.

Table 2: Growth rate index and final infarct volumes

Experiment	G (95% CI) ×(10^{-3})1/min	V_{fit} (95% CI) ×1000 mm^3	r^2
1	4.765 (2.37–7.16)	9.31 (7.08–11.55)	0.92
2	7.951 (4.65–11.25)	17.58 (14.52–20.63)	0.96
3	5.337 (3.629–7.05)	9.467 (8.04–10.89)	0.97
4	9.23 (6.79–11.67)	20.54 (18.41–22.67)	0.98
5	14.20 (5.64–22.75)	21.65 (17.64–25.66)	0.94
6	13.22 (8.79–17.67)	23.95 (21.36–26.54)	0.98

Note:—G indicates growth rate index from fit; V_{fit}, final infarct volume from fit; r^2 = coefficient of determination of fit.

There are limitations to this study. It is quite possible that a similar asymptotic function predictive of infarct volume may be found in humans, but our results may not be readily translatable across species. Unlike controlled experiments, physiologic parameters, occlusion site, age, and time of onset relative to MR imaging acquisition time are highly variable in the clinical setting. The current study was performed in a homogeneous population of canines with controlled physiologic conditions, permanent MCAO at a known occlusion site, and precisely known times of onset and imaging times. Varying metabolic, physiologic, and vascular events during cerebral infarction may directly and indirectly influence pial collateral recruitment under typical clinical circumstances. Additionally, the relative contributions of vasogenic, cytotoxic, and ionic edema were not differentially incorporated into the derived mathematic function. Cytotoxic and ionic edema are thought to have an immediate influence on infarct volume measured by diffusion-weighted imaging, whereas vasogenic edema would be expected to have a delayed and more prolonged impact.[17] Additionally, vasogenic edema due to reperfusion would be expected to have an additive influence at the time of reperfusion as mentioned earlier. Finally, the confined space of the calvaria may influence the infarct growth rate depending on the baseline difference in cerebral volume relative to calvarial volume, which increases with age. Further refinements of this mathematic function would need to consider the relative contributions of reperfusion and the potential variability of pial collateral recruitment with time.

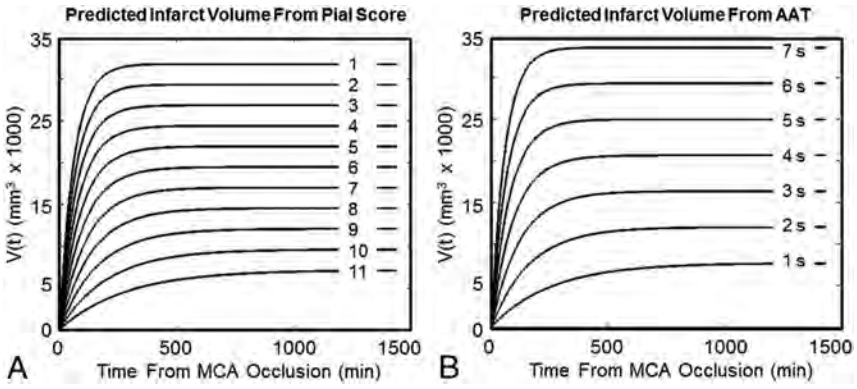

FIG 4. Families of infarct volume growth curves over 24 hours predicted by the pial collateral score and arterial arrival time.

Despite these limitations, the observation that the degree of pial collateral recruitment can estimate infarct volume growth can be incorporated in clinical decision-making. The finding of final infarct volume being dependent on pial collateral recruitment indicates that a variable peripheral zone of benign oligemia also exists in acute ischemic stroke. Finally, the observation that infarct growth rates depend on the time and extent of pial collaterals suggests that the window for potential interventional benefit may be longer in patients with good collaterals versus those with poor collaterals.

CONCLUSIONS

MR imaging–derived cerebral infarct volumes from an experimental MCAO canine model can be mathematically modeled by using an asymptotic function of time governed by final infarct volume and the growth rate index. Because both final infarct volume and the growth rate index can be linearly fitted to pial collateral recruitment, pial collateral assessment may be used to estimate potential infarct growth in the early stages of experimental cerebral ischemia due to MCAO.

Disclosures: Gregory A. Christoforidis—*RELATED*: *Grant*: National Institutes of Health R01-NS093908,* American Heart Association GRNT-20380798.* Timothy J. Carroll—*RELATED*: *Grant*: National Institutes of Health R21-EB017928,* R01-NS093908,* and American Heart Association GRNT-20380798.* *Money paid to the institution.

REFERENCES

1. Olivot JM, Mlynash M, Thijs VN, et al. **Geography, structure and evolution of diffusion and perfusion lesions in DEFUSE.** *Stroke* 2009;40:3245–51 CrossRef Medline
2. Hacke W, Albers G, Al Rawi Y, et al; DIAS Study Group. **The Desmoteplase in Acute Ischemic Stroke Trial (DIAS): a phase II MRI-based 9-hour window acute stroke thrombolysis trial with intravenous desmoteplase.** *Stroke* 2005;36:66–73 CrossRef Medline
3. Schlaug G, Benfield A, Baird AE, et al. **The ischemic penumbra: operationally defined by diffusion and perfusion MRI.** *Neurology* 1999;53:1528–37 CrossRef Medline
4. Fitzek S, Fitzek C, Urban PP, et al. **Time course of lesion development in patients with acute brain stem infarction and correlation with NIHSS score.** *Eur J Radiol* 2001;39:180–85 CrossRef Medline
5. Christoforidis GA, Mohammad Y, Kehagias D, et al. **Angiographic assessment of pial collaterals as a prognostic indicator following intra-arterial thrombolysis for acute ischemic stroke.** *AJNR Am J Neuroradiol* 2005;26:1789–97 Medline
6. Terasaki Y, Liu Y, Hayakawa K, et al. **Mechanisms of neurovascular dysfunction in acute ischemic brain.** *Curr Med Chem* 2014;21:2035–42 Medline
7. Christoforidis GA, Rink C, Kontzialis MS, et al. **An endovascular canine middle cerebral artery occlusion model for the study of leptomeningeal collateral recruitment.** *Invest Radiol* 2011;46:34–40 CrossRef Medline
8. Rink C, Christoforidis G, Abduljalil A, et al. **Minimally invasive neuroradiologic model of preclinical transient middle cerebral artery occlusion in canines.** *Proc Natl Acad Sci U S A* 2008;105:14100–05 CrossRef Medline
9. Schwamm LH, Koroshetz WJ, Sorensen AG, et al. **Time course of lesion development in patients with acute stroke: serial diffusion- and hemodynamic-weighted magnetic resonance imaging.** *Stroke* 1998;29:2268–76 CrossRef Medline
10. Bardutzky J, Shen Q, Henninger N, et al. **Differences in ischemic lesion evolution in different rat strains using diffusion and perfusion imaging.** *Stroke* 2005;36:2000–05 CrossRef Medline
11. Zhang X, Tong F, Li C-X, et al. **Temporal evolution of ischemic lesions in nonhuman primates: a diffusion and perfusion MRI study.** *PLoS One* 2015;10:e0117290 CrossRef Medline
12. Neumann-Haefelin T, Kastrup A, de Crespigny A, et al. **Serial MRI after transient focal cerebral ischemia in rats: dynamics of tissue injury, blood-brain barrier damage, and edema formation.** *Stroke* 2000;31:1965–72; discussion 1972–73 CrossRef Medline
13. Markus R, Reutens DC, Kazui S, et al. **Topography and temporal evolution of hypoxic viable tissue identified by 18F-fluoromisonidazole positron emission tomography in humans after ischemic stroke.** *Stroke* 2003;34:2646–52 CrossRef Medline
14. Saver J. **Time is brain: quantified.** *Stroke* 2006:37:263–66 CrossRef Medline
15. Loubinoux I, Volk A, Borredon J, et al. **Spreading of vasogenic edema and cytotoxic edema assessed by quantitative diffusion and T2 magnetic resonance imaging.** *Stroke* 1997;28:419–26; discussion 426–27 CrossRef Medline
16. Martinon E, Lefevre PH, Thouant P, et al. **A collateral circulation in acute stroke: assessing methods and impact: a literature review.** *J Neuroradiol* 2014;41:97–107 CrossRef Medline
17. Simard JM, Kent TA, Chen M, et al. **Brain oedema in focal ischaemia: molecular pathophysiology and theoretical implications.** *Lancet Neurol* 2007;6:258–68 Medline

The "White Gray Sign" Identifies the Central Sulcus on 3T High-Resolution T1-Weighted Images

O.F. Kaneko, N.J. Fischbein, J. Rosenberg, M. Wintermark, and M.M. Zeineh

ABSTRACT

BACKGROUND AND PURPOSE: The central sulcus is an important anatomic landmark, but most methods of identifying it rely on variable gyral and sulcal patterns. We describe and assess the accuracy of reduced gray-white contrast along the central sulcus, an observation we term the "white gray sign."

MATERIALS AND METHODS: We conducted a retrospective review of 51 fMRIs with a T1-weighted 3D inversion recovery fast-spoiled gradient-echo and concomitant hand-motor fMRI, which served as confirmation for the location of the central sulcus. To measure gray-white contrast across the central and adjacent sulci, we performed a quantitative analysis of 25 normal hemispheres along the anterior and posterior cortices and intervening white matter of the pre- and postcentral gyri. 3D inversion recovery fast-spoiled gradient-echo axial images from 51 fMRIs were then evaluated by 2 raters for the presence of the white gray sign as well as additional established signs of the central sulcus: the bracket, cortical thickness, omega, and T signs.

RESULTS: The mean gray-white contrast along the central sulcus was 0.218 anteriorly and 0.237 posteriorly, compared with 0.320 and 0.295 along the posterior precentral and anterior postcentral sulci, respectively ($P < .001$). Both raters correctly identified the central sulcus in all 35 normal and 16 abnormal hemispheres. The white gray sign had the highest agreement of all signs between raters and was rated as present the most often among all the signs.

CONCLUSIONS: Reduced gray-white contrast around the central sulcus is a reliable sign for identification of the central sulcus on 3D inversion recovery fast-spoiled gradient-echo images.

The central sulcus is an important anatomic landmark that defines the location of the primary motor cortex, a region of the brain critical for all essential motor tasks. Because injury to this region has irreversible consequences and other brain regions cannot compensate for its loss,[1] it is important to clearly identify the central sulcus for surgical planning, especially in the context of focal brain lesions. With knowledge of the location of the central sulcus, DTI and tractography can be used to identify the corticospinal tract emanating from the primary motor cortex. fMRI is a proven technique to identify the primary motor cortex for surgical planning.[2-6] It is still desirable, however, to identify the central sulcus from structural imaging for several reasons: this can provide an estimate of the proximity of a lesion to the motor strip to determine the necessity of fMRI, guide the tasks chosen for fMRI, serve as a surrogate if fMRI is not possible because of patient cooperation and compliance or technical factors, and assist in determining the risks of surgery.[7]

Numerous methods besides fMRI for identifying the central sulcus have been previously described on both CT and MR imaging. Most rely on identifying gyral and sulcal patterns and relationships,[8-13] which can be variable. Others involve complex image reformatting that most clinicians are untrained to produce or interpret.[14,15] Only a few signs, such as the difference in cortical thickness across the central sulcus, are based on differences in the underlying cytoarchitecture of the sensorimotor cortex.[16,17] Histologic studies and postmortem ex vivo high-resolution imaging have shown that in addition to the variation of the thickness of the 6 cellular layers of the sensorimotor cortex, there are also differences in myelin content that should be appreciable on MR imaging.[18-21] Based on this latter histologic finding, we describe the "white gray sign," which refers to the inherent increased T1 signal of the anterior and posterior cortices along the central sulcus, giving this gray matter a more white appearance (Fig 1). Specifically, we measure this contrast and assess the accuracy of this sign in identifying the central sulcus with reference to the criterion standard of fMRI.

Received July 1, 2016; accepted after revision September 20.

From the Department of Radiology, Neuroradiology Section, Stanford University, Stanford, California.

Please address correspondence to Michael Zeineh, MD, PhD, Stanford University, Lucas Center for Imaging Room P271, 1201 Welch Rd, Stanford, CA 94305; e-mail: mzeineh@stanford.edu

http://dx.doi.org/10.3174/ajnr.A5014

MATERIALS AND METHODS

Study Population

Using a retrospective institutional review board–approved review, we identified 51 fMRI examinations from January 2014 to December 2015. We only analyzed 1 hemisphere per patient for which hand-motor fMRI was available. Patient ages ranged from 20–70 years (mean, 42.5 years) and 27 women and 24 men were included. Of the 51 hemispheres examined, 35 were morphologically normal (normal hemispheres were functionally evaluated either for cryptogenic epilepsy surgical planning or as a reference for contralateral pathology). A separate 16 hemispheres had lesions that affected the sensorimotor region of the analyzed hemisphere. Pathologies included AVM ($n = 8$), encephalomalacia ($n = 3$), neoplasm ($n = 2$), cavernous malformation ($n = 2$), and cyst ($n = 1$). In all hemispheres with pathology, fMRI was performed for presurgical planning for eloquent cortex lateralization and/or localization.

Imaging Protocol

Each study was performed at 3T and consisted of 1) a 1.0-mm isotropic 3D inversion recovery fast-spoiled gradient-echo sequence (axial 3D; TR, 9.2 ms; TE, 3.7 ms; TI, 400 ms; matrix, 256 × 256 × 164; field of view, 24 cm × 24 cm × 16.4 cm; in-plane acceleration, 2; 4 minutes, 13 seconds), and 2) an fMRI motor task consisting of 12 blocks of 10 seconds of finger tapping alternating with 10 seconds of rest (2D gradient-echo, echo-planar imaging; TR, 2500 ms; TE, 35 ms; 3-mm section thickness; 20-cm field of view; 64 × 64 matrix size). Both sequences were processed to produce hand-motor activation maps thresholded at a T-score of 2–3 by using DynaSuite Neuro 3.1 (Invivo, Gainesville, Florida). Functional images were interpreted on a PACS workstation.

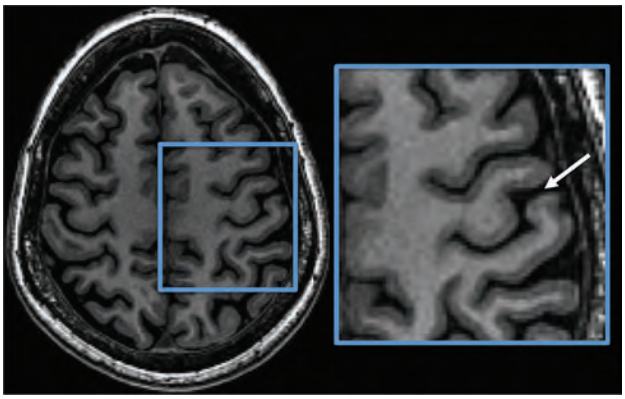

FIG 1. The "white gray sign." Axial high-resolution 3D inversion recovery fast-spoiled gradient-echo T1-weighted image demonstrates decreased gray-white contrast of the anterior and posterior cortices along the central sulcus (*white arrow*).

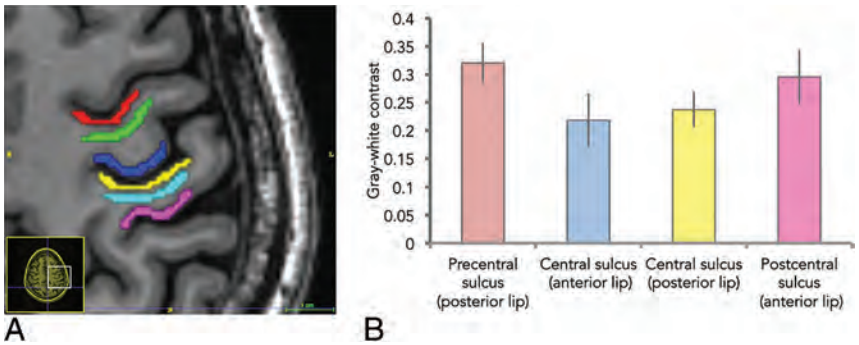

FIG 2. Measurement of gray-white contrast. *A*, Cortical segmentations were drawn along both sides of the central sulcus (royal blue and yellow) as well as along the adjacent banks of the precentral and postcentral sulci (red and pink) and the intervening WM (green and light blue). *B*, Gray-white contrast (± standard deviation bars) along the central sulcus was significantly ($P < .001$) decreased both anteriorly and posteriorly compared with the contrast along the pre- and postcentral sulci, respectively.

Quantitative Analysis of the White Gray Sign

Twenty-five of the normal hemisphere structural MRIs were segmented using ITK-SNAP (www.itksnap.org).[22] Using the fMRI as the reference for the central sulcus, on a single axial section at the level of the upper centrum semiovale, we manually segmented the following cortical regions of interest sequentially from anterior to posterior (Fig 2): cortex along the posterior bank of the precentral sulcus, cortex along the anterior bank of the central sulcus, cortex along the posterior bank of the central sulcus, and cortex along the anterior bank of the postcentral sulcus. For gray-white contrast computation, we manually segmented the white matter within the intervening precentral and postcentral gyri. All segmentations for both the cortices and the WM were at least 30 pixels in volume and thinned to avoid partial volume effect due to averaging with adjacent structures.

Gray-white contrast for the 4 cortical regions was calculated by: (Subjacent WM average signal intensity − GM average signal intensity) / (Subjacent WM average signal intensity). A Student *t* test compared gray-white contrast differences between the precentral sulcus and central sulcus and between the central sulcus and postcentral sulcus using STATA (StataCorp, College Station, Texas).

Qualitative Analysis of the White Gray Sign

To test the performance of the white gray sign clinically and to compare that performance with previously described methods for identifying the central sulcus, 51 hemispheres from fMRI examinations were analyzed. Both normal (including the aforementioned 25 fMRIs) and abnormal hemispheres were analyzed.

Two readers (M.W., N.J.F.) with 16 and 26 years of neuroradiology experience, respectively, evaluated the 51 hemispheres for the presence or absence of the white gray sign as well as the bracket, cortical thickness difference, omega, and T signs (Fig 3). The raters were blinded to the functional data. The following rating scale was used: 1 = sign definitely not present; 2 = sign likely not present; 3 = sign likely present; and 4 = sign definitely present. Each rater also annotated the putative sulcus, and accuracy was confirmed by a coauthor (O.F.K.) with the fMRI hand-motor activation maps.

The 1–4 scale was then dichotomized to summarize the presence or absence of the individual signs (ie, 1–2 = not present; 3–4 = present). Rater agreement was assessed by summing the number of patients in which they agreed on a sign being present or absent divided by the total number of patients.

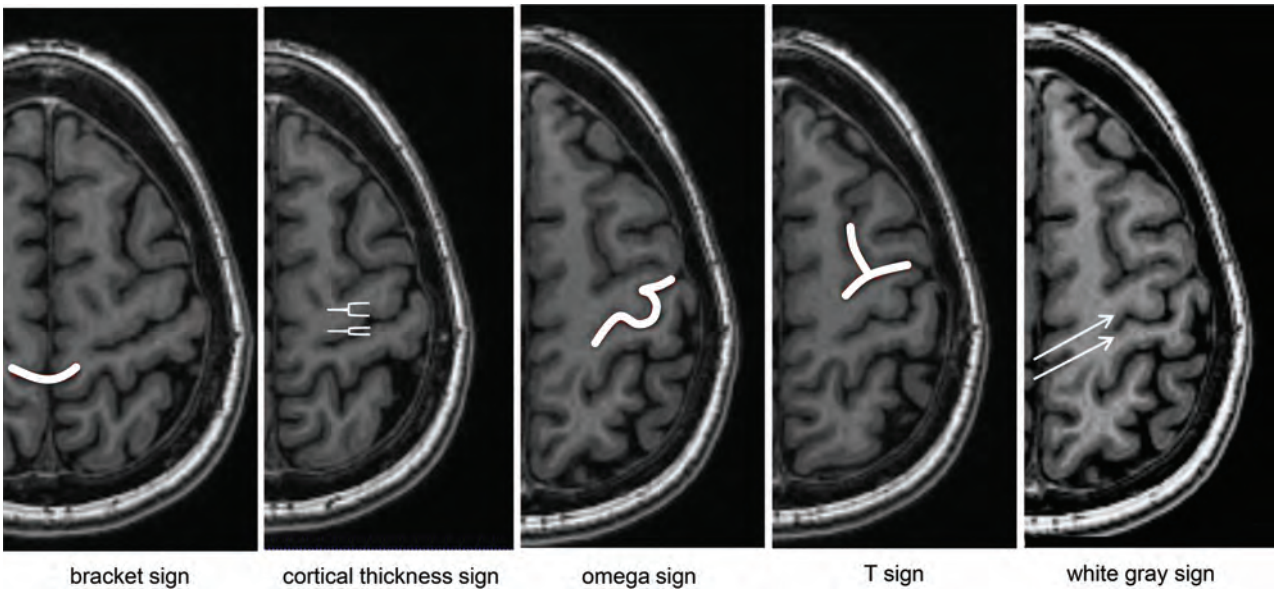

FIG 3. Signs of the central sulcus rated in this study. Bracket = central sulcus points to the marginal sulcus. Cortical thickness = increased cortical thickness along the anterior compared with posterior bank of the central sulcus. Omega = characteristic omega shape of the hand-motor knob. T = superior frontal sulcus meets the precentral gyrus.

Comparison of the white gray sign with other signs of the central sulcus[a]

	Hemispheres	White Gray	Bracket	Thickness	Omega	T
Rater 1	51	45	11 (<.001)[b]	23 (<.001)[b]	37 (.022)	38 (.092)
	35 normal	34	9 (<.001)[b]	15 (<.001)[b]	26	28
	16 abnormal	11	2 (.004)[b]	8 (.375)	11	10
Rater 2	51	51	38 (<.001)[b]	49 (.500)	42 (.004)[b]	27 (<.001)[b]
	35 normal	35	28 (.016)[b]	35	28 (.016)[b]	20 (<.001)[b]
	16 abnormal	16	10 (.031)	14	14 (.500)	7 (<.004)[b]

[a] Proportion of cases where each sign was reported, each compared with the white gray sign within rater. For the comparison of both hemispheres, a Bonferroni-adjusted *P* value of <.0125 was statistically significant correcting for the 4 signs evaluated. For the post-hoc separate evaluation of normal and abnormal hemispheres, the corrected threshold is $P < .025$.

[b] Statistically significant.

Statistical Analysis

Systematic disagreement between raters was assessed by a symmetry test, with a Bonferroni-corrected threshold of 0.01 for the 5 tests evaluated. Differences in presence of the white gray sign compared with the other signs across all hemispheres were tested for each rater by using a McNemar test, with a Bonferroni-corrected threshold of 0.0125 to correct for the 4 comparisons between signs. For cases in which the white gray sign outperformed another sign, a subsequent post hoc analysis did the same comparison separately for normal and abnormal hemispheres, with a Bonferroni-corrected threshold of 0.025.

RESULTS

Quantitative Analysis of Gray-White Contrast around the Central Sulcus

On axial T1-weighted 3D inversion recovery fast-spoiled gradient-echo images of the 25 normal hemispheres, the mean gray-white contrast along the central sulcus was 0.218 ± 0.0356 anteriorly and 0.237 ± 0.0457 posteriorly compared with 0.320 ± 0.0318 and 0.295 ± 0.0485 along the precentral and postcentral sulci, respectively (Fig 2*B*). Differences in gray-white contrast were statistically significant, with *P* values of <.001. In all 25 hemispheres tested, the gray-white contrast was lower along the anterior bank of the central sulcus compared with the neighboring posterior bank of the precentral gyrus. In 23/25 (92%) cases, the contrast was lower along the posterior bank of the central sulcus compared with the neighboring anterior bank of the postcentral sulcus.

Qualitative Analysis of the White Gray Sign and Other Signs of the Central Sulcus

For the rater analyses of the 51 hemispheres, both raters correctly identified the central sulcus in all 35 normal and 16 abnormal hemispheres. Rater agreement for the bracket, cortical thickness, omega, T, and white gray signs was 43.1%, 45.1%, 74.5%, 62.8%, and 88.3%, respectively. The symmetry test was significant for the bracket and thickness signs (both $P < .001$), suggesting a systematic difference between raters in scores for these signs (Fig 4). The asymmetry was not statistically significant for the omega, T, and white gray signs, with *P* values of .267, .019, and .031, respectively. The white gray sign was reported statistically significantly more often than the following signs across all hemispheres: the bracket sign for both raters, the thickness sign for rater 1, and the omega and T signs for rater 2 (Table, Fig 4). The post hoc analysis of normal hemispheres showed that these differences held for the bracket sign for both raters, the thickness sign for rater 1, and the omega and T signs for rater 2.

For those 16 hemispheres that contained lesions affecting the central sulcus, rater 1 found the white gray sign in all 16 hemispheres, whereas rater 2 found the white gray sign in 11/16 hemispheres. An example lesion extending to the precentral gyrus does not interfere with the correct identification of the white gray sign (Fig 5). Performance of the additional signs for the abnormal hemispheres was as follows: bracket (rater 1, 2/16; rater 2, 10/16),

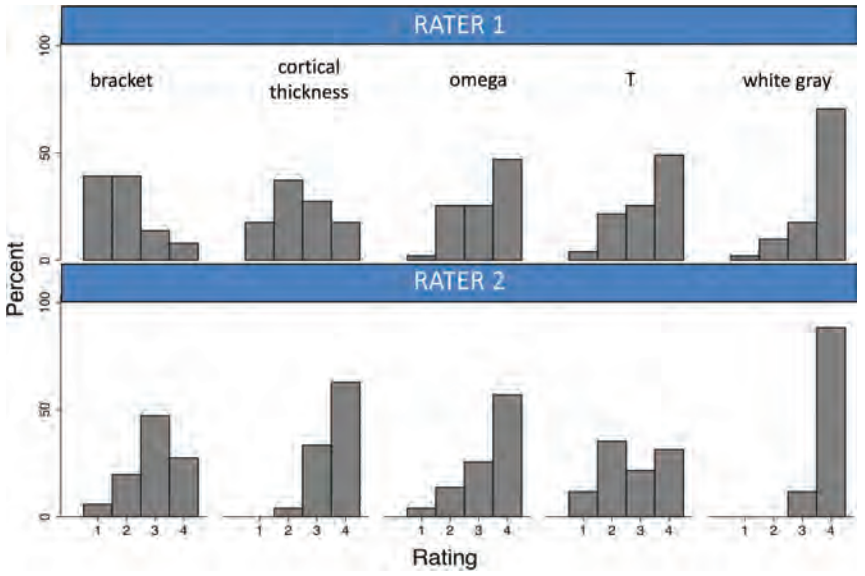

FIG 4. Rater evaluation of signs of the central sulcus in 51 hemispheres (35 normal, 16 with pathology). 1 = definitely not present, 2 = likely not present, 3 = likely present, 4 = definitely present.

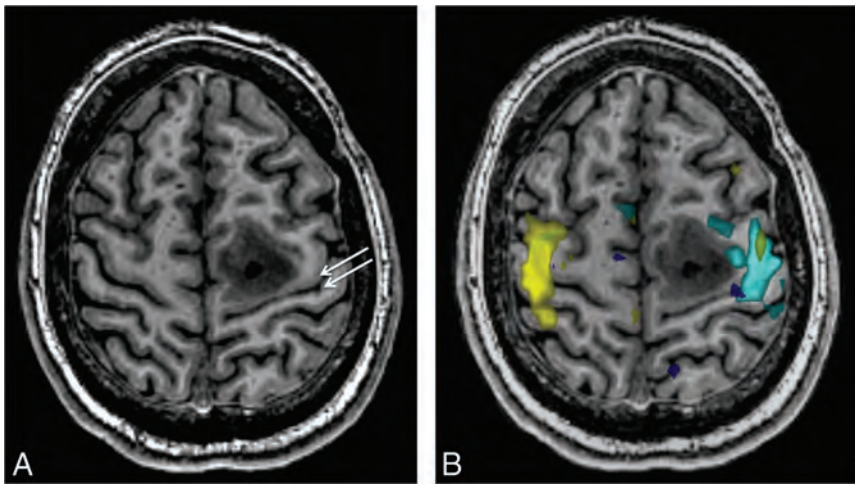

FIG 5. A 22-year-old man with posterior left frontal grade 2 astrocytoma. *A*, Axial 3D inversion recovery fast-spoiled gradient-echo T1-weighted image shows the tumor centered along the anterior aspect of the precentral gyrus. The white gray sign is still noticeable as decreased contrast of the gray-white interface along the central sulcus (*arrows*). This is also appreciable on the contralateral normal side. *B*, Functional data with hand-motor tasks (light blue = right hand, yellow = left hand) confirm the location of the primary motor and somatosensory cortices.

cortical thickness (8/16, 14/16), omega sign (11/16, 14/16), and T sign (10/16, 7/16). The post hoc analysis of abnormal hemispheres showed that the white gray sign was reported statistically significantly more often than the bracket sign for rater 1 and the T sign for rater 2.

DISCUSSION

We describe an additional reliable central sulcus sign that is based upon the physiologic high T1 signal of the cortices along the central sulcus and, consequently, the decreased contrast with the adjacent WM. It is likely that the relatively increased T1 signal demonstrated on high-resolution inversion recovery fast-spoiled gradient-echo images is reflective of the increased myelin content of this tissue. Previously described differences in signal of the motor cortex on T2-FLAIR are also likely secondary to these differences in the underlying myeloarchitecture.[23,24] Thus, increased cortical thickness along the anterior bank of the central sulcus, in combination with the increased T1 signal within the cortex along both sides of the central sulcus, are together 2 distinct imaging markers for cytoarchitecture and myeloarchitecture that are likely to be robust for anatomic delineation.

There are several limitations to the current study. At our institution, all functional MR imaging examinations are performed at 3T; therefore, both the quantitative and qualitative portions of this study were also based only on 3T images, and we cannot assess if this sign would perform similarly at 1.5T. Although some volume averaging with the adjacent WM could occur in the cortical segmentations, in particular along the relatively thin posterior bank of the central sulcus, care was taken to confine the segmentations to cortices. Differences in gray-white contrast were only measured in normal hemispheres. Although the same relationship may not persist in the presence of local edema near a lesion, we have found that qualitatively, the white gray sign is identifiable along the entirety of the central sulcus, and this matches other imaging data regarding myelination along the central sulcus.[25] Regarding the rating portion of the study, both raters accurately identified the central sulcus in all 51 cases; however, it was not determined by which method they came to that conclusion. The 2 raters did not perfectly agree on all the signs, suggesting that these signs can all be subjective and dependent on factors such as reader training. Nevertheless, the white gray sign had the highest agreement and scored the highest among both raters in both normal and pathologic hemispheres. Future studies can evaluate the conspicuity of this finding on sequences other than T1-weighted inversion recovery fast-spoiled gradient-echo, the extension of this finding to other primary cortices, and the relationship with developmental aspects of myelination along the central sulcus.

CONCLUSIONS

We have shown that inherent differences in T1 signal of the cortices along the central sulcus lead to discrete and appreciable differences in gray-white contrast. Clinically, the "white gray sign" is a reliable method for identifying the central sulcus, which was

found to be present in the highest proportion of cases compared with other previously described and well-known signs. Anatomic imaging methods that take advantage of knowledge of underlying cyto- and myeloarchitecture are powerful tools for determining functional segregation of brain structure.

Disclosures: Max Wintermark—*UNRELATED*: *Board Membership*: GE Healthcare and National Football League Advisory Board. Michael Zeineh—*UNRELATED*: *Other*: GE Healthcare, *Comments*: research funding.* *Money paid to the institution.

REFERENCES

1. Miyai I, Suzuki T, Kang J, et al. **Middle cerebral artery stroke that includes the premotor cortex reduces mobility outcome.** *Stroke* 1999;30:1380–83 CrossRef Medline
2. Hingwala D, Thomas B, Radhakrishnan A, et al. **Correlation between anatomic landmarks and fMRI in detection of the sensorimotor cortex in patients with structural lesions.** *Acta Radiol* 2014;55:107–13 CrossRef Medline
3. Lehéricy S, Duffau H, Cornu P, et al. **Correspondence between functional magnetic resonance imaging somatotopy and individual brain anatomy of the central region: comparison with intraoperative stimulation in patients with brain tumors.** *J Neurosurg* 2000;92:589–98 CrossRef Medline
4. Morioka T, Mizushima A, Yamamoto T, et al. **Functional mapping of the sensorimotor cortex: combined use of magnetoencephalography, functional MRI, and motor evoked potentials.** *Neuroradiology* 1995;37:526–30 CrossRef Medline
5. Morioka T, Yamamoto T, Mizushima A, et al. **Comparison of magnetoencephalography, functional MRI, and motor evoked potentials in the localization of the sensory-motor cortex.** *Neurol Res* 1995;17:361–67 Medline
6. Wengenroth M, Blatow M, Guenther J, et al. **Diagnostic benefits of presurgical fMRI in patients with brain tumours in the primary sensorimotor cortex.** *Eur Radiol* 2011;21:1517–25 CrossRef Medline
7. Due-Tonnessen P, Rasmussen I, Berntsen EM, et al. **Identifying the central sulcus in patients with intra-axial lesions: a multicenter study comparing conventional presurgical MRI to topographical analysis and BOLD-fMRI.** *J Comput Assist Tomogr* 2014;38:1–8 CrossRef Medline
8. Naidich TP, Blum JT, Firestone MI. **The parasagittal line: an anatomic landmark for axial imaging.** *AJNR Am J Neuroradiol* 2001;22:885–95 Medline
9. Rodrigues T, Rodrigues M, Paz D, et al. **Is the omega sign a reliable landmark for the neurosurgical team? An anatomical study about the central sulcus region.** *Arq Neuropsiqiatr* 2015;73:934–38 CrossRef Medline
10. Sobel DF, Gallen CC, Schwartz BJ, et al. **Locating the central sulcus: comparison of MR anatomic and magnetoencephalographic functional methods.** *AJNR Am J Neuroradiol* 1993;14:915–25 Medline
11. Yousry TA, Schmid UD, Alkadhi H, et al. **Localization of the motor hand area to a knob on the precentral gyrus. A new landmark.** *Brain* 1997;120(Pt 1):141–57 CrossRef Medline
12. Yousry TA, Schmid UD, Schmidt D, et al. **The central sulcal vein: a landmark for identification of the central sulcus using functional magnetic resonance imaging.** *J Neurosurg* 1996;85:608–17 CrossRef Medline
13. Naidich TP, Valavanis AG, Kubik S. **Anatomic relationships along the low-middle convexity: part I–normal specimens and magnetic resonance imaging.** *Neurosurgery* 1995;36:517–32 CrossRef Medline
14. Hattingen E, Good C, Weidauer S, et al. **Brain surface reformatted images for fast and easy localization of perirolandic lesions.** *J Neurosurg* 2005;102:302–10 CrossRef Medline
15. Wagner M, Jurcoane A, Hattingen E. **The U sign: tenth landmark to the central region on brain surface reformatted MR imaging.** *AJNR Am J Neuroradiol* 2013;34:323–26 CrossRef Medline
16. Biega TJ, Lonser RR, Butman JA. **Differential cortical thickness across the central sulcus: a method for identifying the central sulcus in the presence of mass effect and vasogenic edema.** *AJNR Am J Neuroradiol* 2006;27:1450–53 Medline
17. Meyer JR, Roychowdhury S, Russell EJ, et al. **Location of the central sulcus via cortical thickness of the precentral and postcentral gyri on MR.** *AJNR Am J Neuroradiol* 1996;17:1699–706 Medline
18. Dinse J, Härtwich N, Waehnert MD, et al. **A cytoarchitecture-driven myelin model reveals area-specific signatures in human primary and secondary areas using ultra-high resolution in-vivo brain MRI.** *Neuroimage* 2015;114:71–87 CrossRef Medline
19. Geyer S, Weiss M, Reimann K, et al. **Microstructural parcellation of the human cerebral cortex - from Brodmann's post-mortem map to in vivo mapping with high-field magnetic resonance imaging.** *Front Hum Neurosci* 2011;5:19 CrossRef Medline
20. Annese J, Pitiot A, Dinov ID, et al. **A myelo-architectonic method for the structural classification of cortical areas.** *Neuroimage* 2004;21:15–26 CrossRef Medline
21. Nieuwenhuys R, Broere CA, Cerliani L. **A new myeloarchitectonic map of the human neocortex based on data from the Vogt-Vogt school.** *Brain Struct Funct* 2015;220:2551–73 CrossRef Medline
22. Yushkevich PA, Piven J, Hazlett HC, et al. **User-guided 3D active contour segmentation of anatomical structures: significantly improved efficiency and reliability.** *Neuroimage* 2006;31:1116–28 CrossRef Medline
23. Kakeda S, Korogi Y, Kamada K, et al. **Signal intensity of the motor cortex on phase-weighted imaging at 3T.** *AJNR Am J Neuroradiol* 2008;29:1171–75 CrossRef Medline
24. Kamada K, Kakeda S, Ohnari N, et al. **Signal intensity of motor and sensory cortices on T2-weighted and FLAIR images: intraindividual comparison of 1.5T and 3T MRI.** *Eur Radiol* 2008;18:2949–55 CrossRef Medline
25. Glasser MF, Coalson TS, Robinson EC, et al. **A multi-modal parcellation of human cerebral cortex.** *Nature* 2016;536:171–78 CrossRef Medline

Use of Phase-Contrast MRA to Assess Intracranial Venous Sinus Resistance to Drainage in Healthy Individuals

S. Fall, G. Pagé, J. Bettoni, R. Bouzerar, and O. Balédent

ABSTRACT

BACKGROUND AND PURPOSE: Resistance to blood flow in the cerebral drainage system may affect cerebral hemodynamics. The objective of the present study was to use phase-contrast MRA to quantify resistance to drainage of blood across branches of the venous sinus tree and to determine whether the resistance to drainage values correlated with internal jugular vein outflows.

MATERIALS AND METHODS: We performed whole-head phase-contrast MRA and 2D phase-contrast MR imaging in 31 healthy volunteers. Vascular segmentation was applied to the angiograms, and the internal jugular vein velocities were quantified from the flow images. Resistance to drainage across branches of the venous sinus tree was calculated from the segmented angiograms, by using the Poiseuille equation for laminar flow. Correlations between the values of resistance to drainage and internal jugular vein outflow measurements were assessed by using the Spearman ρ.

RESULTS: The overall mean resistance to drainage of the venous sinus tree was 24 $\pm$ 7 Pa s/cm^3. The mean resistance to drainage of the right side of the venous sinus tree was 42% lower than that of the left side ($P < .001$). There were negative correlations between the values of resistance to drainage and internal jugular vein outflows on both the left side of the venous sinus tree ($R = -0.551$, $P = .002$) and the right side ($R = -0.662$, $P < .001$).

CONCLUSIONS: Phase-contrast MRA is a noninvasive means of calculating the resistance to drainage of blood across the venous sinus tree. Our approach for resistance to drainage quantification may be of value in understanding alterations in the cerebral venous sinus drainage system.

ABBREVIATIONS: AI = asymmetry index; IJV = internal jugular vein; PC-MRA = phase-contrast MR angiography; Rd = resistance to drainage

The cerebral venous sinus system is characterized by anatomic variations[1] associated with marked interindividual variability in blood drainage patterns.[2] The venous compartment is generally compliant, whereas the walls of the sinuses tend to be rigid. In comparison with the intracranial arterial system, the venous sinus system has received less attention in the imaging-based evaluation of cerebrovascular diseases in clinical research, possibly because the pathologies that affect the intracranial venous sinus system are less common than those affecting the arterial system and often present a broad spectrum of clinical manifestations.[3] However, alterations in cerebral hemodynamics are known to be associated with abnormal drainage in the cerebral venous sinus system. For example, impaired intracranial drainage is widely cited as one of the prime causes in idiopathic intracranial hypertension,[4-7] intracranial dural arteriovenous fistula malformation,[8] communicating and noncommunicating hydrocephalus,[9,10] and multiple sclerosis.[11] Nevertheless, a suspected case of venous stenosis must be assessed with caution[12] because misinterpretation can lead to a nonindicated operation (with all its associated non-negligible risks). This point is clearly illustrated by the debate over the involvement of jugular venous stenosis in the pathogenesis of multiple sclerosis. In multiple sclerosis, it has been shown that percutaneous transluminal angioplasty of extracranial veins with suspected alterations is ineffective, may exacerbate underlying disease activity, and can lead to serious complications.[13]

In clinical practice, intraluminal vessel defects and/or pathologic flow velocities of the intracranial drainage system are usually evaluated by using contrast-enhanced or unenhanced MR imaging,[5] CTA,[14] DSA,[15] or transcranial Doppler sonography.[16] Al-

Received April 20, 2016; accepted after revision September 11.

From the BioFlow Image Laboratory (S.F., G.P., O.B.), University of Picardy Jules Verne, Amiens, France; Maxillofacial Department (J.B.) and Medical Image Processing Department (R.B., O.B.), University Hospital of Picardy, Amiens, France; and ICube-IRMA (S.F.), Strasbourg University, Illkirch, France.

The research was funded in part by the French National Research Agency (grant ANR-12-MONU-0010).

Please address correspondence to Sidy Fall, MD, BioFlow Image, University of Picardy Jules Verne, Chemin du Thil, F-80000, Amiens, France; e-mail: fall.sidy@chu-amiens.fr

http://dx.doi.org/10.3174/ajnr.A5013

though unenhanced vascular imaging techniques are less sensitive than contrast-enhanced techniques, they may be of value for an initial evaluation of the venous system in neonates or in patients who are allergic to contrast agents or have kidney dysfunction. Unenhanced 3D phase-contrast MRA (PC-MRA) offers several advantages: It is relatively rapid, is often appropriate for patient follow-up, and is associated with a lower complication rate.[17,18] The results of patient evaluations usually show that a narrower luminal cross-section can produce higher flow resistance and therefore a decrease in flow and an increase in pressure—at least in the region adjacent (proximal) to the lesion. Moreover, venous sinus manometry has shown an elevated sagittal sinus pressure and a significant drop in transverse sinus pressure in patients with idiopathic intracranial hypertension.[19] Other researchers have shown that most patients with idiopathic intracranial hypertension have normal blood flow in the superior sagittal sinus.[7]

The mechanisms linking the cerebral venous outflow rate to intracranial pressure have not been characterized, to our knowledge. However, it is possible that structural factors (such as an increase in the resistance to drainage [Rd] of blood across the branches of the venous sinus pathways) may impact intracranial venous outflow, as has been demonstrated in patients with venous outflow obstruction (in whom an elevated venous back pressure resulted in elevated venous resistance[20]). It is generally assumed that the pressure drop for driving axial flow across a tube increases with the flow resistance. Thus, an increase in venous sinus flow resistance would require an increase in upstream flow pressure for a constant volume flow through this drainage system to be maintained. Hence, the cumulative effects of the Rd across segments of the venous sinus pathways may have a role in cerebral hydrodynamics in general and in intracranial pressure and cerebral compliance in particular.

While the association between intracranial hydrodynamics and the geometric characteristics of the venous sinus system appears to be strong, we are not aware of any quantitative data on the resistance to blood flow in the cerebral drainage system. The objective of the present study was therefore to calculate the Rd of blood across the major dural sinuses and internal jugular veins (IJVs) in healthy volunteers by using phase-contrast MR angiography. We used the well-established Poiseuille equation for laminar flow to calculate the Rd from the PC-MRA data. Furthermore, we explored the relationship between the values of Rd and the IJV flows measured by cine phase-contrast MR imaging.

MATERIALS AND METHODS

Participants

Twenty-nine healthy volunteers (mean age, 26.7 ± 5.5 years; 18 women and 11 men) were recruited. None had a history of neurovascular disease. The study was approved by the regional investigational review board, and all participants gave their written, informed consent.

Image Acquisition

Images were acquired with a 3T MR imaging system (dStream; Philips Healthcare, Best, the Netherlands) equipped with a 32-channel digital head coil, by using a 3D PC-MRA sequence. This sequence exploits the property whereby spins that move through a bipolar gradient field accumulate a phase difference, whereas static spins do not. The bipolar flow-encoding gradients can be applied simultaneously along 3 axes to measure the corresponding flow sensitivities. The sensitivity of the PC-MRA technique can be controlled by using a parameter sequence commonly referred to as "velocity-encoding." More details of this technique have been presented by Dumoulin et al.[21]

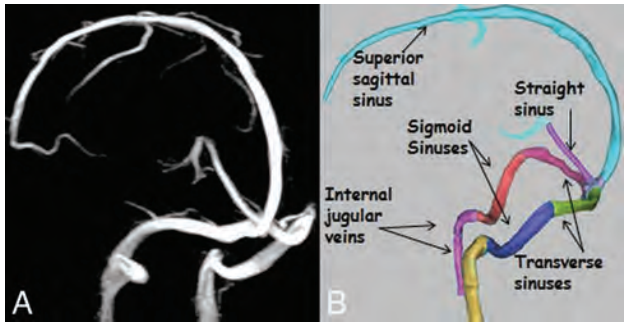

FIG 1. Representative examples of maps of the venous sinus tree. *A*, Maximum-intensity projection of a 3D PC-MRA source image. *B*, The venous sinus tree segmentation was produced by Mimics software.

PC-MRA was performed in the sagittal plane (covering the whole cerebral venous system and some of the IJVs, up to the C3–C4 cervical vertebrae) by using the following parameters: FOV = 220 × 220 mm^2; number of sections = 320; effective spatial resolution = 0.7 × 0.7 mm^2; flip angle = 12°; velocity-encoding = 30 cm/s; TR = 5.5 ms; TE = 3 ms; acquisition time = 6 minutes. Next, 2D PC-MR images were acquired perpendicular to the IJVs near the C2 and C3 vertebrae, by using a gated cine PC-MR imaging pulse sequence. The main scan parameters were as follows: FOV = 120 × 120 mm^2; resulting spatial resolution = 0.5 × 0.5 mm^2; section thickness = 2 mm; TR/TE = 14/8 ms; flip angle = 30°; velocity-encoding = 80 cm/s; cardiac phases = 16. The acquisition times ranged from 1.2 to 1.8 minutes, depending on the heart rate.

Image Processing

The PC-MRA datasets were imported into Mimics software (Materialise, Leuven, Belgium) for 3D, semiautomated segmentation of the cerebral venous sinus tree (represented as the superior sagittal, straight, transverse, and sigmoid sinuses and the IJVs). Threshold-based segmentation was used to extract the venous sinus tree from each angiogram. To this end, the section passing as close as possible to the mesial plane of the straight sinus was selected, and an intensity profile was obtained along a line perpendicular to the sinus. A suitable intensity threshold was then determined from this profile (17%–23% of its maximum intensity, depending on the image quality for each participant). All voxels with signal intensities below this threshold value were masked. Figure 1 shows a typical segmentation of the venous sinus tree. The final segmented geometry was converted into a Standard Tessellation Language file format. The Standard Tessellation Language file was then imported into the Vascular Modeling Toolkit software (www.vmtk.org) for quantification of the length, cross-sectional area, and associated radius at 10-mm intervals along each vessel segment. To avoid possible bias due to anatomic variations, we excluded the anterior portion of the superior sagittal sinus from the calculation.

For the flow images, IJV flow velocities at the C2–C3 cervical vertebrae were quantified throughout the cardiac cycle by using freely available, semiautomatic software (Bio Flow image; http://www.tidam.fr). Details of the flow measurement have been described previously.[22]

Calculation of Resistance and Flows

The Rd of each 10-mm segment was calculated by applying the Poiseuille equation for laminar flow:

$$Rd = \frac{8\mu L}{\pi r_h^4},$$

where L (10 mm) and r_h are the length and the radius of the segment, respectively, and μ is the viscosity of the blood. The total Rd for a selected part of the venous sinus tree was calculated by summing the Rd for all the component 10-mm segments.

The left- or right-sided Rd for the venous sinus tree was calculated by summing the Rd values for the transverse sinus, sigmoid sinus, and IJV on each side of the head. An overall Rd for the venous sinus tree was also calculated by analogy with an electric circuit (Fig 2). Details of the mathematic equation for calculation of the overall Rd are presented in the Appendix.

The flows in each IJV were also added to obtain the total IJV flow. Figure 3 shows the change in mean flow in the IJVs over the cardiac cycle in 1 participant.

Statistical Analysis

Statistical analysis was performed with R statistical and computing software (Version 3.2.3; http://www.r-project.org/). A Wilcoxon matched-pairs test was used to probe for differences between the left and right sides of the venous sinus tree. Correlations between the values of Rd and blood flow measurements of the IJVs were assessed by using the Spearman ρ. The threshold for statistical significance was set at $P < .05$.

We calculated the correlations between the values of Rd and IJV flow measurements for each side of the venous tree and between the overall Rd for the venous sinus tree and the total IJV flow measurements. We also looked at whether there was an association between sidedness in flow and sidedness in Rd in the venous sinus tree. To this end, we calculated 2 asymmetry indices (AIs) for each participant:

The resistance AI, reflecting asymmetry resistance, was the following:

Resistance AI = (left-sided Rd − right-sided Rd) / (left-sided Rd + right-sided Rd).

The flow AI, reflecting IJV flow dominance, was the following:

Flow AI = (left IJV flow − right IJV flow) / (left IJV flow + right IJV flow).

The AIs obtained with these 2 equations ranged from −1 (strong right dominance) to +1 (strong left dominance). The strength of the sidedness (for flow or resistance) was categorized as $+0.2 < AI < +1$ (left-sided dominance), $-0.2 < AI < -1$ (right-sided dominance), and $-0.2 < AI < +0.2$ (codominance).

The correlation between the flow AIs and resistance AIs were also evaluated.

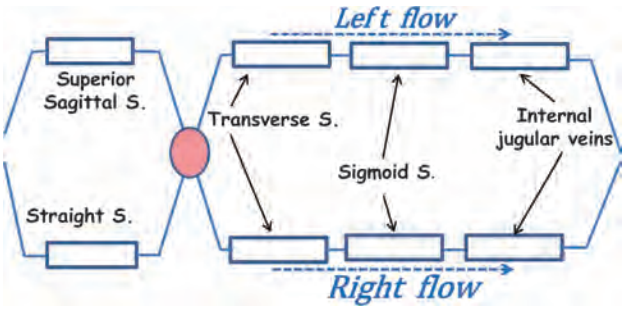

FIG 2. Schematic representation of the modeled venous system. S. indicates sinus.

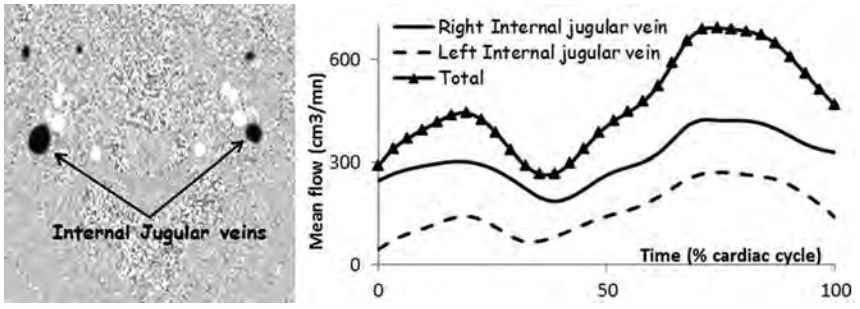

FIG 3. An example of phase-contrast MR imaging showing the 2 IJVs (at the C2–C3 vertebrae) and typical flow curves over the cardiac cycle in 1 participant. The curve marked with *triangles* shows the total mean flow through the left and right IJVs.

RESULTS

The mean values of Rd for each vessel segment and for the venous sinus tree as a whole are summarized in the Table. Significant sidedness was observed for the mean of Rd (left side versus right side, 42.1 ± 17 versus 18.4 ± 10 Pa s/cm^3; $P < .001$) and the measured flows (left side versus right side, 250 ± 108 versus 349 ± 124 cm^3/min; $P = .02$). Left-dominant, right-dominant, and codominant flow was observed in, respectively, 17%, 48%, and 35% of the participants.

Scatterplots of the associations between the values of Rd and flow measurements are shown in Fig 4. There were significant negative correlations between the values of Rd and the flow measurements on both the left side of the venous sinus tree ($R = -0.551$, $P = .002$) and the right side ($R = -0.662$, $P < .001$). When we considered associations between flow dominance and resistance dominance, there was a strong negative correlation between the flow AIs and the resistance AIs ($R = -0.792$, $P < .001$) as illustrated by a scatterplot (Fig 5). There was no significant correlation between total resistance and total venous outflow ($R = -0.359$, $P = .06$).

DISCUSSION

It has been suggested that cerebral venous sinus insufficiency is a major factor in certain neurovascular diseases.[4,5,8-10,23] Apart from evaluations of anatomic abnormalities and the quantification of

narrowed vessels and abnormal flow/pressure patterns,[24,25] little is known about resistance to blood flow in the cerebral venous sinus drainage system. Here, we describe a novel approach for calculating the Rd through the cerebral venous tree; it is based on the application of the Poiseuille equation for laminar flow to data from phase-contrast MRA, a highly sensitive technique for noninvasive imaging of the cerebral venous sinus system.[26]

In the present study, we hypothesized that turbulent flow conditions occur very infrequently. To confirm this hypothesis, we calculated the Reynolds number (*Re*) for the study participants' superior sagittal sinus and IJVs according to the following equation: $Re = \rho VD / \mu$, where V is the maximum velocity, D is the diameter of the luminal cross-section, ρ is the attenuation of blood, and μ is the viscosity of blood. The highest Reynolds number that we obtained was 392, well below the value of 2000 at which turbulent flow conditions can be expected.[27]

The blood flows through the IJVs measured in our study agree with the literature data.[28] We also observed relatively high interindividual variations in both the calculated Rd and outflows. These flow variations have been reported by others[2] and may reflect anatomic variants rather than changes in physiologic conditions.[11] The total venous flow appeared to be correlated with the overall Rd of the venous sinus tree, though the relationship did not achieve statistical significance. One possible explanation is that our representation of the very complex venous sinus pathway was oversimplified; some branches of the venous drainage network were not taken into account in our calculation of the overall resistance. For example, the straight sinus drains the deep venous system through the inferior sagittal sinus and the vein of Galen.[29] The transverse sinus also receives the superior petrosal sinuses and the veins of Labbé, which drain blood from the temporooccipital cortex. Moreover, the drainage pathways include the emissary veins, vertebral veins, and pterygoid plexus; this network may also explain the lack of a statistically significant correlation between the values of the overall Rd and the total IJV flow measurements. We chose to limit our measurements to the major dural sinuses, in view of the high interindividual variations in the venous sinus system.[30]

Another unique feature of the cerebral venous drainage system is its dependence on posture. In the upright position, the IJVs tend to collapse and thus prompt a concomitant rise in flow in the vertebral veins[31]; in the supine position, they are the main drainage pathways for the cerebral outflow. Our participants were imaged in the supine position, which minimized the impact of position on both flow and Rd measurements of the IJVs.

The present findings and previous reports[2,32] show that venous drainage is dominated by the right outflow, reflecting the asymmetry in the resistance between the left and right sides of the venous sinus pathway. Furthermore, the relationship between resistance and flow was highlighted by our observation of a strong, inverse correlation between the resistance AIs and the flow AIs. The presence of an inverse association may indicate a lateralization effect, whereby one side compensates for the other.[2,28] It may also underline the importance of flow resistance in the regulation of cerebral blood outflow. Although our results are preliminary, they suggest that the cumulative effects of resistance to flow along vessel segments may have repercussions on the intracranial hydrodynamics, insofar as cerebral blood outflow may be influenced by the venous sinus resistance to flow. It is also possible that an elevated Rd across the cerebral sinus pathways contributes to the elevation of blood pressure on the venous side of the cerebral vascular tree. An elevation in venous pressure makes the cortical veins stiffer and induces a decrease in craniospinal compliance.[33] Furthermore, several researchers have emphasized the relevance of the venous sinus drainage system in hydrocephalus.[9,10] One hypothesis is that elevated pressure in the venous system may lead to alterations in CSF resorption through the arachnoid granulations. Moreover, other researchers have suggested that reduced cortical vein compliance and reduced superior sagittal sinus flow in normal-pressure hydrocephalus indicate the presence of a sig-

Values of the mean Rd of blood in the study population of healthy adults

	Mean Rd (Pa s/cm^3)
Superior sagittal sinus	20.1 ± 6
Straight sinus	41.2 ± 21
Transverse sinus	
Left	21.5 ± 14
Right	8.5 ± 5
Sigmoid sinus	
Left	11.6 ± 6
Right	4.8 ± 3
Internal jugular vein	
Left	8.5 ± 7
Right	5.1 ± 4
Overall Rd	23.8 ± 7

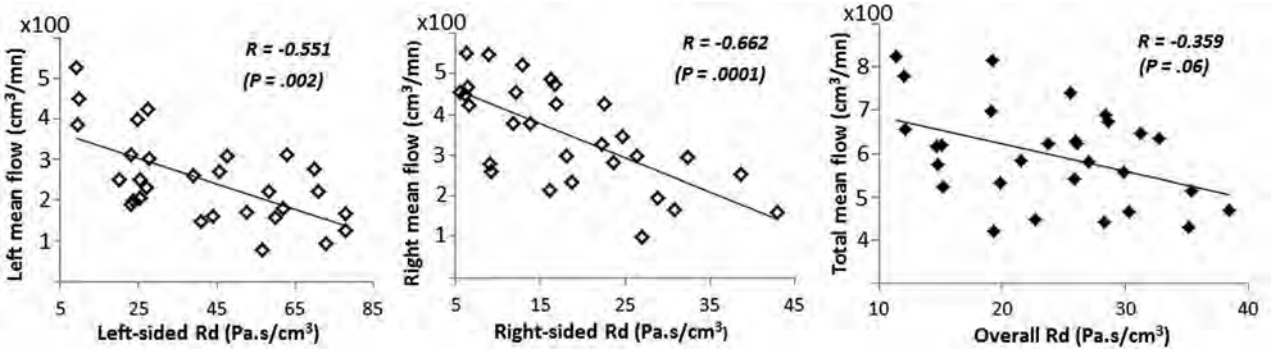

FIG 4. The relationship between mean flow and calculated Rd on the left (left panel) and right (middle panel) sides of the venous sinus tree. The vessels of the left and right sides, respectively, comprise the 3 left or right vessel segments (the transverse sinus, sigmoid sinus, and IJV). The right panel shows the relationship between total mean flow and the overall Rd.

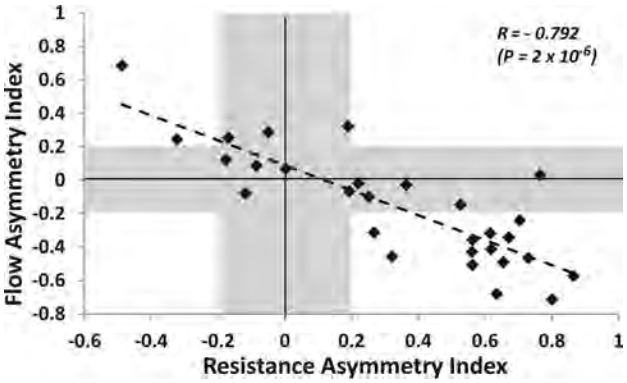

FIG 5. Flow AIs plotted against resistance AIs. *Diamonds* located below the *horizontal gray band* (AI < -0.2) reflect right-sided flows, and those above the *horizontal gray band* (AI $> +0.2$) reflect left-sided flows. *Diamonds* located to the left of the *vertical gray band* (AI < -0.2) reflect right-sided resistance, and those on the right of the *vertical gray band* (AI $> +0.2$) reflect left-sided resistance.

nificant elevation in the resistance to flow through these vessels.[34,35] The balance between cerebral arterial inflow and venous outflow contributes to the maintenance of normal intracranial pressure, which depends not only on the arterial volume input and CSF volume but also on venous outflow.

The effect of intracranial fluid dynamics on intracranial pressure is a major component of the Monro-Kellie[36,37] doctrine. As presented in Wilson's recent review,[38] increasing evidence suggests that a venous pathology is central to the multiple conditions that cause a rise in intracranial pressure. A better understanding of the role of the venous system in neurocritical care is essential. In a prospective controlled study based on a grading system, Farb et al[25] showed sinovenous stenosis in 27 of 29 patients with idiopathic intracranial hypertension and in only 4 of 59 control patients. Moreover, the severity of intracranial hypertension (which depends on the degree of venous congestion) was found to be closely related to the intradural sinus pressure.[39] As the latter rises, slight parenchymal damage may progress to severe cerebral edema and/or hematoma if thrombolysis is delayed. Furthermore, some researchers have suggested that benign intracranial hypertension may be caused by venous hypertension,[19,20] mostly due to stenosis or occlusions of the lateral sinuses. Moreover, it has been shown that dilation of one of the sinuses with a stent may reduce the pressure gradient and produce a striking reduction in symptoms.[40] This venous sinus stent placement technique had a high technical success rate and was highly effective (80%) in reducing the headache associated with benign intracranial hypertension.[41] Nevertheless, sinus stenosis appears to result from elevated CSF pressure (rather than hypertension) in some cases.[42]

Also, there is some evidence that idiopathic intracranial hypertension may be characterized by elevated central venous pressure[20] in the absence of ventricular dilation, a mass lesion, or venous sinus thrombosis.[43,44] Thus, it is possible that the cumulative effects of resistance to blood flow across the venous sinus pathways may lead to a substantial pressure increase in the intracranial drainage system. This question could be addressed (at least in part) by comparing venous sinus Rd measurements in patients versus healthy individuals. However, in the absence of such data, it seems premature to draw conclusions with regard to a possible causal link between venous sinus resistance to blood flow and intracranial hypertension.

The relationships between blood flow velocity, cross-sectional area, pressure drop, and resistance are very complex. A simplified relationship between fluid velocity and pressure can be described by the Bernoulli law, which is based on the fundamental physical law of energy conservation. The equation based on the Bernoulli law can take various forms, which differ in their complexity as a function of the type of fluid flow[45] but can be represented as $(\frac{1}{2})\cdot\rho\cdot V^2 + P + \rho\cdot g\cdot z = Constant$, where ρ is the fluid attenuation, V is the velocity, P is the pressure, z the vertical height relative to a reference location, and g is the gravity constant. The first term of this equation accounts for the kinetic energy, and the 2 last terms represent the potential energy resulting from pressure and gravity. According to this principle, an increase in fluid velocity implies a concomitant decrease in pressure and vice versa. Therefore, if vessel resistance is increased by lumen constriction, the flow velocity rise would imply a decrease in pressure.

However, several assumptions must be made before applying the Bernoulli equation. In particular, the velocities must be uniformly distributed at the cross-sectional area, the fluid must be incompressible, and there must be no loss of energy. These assumptions tend to limit the applicability of the Bernoulli law to structures that are subject to deformation. Moreover, Cebral et al[46] used phase-contrast MR imaging to investigate the flow-area relationship in the internal carotid and vertebral arteries. To the best of our knowledge, a similar study on the cerebral veins has not been performed. The pressure/area/flow relationships in compliant veins are much more complicated to evaluate than in the venous sinuses because the veins are prone to hydrostructural instability and are much more sensitive to slight pressure variations.

The present study had a number of limitations. First, the relatively small sample size must be taken into account when interpreting the results. A second limitation relates to the calculated Rd possibly being influenced by the hydrostatic pressure gradient across the venous sinus wall, which might influence the compliance of the vessels. Third, given that patterns of complex and disturbed flow may occur at branch points in the venous sinus network, the laminar flow required for the validity of the Poiseuille equation may not be met. It is also possible that the image quality was worsened by intravascular signal loss due to turbulence and intravoxel dephasing.[47] Moreover, although the PC-MRA technique may be useful for imaging slowing blood flow[48] and can depict multidirectional flow (such as recirculating flow patterns) with good sensitivity,[49] the choice of an optimal velocity-encoding value that enables avoiding velocity aliasing also constitutes a study limitation.[26] Last, our data were collected from a group of young, healthy participants. Extending this investigation to more representative samples of older individuals (including patients with cerebrovascular/neurovascular disease) would be a valuable goal in the near future.

CONCLUSIONS

The results of this preliminary study suggest that PC-MRA can be used to quantify Rd in the venous sinus drainage system. These measurements may improve our understanding of certain cere-

brovascular diseases. Along with flow measurements, this approach can also be used to calculate a pressure drop across vessel segments by application of the Poiseuille equation for laminar flow: pressure gradient = resistance × flow.

APPENDIX

Calculation of Overall Rd

The overall Rd of the venous sinus system can be calculated by an analogy with an electric circuit (Fig 2). We have the following:

$$Overall\ Rd = \frac{Rd\ SSS \times Rd\ StS}{Rd\ SSS + Rd\ StS} + \frac{R_{left\ side} \times R_{right\ side}}{R_{left\ side} + R_{right\ side}}.$$

Here, *SSS* and *StS* denote the superior sagittal sinus and the straight sinus, respectively, and $R_{\text{left side (or right side)}}$ represents the resistance of the left (or right) side of the venous sinus tree, calculated as the sum of the Rd of the 3-vessel segments (transverse sinus + sigmoid sinus + internal jugular vein):

$$R_{\text{left/right side}} = \text{Rd Tranverse Sinus} + \text{Rd Sigmoid Sinus} + \text{Rd Internal Jugular Vein}.$$

ACKNOWLEDGMENTS

The authors are grateful to the staff members at the Institut Faire Faces (Amiens, France) for technical assistance and thank the study volunteers for their participation.

REFERENCES

1. Grand W, Hopkins LN. *Vasculature of the Brain and Cranial Base: Variations in Clinical Anatomy.* New York: Thieme; 1999
2. Stoquart-Elsankari S, Lehmann P, Villette A, et al. **A phase-contrast MRI study of physiologic cerebral venous flow.** *J Cereb Blood Flow Metab* 2009;29:1208–15 CrossRef Medline
3. Agnelli G, Verso M. **Epidemiology of cerebral vein and sinus thrombosis.** *Front Neurol Neurosci* 2008;23:16–22 CrossRef Medline
4. Dhungana S, Sharrack B, Woodroofe N. **Idiopathic intracranial hypertension.** *Acta Neurol Scand* 2010;121:71–82 CrossRef Medline
5. Bateman GA. **Vascular hydraulics associated with idiopathic and secondary intracranial hypertension.** *AJNR Am J Neuroradiol* 2002; 23:1180–86 Medline
6. Gross CE, Tranmer BI, Adey G, et al. **Increased cerebral blood flow in idiopathic pseudotumour cerebri.** *Neurol Res* 1990;12:226–30 CrossRef Medline
7. Greitz D, Hannerz J, Rähn T, et al. **MR imaging of cerebrospinal fluid dynamics in health and disease: on the vascular pathogenesis of communicating hydrocephalus and benign intracranial hypertension.** *Acta Radiol* 1994;35:204–11 CrossRef Medline
8. Kwon BJ, Han MH, Kang HS, et al. **MR imaging findings of intracranial dural arteriovenous fistulas: relations with venous drainage patterns.** *AJNR Am J Neuroradiol* 2005;26:2500–07 Medline
9. Sainte-Rose C, LaCombe J, Pierre-Kahn A, et al. **Intracranial venous sinus hypertension: cause or consequence of hydrocephalus in infants?** *J Neurosurg* 1984;60:727–36 CrossRef Medline
10. Shulman K, Ransohoff J. **Sagittal sinus venous pressure in hydrocephalus.** *J Neurosurg* 1965;23:169–73 CrossRef Medline
11. Zamboni P, Galeotti R, Menegatti E, et al. **Chronic cerebrospinal venous insufficiency in patients with multiple sclerosis.** *J Neurol Neurosurg Psychiatry* 2009;80:392–99 Medline
12. ElSankari S, Balédent O, van Pesch V, et al. **Concomitant analysis of arterial, venous, and CSF flows using phase-contrast MRI: a quantitative comparison between MS patients and healthy controls.** *J Cereb Blood Flow Metab* 2013;33:1314–21 CrossRef Medline
13. Tsivgoulis G, Faissner S, Voumvourakis K, et al. **"Liberation treatment" for chronic cerebrospinal venous insufficiency in multiple sclerosis: the truth will set you free.** *Brain Behav* 2015;5:3–12 CrossRef Medline
14. Willems PW, Brouwer PA, Barfett JJ, et al. **Detection and classification of cranial dural arteriovenous fistulas using 4D-CT angiography: initial experience.** *AJNR Am J Neuroradiol* 2011;32: 49–53 CrossRef Medline
15. Leach JL, Jones BV, Tomsick TA, et al. **Normal appearance of arachnoid granulations on contrast-enhanced CT and MR of the brain: differentiation from dural sinus disease.** *AJNR Am J Neuroradiol* 1996;17:1523–32 Medline
16. Schoser BG, Riemenschneider N, Hansen HC. **The impact of raised intracranial pressure on cerebral venous hemodynamics: a prospective venous transcranial Doppler ultrasonography study.** *J Neurosurg* 1999;91:744–49 CrossRef Medline
17. Heiserman JE, Dean BL, Hodak JA, et al. **Neurologic complications of cerebral angiography.** *AJNR Am J Neuroradiol* 1994;15:1401–07; discussion 1408–11 Medline
18. Waugh JR, Sacharias N. **Arteriographic complications in the DSA era.** *Radiology* 1992;182:243–46 CrossRef Medline
19. King JO, Mitchell PJ, Thomson KR, et al. **Cerebral venography and manometry in idiopathic intracranial hypertension.** *Neurology* 1995;45:2224–28 CrossRef Medline
20. Karahalios DG, Rekate HL, Khayata MH, et al. **Elevated intracranial venous pressure as a universal mechanism in pseudotumor cerebri of varying etiologies.** *Neurology* 1996;46:198–202 CrossRef Medline
21. Dumoulin CL, Cline HE, Souza SP, et al. **Three-dimensional time-of-flight magnetic resonance angiography using spin saturation.** *Magn Reson Med* 1989;11:35–46 CrossRef Medline
22. Balédent O, Henry-Feugeas MC, Idy-Peretti I. **Cerebrospinal fluid dynamics and relation with blood flow: a magnetic resonance study with semiautomated cerebrospinal fluid segmentation.** *Invest Radiol* 2001;36:368–77 CrossRef Medline
23. Elsankari S, Czosnyka M, Lehmann P, et al. **Cerebral blood and CSF flow patterns in patients diagnosed for cerebral venous thrombosis: an observational study.** *J Clin Imaging Sci* 2012;2:41 CrossRef Medline
24. Donnet A, Metellus P, Levrier O, et al. **Endovascular treatment of idiopathic intracranial hypertension: clinical and radiologic outcome of 10 consecutive patients.** *Neurology* 2008;70:641–47 CrossRef Medline
25. Farb RI, Vanek I, Scott JN, et al. **Idiopathic intracranial hypertension: the prevalence and morphology of sinovenous stenosis.** *Neurology* 2003;60:1418–24 CrossRef Medline
26. Fera F, Bono F, Messina D, et al. **Comparison of different MR venography techniques for detecting transverse sinus stenosis in idiopathic intracranial hypertension.** *J Neurol* 2005;252:1021–25 CrossRef Medline
27. Hatle L, Angelsen B. *Doppler Ultrasound in Cardiology: Physical Principles and Clinical Applications.* Philadelphia: Lea & Febiger; 1982
28. Sundström P, Wåhlin A, Ambarki K, et al. **Venous and cerebrospinal fluid flow in multiple sclerosis: a case-control study.** *Ann Neurol* 2010;68:255–59 CrossRef Medline
29. Suzuki Y, Ikeda H, Shimadu M, et al. **Variations of the basal vein: identification using three-dimensional CT angiography.** *AJNR Am J Neuroradiol* 2001;22:670–76 Medline
30. Curé JK, Van Tassel P, Smith MT. **Normal and variant anatomy of the dural venous sinuses.** *Semin Ultrasound CT MR* 1994;15:499–519 CrossRef Medline
31. Valdueza JM, von Münster T, Hoffman O, et al. **Postural dependency of the cerebral venous outflow.** *Lancet* 2000;355:200–01 CrossRef Medline
32. Lichtenstein D, Saïfi R, Augarde R, et al. **The internal jugular veins are asymmetric: usefulness of ultrasound before catheterization.** *Intensive Care Med* 2001;27:301–05 CrossRef Medline
33. Bateman GA. **The reversibility of reduced cortical vein compliance in normal-pressure hydrocephalus following shunt insertion.** *Neuroradiology* 2003;45:65–70 Medline
34. Bateman GA. **Pulse-wave encephalopathy: a comparative study of**

the hydrodynamics of leukoaraiosis and normal-pressure hydrocephalus. *Neuroradiology* 2002;44:740–48 CrossRef Medline
35. Bateman GA. **Vascular compliance in normal pressure hydrocephalus.** *AJNR Am J Neuroradiol* 2000;21:1574–85 Medline
36. Kellie G. **An account of the appearances observed in the dissection of two of the three individuals presumed to have perished in the storm of the 3rd, and whose bodies were discovered in the vicinity of Leith on the morning of the 4th November 1821 with some reflections on the pathology of the brain.** *Trans Med Chir Soc Edinb* 1824;1:84–169
37. Monro A. *Observations on Structure and Functions of the Nervous System.* Edinburgh, UK: Creech and Johnson; 1783
38. Wilson MH. **Monro-Kellie 2.0: the dynamic vascular and venous pathophysiological components of intracranial pressure.** *J Cereb Blood Flow Metab* 2016;36:1338–50 CrossRef Medline
39. Tsai FY, Wang AM, Matovich VB, et al. **MR staging of acute dural sinus thrombosis: correlation with venous pressure measurements and implications for treatment and prognosis.** *AJNR Am J Neuroradiol* 1995;16:1021–29 Medline
40. Higgins JN, Owler BK, Cousins C, et al. **Venous sinus stenting for refractory benign intracranial hypertension.** *Lancet* 2002;359:228–30 CrossRef Medline
41. Albuquerque FC, Dashti SR, Hu YC, et al. **Intracranial venous sinus stenting for benign intracranial hypertension: clinical indications, technique, and preliminary results.** *World Neurosurg* 2011;75:648–52; discussion 592–95 CrossRef Medline
42. Higgins JNP, Pickard JD. **Lateral sinus stenoses in idiopathic intracranial hypertension resolving after CSF diversion.** *Neurology* 2004;62:1907–08 CrossRef Medline
43. Friedman DI, Jacobson DM. **Diagnostic criteria for idiopathic intracranial hypertension.** *Neurology* 2002;59:1492–95 CrossRef Medline
44. Lee AG, Brazis PW. **Magnetic resonance venography in idiopathic pseudotumor cerebri.** *J Neuroophthalmol* 2000;20:12–13 CrossRef Medline
45. Fung Y. *Biomechanics: Circulation.* New York: Springer; 1997
46. Cebral JR, Castro MA, Putman CM, et al. **Flow-area relationship in internal carotid and vertebral arteries.** *Physiol Meas* 2008;29:585–94 CrossRef Medline
47. Ayanzen RH, Bird CR, Keller PJ, et al. **Cerebral MR venography: normal anatomy and potential diagnostic pitfalls.** *AJNR Am J Neuroradiol* 2000;21:74–78 Medline
48. Bono F, Lupo MR, Lavano A, et al. **Cerebral MR venography of transverse sinuses in subjects with normal CSF pressure.** *Neurology* 2003;61:1267–70 CrossRef Medline
49. Wheaton AJ, Miyazaki M. **Non-contrast enhanced MR angiography: physical principles.** *J Magn Reson Imaging* 2012;36:286–304 CrossRef Medline

Early-Stage Glioblastomas: MR Imaging–Based Classification and Imaging Evidence of Progressive Growth

C.H. Toh and M. Castillo

ABSTRACT

BACKGROUND AND PURPOSE: The serial imaging changes describing the growth of glioblastomas from small to large tumors are seldom reported. Our aim was to classify the imaging patterns of early-stage glioblastomas and to define the order of appearance of different imaging patterns that occur during the growth of small glioblastomas.

MATERIALS AND METHODS: Medical records and preoperative MR imaging studies of patients diagnosed with glioblastoma between 2006 and 2013 were reviewed. Patients were included if their MR imaging studies showed early-stage glioblastomas, defined as small MR imaging lesions detected early in the course of the disease, demonstrating abnormal signal intensity but the absence of classic imaging findings of glioblastoma. Each lesion was reviewed by 2 neuroradiologists independently for location, signal intensity, involvement of GM and/or WM, and contrast-enhancement pattern on MR imaging.

RESULTS: Twenty-six patients with 31 preoperative MR imaging studies met the inclusion criteria. Early-stage glioblastomas were classified into 3 types and were all hyperintense on FLAIR/T2-weighted images. Type I lesions predominantly involved cortical GM ($n = 3$). Type II ($n = 12$) and III ($n = 16$) lesions involved both cortical GM and subcortical WM. Focal contrast enhancement was present only in type III lesions at the gray-white junction. Interobserver agreement was excellent ($\kappa = 0.95$; $P < .001$) for lesion-type classification. Transformations of lesions from type I to type II and type II to type III were observed on follow-up MR imaging studies. The early-stage glioblastomas of 16 patients were pathologically confirmed after imaging progression to classic glioblastoma.

CONCLUSIONS: Cortical lesions may be the earliest MR imaging–detectable abnormality in some human glioblastomas. These cortical tumors may progress to involve WM.

ABBREVIATIONS: GB = glioblastoma; *IDH1* = *isocitrate dehydrogenase 1*

Glioblastoma (GB) is the most common primary malignant brain tumor. It typically appears as a large mass with necrosis, prominent edema, mass effect, and strong heterogeneous contrast enhancement when diagnosed. MR imaging, a noninvasive diagnostic tool with excellent tissue contrast, has the potential to detect small GBs. However, it is uncommon to detect small GBs clinically, probably due to nonspecific or absent symptoms. The serial imaging changes depicting the growth of GBs from small to large tumors are seldom reported.

Received July 25, 2016; accepted after revision September 23.

From the Department of Medical Imaging and Intervention (C.H.T.), Chang Gung Memorial Hospital at Linkou and Chang Gung University College of Medicine, Tao-Yuan, Taiwan; and Department of Radiology (M.C.), University of North Carolina School of Medicine, Chapel Hill, North Carolina.

Please address correspondence to Cheng Hong Toh, MD, PhD, Department of Medical Imaging and Intervention, Chang Gung Memorial Hospital at Linkou, No. 5, Fuxing St, Guishan District, Taoyuan City 333, Taiwan (R.O.C.); e-mail: eldomtoh@hotmail.com

http://dx.doi.org/10.3174/ajnr.A5015

Some reports described small MR imaging lesions that subsequently progressed to GBs.[1-11] These are often described as ill-defined, FLAIR or T2-weighted hyperintensities without discernable mass effect that typically involve both the cortex and subcortical WM, but occasionally appear as only cortical lesions.[2,4,8] Contrast enhancement is not a consistent feature and tends to be focal and nodular when present.[6-8] The commonly affected brain areas include frontal ($n = 4$),[2,3,6,8] parietal ($n = 2$),[7,10] occipital ($n = 1$),[11] temporal ($n = 5$),[2,3,6,7,11] hippocampal ($n = 3$),[1,2,9] and insular ($n = 1$)[9] regions. Because these MR imaging lesions were detected early in the course of the disease, they were frequently referred to as early-stage GBs.[3,5-8,11]

We have noticed different imaging patterns in early-stage GBs. An imaging classification for early-stage GB, however, is not available because most previous studies included only a few such cases. It is important for radiologists to be familiar with early imaging findings and growth patterns of GBs because familiarity may help diagnose small tumors that are symptomatic or incidentally found. Early diagnosis of GB may lead to a higher extent of tumor

resection, which has been demonstrated to correlate with patient survival.[12] In this study, we aimed to classify the imaging patterns of early-stage GBs and to the define the order of appearance of different imaging patterns that occur during the growth of these tumors.

MATERIALS AND METHODS

This retrospective longitudinal observational cohort study was performed in 2 medical centers (Chang Gung Memorial Hospital at Linkou and University of North Carolina Medical Center at Chapel Hill) after institutional review board approval with a waiver of the informed consent requirement. The study was performed in compliance with the Health Insurance Portability and Accountability Act.

A search of the hospital data base was first performed at both institutions for patients diagnosed with glioblastoma between 2006 and 2013. By reviewing their medical records and all available preoperative MR imaging studies, we excluded patients with GBs transformed from histology-proved low-grade gliomas, gliomatosis cerebri, a history of cranial irradiation before the diagnosis of GB, and poor image quality. Patients with preoperative MR imaging studies demonstrating early-stage glioblastomas were included.

Early-stage GBs were defined as small MR imaging lesions detected early in the course of the disease, demonstrating abnormal signal intensity on T2-weighted, FLAIR, and/or postcontrast T1-weighted images but with an absence of the imaging findings of classic GB, such as tumors with necrosis, hemorrhage, prominent edema, and heterogeneous contrast enhancement. These lesions were all subsequently proved by histopathology to be GBs. They did or did not develop into classic GBs on MR imaging, depending on the timing of the operation and the frequency of follow-up studies. At each institution, histologic sections were reviewed by neuropathologists with >15 years of experience, and diagnosis was made according to World Health Organization criteria.

Besides MR imaging findings, clinical information collected from each patient included age, sex, and tumor *isocitrate dehydrogenase* (*IDH1*) gene mutation status determined by immunohistochemistry study, if available.

Imaging Protocols

Because the MR imaging studies were performed at 2 medical centers with 1.5T or 3T clinical MR imaging scanners (Magnetom Espree, Avanto, or Tim Trio; Siemens, Erlangen, Germany; Optima MR450w with GEM Suite or Discovery MR750; GE Healthcare, Milwaukee, Wisconsin; or Intera; Philips, Best, the Netherlands), their imaging parameters were not consistent.

The imaging protocol for 1.5T MR imaging scanners typically included transverse T1WI (TR/TE, 449/12 ms; section thickness, 5 mm; gap, 1 mm; matrix, 256 × 512; and FOV, 210 × 178 mm), transverse FSE T2WI (TR/TE, 4000/90 ms; section thickness, 5 mm; gap, 1 mm; echo-train length, 17; matrix, 304 × 512; and FOV, 210 × 178 mm), transverse FLAIR (TR/TE/TI, 9788/90/2300 ms; section thickness, 5 mm; gap, 1 mm; matrix, 256 × 512; and FOV, 210 × 178 mm), and postcontrast T1WI (TR/TE, 420/11 ms; section thickness, 5 mm; gap, 1 mm; matrix, 256 × 512; and FOV, 210 × 178 mm). For 3T scanners, the typical pulse sequences included transverse T1WI (TR/TE, 250/2.46 ms; section thickness, 4 mm; gap, 1 mm; matrix, 256 × 256; and FOV, 220 × 220 mm), transverse FSE T2WI (TR/TE, 4000/90 ms; section thickness, 4 mm; gap, 1; flip angle, 120°; echo-train length, 17; matrix, 512 × 358; and FOV, 220 × 220 mm), transverse FLAIR (TR/TE/TI, 8200/85/2500 ms; section thickness, 4 mm; gap, 1 mm; matrix, 320 × 256; and FOV, 220 × 220 mm), and postcontrast 3D MPRAGE (TR/TE/TI, 2530/4.03/1100 ms; section thickness, 1 mm; matrix, 256 × 256; and FOV, 256 × 224 mm). A standard dose of 0.1 mmol of gadodiamide (Omniscan; GE Healthcare, Piscataway, New Jersey) or gadopentetate dimeglumine (Magnevist; Bayer HealthCare Pharmaceuticals, Wayne, New Jersey) per kilogram of body weight was administered intravenously for postcontrast T1WI or MPRAGE.

Image Analysis

All available preoperative MR imaging studies for each patient with early-stage GB were reviewed. Two neuroradiologists (C.H.T. and M.C.) with 12 and 26 years of experience, respectively, independently evaluated all lesions for their size, location, involvement of GM and/or WM, MR imaging signal intensity, and contrast-enhancement pattern. Among the imaging features reviewed, involvement of GM and/or WM and contrast-enhancement patterns were used for lesion-type classification. Interobserver differences in lesion type classification were resolved by consensus.

The size of FLAIR/T2-weighted and contrast-enhancing lesions was measured by using a bidimensional method. For each lesion, the largest and perpendicular diameters were measured on a single axial image demonstrating the largest cross-sectional area if the diameters were >1 cm. Morphologic changes, such as lesion enlargement, new contrast enhancement, or transformation to a classic GB, were recorded when follow-up MR imaging studies were available.

Statistical Analysis

The level of interobserver agreement for lesion-type classification was determined by calculating the κ coefficient. SPSS for Windows, Version 20.0 (IBM, Armonk, New York), was used to perform the statistical analyses, and P values <.05 were considered statistically significant.

RESULTS

Between 2006 and 2013, 282 patients were diagnosed with GBs. Among these, 46 were secondary GBs and 9 were gliomatosis cerebri and therefore were excluded. In the remaining 227 patients, 26 patients (18 from Chang Gung Memorial Hospital at Linkou and 8 from University of North Carolina Medical Center at Chapel Hill) with 31 MR imaging studies met the inclusion criteria. None of these 26 patients had a history of cranial irradiation before the diagnosis of GB or poor image quality. MR imaging findings of early-stage GBs were classified into 3 types on the basis of GM and/or WM involvement and patterns of contrast enhancement. The 2 neuroradiologists agreed on lesion-type classification in 30 of 31 MR imaging studies, with excellent interobserver agreement ($\kappa = 0.95$; $P < .001$). Tables 1, 2, and 3 summarize the clinical characteristics of patients who presented with type I, II, and III lesions, respectively.

Type I lesions were those that on the first available study, pre-

Table 1: Clinical characteristics of patients who presented with type I lesions[a]

Patient	Sex/Age (yr)	Symptoms	Lesion Location	Lesion Size (cm)	Duration[b] (mo) Type II	Type III	Classic GB	*IDH1* Mutation
1	M/55	Focal seizure	Right insula and temporal cortex	5	6	NA	11	−
2	M/57	Focal seizure	Left parietal cortex	2.2	NA	NA	7	+
3	M/60	Focal seizure	Right insula and frontal operculum	3	NA	NA	8	−

Note:—NA indicates not available; +, positive; −, negative.

[a] The lesions refer to the FLAIR/T2-weighted hyperintensities predominantly involving cortical GM. Their perpendicular diameters were <1 cm and therefore not measured.

[b] The duration is the time interval between the first and follow-up MR imaging studies showing type II lesions, type III lesions, or classic GB, respectively. NA indicates that the particular lesion type was not detected during the course of follow-up.

Table 2: Clinical characteristics of patients who presented with type II lesions[a]

Patient	Sex/Age (yr)	Symptoms	Lesion Location	Lesion Size (cm)	Duration[b] (mo) Type III	Classic GB	*IDH1* Mutation
1	M/48	LOC	Left temporal	2 × 1.2	NA	12	−
2	F/40	Syncope	Right insula and frontal operculum	4 × 2.5	NA	11	NS
3	F/32	Speech	Left parietal	2.5 × 2	NA	4	−
4	M/33	Headache, LOC	Right insular	3.1 × 2.5	NA	4	NS
5	F/58	Gait disturbance, memory impairment	Right medial frontal	4 × 3	10	13	NS
6	M/48	Focal seizure	Right parietal	3.5 × 2.5	8	10	+
7	F/78	Headache	Right temporal	2.5 × 1	NA	2	−
8	M/41	Focal seizure	Left temporal	3 × 2	1	1.5	−
9	M/40	Generalized seizure	Left parietal	3 × 2.8	NA	NA	NS
10	M/71	Visual TIA	Right occipital	3 × 3	2	NA	NS
11	M/27	Focal seizure	Left frontal	2.2 × 2.8	NA	NA	+

Note:—LOC indicates loss of conscious; NA, not available; NS, not studied; +, positive; −, negative.

[a] The lesions refer to the FLAIR/T2-weighted hyperintensities involving both cortical GM and subcortical WM.

[b] The duration is the time interval between the first and follow-up MR imaging studies showing a type III lesion or classic GB. NA indicates that the particular lesion type was not detected during follow-up. The type II lesions of patients 9 and 11 were resected before they transformed to type III lesions or classic GB.

Table 3: Clinical characteristics of patients who presented with type III lesions[a]

Patient	Sex/Age (yr)	Symptoms	Lesion Location	Lesion Size (cm)	Duration[b] (mo) to Classic GB	*IDH1* Mutation
1	F/95	Facial palsy	Right frontal	3 × 1.5	3	NS
2	M/48	Generalized seizure	Right frontal	4 × 2	NA	−
3	M/69	Focal seizure	Right parietal	2.5 × 1.2	3	−
4	F/59	Slurred speech	Left insular	3 × 1.3	NA	NS
5	F/55	Hand numbness	Right parietal	2.1 × 1.3	NA	−
6	F/69	Leg weakness	Right frontal	3 × 1.2	NA	NS
7	F/35	Leg numbness	Left frontal	2.5 × 1.3	1	−
8	M/65	Generalized seizure	Left parietal	2.6 × 2.6	NA	NS
9	M/45	Generalized seizure	Left temporal	3 × 3	1	NS
10	M/58	Generalized seizure	Left frontal	1.5 × 1	NA	NS
11	M/43	Generalized seizure	Left frontal	3 × 1.8	NA	NS
12	M/62	Generalized seizure	Left temporal	2.4 × 2.3	6	−

Note:—NA indicates not available; NS, not studied; −, negative.

[a] The lesions refer to FLAIR/T2-weighted hyperintensities involving the cortex and subcortical WM, with focal contrast enhancement at the GM-WM junction. The size of contrast-enhancing foci is not shown because they are about ≤1 cm.

[b] The duration is the time interval between the first and follow-up MR imaging studies showing classic GB. NA indicates that type III lesions were resected before progressing to classic GB.

dominantly involved GM (ie, the cerebral cortex). They appeared as T2-weighted or FLAIR hyperintensities without contrast enhancement. Three patients had type I lesions (Fig 1). Type II lesions were T2-weighted or FLAIR hyperintensities involving the cortex and subcortical WM without contrast enhancement. Twelve patients, including one who progressed from a type I lesion, had type II lesions (Fig 2). Type III lesions were hyperintense on T2-weighted and FLAIR images, involved both the cortex and subcortical WM, and demonstrated small focal areas of contrast enhancement at the GM-WM junction. The diameter of enhancing focus was about ≤1 cm in all. Sixteen patients, including 4 who progressed from type II, had type III lesions (Fig 3).

Figure 4 summarizes the morphologic changes of the early-stage GBs in 26 patients as observed in follow-up MR imaging studies. One type I lesion transformed to a type II, and 4 type II lesions transformed to type III. Reverse-order transformation (ie, transformation from a type III lesion to types II and I or from type II to I) was not observed.

Two type II and 8 type III lesions underwent an early operation

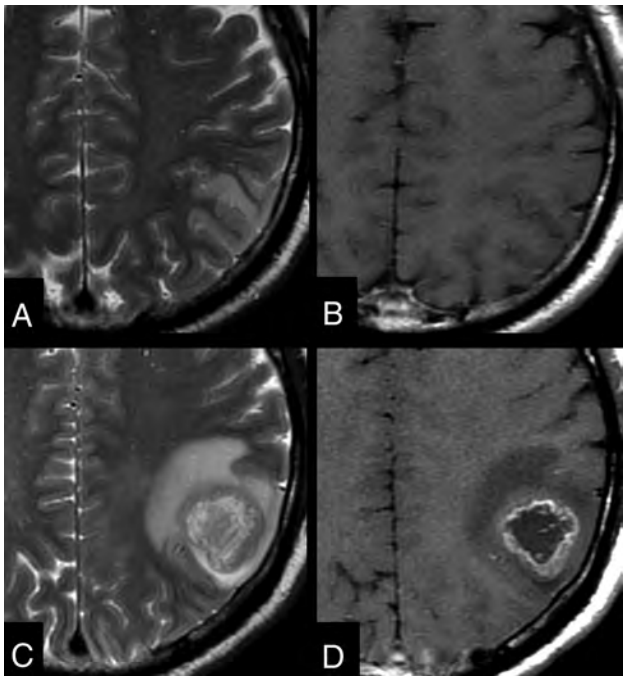

FIG 1. A 57-year-old man with a type I lesion. Axial images show a left parietal cortical lesion, which is hyperintense on the T2-weighted image (*A*) and without enhancement on the contrast-enhanced T1-weighted image (*B*). T2-weighted (*C*) and contrast-enhanced T1-weighted (*D*) images obtained 7 months later show a left parietal glioblastoma.

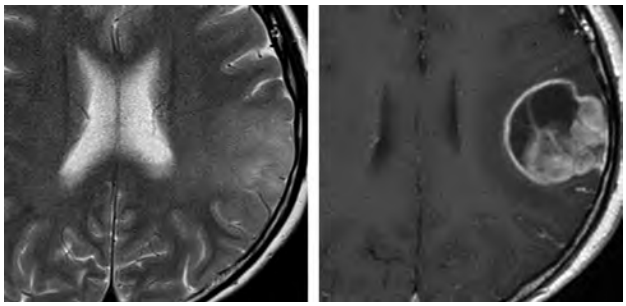

FIG 2. Axial images in a 32-year-old woman with a type II lesion. Left, T2-weighted image shows hyperintensity involving the left parietal cortex and subcortical WM. Right, contrast-enhanced T1-weighted image obtained 4 months later shows a left parietal glioblastoma.

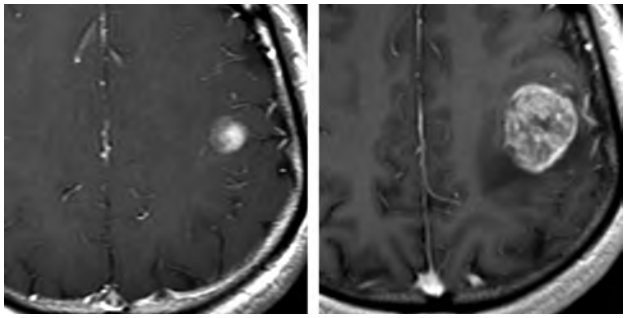

FIG 3. Contrast-enhanced T1-weigthed axial images in a 35-year-old woman with a type III lesion. Left, a cortical/subcortical contrast-enhancing lesion is present in the left frontal region. Right, the lesion transformed to a left frontal glioblastoma after 1 month.

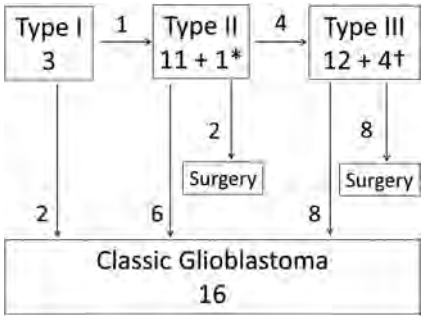

FIG 4. Diagram summarizes the morphologic changes of the 26 early-stage glioblastomas observed in follow-up MR imaging studies. The *asterisk* and *dagger* indicate the number of lesions transformed from type I and type II lesions, respectively.

and were confirmed to be GBs. The early-stage GBs of 16 patients were surgically resected after imaging progression to classic GB was documented. *IDH1* mutation status was available in 14 GBs, with 3 being positive for this mutation. The *IDH1* mutation rate was 21.4% (3 of 14).

DISCUSSION

In this study, we propose an MR imaging–based classification for early-stage GBs. Lesions were classified into 3 types on the basis of the involvement of GM and/or WM and their patterns of contrast enhancement. The 3 types of MR imaging lesions may represent sequential stages of human GB growth. To the best of our knowledge, an MR imaging–based classification for early-stage GBs does not exist.

Among the 3 types of lesions, type I was the earliest, followed by type II, and then type III, according to the morphologic changes observed on follow-up MR imaging studies. The order of appearance suggests that some GBs start as T2-weighted or FLAIR hyperintense lesions in the GM (ie, cerebral cortex [type I]). Then, both the cortex and subcortical WM become involved (type II). Later, focal contrast enhancement develops at the GM-WM junction, within the area of T2-weighted or FLAIR hyperintensity (type III). Enlargement of the contrast-enhancing focus then evolves into the classic appearance of GB.

Our review of the literature shows that there were 19 cases of early-stage GBs with MR imaging studies included when they were published.[1-11] With our proposed classification, 2 of 19 lesions may be classified as type I[2,8]; 12, as type II[1-3,8-11]; and 5, as type III.[4,6-8] Oyama et al[8] emphasized the role of DWI in early tumor detection when they reported a GB that first appeared as a type I lesion, then transformed to a type II lesion, and finally transformed to a classic GB before the operation. A type I lesion reported by Thaler et al[2] was described as a "right medial frontal nondiagnostic T2-weighted hyperintensity."

It is difficult to study the cell of origin and growth of human GB because the tumors are typically large and in their late stage when diagnosed. Therefore, genetically engineered mouse models in which gliomas are induced by manipulation of the mouse genome at the molecular level are important tools for studying gliomagenesis.[13,14] Using mosaic analysis with a double marker genetic mouse model, Liu et al[15] discovered that an oligodendrocyte precursor cell was the cell of origin of malignant gliomas and

that the earliest neoplastic lesions were found in the GM. Furthermore, they observed tumor extension in subcortical regions along WM tracts.[15] Another study also found that a glioblastoma could originate from cortical neurons.[16] However, there is always concern about whether results from animal studies can be transferred to humans. It is not known whether gliomas growing in mice with genetic alterations and different microenvironments resemble spontaneous human GBs.

In our present study, we found that GM lesions were the earliest MR imaging–detectable abnormalities during human GB growth. We believe this finding may serve as indirect evidence, along with that found in the mouse glioma models,[15,16] to suggest that some GBs may originate from GM. Moreover, the WM FLAIR/T2-weighted hyperintensity of type II lesions may correspond to GB infiltration rather than just edema. GBs have also been reported to originate and recur in the subventricular zone, and it is possible that tumors arising in the cortex are due to secondary outward migration of abnormal brain tumor cells.[17,18] These issues are beyond the scope of this article, and we wish to only describe and emphasize a subset of GBs that originate in the cortex and are probably from a different cell origin than periventricular or deep WM GBs.

In the present study, the diagnosis of GB in 16 patients was confirmed after their MR imaging lesions progressed to classic ones. Thus, it is possible that those 16 patients initially had low-grade gliomas, which later transformed to secondary GBs. *IDH1* mutation status has recently been considered a molecular marker of secondary GBs. The reported *IDH1* mutation rates for clinically diagnosed primary and secondary GBs are about 4%–7% and 73%–88%, respectively.[19] Among those 16 patients, *IDH1* mutation status was available in 11 with 2 being positive. The mutation rate of our patients is lower than expected for secondary GBs. As reported in previous studies, the median intervals for low-grade gliomas to transform to GBs ranged from 2.1 to 10.1 years.[20] The MR imaging lesions of those 16 patients progressed to the classic appearance of GBs in <14 months. Among these, the 2 lesions with *IDH1* mutations progressed to classic GB in 7 and 10 months, respectively. In light of rapid progression to GBs and the low incidence of *IDH1* mutation, we believe the MR imaging lesions of those 16 patients were not low-grade gliomas but high-grade from their origin.

The differential diagnosis for type I lesions should include postictal change because focal seizures were the clinical presentation for 3 patients with type I lesions. However, in previous reports, most seizure-induced MR imaging abnormalities were transient and reversible.[21] Permanent structural abnormalities such as gliosis and focal atrophy are more likely to occur in status epilepticus.[21] In this study, no patients with type I lesions had status epilepticus, and their abnormalities in the cerebral cortex persisted even when these lesions transformed to type II or classic GBs. Moreover, seizure-induced abnormalities tend to involve both the cortex and subcortical WM and are seldom limited to GM only.[21] Therefore, our type I lesions likely reflect tumor in GM.

According to the histologic classification of the World Health Organization, the presence of microvascular proliferation or pseudopalisading necrosis differentiates GBs from lower-grade gliomas. These 2 histologic hallmarks are typically present in the contrast-enhancing component of GB.[22,23] Microvascular proliferation is known to result in neovascularity with a disrupted blood-brain barrier and increased permeability to gadolinium-based contrast agents and thus contrast enhancement in GB. Barajas et al[22] reported that tissue samples obtained from nonenhancing tumor components of GBs demonstrated less microvascular proliferation than those from contrast-enhancing components. GBs without contrast enhancement, though relatively rare, have been reported.[23-25] In the study of Utsuki et al,[23] purely non-contrast-enhancing glioblastomas demonstrated only pseudopalisading necrosis and no neovascularity. Although histopathologic diagnosis was only available in 2 type II lesions, we believe that the other 10 type II lesions were also GBs without contrast enhancement. The implication of these observations may be that advanced imaging techniques such as perfusion and permeability may not reflect the true nature of these small GBs as they do in larger, classic ones.

The present study helps radiologists be familiar with imaging findings of early-stage GBs. For a type I or II lesion, early-stage GB should be included in the differential diagnosis in addition to a self-limited non-neoplastic lesion. It is challenging to prospectively diagnose early-stage GBs; therefore, aggressive surgical resection of these lesions is unlikely. Biopsy may be an alternative other than short-interval imaging follow-up. Advanced MR imaging such as diffusion, perfusion, and MR spectroscopy may have a role, but further studies are needed.

There are some limitations to our study. First, the diagnosis of GB was confirmed in only 10 patients who underwent an early operation. Thus, for the other 16 patients, we can only assume that their MR imaging lesions were early-stage GBs because they all eventually developed the typical MR imaging appearance and histopathology of GBs. Second, because our routine MR imaging protocol did not include advanced MR imaging techniques such as diffusion, perfusion, and spectroscopy, we could not assess their roles in early-stage GBs. Third, the MR imaging findings describe only macroscopic growth of GBs and not their microscopic changes. Although GBs may arise from GM, their cell of origin remains unknown. Fourth, tumors included in this study probably represent only a subset of GBs. GBs arising from the hippocampus and subventricular zone may have different growth patterns on MR imaging. Finally, due to a limited number of patients and the retrospective nature of our study, we were unable to determine whether our MR imaging–based classification correlates with outcomes.

CONCLUSIONS

A cortical GM lesion may be the earliest MR imaging–detectable abnormality in some human GBs. GBs may originate from the cortical GM and extend into the subcortical WM. Detection of these lesions while limited to the GM may allow total resection and potentially improve patient outcome.

REFERENCES

1. Nam TS, Choi KH, Kim MK, et al. **Glioblastoma mimicking herpes simplex encephalitis.** *J Korean Neurosurg Soc* 2011;50:119–22 CrossRef Medline

2. Thaler PB, Li JY, Isakov Y, et al. **Normal or non-diagnostic neuroimaging studies prior to the detection of malignant primary brain tumors.** *J Clin Neurosci* 2012;19:4111–14 CrossRef Medline
3. Ideguchi M, Kajiwara K, Goto H, et al. **MRI findings and pathological features in early-stage glioblastoma.** *J Neurooncol* 2015;123:289–97 CrossRef Medline
4. Takagi I, Shakur SF, Lukas RV, et al. **Spontaneous radiographic resolution and subsequent redemonstration of an untreated glioblastoma.** *J Neurosurg* 2011;115:24–29 CrossRef Medline
5. Nishi N, Kawai S, Yonezawa T, et al. **Early appearance of high grade glioma on magnetic resonance imaging.** *Neurol Med Chir (Tokyo)* 2009;49:8–12 CrossRef Medline
6. Simonet Redondo M, Auger Acosta C, Rovira-Gols A, et al. **Neuroimaging findings in the initial phase of development of high grade cortical astrocytomas.** *Radiologia* 2012;54:424–31 CrossRef Medline
7. Rossi R, Figus A, Corraine S. **Early presentation of de novo high grade glioma with epileptic seizures: electroclinical and neuroimaging findings.** *Seizure* 2010;19:470–74 CrossRef Medline
8. Oyama H, Ando Y, Aoki S, et al. **Glioblastoma detected at the initial stage in its developmental: case report.** *Neurol Med Chir (Tokyo)* 2010;50:414–17 CrossRef Medline
9. Cohen-Gadol AA, DiLuna ML, Bannykh SI, et al. **Non-enhancing de novo glioblastoma: report of two cases.** *Neurosurg Rev* 2004;27:281–85 Medline
10. Okamoto K, Ito J, Takahashi N, et al. **MRI of high-grade astrocytic tumors: early appearance and evolution.** *Neuroradiology* 2002;44:395–402 CrossRef Medline
11. Jung TY, Jung S. **Early neuroimaging findings of glioblastoma mimicking non-neoplastic cerebral lesion.** *Neurol Med Chir (Tokyo)* 2007;47:424–27 CrossRef Medline
12. Marko NF, Weil RJ, Schroeder JL, et al. **Extent of resection of glioblastoma revisited: personalized survival modeling facilitates more accurate survival prediction and supports a maximum-safe-resection approach to surgery.** *J Clin Oncol* 2014;32:774–82 CrossRef Medline
13. Chen J, McKay RM, Parada LF. **Malignant glioma: lessons from genomics, mouse models, and stem cells.** *Cell* 2012;149:36–47 CrossRef Medline
14. Jiang Y, Uhrbom L. **On the origin of glioma.** *Ups J Med Sci* 2012;117:113–21 CrossRef Medline
15. Liu C, Sage JC, Miller MR, et al. **Mosaic analysis with double markers reveals tumor cell of origin in glioma.** *Cell* 2011;146:209–21 CrossRef Medline
16. Friedmann-Morvinski D, Bushong EA, Ke E, et al. **Dedifferentiation of neurons and astrocytes by oncogenes can induce gliomas in mice.** *Science* 2012;338:1080–84 CrossRef Medline
17. Das S, Srikanth M, Kessler JA. **Cancer stem cells and glioma.** *Nat Clin Pract Neurol* 2008;4:427–35 CrossRef Medline
18. Achanta P, Sedora Roman NI, Quiñones-Hinojosa A. **Gliomagenesis and the use of neural stem cells in brain tumor treatment.** *Anticancer Agents Med Chem* 2010;10:121–30 CrossRef Medline
19. Ohgaki H, Kleihues P. **The definition of primary and secondary glioblastoma.** *Clin Cancer Res* 2013;19:764–72 CrossRef Medline
20. Sanai N, Chang S, Berger MS. **Low-grade gliomas in adults.** *J Neurosurg* 2011;115:948–65 CrossRef Medline
21. Cianfoni A, Caulo M, Cerase A, et al. **Seizure-induced brain lesions: a wide spectrum of variably reversible MRI abnormalities.** *Eur J Radiol* 2013;82:1964–72 CrossRef Medline
22. Barajas RF Jr, Phillips JJ, Parvataneni R, et al. **Regional variation in histopathologic features of tumor specimens from treatment-naive glioblastoma correlates with anatomic and physiologic MR imaging.** *Neuro Oncol* 2012;14:942–54 CrossRef Medline
23. Utsuki S, Oka H, Miyajima Y, et al. **Glioblastoma without remarkable contrast enhancement on magnetic resonance imaging.** *Int J Clin Med* 2012;3:439–45 CrossRef
24. Pope WB, Sayre J, Perlina A, et al. **MR imaging correlates of survival in patients with high-grade gliomas.** *AJNR Am J Neuroradiol* 2005;26:2466–74 Medline
25. Knopp EA, Cha S, Johnson G, et al. **Glial neoplasms: dynamic contrast-enhanced T2*-weighted MR imaging.** *Radiology* 1999;211:791–98 CrossRef Medline

Even Small Decreases in Blood Pressure during Conscious Sedation Affect Clinical Outcome after Stroke Thrombectomy: An Analysis of Hemodynamic Thresholds

M.K. Whalin, K.M. Halenda, D.C. Haussen, L.C. Rebello, M.R. Frankel, R.Y. Gershon, and R.G. Nogueira

ABSTRACT

BACKGROUND AND PURPOSE: The adverse effects of general anesthesia in stroke thrombectomy have been attributed to intraprocedural hypotension, yet optimal hemodynamic targets remain elusive. Identifying hemodynamic thresholds from patients without exposure to general anesthesia may help separate the effect of hypotension from the effect of anesthesia in thrombectomy outcomes. Therefore, we investigated which hemodynamic parameters and targets best correlate with outcome in patients treated under sedation with monitored anesthesia care.

MATERIALS AND METHODS: We performed a retrospective analysis of a prospectively collected data base of patients with anterior circulation stroke who were successfully reperfused (modified TICI ≥ 2b) under monitored anesthesia care sedation from 2010 to 2015. Receiver operating characteristic curves were generated for the lowest mean arterial pressure before reperfusion, both as absolute values and relative changes from baseline. Cutoffs were tested in binary logistic regression models of poor outcome (90-day mRS > 2).

RESULTS: Two-hundred fifty-six of 714 patients met the inclusion criteria. In a multivariable model, a ≥10% mean arterial pressure decrease from baseline had an OR for poor outcome of 4.38 (95% CI, 1.53–12.56; $P < .01$). Other models revealed that any mean pressure of <85 mm Hg before reperfusion had an OR for poor outcome of 2.22 (95% CI, 1.09–4.55; $P = .03$) and that every 10-mm Hg drop in mean arterial pressure below 100 mm Hg had an OR of 1.28 (95% CI, 1.01–1.62; $P = .04$).

CONCLUSIONS: A ≥10% mean arterial pressure drop from baseline is a strong risk factor for poor outcome in a homogeneous population of patients with stroke undergoing thrombectomy under sedation. This threshold could guide hemodynamic management of patients during sedation and general anesthesia.

ABBREVIATIONS: MAC = monitored anesthesia care; MAP = mean arterial pressure

Retrospective studies have found that performing thrombectomies with the patient under general anesthesia may be associated with worse outcomes,[1,2] possibly because of the increased incidence and severity of hypotension compared with the use of conscious sedation.[3] Hypotension before reperfusion may compromise collateral blood flow and negatively impact outcomes in acute ischemic stroke. Previous investigations demonstrated that a lowest recorded systolic blood pressure of >140 mm Hg during endovascular therapy for acute ischemic stroke is associated with good neurologic outcome.[3] Our group subsequently showed that a lowest mean arterial pressure (MAP) of ≥70 mm Hg is an independent predictor of favorable neurologic outcome.[4]

These studies were limited because they included a mix of patients receiving conscious sedation and general anesthesia. In this setting, the association between general anesthesia and hypotension may make it difficult to discern the independent effects of blood pressure regardless of anesthesia type. We hypothesized that hypotension influences outcome even in those patients not exposed to general anesthesia. Our aim was to determine optimal hemodynamic parameters and thresholds for patients with acute stroke undergoing thrombectomy under conscious sedation with monitored anesthesia care (MAC). Such parameters could be used in future studies of outcome and anesthesia type to determine whether general anesthesia has deleterious effects independent of hypotension.

MATERIALS AND METHODS

After approval from the institutional review board, we retrospectively reviewed the records of 714 patients who underwent endovascular treatment for acute ischemic stroke in the neurointerventional suite of Grady Memorial Hospital from September 2010 to April 2015. Five hundred ninety-nine patients had anterior circulation stroke with 90-day outcome data. We had complete

Received May 11, 2016; accepted after revision September 6.

From the Departments of Anesthesiology (M.K.W., R.Y.G.) and Neurology (D.C.H., L.C.R., M.R.F., R.G.N.) and Discovery Program (K.M.H.), Emory University School of Medicine, Atlanta, Georgia; and the Marcus Stroke and Neuroscience Center (D.C.H., L.C.R., M.R.F., R.G.N.), Grady Memorial Hospital, Atlanta, Georgia.

Please address correspondence to Raul G. Nogueira, MD, 49 Jesse Hill Jr Drive SE, Room 333, Atlanta, GA 30303; e-mail: raul.g.nogueira@emory.edu

http://dx.doi.org/10.3174/ajnr.A4992

hemodynamic data for 309 of the 347 patients treated under MAC. Two-hundred seventy-six of these patients were successfully reperfused (as defined by modified Thrombolysis in Cerebral Infarction 2b/3),[5] with a median procedure time of 64 minutes (interquartile range, 43–96 minutes). We excluded 20 patients (7%) who were not reperfused within 2.5 hours of groin puncture, which left a study population of 256. The baseline characteristics and periprocedural variables of our study population were collected prospectively within the study period (September 2010 to April 2015) from the Marcus Stroke and Neuroscience Center endovascular data base. Good outcome was defined as a 90-day modified Rankin Scale score of 0–2.

Stroke Variables and Procedures

Patients were selected for thrombectomy on the basis of the presence of salvageable tissue on imaging. TICI scores were determined in the angiography suite by the operator. Three-fourths of the procedures were performed with stent retrievers, and the remainder used thromboaspiration. All patients had follow-up imaging to assess hemorrhage. The modified Rankin Scale scores at 90 days were determined by an in-person follow-up appointment. Occasional no-shows were estimated by a structured phone interview.[6]

Anesthesia Variables

Our anesthesia care team includes an attending anesthesiologist supervising a nurse anesthetist or anesthesiologist assistant. More than 95% of our MAC procedures use dexmedetomidine infusions with supplemental fentanyl and midazolam as needed. For most patients with MAC, blood pressure measurements are noninvasive and arterial lines are usually reserved for patients with severe cardiac disease. Infusion regimens vary by practitioner but usually involve a loading dose of 0.5–1 μg/kg delivered during 10 minutes followed by a maintenance infusion of 0.5–1 μg/kg/hour. Although we did not have a formal protocol for hemodynamic management during this time, the target range for systolic blood pressure was usually set between 140 and 180 mm Hg before reperfusion. Phenylephrine was the most commonly used vasopressor. Anesthetic variables, including type of sedation, use of vasopressors, and systolic and diastolic blood pressure values (charted every 5 minutes), were retrieved from the anesthesia records. The baseline systolic and diastolic pressures were determined by averaging the measurements before the start of sedation. The single lowest MAP before successful reperfusion was recorded with its component systolic and diastolic blood pressures. We focused on MAP variables because mean blood pressure is directly measured by the noninvasive cuffs used on most patients, whereas these cuffs use an algorithm to derive systolic and diastolic blood pressure.[7]

Statistical Analysis

All data are expressed as mean ± SD or median with interquartile range as appropriate. Receiver operating characteristic curves were generated to identify hemodynamic cut-points. Between groups, 2-sided comparisons for continuous/ordinal variables were made with the Student *t* test or Mann-Whitney *U* test as appropriate. Categoric variables were compared by χ^2 or Fisher exact tests as appropriate. Variables with a $P < .10$ in these univariate analyses were simultaneously entered into multivariate regression models to identify which were independent predictors of outcome. We used binary logistic regression models with significance set as $P < .05$. Statistical analyses were performed by using SPSS Statistics, Version 23 (IBM, Armonk, New York).

RESULTS

Two hundred fifty-six patients meeting the selection criteria were included in the analysis. The mean age of the study population was 65.2 ± 15.4 years, and the mean NIHSS score was 17.3 ± 5.9. Table 1 presents the clinical characteristics and procedural variables of the groups with good and poor outcomes at 90 days. The groups had similar procedure durations and times from last known healthy to groin puncture, as well as similar rates of IV tPA and stent retriever use. We observed differences in ASPECTS and NIHSS scores and rates of parenchymal hemorrhage between the groups. The poor outcome group also had higher rates of atrial fibrillation and ICA terminus occlusion.

Table 2 shows systolic blood pressure and MAP parameters in the population and their association with outcome. Patients included in the analysis had a mean baseline systolic blood pressure of 157.6 ± 29.3 mm Hg and a MAP of 108.5 ± 18.6 mm Hg. The means for the lowest recorded systolic blood pressure and MAP before successful reperfusion were 118.0 ± 22.0 and 80.7 ± 14.4 mm Hg, respectively. Baseline pressures did not differ between the 2 outcome groups, but all variables related to the lowest pressure before reperfusion were statistically different (Table 2).

Due to collinearity, we incorporated the continuous variables of the lowest MAP, absolute MAP drop, and percentage MAP drop one at a time into binary logistic regression models for predictors of poor outcome. Neither absolute MAP drop nor percentage MAP drop were independent predictors of outcome ($P = .38$ and .16, respectively). The lowest MAP before modified TICI 2b/3 reperfusion was independently associated with poor outcome ($P = .04$). We performed a linear transformation [(100 − lowest MAP)/10] to place this result in a more meaningful clinical context. As shown in Table 3, the odds of poor outcome increased by 28% for every 10 mm Hg that the lowest MAP fell below 100 mm Hg.

We next generated receiver operating characteristic curves to investigate hemodynamic thresholds that could predict neurologic outcome (Fig 1). The areas under the curve for the MAP variables were approximately 0.6, suggesting that they are weaker predictors than the NIHSS score (0.74) or ASPECTS (0.65). For ease of comparison, we linked the pressures to the mRS category that generated curves above the reference line. For example, a lowest MAP of >90 mm Hg was >80% specific for good outcome (Fig 1*A*), whereas a drop in MAP of >40 mm Hg was approximately 80% specific for poor outcome (Fig 1*B*). The trade-off for the high specificities of these extreme values is low sensitivity. The 30% sensitivity of a lowest MAP of >90 mm Hg indicates that many patients whose MAP falls below 90 mm Hg will still have a good outcome.

In multivariate analysis for predictors of poor outcome, the lowest MAP of <85 mm Hg had an OR of 2.23 (95% CI, 1.09–17.7; $P = .03$). The lowest MAP cutoffs of 70 and 80 mm Hg were also independent predictors (OR = 2.15; 95% CI, 1.02–4.56; $P = .04$; and OR = 2.21; 95% CI, 1.12–4.16; $P = .02$, respectively). For blood pressure changes, an absolute MAP drop of >15 mm Hg

Table 1: Univariate analysis of baseline characteristics, procedural variables, and outcomes associated with 90-day mRS > 2[a]

	All Patients (n = 256[b])	90-Day mRS 0–2 (n = 152)	90-Day mRS >2 (n = 104)	P Value
Demographics				
Age (yr)	65.2 ± 15.4	61.5 ± 15.1	70.7 ± 14.1	<.01[c]
Male sex	123 (48%)	76 (50%)	47 (46%)	.49
Current smoker	48 (19%)	30 (20%)	18 (17%)	.61
Hypertension	179 (70%)	102 (67%)	77 (74%)	.23
Diabetes mellitus	58 (23%)	35 (23%)	23 (22%)	.86
Dyslipidemia	92 (36%)	55 (36%)	37 (36%)	.92
Atrial fibrillation	95 (37%)	49 (32%)	46 (44%)	.06[c]
Stroke features				
Baseline NIHSS	17 (13–22)	15 (11–19)	20 (17–24)	<.01[c]
ASPECTS	8 (7–9)	9 (7–9)	7 (6–9)	<.01[c]
Occlusion site				
ICA terminus	46 (18%)	18 (12%)	28 (27%)	<.01[c]
MCA M1	158 (72%)	98 (64%)	60 (58%)	.27
Last healthy to puncture (min)	295 (219–457)	281 (208–460)	305 (236–449)	.34
IV tPA given	113 (44%)	71 (47%)	42 (41%)	.35
Intraprocedural management				
Stent retriever	189 (74%)	115 (76%)	74 (72%)	.44
Procedure time (min)	62 (41–88)	60 (41–81)	66 (40–91)	.23
Vasopressor use	134 (52%)	75 (49%)	59 (57%)	.24
Outcomes				
Parenchymal hemorrhage	19 (7%)	4 (3%)	15 (14%)	<.01[c]
Final infarct volume (cm^3)	20.5 (7.3–60.0)	13.4 (5.4–35.6)	30.6 (17.4–111)	<.01
90-day mRS	2 (1–4)			
Mortality	31 (12%)		31 (30%)	

Note:—M1 indicates the sphenoidal segment of middle cerebral artery.
[a] Results are shown as mean ± SD, median (interquartile range), or number (percentage).
[b] Not all patients had data available for ASPECTS (n = 243), minutes from last known healthy to groin puncture (n = 211), or final infarct volume (n = 217).
[c] Variables with P < .1 added to the multivariate models.

Table 2: Intraprocedural hemodynamic characteristics[a] and their association with 90-day mRS > 2

	All Patients (n = 256)	90-Day mRS 0–2 (n = 152)	90-Day mRS > 2 (n = 104)	P Value[b]
Systolic blood pressure				
Baseline (mm Hg)	158 (135–176)	156 (134–173)	160 (137–180)	.137
Lowest before mTICI 2b/3 (mm Hg)[c]	117 (103–132)	118 (105–135)	115 (99–124)	.047
Absolute drop (mm Hg)[d]	35.5 (17–56)	30.0 (11–51)	41.5 (24–63)	.004
% Pressure drop[e]	22.8% (12–34)	21.4% (9–32)	27.6% (16–37)	.002
Mean arterial pressure				
Baseline (mm Hg)	107 (95–120)	107 (94–118)	107 (95–123)	.473
Lowest before mTICI 2b/3 (mm Hg)	79 (71–89)	81 (72–92)	77 (68–85)	.01
Absolute drop (mm Hg)[d]	24.7 (13–39)	23.8 (11–31)	26.7 (16–42)	.008
% Pressure drop[e]	23.3% (13–34)	22.1% (12–31)	25.6% (18–37)	.004

Note:—mTICI indicates modified TICI.
[a] Reported as median (interquartile range) unless otherwise noted.
[b] Mann-Whitney U test.
[c] Obtained from the systolic component of the lowest observed MAP prior to mTICI 2b/3 reperfusion.
[d] Calculated as the baseline pressure minus the lowest pressure before mTICI 2b/3.
[e] Calculated as the absolute pressure drop divided by the baseline pressure.

was independently associated with poor outcome (OR = 2.33; 95% CI, 1.11–18.6; P = .03). Finally, the largest OR for poor outcome was 4.38 for a MAP drop of >10% (95% CI, 1.53–12.6; P < .01).

Because the lowest MAP predicted an outcome over a range of cutoffs, we next examined how its effect varied by the baseline NIHSS score. Given our sample size, we divided our study population into 3 groups by baseline NIHSS. Subdividing these by the lowest MAP yielded subgroups of 18–26 patients. The rates of good outcome are shown in Fig 2. For less severe strokes (NIHSS score, <15), even patients whose MAP fell below 70 mm Hg had a 78% rate of good outcome. Only 60% of patients with NIHSS scores of ≥15 had good outcomes, even when their MAPs stayed above 90 mm Hg.

DISCUSSION

The optimal hemodynamic management of patients undergoing endovascular therapy for acute ischemic stroke remains a topic of debate among clinicians. The 2014 Society for Neuroscience in Anesthesiology and Critical Care Expert Consensus Statement recommends the use of continuous hemodynamic monitoring with maintenance of systolic blood pressure at 140–180 mm Hg,[8] but these recommendations are not based on data from patients having undergone thrombectomy. Instead, they originate from large epidemiologic studies that examined the associations between poor outcome and baseline hemodynamics or variation during the acute phase of acute ischemic stroke.[9-11] Davis et al[3] have investigated the association between favorable neurologic outcome and the lowest systolic blood pressure of >140 mm Hg based on the same extrapolation. In a subsequent study, our group selected a threshold of MAP of >70 mm Hg after dividing our range of observed MAP into quartiles.[4] Most recently, Löwhagen Hendén et al[12] showed that a >40% fall in MAP during endovascular reperfusion with the patient under general anesthesia is an independent predictor of poor neurologic outcome. We saw a need to more closely examine how various blood pressure changes influence outcome for patients undergoing thrombectomy.

We sought to perform our analysis in a large but relatively homogeneous study population to best observe the relationship between intraprocedural hypotension and outcome. We chose to restrict our analysis to those patients who achieved successful reperfusion (modified TICI 2b/3) because even the best blood pressure control would be unlikely to improve outcome if the vessel remained occluded. Because hypotension has been shown to be collinear with general anesthesia,[3] we restricted our analysis to those patients whose procedures were performed under MAC to eliminate confounding by anesthesia type.

Despite the perceived hemodynamic stability of thrombec-

tomy with the patient under sedation, we observed substantial drops in blood pressure during the procedures. Our baseline and lowest pressures are similar to the MAC/sedation cohorts reported from the Cleveland Clinic ($n = 99$)[13] and Mayo Clinic ($n = 38$).[14] Rates of vasopressor use were also quite similar across the 3 studies. The results from these 3 institutions suggest that it is difficult to replicate the tight hemodynamic control in the Calgary cohort reported by Davis et al.[3] One potential reason might be differences in the depth of sedation or drugs used. Although the former is impossible to determine, we can make crude comparisons of the latter. The Calgary patients received only fentanyl and midazolam for sedation, whereas our institution uses dexmedetomidine infusions with supplemental fentanyl and midazolam if needed. The practice at the Cleveland Clinic mirrors ours except they also use propofol infusions.[13] In contrast, most patients at the Mayo Clinic received only fentanyl and midazolam for sedation but still experienced significant drops in blood pressure.[14] It therefore appears that no particular sedative regimen can ensure tight hemodynamic control.

Table 3: Binary logistic regression model for poor neurologic outcome (90-day mRS > 2)[a]

Variable	OR (95% CI)	*P* Value
Age	1.05 (1.02–1.07)	.001
Atrial fibrillation	1.09 (0.55–2.15)	.805
Baseline NIHSS	1.16 (1.09–1.24)	<.001
ASPECTS	0.80 (0.65–0.97)	.023
ICA terminus occlusion	2.50 (1.14–5.50)	.022
Parenchymal hemorrhage	5.06 (1.30–19.7)	.020
Lowest MAP (per 10-mm Hg drop below 100 mm Hg)[b]	1.28 (1.01–1.62)	.043

[a] Variables with $P < .1$ in univariate analysis were entered simultaneously into a multivariate logistic regression model.

[b] Lowest intraprocedural MAP recorded prior to mTICI 2b/3 reperfusion.

Not only are blood pressure drops common during MAC, but even modest drops in blood pressure can have a dramatic impact on neurologic outcome. This is perhaps best illustrated by our finding that a decrease in MAP from baseline of >10% carries an OR for poor outcome of 4.38. Such tight hemodynamic control may not always be possible, but it should be a goal even with the patient under minimal sedation. From the receiver operating characteristic curves and multivariate models, we found no single MAP threshold. Instead, the lowest MAP showed a dose effect in which each 10-mm Hg drop below 100 mm Hg increased the odds of poor outcome. Although we consistently observed the benefit of keeping the MAP close to baseline, the critical MAP threshold may vary by the severity of the underlying stroke. Patients with an NIHSS score of <15 had high rates of good outcome across a wide range of MAPs, whereas the lowest MAP below 80 mm Hg had a large outcome effect for those with NIHSS scores of >20. For those patients in the middle (NIHSS score, 15–20), the threshold appeared to be 70 mm Hg. Presumably, in a homogeneous cohort of large-vessel occlusion strokes, patients with higher NIHSS severity have poorer collaterals and, thus, are more dependent on blood pressure compared with patients with milder stroke severity.

Low blood pressure has been reported to be an independent risk factor for poor outcome in 2 mixed populations of MAC and patients under general anesthesia [3,4] and 1 pure general anesthesia group.[12] We found that this relationship holds true even in populations with no general anesthesia. What remains unknown, however, is whether intervention to correct hypotension can actually improve outcomes. One group recently reported their experience instituting hemodynamic parameters for their patients undergoing thrombectomy.[15] They noted similar blood pressures in the groups with poor and favorable outcomes but that the cumulative dose of norepinephrine was independently associated with poor outcome.[15] These data raise the possibility that vasopressors may improve peripheral blood pressures without improving blood flow to the ischemic penumbra. Future work might approach this question through a prospective, randomized trial evaluating strict blood pressure control by using vasopressors in comparison with usual anesthesia care. Until the results of such a trial are available, it seems reasonable to minimize hypotension during endovascular thrombectomies for acute ischemic stroke.

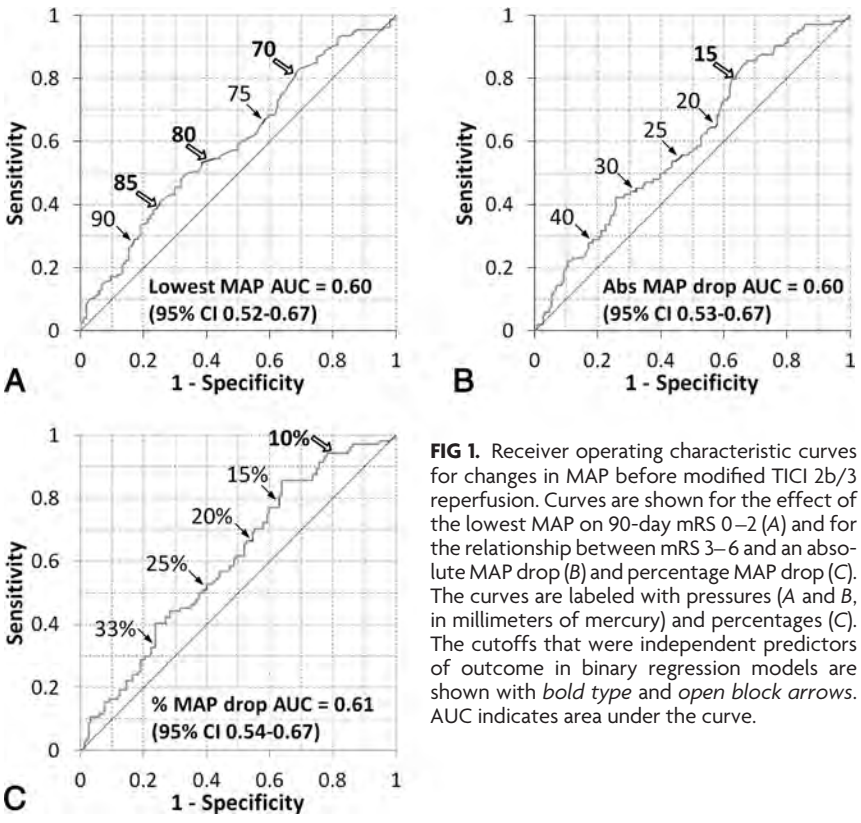

FIG 1. Receiver operating characteristic curves for changes in MAP before modified TICI 2b/3 reperfusion. Curves are shown for the effect of the lowest MAP on 90-day mRS 0–2 (*A*) and for the relationship between mRS 3–6 and an absolute MAP drop (*B*) and percentage MAP drop (*C*). The curves are labeled with pressures (*A* and *B*, in millimeters of mercury) and percentages (*C*). The cutoffs that were independent predictors of outcome in binary regression models are shown with *bold type* and *open block arrows*. AUC indicates area under the curve.

The present study has several limitations. Although larger than the previous studies, it remains retrospective in nature. As with all such studies, missing data may bias the results in unpredictable ways. For

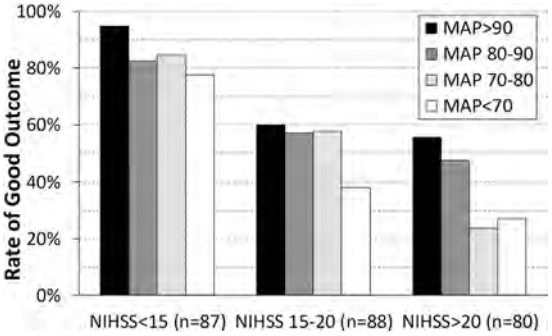

FIG 2. Rates of good neurologic outcome (90-day mRS of 0–2) by baseline NIHSS score and the lowest MAP measured before modified TICI 2b/3 reperfusion. Subdividing the NIHSS groups into 4 MAP categories yielded subgroups of similar size ($n = 18–26$).

example, we did not collect prestroke mRS scores. The lowest blood pressures before reperfusion were captured from the anesthesia records as the lowest MAP rather than lowest systolic pressure. However, our rationale was that most blood pressure data were acquired by using noninvasive oscillometric cuff sphygmomanometers, which measure the MAP and derive systolic and diastolic pressures from an algorithm.[7] Additionally, our choice of a study population with minimal confounders may limit the generalizability of our results to other patients undergoing thrombectomy, such as those with posterior circulation stroke or patients receiving general anesthesia. Nevertheless, the hemodynamic variables we identified may provide a useful way to control for the effect of hypotension in future studies on the effect of anesthesia on outcome.

CONCLUSIONS

Significant decreases in blood pressure occur during thrombectomies performed under MAC sedation. Our data support the hypothesis that hypotension influences outcome in patients not exposed to general anesthesia. Every 10-mm Hg drop in MAP below 100 mm Hg before reperfusion increased the odds of poor outcome by an estimated 28% (95% CI, 1%–62%). Even a 10% drop in MAP from the initial value seen in the angiography suite was a strong independent risk factor for poor outcome. These results suggest that clinicians should be just as vigilant in maintaining blood pressure for patients under MAC or conscious sedation as they are for those under general anesthesia.

Disclosures: Diogo C. Haussen—*UNRELATED*: *Other Relationships*: consultant for Codman (unpaid). Michael R. Frankel—*UNRELATED*: *Grants/Grants Pending*: Stryker, *Comments*: I am a coinvestigator on a clinical trial called DWI/PWI and CTP Assessment in the Triage of Wake-Up and Late Presenting Strokes Undergoing Neurointervention (DAWN), which tests whether thrombectomy using a device supplied by Stryker is effective in patients who are between 6 and 24 hours from symptom onset. I do not receive direct payment or direct salary support for this activity. I am just a coinvestigator. I was also a coinvestigator on the following clinical trials: A Randomized, Concurrent Controlled Trial to Assess the Safety and Effectiveness of the Separator 3D as a Component of the Penumbra System in the Revascularization of Large Vessel Occlusion in Acute Ischemic Stroke (Penumbra3D), Stent-Retriever Thrombectomy After Intravenous t-PA vs t-PA Alone in Stroke (SWIFT PRIME), and the Randomized, Concurrent Controlled Trial to Assess the Penumbra System's Safety and Effectiveness in the Treatment of Acute Stroke (THERAPY) (industry-sponsored studies), which involved thrombectomy and used devices in patients who were included in the present article. I received no direct payment or direct salary support.* Raul G. Nogueira—*RELATED*: *Fees for Participation in Review Activities such as Data Monitoring Boards, Statistical Analysis, Endpoint Committees, and the Like*: Stryker Neurovascular, Medtronic, Penumbra, *Comments*: Stryker Neurovascular (Randomized Trial Evaluating Performance of the Trevo Retriever Versus the Merci Retriever in Acute Ischemic Stroke [TREVO-2]; DAWN; Principal Investigator, no compensation); Medtronic (SOLITAIRE FR With the Intention for Thrombectomy [SWIFT] trial steering committee, modest compensation; [SWIFT-PRIME], Steering Committee, no compensation; Solitaire FR Thrombectomy for Acute Revascularization [STAR] trial Angiographic Core Lab, significant compensation); and Penumbra (A Randomized, Concurrent Controlled Trial to Assess the Safety and Effectiveness of the Separator 3D as a Component of the Penumbra System in the Revascularization of Large Vessel Occlusion in Acute Ischemic Stroke [Penumbra 3D], Executive Committee, no compensation); Editor-In-Chief of the journal *Interventional Neurology* (no compensation). *Money paid to the institution.

REFERENCES

1. Abou-Chebl A, Lin R, Hussain MS, et al. **Conscious sedation versus general anesthesia during endovascular therapy for acute anterior circulation stroke: preliminary results from a retrospective, multicenter study.** *Stroke* 2010;41:1175–79 CrossRef Medline
2. Abou-Chebl A, Zaidat OO, Castonguay AC, et al. **North American SOLITAIRE Stent-Retriever Acute Stroke Registry: choice of anesthesia and outcomes.** *Stroke* 2014;45:1396–401 CrossRef Medline
3. Davis MJ, Menon BK, Baghirzada LB, et al; Calgary Stroke Program. **Anesthetic management and outcome in patients during endovascular therapy for acute stroke.** *Anesthesiology* 2012;116:396–405 CrossRef Medline
4. Whalin MK, Lopian S, Wyatt K, et al. **Dexmedetomidine: a safe alternative to general anesthesia for endovascular stroke treatment.** *J Neurointerv Surg* 2014;6:270–75 CrossRef Medline
5. Zaidat OO, Yoo AJ, Khatri P, et al; Cerebral Angiographic Revascularization Grading (CARG) Collaborators, STIR Revascularization working group, STIR Thrombolysis in Cerebral Infarction (TICI) Task Force. **Recommendations on angiographic revascularization grading standards for acute ischemic stroke: a consensus statement.** *Stroke* 2013;44:2650–63 CrossRef Medline
6. Bruno A, Akinwuntan AE, Lin C, et al. **Simplified modified Rankin Scale questionnaire: reproducibility over the telephone and validation with quality of life.** *Stroke* 2011;42:2276–79 CrossRef Medline
7. Amoore JN. **Oscillometric sphygmomanometers: a critical appraisal of current technology.** *Blood Press Monit* 2012;17:80–88 CrossRef Medline
8. Talke PO, Sharma D, Heyer EJ, et al. **Society for Neuroscience in Anesthesiology and Critical Care Expert Consensus Statement: anesthetic management of endovascular treatment for acute ischemic stroke*—endorsed by the Society of NeuroInterventional Surgery and the Neurocritical Care Society.** *J Neurosurg Anesthesiol* 2014;26:95–108 CrossRef Medline
9. Leonardi-Bee J, Bath PM, Phillips SJ, et al; IST Collaborative Group. **Blood pressure and clinical outcomes in the International Stroke Trial.** *Stroke* 2002;33:1315–20 CrossRef Medline
10. Castillo J, Leira R, Garcia MM, et al. **Blood pressure decrease during the acute phase of ischemic stroke is associated with brain injury and poor stroke outcome.** *Stroke* 2004;35:520–26 CrossRef Medline
11. Ritter MA, Kimmeyer P, Heuschmann PU, et al. **Blood pressure threshold violations in the first 24 hours after admission for acute stroke: frequency, timing, predictors, and impact on clinical outcome.** *Stroke* 2009;40:462–68 CrossRef Medline
12. Löwhagen Hendén P, Rentzos A, Karlsson JE, et al. **Hypotension during endovascular treatment of ischemic stroke is a risk factor for poor neurological outcome.** *Stroke* 2015;46:2678–80 CrossRef Medline
13. John S, Thebo U, Gomes J, et al. **Intra-arterial therapy for acute ischemic stroke under general anesthesia versus monitored anesthesia care.** *Cerebrovasc Dis* 2014;38:262–67 CrossRef Medline
14. Jagani M, Brinjikji W, Rabinstein AA, et al. **Hemodynamics during anesthesia for intra-arterial therapy of acute ischemic stroke.** *J Neurointerv Surg* 2016;8:883–88 CrossRef Medline
15. Mundiyanapurath S, Stehr A, Wolf M, et al. **Pulmonary and circulatory parameter guided anesthesia in patients with ischemic stroke undergoing endovascular recanalization.** *J Neurointerv Surg* 2016;8:335–41 CrossRef Medline

Endovascular Stroke Treatment of Nonagenarians

M. Möhlenbruch, J. Pfaff, S. Schönenberger, S. Nagel, J. Bösel, C. Herweh, P. Ringleb, M. Bendszus, and S. Stampfl

ABSTRACT

BACKGROUND AND PURPOSE: Although endovascular treatment has become a standard therapy in patients with acute stroke, the benefit for very old patients remains uncertain. The purpose of this study was the evaluation of procedural and outcome data of patients ≥90 years undergoing endovascular stroke treatment.

MATERIALS AND METHODS: We retrospectively analyzed prospectively collected data of patients ≥90 years in whom endovascular stroke treatment was performed between January 2011 and January 2016. Recanalization was assessed according to the TICI score. The clinical condition was evaluated on admission (NIHSS, prestroke mRS), at discharge (NIHSS), and after 3 months (mRS).

RESULTS: Twenty-nine patients met the inclusion criteria for this analysis. The median prestroke mRS was 2. Successful recanalization (TICI ≥ 2b) was achieved in 22 patients (75.9%). In 9 patients, an NIHSS improvement ≥ 10 points was noted between admission and discharge. After 3 months, 17.2% of the patients had an mRS of 0–2 or exhibited prestroke mRS, and 24.1% achieved mRS 0–3. Mortality rate was 44.8%. There was only 1 minor procedure-related complication (small SAH without clinical sequelae).

CONCLUSIONS: Despite high mortality rates and only moderate overall outcome, 17.2% of the patients achieved mRS 0–2 or prestroke mRS, and no serious procedure-related complications occurred. Therefore, very high age should not per se be an exclusion criterion for endovascular stroke treatment.

It is expected that the elderly population will grow substantially over the next few decades, with a doubling of the percentage of people over 80 years in the United States as well as in the European Union by 2050.[1,2] The risk of stroke, a leading cause of disability and death, increases with age,[3] and patients older than 80 years have the highest incidence.[4]

In studies assessing the outcomes of patients with stroke after endovascular treatment, patients are frequently separated into groups <80 years versus ≥80 years. Age greater than 80 years was found to be associated with a poorer clinical outcome and increased mortality,[5] though revascularization success rates were comparable with those of younger patients.[6] However, recent large prospective trials on endovascular stroke treatment had no upper age limit,[7,8] and the subgroup analysis in the Multicenter Randomized Clinical Trial of Endovascular Treatment for Acute Ischemic Stroke in the Netherlands (MR CLEAN) trial showed a treatment effect in all predefined subgroups, including the subgroup based on age (<80 years versus ≥80 years). Therefore, patients ≥80 years regularly undergo endovascular stroke treatment in our institution if they are eligible. Increasingly, we also treat nonagenarians (patients ≥ 90 years), though in the literature, most reports on the older age group include patients between 80 and 90 years, and only few data on patients older than 90 years exist. The oldest documented patient who underwent endovascular stroke treatment was a 103-year-old woman[9] who recovered well.

In this study, we summarize our experience of endovascular stroke treatment in patients ≥90 years of age between January 2011 and January 2016.

MATERIALS AND METHODS

Patient Selection

Approval for collection of interventional and clinical data was given by the local ethics committee.

We retrospectively analyzed prospectively collected data of patients with acute stroke who were treated between January 2011 and January 2016. They met the following inclusion criteria: age ≥90 years, reasonable cognitive and functional prestroke status (no advanced dementia, only mild to moderate disabilities), no signs of

Received May 24, 2016; accepted after revision August 19.

From the Departments of Neuroradiology (M.M., J.P., C.H., M.B., S. Stampfl) and Neurology (S. Schönenberger, S.N., J.B., P.R.), University Hospital Heidelberg, Heidelberg, Germany.

Please address correspondence to Sibylle Stampfl, MD, Department of Neuroradiology, University Hospital Heidelberg, Im Neuenheimer Feld 400, 69120 Heidelberg, Germany; e-mail: sibylle.stampfl@med.uni-heidelberg.de

http://dx.doi.org/10.3174/ajnr.A4976

Baseline characteristics and overview of angiographic and clinical outcome data

Demographics	
Mean age, yr (range)	91.9 (90–99)
Sex (F/M)	19/10
Medical history, No. of patients	
Hypertension	25
Atrial fibrillation	20
Diabetes mellitus	7
Coronary artery disease	5 (n = 1 status after myocardial infarction)
Cardiac insufficiency	8
Peripheral artery disease	3 (n = 2 with femoropopliteal bypass surgery)
Previous stroke	8 (lacunar ischemia or partial MCA, PCA, or PICA infarction with good recovery; transient ischemic attack, n = 1)
Renal insufficiency	9
History of cancer	3 (multiple myeloma, breast cancer, basalioma)
Coxarthrosis	5 (state after hip fracture, n = 1)
Clinical presentation and outcome	
Prestroke mRS, median (IQR)	2 (1–3)
Initial NIHSS, median (IQR)	20 (16.5–22.5)
mRS of surviving patients at 90 days, median (IQR)	4 (2.25–5)
Mortality, No. of patients (%)	13 (44.8)
Occlusion site, No. of patients (%)	
ICA terminus	4 (13.8)
ICA/MCA	5 (17.2)
M1 segment	12 (41.4)
M2 segment	4 (13.8)
Vertebrobasilar	4 (13.8)
Angiographic outcome, No. of patients (%)	
TICI 0	4 (13.8)
TICI 1	0 (0)
TICI 2a	3 (10.3)
TICI 2b	12 (41.4)
TICI 3	10 (34.5)

Note:—IQR indicates interquartile range; PCA, posterior cerebral artery.

major infarction (>one-third of the MCA territory) on baseline CT or MR imaging, and CTA- or MRA-proved major intracranial vessel occlusion.

Interventional Procedure

All procedures were performed under general anesthesia or conscious sedation. As vascular access, an 8F sheath was placed in the right femoral artery. Then, an 8F catheter was advanced into the common carotid artery of the occluded side. In patients with occlusion of the posterior circulation, a long 7F sheath was placed in the right femoral artery with the tip of the sheath in the subclavian artery. Subsequently, a 5F Sofia catheter (MicroVention, Tustin, California) or a 5F Neuron catheter (Penumbra, Alameda, California) was positioned within the ICA close to the thrombus. The microcatheter tip was placed distal to the thrombus, and the stent-retriever device was advanced through the microcatheter. Then, a stent-retriever device (Solitaire [Covidien, Irvine, California]; Trevo [Stryker, Kalamazoo, Michigan]) was deployed by pulling back the microcatheter. Angiographic runs were performed to control flow restoration. Device and microcatheter were simultaneously pulled back under continuous aspiration through the intermediate catheter, which was applied by using a 20- to 60-mL syringe. Again, angiographic runs were performed to document the result. If no sufficient recanalization was achieved, thrombectomy was repeated.

Evaluation of Angiographic Data

Successful recanalization was defined as TICI (Thrombolysis in Cerebral Infarction) score 2b/3.[10] Angiographic images were evaluated in consensus by 2 neuroradiologists (S.Stampfl, M.M.) regarding the following aspects: site of occlusion, time to interventional treatment (symptom onset to first angiographic image), time to revascularization (time between the first and the final angiographic image), pre- and postprocedural TICI, and procedure-related complications. Furthermore, it was noted if IV rtPA was administered.

Evaluation of Outcome Data

Follow-up CT was performed after 24–36 hours or earlier in case of clinical deterioration. All patients were treated on a specialized neuro–intensive care unit or a certified stroke unit. NIHSS was used to quantify neurologic deficit; here, we analyzed admission and discharge NIHSS. After 90 days, the mRS was assessed by a semistandardized telephone interview or during an outpatient visit by a trained investigator not blinded to the type of treatment. Favorable clinical outcome was defined as mRS 0–2 or achieving prestroke mRS at 3 months.

Intracranial hemorrhage was classified according to the second European-Australasian Acute Stroke Study classification.[11]

Statistics

All data were collected in a data base. Continuous data are described by median and interquartile range or mean and standard deviation. Statistical analysis was performed by using GraphPad Prism 5.0 (GraphPad Software, San Diego, California).

RESULTS

Patient Selection

The Table gives an overview of baseline characteristics and angiographic and clinical data.

Overall, 29 nonagenarians from a cohort of 615 patients with interventional stroke treatment underwent endovascular treatment for acute stroke between January 2011 and January 2016. Mean age was 91.9 years (range, 90–99 years; 19 women, 10 men). In 12 patients, time of symptom onset remained uncertain. In the other patients, the median time of symptom onset to time of the first image was 206 minutes (range, 91–321 minutes). Four patients presented with basilar artery occlusions. The other patients had occlusions of the anterior circulation (ICA terminus, n = 4; ICA terminus + MCA, n = 5; M1 segment, n = 12; M2 segment n = 4).

In 17 patients, additional IV rtPA was administered as part of

the bridging concept combining IV thrombolysis (0.9 mg/kg body weight, with 10% administered as a bolus) and endovascular therapy.

The median prestroke mRS was 2 (range, 0–4; interquartile range, 1–3). Three patients presented with a prestroke mRS of 4 mainly because of orthopedic diseases, but they had a good prestroke cognitive function, or the prestroke mRS was uncertain at admission.

Most patients had a history of hypertension ($n = 25$) and atrial fibrillation ($n = 20$). Eight patients had a history of stroke (lacunar ischemia, $n = 3$; partial MCA infarction, $n = 2$; partial posterior cerebral artery infarction, $n = 1$; partial PICA infarction, $n = 2$), but they had recovered well with only minor disabilities remaining. One patient had a history of multiple myeloma (classified as stable). One patient had a history of basalioma. Another patient underwent breast cancer treatment in the 1980s.

Median NIHSS at admission was 20 (interquartile range, 16.5–22.5).

Evaluation of Angiographic Data

Before the procedure, TICI was 0 in all patients. In 22 patients (75.9%), recanalization was successful (TICI 2b, $n = 12$; TICI 3, $n = 10$). In 4 patients (basilar artery occlusion, $n = 1$; ICA occlusion, $n = 1$; M1 occlusion, $n = 2$), the procedure was futile (no stable guide-catheter position because of extensive vessel elongation and kinking, $n = 3$; no passage of the occluded ICA lumen possible, $n = 1$). In the other patients, the final recanalization result was achieved 77 minutes after groin puncture (median; range, 19–142 minutes).

In 2 patients who were treated in 2011, permanent Solitaire stent implantation in the MCA was performed to maintain sufficient revascularization. In these patients, tirofiban was administered for 24 hours (overlapping with aspirin and clopidogrel). In 1 patient with high-grade ICA stenosis, additional carotid stent implantation was necessary to access the intracranial lesion. This patient received a loading dose of aspirin and 2000 IU heparin.

Evaluation of Outcome Data

Nine patients (31%) improved ≥10 NIHSS points between admission and discharge. After 90 days, the mortality rate was 44.8% (13 patients). In 9 of these patients, life-prolonging care was withdrawn because of advance directives or because of the presumed wishes of the patient. All patients died because of the infarction extent or non-neurologic stroke-related complications such as pneumonia.

The median mRS of the surviving patients was 4 (interquartile range, 2.25–5). Favorable clinical outcome (mRS 0–2) or prestroke mRS was regained in 17.2% of the patients (mRS 0–2, $n = 4$ [13.8%]; mRS 3, $n = 3$ [10.3%]; mRS 4–5, $n = 9$ [31%]).

Complications

In 1 patient, vessel perforation with subsequent small SAH occurred during thrombectomy. However, this did not increase morbidity, and the patient presented with a mRS of 3 after 90 days (prestroke mRS was also 3).

Intraparenchymal hemorrhage occurred as follows: HI1 (small petechiae), $n = 1$; HI 2 (confluent petechiae), $n = 1$; PH 1 (<30% of the infarcted area, with some mild space-occupying effect), $n = 3$. Permanent ICA or MCA stent implantation had not been performed in any of these patients.

DISCUSSION

Safety and efficacy of endovascular stroke therapy has been proved in several trials.[7,8] Accordingly, an increasing number of elderly patients with stroke undergo recanalization procedures. In this study, we report our experience with endovascular stroke therapy in nonagenarians. To our knowledge, this is the first report on endovascular treatment of a larger patient cohort in this age group. The outcome of our study patients is limited, with a mortality rate of 44.8% and a median mRS of 4 in the surviving patients after 3 months. However, interpreting these results, we have to consider several facts. First of all, it is known that the higher incidence of prestroke comorbidity and poststroke nonneurologic complications such as pneumonia lead to a higher poststroke mortality and disability in elderly patients with stroke.[6,12-15] Singer et al[16] reported a highly age-related clinical outcome: in the lowest age quartile (<56 years), 60% experienced a favorable outcome, contrary to 17% in the highest age quartile (>77 years). Prestroke mRS of elderly patients with stroke is usually worse compared with younger patients and mainly contributes to the limited outcome. In a single-center study, approximately one-third of the elderly (>80 years) patients with stroke treated with intra-arterial therapy had a baseline mRS >1, and 59% had died after 3 months.[17] In another study, prestroke mRS was 3–4 in 13% of the patients,[18] with a mortality rate of 48% at 3 months. Similarly, only in a minority of our study patients was the prestroke mRS 0 or 1. Restoring the prestroke condition is the best achievable result in most patients. Although this could be obtained in only 17.2% of our study patients, an NIHSS improvement ≥10 points between admission and discharge was observed in 31%. Furthermore, in 24% of our patients, mRS of 0–3 was achieved, which seems an acceptable result in our aged study population. This should be taken into account because without therapy, outcome of patients with stroke in the 10th decade of life is probably even worse. In a publication from 1999 evaluating the natural course of stroke, it was described that in the older age group (>80 years), 45% of the patients had a prestroke mRS of 2–5, and the mortality rate was 44.6% after 3 months,[19] which is almost identical to the mortality rate in our study. However, patients in our study are at least 10 years older with a presumably worse prognosis.

It has been discussed that the greater likelihood of withdrawing life-prolonging care because of advance directives or presumed wishes of the patient contributes to the higher mortality rate in very old patients.[17] Life-prolonging care was withdrawn in most patients in our study who died. However, the possible outcome without care withdrawal is unknown and, of course, the prognosis in these patients was dismal.

As a consequence of the reported worse outcome of elderly patients with stroke, some prospective trials included only patients younger than 80 years[20] or 85 years.[21,22]

In contrast, a recently published report found that endovascular therapy improved the outcome and reduced the risk of hospital-acquired infections in patients ≥80 years with acute stroke.[23] In most of the recent large randomized trials, there was no upper

age limit,[7,8,24] and the oldest patient in the MR CLEAN trial was 96 years old.[7] A subgroup analysis of the MR CLEAN trial showed a treatment effect in all subgroups, including the one based on age.[7] In fact, endovascular treatment was even more beneficial for elderly patients with stroke.

Correspondingly, a subgroup analysis of the Endovascular Treatment for Small Core and Proximal Occlusion Ischemic Stroke (ESCAPE) trial[24] documented a benefit in the endovascular treatment group even in elderly patients.

In these subgroup analyses as well as in other studies,[6,25] patients were separated into groups <80 years versus ≥80 years. However, with endovascular stroke therapy emerging, neurointerventionalists are increasingly faced with the question of whether to offer this treatment even to nonagenarians. It always remains an individual decision and should depend on the patient's prestroke cognitive and functional condition in addition to the regularly used clinical and imaging criteria. In our study, the decision for endovascular treatment was always based on the consensus of an interdisciplinary stroke team, and not only the prestroke disability, but also the prestroke cognitive function was taken into account. Therefore, in some cases, even patients with a moderately severe disability (corresponding to mRS 4) were treated because they participated in life despite their physical handicap or because prestroke mRS was uncertain at admission. However, we have to admit that the 3 patients with prestroke mRS 4 had a bad outcome (mRS 5, $n = 1$; mRS 6, $n = 2$), and it remains controversial if such patients should be treated in the future.

Endovascular stroke therapy in elderly patients is potentially more complicated because of age-related vessel elongation and calcification, and these difficult vascular access conditions might result in lower success rates. Indeed, vascular access was not possible in 13.8% of our patients (compared with approximately 4%–5% as reported in the literature[26,27]) and, accordingly, thrombectomy could not be performed. Importantly, the failed attempts were not associated with complications. During decision-making, one should also keep in mind that the complication rate of endovascular stroke therapy is low, and the possible advantages outweigh the risks.

Our study has several limitations. First of all, it is a retrospective single-center analysis; the number of patients is relatively small, and the study group is heterogeneous (inclusion of patients with occlusion in the anterior as well as in the posterior circulation). However, to our knowledge, there is no other report about a series of patients with stroke in this age group treated with thrombectomy.

Another limitation is that we do not have a control group of elderly patients with stroke who were not treated with thrombectomy or received IV lysis alone.

Furthermore, in elderly patients, the cognitive dimension is at least as important as disability. However, the cognitive function was not evaluated in our study.

CONCLUSIONS

The aged population in this study had a high mortality with an overall limited outcome after 3 months. Furthermore, the vascular approach is more complicated in the elderly population, and the revascularization rates achieved are slightly lower. However, increased age did not seem to be associated with higher procedural complication rates. Almost every fifth carefully selected patient achieved a good clinical result (mRS 0–2 or restoration of prestroke mRS). Hence, thrombectomy should not be withheld from nonagenarians. Exclusion of patients from endovascular treatment on the basis of age alone doesn't seem to be justified.

Disclosures: Markus Möhlenbruch—*UNRELATED*: *Board Membership*: Codman; *Consultancy*: Acandis, Codman, MicroVention, Phenox; *Payment for Lectures (including service on Speakers Bureaus)*: Codman, MicroVention, Phenox. Johannes Pfaff—*UNRELATED*: *Grants/Grants Pending*: Siemens Healthineers*; *Payment for Lectures (including service on Speakers Bureaus)*: Siemens Healthineers, *Comments*: payment for lectures during the Deutsche Röntgenkongress 2015 (German X-Ray Congress); *Travel/Accommodations/Meeting Expenses Unrelated to Activities Listed*: Stryker Neurovascular, *Comments*: annual meeting of the Deutsche Gesellschaft für Neuroradiologie 2015 (German Society for Neuroradiology). Simon Nagel—*UNRELATED*: *Consultancy*: Brainomix; *Payment for Lectures (including service on Speakers Bureaus)*: Bayer, Pfizer, Medtronic; *Travel/Accommodations/Meeting Expenses Unrelated to Activities Listed*: Böhringer Ingelheim. Julian Bösel—*UNRELATED*: *Payment for Lectures (including service on Speakers Bureaus)*: Bard, Zoll, Seiratherm, Sedana, *Comments*: speaker honoraria; *Travel/Accommodations/Meeting Expenses Unrelated to Activities Listed*: Bard, Zoll, Seiratherm, Sedana, *Comments*: travel support. Peter Ringleb—*UNRELATED*: *Consultancy*: Boehringer Ingelheim, Covidien*; *Payment for Lectures (including service on Speakers Bureaus)*: Boehringer Ingelheim, Bayer, BMS, Pfizer, Daichii Sankyo*; *Travel/Accommodations/Meeting Expenses Unrelated to Activities Listed*: Boehringer Ingelheim, Bayer, Pfizer.* Martin Bendszus—*UNRELATED*: *Board Membership*: DSMB Vascular Dynamics; *Consultancy*: Roche, Guerbet, Codman; *Grants/Grants Pending*: DFG, Hopp Foundation, Novartis, Siemens, Guerbet, Stryker, Covidien*; *Payment for Lectures (including service on Speakers Bureaus)*: Novartis, Roche, Guerbet, Teva, Bayer, Codman. *Money paid to the institution.

REFERENCES

1. Vincent GK, Velkoff VA. The next four decades. The older population in the United States: 2010–50. Population estimates and projections. https://www.census.gov/prod/2010pubs/p25-1138.pdf. Accessed April 1, 2016
2. Population projections 2004–2050. EU25 population rises until 2025, then falls. Eurostat news release 48/2005; April 8, 2005. http://ec.europa.eu/eurostat/web/products-press-releases/-/3-08042005-AP. Accessed October 3, 2016
3. Wolf PA, D'Agostino RB, Belanger AJ, et al. **Probability of stroke: a risk profile from the Framingham Study.** *Stroke* 1991;22:312–18 CrossRef Medline
4. Mozaffarian D, Benjamin EJ, Go AS, et al. **Heart disease and stroke statistics–2015 update: a report from the American Heart Association.** *Circulation* 2015;27 131:e29–322 CrossRef Medline
5. Villwock MR, Singla A, Padalino DJ, et al. **Acute ischaemic stroke outcomes following mechanical thrombectomy in the elderly versus their younger counterpart: a retrospective cohort study.** *BMJ Open* 2014;4:e004480 CrossRef Medline
6. Castonguay AC, Zaidat OO, Novakovic R, et al. **Influence of age on clinical and revascularization outcomes in the North American Solitaire Stent-Retriever Acute Stroke Registry.** *Stroke* 2014;45:3631–36 CrossRef Medline
7. Berkhemer OA, Fransen PS, Beumer D, et al. **A randomized trial of intraarterial treatment for acute ischemic stroke.** *N Engl J Med* 2015;372:11–20 CrossRef Medline
8. Campbell BC, Mitchell PJ, Kleinig TJ, et al. **Endovascular therapy for ischemic stroke with perfusion-imaging selection.** *N Engl J Med* 2015;372;1009–18 CrossRef Medline
9. Boo S, Duru UB, Smith MS, et al. **Successful endovascular stroke therapy in a 103-year-old woman.** *J Neurointerv Surg* 2015 Nov 9. [Epub ahead of print] CrossRef Medline
10. Higashida RT, Furlan AJ, Roberts H, et al. **Trial design and reporting standards for intra-arterial cerebral thrombolysis for acute ischemic stroke.** *Stroke* 2003;34:e109–37 CrossRef Medline
11. Hacke W, Kaste M, Fieschi C, et al. **Randomised double-blind placebo-controlled trial of thrombolytic therapy with intravenous alteplase in acute ischaemic stroke (ECASS II). Second European-**

Australasian Acute Stroke Study Investigators. *Lancet* 1998;352:1245–51 CrossRef Medline
12. Qureshi AI, Suri MF, Georgiadis AL, et al. **Intra-arterial recanalization techniques for patients 80 years or older with acute ischemic stroke: pooled analysis from 4 prospective studies.** *AJNR Am J Neuroradiol* 2009;30:1184–89 CrossRef Medline
13. Broussalis E, Weymayr F, Hitzl W, et al. **Endovascular mechanical recanalization of acute ischaemic stroke in octogenarians.** *Eur Radiol* 2016;26:1742–50 CrossRef Medline
14. Sharma JC, Fletcher S, Vassallo M. **Strokes in the elderly—higher acute and 3-month mortality—an explanation.** *Cerebrovasc Dis* 1999;9:2–9 CrossRef
15. Denti L, Scoditti U, Tonelli C, et al. **The poor outcome of ischemic stroke in very old people: a cohort study of its determinants.** *J Am Geriatr Soc* 2010;58:12–17 CrossRef Medline
16. Singer OC, Haring HP, Trenkler J, et al. **Age dependency of successful recanalization in anterior circulation stroke: the ENDOSTROKE study.** *Cerebrovasc Dis* 2013;36:437–45 CrossRef Medline
17. Chandra RV, Leslie-Mazwi TM, Oh DC, et al. **Elderly patients are at higher risk for poor outcomes after intra-arterial therapy.** *Stroke* 2012;43:2356–61 CrossRef Medline
18. Kurre W, Aguilar-Pérez M, Niehaus L, et al. **Predictors of outcome after mechanical thrombectomy for anterior circulation large vessel occlusion in patients aged ≥80 years.** *Cerebrovasc Dis* 2013;36:430–36 CrossRef Medline
19. Di Carlo A, Lamassa M, Pracucci G, et al. **Stroke in the very old: clinical presentation and determinants of 3-month functional outcome: a European perspective. European BIOMED Study of Stroke Care Group.** *Stroke* 1999;30:2313–19 CrossRef Medline
20. Jovin TG, Chamorro A, Cobo E, et al. **Thrombectomy within 8 hours after symptom onset in ischemic stroke.** *N Engl J Med* 2015;372:2296–306 CrossRef Medline
21. Saver JL, Goyal M, Bonafe A, et al. **Stent-retriever thrombectomy after intravenous t-PA vs. t-PA alone in stroke.** *N Engl J Med* 2015;372:2285–95 CrossRef Medline
22. Jansen O, Macho JM, Killer-Oberpfalzer M, et al. **Neurothrombectomy for the treatment of acute ischemic stroke: results from the TREVO study.** *Cerebrovasc Dis* 2013;36:218–25 CrossRef Medline
23. Hwang K, Hwang G, Kwon OK, et al. **Endovascular treatment for acute ischemic stroke patients over 80 years of age.** *J Cerebrovasc Endovasc Neurosurg* 2015;17:173–79 CrossRef Medline
24. Goyal M, Demchuk AM, Menon BK, et al. **Randomized assessment of rapid endovascular treatment of ischemic stroke.** *N Engl J Med* 2015;372:1019–30 CrossRef Medline
25. To CY, Rajamand S, Mehra R, et al. **Outcome of mechanical thrombectomy in the very elderly for the treatment of acute ischemic stroke: the real world experience.** *Acta Radiol Open* 2015;4:2058460115599423 CrossRef Medline
26. Wiesmann M, Kalder J, Reich A, et al. **Feasibility of combined surgical and endovascular carotid access for interventional treatment of ischemic stroke.** *J Neurointervent Surg* 2016;8:571–75 CrossRef Medline
27. Ribo M, Flores A, Rubiera M, et al. **Difficult catheter access to the occluded vessel during endovascular treatment of acute ischemic stroke is associated with worse clinical outcome.** *J Neurointervent Surg* 2013;5(suppl 1):i70–73 CrossRef Medline

Diffusion-Weighted Imaging–Detected Ischemic Lesions following Endovascular Treatment of Cerebral Aneurysms: A Systematic Review and Meta-Analysis

K.M. Bond, W. Brinjikji, M.H. Murad, D.F. Kallmes, H.J. Cloft, and G. Lanzino

ABSTRACT

BACKGROUND AND PURPOSE: Endovascular treatment of intracranial aneurysms is associated with the risk of thromboembolic ischemic complications. Many of these events are asymptomatic and identified only on diffusion-weighted imaging. We performed a systematic review and meta-analysis to study the incidence of DWI positive for thromboembolic events following endovascular treatment of intracranial aneurysms.

MATERIALS AND METHODS: A comprehensive literature search identified studies published between 2000 and April 2016 that reported postprocedural DWI findings in patients undergoing endovascular treatment of intracranial aneurysms. The primary outcome was the incidence of DWI positive for thromboembolic events. We examined outcomes by treatment type, sex, and aneurysm characteristics. Meta-analyses were performed by using a random-effects model.

RESULTS: Twenty-two studies with 2148 patients and 2268 aneurysms were included. The overall incidence of DWI positive for thromboembolic events following endovascular treatment was 49% (95% CI, 42%–56%). Treatment with flow diversion trended toward a higher rate of DWI positive for lesions than coiling alone (67%; 95% CI, 46%–85%; versus 45%; 95% CI, 33%–56%; $P = .07$). There was no difference between patients treated with coiling alone and those treated with balloon-assisted (44%; 95% CI, 29%–60%; $P = .99$) or stent-assisted (43%; 95% CI, 24%–63%; $P = .89$) coiling. Sex, aneurysm rupture status, location, and size were not associated with the rate of DWI positive for lesions.

CONCLUSIONS: One in 2 patients may have infarcts on DWI following endovascular treatment of intracranial aneurysms. There is a trend toward a higher incidence of DWI-positive lesions following treatment with flow diversion compared with coiling. Patient demographics and aneurysm characteristics were not associated with DWI-positive thromboembolic events.

Coil embolization and flow diversion have proved highly efficacious options for the endovascular treatment of intracranial aneurysms. However, both techniques are associated with potential periprocedural complications, including aneurysm rupture, transient ischemic attacks, and ischemic stroke. Small, silent infarcts caused by thromboemboli are often seen on postprocedural diffusion-weighted imaging. While many of these lesions remain ostensibly asymptomatic, the long-term effects of such tiny infarcts remain unclear.[1-3]

Previous studies have reported that the rate of ischemic lesions on postoperative DWI ranges from 10% to 77% following coil embolization[4-15] and 51% to 63% following therapy with flow diversion.[16-19] However, baseline clinical and angiographic risk factors for postoperative DWI lesions, to our knowledge, have not been fully elucidated previously. We performed a systematic review and meta-analysis for the following: 1) to determine the overall incidence of perioperative infarcts on DWI in patients undergoing endovascular treatment of intracranial aneurysms; and 2) to demonstrate the relationship between treatment type, patient demographics, and aneurysm characteristics with postoperative infarcts on DWI.

MATERIALS AND METHODS

Literature Search and Inclusion Criteria

This systematic review and meta-analysis are reported in accordance with the Preferred Reporting Items for Systematic Reviews and Meta-Analysis (PRISMA; http://www.bmj.com/content/339/bmj.b2535) guidelines. An experienced librarian conducted a comprehensive literature search of PubMed, Ovid MEDLINE, and Ovid EMBASE with input from the authors. The search was

Received May 18, 2016; accepted September 6.

From the Mayo Medical School (K.M.B.), Department of Radiology (W.B., D.F.K., H.J.C.), Center for Science of Healthcare Delivery (M.H.M.), and Department of Neurologic Surgery (G.L.), Mayo Clinic, Rochester, Minnesota.

Please address correspondence to Waleed Brinjikji, MD, Mayo Clinic, Department of Radiology, 200 1st St SW, Rochester, MN 55905; e-mail: brinjikji.waleed@mayo.edu; @WBrinjikji

http://dx.doi.org/10.3174/ajnr.A4989

Table 1: Summary of studies included in meta-analysis

Study	Design	No. of Patients	Mean Age	Sex		Aneurysms			Circulation		Treatment	Time until Imaging (hr)	Risk of Bias
				M	F	Ruptured	Unruptured	Total	Anterior	Posterior			
Altay et al, 2011[12]	R	184	58.8	44	154[a]	65	133	198	147	51	C, SAC, BAC	<72	M
Biondi et al, 2000[25]	R	20	50	5	15	11	9	20	16	4	C	2–4 and 24–48	M
Brasiliense et al, 2016[16]	P	59	59	11	48	70	0	70	60	10	FD	24	M
Cronqvist et al, 2005[32]	P	40	49.4	13	27	16	30	46	38	8	C	18–52	M
Hahnemann et al, 2014[7]	R	75	52.6	21	54	0	75	75	35	40	SAC	<120	H
Heller et al, 2013[17]	P	76	56	11	65	68	10	78	53	25	SAC	24–48	H
Iosif et al, 2015[18]	P	38	53	7	31	–	–	49	48	1	FD	<48	H
Ishibashi et al, 2006[15]	R	74	–	–	–	29	45	74	63	11	C, BAC	<48	H
Kang et al, 2013[6]	R	343	–	99	283[a]	0	382	382	323	59	C, SAC, BAC	–	M
Kang et al, 2013[24]	P	40	54.8	13	27	0	40	40	33	7	C, SAC	<24	M
Kim et al, 2013[11]	R	90	58	20	72[a]	0	92	92	78	14	C	<24	M
Kim et al, 2014[10]	R	58	–	23	35	0	62	62	–	–	C, SAC	23–46	M
Kim et al, 2016[27]	R	309	–	84	225	0	338	338	306	32	C, SAC	24–48	M
McGuinness et al, 2015[33]	P	31	56	4	27	8	25	33	30	3	FD	48–240	H
Nagahata et al, 2011[34]	R	14	58.6	1	13	0	14	14	14	0	C, BAC	<96	M
Nishikawa et al, 2013[4]	R	154	58.8	37	117	0	157	157	108	49	C, SAC, BAC	48–120	M
Park et al, 2016[5]	R	271	57.2	68	203	0	271	271	226	45	C, SAC, BAC	24	L
Rordorf et al, 2001[9]	P	14	57.2	4	10	0	14	14	14	0	C, BAC	<48	M
Sim and Shin, 2012[8]	P	39	57.7	11	28	26	13	39	32	7	C, SAC, BAC	<48	M
Soeda et al, 2003[13]	R	26	60	8	18	0	26	26	0	26	C, BAC	48–120	M
Takigawa et al, 2014[14]	R	119	62.9	30	89	0	119	119	95	24	SAC, BAC	24	M
Tan et al, 2015[19]	R	74	60	12	62	0	74	74	58	16	FD	<24	M

Note:—R indicates retrospective; P, prospective; C, coiling only; SAC, stent-assisted coiling; BAC, balloon-assisted coiling; FD, flow diversion; H, high; M, moderate; L, low; –, data was not available.

[a] Authors reported sex distribution by number of aneurysms.

performed by using the following keywords: "coiling," "pipeline," "flow diverter," "aneurysm," "endovascular," "diffusion," "restricted diffusion," "MR imaging," and "stroke" in both "AND" and "OR" combinations. The search was limited to English articles published from 2000 to April 2016. The inclusion criteria were the following: 1) consecutive series of ≥10 patients who underwent endovascular treatment of intracranial aneurysms with endosaccular coiling or flow diversion, and 2) DWI examination performed within 5 days of endovascular treatment in all patients. Exclusion criteria were the following: 1) <10 patients in the series, 2) series that reported outcomes of parent artery occlusion, 3) studies in which only symptomatic patients underwent postoperative DWI imaging, 4) studies that did not provide the number of patients who had no lesions on DWI, and 5) studies for which an English translation was not available. Two independent reviewers determined whether the articles met the inclusion and exclusion criteria for this systematic review and meta-analysis. The following baseline information was extracted from each study: number of patients, mean age, sex distribution, mean aneurysm size, aneurysm location, and rupture status.

Outcomes and Patient Groups

The primary outcome of this study was the overall rate of DWI positive for thromboembolic events following endovascular aneurysm treatment. We also performed subgroup analyses stratified by treatment type (ie, coiling, stent-assisted coiling, balloon-assisted coiling, and flow diversion), patient sex (male versus female), aneurysm size (small versus large/giant), aneurysm location (anterior versus posterior circulation), and aneurysm rupture status (ruptured versus unruptured). Small aneurysms were defined as those with a maximum diameter of <10 mm.

Risk of Bias Assessment

We selected items from the Newcastle-Ottawa Scale for nonrandomized trials to fit the type of included studies. We queried the following study characteristics: 1) patient groups clearly defined, 2) outcomes clearly reported, 3) outcomes clearly reported for each patient group studied, 4) imaging interpreted by an independent reader or interpreted by the operator, 5) readers blinded to the clinical status of the patient, 6) multiple readers used and interobserver agreement assessed, and 7) the study followed a predefined study protocol in which all patients underwent MR imaging at the same time point.

Statistical Analysis

We estimated from each study the cumulative incidence (event rate at the end of the study) and 95% confidence interval. Because we anticipated marked heterogeneity in the populations and interventions across the various included studies, a random-effects model was used to pool incident rates across studies.[20] Variance was estimated by using the Freeman-Tukey Double Arcsine Transformation.[21,22] The I^2 statistic was used to express the proportion of inconsistency that is not attributable to chance.[23] Analysis was conducted by using the STATA Statistical Software for 2015: Release 14 (StataCorp, College Station, Texas).

RESULTS

Search Results and Patient Population

The literature search yielded 533 records, of which 424 were deemed irrelevant by reading the title and abstract alone. Of the remaining 109 records, 45 were duplicates, abstracts only, or review articles. Forty-two did not meet our minimum sample size criterion of ≥10 patients or did not provide data for the number

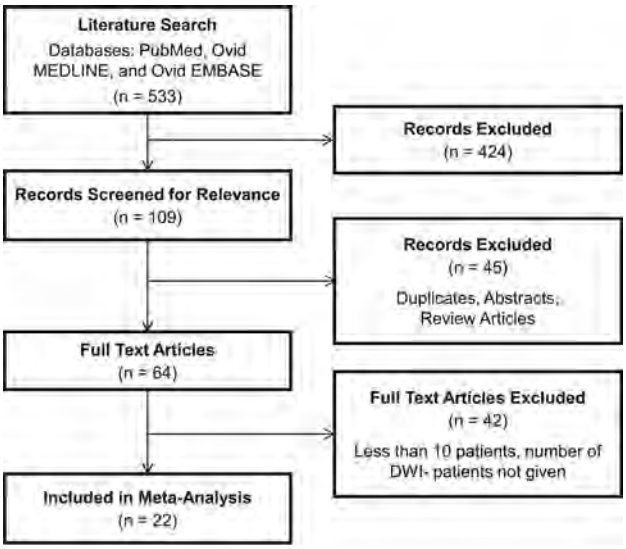

FIG 1. Flow chart illustrating study selection.

Table 2: Incidence of ischemic strokes as measured by restricted diffusion with DWI

	% DWI+ (95% CI)	I^2	*P* Value
Overall	49 (42–56)	90	–
Location			
Anterior	35 (25–47)	76	.83
Posterior	31 (9–59)	87	
Treatment type			
Coiling alone	45 (33–56)	86	Ref
Balloon-assisted coiling	44 (29–60)	54	.99
Stent-assisted coiling	43 (24–63)	93	.89
Flow diversion	67 (46–85)	87	.07
Sex			
Male	32 (17–48)	58	.47
Female	41 (28–54)	84	
Rupture status			
Ruptured	42 (17–69)	90	.87
Unruptured	44 (35–53)	87	
Size			
Small	52 (39–65)	62	.55
Large	61 (34–86)	38	

Note:—Ref indicates reference.

of patients with no DWI positive for lesions. Twenty-two studies met all of our inclusion criteria and were included in the meta-analysis. A summary of these studies is provided in Table 1. The PRISMA flow diagram is provided in Fig 1.

In total, 2148 patients with 2268 aneurysms were included in this study. Five hundred ninety-two aneurysms were treated with coiling alone; 376, with stent-assisted coiling; 162, with balloon-assisted coiling; and 178, with flow diversion. Two hundred ninety-two aneurysms had ruptured at the time of treatment, while 1927 aneurysms remained unruptured. Four hundred thirty-six aneurysms were located in the anterior circulation, and 129 were in the posterior circulation.

Study Outcomes

The rates of postprocedural DWI positive for thromboembolic events are summarized in Table 2. Overall, 49% of all patients had DWI positive for lesions following endovascular treatment of cerebral aneurysms (95% CI, 42%–56%) (Fig 2). The rate of infarcts in patients treated with simple coiling was 45% (95% CI, 33%–56%). This was no different from those treated with balloon-assisted coiling (44%; 95% CI, 29%–60%; $P = .99$) or stent-assisted coiling (43%; 95% CI, 24%–63%; $P = .89$). The rate of DWI positive for lesions in patients treated with flow diversion was 67% and approached statistical significance (95% CI, 46%–85%; $P = .07$) (Fig 3).

Patient sex was not associated with the rate of DWI positive for lesions because 32% (95% CI, 17%–48%) of men and 41% (95% CI, 28%–54%) of women had postoperative infarcts ($P = .47$). In comparing aneurysm size, the rate of DWI positive for thromboembolic events was 52% (95% CI, 39%–65%) for small aneurysms and 61% (95% CI, 34%–86%) for large aneurysms ($P = .55$). The rate of infarcts was not different between patients with aneurysms in the anterior circulation (35%; 95% CI, 25%–47%) and posterior circulation (31%; 95% CI, 9%–59%; $P = .83$). Aneurysm rupture status was not associated with the rate of stroke because 42% (95% CI, 17%–69%) of patients with ruptured aneurysms and 44% (95% CI, 35%–53%; $P = .87$) of those with unruptured aneurysms had DWI positive for lesions.

Study Heterogeneity and Risk of Bias

I^2 values were >50% for all outcomes, with the exception of postoperative infarct rate for large aneurysms, indicating substantial heterogeneity. Of the 22 studies included in this meta-analysis, 14 were retrospective and 8 were prospective. Five studies had a high risk of bias, 16 studies had a moderate risk of bias, and 1 study had a low risk of bias as determined by our modified Newcastle-Ottawa Scale criterion.

DISCUSSION

This systematic review and meta-analysis demonstrated that the overall incidence of DWI positive for thromboembolic events following endovascular treatment of intracranial aneurysms is approximately 50%, with no significant difference between coiling with and without adjunct devices. In addition, there was no association between postoperative DWI positive for lesions and patient sex or aneurysm location, size, or rupture status. There was a trend toward a higher infarct rate among patients treated with flow diversion compared with traditional endovascular coiling techniques; however, this did not reach statistical significance. Because these so-called "clinically silent strokes" have been associated with cognitive decline, depression, and future stroke, these findings highlight the importance of finding new techniques aimed at reducing perioperative infarcts.[1-3,24]

Several studies have identified risk factors for both symptomatic and asymptomatic lesions positive on DWI following treatment with traditional endovascular techniques. These include large aneurysm size, female sex, age, atherosclerotic disease, and protruding loops of coil.[8,13,25,26] Some studies have found that balloon-assisted and stent-assisted coiling increased the risk of thromboembolic complications, while others found no association.[5,6,8-10,13-15,27] In contrast, our large study demonstrates that no anatomic or demographic risk factors are associated with this particular postoperative complication. Prior studies have demonstrated that aggressive antiplatelet and anticoagulation therapy is also associated with a reduction in perioperative ischemic

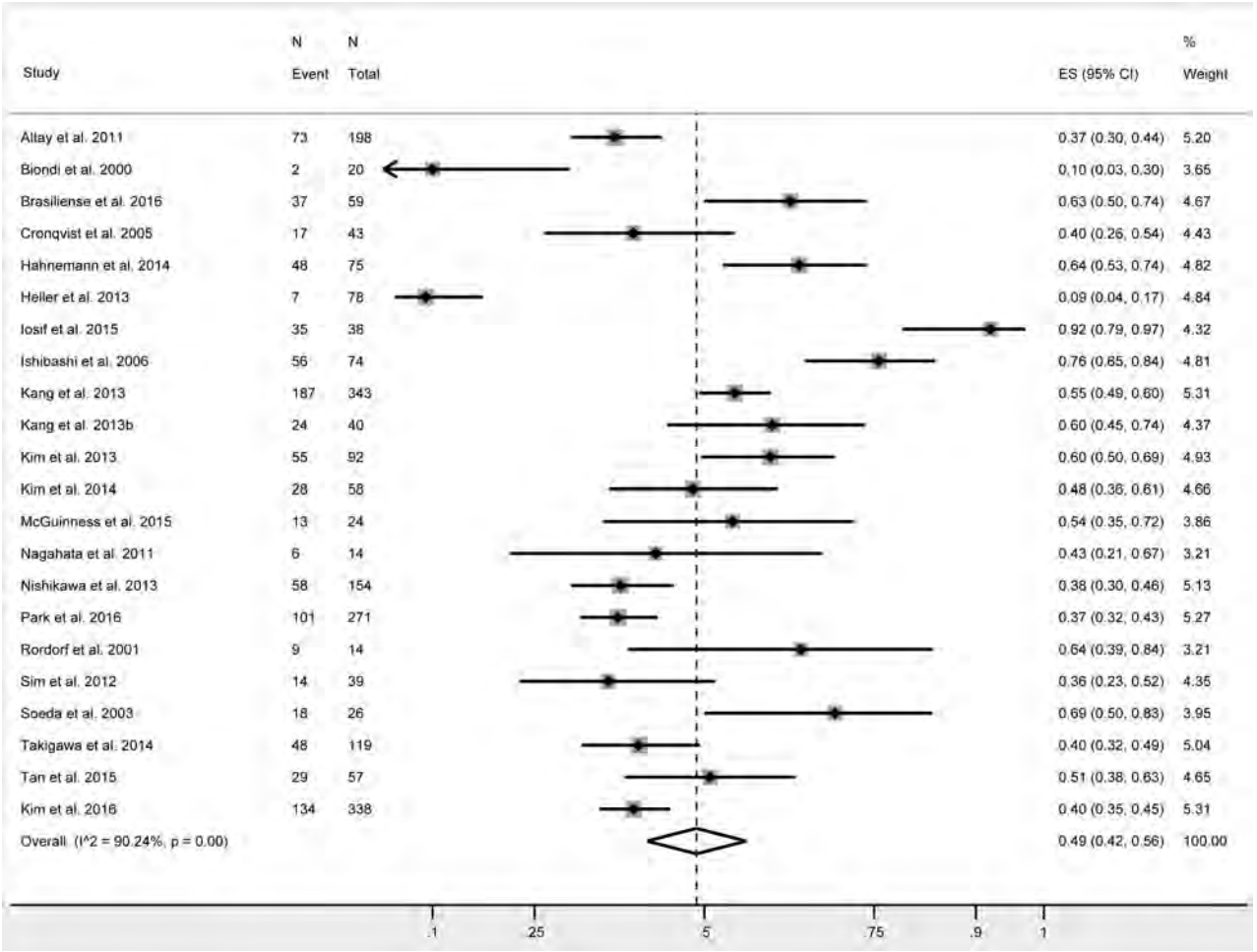

FIG 2. Forest plot demonstrating the overall rate of silent infarcts following endovascular aneurysm treatment.

events,[28] but our meta-analysis did not consider this parameter because it was inconsistently reported by the included studies.

One of the interesting findings from our meta-analysis was the trend toward a higher rate of silent infarcts in patients treated with flow diverters compared with those treated with coils alone. While both coils and flow diverters are inherently thrombogenic, treatment with flow diversion is generally associated with a higher rate of thromboembolic complications than with coiling alone.[19] Because flow diverters are high-density metal constructs with large endoluminal surface areas, these devices pose a higher risk of thrombosis in the lumen of the parent artery. Shearing stress from blood flow through the device can cause these thrombi to embolize. In contrast, thrombi that form on lower density coils are less likely to embolize into the bloodstream because of the placement of the coil in the aneurysm sac outside the cerebral circulation.[29]

The high rate of asymptomatic DWI positive for lesions raises questions about the clinical relevance of these tiny strokes. Most thromboembolic events likely do not present as focal neurologic deficits simply because they occur in noneloquent locations. However, many of these so-called "clinically silent" lesions may actually give rise to nongross neurologic deficits. Thus, studies have prospectively explored the relationship between DWI positive for lesions and neuropsychological examination performance and have yielded variable results. Studies from the cardiac literature have found that patients with DWI lesions post-cardiac endovascular and surgical procedures have reduced cognitive function on neuropsychological examinations.[30,31] However, studies from the coiling and flow-diversion literature have demonstrated no association between the presence of DWI lesions and neuropsychological examination performance.[24,18] Given these conflicting results, the relevance of DWI positive for lesions to cognitive function remains uncertain, and further study is needed to evaluate the long-term consequences of these infarcts.

Limitations

Our study has several limitations. Many of the studies included in our analysis were retrospective, noncomparative, and nonrandomized. There was substantial variability in methods and the detail in which outcomes were reported. For example, the type of antiplatelet therapy and the time elapsed between the procedures and imaging were inconsistent between studies. Additionally, many articles gave an incomplete account of patient demographics, symptomatic status, and neurologic outcomes. Our study also has publication bias, and we acknowledge the methodologic differences between institutions and the tendency for retrospective studies to only publish positive results. We did not compare outcomes based on the type of anticoagulation and antiplatelet therapy, a parameter that likely influences clot formation and isch-

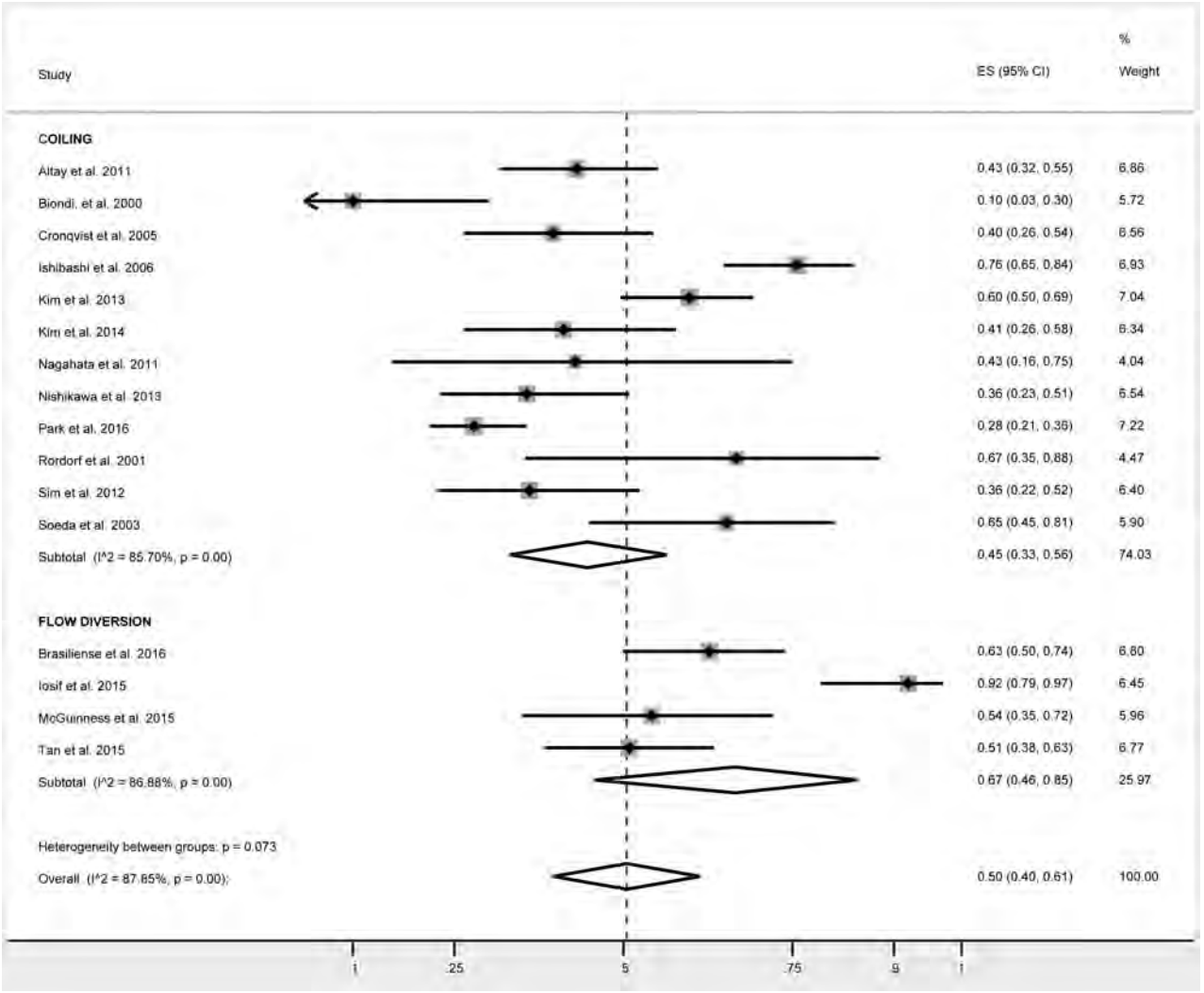

FIG 3. Forest plot demonstrating the overall rate of silent infarcts following treatment with coiling and flow diversion.

emic stroke incidence. Similarly, we did not consider the lesion load of each patient and the relationship of this value to predicting symptoms. MR imaging techniques likely differ from institution to institution. It is possible that differences in MR imaging field strength, B0 values, and section thickness affect the overall rate of DWI lesion detection. It is important to consider these limitations when interpreting the results of this meta-analysis.

CONCLUSIONS

Our meta-analysis, which included >2000 patients undergoing endovascular treatment of intracranial aneurysms, demonstrated that the overall rate of postoperative DWI positive for thromboembolic events is approximately 50%, with no differences when comparing coiling techniques, aneurysm characteristics, or patient sex. There was a trend toward a higher rate of thromboembolic complications among those treated with flow diverters compared with those treated with coiling alone. Because the long-term effects of these so-called silent infarcts are unclear, further work is needed to develop techniques to reduce the rate of thromboembolic complications associated with endovascular aneurysm treatment. Given the limitations of this meta-analysis, prospective studies with uniform methods are needed to confirm these results.

Disclosures: David F. Kallmes—*UNRELATED*: *Board Membership*: GE Healthcare, *Comments*: Cost-Effectiveness Board*; *Consultancy*: Medtronic, Minnetronix, *Comments*: planning clinical trials, Data and Safety Monitoring Board Chair*; *Grants/Grants Pending*: MicroVention, Medtronic, SurModics, Sequent, NeuroSigma, Codman, *Comments*: clinical trials and preclinical research*; *Travel/Accommodations/Meeting Expenses Unrelated to Activities Listed*: Medtronic, *Comments*: presentation at an FDA panel meeting.* Giuseppe Lanzino—*UNRELATED*: *Consultancy*: Covidien/Medtronic.* *Money paid to the institution.

REFERENCES

1. Kang DW, Lattimore SU, Latour LL, et al. **Silent ischemic lesion recurrence on magnetic resonance imaging predicts subsequent clinical vascular events.** *Arch Neurol* 2006;63:1730–33 CrossRef Medline
2. Vermeer SE, Prins ND, den Heijer T, et al. **Silent brain infarcts and the risk of dementia and cognitive decline.** *N Engl J Med* 2003;348:1215–22 CrossRef Medline
3. Choi SH, Na DL, Chung CS, et al**. Diffusion-weighted MRI in vascular dementia.** *Neurology* 2000;54:83–89 CrossRef Medline
4. Nishikawa Y, Satow T, Takagi T, et al. **Efficacy and safety of single**

versus dual antiplatelet therapy for coiling of unruptured aneurysms. *J Stroke Cerebrovasc Dis* 2013;22:650–55 CrossRef Medline
5. Park JC, Lee DH, Kim JK, et al. **Microembolism after endovascular coiling of unruptured cerebral aneurysms: incidence and risk factors.** *J Neurosurg* 2016;124:777–83 CrossRef Medline
6. Kang DH, Kim BM, Kim DJ, et al. **MR-DWI-positive lesions and symptomatic ischemic complications after coiling of unruptured intracranial aneurysms.** *Stroke* 2013;44:789–91 CrossRef Medline
7. Hahnemann ML, Ringelstein A, Sandalcioglu IE, et al. **Silent embolism after stent-assisted coiling of cerebral aneurysms: diffusion-weighted MRI study of 75 cases.** *J Neurointerv Surg* 2014;6:461–65 CrossRef Medline
8. Sim SY, Shin YS. **Silent microembolism on diffusion-weighted MRI after coil embolization of cerebral aneurysms.** *Neurointervention* 2012;7:77–84 CrossRef Medline
9. Rordorf G, Bellon RJ, Budzik RF Jr, et al. **Silent thromboembolic events associated with the treatment of unruptured cerebral aneurysms by use of Guglielmi detachable coils: prospective study applying diffusion-weighted imaging.** *AJNR Am J Neuroradiol* 2001; 22:5–10 Medline
10. Kim B, Kim K, Jeon P, et al. **Thromboembolic complications in patients with clopidogrel resistance after coil embolization for unruptured intracranial aneurysms.** *AJNR Am J Neuroradiol* 2014;35: 1786–92 CrossRef Medline
11. Kim MJ, Lim YC, Oh SY, et al. **Thromboembolic events associated with electrolytic detachment of Guglielmi detachable coils and target coils: comparison with use of diffusion-weighted MR imaging.** *J Korean Neurosurg Soc* 2013;54:19–24 CrossRef Medline
12. Altay T, Kang HI, Woo HH, et al. **Thromboembolic events associated with endovascular treatment of cerebral aneurysms.** *J Neurointerv Surg* 2011;3:147–50 CrossRef Medline
13. Soeda A, Sakai N, Murao K, et al. **Thromboembolic events associated with Guglielmi detachable coil embolization with use of diffusion-weighted MR imaging, part II: detection of the microemboli proximal to cerebral aneurysm.** *AJNR Am J Neuroradiol* 2003;24: 2035–38 Medline
14. Takigawa T, Suzuki K, Sugiura Y, et al. **Thromboembolic events associated with single balloon-, double balloon-, and stent-assisted coil embolization of asymptomatic unruptured cerebral aneurysms: evaluation with diffusion-weighted MR imaging.** *Neuroradiology* 2014;56: 1079–86 CrossRef Medline
15. Ishibashi T, Murayama Y, Saguchi T, et al. **Thromboembolic events during endovascular coil embolization of cerebral aneurysms.** *Interv Neuroradiol* 2006;12:112–16 Medline
16. Brasiliense LB, Stanley MA, Grewal SS, et al. **Silent ischemic events after Pipeline embolization device: a prospective evaluation with MR diffusion-weighted imaging.** *J Neurointerv Surg* 2016 Jan 8. [Epub ahead of print] Medline
17. Heller RS, Dandamudi V, Calnan D, et al. **Neuroform intracranial stenting for aneurysms using simple and multi-stent technique is associated with low risk of magnetic resonance diffusion-weighted imaging lesions.** *Neurosurgery* 2013;73:582–90; discussion 590–91 CrossRef Medline
18. Iosif C, Camilleri Y, Saleme S, et al. **Diffusion-weighted imaging-detected ischemic lesions associated with flow-diverting stents in intracranial aneurysms: safety, potential mechanisms, clinical outcome, and concerns.** *J Neurosurg* 2015;122:627–36 CrossRef Medline
19. Tan LA, Keigher KM, Munich SA, et al. **Thromboembolic complications with Pipeline Embolization Device placement: impact of procedure time, number of stents and pre-procedure P2Y12 reaction unit (PRU) value.** *J Neurointerv Surg* 2015;7:217–21 CrossRef Medline
20. DerSimonian R, Laird N. **Meta-analysis in clinical trials.** *Control Clin Trials* 1986;7:177–88 CrossRef Medline
21. Barendregt JJ, Doi SA, Lee YY, et al. **Meta-analysis of prevalence.** *J Epidemiol Community Health* 2013;67:974–78 CrossRef Medline
22. Freeman MF, Tukey JW. **Transformations related to the angular and the square root.** *The Annals of Mathematical Statistics* 1950;21: 607–11 CrossRef
23. Higgins JP, Thompson SG, Deeks JJ, et al. **Measuring inconsistency in meta-analyses.** *BMJ* 2003;327:557–60 CrossRef Medline
24. Kang DH, Hwang YH, Kim YS, et al. **Cognitive outcome and clinically silent thromboembolic events after coiling of asymptomatic unruptured intracranial aneurysms.** *Neurosurgery* 2013;72:638–45; discussion 645 CrossRef Medline
25. Biondi A, Oppenheim C, Vivas E, et al. **Cerebral aneurysms treated by Guglielmi detachable coils: evaluation with diffusion-weighted MR imaging.** *AJNR Am J Neuroradiol* 2000;21:957–63 Medline
26. Soeda A, Sakai N, Sakai H, et al. **Thromboembolic events associated with Guglielmi detachable coil embolization of asymptomatic cerebral aneurysms: evaluation of 66 consecutive cases with use of diffusion-weighted MR imaging.** *AJNR Am J Neuroradiol* 2003;24: 127–32 Medline
27. Kim MS, Jo KI, Yeon JY, et al. **Association between postprocedural infarction and antiplatelet drug resistance after coiling for unruptured intracranial aneurysms.** *AJNR Am J Neuroradiol* 2016;37: 1099–105 CrossRef Medline
28. Pelz DM, Lownie SP, Fox AJ. **Thromboembolic events associated with the treatment of cerebral aneurysms with Guglielmi detachable coils.** *AJNR Am J Neuroradiol* 1998;19:1541–47 Medline
29. Derdeyn CP, Cross DT 3rd, Moran CJ, et al. **Postprocedure ischemic events after treatment of intracranial aneurysms with Guglielmi detachable coils.** *J Neurosurg* 2002;96:837–43 CrossRef Medline
30. Lund C, Nes RB, Ugelstad TP, et al. **Cerebral emboli during left heart catheterization may cause acute brain injury.** *Eur Heart J* 2005;26: 1269–75 CrossRef Medline
31. Restrepo L, Wityk RJ, Grega MA, et al. **Diffusion- and perfusion-weighted magnetic resonance imaging of the brain before and after coronary artery bypass grafting surgery.** *Stroke* 2002;33:2909–15 CrossRef Medline
32. Cronqvist M, Wirestam R, Ramgren B, et al. **Diffusion and perfusion MRI in patients with ruptured and unruptured intracranial aneurysms treated by endovascular coiling: complications, procedural results, MR findings and clinical outcome.** *Neuroradiology* 2005;47: 855–73 CrossRef Medline
33. McGuinness BJ, Memon S, Hope JK. **Prospective study of early MRI appearances following flow-diverting stent placement for intracranial aneurysms.** *AJNR Am J Neuroradiol* 2015;36:943–48 CrossRef Medline
34. Nagahata M, Kondo R, Saito S, et al. **Which factors increase procedural thromboembolic events in patients with unruptured paraclinoid internal carotid artery aneurysm treated by coil embolization?** *Neuroradiol J* 2011;24:712–14 CrossRef Medline

Middle Cerebral Artery Bifurcation Aneurysms Treated by Extrasaccular Flow Diverters: Midterm Angiographic Evolution and Clinical Outcome

C. Iosif, C. Mounayer, K. Yavuz, S. Saleme, S. Geyik, H.S. Cekirge, and I. Saatci

ABSTRACT

BACKGROUND AND PURPOSE: Flow diverters have been increasingly used lately in off-label, distal intracranial aneurysm treatments. Our aim was to evaluate the effectiveness of flow diverters in the treatment of middle cerebral artery bifurcation aneurysms and to analyze midterm angiographic patterns of regional flow modifications for safety and clinical outcomes.

MATERIALS AND METHODS: Consecutive patients treated from January 2010 to December 2014 by the authors by using endovascular flow-diverting stents for MCA bifurcation aneurysms were evaluated retrospectively with prospectively maintained data. All patients had been followed for at least 12 months after treatment, with at least 2 control angiograms; regional flow-related angiographic modifications were registered by using a new angiographic outcome scale for flow diverters. Data were analyzed with emphasis on procedure-related events, angiographic results, and clinical outcome.

RESULTS: Fifty-eight patients were included in the study, with 63 MCA bifurcation aneurysms; 13 of these were large and giant. Pretreatment mRS was 0 for 12 patients (20.7%), 1 for 41 (70.7%), and 2 for 5 patients (8.6%). Six-month control revealed mRS 0–2 for 57 (98.3%) patients and 3 for 1 (1.7%) patient. Procedure-related morbidity and mortality were 8.6% (5/58) and 0%, respectively. From 95% of still circulating immediate postprocedure angiographic outcomes, 68% progressed to aneurysm occlusion at 6 months and 95%, to occlusion at 12 months, with a 0% aneurysm rupture rate.

CONCLUSIONS: Flow diverters seem to be an effective treatment alternative for complex MCA bifurcation aneurysms, with reasonable complication rates. Longer angiographic follow-ups are needed to assess the morphologic outcome; immediate subtotal occlusions do not seem to be related to rupture.

ABBREVIATION: FD = flow diverter

Flow-diverter (FD) stents have provided a paradigm shift in endovascular cerebral aneurysm treatment. Initially approved for carotid aneurysms, their use has been extended to include distal intracranial localizations such as MCA aneurysms.[1] Covering intracranial arteries with FDs has recently been the subject of debate. While for localizations such as the posterior communicating artery,[2] side branch coverage does not seem to have clinical consequences for patients, controversy exists regarding MCA branches.

The objectives of our study were to evaluate the clinical and midterm angiographic outcomes of FD stent placement for MCA bifurcation aneurysms with emphasis on the regional flow-induced modifications and their impact; the analysis was performed by using an angiographic classification[3] that takes into account the hemodynamic evolution of the aneurysm and the regional anatomy with time.

MATERIALS AND METHODS

This clinical study included consecutive patients treated by multiple operators in several centers with endovascular flow-diverting stents for saccular MCA bifurcation aneurysms, ruptured and unruptured, during 5 consecutive years (January 2010 to December 2014). The prospectively maintained records of the patients were retrospectively evaluated by 2, and in case of inconsistency, by 3 investigators independently. Initial data of 39 aneurysms were published in 2 previous studies.[4,5]

Received July 22, 2016; accepted after revision September 15.

From the Interventional Neuroradiology Department (C.I., C.M., S.S.), Dupuytren University Hospital (Centre Hospitalier Universitaire Limoges), Limoges, France; Interventional Neuroradiology Department (K.Y.), Ankara University, School of Medicine, Ankara, Turkey; Interventional Neuroradiology Department (S.G.), Memorial HealthCare Group, Istanbul, Turkey; Interventional Neuroradiology Department (I.S.), Yuksek Ihtisas University, Koru Hospital, Ankara, Turkey; and Interventional Neuroradiology Department (H.S.C.), Koru Hospital and Bayındır Hospital, Ankara, Turkey.

Please address correspondence to Christina Iosif, MD, MSc, PhD, 2 Ave Martin Luther King, 87042 Limoges, France; e-mail: christina.iosif@gmail.com, christinaiosif@yahoo.gr

Indicates open access to non-subscribers at www.ajnr.org

http://dx.doi.org/10.3174/ajnr.A5022

Endovascular Technique and Procedure-Related Medication

Therapeutic decisions were made by multidisciplinary consensus between interventional neuroradiologists and neurosurgeons. They were based on patient history, clinical presentation, and DSA; cases considered unfavorable for conventional endovascular treatment and failures or retreatment after previous endovascular or surgical procedures were selected. The patients' preferences were also taken into account, after having been informed of the risks of all potential alternatives. Written consent was always obtained before the intervention.

Antiaggregation protocols have been previously described.[4,6] No patient was treated with <40% platelet inhibition. Since January 2013, the protocol was modified by 2 operators (H.S.C., I.S.): Prasugrel replaced the dual antiplatelet regimen of clopidogrel and aspirin. All patients remained on dual antiaggregation or prasugrel for at least 6 months, continuing with aspirin monotherapy thereafter.

Therapeutic procedure details have been previously reported.[5,7] For uncomplicated cases, single FD coverage and slight oversizing of 0.25 or 0.5 mm in diameter were favored, except for large and giant aneurysms. Systematic oversizing was done to decrease mesh density across the aneurysm neck, to obtain a slower progressive aneurysm occlusion with less risk of abrupt occlusion of the vessel coming off the sac. The presence of clips or stents was not a contraindication for the use of FDs in this study, but the treatment strategy and technical details remained at the discretion of the treating physicians.

Clinical and Imaging Assessment

Patients were clinically assessed with the modified Rankin Scale at each time point. Clinical statuses after treatment and eventual neurologic deficits at discharge or at follow-up were recorded. Any delayed clinical event, transient or permanent, was noted.

Immediate postdeployment DSA included DynaCT (Siemens, Erlangen, Germany) or VasoCT (Philips Healthcare, Best, the Netherlands) with diluted iodinated contrast medium, to assess stent apposition to the arterial wall, in addition to standard and working projections. At least 2 DSAs were performed at 6 and at least 12 months postintervention, including 2D and 3D selective angiographic runs. Results were evaluated according to the Cekirge-Saatci grading scale.[3] Symptomatic narrowing or occlusion indicated occurrence of any transient or permanent symptoms attributed to compromise of the relevant branch; "reopening" indicated that a branch was enhanced better on a later DSA than in a previous study.

Statistical Analysis

The Fisher exact test was used for quantitative data after verifying normality by the De Agostino-Pearson test; the χ^2 test was used for qualitative data. Statistical analyses were performed with appropriate software (Statistica; StatSoft, Tulsa, Oklahoma); the level of statistical significance was $P \leq .05$.

RESULTS

Baseline Population Characteristics

In the 5-year period, 58 consecutive patients (17 men, 41 women; mean age, 52.4 ± 11.1 years; range, 25–74 years) with 63 MCA bifurcation aneurysms were included in this study. Pretreatment mRS was 0 for 12 patients (20.7%), 1 for 41 (70.7%), and 2 for 5 patients (8.6%).

Aneurysm Characteristics

There were 10 large (15.9%) and 3 (4.8%) giant aneurysms, with the remainder being small. Thirty-eight of 63 aneurysms (60.3%) were in the right MCA, and 39.7%, in the left MCA. One aneurysm was treated on day 11 and another on day 1 post-aneurysm rupture (the latter aneurysm had been clipped 1 year before); 9 aneurysms were previously ruptured but were treated after the acute phase.

Fifty-two aneurysms had FDs as the first treatment, and 11, as the retreatment; among the latter group, 1 was a clipping failure and 10 were recurrences (1 previously clipped and 9 previously coiled aneurysms). Before FD treatment, 5/11 were classified as having a neck remnant (45.5%), and 6/11, as having an aneurysm remnant (54.5%), according to the Raymond-Roy classification. The first-treatment aneurysms had a mean aspect ratio of 1.6 ± 0.7 (65%, ≤1.6, and 34.6%, ≤1.2) and a mean dome-to-neck ratio of 1.4 ± 0.5 (73%, ≤1.5).

Treatment and Technical Outcomes

Fifty-seven aneurysms (90.5%) were treated with the Pipeline Embolization Device (PED; Covidien, Irvine, California), 5 (7.9%) were treated with the Flow-Redirection Endoluminal Device (FRED; MicroVention, Tustin, California), and 1 (1.6%), with the Silk flow diverter (Balt Extrusion, Montmorency, France). Most of the aneurysms were treated with single FD coverage (58/63, 92.1%), 2 were covered in a telescopic fashion (3.2%), and there was adjunctive use of coils due to the large size for 3 aneurysms (4.8%). In 3 other cases of single-FD coverage, the FD was deployed in a previously existing conventional intracranial stent.

Of the 63 aneurysms, 23 (36.5%) were treated with prasugrel, and 40 (63.5%), with double antiaggregation with clopidogrel and aspirin. Among the patients medicated with clopidogrel, 10 were rescheduled because of a low level of platelet inhibition and the need for increasing the drug dose and retesting.

Periprocedural complications were absent for 95.3% (60/63) of the treatments, while periprocedural thrombus formation was encountered in 4.8% (3/63) of the cases; the latter was clinically evident as worsening of the clinical situation on awakening in 1 case and resulted in an increase of 2 points on the mRS score at discharge. The absence of peri- or postprocedure rupture (early or delayed) was ensured for all cases during the entire follow-up period.

Clinical Outcomes

Clinical mRS outcomes at discharge from the hospital were 0 for 12 (20.7%) patients, 1 for 41 (70.7%) patients, 2 for 3 (5.2%) patients, and 2 for 2 (3.4%) patients. During the postprocedure hospitalization, 6.9% of the patients (4/58) developed procedure-related ischemic events. One patient (1.7%), with a giant aneurysm, developed a perianeurysmal brain inflammatory reaction in the fourth postprocedural week, which progressively resolved under steroids. One patient (1.7%) developed ischemic stroke at 3

Table 1: Modifications of the mRS throughout the follow-up period

PRE tx		Discharge mRS (*n* = 58)				6-Month mRS (*n* = 58)				≥12-Month mRS (*n* = 58)		
mRS	No. of Patients	0	1	2	3	0	1	2	3	0	1	2
0	12	12	0	0	0	12	0	0	0	12	0	0
1	41	0	37	1[a]	2[a]	26	11	4[a]	1[a]	30	9	3
2	5	0	4	1	1[a]	3	1	0	0[a]	3	1	0
Total	58	12	41	2	3	41	12	4	1	45	10	3

Note:—PRE tx indicates pretreatment values.

[a] Number of patients with clinical worsening in regard to pretreatment clinical status.

Table 2: Immediate postprocedure angiographic results and angiographic outcomes in controls

Cekirge-Saatci Evaluation Scale	Immediate Angiographic Outcome	≥12-Month Angiographic Outcome	Third (Midterm) Angiographic Outcome
1a	3 (4.8%)	18 (28.6%)	16 (40.0%)
1b	0	14 (22.2%)	10 (25.0%)
1c	0	13 (20.6%)	8 (20.0%)
2	0	2 (3.2%)	0
3	1 (1.6%)	1 (1.6%)	1 (2.5%)
4a	30 (47.6%)	0	0
4b	29 (46%)	0	0
5	0	15 (23.8%)	5 (12.5%)
Total	63 (100%)	63 (100%)	40 (100%)
	χ^2, 48.175; *df*, 3	χ^2, 24.524; *df*, 5	χ^2,15.750; *df*, 4
	Significance level, $P < .0001$	Significance level, $P = .0002$	Significance level, $P = .0034$

months postintervention following discontinuation of clopidogrel without consulting the physician.

At 6-month control, mRS scores were 0 for 41 (70.7%) patients, 1 for 12 (20.7%) patients, 2 for 4 (6.9%) patients, and 3 for 1 (1.7%) patient. Clinical outcome at 6 months was good (mRS 0–2) in all except 1 patient (98.3%). Clinical evaluation at the latest follow-up showed an mRS score of 0 for 45 (77.6%) patients, 1 for 10 (17.2%) patients, and 2 for 3 (5.2%) patients. Modifications of the mRS throughout the follow-up period in regard to pretreatment status are shown in Table 1.

The permanent complication rate with poor prognosis (mRS > 2) was 0%. Procedure-related morbidity was 8.6% (5/58). Absence of aneurysm rupture and 0% procedure-related mortality were ensured for the population throughout the follow-up period. Among the patients who had ischemic events or transient symptoms, 4 were treated with clopidogrel and 1, with a prasugrel regimen.

Immediate Postprocedure Angiographic Results and Angiographic Outcomes

Immediate postprocedure angiographic results and angiographic outcomes in controls are summarized in Table 2. Mean follow-up time for the entire group of patients was 22 ± 9 months (95% CI of the mean, 19–24 months). Mean follow-up time for the third control was 28 ± 9 months (95% CI of the mean, 19–60 months). Overall, all except 1 aneurysm (1/40, 2.5%), controlled for >2 years postfollow-up, were either totally occluded or had stable remodeled regional angioarchitecture.

Statistical comparison of the 12-month with the 6-month DSA showed a statistically significant increase in the total occlusion rates for the 12-month controls (χ^2, 113.088; *df*, 25; significance level, $P < .0001$). The statistical comparison between the 12-month and the late midterm DSAs for the patients who had >2 angiographic follow-ups showed that all circulating aneurysms and 55.6% of the stable remodelling cases progressed to total occlusion (χ^2, 19.118; *df*, 2; significance level, $P = .0001$).

From a 5% aneurysm occlusion rate on the immediate postprocedure angiograms, the series progressed to a 94.8% aneurysm occlusion rate at 12 months. None of the aneurysms in this series regressed from partial filling, stable remodelling, or total occlusion to aneurysm recirculation with time.

Covered Branch Analysis and Hemodynamic Impact

Angiographic outcomes regarding jailed branches are summarized in Table 3. The jailed branches were unchanged in 54% of the cases at 6-month follow-up angiography, with stability in the further follow-ups up to 85%. Symptomatic branch occlusion occurred in 2/63 (3.2%), both noted within first 6 months.

Three patients in the study had transient symptoms (DWI negative for ischemic events on MR imaging) attributed to hemodynamic factors during the first postprocedural months. These occurred on mean postprocedural day 33.6 ± 8.6 and resolved completely within 48 hours. One of the patients who developed postprocedure stroke at 24 hours postintervention showed sluggish flow on the final control angiogram at the end of the procedure.

DISCUSSION

MCA bifurcation aneurysm therapeutic strategy has been in dispute for the past few years. While clipping remains the mainstream treatment for these lesions, recent advances in the endovascular therapeutic approaches have involved several alternatives, including balloon remodelling, stent-assisted coiling, and, lately, the use of intra-/extrasaccular flow disrupters. Recent reviews failed to show a clear superiority of one approach over the other[8]; nevertheless, surgery remains the mainstream approach for many cases. At the same time, complex cases, such as those with neighboring aneurysms[9] and previous endovascular or sur-

Table 3: Angiographic outcomes regarding jailed branches

Jailed Branch Fate	6-Month Follow-Up		12-Month Follow-Up		3rd (Midterm) Follow-Up	
Asymptomatic narrowing	18	28.6%	10	15.9%	5	12.5%
Symptomatic narrowing	0	0	0	0	0	0
Asymptomatic occlusion	9	14.3%	0	0	1	2.5%
Symptomatic occlusion	2	3.2%	0	0	0	0
Better opacification or "reopening"	0	0	5	7.9%	0	0
No change	34	54.0%	48	76.2%	34	85.0%
Total	63	100.0%	63	100%	40	100%
	χ^2, 36.365; *df*, 3 Significance level, $P < .0001$		χ^2, 52.667; *df*, 2 Significance level, $P < .0001$		χ^2, 48.650; *df*, 2 Significance level, $P < .0001$	

gical failures,[10] emphasize the need for more alternatives in the neurovascular physician's therapeutic armamentarium.

FD treatments are increasingly being used for distal intracranial aneurysms. Some recent data even suggest better clinical outcomes with FDs than with stent-assisted coiling.[11] A recent study by Caroff et al[12] in 15 patients with MCA bifurcation aneurysms challenged previous studies with endovascular flow-diversion treatments in MCA locations,[4,6,13] including large and fusiform aneurysms,[14] by reporting a 43% ischemic complication rate.

In our study, apart from 1 perianeurysmal inflammatory reaction, reversible with steroid treatment, all other complications were ischemic but were limited to an acceptable rate (8.6%). Three of 4 thrombotic ischemic events in the study occurred with patients treated with clopidogrel, and 1, with prasugrel. Even though all patients were systematically double-tested for resistance, lower thrombotic complications seemed to occur after switching to prasugrel.

Apart from 1 patient in whom clopidogrel was discontinued unauthorized at 3 months, the other 4 cases occurred in the early postprocedural period. In only 1 case was sluggish flow observed in an artery covered by a flow-diverter device in this study. We attribute such a low rate of sluggish flow to 2 main reasons: The first was because we systematically avoided device undersizing, actually preferring oversized FD deployment, resulting in decreased mesh density. The second reason could be the terminal nature of jailed branches. Recent laboratory data showed that terminal-type arteries, when jailed, tend to maintain poststenting flow rates similar to the prestenting ones in the acute poststenting phase; this scenario, in turn, seems related to decreased neointimal coverage of the jailed ostia at 3-month control.[15-17]

In accordance with previous reports, transient symptoms were noted during the first follow-up months.[18] In our opinion, they were not related to in situ thrombotic events but rather to hemodynamic parameters. These events were not positively correlated with branch remodelling or occlusion; on the contrary, they were likely the expression of a regional decrease in perfusion, related to the presence of a moderately developed pial network, which might decrease the pressure gradient inside the jailed branch[17] but was not yet sufficient to compensate for the perfusion requirement.

Progressive vasodilation and compensatory mechanisms were capable of resolving this matter as follows: Either the pial network was insufficient; thus, on follow-up, the jailed branch remained patent (Fig 1) or even became larger than that in previous controls; or the pial network would progressively augment, allowing at the same time, a progressive remodelling (ie, narrowing of the jailed branch; Fig 2). Overall in this study, early complications occurred mainly due to in situ thrombosis, probably related to undetected antiaggregation failures; late complications occurred due to either noncompliance with the antiaggregation regimen or hemodynamic effects. The latter resolved within hours and was not related to side branch occlusions.

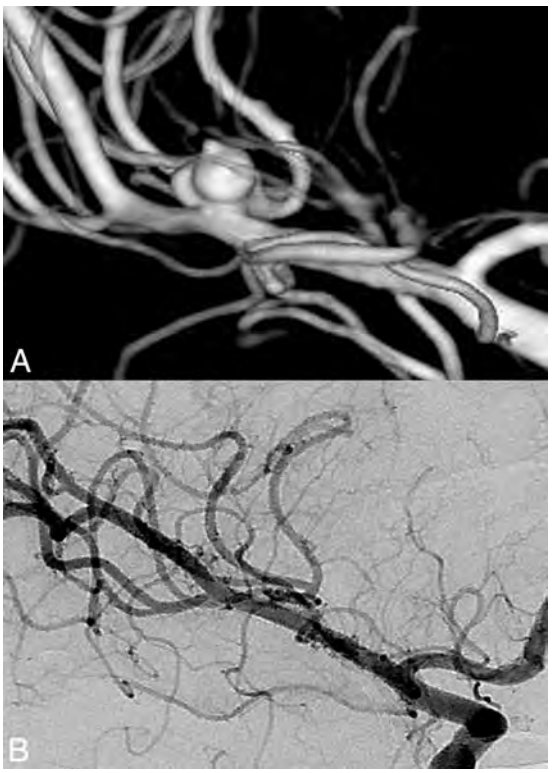

FIG 1. Pretreatment 3D image (*A*) shows a multilobulated right MCA aneurysm with a bleb. Note that the superior trunk originates from the sac. Control DSA 1 year after Pipeline Embolization Device placement. An image at a corresponding angle (*B*) demonstrates total occlusion of the aneurysm with the branch coming off the patent sac (Cekirge-Saatci class 1a occlusion).

Contrary to the recent published results from a clinical study on fusiform/dissecting MCA aneurysms, which positively associated total occlusion rates with side branch occlusion,[19] our results did not show a correlation between side branch and saccular occlusion. On the contrary, an important percentage of the jailed branches remained patent. Furthermore, in cases in which the jailed branch showed transient symptoms during the initial postprocedural months, these branches tended to show unchanged caliber in the control angiographies.

Six-month angiographic controls in our study already showed important results in terms of aneurysm patency, but longer fol-

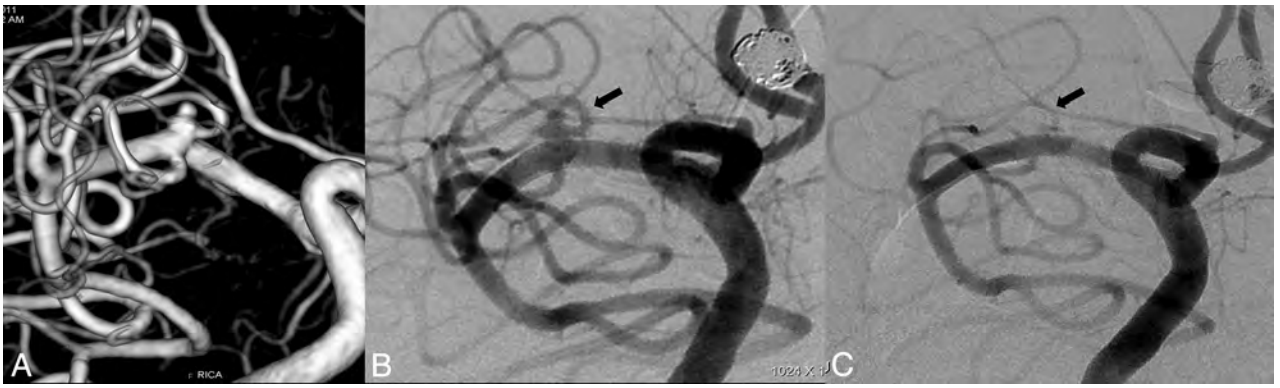

FIG 2. Pretreatment 3D (*A*) and 2D (*B*) images show a small, irregular right MCA aneurysm with an early bifurcating branch (*arrow*) originating from the sac. Corresponding DSA obtained 1 year after PED treatment (*C*) confirms the total occlusion of the aneurysm; the branch coming off the sac (*arrow*) is reduced in caliber (Cekirge-Saatci class 1b occlusion).

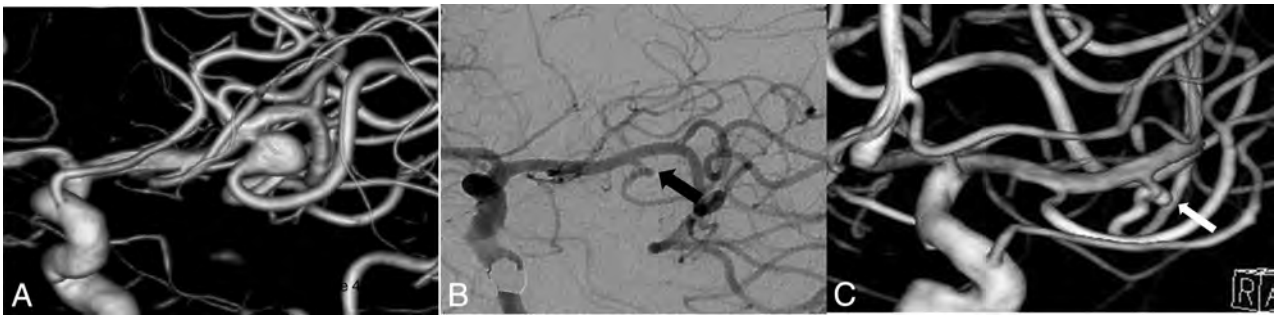

FIG 3. Pretreatment 3D image (*A*) shows a left MCA aneurysm with the inferior trunk coming off the sac. Posttreatment 1- (*B*) and 2-year (*C*) angiograms confirm the stable occlusion of the sac with the patent inferior trunk (*arrow*) having a tortuous origin (Cekirge-Saatci class 5 occlusion).

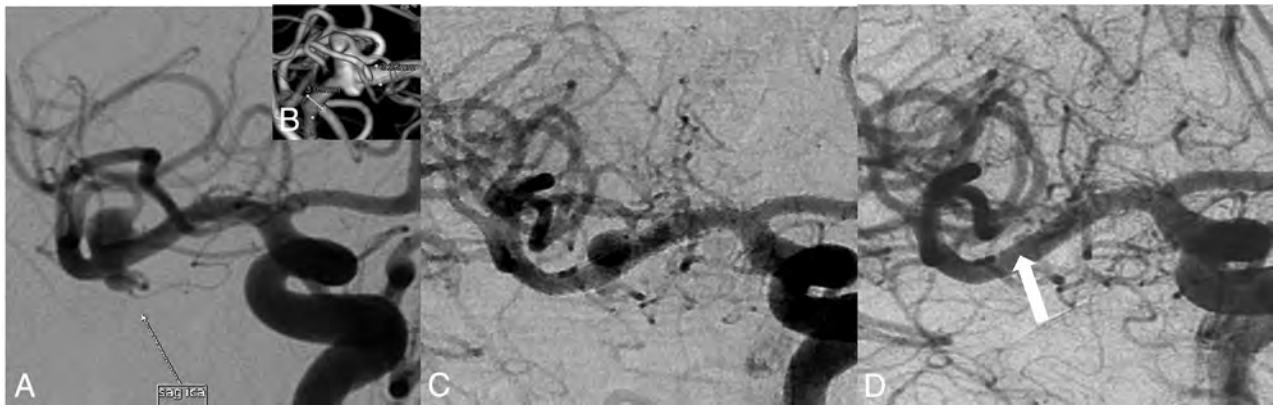

FIG 4. Pretreatment 2D (*A*) and 3D (*B*) images show an irregular right MCA aneurysm with a bleb. Note that the aneurysm has no neck, and a branch is originating from the sac. Six-month control DSA image at a corresponding angle (*C*) reveals the sac decreased in size, but still filling (class 2). Correlative 1-year control DSA image demonstrates total occlusion of the aneurysm sac with the relevant branch filling retrogradely (*white arrow*) (ie, Cekirge-Saatci class 1c occlusion).

low-ups revealed even further significant increases in total occlusion rates, as opposed to the study by Topcuoglu et al.[19] In this study, 93% of immediate postprocedure circulating aneurysms progressed to 68% occlusion at 6 months and to 95% occlusion at 1 year. In this series, the rupture rate was 0% within the first year and beyond, similar to other recently published data.[4,12,13]

In this cohort of MCA bifurcation aneurysms, the flow-diversion effect, even though angiographically slow and progressive, still protected the aneurysms from rupture throughout the follow-up period (Fig 3). Angiographic assessment should probably be performed systematically later than the usual one (ie, 6 months) performed for other endovascular techniques (Fig 4). To our understanding, the Cekirge-Saatci angiographic evaluation scale seems more adapted for the evaluation of FD treatment, providing a more comprehensive evaluation not only of aneurysmal occlusion but of the whole hemodynamic modification process with time.

A recent study argued that the apparent shape of the covered branches and their disposition[20] as to the aneurysm sac play an important role in both side branch patency and aneurysm occlu-

sion. However, our observation is different in that these issues are more relevant to the terminal nature of the MCA bifurcation branches and the variability in pial anastomoses. The pressure gradient along a terminal artery is expected to persist after jailing, thus allowing the branch to remain patent.[21] This feature may delay the process of aneurysm remodelling toward occlusion, but as found in the study presented herein, in the later follow-up, the aneurysms were occluded, with occlusion of the jailed branch not being a prerequisite.

In accordance with other reported cases,[6,22] some patients exhibited an increased caliber of the jailed branch on later angiographic follow-up. These observations support the hypothesis that side branch remodelling after flow diversion is a hemodynamic process of constant re-adaptation, which can potentially evolve either way, not only toward progressive occlusion but also toward limiting endothelial coverage.[15,17]

Similar to our results, other recent publications have shown good clinical and anatomic results with flow diverters for MCA bifurcation aneurysms. Zanaty et al,[13] in their series of complex large, giant, and bifurcation MCA aneurysms treated with the PED, reported its effectiveness with reasonable complication rates.

Recent studies report promising results from intrasaccular flow-disrupting devices; nevertheless, initial complete occlusion rates were relatively low.[23] Endosaccular flow disrupters have a specific shape and are made of nitinol filaments, which preserve their shape-memory properties; thus, they may not be adapted to every aneurysm anatomy or side branch configuration. Additionally, their hyperelastic properties along with the thrombus formation inside the device presumably play a role in the deformation described in the follow-up of some cases.

Even though surgical clipping has been considered a stable treatment of aneurysm recurrences, several studies have shown that this is not an absolute fact; clipped aneurysms may recur.[24] Retreatment in these cases can be complicated for both the endovascular and surgical approaches. Adhesions from previous surgery, massive periprocedural bleeding, and anatomic complexity are issues to consider in microsurgical retreatment.[24] Successful endovascular retreatments, though feasible,[25,26] may be technically challenging for conventional techniques. Recent bibliographic data showed good outcomes with FDs in aneurysm recurrences after surgical clipping.[25,27] In 2 series presented by Cekirge et al[25] and Ding et al,[27] 2 cases of clip failures and 3 cases of previous stent treatments were successfully retreated by FD embolization with very good results.

Large or giant, partially thrombosed aneurysms may be equally challenging for classic endovascular and microsurgical techniques; in this series, almost 21% of the cases were large/giant aneurysms. Flow diversion may not be the first-choice treatment for every MCA aneurysm, but complex cases may be successfully addressed, provided that some technical rules are respected, such as effective antiaggregation, careful sizing with slight oversizing, and meticulous control of stent apposition.

FDs are devices that appear to work in synergy with the dynamic vascular remodelling processes of brain; the technical strategy is to favor the regional remodelling to the patient's advantage. We are still a long way from completely understanding and exploiting the full potential of these processes. Further research is needed, and until then, moderation in our conclusions would be more appropriate. FD use should be reserved for complex cases, and its results are to be evaluated with longer follow-ups. Nevertheless, taking extrasaccular flow diverters out of our therapeutic armamentarium for MCA bifurcation aneurysms seems just as imprudent as using them as first-line treatment.

Limitations

Even though the clinical and angiographic data bases for this cohort were maintained prospectively, the study design is retrospective; furthermore, the number of patients remains limited. Nevertheless, the conclusions of this study should be investigated with larger, multicenter studies.

CONCLUSIONS

Flow diverters seem to be an effective treatment alternative for complex MCA bifurcation aneurysms, with reasonable complication rates. An effective antiaggregation regimen is mandatory. Longer angiographic follow-ups are needed to assess the morphologic outcome; immediate subtotal occlusion was not related to rupture in the present study. The new angiographic scale seems adapted to the evaluation of the regional vascular remodelling post-FD stent placement.

Disclosures: H. Saruhan Cekirge—*UNRELATED*: *Consultancy*: Medtronic, MicroVention, Sequent Medical. Isil Saatci—*UNRELATED*: *Consultancy*: Medtronic.

REFERENCES

1. Pistocchi S, Blanc R, Bartolini B, et al. **Flow diverters at and beyond the level of the circle of Willis for the treatment of intracranial aneurysms.** *Stroke* 2012;43:1032–38 CrossRef Medline
2. Brinjikji W, Lanzino G, Cloft HJ, et al. **Patency of the posterior communicating artery after flow diversion treatment of internal carotid artery aneurysms.** *Clin Neurol Neurosurg* 2014;120:84–88 CrossRef Medline
3. Cekirge HS, Saatci I. **A new aneurysm occlusion classification after the impact of flow modification.** *AJNR Am J Neuroradiol* 2016;37:19–24 CrossRef Medline
4. Yavuz K, Geyik S, Saatci I, et al. **Endovascular treatment of middle cerebral artery aneurysms with flow modification with the use of the Pipeline embolization device.** *AJNR Am J Neuroradiol* 2014;35:529–35 CrossRef Medline
5. Saleme S, Iosif C, Ponomarjova S, et al. **Flow-diverting stents for intracranial bifurcation aneurysm treatment.** *Neurosurgery* 2014;75:623–31; quiz 631 CrossRef Medline
6. Iosif C, Camilleri Y, Saleme S, et al. **Diffusion-weighted imaging-detected ischemic lesions associated with flow-diverting stents in intracranial aneurysms: safety, potential mechanisms, clinical outcome, and concerns.** *J Neurosurg* 2015;122:627–36 CrossRef Medline
7. Saatci I, Yavuz K, Ozer C, et al. **Treatment of intracranial aneurysms using the Pipeline flow-diverter embolization device: a single-center experience with long-term follow-up results.** *AJNR Am J Neuroradiol* 2012;33:1436–46 CrossRef Medline
8. Santiago-Dieppa DR, Pannell JS, Khalessi AA. **Endovascular and surgical options for ruptured middle cerebral artery aneurysms: review of the literature.** *Stroke Res Treat* 2014;2014:315906 CrossRef Medline
9. Nussbaum ES, Defillo A. **Surgical management and alternative strategies for neighboring intracranial aneurysms.** *J Neurosurg Sci* 2012;56:345–48 Medline
10. Becske T, Kallmes DF, Saatci I, et al. **Pipeline for uncoilable or failed**

aneurysms: results from a multicenter clinical trial. *Radiology* 2013; 267:858–68 CrossRef Medline
11. Zhang Y, Zhou Y, Yang P, et al. **Comparison of the flow diverter and stent-assisted coiling in large and giant aneurysms: safety and efficacy based on a propensity score-matched analysis.** *Eur Radiol* 2016; 26:2369–77 CrossRef Medline
12. Caroff J, Neki H, Mihalea C, et al. **Flow-diverter stents for the treatment of saccular middle cerebral artery bifurcation aneurysms.** *AJNR Am J Neuroradiol* 2016;37:279–84 CrossRef Medline
13. Zanaty M, Chalouhi N, Tjoumakaris SI, et al. **Flow diversion for complex middle cerebral artery aneurysms.** *Neuroradiology* 2014;56: 381–87 CrossRef Medline
14. Fischer S, Perez MA, Kurre W, et al. **Pipeline embolization device for the treatment of intra- and extracranial fusiform and dissecting aneurysms: initial experience and long-term follow-up.** *Neurosurgery* 2014;75:364–74; discussion 374 CrossRef Medline
15. Iosif C, Saleme S, Ponsonnard S, et al. **Intravascular optical coherence tomography for the evaluation of arterial bifurcations covered by flow diverters.** *J Neurointerv Surg* 2016 Jan 27. [Epub ahead of print] CrossRef Medline
16. Iosif C, Berg P, Ponsonnard S, et al. **Role of terminal and anastomotic circulation in the patency of arteries jailed by flow-diverting stents: from hemodynamic changes to ostia surface modifications.** *J Neurosurg* 2016:1–12 [Epub ahead of print] Medline
17. Iosif C, Berg P, Ponsonnard S, et al. **Role of terminal and anastomotic circulation in the patency of arteries jailed by flow-diverting stents: animal flow model evaluation and preliminary results.** *J Neurosurg* 2016;125:898–908 CrossRef Medline
18. Gawlitza M, Januel AC, Tall P, et al. **Flow diversion treatment of complex bifurcation aneurysms beyond the circle of Willis: a single-center series with special emphasis on covered cortical branches and perforating arteries.** *J Neurointerv Surg* 2016;8:481–87 CrossRef Medline
19. Topcuoglu OM, Akgul E, Daglioglu E, et al. **Flow diversion in middle cerebral artery aneurysms: is it really an all-purpose treatment?** *World Neurosurg* 2016;87:317–27 CrossRef Medline
20. Washington CW, Ju T, Zipfel GJ, et al. **Middle cerebral artery bifurcation aneurysms: an anatomic classification scheme for planning optimal surgical strategies.** *Neurosurgery* 2014;10(suppl 1):145–53; discussion 153–55 CrossRef Medline
21. **Epilepsy: a clinical and experimental research—Proceedings of the Second European Regional Conference on Epilepsy, Warsaw, October 5–7, 1978.** *Monogr Neural Sci* 1980;5:1–306 Medline
22. Berge J, Biondi A, Machi P, et al. **Flow-diverter Silk stent for the treatment of intracranial aneurysms: 1-year follow-up in a multicenter study.** *AJNR Am J Neuroradiol* 2012;33:1150–55 CrossRef Medline
23. Pierot L, Spelle L, Molyneux A, et al. **Clinical and anatomical follow-up in patients with aneurysms treated with the WEB device: 1-year follow-up report in the cumulated population of 2 prospective, multicenter series (WEBCAST and French Observatory).** *Neurosurgery* 2016;78:133–41 CrossRef Medline
24. Spiotta AM, Hui F, Schuette A, et al. **Patterns of aneurysm recurrence after microsurgical clip obliteration.** *Neurosurgery* 2013;72: 65–69; discussion 69 CrossRef Medline
25. Cekirge HS, Islak C, Firat MM, et al. **Endovascular coil embolization of residual or recurrent aneurysms after surgical clipping.** *Acta Radiol* 2000;41:111–15 CrossRef Medline
26. Lubicz B, Leclerc X, Gauvrit JY, et al. **Endovascular treatment of remnants of intracranial aneurysms following incomplete clipping.** *Neuroradiology* 2004;46:318–22 CrossRef Medline
27. Ding D, Starke RM, Evans AJ, et al. **Endovascular treatment of recurrent intracranial aneurysms following previous microsurgical clipping with the Pipeline Embolization Device.** *J Clin Neurosci* 2014;21:1241–44 CrossRef Medline

Testing Stenting and Flow Diversion Using a Surgical Elastase-Induced Complex Fusiform Aneurysm Model

R. Fahed, T.E. Darsaut, I. Salazkin, J.-C. Gentric, M. Mazighi, and J. Raymond

ABSTRACT

BACKGROUND AND PURPOSE: Rabbit elastase-induced saccular aneurysms have been commonly used for preclinical testing of endovascular devices, including flow diverters. However, all tested devices have been shown to be capable of aneurysm occlusion with this model. We aimed to create a more challenging model to test and discriminate among neurovascular devices of varying efficacies.

MATERIALS AND METHODS: With a surgical approach that included elastase infusion and balloon dilation, we attempted the creation of complex fusiform aneurysms in 16 rabbits, with standard saccular carotid aneurysms created in 15 other animals. Aneurysms were randomly allocated to one of the following treatments: flow diversion ($n = 8$), high-porosity stent ($n = 6$), double high-porosity stent ($n = 5$), and control ($n = 6$). Angiographic assessment and pathologic analyses were performed at 3 months.

RESULTS: Creation of complex fusiform and standard saccular aneurysms was successful in 12/16 and 13/15 attempts, respectively. All saccular ($n = 4$) or complex fusiform ($n = 4$) aneurysms treated with flow diverters were successfully occluded. Three of 3 saccular compared with 0/2 complex fusiform aneurysms were occluded by double high-porosity stents. One of 3 saccular and 0/3 complex fusiform aneurysms were occluded by a single high-porosity stent. Both aneurysm types shared the same pathologic findings when untreated: The aneurysm wall lacked an elastic layer and smooth muscle cells, while the lumen was lined with neointima of varying thickness. Neointimal coverage of the devices was complete when aneurysms were occluded, while leaks were always associated with aneurysm remnants.

CONCLUSIONS: Challenging fusiform aneurysms can be created in rabbits by using a surgical modification of the elastase method.

ABBREVIATIONS: FD = flow diverter; HPS = high-porosity stent

Flow diverters (FDs) are a class of braided stents used to treat intracranial aneurysms.[1] Compared with high-porosity stents (HPSs) used mainly for stent-assisted coiling of the aneurysmal sac, FDs are lower porosity devices designed to occlude aneurysms by repairing the parent vessel. FDs have been shown to be more effective at occluding experimental canine aneurysms compared with high-porosity stents.[2]

A number of experimental aneurysm models are available to test neurovascular devices.[3-5] The most commonly used model is the rabbit elastase-induced saccular aneurysm model.[6-9] The model can be created by using endovascular techniques with low morbidity.[10] However, most studies conducted with this model have shown high occlusion rates irrespective of the device used.[6,11-16] It remains unclear whether the saccular rabbit elastase model is sufficiently challenging to test flow diversion because complete occlusions have been reported by using non-flow-diverting high-porosity stents.[11,12] An insufficiently challenging model could result in an overestimation of device efficacy. It may also be incapable of comparing more or less effective flow-diverting devices or may be of limited utility in the exploration of reasons for or mechanisms of treatment failure.

The main objective of the present study was to create and test a rabbit aneurysm model that could offer a more challenging test

Received June 14, 2016; accepted after revision September 29.

From the Centre Hospitalier de l'Université de Montréal (R.F., I.S., J.R.), Interventional Neuroradiology Research Laboratory, Notre-Dame Hospital, Montreal, Quebec, Canada; Department of Surgery (T.E.D.), Division of Neurosurgery, University of Alberta Hospital, Mackenzie Health Sciences Centre, Edmonton, Alberta, Canada; Department of Radiology (J.-C.G.), Division of Neuroradiology, Centre Hospitalo-Universitaire Cavale Blanche, Brest, France; and Department of Interventional Neuroradiology (M.M.), Fondation Ophtalmologique Adolphe de Rothschild, Paris, France.

This work was supported by a research grant from La Fondation pour la Recherche Médicale to Robert Fahed (grant No. DEA20140630151). FDs, stents, and microcatheters were gifts from MicroVention (Tustin, California).

Please address correspondence to Jean Raymond, MD, Centre Hospitalier de l'Université de Montréal, Notre-Dame Hospital, Department of Radiology, 1560 Sherbrooke East, Pavilion Simard, Suite Z12909, Montreal, Quebec, Canada H2L 4M1; e-mail: jean.raymond@umontreal.ca

Indicates article with supplemental on-line appendix and table.

http://dx.doi.org/10.3174/ajnr.A5018

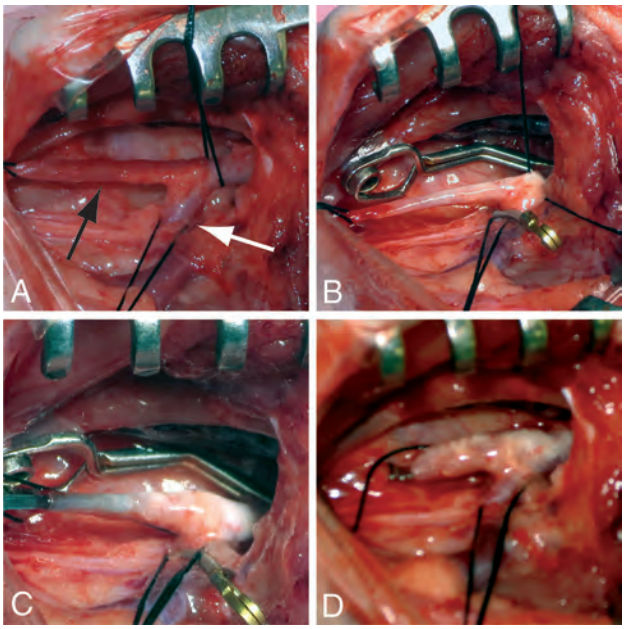

FIG 1. Surgical elastase-induced aneurysm creation. *A*, The right common carotid (*black arrow*), subclavian (*white arrow*), and brachiocephalic arteries are encircled with ligatures. *B*, Under temporary clip occlusion, elastase is injected into the lumen and adventitia of the carotid (both models) and subclavian arteries (fusiform model only). *C*, A 3F Fogarty balloon catheter is introduced into the carotid artery for angioplasty. *D*, The distal right carotid artery is occluded, and clips are removed.

of neurovascular devices such as FDs and discriminate among devices of varying efficacies.

MATERIALS AND METHODS

This article was written in accordance with the Animal Research: Reporting of In Vivo Experiments guidelines.[17] Protocols for animal experimentation were approved by the Institutional Animal Care Committee in accordance with guidelines of the Canadian Council on Animal Care. Aneurysms were created in New Zealand white rabbits (*Oryctolagus cuniculus*; mean weight, 3–4 kg). Details of the animal housing and husbandry, anesthesia, and surgical protocols can be found in the On-line Appendix.

Surgical Elastase Aneurysm Creation

Two types of rabbit aneurysms were created by using elastase: complex fusiform and saccular aneurysms. In 16 rabbits, under general anesthesia, complex fusiform aneurysms were created as follows: A 2- to 3-cm vertical skin incision was made over the right parasternal area. The right carotid artery was located and encircled with ligature (Silk 4–0; Ethicon, Laurel, Maryland), along with the brachiocephalic trunk and the subclavian artery proximal to the vertebral artery (Fig 1*A*). Strips of latex were placed under isolated arteries to protect the underlying cervical plexus from incubation with elastase. Encircled arteries were temporarily occluded. We then injected approximately 100 IU of porcine elastase (9.80 U/mg of protein; 100 U/mL; Worthington Biochemical, Lakewood, New Jersey) into the lumen of the carotid artery, allowing the elastase to enter the subclavian artery. Elastase was also injected into the adventitia of both arteries with a 31-ga needle (Fig 1*B*). After 20 minutes of elastase incubation, without irrigating the elastase away, a 3F Fogarty balloon catheter (Baxter Healthcare, Irvine, California) was retrogradely introduced into the right carotid artery and progressively inflated at different insertion depths with up to 0.3 mL of saline for 3 minutes in the right subclavian and carotid arteries, including the ostium (Fig 1*C*). The balloon catheter was then removed, and the right carotid artery was permanently occluded with clips. Temporary clips were removed, and hemostasis was obtained, covering the arteries with pledgets of collagen sponges when necessary (SURGIFOAM Absorbable Gelatin Sponge; Ethicon) (Fig 1*D*). The surgical incision was closed by using Vicryl 4–0 for deep layers and Prolene 6–0 (Ethicon) for skin.

In an additional group of 15 rabbits, we created a saccular right carotid artery aneurysm model by using the same surgical procedure as above, but the elastase treatment and balloon dilation were limited to the right carotid artery.

Stents and Flow Diverters

Stents, flow diverters, and delivery systems were gifts from MicroVention (Tustin, California).

The Low-Profile Visualized Intraluminal Support Device (LVIS; MicroVention) is a self-expanding high-porosity braided stent (not a flow diverter), with an in vitro porosity of 89% ± 1.5% and a pore density of 0.6 ± 0.5 full pores/mm^2 (in 3.5-mm straight glass tubes).[2] Double overlapping LVIS stents (double HPS) result in varying porosities (up to 75.8% ± 1.2%) and pore densities (up to 2.3 ± 2.1 full pores/mm^2 in optimal in vitro conditions), depending on the extent of overlap of the 2 stents.[2]

The Flow-Redirection Endoluminal Device (FRED; MicroVention) is an FD made of an inner sleeve of low-porosity/high-density mesh sutured inside an outer LVIS (values measured in 3.5-mm glass tubes).[2]

The diameters and lengths of the LVIS HPSs were 3.0 × 25 mm, 3.0 × 41 mm, and 4.5 × 23 mm, respectively, while those of the FRED FDs were 4.0 × 23 mm and 4.5 × 20 mm.

Endovascular Treatment

Endovascular treatment was performed 2–3 weeks after aneurysm creation. All animals were administered aspirin (10 mg/kg by mouth) and clopidogrel (10 mg/kg by mouth) for 2 days before the procedure and for 1 month thereafter.

Through a right femoral artery cut-down, a 4F vascular sheath was introduced, through which a microcatheter (Headway 21 or Headway 27; MicroVention) was advanced into the right brachiocephalic artery. A 4F diagnostic catheter (Glidecath; Terumo, Tokyo, Japan) was used for additional support when necessary.

Aneurysm dimensions and parent arteries were measured by using a Leonardo workstation with syngo software (Siemens, Erlangen, Germany). Assuming that aneurysms were ellipsoid, we calculated aneurysm volumes by using the AngioCalc Web site (http://www.angiocalc.com).

Animals with patent aneurysms ($n = 25$) were randomly allocated treatment by drawing lots: flow diversion ($n = 8$), double overlapping high-porosity stent placement ($n = 5$), single high-porosity stent placement ($n = 6$), and control ($n = 6$).

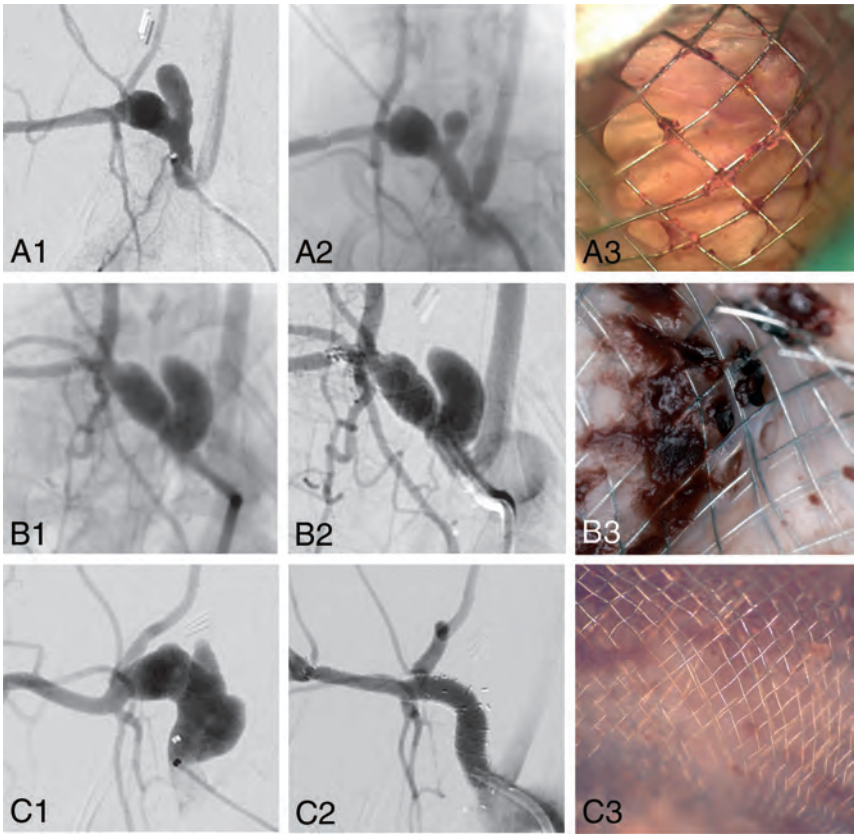

FIG 2. Treatment results (complex fusiform aneurysms). Preimplantation (*A1*, *B1*, *C1*) and 3-month follow-up angiography (*A2*, *B2*, *C2*) and microscopic photography (*A3*, *B3*, *C3*) of complex fusiform aneurysms treated with a single HPS (*A*), double overlapping HPSs (*B*), and flow diversion (*C*) (2 FDs were required). Note angiographic cure after flow diversion, with complete neointimal coverage of the FD. For reference, the diameter of the device wire measures 53 μm.

Angiography

Follow-up angiography was performed 3 months after treatment. Through a surgical left femoral artery cut-down, a 4F catheter (Glidecath) or a Headway microcatheter was advanced into the aortic arch and the right subclavian artery. The patency of parent vessels and jailed branches was assessed, as well as angiographic aneurysm occlusion according to the grading scales of Kamran et al[18] for fusiform and saccular aneurysms. A successful treatment was defined as an angiographic score of 3 or 4. Angiographic assessment was performed by 2 independent readers (R.F., T.E.D.), with discrepancies resolved in a consensus session.

We hypothesized that devices of decreasing porosity (from a single HPS to a double overlapping HPS to an FD) would increasingly be able to occlude aneurysms and that successful aneurysm occlusion would occur less frequently in the complex fusiform compared with the simple saccular aneurysm model.

Pathology

After 3-month angiography, animals were euthanized by barbiturate overdose. Aneurysm and arterial constructs were removed en bloc and fixed in formalin for 1 week. Specimens were examined under a microscope and photographed. Aneurysms, arteries, stents, and FDs were cut longitudinally to confirm arterial patency and assess aneurysm occlusion.

We carefully dissected some specimens, removing individual stent wires, to permit pathologic sectioning without metal. In other specimens, aneurysms and representative samples of tissues covering the metallic devices were biopsied under the surgical microscope. Sections were stained with hematoxylin-eosin and Movat pentachrome.

Statistics

Aneurysm dimensions were compared by using the Student *t* test. Dichotomized angiographic results (Kamran et al[18] grades 3–4 [defined as successful aneurysm treatment] versus grades 0–2) following various treatments were compared by using the Fisher exact test. A *P* value of .05 was significant.

RESULTS

Aneurysm Creation and Treatment

Aneurysm dimensions are presented in the On-line Table. The mean diameter of the fusiform aneurysms was 54.6% ± 27.2% larger than the upstream normal vessel. Complex fusiform aneurysms were successfully created in 12/16 rabbits. The complex morphology resulted from the combination of a fusiform subclavian aneurysm of varying size, with a "daughter sac" composed of the dilated right carotid artery origin. Two animals had immediate complications (1 vessel rupture during angioplasty; 1 postoperative right limb palsy; both animals were immediately euthanized). In 2 other animals, the parent vessels were occluded at 3 weeks. These 4 animals were excluded from analyses.

The creation of saccular aneurysms was successful in 13/15 rabbits (1 vessel rupture during angioplasty; 1 spontaneous aneurysm occlusion at 3 weeks.). These 2 animals were excluded, leaving a total of 25 aneurysms for analyses.

Complex fusiform aneurysms were significantly larger than saccular aneurysms (mean aneurysm volumes, 207.3 ± 156.9 mm^3, compared with 44.8 ± 16.7 mm^3, respectively; $P = .001$).

All endovascular procedures were performed without morbidity or mortality. One animal in the fusiform aneurysm group required 2 telescoping FDs to cross the entire aneurysmal segment.

Angiographic Results

Angiographic results are presented in the On-line Table and Figs 2 and 3.

Angiographic results were significantly different among treatments ($P = .0001$), with flow diversion leading to occlusion more frequently than treatment with a single or double high-porosity stent ($P = .03$). Overall angiographic results of all treated saccular and fusiform aneurysms were not significantly different ($P = .24$).

Aneurysms in animals with complex fusiform aneurysms treated with flow diverters were successfully occluded, while those in control animals and those treated with single high-porosity stents remained

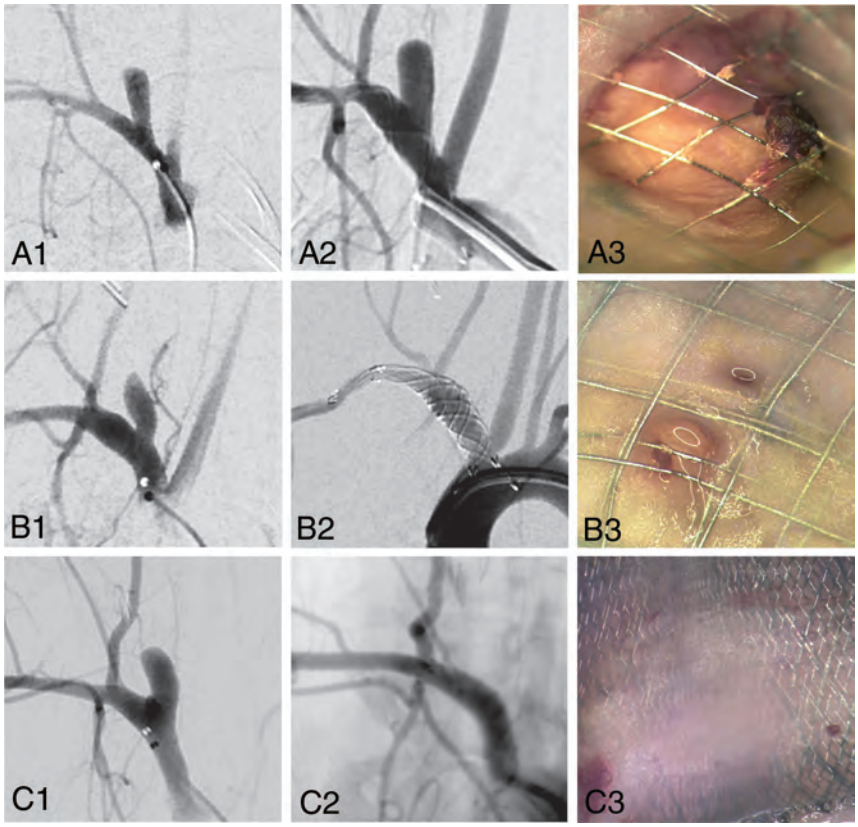

FIG 3. Treatment results (saccular aneurysms). Preimplantation (*A1*, *B1*, *C1*) and 3-month follow-up angiography (*A2*, *B2*, *C2*) and microscopic photography (*A3*, *B3*, *C3*) of saccular aneurysms treated with a single HPS (*A*), double overlapping HPSs (*B*), and flow diversion (*C*). Note complete aneurysm occlusion after double HPS placement and flow diversion. For reference, the diameter of the device wire measures 53 μm.

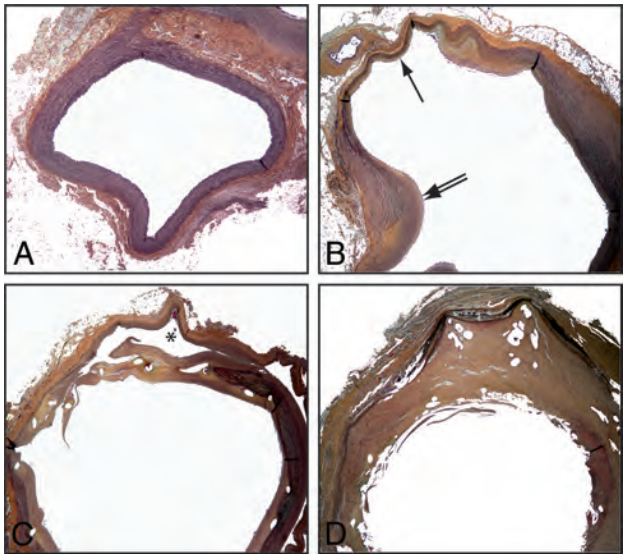

FIG 4. Pathology of untreated, stented, and flow-diverted fusiform aneurysms. The standard saccular model shows a subclavian of normal diameter with a continuous elastic lamina and no neointima formation (*A*). In comparison, the complex fusiform aneurysm is composed of a dilated thinned wall with a discontinuous media (*black arrow*) and neointima formation (*double arrow*). In case of treatment failure with HPS (*C*), the stent struts were covered with a thin, discontinuous neointima with leaks responsible for the residual aneurysm (partially shown, *black asterisk*). Successful occlusion of fusiform aneurysms by an FD (*D*) was associated with thick and complete neointimal coverage of the FD. (Movat staining, original magnification ×50.)

patent. Treatment with double overlapping HPSs did not lead to aneurysm occlusion in either of the 2 fusiform aneurysms in which it was attempted. All saccular aneurysms treated with FDs or double overlapping HPSs were occluded. One of 3 saccular aneurysms treated with a single HPS was occluded, while the 2 others remained patent, as did all control aneurysms.

None of the jailed branches were occluded in either model. One animal treated with 2 overlapping HPSs had a distal occlusion of the subclavian artery at 3-month follow-up.

Pathology

Untreated saccular or fusiform aneurysms shared similar pathologic features 3 months following creation (Figs 4*A* and 5*A*). Compared with the normal arterial wall (Fig 4*B*), the aneurysmal wall lacked elastic layers and smooth-muscle cells. The lumen was lined with neointima of varying thickness. Inflammatory cells were infrequent.

In the saccular model, the architecture of the normal artery could be recognized at the neck of the aneurysm (the origin of the right carotid artery as it arises from the brachiocephalic trunk), with reappearance of organized elastic layers (Fig 5*B*). Some partially organized thrombus could always be found within the fundus of the saccular aneurysm, close to the arterial ligature (Fig 4*A*). In the fusiform model, the walls of the brachiocephalic trunk and subclavian arteries showed features similar to those of the elastase-treated carotid aneurysms, though the neointimal lining of the aneurysm wall was usually not as thick (Fig 4*A*). The wires of all implanted devices closely apposed to the parent vessels at the level of landing zones were covered with neointima of variable thickness. There was no difference in the distribution of neointima covering the proximal or distal ends of the devices. In all cases of incomplete aneurysm occlusion, the neointima covering the stents was incomplete at the level of the aneurysm, leaving large (HPS) (Figs 4*C* and 5*C*) or small gaps (double HPSs) responsible for leaks associated with aneurysm remnants. The wires sometimes seemed bare; at other times, they were covered with neointima, or alternatively with clot. FDs were always completely covered with thick neointima (Figs 4*D* and 5*D*).

Aneurysms that were angiographically occluded were sometimes difficult or impossible to recognize at the time of specimen preparation because they had shrunk to the point of being indistinguishable from the other postsurgical fibrous tissues. In some specimens, all that remained was an area of fibrous thickening of the parent vessel now reconstructed by the FD (Fig 4*D*). In some others, the saccular (carotid) portion of the aneurysm could be recognized, but the lumen was completely filled with fibrous tissue. There was little inflammation, except for some small areas near the arterial wall where hemosiderin-laden macrophages and giant cells were found (Fig 5*D*).

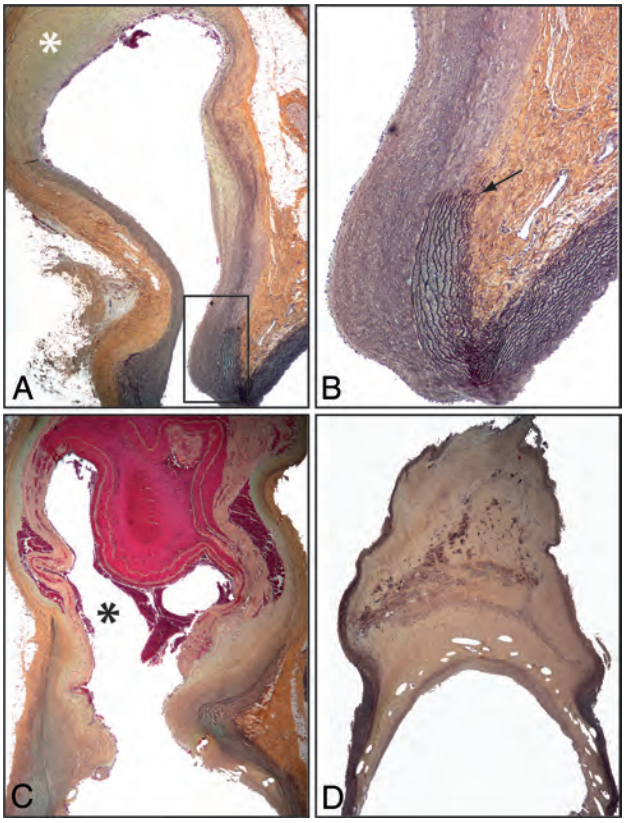

FIG 5. Pathology of untreated, stented, and flow-diverted saccular aneurysms. The saccular aneurysm has an organized thrombus in its dome (*white asterisk* in *A*), with a thin wall with interruption of the elastic lamina at the neck (*A*, magnified view in *B*, *black arrow*). In case of treatment failure, the neck was wide open with a persistent aneurysmal cavity (*black asterisk*), which was only partially filled with unorganized thrombus (*C*), whereas in case of treatment success, the stent struts were covered with a thick and continuous neointima and the aneurysm cavity was filled with organized thrombus containing areas of hemosiderin (*D*) (Movat staining, original magnification ×50).

DISCUSSION

The surgical approach we describe allows the creation of a complex fusiform aneurysm model in addition to the standard right carotid saccular model. The new model can be used to provide a challenging test of stents and flow diverters. The model could be used to compare devices of varying efficacy or to explore potential causes of treatment failures.

Elastase-induced rabbit carotid aneurysm models are those most frequently used to test endovascular devices.[6] Although they are popular, one can question the extent to which tested devices have been challenged, given that virtually all devices have been shown to be successful in occluding aneurysms, including first-[13] or second-[14] generation coils, high-porosity stents,[11,12] and flow diverters.[15,16,19] A number of technical modifications have been described to overcome this limitation, including attempts to increase the size of aneurysms to make the model more challenging, by adjusting the position of the inflated balloon or the location of carotid ligation.[15-18,20] We suspect that the main limitation of this type of aneurysm creation is the size of the artery selected for elastase infusion and balloon dilation. Modified surgical approaches have been published as well, but they were limited to elastase incubation and balloon angioplasty of the carotid artery.[21-23] Other techniques to create fusiform aneurysms with intraluminal injections of elastase[24,25] have reported lesions of smaller dimensions (mean aneurysm width, 3.1 ± 0.4 mm, compared with 5.1 ± 1.2 mm with our technique).

The surgical model we describe allows the operator the freedom to choose which parent vessel will become aneurysmal and thus form a complex aneurysm comprising a saccular lobule originating from a dilated fusiform segment. Attempting to create too large an aneurysm from too small a vessel may lead to vascular rupture or parent vessel occlusion, as we encountered in this exploratory work. Other surgical rabbit models include carotid lateral wall and bifurcation aneurysms made from venous pouches.[26-28] So far, flow diversion of these rabbit bifurcation aneurysms has not been studied, but FDs were shown to nearly always occlude the surgical sidewall aneurysms.[29]

More complex aneurysm models have been constructed in canines.[5,29-31] Some models were so challenging that aneurysms remained patent despite implantation of multiple flow diverters.[31,32] The complex fusiform aneurysms created in this work were larger than the standard rabbit elastase carotid model, but they remain of modest size compared with most canine vein pouch aneurysms.[33]

Rabbit aneurysm models may still have a number of advantages, including simpler logistics, reduced costs, and less technically demanding procedures, while avoiding the difficulties of using dogs for research. Creation of these aneurysms still required surgical expertise. The surgical procedures detailed here may be simpler than those for canine venous pouch aneurysms,[5] but procedural complications (arterial rupture and brachial plexus injury) nonetheless occurred. The mortality rate (3/31 animals) remained comparable with that of the standard rabbit elastase method.[10]

Although others have shown successful occlusion of elastase aneurysms with HPSs,[10,11] in this work, HPSs could not reliably occlude either the surgically created saccular or fusiform aneurysms. The surgical modification to the elastase model performed in this work may permit discrimination between endovascular treatments of various efficacies. We were unable to demonstrate statistically significant differences in angiographic results between the 2 surgically created models, which would have required more animals and resources than were available. Nonetheless, the fusiform aneurysms were larger, more complex, and more challenging to treat, and they may offer a more challenging test of endovascular devices than the standard saccular model.

This study has several limitations: The number of animals was small, and follow-up beyond 3 months was not performed. The patency of untreated elastase-induced saccular aneurysms has previously been shown to be durable for up to 5 years.[34] When creating the saccular, carotid stump aneurysms, modest dilation of the subclavian artery can occur. This has previously been described following the endovascular method of producing carotid stump aneurysms as well.[16] Fusiform aneurysms were of various sizes. Further refinements in the technique of aneurysm creation may be necessary to reproducibly yield aneurysms of constant dimensions. The method has only been used in a single laboratory. Proof of reproducibility from other centers would be welcome. Experimentally created aneurysms differ from spontaneous intracranial aneurysms, and rabbit biology differs from human biology. Any extrapolation of these results must remain cautious.

CONCLUSIONS

Fusiform rabbit aneurysms can be created by using a surgical modification of the elastase method.[7] This model may offer a more challenging test to compare different endovascular devices.

Disclosures: Robert Fahed—*RELATED*: *Grant*: La Fondation pour la Recherche Médicale (grant No. DEA20140630151), *Comments*: The Fondation pour la Recherche Médicale had no role in this study. Tim E. Darsaut—*UNRELATED*: *Grants/Grants Pending*: Canadian Institute of Health Research, *Comments*: peer-reviewed operating grant for the Collaborative Unruptured Endovascular vs Surgery Study (co-Principal Investigator).* Jean Raymond—*UNRELATED*: *Grants/Grants Pending*: Canadian Institute of Health Research for the Collaborative Unruptured Endovascular vs Surgery Study; Unrestricted investigator-led grant for the Does Embolization With Larger Coils Lead to Better Treatment of Aneurysms Trial (DELTA) from DePuy Synthes Johnson & Johnson Medical Companies*; *Other*: MicroVention, *Comments*: stents, flow diverters, and delivery systems were gifts from MicroVention (Tustin, California).* *Money paid to the institution.

REFERENCES

1. Brinjikji W, Murad MH, Lanzino G, et al. **Endovascular treatment of intracranial aneurysms with flow diverters: a meta-analysis.** *Stroke* 2013;44:442–47 CrossRef Medline
2. Darsaut TE, Bing F, Salazkin I, et al. **Flow diverters can occlude aneurysms and preserve arterial branches: a new experimental model.** *AJNR Am J Neuroradiol* 2012;33:2004–09 CrossRef Medline
3. Bouzeghrane F, Naggara O, Kallmes DF, et al; International Consortium of Neuroendovascular Centres. **In vivo experimental intracranial aneurysm models: a systematic review.** *AJNR Am J Neuroradiol* 2010;31:418–23 CrossRef Medline
4. Naggara O, Darsaut TE, Salazkin I, et al. **A new canine carotid artery bifurcation aneurysm model for the evaluation of neurovascular devices.** *AJNR Am J Neuroradiol* 2010;31:967–71 CrossRef Medline
5. Fahed R, Gentric JC, Salazkin I, et al. **Flow diversion of bifurcation aneurysms is more effective when the jailed branch is occluded: an experimental study in a novel canine model.** *J Neurointerv Surg* 2016 Apr 11. [Epub ahead of print] CrossRef Medline
6. Fahed R, Raymond J, Ducroux C, et al. **Testing flow diversion in animal models: a systematic review.** *Neuroradiology* 2016;58:375–82 CrossRef Medline
7. Cloft HJ, Altes TA, Marx WF, et al. **Endovascular creation of an in vivo bifurcation aneurysm model in rabbits.** *Radiology* 1999;213:223–28 CrossRef Medline
8. Brinjikji W, Ding YH, Kallmes DF, et al. **From bench to bedside: utility of the rabbit elastase aneurysm model in preclinical studies of intracranial aneurysm treatment.** *J Neurointerv Surg* 2016;8:521–25 CrossRef Medline
9. Altes TA, Cloft HJ, Short JG, et al. **1999 ARRS Executive Council Award: creation of saccular aneurysms in the rabbit: a model suitable for testing endovascular devices—American Roentgen Ray Society.** *AJR Am J Roentgenol* 2000;174:349–54 CrossRef Medline
10. Lewis DA, Ding YH, Dai D, et al. **Morbidity and mortality associated with creation of elastase-induced saccular aneurysms in a rabbit model.** *AJNR Am J Neuroradiol* 2009;30:91–94 Medline
11. Krings T, Hans FJ, Möller-Hartmann W, et al. **Treatment of experimentally induced aneurysms with stents**. *Neurosurgery* 2005;56:1347–59; discussion 1360 CrossRef Medline
12. Hans FJ, Krings T, Möller-Hartmann W, et al. **Endovascular treatment of experimentally induced aneurysms in rabbits using stents: a feasibility study.** *Neuroradiology* 2003;45:430–34 CrossRef Medline
13. Kallmes DF, Helm GA, Hudson SB, et al. **Histologic evaluation of platinum coil embolization in an aneurysm model in rabbits.** *Radiology* 1999;213:217–22 CrossRef Medline
14. Ding YH, Dai D, Lewis DA, et al. **Angiographic and histologic analysis of experimental aneurysms embolized with platinum coils, Matrix, and HydroCoil.** *AJNR Am J Neuroradiol* 2005;26:1757–63 Medline
15. Kallmes DF, Ding YH, Dai D, et al. **A second-generation, endoluminal, flow-disrupting device for treatment of saccular aneurysms.** *AJNR Am J Neuroradiol* 2009;30:1153–58 CrossRef Medline
16. Kallmes DF, Ding YH, Dai D, et al. **A new endoluminal, flow-disrupting device for treatment of saccular aneurysms.** *Stroke* 2007;38:2346–52 CrossRef Medline
17. Kilkenny C, Browne W, Cuthill IC, et al; National Centre for the Replacement, Refinement and Reduction of Amimals in Research. **Animal research: reporting in vivo—the ARRIVE guidelines.** *J Cereb Blood Flow Metab* 2011;31:991–93 CrossRef Medline
18. Kamran M, Yarnold J, Grunwald IQ, et al. **Assessment of angiographic outcomes after flow diversion treatment of intracranial aneurysms: a new grading schema.** *Neuroradiology* 2011;53:501–08 CrossRef Medline
19. Sadasivan C, Cesar L, Seong J, et al. **An original flow diversion device for the treatment of intracranial aneurysms: evaluation in the rabbit elastase-induced model.** *Stroke* 2009;40:952–58 CrossRef Medline
20. Ding YH, Dai D, Danielson MA, et al. **Control of aneurysm volume by adjusting the position of ligation during creation of elastase-induced aneurysms: a prospective study.** *AJNR Am J Neuroradiol* 2007;28:857–59 Medline
21. Hoh BL, Rabinov JD, Pryor JC, et al. **A modified technique for using elastase to create saccular aneurysms in animals that histologically and hemodynamically resemble aneurysms in human.** *Acta Neurochir* 2004;146:705–11 Medline
22. Wang K, Huang Q, Hong B, et al. **Neck injury is critical to elastase-induced aneurysm model.** *AJNR Am J Neuroradiol* 2009;30:1685–87 CrossRef Medline
23. Ding YH, Danielson MA, Kadirvel R, et al. **Modified technique to create morphologically reproducible elastase-induced aneurysms in rabbits.** *Neuroradiology* 2006;48:528–32 CrossRef Medline
24. Alaqeel A, Meek C, Wong J, et al. **A novel fusiform aneurysmal model in a rabbit carotid: a combination of pericarotid calcium chloride and elastase incubation.** *Can J Neurol Sci* 2015;42:S12 CrossRef
25. Reinald N, Fournier B, Naveau A, et al. **Fusiform aneurysm model in rabbit carotid artery.** *J Vasc Res* 2010;47:61–68 CrossRef Medline
26. Ding YH, Tieu T, Kallmes DF. **Experimental testing of a new generation of flow diverters in sidewall aneurysms in rabbits.** *AJNR Am J Neuroradiol* 2015;36:732–36 CrossRef Medline
27. Sherif C, Marbacher S, Erhardt S, et al. **Improved microsurgical creation of venous pouch arterial bifurcation aneurysms in rabbits.** *AJNR Am J Neuroradiol* 2011;32:165–66 CrossRef Medline
28. Sherif C, Herbich E, Plasenzotti R, et al. **Very large and giant microsurgical bifurcation aneurysms in rabbits: proof of feasibility and comparability using computational fluid dynamics and biomechanical testing.** *J Neurosci Method* 2016;268:7–13 CrossRef Medline
29. Darsaut TE, Bing F, Makoyeva A, et al. **Flow diversion of giant curved sidewall and bifurcation experimental aneurysms with very-low-porosity devices.** *World Neurosurg* 2014;82:1120–26 CrossRef Medline
30. Darsaut TE, Bing F, Salazkin I, et al. **Flow diverters failing to occlude experimental bifurcation or curved sidewall aneurysms: an in vivo study in canines.** *J Neurosurg* 2012;117:37–44 CrossRef Medline
31. Darsaut TE, Bing F, Salazkin I, et al. **Testing flow diverters in giant fusiform aneurysms: a new experimental model can show leaks responsible for failures.** *AJNR Am J Neuroradiol* 2011;32:2175–79 CrossRef Medline
32. Raymond J, Darsaut TE, Makoyeva A, et al. **Endovascular treatment with flow diverters may fail to occlude experimental bifurcation aneurysms.** *Neuroradiology* 2013;55:1355–63 CrossRef Medline
33. Gentric JC, Darsaut TE, Makoyeva A, et al. **The success of flow diversion in large and giant sidewall aneurysms may depend on the size of the defect in the parent artery.** *AJNR Am J Neuroradiol* 2014;35:2119–24 CrossRef Medline
34. Ding Y, Dai D, Kadirvel R, et al. **Five-year follow-up in elastase-induced aneurysms in rabbits.** *AJNR Am J Neuroradiol* 2010;31:1236–39 CrossRef Medline

Collar Sign in Incompletely Occluded Aneurysms after Pipeline Embolization: Evaluation with Angiography and Optical Coherence Tomography

C.J. Griessenauer, R. Gupta, S. Shi, A. Alturki, R. Motiei-Langroudi, N. Adeeb, C.S. Ogilvy, and A.J. Thomas

ABSTRACT

BACKGROUND AND PURPOSE: Flow diversion with the Pipeline Embolization Device has emerged as an attractive treatment for cerebral aneurysms. Processes involved in aneurysm occlusion include changes in intra-aneurysmal hemodynamics and endothelialization of the device. Here, we call attention to a radiographic sign not previously reported that is detected in incompletely occluded aneurysms after treatment with the Pipeline Embolization Device at angiographic follow-up and referred to as the "collar sign."

MATERIALS AND METHODS: A retrospective review of all patients who underwent placement of a Pipeline Embolization Device for cerebral aneurysms between January 2014 and May 2016 was performed. All aneurysms found to show the collar sign at follow-up were included. Optical coherence tomography was performed in 1 case.

RESULTS: One hundred thirty-five aneurysms were treated in 115 patients. At angiographic follow-up, 17 (10.7%) aneurysms were found to be incompletely occluded. Ten (58.8%) of these aneurysms (average diameter, 7.9 ± 5.0 mm) were found to have the collar sign at angiographic follow-up (average, 5.5 ± 1.0 months). Four (40.0%) of the aneurysms underwent a second angiographic follow-up (average, 11.0 ± 0.9 months) after treatment, and again were incompletely occluded and showing the collar sign. Two patients underwent retreatment with a second Pipeline Embolization Device. Optical coherence tomography showed great variability of endothelialization at the proximal end of the Pipeline Embolization Device.

CONCLUSIONS: The collar sign appears to be indicative of endothelialization, but continued blood flow into the aneurysm. This is unusual given the processes involved in aneurysm occlusion after placement of the Pipeline Embolization Device and has not been previously reported.

ABBREVIATIONS: OCT = optical coherence tomography; PED = Pipeline Embolization Device

Flow diversion with the Pipeline Embolization Device (PED; Covidien, Irvine, California) has emerged as an attractive treatment option for cerebral aneurysms, resulting in 6-month occlusion rates higher than 90%.[1-3] Serving as a scaffold for endothelialization, the PED is believed to divert blood flow away from the aneurysm, inducing thrombosis and collagenization within its sac.[4] The relative contribution of the 2 processes, namely endothelialization and blood stasis followed by clot formation, in leading to aneurysm occlusion and shrinkage remains poorly understood. However, visualization of complete obliteration of the lesion via DSA is believed to coincide with endothelialization across the neck of the lesion. Here, we report on a series of incompletely occluded aneurysms after PED placement where a gap in contrast opacification between parent vessel and aneurysm dome, or "collar sign," was observed upon angiographic follow-up. Optical coherence tomography (OCT) was performed in 1 case.

MATERIALS AND METHODS

After obtaining institutional review board approval, a retrospective review of all patients who underwent flow-diversion treatment for intracranial aneurysms with the PED at our institution between January 2014 and May 2016 was performed. All aneurysms were followed up with DSA, generally at 6 months after PED placement, by using standard anteroposterior and lateral projections and high-magnification views. Injections were performed from the ICA in all cases. All aneurysms found to show the collar sign at angiographic follow-up were included. Follow-up images were reviewed by at least 2 physicians with subspecialty training in neuroendovascular surgery.

Received August 12, 2016; accepted after revision September 15.

From the Neurosurgical Service, Beth Israel Deaconess Medical Center, Harvard Medical School, Boston, Massachusetts.

Please address correspondence to Christoph J. Griessenauer, MD, 110 Francis St, Boston, MA 02215-5501; e-mail: christoph.griessenauer@gmail.com

Indicates article with supplemental on-line table.

http://dx.doi.org/10.3174/ajnr.A5010

Optical Coherence Tomography Procedure

OCT was performed in 1 case (case 10). A 6F guide catheter was placed in the right ICA. Baseline intracranial angiograms were obtained and 5000 U of IV heparin were administered. A Navien intracranial support catheter (Covidien) was positioned in the cavernous ICA. A 0.014-inch Synchro Standard microwire (Stryker Neurovascular, Kalamazoo, Michigan) was advanced through the Navien, past the aneurysm, and positioned in the MCA. Next, a 2.7F Dragonfly OCT imaging catheter (St. Jude Medical, St. Paul, Minnesota) was advanced over the microwire. Attempts to negotiate the carotid siphon past the aneurysm with the Dragonfly OCT catheter failed. These attempts included alternative distal access catheters and stiffer microwires, such as the 0.014-inch Transend (Stryker Neurovascular). After several attempts, there was profound spasm in the ICA, and the decision was made to only perform OCT of the proximal end of the PED in the horizontal segment of the cavernous ICA. The guide catheter was connected to a power injector. An OCT acquisition over 2.7 seconds was done during power injection of contrast to trigger the internalized automated "pull-back" method that renders catheter manipulation unnecessary during image acquisition and to transiently clear red blood cells from the imaging area.[5,6] Image processing and data analysis were done using a commercially available OCT system (Ilumien System; St. Jude Medical).

RESULTS

A total of 135 aneurysms were treated at our institution with PEDs in 115 patients between January 2014 and May 2016. Ninety of these aneurysms (66.7%) underwent angiographic follow-up, at which point 73 (81.1%) were found to be completely occluded and 5 (5.6%) were >90% occluded. Of 17 aneurysms that were incompletely occluded, 10 (58.8%) aneurysms (average diameter, 7.9 ± 5.0 mm) in 9 patients (average age, 54.2 ± 14.5 years) were found to have a collar sign with variable thickness at first angiographic follow-up (average, 5.5 ± 1.0 months). Two aneurysms underwent retreatment with a second PED device. Seven (70.0%) aneurysms were paraophthalmic ICA aneurysms, but the collar sign was also observed in MCA, ICA bifurcation, and posterior communicating artery aneurysms (1 aneurysm each). No procedural complications occurred. Satisfactory wall apposition as demonstrated on fluoroscopy was achieved in all cases. Four (40.0%) of the aneurysms underwent a second angiographic follow-up (average, 11.0 ± 0.9 months) after treatment, and again were incompletely occluded showing the collar sign (Fig 1). Opacification of parent vessel and aneurysm occurred simultaneously with injection of the ICA, reducing the possibility for retrograde aneurysm filling via external carotid artery or other collaterals. The collar sign was observed were in both clopidogrel responders and nonresponders treated with ticagrelor (On-line Table).

Optical Coherence Tomography Findings

Because of inability to negotiate the carotid siphon with the OCT catheter past the aneurysm, only the proximal end of the PED in the horizontal segment of the cavernous ICA could be imaged with OCT (Fig 2). Interestingly, there was great variability of endothelialization of the PED. There were portions where the PED

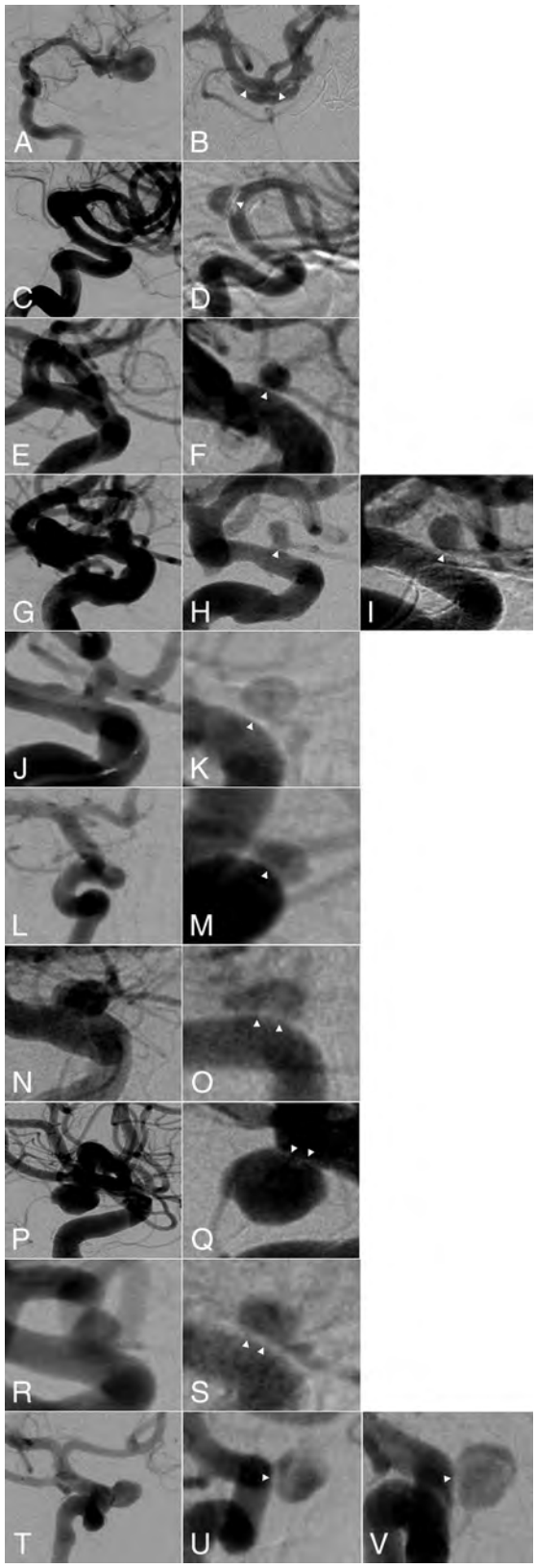

FIG 1. DSA showing collar sign in incompletely occluded aneurysms after Pipeline embolization. Each line represents 1 aneurysm corresponding to the On-line Table. The left column shows the aneurysm before Pipeline embolization. The right column shows the residual aneurysm with the collar sign (*white arrowheads*) after Pipeline placement at last follow-up. For aneurysms 4 and 10, both first and second angiographic follow-up are shown.

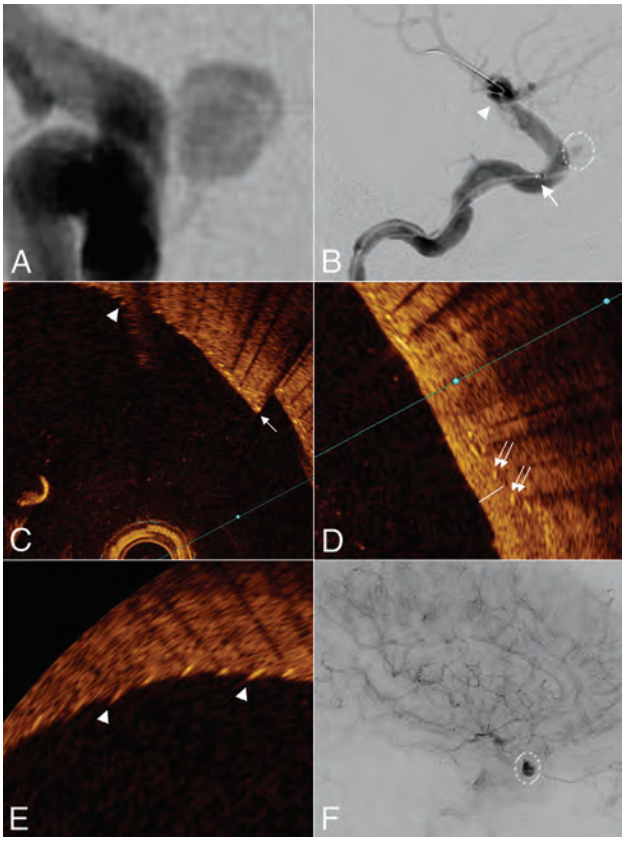

FIG 2. Case 10. DSA showing collar sign in incompletely occluded paraophthalmic ICA aneurysm after Pipeline embolization (*A*). Lateral DSA of the ICA showing the aneurysm (*white dashed line*) and position of the tip (*arrowhead*) and the beginning of the scanning portion (*arrow*) of the OCT catheter (*B*). OCT images showing variable degree of endothelialization (*C–E*). There are portions where the PED struts lay bare (*arrowheads*) or are covered with thin endothelium (*arrow*) or robust neointima (*double arrow* and *white line* showing the distance from lumen to PED struts). After treatment with a second PED, there is stasis of contrast within the aneurysm (*F*).

struts laid bare or were covered by thin endothelium or robust neointima. The degree of endothelialization was even variable on the same cross-section.

DISCUSSION

Here, we report on a series of patients with incompletely occluded cerebral aneurysms after PED placement where the parent vessel appeared to be separate from the aneurysm on angiographic follow-up. We decided to use the term "collar sign" to describe this observation. The main purpose of this article was to report this interesting observation and spark discussion among neurointerventionalists about its significance.

Potential Mechanisms Underlying the Collar Sign

Given the contiguous nature of this sign with the endothelial lining of the parent vessel, it appears to represent endothelialization on the surface of the stent adjacent to the neck of the aneurysm. Why there is continued blood flow into the aneurysm, however, is unclear. Small channels, not readily apparent on DSA, must remain, connecting the parent vessel with the aneurysm. It has been postulated that endothelialization, rather than intra-aneurysmal hemodynamic changes, are primarily responsible for aneurysm obliteration after PED placement. After performing immunohistochemical analysis in rabbit models, Kadirvel et al[7] found that endothelial cells derived from the parent vessel rather than from progenitor cells from the bone marrow are responsible for neointimal growth after flow-diverter placement, supporting previous results in mice models. They further found that smooth muscle cells derived from the parent vessel and the aneurysm itself also served as the scaffold for neointimal formation. The presence of inflammatory cells, including macrophages and monocytes, within the portion of the device covering the aneurysm neck was observed in cases of incomplete obliteration and was associated with disorganized thrombus formation at 8 weeks after flow-diverter placement. The macrophages and monocytes formed islands at the neck of the aneurysms without associated endothelial, smooth muscle, and progenitor cells. Similar processes may, in part, be responsible for the collar sign observed on follow-up DSA in humans, and it may represent an angiographic correlate for inflammatory-driven aberrant endothelialization. Along the same lines, Dai et al[8] reported a case of a patient who underwent PED placement for a basilar tip aneurysm. At 4 months, the aneurysm was occluded, but at 1 year, it had recanalized, and the patient died from brain stem compression. Microscopic analysis of the aneurysm revealed channels extending through thick, newly formed islands of intima from the parent vessel to the sac of the aneurysm containing fresh blood clot. The aneurysm was filled with disorganized thrombus. The collar sign on the DSAs obtained in the present series of patients were mostly homogeneous in appearance with variable thickness, even though they contained rare regions speckled with contrast, indicative of blood flow through this layer. OCT performed in 1 case showed variable degrees of endothelialization at the proximal end of the PED, ranging from no coverage of the PED struts to thick neointima. Unfortunately, the area of the collar sign could not be imaged because of inability to negotiate the carotid siphon with the OCT catheter. In animal models, OCT has been used to assess PED wall apposition[9] and side branches covered by the PED.[10,11] We are not aware of any prior use of OCT after PED placement in humans.

Clinical Implications of the Collar Sign

The implications of the collar sign are unclear. Initially, we assumed that incompletely occluded aneurysms with this associated sign at 6 months would likely be occluded at subsequent follow-up. However, all patients who had additional angiographic follow-up past the 6-month mark continued to have aneurysm filling, with no notable change in the collar sign appearance. Given that flow diversion is associated with high rates of complete occlusion at 6-month follow-up,[2,12-14] these aneurysms only represent a small fraction of all aneurysms treated with the PED. Nevertheless, it is important to consider. If the collar sign at 6 months is not predictive of occlusion in the future, early treatment with a second PED may be warranted. In the current series, this approach was pursued in 2 aneurysms, with close follow-up on the others.

CONCLUSIONS

Pipeline embolization is associated with high rates of occlusion of cerebral aneurysms. Two mechanisms underlying occlusion have been proposed for the device: 1) diversion of blood flow away

from the fundus of the lesion, resulting in subsequent thrombus formation and aneurysm shrinkage; and 2) endothelialization of the neck of the aneurysm over time. Here, we report on a series of patients who underwent PED placement and were found to have incomplete occlusion of their aneurysms at angiographic follow-up, with a characteristic collar sign visible on angiography. They appear to represent endothelialization along the neck of the aneurysm with continued filling of the lesions. Subsequent follow-ups in a subset of these patients demonstrated residual blood flow into these aneurysms and continued incomplete endothelialization across the neck, warranting retreatment.

Disclosures: Ajith Thomas—*UNRELATED*: *Consultancy*: Stryker, *Comments*: data safety monitoring board of SCENT trial*; *Expert Testimony*: testimony related to aneurysm treatment. *Money paid to the institution.

REFERENCES

1. Alderazi YJ, Shastri D, Kass-Hout T, et al. **Flow diverters for intracranial aneurysms.** *Stroke Res Treat* 2014;2014:415653 CrossRef Medline
2. Szikora I, Berentei Z, Kulcsar Z, et al. **Treatment of intracranial aneurysms by functional reconstruction of the parent artery: the Budapest experience with the Pipeline embolization device.** *AJNR Am J Neuroradiol* 2010;31:1139–47 CrossRef Medline
3. Griessenauer CJ, Ogilvy CS, Foreman PM, et al. **Pipeline Embolization Device for small paraophthalmic artery aneurysms with an emphasis on the anatomical relationship of ophthalmic artery origin and aneurysm.** *J Neurosurg* 2016 Mar 4:1–8. [Epub ahead of print] CrossRef Medline
4. D'Urso PI, Lanzino G, Cloft HJ, et al. **Flow diversion for intracranial aneurysms: a review.** *Stroke* 2011;42:2363–68 CrossRef Medline
5. Attizzani GF, Jones MR, Given CA 2nd, et al. **Frequency-domain optical coherence tomography assessment of very late vascular response after carotid stent implantation.** *J Vasc Surg* 2013;58:201–04 CrossRef Medline
6. Griessenauer CJ, Foreman PM, Deveikis JP, et al. **Optical coherence tomography of traumatic aneurysms of the internal carotid artery: report of 2 cases.** *J Neurosurg* 2016;124:305–09 CrossRef Medline
7. Kadirvel R, Ding YH, Dai D, et al. **Cellular mechanisms of aneurysm occlusion after treatment with a flow diverter.** *Radiology* 2014;270:394–99 CrossRef Medline
8. Dai D, Ding YH, Kelly M, et al. **Histopathological findings following Pipeline embolization in a human cerebral aneurysm at the basilar tip.** *Interv Neuroradiol* 2016;22:153–57 CrossRef Medline
9. van der Marel K, Gounis MJ, Weaver JP, et al. **Grading of Regional Apposition after Flow-Diverter Treatment (GRAFT): a comparative evaluation of VasoCT and intravascular OCT.** *J Neurointerv Surg* 2016;8:847–52 CrossRef Medline
10. Iosif C, Saleme S, Ponsonnard S, et al. **Intravascular optical coherence tomography for the evaluation of arterial bifurcations covered by flow diverters.** *J Neurointerv Surg* 2016 Jan 27. [Epub ahead of print] CrossRef Medline
11. Lopes DK, Johnson AK. **Evaluation of cerebral artery perforators and the Pipeline embolization device using optical coherence tomography.** *J Neurointerv Surg* 2012;4:291–94 CrossRef Medline
12. Kan P, Siddiqui AH, Veznedaroglu E, et al. **Early postmarket results after treatment of intracranial aneurysms with the Pipeline embolization device: a U.S. multicenter experience.** *Neurosurgery* 2012;71:1080–87, discussion 1087–88 CrossRef Medline
13. O'Kelly CJ, Spears J, Chow M, et al. **Canadian experience with the Pipeline embolization device for repair of unruptured intracranial aneurysms.** *AJNR Am J Neuroradiol* 2013;34:381–87 CrossRef Medline
14. Yu SC, Kwok CK, Cheng PW, et al. **Intracranial aneurysms: midterm outcome of Pipeline embolization device–a prospective study in 143 patients with 178 aneurysms.** *Radiology* 2012;265:893–901 CrossRef Medline

Ascending and Descending Thoracic Vertebral Arteries

P. Gailloud, L. Gregg, M.S. Pearl, and D. San Millan

ABSTRACT

SUMMARY: Thoracic vertebral arteries are anastomotic chains similar to cervical vertebral arteries but found at the thoracic level. Descending thoracic vertebral arteries originate from the pretransverse segment of the cervical vertebral artery and curve caudally to pass into the last transverse foramen or the first costotransverse space. Ascending thoracic vertebral arteries originate from the aorta, pass through at least 1 costotransverse space, and continue cranially as the cervical vertebral artery. This report describes the angiographic anatomy and clinical significance of 9 cases of descending and 2 cases of ascending thoracic vertebral arteries. Being located within the upper costotransverse spaces, ascending and descending thoracic vertebral arteries can have important implications during spine interventional or surgical procedures. Because they frequently provide radiculomedullary or bronchial branches, they can also be involved in spinal cord ischemia, supply vascular malformations, or be an elusive source of hemoptysis.

ABBREVIATIONS: ISA = intersegmental artery; SIA = supreme intercostal artery; VA = vertebral artery

The cervical portion of the vertebral artery (VA) is formed by a series of anastomoses established between the first 6 cervical intersegmental arteries (ISAs) and one of the carotid-vertebral anastomoses, the proatlantal artery.[1-3] The VA is labeled a "postcostal" anastomotic chain (ie, located behind the costal process of cervical vertebrae or dorsal to the rib itself at the thoracic level) to emphasize its location within the transverse foramina. A thoracic VA is a similar postcostal vessel found at the thoracic level.[4]

A thoracic VA was originally defined as a proximal VA branch curving medially and caudally to enter the ipsilateral C7 transverse foramen or first costotransverse space (Fig 1, right).[5] Atypical forms, common in birds and mammals but rare in humans,[5,6] include thoracic VAs originating from the supreme intercostal or deep cervical arteries.

Another anastomotic chain found within the upper costotransverse spaces differs from a descending thoracic VA by its caudal origin from a thoracic ISA and its ascending course.[7] This exceptional variant corresponds to an ascending thoracic VA (Fig 1, left) and should not be confused with variants such as a vertebral arteria lusoria[8-13] or persistent left seventh cervical ISA of aortic origin.[14]

This report discusses 9 angiographic observations of descending thoracic VAs and 2 cases of ascending thoracic VAs.

CASE SERIES

Descending Thoracic Vertebral Arteries

Nine typical descending thoracic VAs were documented by DSA in 9 patients between 2006 and 2015 (Table). The variation was unilateral in 8 instances. In 1 patient, a contralateral thoracic VA was documented by CTA only. The bifurcation into the cervical and thoracic VAs was found at C7–T1 (5 instances, 56%) or C6–C7 (4 instances, 44%). The descending thoracic VA was right-sided in 8 cases (89%).

The ISAs provided by the descending thoracic VAs were either complete (ie, including medial, dorsal, and lateral branches) or incomplete, with only the medial branch present; the other branches then came from the supreme intercostal artery (SIA). Most commonly, the descending thoracic VA provided the second (T2) and third (T3) thoracic ISAs completely, as well as 1 or more partial ISA proximally (T1 in 5 cases, C7 and T1 in 1 case). Isolated medial branches were also noted at C7 or T2 (once each). In 2 observations, the descending thoracic VAs were extending out of the FOV after branching off the third thoracic ISA (T3). Descending thoracic VAs branched off important anterior radiculomedullary arteries in 5 instances (56%), 4 times at T2 and once at T1.

Received August 5, 2016; accepted after revision September 23.

From the Division of Interventional Neuroradiology (P.G., L.G., M.S.P., D.S.M.), The Johns Hopkins Hospital, Baltimore, Maryland; and Neuroradiology Unit (D.S.M.), Service of Diagnostic and Interventional Radiology, Sion Hospital, Centre Hospitalier du Valais Romand, Romand, Switzerland.

Please address correspondence to P. Gailloud, MD, Division of Interventional Neuroradiology, The Johns Hopkins Hospital, 1800 E Orleans St, Bloomberg 7218, Baltimore, MD 21287; e-mail: phg@jhmi.edu

http://dx.doi.org/10.3174/ajnr.A5016

Case 1. Right descending thoracic VA documented (Fig 2) in a 64-year-old man.

Case 2. Right descending thoracic VA documented in a 67-year-old woman (Fig 3).

Case 3. Bilateral descending thoracic VAs documented in a 59-year-old woman (Fig 4).

Case 4. Right descending thoracic VA documented in 30-year-old man (Fig 5*A*, *-B*). An ipsilateral costocervical angiogram illustrates the characteristics distinguishing a descending thoracic VA from an SIA (Fig 5*C*, *-D*).

Case 5. A 47-year-old woman with a right descending thoracic VA branching off the third thoracic ISA as well as a conspicuous bronchial artery (Fig 6).

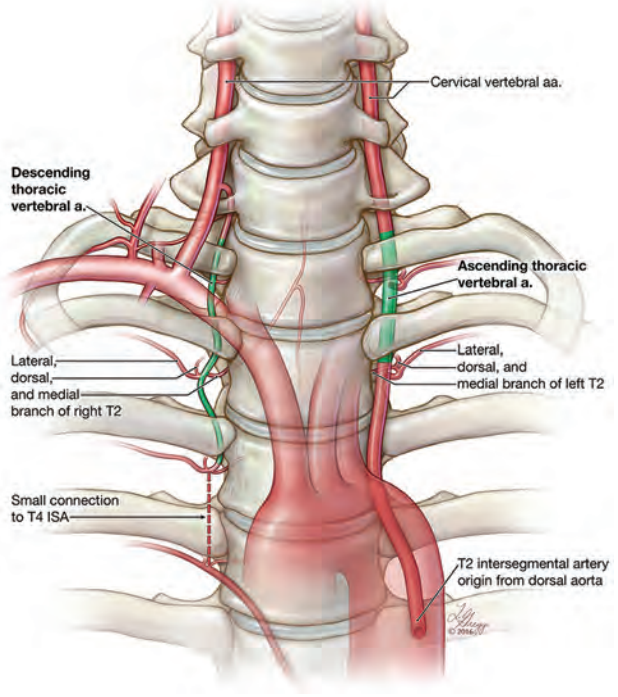

FIG 1. Schematic representation of ascending and descending thoracic vertebral arteries. In its most typical form, a descending thoracic VA (right side) originates from the pretransverse segment (V1) of the cervical VA and curves sharply medially and caudally to enter the last transverse foramen or the first costotransverse space. It then continues caudally, passing through 1 or more costotransverse space, generally branching off a complete set of branches for the second and third thoracic ISAs (T2 and T3) and the medial branch of the first thoracic ISA (T1). In about 50% of cases, a descending thoracic VA provides an important contribution to the spinal cord vascularization. An ascending thoracic VA (left side) is the cranial prolongation of a thoracic ISA, which passes through 1 or more costotransverse space before continuing as a normal cervical VA. Strictly speaking, the thoracic VA segment only corresponds to the portion of the vessel delimited by costotransverse spaces (highlighted in green).

Ascending Thoracic Vertebral Arteries

Case 1. A 20-year-old man with bullet fragments in the posterior fossa. The right VA injection showed minimal reflux into the left V4 segment, with prompt wash-off indicating the presence of a patent left VA, which was identified as the cranial continuation of the left T2 ISA (Fig 7*A*, *-B*). Enlargement of the left T1 and T2 costotransverse spaces was noted (Fig 7*C*).

Case 2. A 64-year-old man investigated for gait disturbance. A left VA originating from the thoracic aorta and passing through the left T2 and T1 costotransverse spaces (Fig 8*A*) is identified as a left T2 ISA (Fig 8*B*).

DISCUSSION

Developmental Anatomy of the VA

His[15] divided the VA into cranial and cervical portions on the basis of their developmental history. Appearing first, the cranial portion principally consists of the proatlantal artery, which is associated with the first cervical nerve. The anterior radiculomedullary branch stemming from the proatlantal artery becomes the distal VA; it divides into ascending and descending rami, which respectively turn into the proximal basilar artery and the vertebral root of the anterior spinal artery.[16-18] The cervical portion of the VA subsequently forms as a succession of anastomoses between the first 6 ISAs, which connect cranially with the proatlantal artery and caudally with the subclavian artery (sixth ISA).[2] The final configuration of the VA depends on which primitive ISA becomes its adult origin. Most often, the proximal VA, being derived from the sixth cervical ISA, originates from the subclavian artery and enters the C6 transverse foramen. Variations are identified by the level at which they enter the transverse canal rather than by their origin. For example, a VA derived from the seventh cervical ISA always enters the C7 transverse foramen but can arise from the aorta or from the subclavian artery via the SIA.[19]

A thoracic VA is an anastomotic chain passing through 1 or more costotransverse space.[4,19]

Nine angiographic observations of the descending thoracic vertebral artery

Patient	Sex	Age (yr)	Level	Side	ISA		Branches	
					Complete	Partial	ARMA	Br
1	M	64	C7–T1	R	T2–T3	Medial C7–T1	T2	Yes
2	W	67	C7–T1	R	T2–T4?[a]	Medial T1	T1	No
3	W	59	C6–C7	L	T2–T3	Medial T1	T2	No
4	M	30	C6–C7	R	T2	Medial C7	T2	No
5	W	47	C6–C7	R	T3	Medial T2	–	Yes
6	M	18	C7–T1	R	T2–T3	Medial T1	T2	No
7	W	56	C7–T1	R	T2–T3	Medial T1	–	No
8	W	60	C7–T1	R	T2–T4?[a]	Medial T1	–	No
9	W	31	C6–C7	R	T1–T2	?[b]	–	No

Note:—ARMA indicates anterior radiculomedullary artery; Br, bronchial artery; R, right; L, left; –, none; M, man; W, woman.

[a] Question mark indicates that the caudal extension of the descending thoracic VA was beyond the FOV.

[b] Question mark indicates that motion artifacts prevented evaluating the presence of a proximal medial branch.

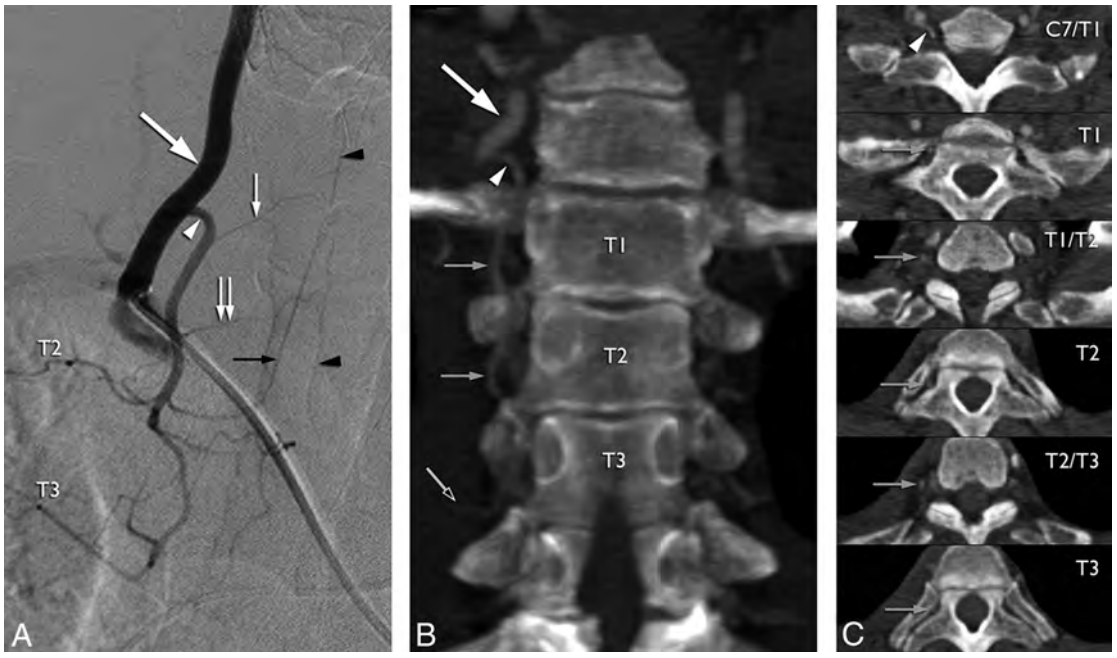

FIG 2. A 64-year-old man with a right descending thoracic vertebral artery. *A*, DSA, right VA injection, posteroanterior projection, shows a VA originating from the subclavian artery and dividing into ascending cervical (*large white arrow*) and descending thoracic (*white arrowhead*) VAs at the C7–T1 level. The descending thoracic VA provides the medial branches of C7 (*small white arrow*) and T1 (*double small white arrow*) and complete sets of branches for the T2 and T3 ISAs. The second thoracic ISA provides a prominent anterior radiculomedullary artery (*small black arrow*), which supplies the anterior spinal artery (*black arrowheads*). *B*, CTA, coronal reconstruction at the level of the transverse foramina. The ascending (*large white arrow*) and descending (*white arrowhead*) branches of the VA are identified. The *small gray arrows* point to the descending thoracic VA down to its termination at T3 (*small black arrow*). *C*, CTA, multilevel axial reconstructions, shows the course of the descending thoracic VA (*small gray arrows*) from its origin at C7–T1 (*white arrowhead*).

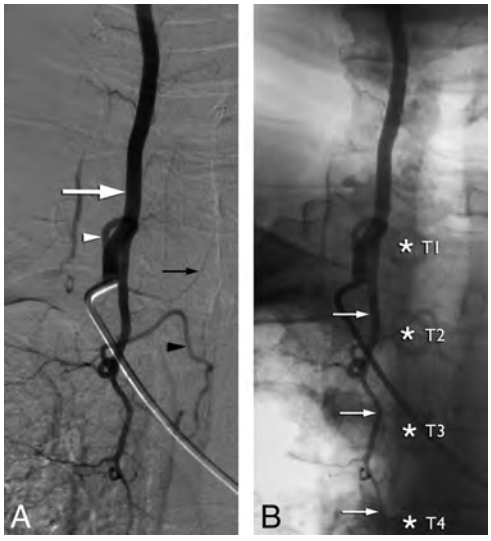

FIG 3. A 67-year-old woman with a right descending thoracic vertebral artery. *A*, DSA, right VA injection, posteroanterior projection. The VA divides into ascending cervical (*large white arrow*) and descending thoracic (*white arrowhead*) VAs at the C7–T1 level. The descending thoracic VA provides the medial branch of T1, which gives off a prominent anterior radiculomedullary artery (*small black arrow*). Note that the descending thoracic VA extends beyond the FOV and may provide additional ISAs. A prominent T2 dorsal (muscular) branch is seen coursing medially and caudally (*black arrowhead*) and should not be confused with a bronchial artery. *B*, DSA, right VA injection, nonsubtracted posteroanterior projection, documents the close relationship between the descending thoracic VA and the cervical pedicles (*asterisks*), notably at the level of the transverse foramina (*small white arrows*).

Walsham[4] described thoracic VAs in the following manner: "The artery would here appear to be homologous to the vertebral artery in the neck, as both lie between homologous parts, the anterior part of the transverse process of the cervical vertebra being the homolog of the neck and head of the dorsal rib, and the posterior part of the cervical transverse process that of the transverse process of the dorsal vertebra."

While any postcostal anastomosis established between 2 or more thoracic ISAs answers this definition (eg, a T3–T4 intercostal trunk linked by a postcostal anastomosis), the term "thoracic VA" is generally reserved for variants connected with or continuing as a cervical VA. These variations can be divided into 2 groups with similar developmental mechanisms but different connection patterns: the ascending and descending thoracic VAs. Descending thoracic VAs generally share a common origin with the cervical VA but may also be connected to the SIA or deep cervical artery (atypical forms of Krassnig[5]) (Figs 9 and 10, right).[20] An alternate configuration reported by Bühler[21] consists of a first thoracic ISA originating from the aorta and continuing as a descending thoracic VA to branch off additional ISAs (Fig 10, left).

Ascending thoracic VAs arise from the thoracic aorta and continue cranially as a cervical VA.[7] A thoracic VA can occasionally show mixed characteristics by connecting both at the cervical and thoracic levels (eg, Walsham's case[4]).[7] Dubreuil-Chambardel[7] reviewed the cases of ascending and descending thoracic vertebral arteries published before 1926.

Two configurations developmentally similar to thoracic VAs must be distinguished from this group of variations because they fail to pass through at least 1 costotransverse space. These include more

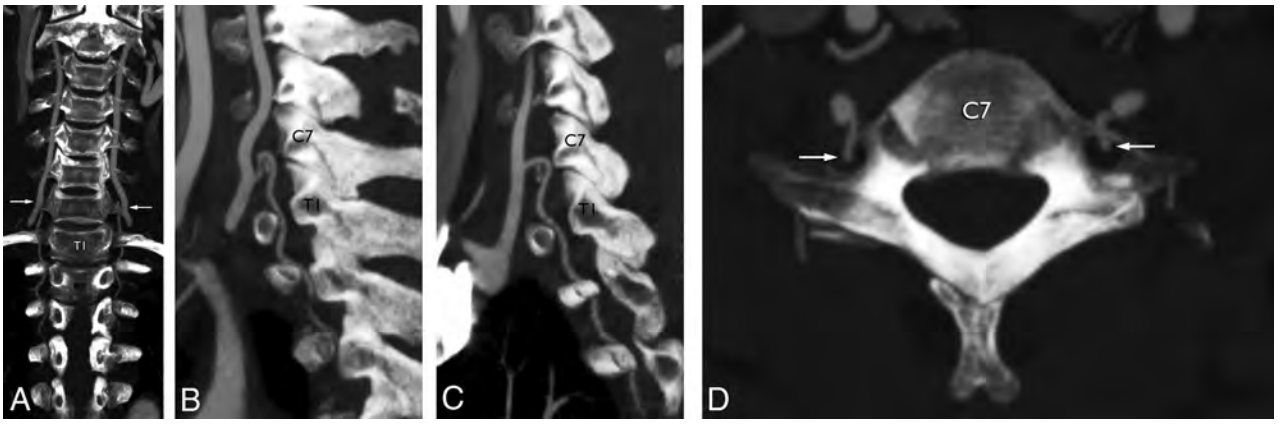

FIG 4. A 59-year-old woman with bilateral descending thoracic vertebral arteries. *A*, CTA, coronal reconstruction at the level of the transverse foramina, documents bilateral and symmetric descending thoracic VAs, both originating at C6–C7 (*arrows*) and ending at T4 on the right and T3 on the left. *B*, CTA, sagittal reconstruction at the level of the left transverse foramina. Note that the level of the variant (C6–C7) is indicated by its tight curve over the anterior margin of the transverse foramen rather than by the actual level of the bifurcation of the common VA trunk (C7–T1). *C*, CTA, sagittal reconstruction at the level of the right transverse foramina. *D*, CTA, axial reconstruction, shows the sharp posterior turn of the descending thoracic VA to pass through the C7 transverse foramina (*white arrows*).

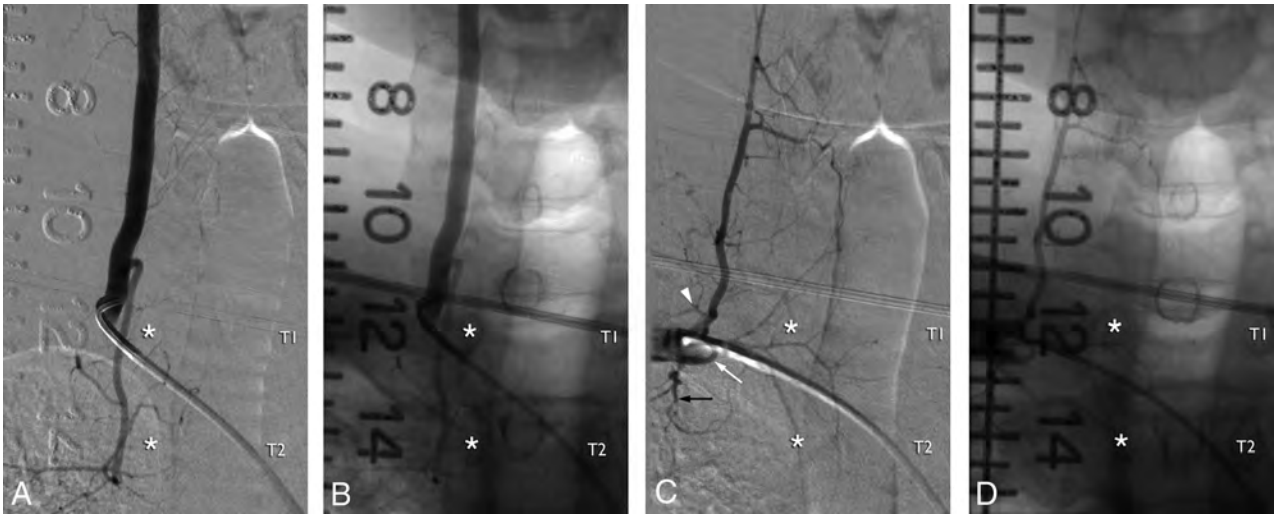

FIG 5. A 30-year-old man with a right-sided descending thoracic vertebral artery. *A*, DSA, right VA injection, posteroanterior projection, subtracted view. Note the typical appearance of the descending thoracic VA, which provides, in this case, medial branches for C7 and T1 and a full set of intersegmental braches for T2 (the *asterisks* indicate the right T1 and T2 pedicles in all images). *B*, DSA, right VA injection, posteroanterior projection, nonsubtracted view. *C*, DSA, right costocervical trunk injection, posteroanterior projection, subtracted view. The existence of a supreme intercostal artery (*white arrow*) is independent of the presence of a descending thoracic VA. In this case, the supreme intercostal artery provides the C7 ISA (*arrowhead*) and the lateral branch of the T1 ISA (*black arrow*). *D*, DSA, right costocervical trunk injection, nonsubtracted posteroanterior projection. Contrary to a descending thoracic VA, the supreme intercostal artery lies away from the vertebral pedicles (hence outside the costotransverse spaces).

cranially bifurcating trunks with a descending branch that remains within the cervical region (Fig 11*A*) and VAs of aortic origin entering the seventh transverse foramen (Fig 11*B*). The latter corresponds to persistent seventh cervical ISAs; their aortic origin remains close to the left subclavian artery.[14] A vertebral arteria lusoria[8] (ie, a right VA originating distal to the left subclavian artery) also known as a "distal aortic origin of the VA" or "fourth branch of the aortic arch,"[9-13] must be distinguished from a thoracic VA as well (though a vertebral arteria lusoria of low origin with a thoracic component is conceivable but, to our knowledge, not reported).

Descending Thoracic Vertebral Arteries

The first case of a descending thoracic VA known to the authors was reported by Quain in 1844 (Fig 12).[22] Pensa[23] confirmed the observation of Quain in 1905 and documented the concomitant existence of thoracic VAs and SIAs (Fig 13). Approximately 70 years later, Newton and Mani[24] offered the first angiographic documentation of a descending thoracic VA (labeled as a "vertebral origin of the SIA"), while Chiras et al[25] published a correctly identified bilateral observation in 1982.

It is important to distinguish descending thoracic VAs from SIAs (both are usually present simultaneously[19]). A major difference is topographic in nature: A thoracic VA is a postcostal vessel passing through costotransverse spaces, while an SIA is a precostal vessel lying in a more lateral position (Figs 1 and 5). Other variations that should not be confused with a descending thoracic VA include VAs originating from the SIA via the seventh cervical ISA (which is often mislabeled as an SIA or costocervical trunk origi-

nating from the VA) (Fig 14) and aberrant bronchial arteries arising from the proximal VA (Fig 15). On the other hand, a VA originating from the SIA via a thoracic ISA (eg, T1 or T2) and entering the first or second costotransverse space would represent an atypical form of an ascending thoracic VA.

Note that in Pensa's illustration,[23] the descending thoracic VA does not give off the lateral branch of T1 (Fig 8). This observation is consistent with our findings: In all except 1 case, the descending thoracic VA branched off at least 1 incomplete proximal ISA, most commonly T1. Adachi et al[19] reported 4 observations of right-sided descending thoracic VAs entering the seventh transverse foramen, all coursing down through the first 3 costotransverse spaces, as in the current report.

The prevalence of descending thoracic VAs may be approximated by considering that 9 cases were documented at our institution (Division of Interventional Neuroradiology, The Johns Hopkins Hospital) during a 5-year period, with an average caseload of approximately 300 diagnostic angiograms per year, hence a prevalence of about 0.6%.

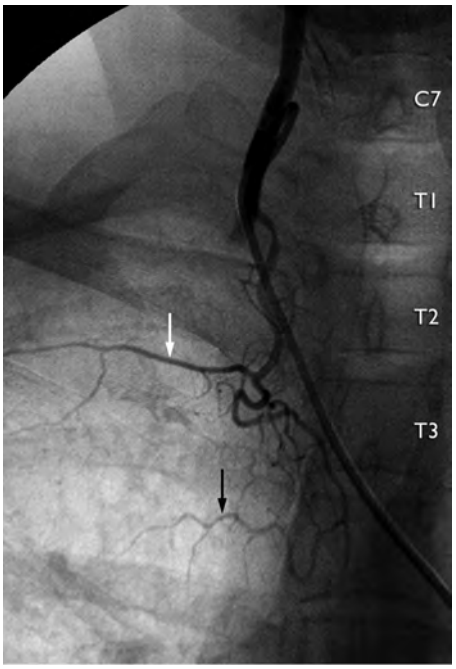

FIG 6. A 47-year-old woman with a right descending thoracic VA. This typical descending thoracic VA provides, in addition to the second thoracic ISA (*white arrow*), a prominent bronchial artery (*black arrow*).

Ascending Thoracic Vertebral Artery

While Adachi et al[19] recorded the existence of ascending thoracic VAs in his anatomic material (Fig 16), no angiographic observation has, to our knowledge, been published so far. In one of our patients with suspected VA dissection, the left VA was found to originate from the second left thoracic ISA (T2). Enlarged left costotransverse spaces at T1 and T2 consistent with the passage of a left ascending thoracic VA were visible on a chest CT. Our second observation was incidental.

Comparative Anatomy

The existence of animal species with vascular configurations matching human anatomic variants helps authenticate these variations and understand their development.[26] Pensa[23] published 2 avian examples of adult anatomy respectively equivalent to typical ascending and descending thoracic VAs in the chicken and the pigeon (Fig 17), while descending thoracic VAs of costocervical origin (atypical form of Krassnig[5]) seem constant in dogs.[6]

Comparative data may also predict variations not yet documented in humans. For example, all 7 pairs of intercostal arteries

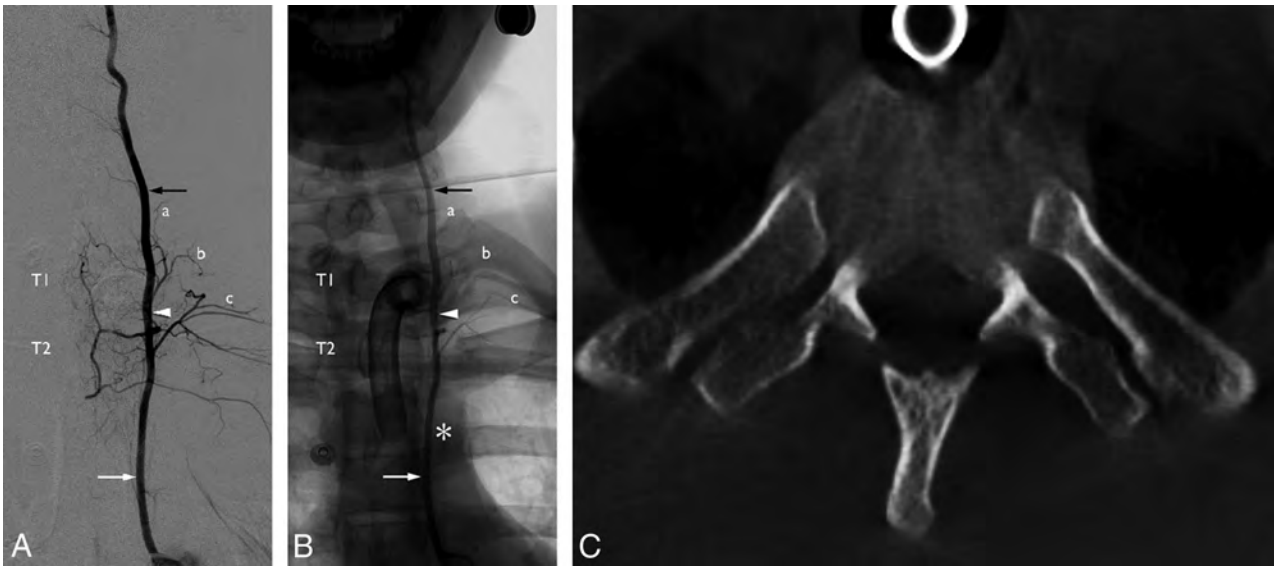

FIG 7. A 20-year-old man with a left ascending thoracic VA. *A*, DSA, left T2 ISA injection, posteroanterior projection, subtracted view. The T2 ISA (*white arrow*) provides the second intercostal artery (c) before crossing through the T2 costotransverse space (*white arrowhead*). It then branches off contributions for the T1 (b) and C7 (a) ISAs and continues cranially as the cervical VA (*black arrow*). *B*, DSA, left T2 ISA injection, posteroanterior projection, nonsubtracted view. The *asterisk* indicates the approximate level of the origin of the left subclavian artery from the aortic arch, illustrating the distance separating the latter from the left T2 ostium. *C*, CT, axial view at the T2 level, shows a marked asymmetry of the size of the T2 costotransverse spaces. This sign should be taken into consideration when planning an upper thoracic spine procedure—for example, when choosing a needle path for a vertebral biopsy or a vertebroplasty.

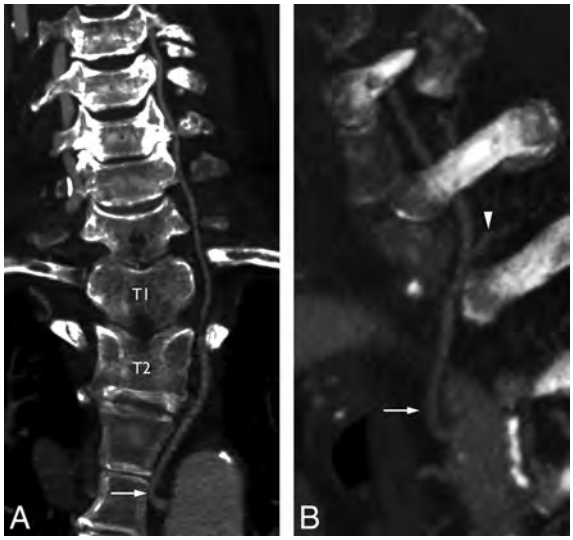

FIG 8. A 64-year-old man with a left ascending thoracic VA. *A*, CTA, coronal MIP reconstruction, shows the origin of the left T2 ISA (*white arrow*) and its passage through the T2 and T1 costotransverse spaces. The vessel then continues cranially as the cervical VA. *B*, CTA, oblique MIP reconstruction, documents the T2 posterior intercostal artery (*arrowhead*), therefore identifying the ascending thoracic VA as being derived from the second thoracic ISA (*arrow*).

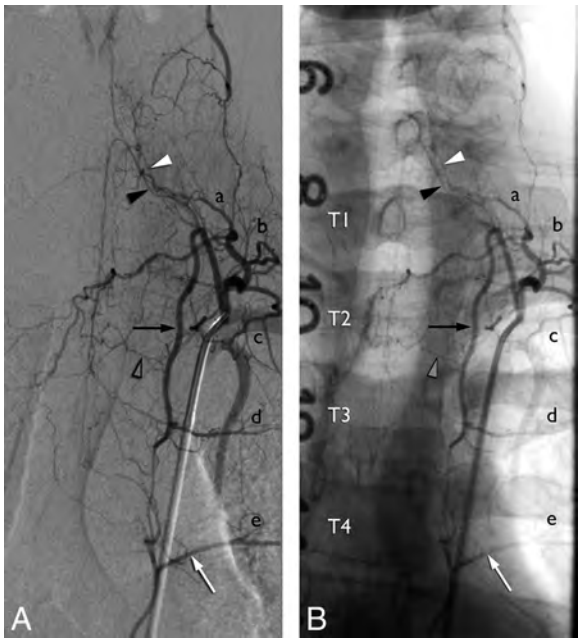

FIG 9. A 31-year-old woman with an atypical descending thoracic VA. *A*, DSA, left supreme intercostal artery injection, posteroanterior projection, subtracted view shows an example of a descending thoracic VA originating from the supreme intercostal artery (atypical form of Krassnig[5]); in this case, there is no connection with the cervical VA. The supreme intercostal artery provides the C7 (a) and T1 (b) ISAs as well as the lateral branch of the T2 ISA (c). A prominent ascending branch curves sharply downward to enter the first costotransverse space and continues caudally as a descending thoracic VA (*black arrow*) passing through the T2 and T3 the costotransverse spaces. This descending thoracic VA provides the T3 ISA (d) and the medial branch of the T2 ISA (*gray arrowhead*). Note the opacification of the T4 ISA (e) via a small paravertebral anastomotic connection (as shown in Fig 1, right side). The C7 ISA provides both an anterior (*black arrowhead*) and a posterior (*white arrowhead*) radiculomedullary artery. *B*, DSA, left supreme intercostal artery injection, posteroanterior projection, nonsubtracted view of same image.

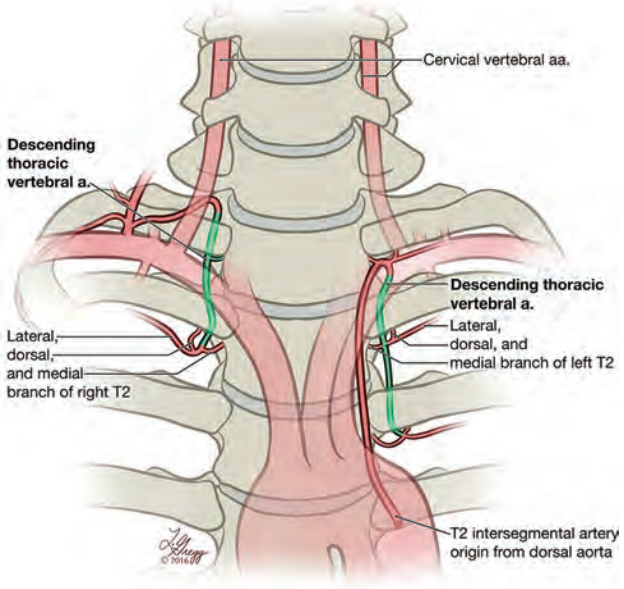

FIG 10. Schematic representation of 2 types of descending thoracic VA variants. The descending thoracic VA (atypical form of Krassnig[5]) depicted on the right side is, as in Fig 9, connected with the supreme intercostal artery rather than the cervical VA. In the configuration shown on the left side (atypical form of Bühler[21]), the descending thoracic VA is the downward continuation of a thoracic ISA of aortic origin. a. indicates artery.

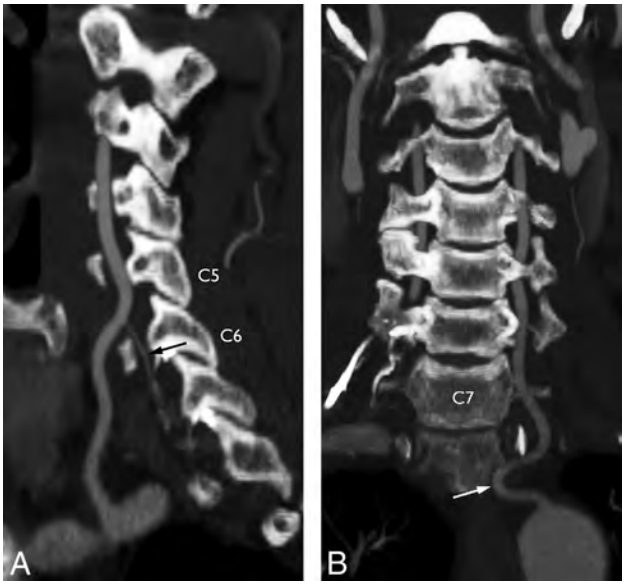

FIG 11. Examples of vertebral configurations similar to but distinct from thoracic VAs. *A*, CTA, sagittal MIP reconstruction. This case shows a descending branch with an appearance similar to that of a descending thoracic VA (*arrow*). However, the bifurcation is located at C5–C6, and the descending branch stops at C7, short of the first costotransverse space. There is, therefore, no thoracic segment. *B*, CTA, coronal MIP reconstruction, shows a vertebral artery originating from the aorta distal to the subclavian artery and entering the seventh transverse foramen (*arrow*). This vessel corresponds to a persistent seventh ISA and has no thoracic component.

in the European pond turtle are branches of an anastomotic chain similar in nature to a VA,[23] an observation suggesting that such extensive longitudinal vertebral chains may, as extreme variants, exist in humans as well.

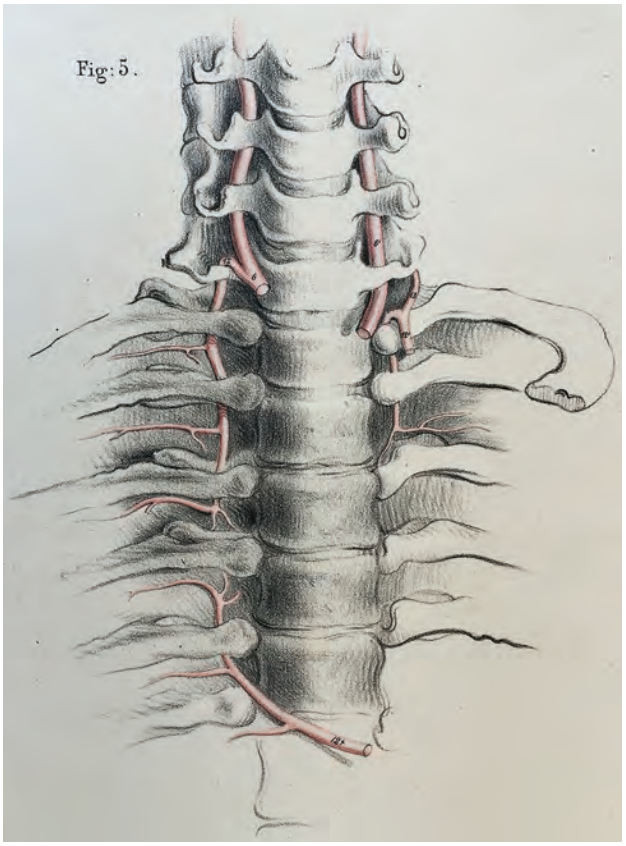

FIG 12. First known representation of a descending thoracic vertebral artery by Joseph Maclise for Richard Quain in 1844 (Fig 5, Plate XXII).[22] The figure accurately depicts a typical descending thoracic VA on the right side (12) and an atypical form on the left (12′), as later defined by Krassnig.[5] While both vessels are clearly coursing within the costotransverse spaces, the distinction from the supreme (or superior) intercostal arteries has not yet been established. The original legend is the following: "The left vertebral enters the last cervical vertebra. On the right side the superior intercostal artery is derived from the vertebral, and passes downwards into the thorax through the foramen in the transverse process of the seventh cervical vertebra, and afterward between the necks of the ribs and the corresponding transverse processes of the dorsal vertebræ. It will be observed that the superior intercostal of the other side descends also between the ribs and the processes of the vertebræ; and that the first aortic intercostal branch occupies a similar position in reference to the bones." 6 indicates right vertebral, 6′, left vertebral; 12, right superior intercostal; 12′, left superior intercostal; 12†, first aortic intercostal; 13, deep cervical (arteria profunda cervicis).

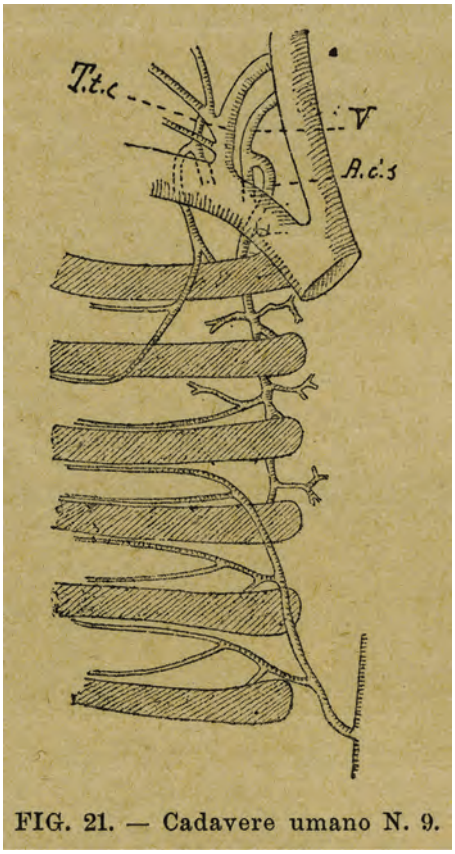

FIG 13. Reproduction of the original Fig 21 of Pensa,[23] showing an example of a typical descending thoracic VA providing T1 partially and T2 entirely. The supreme intercostal artery (originating from an unlabeled costocervical trunk) is clearly distinguished from the thoracic VA, both in the illustration and in the Pensa's text, the latter emphasizing the respective precostal and retrocostal locations of the 2 vessels. However, the nomenclature remains uncertain; Pensa labeled the descending thoracic VA as an arteria intercostalis suprema (A.i.s). V indicates vertebral artery; T.t.c, thyrocervical trunk.

Clinical Relevance

Spine surgeons and interventionists must be aware of the existence of thoracic VAs because their injury during a vertebral procedure may prove significant, notably in cases of ascending thoracic VAs supplying the posterior fossa. One or more abnormally conspicuous costotransverse space may be the only sign indicating the presence of such a variant on preoperative imaging (Fig 7*C*).

These variants also have a significant angiographic importance. Thoracic VAs may, through one of their frequent radiculomedullary branches, supply a spinal vascular malformation or be involved in the development of spinal cord ischemia. Similarly, because ascending thoracic VAs participate in the vascularization of the posterior fossa, they may play a role in vertebrobasilar in-

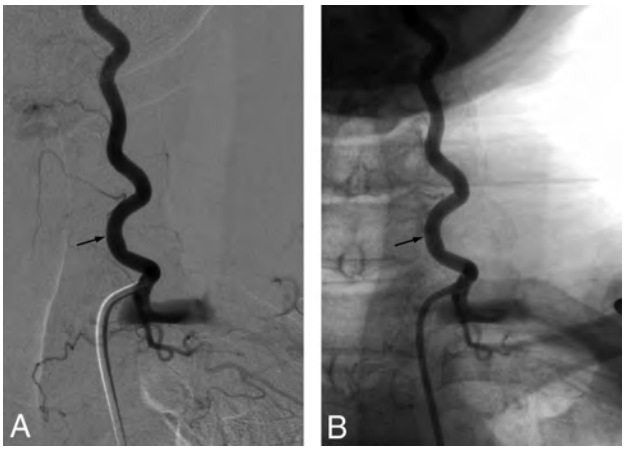

FIG 14. Vertebral artery variant in a 55-year-old woman. This left vertebral injection (posteroanterior projection, subtracted, *A*, and nonsubtracted, *B*, images) documents a vertebral artery that originates from the supreme intercostal artery (ie, a persistent seventh ISA) and enters the transverse canal at C7 (*arrow*). Because the vertebral artery becomes dominant in the adult stage, it falsely suggests an opposite relationship (ie, a supreme intercostal artery of vertebral origin).

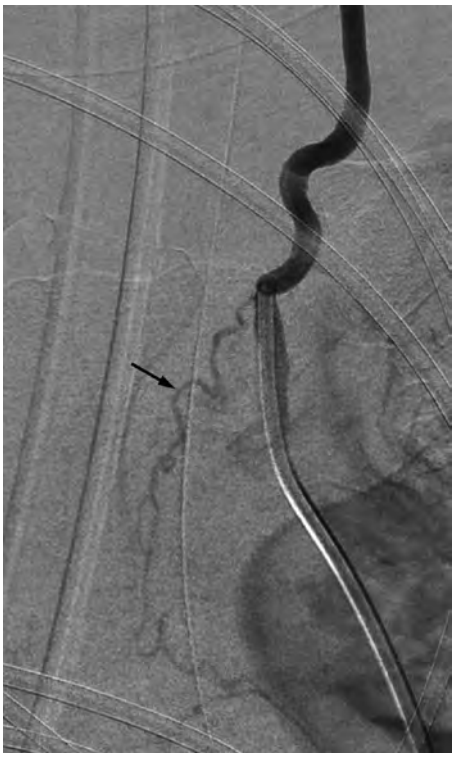

FIG 15. Vertebral artery variant in a 58-year-old woman. Left vertebral injection (posteroanterior projection) documents a prominent aberrant bronchial branch (*arrow*) of vertebral origin.

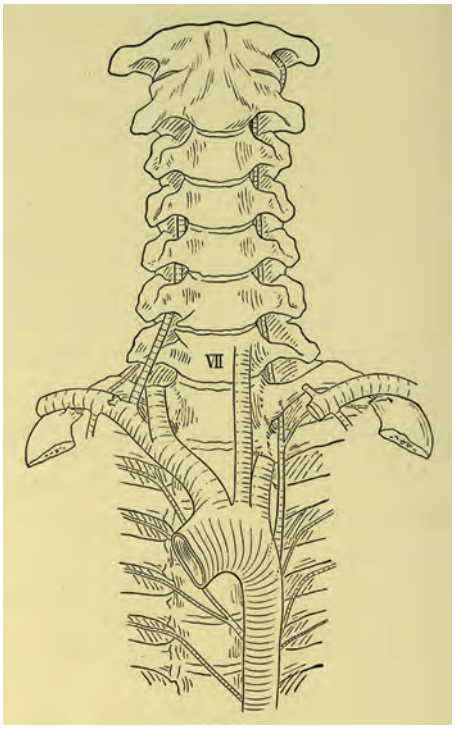

FIG 16. Reproduction of the original Fig 16 (Vol. 1, page 36) of Adachi.[19] Adachi presents a left ascending thoracic VA originating from the aorta at the T3–T4 level and passing behind the head of the first rib to enter the first costotransverse space before continuing cranially as the left cervical vertebral artery.

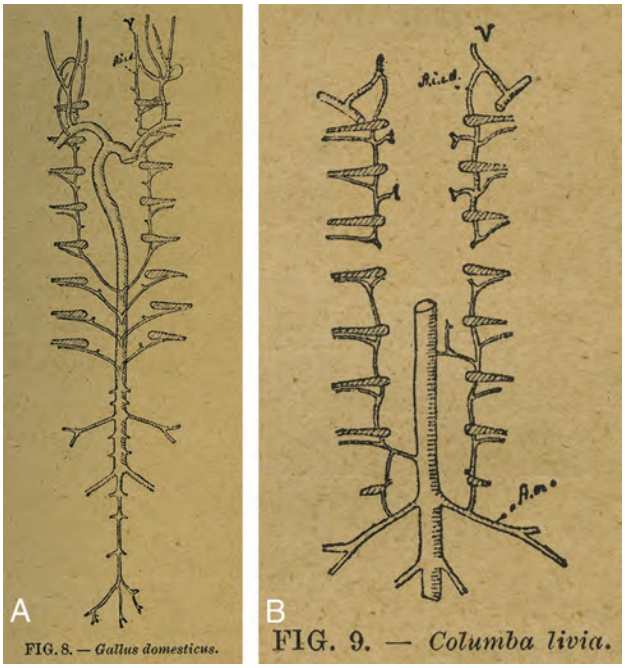

FIG 17. Examples of ascending and descending thoracic aortas in birds (from Pensa[23]). *A*, Bilateral ascending thoracic vertebral arteries in the chicken (*Gallus domesticus*); note a cranial anastomosis with the costocervical trunk. *B*, Bilateral descending thoracic vertebral arteries in the domestic pigeon (*Columba livia*). V indicates vertebral artery; Ai.c.d., arteria intercostalis communis descendens; A.cr., arteria cruralis.

sufficiency or supply an intracranial aneurysm or vascular malformation. They can also represent a source of embolic material, either of atheromatous or iatrogenic origin.

Finally, the possibility that a descending thoracic VA can contribute to the bronchial vascularization must be kept in mind when investigating a hemoptysis of elusive origin.

In summary, thoracic VAs are anastomotic chains similar to normal cervical VAs but extending through at least 1 costotransverse space. They can be divided into ascending and descending types that differ by their origin, course, and clinical implications.

Disclosures: Philippe Gailloud—*UNRELATED*: *Grants/Grants Pending*: Siemens*; *Consultancy*: Codman Neurovascular. Monica S. Pearl—*UNRELATED*: *Grants/Grants Pending*: National Institutes of Health.* *Money paid to the institution.

REFERENCES

1. Padget DH. **Designation of the embryonic intersegmental arteries in reference to the vertebral artery and subclavian stem.** *Anat Rec* 1954;119:349–56 Medline
2. Hochstetter F. **Uber die Entwicklung der A. Vertebralis beim Kaninchen, nebst Bemerkungen über die Entstehung des Ansa Vieussenii.** *Morphol Jahrb* 1890;16:572–86
3. Schmeidel G. **Die Entwicklung der Arteria vertebralis des Menschen.** *Morphol Jahrb* 1933;71:315–435
4. Walsham WJ. **Abnormal origin and distribution of the upper seven right intercostal arteries, with remarks.** *J Anat Physiol* 1882;16:441–62 Medline
5. Krassnig M. **Von der Arteria vertebralis thoracica der Säuger und Vögel.** *Beiträge und Referate zur Anatomie und Entwickelungsgeschichte* 1913;49:523–609 CrossRef
6. Wenthe M, Waibl H, Meyer W. **Some observations on the arteria vertebralis thoracica in the dog.** *Kasetsart Veterinarians* 2009;19:65–69

7. Dubreuil-Chambardel L. *Traité des Variations du Système Artériel: Variations des Artères du Membre Supérieur.* Paris: Masson et Cie; 1926:37–44
8. Lacout A, Khalil A, Figl A, et al. **Vertebral arteria lusoria: a life-threatening condition for oesophageal surgery.** *Surg Radiol Anat* 2012;34:381–83 CrossRef Medline
9. Higashi N, Shimada H, Simamura E, et al. **Right vertebral artery as the fourth branch of the aortic arch.** *Anat Sci Int* 2008;83:314–18 CrossRef Medline
10. Lemke AJ, Benndorf G, Liebig T, et al. **Anomalous origin of the right vertebral artery: review of the literature and case report of right vertebral artery origin distal to the left subclavian artery.** *AJNR Am J Neuroradiol* 1999;20:1318–21 Medline
11. Sakamoto H. **A case of the right vertebral artery as the last branch of the aortic arch (author's transl)** [in Japanese]. *Kaibogaku Zasshi* 1980;55:503–08 Medline
12. Mukkannavar SB, Kuthe SA, Mishra AK, et al. **Aberrant right vertebral artery from descending thoracic aorta.** *Ann Thorac Surg* 2013; 96:1074–76 CrossRef Medline
13. Hsu DP, Alexander AD, Gilkeson RC. **Anomalous vertebral artery origins: the first and second reports of two variants.** *J Neurointerv Surg* 2010;2:160–62 CrossRef Medline
14. Koenigsberg RA, Pereira L, Nair B, et al. **Unusual vertebral artery origins: examples and related pathology.** *Catheter Cardiovasc Interv* 2003;59:244–50 CrossRef Medline
15. His W. *Anatomie Menschlicher Embryonen, III: Zur Geschichte der Organe.* Leipzig: Verlag von F.C.W. Vogel; 1885:193
16. Kadyi H. *Über die Blutgefässe des Menschlichen Rückenmarkes.* Lemberg: Gubrynowicz & Schmidt; 1889:26
17. Charpy A. *Système Nerveux.* Paris: Masson et Cie; 1902
18. Kappers A, Strasburger EH, Addens JL. *Anatomie Comparée du Système Nerveux.* Harleem: Bohn; 1947:532
19. Adachi B. *Das Arteriensystem der Japaner.* Kyoto: Kaiserlich-japanische Universität zu Kyoto, in kommission bei "Maruzen Co."; 1928: 33–36, 191–92
20. Barkow HC. *Die Angiologische Sammlung im Anatomischen Museum der Königlichen Universitätzu Breslau.* Breslau: Hirt; 1869:XL–LI
21. Bühler A. **Varietät der ersten fünf intercostalarterien.** *Gegenbaurs Morphologisches Jahrbuch* 1904;32:189–94
22. Quain R, Maclise J. *The Anatomy of the Arteries of the Human Body, with its Applications to Pathology and Operative Surgery: In Lithographic Drawings with Practical Commentaries.* London: Taylor and Walton; 1844:142 (Plate 22)
23. Pensa A. **Studio sulla morfologia e sullo sviluppo della arteria intercostalis suprema e delle aa. intercostales.** *Ricer Lab Anat Univ Roma* 1905;11:33–142
24. Newton T, Mani R. **The vertebral artery.** In: Newton T, Potts D, eds. *Radiology of the Skull and Brain: Angiography.* Vol 2. Book 2. St. Louis: Mosby; 1974:1659–709
25. Chiras J, Launay M, Gaston A, et al. **Thoracic vertebral artery: an anomaly of the vertebral artery.** *Neuroradiology* 1982;24:67–70 CrossRef Medline
26. Bremer JL. **The origin of the renal artery in mammals and its anomalies.** *Am J Anat* 1915;18:179–200 CrossRef

Reduction of Motion Artifacts and Noise Using Independent Component Analysis in Task-Based Functional MRI for Preoperative Planning in Patients with Brain Tumor

E.H. Middlebrooks, C.J. Frost, I.S. Tuna, I.M. Schmalfuss, M. Rahman, and A. Old Crow

ABSTRACT

BACKGROUND AND PURPOSE: Although it is a potentially powerful presurgical tool, fMRI can be fraught with artifacts, leading to interpretive errors, many of which are not fully accounted for in routinely applied correction methods. The purpose of this investigation was to evaluate the effects of data denoising by independent component analysis in patients undergoing preoperative evaluation for glioma resection compared with more routinely applied correction methods such as realignment or motion scrubbing.

MATERIALS AND METHODS: Thirty-five functional runs (both motor and language) in 12 consecutive patients with glioma were analyzed retrospectively by double-blind review. Data were processed and compared with the following: 1) realignment alone, 2) motion scrubbing, 3) independent component analysis denoising, and 4) both independent component analysis denoising and motion scrubbing. Primary outcome measures included a change in false-positives, false-negatives, *z* score, and diagnostic rating.

RESULTS: Independent component analysis denoising reduced false-positives in 63% of studies versus realignment alone. There was also an increase in the *z* score in areas of true activation in 71.4% of studies. Areas of new expected activation (previous false-negatives) were revealed in 34.4% of cases with independent component analysis denoising versus motion scrubbing or realignment alone. Of studies deemed nondiagnostic with realignment or motion scrubbing alone, 65% were considered diagnostic after independent component analysis denoising.

CONCLUSIONS: The addition of independent component analysis denoising of fMRI data in preoperative patients with glioma has a significant impact on data quality, resulting in reduced false-positives and an increase in true-positives compared with more commonly applied motion scrubbing or simple realignment methods.

ABBREVIATIONS: BOLD = blood oxygen level–dependent; ICA = independent component analysis; DVARS = root-mean-square of the derivatives of the differentiated time courses of every brain voxel for each acquired volume; MD = mean displacement; TC = task correlation

Functional MR imaging has become a widely used tool for examining the function of the brain, during both tasks and rest. Currently, the primary clinical impact of fMRI is in presurgical planning, including both epilepsy and tumor applications. The use of preoperative structural and functional images during brain tumor resection has been shown to decrease the duration of the operation, reduce operative complications, and improve patient survival.[1,2] Unfortunately, fMRI comes with limitations, several of which can lead to impactful interpretive errors.

Blood oxygen level–dependent (BOLD) functional MR imaging relies on the detection of subtle signal changes related to the relationship of oxy- and deoxyhemoglobin as a surrogate marker of neuronal activity.[3,4] Ideally, signal change should not exist outside that created by perturbations of this balance in oxygenated and deoxygenated blood; unfortunately, numerous other contributions to the signal change confound fMRI data, such as artifacts related to head motion, physiologic noise, and scanner-related noise.[5-8] In fact, at higher magnetic field strengths, including 3T, the dominant signal in BOLD imaging has been shown to be related to physiologic noise.[9]

Unfortunately, many of the methods routinely used to correct for these artifacts do not fully account for their effect on the data.[5,10-12] For example, the regularly used "motion correction" algorithms in many fMRI processing programs simply result in spatial realignment of individual voxels for the scan duration. Used in this context, the term "motion correction" is a misnomer.

Received June 26, 2016; accepted after revision September 7.

From the Department of Radiology (E.H.M.), University of Alabama at Birmingham, Birmingham, Alabama; Department of Biology (C.J.F.), University of Louisville, Louisville, Kentucky; Medical Imaging Consultants (C.J.F.), Gainesville, Florida; Departments of Radiology (I.S.T., I.M.S., A.O.C.) and Neurosurgery (M.R.), College of Medicine, University of Florida, Gainesville, Florida; and North Florida/South Georgia Veterans Administration (I.M.S.), Gainesville, Florida.

Please address correspondence to Erik H. Middlebrooks, MD, Department of Radiology, University of Alabama at Birmingham, 619 19th St S, JT 3N, Birmingham, AL 35249-6830; e-mail: ehmiddlebrooks@gmail.com

Indicates article with supplemental on-line tables.

Indicates article with supplemental on-line photos.

http://dx.doi.org/10.3174/ajnr.A4996

It is essential to understand that these typical rigid-body motion-correction algorithms do not account for significant variance in the data produced by myriad motion-related artifacts.[10,11,13] Two major culprits are those related to a changing susceptibility profile in the scanner and the effect of the spatial location of spin magnetization saturation, more commonly referred to as spin-history artifacts.[11] Likewise, numerous other prospective and retrospective methods designed to account for motion-, physiologic-, and scanner-related effects have shown limited improvement.[14-18]

The use of independent component analysis (ICA) for removing the nuisance effects in fMRI data has grown in popularity.[19-21] Fundamentally, ICA separates a mixture of signals in a dataset into its individual signal components. ICA is commonly explained with the analogy of a cocktail party, in which the recorded, indistinct sound from numerous conversations can be deconstructed into individual voices. ICA denoising has been shown to increase statistical significance and sensitivity, resulting in fewer false-positives and false-negatives.[22] The goal of our study was to evaluate the role of ICA denoising on fMRI data of patients undergoing preoperative planning for brain tumor resection.

MATERIALS AND METHODS

The requirement for informed consent was waived in this Health Insurance Portability and Accountability Act–compliant retrospective study, which was approved by the University of Florida institutional review board. Thirty-five runs from 12 consecutive patients undergoing preoperative planning for glioma resection were retrospectively reviewed. Various language (semantic decision [6/35], sentence completion [3/35], word generation [5/35], picture naming [3/35]) and motor (finger [6/35], foot [4/35], tongue [2/35], face [6/35]) paradigms were used. See On-line Table 1 for details of the task designs. All patients were trained on the tasks by the administering physician (E.H.M.).

Image Acquisition

MR imaging data were acquired on a 3T Verio scanner (Siemens, Erlangen, Germany) with a 12-channel head coil. In an attempt to minimize head motion, the head was tightly packed with moldable foam. The importance of reducing head motion was explained to patients. A volumetric T1-weighted MPRAGE sequence with a voxel size of $1 \times 1 \times 1$ mm, TR = 2530 ms, TE = 3.5 ms, TI = 1100 ms, and flip angle = 7° was obtained. BOLD-EPI images used a $3.5 \times 3.5 \times 3.5$ mm voxel size with a 0.7-mm intersection gap, TR = 2000 ms, TE = 30 ms, and flip angle = 78°, with an oblique axial interleaved acquisition. All patients were monitored and scanned by the administering physician (E.H.M.).

Data Processing

Echo-planar images were processed with the fMRIB Software Library (FSL, Version 5.0; http://www.fmrib.ox.ac.uk/fsl).[23] Preprocessing of all datasets included realignment (Motion Correction using FMRIB's Linear Image Registration Tool [MCFLIRT]; http://fsl.fmrib.ox.ac.uk/fsl/fslwiki/MCFLIRT),[24] section-timing correction, and spatial smoothing (5-mm full width at half maximum). The preprocessed data were then processed using 4 differing methods. First, the preprocessed, realigned data were processed without any further manipulation. Second, motion scrubbing was performed by regressing individual volumes that exceeded a strict threshold for excessive section-signal variation based primarily on mean displacement and root-mean-square of the derivatives of the differentiated time courses of every brain voxel for each acquired volume (DVARS), as described in Power et al.[25] Third, ICA analysis was performed (Multivariate Exploratory Linear Optimized Decomposition into Independent Components [MELODIC]; http://fsl.fmrib.ox.ac.uk/fsl/fslwiki/MELODIC), and nuisance components were manually identified by visual inspection of components by an experienced ICA user (E.H.M.) and were removed by using the fsl_regfilt command. The methodology of characterizing components as noise- or task-related signal is based on the methodology used in the excellent review presented in Kelly et al.[26] Last, both ICA denoising and motion scrubbing were performed, as previously described.

Data were analyzed using the FSL General Linear Model (http://fsl.fmrib.ox.ac.uk/fsl/fslwiki/GLM) with cluster thresholding in FMRIB Expert Analysis Tool (FEAT; http://fsl.fmrib.ox.ac.uk/fsl/fslwiki/FEAT). Identical threshold levels were applied to all 4 processing methods to determine the effects of the 4 processing pipelines on statistical significance. Processed EPI data were then linearly registered to the T1-weighted structural images (FMRIB Linear Image Registration [FLIRT]; http://www.fmrib.ox.ac.uk). Data for all 4 processing methods were overlaid to detect differences in each methodology. Two neuroradiologists with functional imaging experience (E.H.M., I.S.T.) independently and blindly evaluated the overlaid data to assess the presence or absence of expected activation based on the task, amount of noise, and change in statistical significance (z score variance) of the activated areas and whether any or all of the processing methods were considered diagnostic. Diagnostic studies were defined as showing all expected areas of activation for the given task regardless of tumor location, to minimize the subjectivity of the meaning of diagnostic versus nondiagnostic. The subjective measures of noise, new real areas of activation, and diagnostic ability for each method resulted in 560 individual binary data points, which were entered in to an assessment of reader agreement. Disagreements were settled by a third blinded reader (I.M.S.).

Data Analysis

We extensively evaluated image quality and tabulated 3 primary motion parameters: mean displacement (MD), task correlation (TC), and DVARS. For MD, each functional run was placed in 1 of 3 categories from none/mild, moderate, to severe, as follows: $<$1-mm MD throughout the study, 1- to 2-mm MD in $\leq$4 spikes, or any MD of $>$2 mm or $>$1 mm for $>$4 spikes. Likewise, DVARS was categorized as the following: no spikes of $>$5% signal change from volume to volume, 1–5 spikes of $>$5%, or $>$5 spikes of $>$5%. TC was categorized as $r < 0.05$, $0.05 \leq r < 0.2$, or $r \geq 0.2$.

Due to the ordinal and nominal nature of the data, contingency analysis was used with motion parameters (ordinal) as independent measurements to evaluate their relationships to the nominal, binary (yes/no) response outcome measures. The Cochran-Armitage exact test for trend was appropriate to capture the power of the ordinal motion parameter measurements to assess statistical significance; the Fisher exact test was used when the motion parameter data were collapsed into binary variables

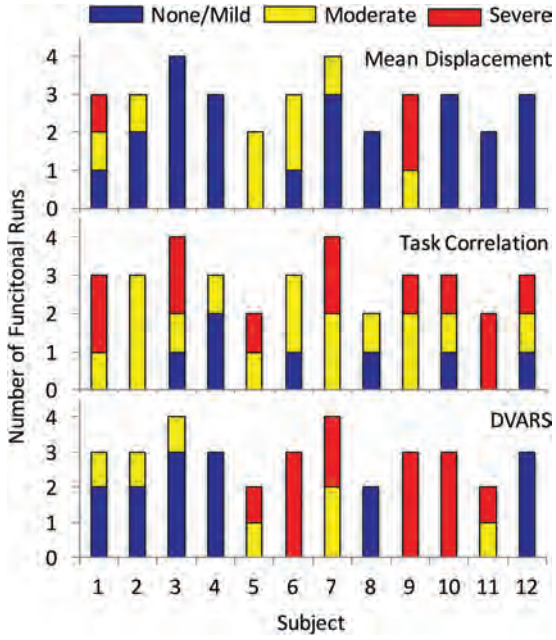

FIG 1. Distribution of motion parameters in each individual subject showing the number of functional runs characterized as having a none/mild, moderate, or severe rating in each of the 3 recorded parameters (DVARS, task-correlated motion, and MD).

(eg, assessing ICA-salvaged diagnostic studies). χ^2 was used to assess expected-versus-observed effects among the 12 subjects, including subject-level variation of the motion parameter severity and comparing the number of diagnostic-versus-nondiagnostic scans when realignment alone, motion scrubbing, ICA, or both ICA and motion scrubbing was applied.

RESULTS

The 2 readers' independent evaluations agreed in 97% (546/560) of individual recorded data points; only 14 evaluations required a tie-breaker with a blinded third reader (On-line Table 2).

Motion Parameters

The individual motion parameters are illustrated in Fig 1. A severe rating was present in 1 of the 3 motion parameters in 60% (21/35) of studies and in >1 motion parameter in 17% (6/35) of studies. MD and DVARS were patient-specific: Half of patients had none/mild MD ($\chi^2 = 35.5$, $P = .034$), while half of patients accounted for nearly all (17/20) moderate or severe DVARS ($\chi^2 = 39.3$, $P = .013$). In contrast, task-correlated motion of >0.05 was observed in at least 1 paradigm in all 12 patients, with severe task-correlated motion distributed across 8 patients ($\chi^2 = 20.6$, $P = .547$). While there were no statistical differences in motion parameters between language and motor studies, motor tasks accounted for 8 of the 12 severe TC motion studies (On-line Fig 1).

fMRI Statistical Analyses

ICA denoising resulted in demonstrable improvement in overall fMRI quality. ICA denoising decreased the level of noise (false-positives) in the activation maps in 63% (22/35) of cases compared with realignment alone. A reduction in noise after ICA denoising was not correlated with any individual motion parameter or combination thereof. ICA also improved the statistical significance in regions of expected activation in 71.4% (25/35) of cases compared with realignment or motion scrubbing alone. ICA improved fMRI statistics, as assessed by an increase in the z score in areas of expected activation, in almost all scans with high MD (7/8 and 3/3 cases of moderate and severe MD, respectively; $z = -1.75$, $P = .040$). Additionally, ICA improved fMRI statistics with moderate or high TC ($z = -1.80$, $P = .036$) and when MD and TC were considered together ($z = -1.92$, $P = .049$). New expected areas of activation (previous false-negatives) were present only after ICA denoising in 34.3% (12/35) of the datasets and were not correlated with any motion parameter. Motion scrubbing alone did not reveal new areas of expected activation (previous false-negatives) compared with realignment alone or ICA. The combination of ICA and motion scrubbing showed no difference from ICA alone.

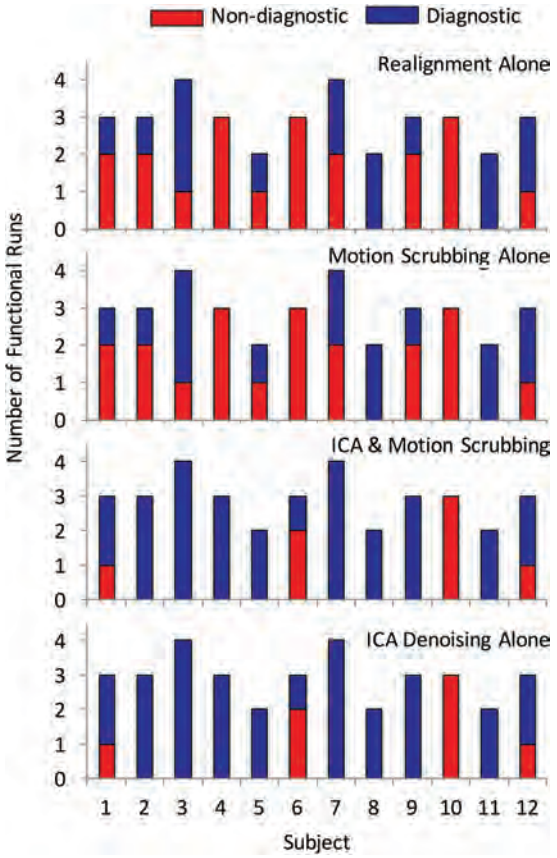

FIG 2. Distribution of diagnostic and nondiagnostic scans for each correction method per subject.

Diagnostic Quality

Most important, ICA denoising improved the diagnostic value of the fMRI studies (Fig 2). After realignment alone, 10 of the 12 patients had at least 1 nondiagnostic scan ($\chi^2 = 14.9$, $P = .186$; Fig 2, upper graph), with 3 patients having all nondiagnostic-quality scans. In all, 57% (20/35) of scans were deemed nondiagnostic when corrected with realignment only. ICA denoising rendered diagnostic 65% (13/20) of the previously nondiagnostic scans, increasing the overall percentage of diagnostic scans from 42.9% to 80.0% ($\chi^2 = 6.3$, $P < .001$). Moreover, ICA denoising improved the diagnostic outcome for 11 of 12 patients, with 8 pa-

tients having all scans of diagnostic quality ($\chi^2 = 22.5$, $P = .021$; Fig 2, lower graph). Notably, all 7 scans (in 4 patients) that remained nondiagnostic after ICA denoising contained severe TC and/or DVARS ($z = 2.76$, $P = .004$). In contrast, motion scrubbing failed to improve any of these scans to the point of being diagnostic (Fig 2, second graph), which is in line with the failure of motion scrubbing to reveal any new areas of activation compared with motion correction alone.

Motion scrubbing alone increased the statistical significance in expected areas of activation in 20% (7/35) of the scans compared with realignment alone but only showed improved statistical significance versus ICA denoising in 1 case (with low MD, severe TC, and moderate DVARS). Motion scrubbing had the greatest effect in those scans with moderate-severe ratings in TC alone ($z = -1.75$, $P = .040$) or to a lesser extent when MD and TC were considered together ($z = -1.67$, $P = .054$). The addition of motion scrubbing to ICA denoising did not show any improvement over ICA denoising alone.

DISCUSSION

Based on the previously reported success of ICA in improving data quality in both task-based and resting-state fMRI studies, our goal was to investigate its utility in preoperative planning for patients undergoing resection for gliomas. We found improvement in statistical significance and decreased noise, resulting in fewer false-positives and, perhaps more important, an increase in true-positives, similar to findings in studies in patients without tumors.[20,27,28] We also found that a proportion of studies, otherwise nondiagnostic when processed with traditional methods, were diagnostic after ICA denoising.

As previously discussed, underlying motion-related artifacts, physiologic noise, and scanner-related noise, which are ubiquitous in fMRI, have serious detrimental effects on fMRI interpretation. The first of these, subject motion, is becoming an increasingly recognized cause of fMRI misinterpretation. For example, a prominent theory in autism that touted decreased long-range connections was eventually shown to be related to increased head motion in the autistic group relative to controls.[12,29] For any user of fMRI, it is essential to have a thorough understanding of motion and related artifacts. An important tenet of high-quality fMRI is homogeneity of the B0 magnetic field. When an object is introduced into the bore of the scanner, the field becomes distorted and is corrected for with a shimming procedure. However, if the object moves once in the bore, this shim effect is lost and the susceptibility profile of the object changes. This change can result in drastic changes in signal intensity and geometric distortion that cannot be corrected by typical realignment procedures.[11,13] Shifts as small as 2° can potentially create large areas of false-positive activation regardless of intensive thresholding.[13]

A second major consideration regarding patient motion in fMRI is signal change as a result of spin-history artifacts. Given the typical short TRs in fMRI, the brain achieves a steady-state of incomplete longitudinal magnetization recovery after a few TRs. This recovery is slightly out of phase in any individual section. Once the head moves, these voxels will be shifted into a different plane, resulting in either a lower- or higher-than-expected amount of recovery in sections obtained prior or subsequent to the reference section, respectively. This unexpected change in magnetization recovery can have a substantial effect on signal intensity.[11] While abrupt motion with a large amount of displacement can have noticeable effects on the signal intensity, minimal amounts of motion (<1-mm displacement) can have a substantial impact on the data if the motion is frequent. Because this movement is low-amplitude, one cannot expect to see significant outliers in mean signal intensity across volumes. Spin-history artifacts are best assessed by DVARS, which assesses the volume-to-volume signal change.[25] In our data, we found this frequent, low-amplitude motion (<1 mm) effect to be the most common source of nondiagnostic studies.

Third, when signal fluctuations from artifacts, such as the previously mentioned spin-history artifacts and susceptibility changes, create a time-series similar to the experimental design, commonly referred to as "task-correlated motion," the artifactual component is generally inseparable from task-related signal change.[8,28,30] Our results show that task-correlated motion has a strong prevalence in nondiagnostic studies, including studies that are not even improved by ICA denoising. Although neurovascular uncoupling could potentially be the source of these nondiagnostic studies, the prevalence of task-correlated motion suggests that this may also be an etiology. Given the impact of TC on study outcomes, the assessment of this parameter should be a routine part of fMRI data quality analysis.

Physiologic noise is also a major source of variance in BOLD fMRI data and is primarily related to fluctuations in basal metabolism, cardiac and respiratory effects, and subtle motion effects from brain pulsation. In fact, it has been shown that physiologic noise at a higher field strength (3T) is the dominant source of noise in fMRI and even counteracts much of the gain in signal-to-noise ratio and contrast-to-noise ratio when moving to higher magnetic field strengths.[9,31] Due to the typically short TRs used in fMRI, the frequency of these artifacts results in their aliasing into the task-related signal.[7] Because this noise is structured, nonwhite noise, it does not meet the statistical assumption that errors are independent and identically distributed; therefore, it will have a significant impact on most statistical modeling.[32] Similarly, scanner-related noise, such as thermal noise, drift, and imperfections in the coil, radiofrequency, gradient, and shim subsystems and various other minor contributors, produces similar effects.[9] Our study revealed a large decrease in false-positives with use of ICA versus other methods; however, the ICA decrease in false-positives did not correlate with any motion parameters. This finding could suggest that removal of physiologic and scanner noise is also a major contributor to improvement seen with ICA versus other methods.

Many attempts have been made to reduce artifacts in fMRI; however, they remain extremely problematic. There are generally 2 types of artifact-correction systems, hypothesis-driven and data-driven. Hypothesis-driven systems include prospective motion-correction systems, such as the use of navigator sequences,[33,34] optical motion tracking,[16,18,35] or methods of measuring physiologic parameters during the scan (ie, heart rate, respiratory rate, and so forth) that are then used to apply filters to the data or used as nuisance regressors.[7,14] Unfortunately, these methods have been difficult to implement due to inaccurate cardiac or respiratory peak detection, variability in results with differing TRs, lag in the motion data, and

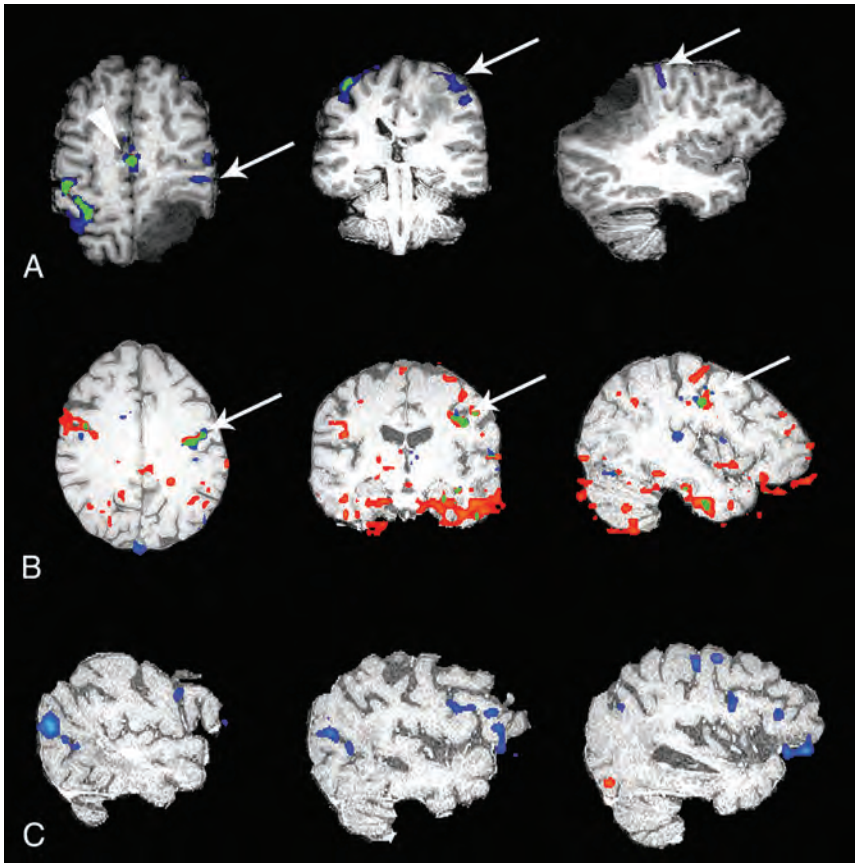

FIG 3. Processed fMRI data from 3 different subjects. Each case shows ICA-denoised data in blue, motion-scrubbed data in red, and overlapping areas of ICA-denoised data and motion-scrubbed data in green. The first case (*A*) is a motor finger task in a patient with a left parietal glioma. The primary motor cortex for the right finger (*arrow*) is only seen after ICA denoising. Likewise, the supplementary motor area (*arrowhead*) shows a slight increase in statistical significance. The second subject (*B*) is undergoing a motor face task with severe task-correlated motion and severe DVARS showing no major change in the primary motor face cortex (*arrow*); however, the number of motion-related false-positives (noise) is markedly reduced. The third case (*C*) is a semantic decision task in which no meaningful activation is present on the motion-scrubbed data. Expected areas of activation in the anterior and posterior language areas are clearly present after ICA denoising.

increased radiofrequency pulses resulting in decreased temporal resolution. Furthermore, no single method accounts for all sources of noise present in the data.[5,7,32,36]

Data-driven approaches, such as removal or regression of volumes with signal changes above a threshold (motion scrubbing) or regression of motion parameters, do not account for all sources of artifacts and have limited effect.[5,25] The limited effect on quality improvement is evident when volumes are discarded on the basis of motion parameters alone, because motion artifacts can have serious detrimental effects, even with minor head motion (<1 mm).[8] Thus, more thorough parameters are needed when using motion scrubbing, such as DVARS or frame-wise displacement, which can detect very subtle artifactual changes in signal.[25] Furthermore, motion scrubbing results in decreased statistical power, particularly in data with numerous motion-affected volumes, while images with detrimental artifacts that do not meet the threshold for rejection still exist. Regression of the motion parameters can also have deleterious effects if the motion is correlated with the task and therefore must be used with extreme caution in task-based experiments.[6] Even with these considerations, the overall improvement gained by these methods is minimal.[5,12,25] This outcome is also likely due, in part, to the lack of accounting for physiologic and scanner-related noise.

There has been an increasing interest in the use of ICA to denoise fMRI data to improve the sensitivity and specificity of results. The methodology behind ICA is beyond the scope of this article (see Stone[37] for an excellent introduction), but in short, ICA deconstructs an fMRI time-series into unique components (each having a spatial map and the corresponding time course), which are maximally spatially independent.[19,22,28,37] These components can then be classified as either artifactual/noise versus task-related activity (see Kelly et al,[26] for an excellent review). In addition to manual identification, numerous methods of automated classification have been described, primarily by using machine-learning algorithms, but a discussion of these methods is beyond the scope of this article.[38-43] The artifactual components consist of a variety of physiologic processes, motion-related artifacts, scanner-related noise, aliasing, and so forth. Once identified, these artifactual components can be removed from the dataset before statistical analysis, such as with the General Linear Model. The improved statistical modeling results in increased sensitivity and specificity, with reduction of false-positives and increased true-positives (Fig 3).[20,27,28]

Previous studies evaluating the use of ICA in task-based presurgical fMRI have yielded mixed results.[21,44,45] While these studies were the first to explore ICA in the presurgical setting, they relied on the extraction of a single component from the ICA analysis results that best modeled the task. This approach can be problematic because task-related activation can often be distributed across multiple components.[46] An approach rendering the most accurate and reliable results is to remove those components reflecting structured or random noise during preprocessing and then to process the denoised dataset with statistical modeling. Additionally, these studies were performed at 1.5T, in which physiologic noise and susceptibility-related changes are substantially lower than at 3T, so the results may not be directly applicable to higher field strengths.

The results of this study highlight the benefits of ICA denoising in presurgical mapping for tumor resection, even at higher field strengths. The reduction in false-positives related to these nuisance variables also reduces the number of surgical false-positives. Furthermore, this reduction has the effect of providing the surgeon with "cleaner" activation maps. Additionally, we have demonstrated that in some cases, true-positive activation was only identified with the use of ICA denoising, the lack of which could have had detrimental effects on the operation (Fig 4). The

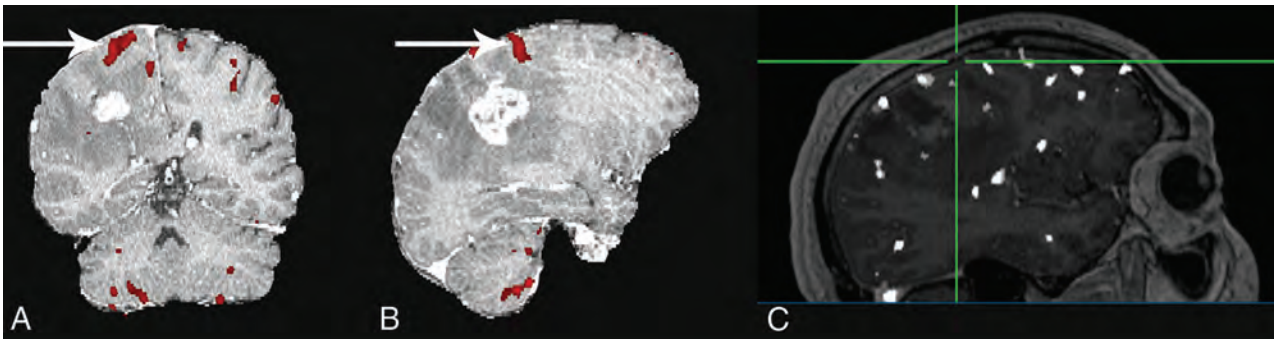

FIG 4. *A* and *B*, Images for a subject undergoing a motor finger task showing areas in which the *z* score increased (red) after ICA denoising compared with motion scrubbing. The *arrow* illustrates increased statistical significance in the left finger primary motor cortex adjacent to the tumor. The location of the primary motor cortex for the left finger was confirmed surgically and is shown on the intraoperative map (*C*), where the crosshairs correspond to primary finger motor cortex. The white "blobs" in *C* show the thresholded maps for the realignment-only data where there is no activation in the area of the primary motor cortex.

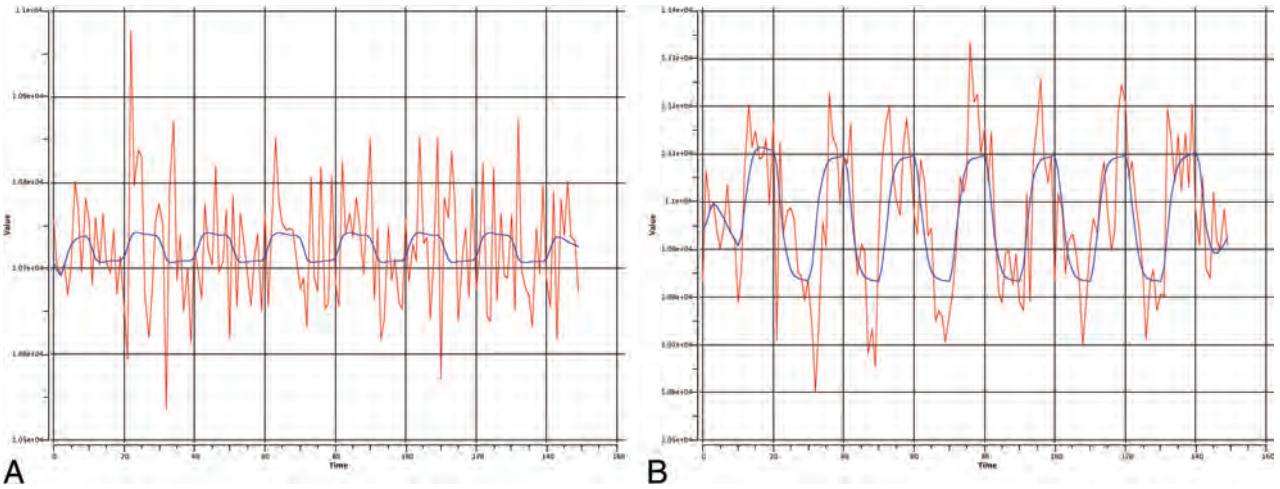

FIG 5. Signal intensity with time from 1 voxel is shown before (*A*) and after (*B*) ICA denoising with the expected hemodynamic response in blue. One can appreciate the amount of overlapping noise from a variety of artifacts resulting in a poor fit with the ideal curve. These noise effects are largely removed after ICA denoising, and the subsequent denoised time course shows a substantially improved fit with the task design.

appearance of otherwise undetected activation is likely due to improved statistical significance achieved by the removal of overlapping nuisance signal or artifacts in the area of true activation (Fig 5). This effect was most dramatic in patients with a higher incidence of motion-induced artifacts. However, when motion was correlated with the task, the motion-induced signal changes were generally indistinguishable from the task itself and any improvement in data quality with ICA denoising, as well as motion scrubbing, was often negligible. Last, we have shown an overall improvement in statistical significance of activated voxels with the use of ICA denoising.

Notable limitations of the current study include its retrospective nature. Because limited evidence exists on the effects of ICA denoising in the surgical setting, we do not believe that the prospective use of this technique is yet warranted. In this retrospective design, a strong inherent bias is present when assessing whether the results would alter patient treatment or decision-making, and as such, this assessment was not included in the analysis. Additionally, precise intraoperative mapping data were not collected in a structured fashion; this omission limits the ability to directly correlate with surgical data in all patients. Likewise, an inherent limitation of many surgical mapping studies is the inability to test all activation sites from limited craniotomies. To address these limitations, we relied on a double-blind expert review of activation maps to assess activation in expected areas on the basis of the task administered. We believe these limitations do not detract from the objective of this study in identifying data-quality improvement with ICA denoising relative to other standard methods of fMRI data denoising. Future prospective studies should be aimed at evaluating the impact on decision-making and patient outcomes.

CONCLUSIONS

The addition of ICA denoising of fMRI data in preoperative patients with glioma has a significant impact in data quality, resulting in reduced false-positives and an increase in true-positives compared with more commonly applied motion scrubbing or simple realignment methods.

REFERENCES

1. Pillai JJ. **The evolution of clinical functional imaging during the past 2 decades and its current impact on neurosurgical planning.** *AJNR Am J Neuroradiol* 2010;31:219–25 CrossRef Medline
2. Krings T, Reinges MH, Erberich S, et al. **Functional MRI for presurgical planning: problems, artefacts, and solution strategies.** *J Neurol Neurosurg Psychiatry* 2001;70:749–60 CrossRef Medline

3. Ogawa S, Lee TM, Kay AR, et al. **Brain magnetic resonance imaging with contrast dependent on blood oxygenation.** *Proc Natl Acad Sci U S A* 1990;87:9868–72 CrossRef Medline
4. Ogawa S, Menon RS, Tank DW, et al. **Functional brain mapping by blood oxygenation level-dependent contrast magnetic resonance imaging: a comparison of signal characteristics with a biophysical model.** *Biophys J* 1993;64:803–12 CrossRef Medline
5. Xu Y, Tong Y, Liu S, et al. **Denoising the speaking brain: toward a robust technique for correcting artifact-contaminated fMRI data under severe motion.** *Neuroimage* 2014;103:33–47 CrossRef Medline
6. Johnstone T, Ores Walsh KS, Greischar LL, et al. **Motion correction and the use of motion covariates in multiple-subject fMRI analysis.** *Hum Brain Mapp* 2006;27:779–88 CrossRef Medline
7. Biswal B, DeYoe EA, Hyde JS. **Reduction of physiological fluctuations in fMRI using digital filters.** *Magn Reson Med* 1996;35:107–13 CrossRef Medline
8. Field AS, Yen YF, Burdette JH, et al. **False cerebral activation on BOLD functional MR images: study of low-amplitude motion weakly correlated to stimulus.** *AJNR Am J Neuroradiol* 2000;21:1388–96 Medline
9. Krüger G, Glover GH. **Physiological noise in oxygenation-sensitive magnetic resonance imaging.** *Magn Reson Med* 2001;46:631–37 CrossRef Medline
10. Wilke M. **Isolated assessment of translation or rotation severely underestimates the effects of subject motion in fMRI data.** *PLoS One* 2014;9:e106498 CrossRef Medline
11. Friston KJ, Williams S, Howard R, et al. **Movement-related effects in fMRI time-series.** *Magn Reson Med* 1996;35:346–55 CrossRef Medline
12. Power JD, Barnes KA, Snyder AZ, et al. **Spurious but systematic correlations in functional connectivity MRI networks arise from subject motion.** *Neuroimage* 2012;59:2142–54 CrossRef Medline
13. Wu DH, Lewin JS, Duerk JL. **Inadequacy of motion correction algorithms in functional MRI: role of susceptibility-induced artifacts.** *J Magn Reson Imaging* 1997;7:365–70 CrossRef Medline
14. Glover GH, Li TQ, Ress D. **Image-based method for retrospective correction of physiological motion effects in fMRI: RETROICOR.** *Magn Reson Med* 2000;44:162–67 Medline
15. Goto M, Abe O, Miyati T, et al. **Head motion and correction methods in resting-state functional MRI.** *Magn Reson Med Sci* 2016;15:178–86 CrossRef Medline
16. Todd N, Josephs O, Callaghan MF, et al. **Prospective motion correction of 3D echo-planar imaging data for functional MRI using optical tracking.** *Neuroimage* 2015;113:1–12 CrossRef Medline
17. Muraskin J, Ooi MB, Goldman RI, et al. **Prospective active marker motion correction improves statistical power in BOLD fMRI.** *Neuroimage* 2013;68:154–61 CrossRef Medline
18. Schulz J, Siegert T, Bazin PL, et al. **Prospective slice-by-slice motion correction reduces false positive activations in fMRI with task-correlated motion.** *Neuroimage* 2014;84:124–32 CrossRef Medline
19. McKeown MJ, Makeig S, Brown GG, et al. **Analysis of fMRI data by blind separation into independent spatial components.** *Hum Brain Mapp* 1998;6:160–88 Medline
20. Biswal BB, Ulmer JL. **Blind source separation of multiple signal sources of fMRI data sets using independent component analysis.** *J Comput Assist Tomogr* 1999;23:265–71 CrossRef Medline
21. Quigley MA, Haughton VM, Carew J, et al. **Comparison of independent component analysis and conventional hypothesis-driven analysis for clinical functional MR image processing.** *AJNR Am J Neuroradiol* 2002;23:49–58 Medline
22. Thomas CG, Harshman RA, Menon RS. **Noise reduction in BOLD-based fMRI using component analysis.** *Neuroimage* 2002;17:1521–37 CrossRef Medline
23. Smith SM, Jenkinson M, Woolrich MW, et al. **Advances in functional and structural MR image analysis and implementation as FSL.** *Neuroimage* 2004;23(suppl 1):S208–19 CrossRef Medline
24. Jenkinson M, Bannister P, Brady M, et al. **Improved optimization for the robust and accurate linear registration and motion correction of brain images.** *Neuroimage* 2002;17:825–41 CrossRef Medline
25. Power JD, Mitra A, Laumann TO, et al. **Methods to detect, characterize, and remove motion artifact in resting state fMRI.** *Neuroimage* 2014;84:320–41 CrossRef Medline
26. Kelly RE Jr, Alexopoulos GS, Wang Z, et al. **Visual inspection of independent components: defining a procedure for artifact removal from fMRI data.** *J Neurosci Methods* 2010;189:233–45 CrossRef Medline
27. McKeown MJ, Hansen LK, Sejnowsk TJ. **Independent component analysis of functional MRI: what is signal and what is noise?** *Curr Opin Neurobiol* 2003;13:620–29 CrossRef Medline
28. Kochiyama T, Morita T, Okada T, et al. **Removing the effects of task-related motion using independent-component analysis.** *Neuroimage* 2005;25:802–14 CrossRef Medline
29. Power JD, Fair DA, Schlaggar BL, et al. **The development of human functional brain networks.** *Neuron* 2010;67:735–48 CrossRef Medline
30. Desmond JE, Atlas SW. **Task-correlated head movement in fMR imaging: false activations can contaminate results despite motion correction.** *AJNR Am J Neuroradiol* 2000;21:1370–71 Medline
31. Krüger G, Kastrup A, Glover GH. **Neuroimaging at 1.5 T and 3.0 T: comparison of oxygenation-sensitive magnetic resonance imaging.** *Magn Reson Med* 2001;45:595–604 CrossRef Medline
32. Lund TE, Madsen KH, Sidaros K, et al. **Non-white noise in fMRI: does modelling have an impact?** *Neuroimage* 2006;29:54–66 CrossRef Medline
33. White N, Roddey C, Shankaranarayanan A, et al. **PROMO: real-time prospective motion correction in MRI using image-based tracking.** *Magn Reson Med* 2010;63:91–105 CrossRef Medline
34. Ward HA, Riederer SJ, Grimm RC, et al. **Prospective multiaxial motion correction for fMRI.** *Magn Reson Med* 2000;43:459–69 Medline
35. Rotenberg D, Chiew M, Ranieri S, et al. **Real-time correction by optical tracking with integrated geometric distortion correction for reducing motion artifacts in functional MRI.** *Magn Reson Med* 2013;69:734–48 CrossRef Medline
36. Dold C, Zaitsev M, Speck O, et al. **Advantages and limitations of prospective head motion compensation for MRI using an optical motion tracking device.** *Acad Radiol* 2006;13:1093–103 CrossRef Medline
37. Stone JV. **Independent component analysis: an introduction.** *Trends Cogn Sci* 2002;6:59–64 CrossRef Medline
38. Bhaganagarapu K, Jackson GD, Abbott DF. **An automated method for identifying artifact in independent component analysis of resting-state FMRI.** *Front Hum Neurosci* 2013;7:343 CrossRef Medline
39. Sochat V, Supekar K, Bustillo J, et al. **A robust classifier to distinguish noise from fMRI independent components.** *PLoS One* 2014;9:e95493 CrossRef Medline
40. Salimi-Khorshidi G, Douaud G, Beckmann CF, et al. **Automatic denoising of functional MRI data: combining independent component analysis and hierarchical fusion of classifiers.** *Neuroimage* 2014;90:449–68 CrossRef Medline
41. Tohka J, Foerde K, Aron AR, et al. **Automatic independent component labeling for artifact removal in fMRI.** *Neuroimage* 2008;39:1227–45 CrossRef Medline
42. De Martino F, Gentile F, Esposito F, et al. **Classification of fMRI independent components using IC-fingerprints and support vector machine classifiers.** *Neuroimage* 2007;34:177–94 CrossRef Medline
43. Pruim RH, Mennes M, van Rooij D, et al. **ICA-AROMA: A robust ICA-based strategy for removing motion artifacts from fMRI data.** *Neuroimage* 2015;112:267–77 CrossRef Medline
44. Moritz CH, Haughton VM, Cordes D, et al. **Whole-brain functional MR imaging activation from a finger-tapping task examined with independent component analysis.** *AJNR Am J Neuroradiol* 2000;21:1629–35 Medline
45. Caulo M, Esposito R, Mantini D, et al. **Comparison of hypothesis- and a novel hybrid data/hypothesis-driven method of functional MR imaging analysis in patients with brain gliomas.** *AJNR Am J Neuroradiol* 2011;32:1056–64 CrossRef Medline
46. McKeown MJ. **Detection of consistently task-related activations in fMRI data with hybrid independent component analysis.** *Neuroimage* 2000;11:24–35 CrossRef Medline

Microstructure of the Default Mode Network in Preterm Infants

J. Cui, O. Tymofiyeva, R. Desikan, T. Flynn, H. Kim, D. Gano, C.P. Hess, D.M. Ferriero, A.J. Barkovich, and D. Xu

ABSTRACT

BACKGROUND AND PURPOSE: Diffusion and fMRI has been providing insights to brain development in addition to anatomic imaging. This study aimed to evaluate the microstructure of white matter tracts underlying the default mode network in premature infants by using resting-state functional MR imaging in conjunction with diffusion tensor imaging–based tractography.

MATERIALS AND METHODS: A cohort of 44 preterm infants underwent structural T1-weighted imaging, resting-state fMRI, and DTI at 3T, including 21 infants with brain injuries and 23 infants with normal-appearing structural imaging as controls. Neurodevelopment was evaluated with the Bayley Scales of Infant Development at 12 months' adjusted age. Probabilistic independent component analysis was applied to resting-state fMRI data to explore resting-state networks. The localized clusters of the default mode network were used as seeding for probabilistic tractography. The DTI metrics (fractional anisotropy, mean diffusivity, axial diffusivity, and radial diffusivity) of the reconstructed primary tracts within the default mode network–cingula were measured.

RESULTS: Results revealed decreased fractional anisotropy (0.20 ± 0.03) and elevated radial diffusivity values (1.24 ± 0.16) of the cingula in the preterm infants with brain injuries compared with controls (fractional anisotropy, 0.25 ± 0.03; $P < .001$; radial diffusivity, 1.06 ± 0.16; $P = .001$). The Bayley Scales of Infant Development cognitive scores were significantly associated with cingulate fractional anisotropy ($P = .004$) and radial diffusivity ($P = .021$); this association suggests that the microstructural properties of interconnecting axonal pathways within the default mode network are of critical importance in the early neurocognitive development of infants.

CONCLUSIONS: This study of combined resting-state fMRI and DTI at rest suggests that such studies may allow the investigation of key functional brain circuits in premature infants, which could function not only as diagnostic tools but also as biomarkers for long-term neurodevelopmental outcomes.

ABBREVIATIONS: AD = axial diffusivity; BI = brain injuries; BSID-III = Bayley Scales of Infant Development; DMN = default mode network; FA = fractional anisotropy; GA = gestational age; IVH = intraventricular hemorrhage; MD = mean diffusivity; RD = radial diffusivity; RSNs = resting-state networks; WMI = white matter injury

Prematurely born infants face heightened risks of brain injuries, such as intraventricular hemorrhage (IVH) and white matter injury (WMI). The brain injuries may disrupt normal cerebral development and result in long-term neurodevelopmental disabilities, including cognitive impairment, behavioral problems, and psychiatric alterations.[1-3] A brain neural network is a series of interconnected neurons whose information is continuously processed and transported between structurally and functionally linked brain regions.[4] The maturation of neural networks plays an important role in cortical development because neural activity is essential for refining and shaping the intricate circuitry of the nervous system.[5] Recently, a growing number of studies have used noninvasive resting-state fMRI to characterize these networks during brain development.[6-11]

Resting-state fMRI enables the detection of spontaneous spatially coherent fluctuations of the blood oxygen level–dependent signals at rest.[12] Application of resting-state fMRI has led to the identification of the resting-state networks (RSNs) encompassing regions of the brain involved in attention, language, behavior, and cognitive function.[13,14] Resting-state fMRI is a promising technique for the study of cerebral development in infants because no specific task performance or cognitive ability is required.[7-11,15]

Received March 9, 2016; accepted after revision September 6.

From the Departments of Radiology and Biomedical Imaging (J.C., O.T., R.D., T.F., H.K., C.P.H., A.J.B., D.X.) and Pediatrics and Neurology (D.G., D.M.F.), University of California, San Francisco, San Francisco, California.

This work was supported by National Institutes of Health grants R01EB009756, R01HD072074, R01NS046432, R21AT009173, and P01NS082330.

Please address correspondence to Duan Xu, PhD, 1700 4th St, BH102, UCSF Box 2512, San Francisco, CA 94143-2512; e-mail: Duan.Xu@ucsf.edu

Indicates open access to non-subscribers at www.ajnr.org

Indicates article with supplemental on-line tables.

Indicates article with supplemental on-line photo.

http://dx.doi.org/10.3174/ajnr.A4997

Several recent studies have observed the emergence of RSNs in the brains of preterm infants, noting that visual, auditory, somatosensory, motor, default mode, frontoparietal, and executive control networks develop at different rates.[7-11,16] Among the RSNs, the most widely studied is the default mode network (DMN), which is associated with cognitive development.[17-19] In adults, the DMN consists of the medial prefrontal cortex, the posterior cingulate cortex/precuneus, the inferior parietal cortex, and their associated connections. Functional "connectivity" between the main nodes is supported by an underlying structure of white matter pathways, with the cingulum as the key tract that interconnects the anterior and posterior core regions of the DMN.[20] Damage to the cingulum may result in a broad range of brain disorders.[17-19] Until now, little was known about the characteristics of the structural pathways underlying the DMN in premature infants. Here, we implemented resting-state fMRI, combined with diffusion tensor imaging–based tractography, to characterize the white matter pathways within the premature infant DMN.

DTI assesses random motion of water molecules within biologic tissue and provides insight into microstructure.[21,22] In the tensor model, which has 3 eigenvalues that represent the magnitude of diffusion in 3 orthogonal axis directions,[21] fractional anisotropy (FA) is calculated from the variance of the 3 eigenvalues to indicate the degree of anisotropy.[23] Mean diffusivity (MD) is the average of the 3 eigenvalues and a scalar measure of the total diffusion.[24] The eigenvector corresponding to the maximum diffusivity is assumed to be directed parallel to the largest group of white matter fibers. Its eigenvalue is referred to as axial diffusivity (AD). The secondary and tertiary eigenvectors oriented perpendicular to the primary eigenvector and the average of their eigenvalues are referred to as "radial diffusivity" (RD). The aims of the present study were the following: 1) to determine the structural pathway of the DMN in these 2 groups of infants (injured and control) and to compare the DTI measures between them; and 2) to further investigate their correlation with longitudinal brain neurocognitive development. We hypothesized that significantly different diffusion parameters would be found in infants with brain injuries compared with normally developing infants. It was also hypothesized that the microstructural architecture inferred by water diffusion of the cingula would be associated with cognitive functioning.

MATERIALS AND METHODS

Subjects

Fifty-one preterm infants, 25 males and 26 females, born prematurely between 24.7 and 32.3 gestational weeks (mean, 28.8 ± 1.8 weeks) underwent MR imaging at 29.8~35.6 gestational weeks (32.2 ± 1.5 weeks). All datasets were visually inspected, and 7 were excluded due to the severe motion artifacts. The datasets of the remaining 44 infants who had a complete and successful (no signal loss or severe artifacts) MR imaging session were included. Radiologic assessments were completed by neuroradiologists experienced in neonatal imaging, including the IVH and WMI scoring systems as follows: IVH score: 0, absent; 1, germinal matrix hemorrhage; 2, intraventricular hemorrhage, volume of blood of <50% of the ventricular volume; 3, intraventricular hemorrhage, volume of blood of >50% of the ventricular volume; and 4, periventricular hemorrhagic infarction. WMI scores were the following: 0, absent; 1, minimal, up to 3 foci of WMI, each <2 mm; 2, moderate, >3 foci of WMI of <2 mm or any foci of >2 mm; and 3, severe, >5% of hemisphere involved. The infants were divided into 2 groups: 21 infants with brain injuries (BI) (13 males and 8 females; gestational age [GA], 29.1 ± 1.9 weeks) and 23 infants with normal-appearing brains (13 males and 10 females; GA, 29.1 ± 1.5 weeks); the latter were controls. A subset of participants (13 of 44 infants) had 12-month follow-up neurodevelopmental studies, and the developmental outcome was evaluated with the Bayley Scales of Infant Development (BSID-III), which has separate composite scores for cognitive, motor, and language skills. The study was approved by the institutional review board, and written inform consent was given by the infants' parents.

MR Imaging Acquisition

Scans were obtained by using a 3T GE MR750 scanner (GE Healthcare, Milwaukee, Wisconsin). Structural 3D sagittal T1 inversion recovery–prepared fast-spoiled gradient-echo images were obtained with the following parameters: flip angle = 15°, FOV = 18 cm, and voxel size = 1 × 1 × 1 mm. T2*-weighed functional MR imaging scans were collected with a gradient-echo pulse sequence (TR/TE/flip angle = 2 s/20 ms/90°, FOV = 24 cm, voxel size = 4 × 4 × 4 mm, and no gap). Whole-brain DTI was acquired with a spin-echo echo-planar imaging diffusion sequence (FOV = 25.6 cm, acquisition matrix = 128 × 128, TR/TE = 5 s/minimum, voxel size = 2 × 2 × 2 mm). Diffusion gradients were applied in 30 noncollinear and noncoplanar directions with b=600 s/mm^2.

Functional Image Processing

Data processing was performed by using FSL, Release 5.0 (http://www.fmrib.ox.ac.uk/fsl). Preprocessing procedures included the following: motion correction with MCFLIRT (http://fsl.fmrib.ox.ac.uk/fsl/fslwiki/MCFLIRT)[25]; section-timing correction; brain extraction with the FSL Brain Extraction Tool (BET; http://fsl.fmrib.ox.ac.uk/fsl/fslwiki/BET)[26]; spatial smoothing with a Gaussian kernel of full width at half maximum of 6 mm; and high-pass temporal filtering with 100 seconds. Functional MR imaging data were aligned to the T1-weighted image with 12 *df*. The structural scan was aligned with the Montreal Neurological Institute pediatric atlas (http://www.bic.mni.mcgill.ca/ServicesAtlases/NIHPD-obj2) by using nonlinear registration. Transformation of the functional results into Montreal Neurological Institute space was performed following concatenation of the 2 alignments into a single matrix. All spatially normalized fMRI data were resampled to 1-mm^3 resolution. FSL Multivariate Exploratory Linear Decomposition into Independent Components (MELODIC; http://fsl.fmrib.ox.ac.uk/fsl/fslwiki/MELODIC[27]) was used to perform an independent component analysis on the fMRI data of all the subjects (n = 44) and to automatically estimate the dimensions of the independent components.

Diffusion Image Processing

DTI data were processed with the FMRIB Diffusion Toolbox (FDT; http://fsl.fmrib.ox.ac.uk/fsl/fslwiki/FDT).[28] A standard

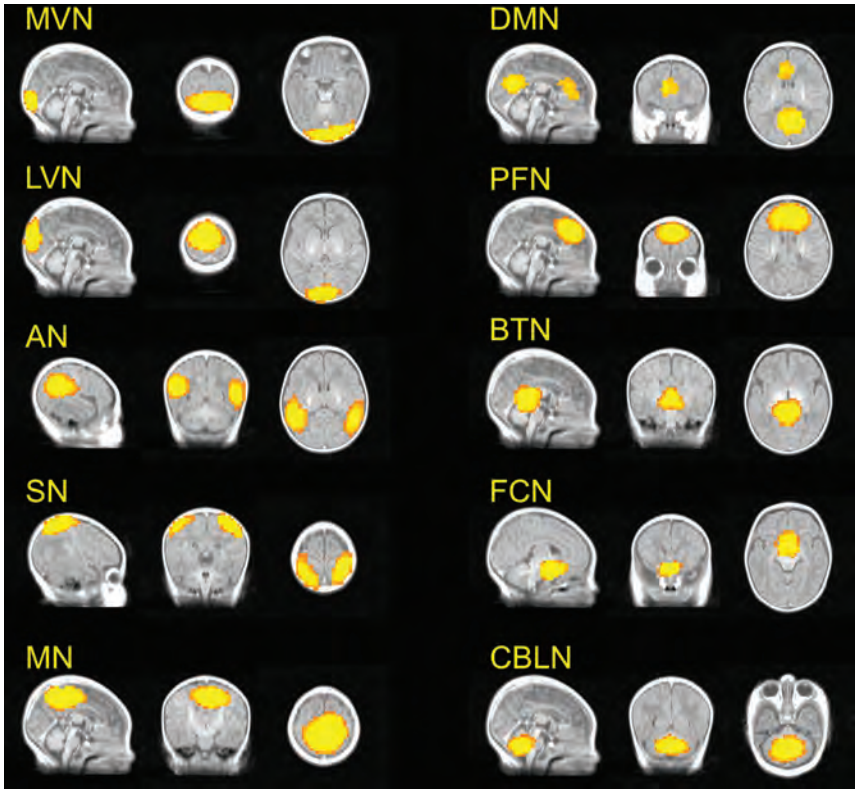

FIG 1. RSNs ($z > 2.6$) identified by group independent component analysis in preterm infants ($n = 44$). MVN indicates medial visual network; LVN, lateral visual network; AN, auditory network; SN, salience network; MN, motor network; PFN, prefrontal network; BTN, brain stem and thalami; FCN, frontal cortical network; and CBLN, cerebellum network.

FDT multistep procedure was performed, including the following: 1) image-quality check (any gradient directions with signal dropouts caused by excessive motion were removed and not included in the analysis[29]); 2) motion and eddy current correction; 3) correction of gradient directions for any image rotation during the previous motion and eddy current correction; 4) removal of skull and nonbrain tissue by using the BET; 5) tensor reconstruction by using a weighted least-squares fit was performed via DTIFit (http://fsl.fmrib.ox.ac.uk/fsl/fsl-4.1.9/fdt/fdt_dtifit.html) within FDT to create DTI scalar images, including FA, MD, and 3 eigenvalues. The RD maps were computed as the average of the 2 minor eigenvalue images. The MD, AD, and RD values were reported in square millimeters/second $\times 10^{-3}$.

Probabilistic Tractography

Fiber tracking was performed by using ProbtrackX (http://fsl.fmrib.ox.ac.uk/fsl/fslwiki/FDT/UserGuide#PROBTRACKX_-_probabilistic_tracking_with_crossing_fibres) in FSL.[30] First, diffusion parameters were estimated at each voxel by using BedpostX (http://fsl.fmrib.ox.ac.uk/fsl/fslwiki/FDT/UserGuide#BEDPOSTX). ProbtrackX was then used to estimate the distribution of connections with 5000 streamline samples, a step length of 0.5 mm, and a curvature threshold of 0.2. We used the localized regions of the DMN ($z > 2.6$) in the resting-state fMRI analysis as seed regions. Seed regions were transformed from standard space (Montreal Neurological Institute pediatric 1-mm^3 standard brain) to each individual diffusion space by using a nonlinear transform (standard2diff) with 12 *df*. Generated pathways are volumes in which values at each voxel represent the number of streamlines passing through that voxel and, therefore, the probability of a connection between paired seed regions. To remove background noise, we thresholded pathways in each individual to include only voxels with at least 100 samples passing through them (of 5000 initiated streamline samples).[31] Pathways in each subject were binarized and overlaid to produce population probability maps for each pathway, in which voxel values represent the number of subjects in whom a pathway is present. The population probability maps were thresholded at 50% of the maximum number of participants who had overlapping connections between paired seed regions to generate a group tract map.[32,33] The obtained group tract map was then transformed to individual diffusion space and binarized to mask the FA, MD, AD, and RD maps for DTI metrics measurement.

Statistical Analysis

Statistical analysis was performed by using SPSS Statistics 22 (IBM, Armonk, New York). The Kolmogorov-Smirnov test of normality was used to confirm the normal distribution of BSID-III scores and DTI metrics ($P > .05$). A 2-tailed independent-samples *t* test was used to compare the birth GA, postmenstrual age at scan, and birth weights between the 2 groups. General linear regression was performed to compare the DTI metrics between groups, correcting for the birth GA, postmenstrual age at scan, sex, and birth weights. To investigate the association between the DTI metrics and BSID-III cognitive scores, we performed partial correlations; and the birth GA, postmenstrual age at scan, sex, and birth weights were also included as nuisance covariates.

RESULTS

Demographics

The 2-tailed independent-samples *t* test demonstrated that there was no significant difference in birth GA (BI, 29.1 ± 1.9 weeks; control, 29.1 ± 1.6 weeks; $P = .96$), GA at scanning (BI, 32.4 ± 1.6 weeks; control, 32.2 ± 1.5 weeks; $P = .76$), and birth weights (BI, 1278 ± 290 g; control,1241 ± 273 g; $P = .65$) between groups. The detailed demographic information of the infants is summarized in On-line Table 1.

RSNs

Forty-three independent components were obtained from group independent component analysis decomposition across all the subjects ($n = 44$). RSNs were identified on the basis of the location and the frequency spectrum. Ten known RSNs were selected (Fig 1), including the medial visual network, lateral visual network, auditory network, salience network, motor network, DMN,

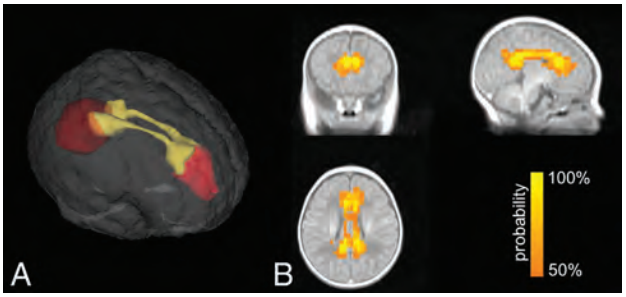

FIG 2. Group tract map of the reconstructed cingula. Each voxel value represents the probability that subjects had some cingula in it.

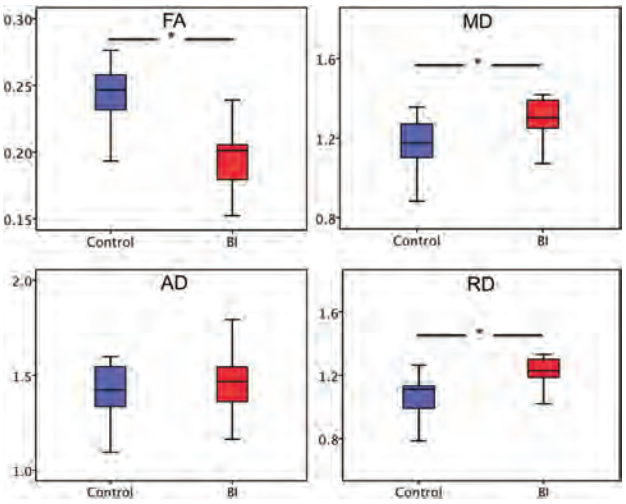

FIG 3. Boxplots illustrate the group differences in DTI metrics. The *asterisk* indicates $P < .05$.

prefrontal network, brain stem and thalami network, frontal cortical network, and cerebellum network. Fourteen additional RSNs were found as the subnetworks of these 10 RSNs, such as the visual network and prefrontal network as well as the subcomponents of some known RSNs, such as the frontoparietal network and executive control network (On-line Figure). Only noise or artifacts were found in the remaining 19 RSNs. The RSN of interest in the current study is the DMN. As shown in Fig 1, the DMN generated from the group independent component analysis on 44 preterm infants contains the regions of the medial prefrontal cortex (cluster size = 162 voxels) and posterior cingulate cortex/precuneus (411 voxels).

Group Comparison in DTI Metrics of the Reconstructed Cingula

As shown in Fig 2, the bilateral cingulum bundles, which are the primary fiber tracts connecting the medial prefrontal cortex and the posterior cingulate cortex/precuneus, were reconstructed. Figure 3 shows the group comparison in DTI metrics of the reconstructed cingula. The FA values in the BI group (0.20 ± 0.03) were significantly lower than those in the control group (0.25 ± 0.03, $F = 26.79$, $P < .001$). The MD and RD values were both elevated in the BI group (MD, 1.32 ± 0.17; RD, 1.24 ± 0.16) compared with the control group (MD, 1.19 ± 0.16; $F = 6.44$, $P = .015$; RD, 1.06 ± 0.16; $F = 13.35$, $P = .001$). No significant difference was found in AD between the 2 groups (BI, 1.47 ± 0.19; control, 1.44 ± 0.18; $F = 0.12$, $P = .731$).

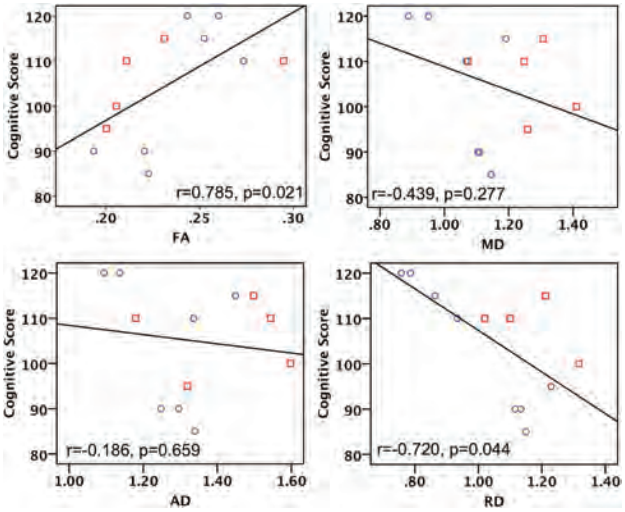

FIG 4. Scatterplots illustrate the correlation between BSID-III cognitive scores and DTI metrics in 13 infants, including 6 with brain injuries (*red rectangle*) and 7 controls (*blue circle*). It was found that the cognitive score is positively associated with FA and negatively associated with RD.

Association between DTI Metrics and BSID-III Scores

As shown in Fig 4, the cognitive scores were positively correlated with the FA values ($r = 0.848$, $P = .004$) and negatively correlated with the RD values ($r = -0.746$, $P = .021$). In addition to cognitive scores, we also examined the association between the DTI metrics and the language and motor scores. Language scores were positively associated with the FA values ($r = 0.782$, $P = .013$) but not significantly correlated with the MD, AD, or RD values. The motor scores were not correlated with the DTI metrics (On-line Table 2).

DISCUSSION

In the present study, resting-state fMRI was used to identify key RSNs and localize the medial prefrontal cortex and posterior cingulate cortex/precuneus within the DMN in prematurely born infants. We found that the DTI metrics within the cingula, the primary fiber tracts connecting the medial prefrontal cortex and posterior cingulate cortex/precuneus, were altered in the preterm infants with brain injuries. DTI abnormalities within the cingula were also significantly associated with decreased cognitive scores at 12 months of age. Our findings support the hypothesis that microstructural abnormalities of the DMN are present in preterm infants with brain injuries and are associated with impaired neurocognitive development. To the best of our knowledge, this is the first investigation of the microstructure of a specific neural network relevant to the neurocognitive development in preterm infants.

In 2007, Fransson et al[10] performed the first study of RSN development in 12 preterm infants at 41 weeks' postmenstrual age. A presumed precursor of the DMN was observed in Fransson et al.[8,9] Gao et al[11] explored the temporal and spatial development within the DMN and observed a primitive and incomplete DMN in 2-week-old neonates. Doria et al[7] performed a longitudinal investigation to explore early development of RSNs from 29 weeks' postmenstrual age to term-equivalent age in 62 preterm infants. In line with the previous studies, the main architecture of the DMN, including the medial prefrontal cortex and posterior

cingulate cortex/precuneus, was observed in our study, while other regions that are commonly observed in the DMNs of adults were not found, such as inferior parietal cortex, lateral temporal cortex, and hippocampal regions. Emerging evidence suggests that the posterior cingulate cortex and medial prefrontal cortex are consistently observed in the DMN and serve as 2 main "hubs" involved in different aspects of cognitive function.[11,34] The medial prefrontal cortex might be involved in self-referential activity, mentalizing processes, and theory of mind, while the posterior cingulate cortex is more associated with implicit memory.[35] As the structural foundation of the functional connectivity between these 2 hubs, the underlying white matter tracts, therefore, are vital to the neural signal transmission between the medial prefrontal cortex and posterior cingulate cortex.

By combining probabilistic independent component analysis and probabilistic tract reconstruction, we provide in vivo evidence that the microstructural architecture of the primary white matter tract within the DMN-cingula is disrupted in preterm infants with brain injuries. The BI group showed significantly lower FA and elevated MD and RD values compared with the control group. This change in DTI metrics of the white matter was consistent with the previous DTI studies in preterm infants.[15,36-38] Counsell et al[36] found that the apparent diffusion coefficient values were significantly higher in the infants with white matter injury than that in the infants with normal-appearing white matter in the frontal, central, and posterior white matter at the level of the centrum semiovale in 50 preterm infants at term-equivalent age. Thompson et al[37] scanned 116 infants and found that perinatal white matter abnormality and IVH were associated with increased diffusivity in the white matter of very preterm infants. Very recently, Morita et al[38] evaluated the cerebellar and cerebral white matter of 42 preterm infants and found that preterm infants with IVH had lower FA values compared with infants without IVH. Until now, no studies have assessed the microstructure of the cingulum bundles in the preterm infant with brain injuries, to our knowledge. Our results first revealed the altered FA, MD, and RD values of the cingula in the BI group compared with the normal-appearing preterm infants. In preterm infants, low FA likely indicates low axonal fiber density, delayed premyelination, or increased water content. In our study, increases in RD with little change in AD were observed in the preterm infants with brain injuries. This finding suggests that the changes in anisotropy are not simply explained by changes in brain-water content and more likely reflect the microstructural changes, causing decreased hindrance to water diffusion perpendicular to the direction of axonal fibers.

Within the cingula, we found that higher FA was associated with decreased cognitive abilities, and lower RD correlated with better cognitive and language scores of infants at 12 months of age. This finding is in accordance with the previous longitudinal studies in preterm infant neurodevelopment.[37,39] van Kooij et al[40] performed Tract-Based Spatial Statistics (TBSS; http://fsl.fmrib.ox.ac.uk/fsl/fslwiki/TBSS) analysis on 63 preterm infants and found that the FA in the corpus callosum at term-equivalent age was positively correlated with cognitive outcome (measured by the BSID-III) at 2-year corrected age. Thompson et al[37] found that higher RD was associated with increased risk of impairment in motor and executive functions at 7 years of age in premature-born children. Currently, the results of our study demonstrate a correlation between cognitive performance and the cingula white matter microstructure measured at an early and critical phase of neurologic development. Previous studies have reported diffusivity decreasing and anisotropy increasing with increasing GA,[41-43] and they are, therefore, signs of physiologic maturation. Indeed, these trends of diffusion metrics with progressive white matter maturation have been shown to continue throughout infancy and childhood. Using partial correlation to exclude the effects of aging, our study reveals that microstructural changes or delayed maturation in the developing white matter of the cingula might result in long-term neurocognitive impairment.

Several limitations to the present study should be considered. First, we did not delineate the anatomic representations of RSNs in the BI or control group separately. Preliminary results have demonstrated significant differences in RSN development in preterm infants with common forms of neuropathology.[44] In a future study, we will apply independent component analysis with dual regression to resting-state fMRI data to investigate the altered brain circuits in preterm infants with brain injuries. Second, we focused on the DMN and its underlying primary white matter tract–cingulum bundles in this study. Other brain regions and neuronal tracts may be associated with neurocognitive development in infants. Nonhypothesized DTI analysis, such as TBSS, would be helpful to investigate the specificity of this effect. Third, the sample size ($n = 13$, including 6 with brain injuries) of our follow-up study was small. We are continuing to enroll additional subjects in the longitudinal study to explore the association between DTI metrics and neurodevelopment outcome for each group. Last, there may be microhemorrhages that may influence the diffusion measurements; however, as indicated by the results, the MD in the BI group is elevated in comparison with the control group; this finding suggests that susceptibility effects from microbleeds are small.

CONCLUSIONS

This study employed a multimodal imaging approach to evaluate the microstructural architecture of the DMN in preterm infants. Our results provide evidence that the microstructure of the primary white matter tracts connecting the medial prefrontal cortex and the posterior cingulate cortex/precuneus within the DMN-cingula were disrupted in the preterm infants with brain injuries. Our findings reveal that higher degree of microstructural architecture of the cingula is associated with better neurocognitive abilities at 12 months, which suggests that the microstructural properties of the interconnecting axonal pathways between the 2 main hubs within the DMN play a critical role in the infants' neurodevelopment.

Disclosures: Olga Tymofiyeva—*RELATED*: *Grant*: National Institutes of Health.* *Christopher P. Hess—RELATED*: *Grant*: National Institutes of Health*; *UNRELATED*: *Expert Testimony*: medicolegal; *Grants/Grants Pending*: GE Healthcare, Quest Diagnostics, Cerebrotech*; *Travel/Accommodations/Meeting Expenses Unrelated to Activities Listed*: Siemens. Donna M. Ferriero—*RELATED*: *Grant*: National Institutes of Health*; *Support for Travel to Meetings for the Study or other Purposes*: National Institutes of Health*; *UNRELATED*: *Grants/Grants Pending*: National Institutes of Health*; *Royalties*: Elsevier. Anthony J. Barkovich—*RELATED*: *Grant*: National Institutes of Health.* Duan Xu—*RELATED*: *Grant*: National Institutes of Health.* *Money paid to the institution.

REFERENCES

1. Panigrahy A, Wisnowski JL, Furtado A, et al. **Neuroimaging biomarkers of preterm brain injury: toward developing the preterm connectome.** *Pediatr Radiol* 2012;42(suppl 1):S33–61 CrossRef Medline
2. Douglas-Escobar M, Weiss MD. **Biomarkers of brain injury in the premature infant.** *Front Neurol* 2012;3:185 CrossRef Medline
3. Miller SP, Cozzio CC, Goldstein RB, et al. **Comparing the diagnosis of white matter injury in premature newborns with serial MR imaging and transfontanel ultrasonography findings.** *AJNR Am J Neuroradiol* 2003;24:1661–69 Medline
4. Amit DJ. *Modeling Brain Function: The World of Attractor Networks*. New York: Cambridge University Press; 1989
5. Penn AA, Shatz CJ. **Brain waves and brain wiring: the role of endogenous and sensory-driven neural activity in development.** *Pediatr Res* 1999;45:447–58 CrossRef Medline
6. Smyser CD, Snyder AZ, Neil JJ. **Functional connectivity MRI in infants: exploration of the functional organization of the developing brain.** *Neuroimage* 2011;56:1437–52 CrossRef Medline
7. Doria V, Beckmann CF, Arichi T, et al. **Emergence of resting state networks in the preterm human brain.** *Proc Natl Acad Sci U S A* 2010;107:20015–20 CrossRef Medline
8. Fransson P, Aden U, Blennow M, et al. **The functional architecture of the infant brain as revealed by resting-state fMRI.** *Cereb Cortex* 2011;21:145–54 CrossRef Medline
9. Fransson P, Skiöld B, Engström M, et al. **Spontaneous brain activity in the newborn brain during natural sleep–an fMRI study in infants born at full term.** *Pediatr Res* 2009;66:301–05 CrossRef Medline
10. Fransson P, Skiöld B, Horsch S, et al. **Resting-state networks in the infant brain.** *Proc Natl Acad Sci U S A* 2007;104:15531–36 CrossRef Medline
11. Gao W, Zhu H, Giovanello KS, et al. **Evidence on the emergence of the brain's default network from 2-week-old to 2-year-old healthy pediatric subjects.** *Proc Natl Acad Sci U S A* 2009;106:6790–95 CrossRef Medline
12. Biswal B, Yetkin FZ, Haughton VM, et al. **Functional connectivity in the motor cortex of resting human brain using echo-planar MRI.** *Magn Reson Med* 1995;34:537–41 CrossRef Medline
13. Fox MD, Raichle ME. **Spontaneous fluctuations in brain activity observed with functional magnetic resonance imaging.** *Nat Rev Neurosci* 2007;8:700–11 CrossRef Medline
14. Smith SM, Fox PT, Miller KL, et al. **Correspondence of the brain's functional architecture during activation and rest.** *Proc Natl Acad Sci U S A* 2009;106:13040–45 CrossRef Medline
15. Thompson DK, Inder TE, Faggian N, et al. **Corpus callosum alterations in very preterm infants: perinatal correlates and 2 year neurodevelopmental outcomes.** *Neuroimage* 2012;59:3571–81 CrossRef Medline
16. Smyser CD, Inder TE, Shimony JS, et al. **Longitudinal analysis of neural network development in preterm infants.** *Cereb Cortex* 2010;20:2852–62 CrossRef Medline
17. Raichle ME, MacLeod AM, Snyder AZ, et al. **A default mode of brain function.** *Proc Natl Acad Sci U S A* 2001;98:676–82 CrossRef Medline
18. Palacios EM, Sala-Llonch R, Junque C, et al. **Resting-state functional magnetic resonance imaging activity and connectivity and cognitive outcome in traumatic brain injury.** *JAMA Neurol* 2013;70:845–51 CrossRef Medline
19. Buckner RL, Andrews-Hanna JR, Schacter DL. **The brain's default network: anatomy, function, and relevance to disease.** *Ann N Y Acad Sci* 2008;1124:1–38 CrossRef Medline
20. Hagmann P, Cammoun L, Gigandet X, et al. **Mapping the structural core of human cerebral cortex.** *PLoS Boil* 2008;6:e159 CrossRef Medline
21. Basser PJ, Mattiello J, LeBihan D. **MR diffusion tensor spectroscopy and imaging.** *Biophys J* 1994;66:259–67 CrossRef Medline
22. Hagmann P, Jonasson L, Maeder P, et al. **Understanding diffusion MR imaging techniques: from scalar diffusion-weighted imaging to diffusion tensor imaging and beyond.** *Radiographics* 2006;26(suppl 1):S205–23 Medline
23. Beaulieu C. **The basis of anisotropic water diffusion in the nervous system: a technical review.** *NMR Biomed* 2002;15:435–55 CrossRef Medline
24. Schmithorst VJ, Yuan W. **White matter development during adolescence as shown by diffusion MRI.** *Brain Cogn* 2010;72:16–25 CrossRef Medline
25. Jenkinson M, Bannister P, Brady M, et al. **Improved optimization for the robust and accurate linear registration and motion correction of brain images.** *Neuroimage* 2002;17:825–41 CrossRef Medline
26. Smith SM. **Fast robust automated brain extraction.** *Hum Brain Mapp* 2002;17:143–55 CrossRef Medline
27. Beckmann CF, Smith SM. **Probabilistic independent component analysis for functional magnetic resonance imaging.** *IEEE Trans Med Imaging* 2004;23:137–52 CrossRef Medline
28. Smith SM, Jenkinson M, Woolrich MW, et al. **Advances in functional and structural MR image analysis and implementation as FSL.** *Neuroimage* 2004;23(suppl 1):S208–19 CrossRef Medline
29. Chen Y, Tymofiyeva O, Hess CP, et al. **Effects of rejecting diffusion directions on tensor-derived parameters.** *Neuroimage* 2015;109:160–70 CrossRef Medline
30. Behrens TE, Berg HJ, Jbabdi S, et al. **Probabilistic diffusion tractography with multiple fibre orientations: what can we gain?** *Neuroimage* 2007;34:144–55 CrossRef Medline
31. Johansen-Berg H, Della-Maggiore V, Behrens TE, et al. **Integrity of white matter in the corpus callosum correlates with bimanual co-ordination skills.** *Neuroimage* 2007;36(suppl 2):T16–21 CrossRef Medline
32. Mayer KM, Vuong QC. **TBSS and probabilistic tractography reveal white matter connections for attention to object features.** *Brain Struct Funct* 2014;219:2159–71 CrossRef Medline
33. Cui J, Tkachenko O, Gogel H, et al. **Microstructure of frontoparietal connections predicts individual resistance to sleep deprivation.** *Neuroimage* 2015;106:123–33 CrossRef Medline
34. Uddin LQ, Kelly AM, Biswal BB, et al. **Functional connectivity of default mode network components: correlation, anticorrelation, and causality.** *Hum Brain Mapp* 2009;30:625–37 CrossRef Medline
35. Lou HC, Luber B, Crupain M, et al. **Parietal cortex and representation of the mental self.** *Proc Natl Acad Sci U S A* 2004;101:6827–32 CrossRef Medline
36. Counsell SJ, Allsop JM, Harrison MC, et al. **Diffusion-weighted imaging of the brain in preterm infants with focal and diffuse white matter abnormality.** *Pediatrics* 2003;112:1–7 CrossRef Medline
37. Thompson DK, Lee KJ, Egan GF, et al. **Regional white matter microstructure in very preterm infants: predictors and 7 year outcomes.** *Cortex* 2014;52:60–74 CrossRef Medline
38. Morita T, Morimoto M, Yamada K, et al. **Low-grade intraventricular hemorrhage disrupts cerebellar white matter in preterm infants: evidence from diffusion tensor imaging.** *Neuroradiology* 2015;57:507–14 CrossRef Medline
39. Partridge SC, Mukherjee P, Henry RG, et al. **Diffusion tensor imaging: serial quantitation of white matter tract maturity in premature newborns.** *Neuroimage* 2004;22:1302–14 CrossRef Medline
40. van Kooij BJ, de Vries LS, Ball G, et al. **Neonatal tract-based spatial statistics findings and outcome in preterm infants.** *AJNR Am J Neuroradiol* 2012;33:188–94 CrossRef Medline
41. Berman JI, Mukherjee P, Partridge SC, et al. **Quantitative diffusion tensor MRI fiber tractography of sensorimotor white matter development in premature infants.** *Neuroimage* 2005;27:862–71 CrossRef Medline
42. Hüppi PS, Murphy B, Maier SE, et al. **Microstructural brain development after perinatal cerebral white matter injury assessed by diffusion tensor magnetic resonance imaging.** *Pediatrics* 2001;107:455–60 CrossRef Medline
43. Miller SP, Vigneron DB, Henry RG, et al. **Serial quantitative diffusion tensor MRI of the premature brain: development in newborns with and without injury.** *J Magn Reson Imaging* 2002;16:621–32 CrossRef Medline
44. Smyser C, Lambeth J. **Perinatal factors affecting development of neural networks in preterm infants.** In: *Proceedings of the Annual Meeting of the Pediatric Academic Societies, Vancouver, Canada*, May 1–4, 2010: *E*-PAS2010 2010:4150

Brain Network Architecture and Global Intelligence in Children with Focal Epilepsy

M.J. Paldino, F. Golriz, M.L. Chapieski, W. Zhang, and Z.D. Chu

ABSTRACT

BACKGROUND AND PURPOSE: The biologic basis for intelligence rests to a large degree on the capacity for efficient integration of information across the cerebral network. We aimed to measure the relationship between network architecture and intelligence in the pediatric, epileptic brain.

MATERIALS AND METHODS: Patients were retrospectively identified with the following: 1) focal epilepsy; 2) brain MR imaging at 3T, including resting-state functional MR imaging; and 3) full-scale intelligence quotient measured by a pediatric neuropsychologist. The cerebral cortex was parcellated into approximately 700 gray matter network "nodes." The strength of a connection between 2 nodes was defined by the correlation between their blood oxygen level–dependent time-series. We calculated the following topologic properties: clustering coefficient, transitivity, modularity, path length, and global efficiency. A machine learning algorithm was used to measure the independent contribution of each metric to the intelligence quotient after adjusting for all other metrics.

RESULTS: Thirty patients met the criteria (4–18 years of age); 20 patients required anesthesia during MR imaging. After we accounted for age and sex, clustering coefficient and path length were independently associated with full-scale intelligence quotient. Neither motion parameters nor general anesthesia was an important variable with regard to accurate intelligence quotient prediction by the machine learning algorithm. A longer history of epilepsy was associated with shorter path lengths ($P = .008$), consistent with reorganization of the network on the basis of seizures. Considering only patients receiving anesthesia during machine learning did not alter the patterns of network architecture contributing to global intelligence.

CONCLUSIONS: These findings support the physiologic relevance of imaging-based metrics of network architecture in the pathologic, developing brain.

ABBREVIATIONS: BOLD = blood oxygen level–dependent; IQ = intelligence quotient

Epilepsy is a common neurologic condition defined by recurrent, unprovoked seizures that affect 1% of the population, including 1 in 200 children.[1] In contrast to epilepsies encountered in the adult population, developmental lesions are the most frequent source of medically intractable seizures in children.[2] Surgical resection in the setting of such focal epilepsies represents an attractive management option.[3] However, even in the most highly selected cohorts, outcomes remain highly variable.[4] Evidence suggests that such inconsistencies may reflect so-called "focal" epilepsies being, in many cases, associated with extensive alterations of the cerebral network.[3,5,6]

With advances in MR imaging, the architecture of the cerebral network is now accessible to systematic study.[7] Resting-state functional MR imaging, which measures the blood oxygen level–dependent (BOLD) signal with time, is one method by which a neural network can be constructed. Because the sequence is task-free, it is of great potential value to young or developmentally impaired children, in whom cooperation with task-based functional imaging and neuropsychological evaluation may not be possible. Regions of the brain that interact to contribute a given function continue to exhibit similar BOLD fluctuations at rest.[8] Hence, with resting-state fMRI, the strength of a connection between brain regions is inferred on the basis of the degree of correlation between their BOLD signal time courses. Connectivity defined in this manner can then be used to create a comprehensive

Received March 28, 2016; accepted after revision August 29.

From the Departments of Radiology (M.J.P., F.G., Z.D.C.) and Psychology (M.L.C.) and Outcomes and Impact Service (W.Z.), Texas Children's Hospital, Houston, Texas.

Paper previously presented at: Annual Meeting of the American Society of Neuroradiology, May 21–26, 2016; Washington, DC.

Please address correspond Michael J. Paldino, MD, Texas Children's Hospital, Department of Radiology, 6621 Fannin St, Houston, TX 77030; e-mail: Michael.paldino@gmail.com

http://dx.doi.org/10.3174/ajnr.A4975

map of connections in the brain.[7] Within this framework, the brain is represented as a collection of "nodes," or anatomic elements in the network, and the connection between each pair of nodes is represented by an "edge."

Once constructed, the architecture of the network can be summarized at the whole-brain scale according to graph theory.[9] An array of graph theory metrics has been described, each of which has the potential to capture specific topologic features of the network.[9] In general terms though, most metrics measure, in some way, the degree to which the network supports either integration across or functional subspecialization within the brain. Previous studies using network metrics derived from resting-state fMRI have demonstrated differences from normal in various disease states, including epilepsy.[10-14] More recently, incremental "dose-response" relationships between brain network efficiency, as quantified by graph theory, and global intelligence have been reported in both adults[15,16] and healthy children.[17] Although these findings point to the potential for network metrics to provide physiologically meaningful markers of cognitive function, few data exist regarding these relationships in the pathologic setting. Nor is it known whether such markers maintain their physiologic meaning when imaging is performed with the patient under general anesthesia, a state of consciousness known to alter neurovascular coupling and BOLD synchrony.[18]

The goals of this study were 2-fold: to determine which metrics of global network architecture are most closely related to intelligence in the pediatric, epileptic brain; and to determine whether such relationships continue to emerge when functional images are acquired with the patient under anesthesia.

MATERIALS AND METHODS

This Health Insurance Portability and Accountability Act–compliant study was approved by the local institutional review board. Informed consent was waived. Patients were identified retrospectively from the medical record with the following inclusion criteria: 1) pediatric age group (21 years of age or younger); 2) diagnosis of focal epilepsy[19] by a pediatric epileptologist based on clinical history and seizure semiology; 3) MR imaging of the brain performed at 3T, including a resting-state fMRI sequence; and 4) full-scale intelligence quotient (IQ) measured according to an age-appropriate version of the Wechsler Intelligence Scales administered by a pediatric neuropsychologist within 3 months of the MR imaging. Refinements to the above-defined population were planned on the basis of the following exclusions: 1) any brain operation performed before the MR imaging, and 2) motion or other artifactual degradation of image quality.

MR Imaging

All imaging was performed on a 3T Achieva system (Philips Healthcare, Best, the Netherlands) with a 32-channel phased array coil. We obtained the following sequences: 1) structural images: sagittal volumetric T1-weighted images (TR/TE, 7.2/2.9 ms; 1 acquisition; flip angle, 7°; TI, 1100 ms; FOV, 22 cm; voxel, 1 × 1 × 1 mm); 2) resting-state fMRI: axial single-shot EPI fMRI (TR/TE, 2000/30 ms; flip angle, 80°; 1 acquisition; FOV, 24 cm; matrix, 64 × 64; voxel, 3.75 × 3.75 × 3.75 mm; 300 volumes; duration, 10 minutes) performed in the resting state. Patients not receiving anesthesia during the examination were instructed to lie quietly in the scanner with their eyes closed. All images were visually inspected for artifacts, including susceptibility and subject motion.

Image Processing and Analysis

Network Node Definition. A processing pipeline was implemented by using Matlab scripts (Version 7.13; MathWorks, Natick, Massachusetts), in which adapter functions were embedded to execute FreeSurfer reconstruction (Version 5.3.0; http://surfer.nmr.mgh.harvard.edu), and several tools in the FSL suite (http://www.fmrib.ox.ac.uk/fsl).[20] First, reconstruction of cerebral cortical surfaces was performed on the T1 structural image by using FreeSurfer. This processing stream includes motion correction, skull stripping, intensity normalization, segmentation of white matter and gray matter structures, parcellation of the gray matter–white matter boundary, and surface deformation following intensity gradients, which optimally place the gray matter/white matter and gray matter/CSF borders at the location where the greatest shift in intensity defines the transition between tissue classes.[21,22] FreeSurfer outputs were visually inspected for accuracy by using the FreeView software (http://surfer.nmr.mgh.harvard.edu), to assure appropriate placement of the pial and gray-white surfaces for each patient.

Next, a self-developed Matlab program was applied to the FreeSurfer outputs, including the pial and gray-white surfaces, to further subdivide the 75 standard parcels according to their surface area (as defined on the FreeSurfer gray-white surface mesh). During this process, each cortical parcel was iteratively divided into 2 new parcels of equal size until the surface area of each parcel was less than a predefined threshold value of 350 mm^2. Each surface parcel was then converted into a volume mask of gray matter at that region; each resulting volume of interest formed a node on the network. The number of nodes in each patient's network ranged from 539 to 841 (mean, 690.7 ± 66.3).

Network Edge Definition. The first 5 images in each resting-state sequence were discarded to allow magnetization to reach equilibrium. Preprocessing and independent component analysis of the functional datasets were performed by using FSL MELODIC (http://fsl.fmrib.ox.ac.uk/fsl/fslwiki/MELODIC), including motion correction, section-timing correction, brain extraction, spatial smoothing (Gaussian kernel of full width at half maximum of 5 mm), and high-pass temporal filtering equivalent to a wavelength of 100 seconds (0.01 Hz). Noise related to motion and other physiologic nuisance was addressed according to an independent component analysis technique.[23] Nonsignal components were removed manually by an expert operator with 5 years of experience using independent component analysis in this patient population. Although the optimal strategies for noise removal in fMRI remain the subject of debate,[24,25] an independent component analysis technique was selected because it has been shown to minimize the impact of motion on network metrics while, at the same time, decreasing the loss of temporal *df* and preserving the signal of interest across a variety of resting-state datasets.[24] Motion parameters measured during preprocessing were summarized for each patient as "translation" (the root mean

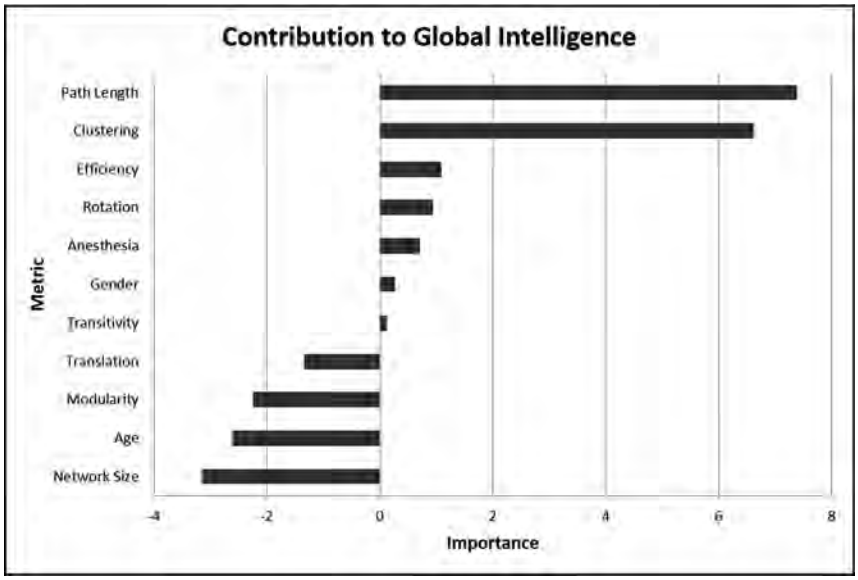

FIG 1. The importance of global metrics of network architecture with respect to full-scale intelligence quotient. The independent contribution of each metric was estimated as the error of the prediction of IQ of the machine learning algorithm compared with the error that results when that metric is negated. The most negative value of importance defines the limit of noise. Hence, variables with importance greater in magnitude than the most negative variable are significant.

Table 1: Metrics of network architecture

Metric	Description
Clustering coefficient	The fraction of the nodes of a given neighbor that are also neighbors of each other; reflects segregation/subspecialization in the network
Transitivity	The fraction of node triplets in the network that form a completely connected triangle; reflects segregation/functional subspecialization in the network
Modularity	The degree to which nodes tend to segregate into relatively independent modules; reflects segregation/subspecialization within the network
Characteristic path length	Minimum number of edges required to traverse the distance between 2 nodes averaged over the network; reflects the ease of information transfer across the network
Global efficiency	Inverse of the mean characteristic path length averaged over the network; reflects integration in the network

square of the 3 translational parameters) and "rotation" (root mean square of 3 rotational parameters). These translation and rotation estimates were then included as covariates in the machine learning analysis (see below). The functional image volume for each patient was registered to that individual's skull-stripped structural T1 dataset by using the FMRIB Linear Image Registration Tool (FLIRT; http://www.fmrib.ox.ac.uk). The inverse transformation matrix was calculated in this step and was subsequently used to transform all masks from structural to functional space. All registrations were inspected for accuracy. Voxelwise BOLD signal time-series were averaged over each node. The strength of an edge (connection) between 2 nodes was specifically defined as the absolute value of the Pearson correlation coefficient between their BOLD time-series.

Graph Construction and Network Metric Calculation. Weighted, undirected connection matrices were constructed, consisting of the pair-wise correlation between BOLD time-series over all network nodes (see an example in Fig 1). Graphs for each patient were thresholded according to a Bonferroni-corrected P value as follows[26]: 1) The P value for each pair-wise correlation in the connection matrix was multiplied by $(N^2 - N) / 2$ to correct for multiple comparisons, and 2) edges with a corrected P value $> .05$ were then set to zero.

For each weighted, undirected connection matrix, the following topologic properties were calculated by using Matlab scripts provided in The Brain Connectivity Toolbox (http://www.brain-connectivity-toolbox.net): clustering coefficient, transitivity, modularity, characteristic path length, and global efficiency. A brief description for each metric is provided in Table 1. To account for the differences in brain volume, and therefore intrinsic network size, that are inherent to a pediatric population, we normalized each raw network metric to the corresponding metric computed on a random network of identical size.[27]

Statistical Analyses

Statistical testing was performed by using the R statistical software package, Version 3.0.2 (http://www.r-project.org). A machine learning method was used to quantify the independent contribution of the measured network metrics to global intelligence. In other words, the importance of each network metric was computed after adjusting for the contribution of all other network metrics (as well as for age, sex, translational and rotational motion [measured during fMRI preprocessing in FSL], and the use of anesthesia during MR imaging). This analysis was accomplished by using a random forest approach, which has been previously described in detail.[28] In short, this ensemble learning method operates by constructing a multitude of decision trees during training and outputting the mean of predictions from individual trees. It is based on bootstrap aggregating, or bagging, in which numerous models are fitted during individual bootstrap samples and then are combined by averaging. During training, approximately one-third of the cohort is omitted at random from the training set: This omitted portion of the dataset is considered "out-of-bag." The IQ of each individual held out of bag is then predicted on the basis of the "learned" model. This process is repeated 1000 times, each time with a new, randomly selected out-of-bag cohort. The independent contribution of an individual variable is estimated by measuring the error for IQ prediction in the out of bag cohort compared with the error that results when that particular variable is negated during bagging. This method was

selected for 1 main reason: Other statistical methods, including regression, generate a model based on data from a given cohort and then assess the fit of the model on the same individuals. This machine learning algorithm, by contrast, tests the predictive capacity of the generated model on a subset of the cohort held out of bag. In other words, the capacity of the model to predict IQ is tested in a previously unseen subset of patients. Machine learning approaches, therefore, represent an attractive method by which metrics derived from quantitative imaging can be assessed with respect to their potential translation into clinically meaningful information at the level of a single patient.[29]

For all variables deemed important above, the relationships to global intelligence were further quantified by using linear regression. The goal of this step was not to confirm the importance of the variables above but rather to demonstrate graphically the nature of the relationships measured by the machine learning algorithm. A potential relationship between important variables and the span of epilepsy history was also assessed by linear regression.

Finally, the impact of anesthesia on the relationship between network architecture and intelligence was interrogated as follows: 1) the Wilcoxon rank sum test (corrected for multiple comparisons) was used to assess potential differences in network metrics between sedated and nonsedated patients (corrected $\alpha = .05$); 2) the machine learning analysis was repeated, this time only considering the subset of patients who underwent anesthesia during the MR imaging examination; and 3) for variables deemed important in step 2, the relationships to global intelligence were again demonstrated graphically by using linear regression.

Table 2: Anesthetic medications administered during MR imaging

Drug Combination	No. of Patients	Age Range (median) (yr)
Propofol only	9	9–17 (11)
Propofol + sevoflurane	6	8–16 (14)
Propofol + Dex	4	4–19 (15)
Propofol + sevoflurane + Dex	1	11–11 (11)
None	10	9–19 (16)

Note:—Dex indicates dexmedetomidine.

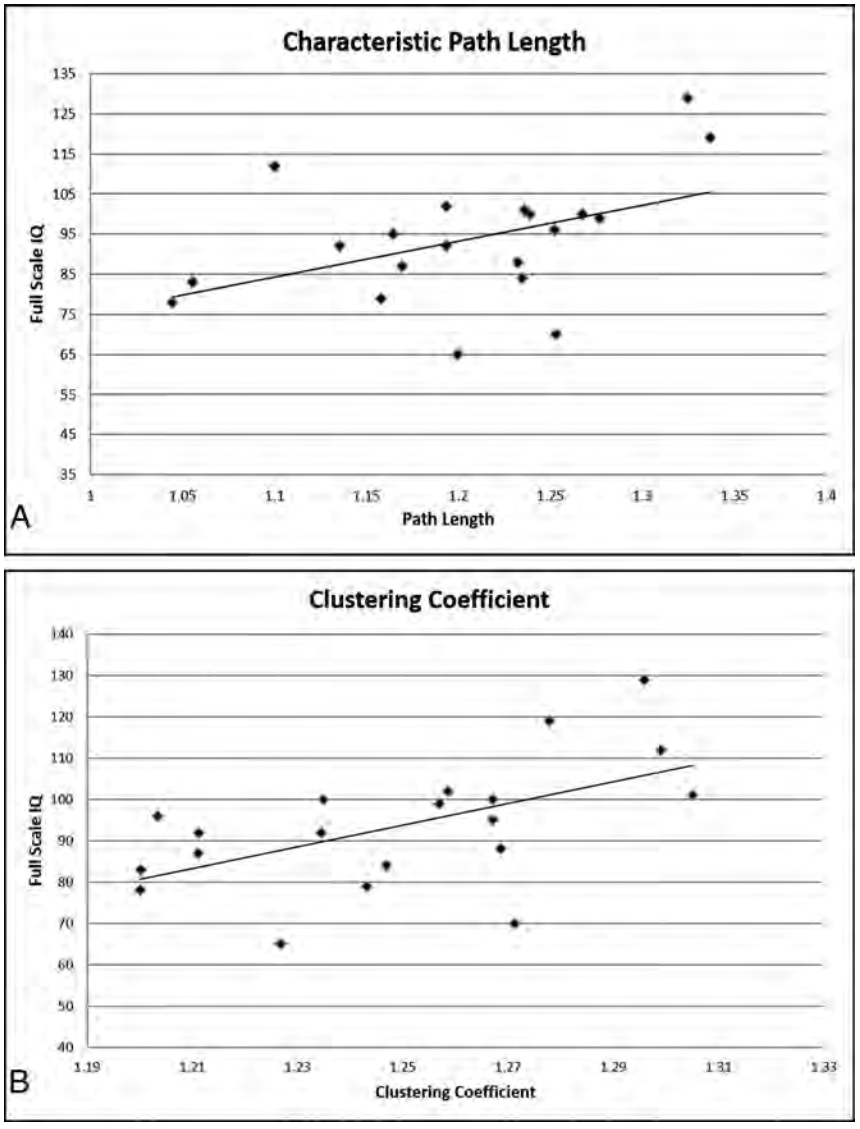

FIG 2. Graphic representation of the relationships of path length (*A*) and clustering coefficient (*B*) to the full-scale intelligence quotient.

RESULTS

Patients

Imaging was performed from June 2013 to June 2015. Forty patients met the inclusion criteria. Ten were excluded on the basis of prior brain surgery. Thirty patients with focal epilepsy (age range, 4–18 years; median age, 13 years; 15 males) composed the final study group. Of this cohort, 5 patients had structurally normal brains and 25 patients had demonstrable structural abnormalities at MR imaging, including focal cortical dysplasia ($n = 9$), mesial temporal sclerosis ($n = 6$), low-grade tumor ($n = 4$), a single epileptogenic tuber in the setting of tuberous sclerosis ($n = 3$), subependymal gray matter heterotopia ($n = 1$), hypothalamic hamartoma ($n = 1$), and prior hypoxic-ischemic insult ($n = 1$). An age-appropriate version of the Wechsler Intelligence Scales was successfully administered in all patients; full-scale intelligence quotient in the cohort ranged from 49 to 129 (median, 88). Of the total study group, 20 patients required general anesthesia during the imaging examination on the basis of guidelines from the American Academy of Pediatrics.[30] The specific medications administered during MR imaging are provided in Table 2.

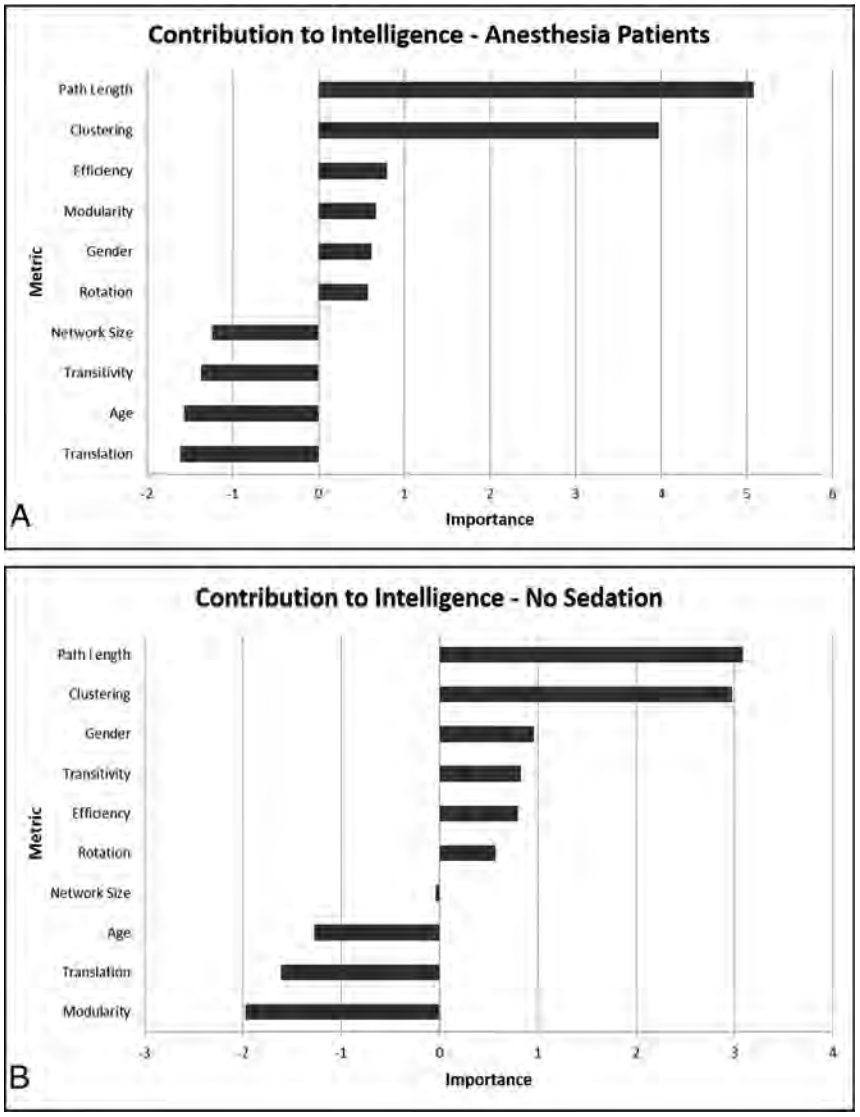

FIG 3. The importance of global metrics of network architecture with respect to the full-scale intelligence quotient for patients requiring anesthesia (*A*) and those who were nonsedated (*B*).

Network Architecture and Intelligence

All brains demonstrated small-world organization, characterized by high clustering coefficients and path lengths approaching those of a random graph. In general terms, both segregation (functional subspecialization) and integration in the network were important contributors to global brain function. In particular, after accounting for age and sex, the clustering coefficient and path length were independently associated with full-scale IQ (Fig 1). Both clustering coefficient ($r = 271$; $P = .0018$) and path length ($r = 107$; $P = .0016$) were directly related to full-scale IQ (Fig 2). Notably, neither motion parameters nor general anesthesia was an important variable with regard to accurate IQ prediction by the machine learning algorithm (Fig 1). Network size (the number of nodes in a patient's network) similarly did not impact the relationship between metrics and IQ (Fig 1). A longer history of epilepsy was associated with shorter path lengths ($P = .008$), consistent with reorganization of the network on the basis of seizures. Clustering coefficient, by contrast, was not related to seizure history ($P = .81$).

Regarding the potential impact of general anesthesia on the utility of network construction, network metrics in patients who required anesthesia during MR imaging did not differ significantly from those in nonsedated patients (P range, .51–.87). Furthermore, considering only patients requiring anesthesia during machine learning did not alter the patterns of network architecture contributing to global intelligence (Fig 3). Finally, for the entire cohort, clustering coefficient ($r = 262$; $P = .01$) and path length ($r = 89$; $P = .04$) were both directly related to full-scale IQ in this subset of children (Fig 4).

DISCUSSION

We report 2 main findings in children with focal epilepsy: 1) Two metrics of network architecture, clustering coefficient and path length, were independently associated with full-scale IQ; and 2) these relationships between network architecture and global intelligence persisted in patients whose functional images were acquired while they were under general anesthesia.

Most higher order functions of the human brain are not accomplished by individual functional centers compartmentalized to a particular region of the cortex. Rather, they emerge from parallel processing within subspecialized but distributed functional systems. A complex neural network, formed by some 10^{10} neurons, forms the structural substrate for efficient interaction between local and distributed areas of the cerebrum. Within this network, segregation into relatively independent local neighborhoods provides an architectural framework for functional subspecialization. Yet a complete range of function only emerges from efficient integration of these subspecialized neighborhoods across the entire brain. While these 2 properties might seem to be mutually antagonistic—efficient integration is best supported by a random network with a high proportion of long-range edges (short path length), while segregation requires a network with primarily local connections (high clustering coefficient)—the recent description of small-world networks by Watts and Strogatz[31] has provided critical insight toward resolving this inconsistency. They observed that within the framework of mathematic models, the addition of a small number of long-range connections to a locally connected graph has little effect on the clustering coefficient but reduces the path length to approximately that of a random graph. In graph theoretic terms, then, small-world networks have both high clustering coefficients, like regular networks, and short path lengths, like random networks. Hence,

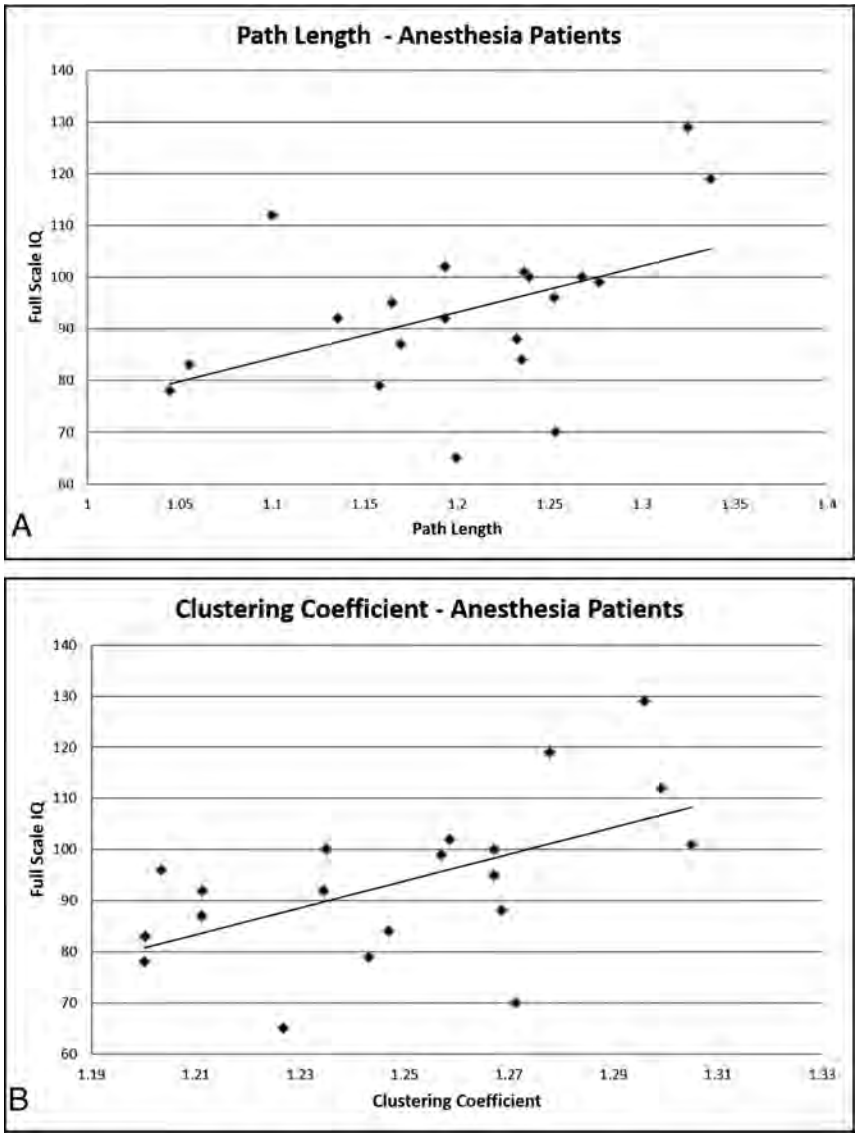

FIG 4. Graphic representation of the relationships of path length (*A*) and clustering coefficient (*B*) to full-scale intelligence quotient for patients requiring anesthesia.

small-world organization is an effective means by which both functional subspecialization and integration can be concomitantly supported by the same network. It has been suggested that small-world properties and the resulting efficiency of the network constitute the biologic underpinnings of cognitive function in the human brain.[15,17,32] We observed that both segregation (clustering coefficient) and integration (path length) were important features of the network with regard to global intelligence, consistent with this idea. In addition, these same relationships were detected in the subset of patients anesthetized according to various drug regimens that included propofol. This last point has important implications for both the pediatric and epilepsy populations, many of whom require anesthesia during MR imaging acquisition. Together, our findings suggest that the metrics of network architecture have the capacity to probe physiologically relevant features of the neural network in a clinical population of children with epilepsy.

In our cohort, shorter path lengths were associated with lower full-scale IQ scores. This relationship was largely mediated by seizure history; a long history of epilepsy portended short path length, suggesting that ongoing seizures are associated with rewiring of the cerebral network. These findings reinforce the idea that network metrics in epileptic brains may not have the same physiologic meaning as in healthy subjects. Synaptic efficacy, according to the Hebbian theory on neural plasticity, arises from repeat and persistent stimulation.[33] In this manner, connections contributing to useful and efficient subnetworks are strengthened with time, while those associated with less functional/inefficient networks are pruned.[34] In the setting of epilepsy, however, synapses are strengthened along pathways related to seizure propagation, essentially hijacking Hebbian processes.[35] Connectivity in this setting is potentiated without regard to network function, resulting in aberrant and potentially maladaptive pathways.[36,37] Consistent with this idea, Liao et al[38] observed shorter path lengths, also related to seizure history, in young adults with temporal lobe epilepsy. Our findings suggest that similar network reorganization occurs in the pediatric population and, furthermore, that such alterations are indeed maladaptive. In an older cohort of adult patients, Vlooswijk et al[39] observed increased path lengths in patients with cryptogenic localization–related epilepsy. Together these findings raise the possibility that the impact of seizures on the cerebral network may be exaggerated in young patients, whose cellular processes are primed to allow cerebral growth and reorganization.

To our knowledge, these are the first data using network architecture as a marker for full-scale IQ in children with epilepsy. However, our results are consistent with work in healthy adults[15,16] and children[17] that has demonstrated consistent relationships between network architecture and intelligence. As discussed above, the specific nature of these relationships is likely to reflect the pathophysiologic mechanisms at play in a given patient population. Hence, at any given time point, an individual's network will reflect not only the trajectories of normal brain development but also the cumulative impact of their particular CNS pathology. Previous studies have reported global network abnormalities in both adults[38-40] and children[41,42] with localization-related epilepsies. Our results extend this previous work to provide evidence that such network reorganization is physiologically meaningful with respect to brain function.

The question of general anesthesia is a complicated one

because it can be accomplished according to a variety of drug regimens, each of which may have a different effect on resting-state networks.[43] Of particular relevance to our work, several groups have reported a relative decrease in connectivity within frontoparietal[44] and whole-brain[45] networks during propofol-induced loss of consciousness. However, these studies did not include an assessment of how well the topology of the constructed brain networks paralleled their ultimate function. Our work suggests that despite relative changes that likely occur with regard to the intrinsic characteristics of the resting-state signal, the resulting network construction retains the capacity to capture important physiologic features of the cerebral network. This idea is consistent with the findings of Liu et al,[46] whose work with electrocorticography has suggested that long-range coordination of neural activity within large-scale brain networks is a core aspect of the physiology of the brain and does not depend on the state of consciousness.

This study has several limitations. First, it was conducted in a cohort of pediatric patients with focal epilepsy. Generalization of these results to patients with other CNS disorders, or to adults with epilepsy, may not be valid. Second, due to the study design, it was not possible to evaluate the relative changes in resting-state raw signal and the resulting functional networks that occurred after loss of consciousness under anesthesia. Along similar lines, due to the small number of patients in each group, the impact of different drug regimens (and their respective doses) on network construction could not be interrogated. Thus, although the physiologic relevance of network metrics was retained across the population, the possibility remains that the use of anesthesia altered, at least in relative fashion, the observed relationships. We also cannot exclude the possibility that anesthesia may completely abrogate accurate network reconstruction in some subsets of individual patients. However, the purpose of this study was not to define the exact impact of anesthetic agents on resting-state networks. Rather, we sought to determine whether it is generally feasible to obtain physiologically relevant information from images acquired with the patient under anesthesia according to the general clinical workflow within a radiology department. Future inquiry regarding the specific drug regimens that allow construction of networks that most closely parallel the true physiology of the brain would be of great future value to this field of study.

CONCLUSIONS

We report 2 main findings in children with focal epilepsy: 1) Metrics of network architecture derived from resting-state functional networks were important contributors to full-scale IQ, and 2) the relationships between network architecture and intelligence were robust to general anesthesia. Our results suggest that imaging-based markers of network architecture indeed capture physiologically relevant information with regard to the function of the pathologic brain and, furthermore, that this information can be acquired with the patient under general anesthesia. In sum, our findings support the potential for resting-state fMRI to provide clinically meaningful markers of network function in children with epilepsy.

REFERENCES

1. Boyle CA, Decouflé P, Yeargin-Allsopp M. **Prevalence and health impact of developmental disabilities in US children.** *Pediatrics* 1994; 93:399–403 Medline
2. Phi JH, Cho BK, Wang KC, et al. **Longitudinal analyses of the surgical outcomes of pediatric epilepsy patients with focal cortical dysplasia.** *J Neurosurg Pediatr* 2010;6:49–56 CrossRef Medline
3. Duchowny M. **Clinical, functional, and neurophysiologic assessment of dysplastic cortical networks: implications for cortical functioning and surgical management.** *Epilepsia* 2009;50(suppl 9):19–27 CrossRef Medline
4. Westerveld M, Sass KJ, Chelune GJ, et al. **Temporal lobectomy in children: cognitive outcome.** *J Neurosurg* 2000;92:24–30 CrossRef Medline
5. Duchowny M, Jayakar P, Levin B. **Aberrant neural circuits in malformations of cortical development and focal epilepsy.** *Neurology* 2000;55:423–28 Medline
6. Yasuda CL, Valise C, Saude AV, et al. **Dynamic changes in white and gray matter volume are associated with outcome of surgical treatment in temporal lobe epilepsy.** *Neuroimage* 2010;49:71–79 CrossRef Medline
7. Hagmann P, Cammoun L, Gigandet X, et al. **Mapping the structural core of human cerebral cortex.** *PLoS Biol* 2008;6:e159 CrossRef Medline
8. Biswal BB, van Kylen J, Hyde JS. **Simultaneous assessment of flow and BOLD signals in resting-state functional connectivity maps.** *NMR Biomed* 1997;10:165–70 Medline
9. Rubinov M, Sporns O. **Complex network measures of brain connectivity: uses and interpretations.** *Neuroimage* 2010;52: 1059–69 CrossRef Medline
10. He H, Sui J, Yu Q, et al. **Altered small-world brain networks in schizophrenia patients during working memory performance.** *PLoS One* 2012;7:e38195 CrossRef Medline
11. Göttlich M, TF, Heldmann M, et al. **Altered resting state brain networks in Parkinson's disease.** *PLoS One* 2013;8:e77336 CrossRef Medline
12. Brier MR, Thomas JB, Fagan AM, et al. **Functional connectivity and graph theory in preclinical Alzheimer's disease.** *Neurobiol Aging* 2014;35:757–68 CrossRef Medline
13. Sanz-Arigita EJ, Schoonheim MM, Damoiseaux JS, et al. **Loss of 'small-world' networks in Alzheimer's disease: graph analysis of FMRI resting-state functional connectivity.** *PLoS One* 2010;5: e13788 CrossRef Medline
14. van Diessen E, Zweiphenning WJ, Jansen FE, et al. **Brain network organization in focal epilepsy: a systematic review and meta-analysis.** *PLoS One* 2014;9:e114606 CrossRef Medline
15. Li Y, Liu Y, Li J, et al. **Brain anatomical network and intelligence.** *PLoS Comput Biol* 2009;5:e1000395 CrossRef Medline
16. van den Heuvel MP, Stam CJ, Kahn RS, et al. **Efficiency of functional brain networks and intellectual performance.** *J Neurosci* 2009;29: 7619–24 CrossRef Medline
17. Kim DJ, Davis EP, Sandman CA, et al. **Children's intellectual ability is associated with structural network integrity.** *Neuroimage* 2016; 124(pt A):550–56 CrossRef Medline
18. Peltier SJ, Kerssens C, Hamann SB, et al. **Functional connectivity changes with concentration of sevoflurane anesthesia.** *Neuroreport* 2005;16:285–88 CrossRef Medline
19. Berg AT, Berkovic SF, Brodie MJ, et al. **Revised terminology and concepts for organization of seizures and epilepsies: report of the ILAE Commission on Classification and Terminology, 2005–2009.** *Epilepsia* 2010;51:676–85 CrossRef Medline
20. Smith SM, Jenkinson M, Woolrich MW, et al. **Advances in functional and structural MR image analysis and implementation as FSL.** *Neuroimage* 2004;23(suppl 1):S208–19 CrossRef Medline
21. Fischl BL, Liu A, Dale AM. **Automated manifold surgery: constructing geometrically accurate and topologically correct models of the human cerebral cortex.** *IEEE Trans Med Imaging* 2001;20:70–80 CrossRef Medline

22. Fischl B, Salat DH, van der Kouwe AJ, et al. **Sequence-independent segmentation of magnetic resonance images.** *Neuroimage* 2004: (suppl 1):S69–84 CrossRef Medline
23. Thomas CG, Harshman RA, Menon RS. **Noise reduction in BOLD-based fMRI using component analysis.** *Neuroimage* 2002;17: 1521–37 CrossRef Medline
24. Pruim RH, Mennes M, Buitelaar JK, et al. **Evaluation of ICA-AROMA and alternative strategies for motion artifact removal in resting state fMRI.** *Neuroimage* 2015;112:278–87 CrossRef Medline
25. Bright MG, Murphy K. **Is fMRI "noise" really noise? Resting state nuisance regressors remove variance with network structure.** *Neuroimage* 2015;114:158–69 CrossRef Medline
26. Weisstein E. Bonferroni Correction**.** From MathWorld–A Wolfram Web Resource. http://mathworld.wolfram.com/BonferroniCorrection.html. Accessed August 5, 2016
27. Rubinov M, Sporns O. **Weight-conserving characterization of complex functional brain networks.** *Neuroimage* 2011;56: 2068–79 CrossRef Medline
28. Breiman L. **Random forests.** *Machine Learning* 2001;45:5–32 CrossRef
29. Paldino MJ, Hedges K, Zhang W. **Independent contribution of individual white matter pathways to language function in pediatric epilepsy patients.** *Neuroimage Clin* 2014;6:327–32 CrossRef Medline
30. Coté CJ, Wilson S; American Academy of Pediatrics; American Academy of Pediatric Dentistry. **Guidelines for monitoring and management of pediatric patients before, during, and after sedation for diagnostic and therapeutic procedures: update 2016.** *Pediatrics* 2016;138:pii: e20161212 CrossRef Medline
31. Watts DJ, Strogatz SH. **Collective dynamics of 'small-world' networks.** *Nature* 1998;393:440–42 CrossRef Medline
32. Pamplona GS, Santos Neto GS, Rosset SR, et al. **Analyzing the association between functional connectivity of the brain and intellectual performance.** *Front Hum Neurosci* 2015;9:61 CrossRef Medline
33. Chaudhury S, Sharma V, Kumar V, et al. **Activity-dependent synaptic plasticity modulates the critical phase of brain development.** *Brain Dev* 2016;38:355–63 CrossRef Medline
34. Cruikshank SJ, Weinberger NM. **Evidence for the Hebbian hypothesis in experience-dependent physiological plasticity of neocortex: a critical review.** *Brain Res Brain Res Rev* 1996;22:191–228 CrossRef Medline
35. Hernan AE, Holmes GL, Isaev D, et al. **Altered short-term plasticity in the prefrontal cortex after early life seizures.** *Neurobiol Dis* 2013; 50:120–26 CrossRef Medline
36. Galicia E, Imai K, Mohamed IS, et al. **Changing ictal-onset EEG patterns in children with cortical dysplasia.** *Brain Dev* 2009;31:569–76 CrossRef Medline
37. Koh S, Mathern GW, Glasser G, et al. **Status epilepticus and frequent seizures: incidence and clinical characteristics in pediatric epilepsy surgery patients.** *Epilepsia* 2005;46:1950–54 CrossRef Medline
38. Liao W, Zhang Z, Pan Z, et al. **Altered functional connectivity and small-world in mesial temporal lobe epilepsy.** *PLoS One* 2010;5: e8525 CrossRef Medline
39. Vlooswijk MC, Vaessen MJ, Jansen JF, et al. **Loss of network efficiency associated with cognitive decline in chronic epilepsy.** *Neurology* 2011;77:938–44 CrossRef Medline
40. DeSalvo MN, Douw L, Tanaka N, et al. **Altered structural connectome in temporal lobe epilepsy.** *Radiology* 2014;270:842–48 CrossRef Medline
41. Vaessen MJ, Braakman HM, Heerink JS, et al. **Abnormal modular organization of functional networks in cognitively impaired children with frontal lobe epilepsy.** *Cereb Cortex* 2013;23:1997–2006 CrossRef Medline
42. Widjaja E, Zamyadi M, Raybaud C, et al. **Disrupted global and regional structural networks and subnetworks in children with localization-related epilepsy.** *AJNR Am J Neuroradiol* 2015;36:1362–68 CrossRef Medline
43. Kalthoff D, Po C, Wiedermann D, et al. **Reliability and spatial specificity of rat brain sensorimotor functional connectivity networks are superior under sedation compared with general anesthesia.** *NMR Biomed* 2013;26:638–50 CrossRef Medline
44. Boveroux P, Vanhaudenhuyse A, Bruno MA, et al. **Breakdown of within- and between-network resting state functional magnetic resonance imaging connectivity during propofol-induced loss of consciousness.** *Anesthesiology* 2010;113:1038–53 CrossRef Medline
45. Monti MM, Lutkenhoff ES, Rubinov M, et al. **Dynamic change of global and local information processing in propofol-induced loss and recovery of consciousness.** *PLoS Comput Biol* 2013;9:e1003271 CrossRef Medline
46. Liu X, Yanagawa T, Leopold DA, et al. **Robust long-range coordination of spontaneous neural activity in waking, sleep and anesthesia.** *Cereb Cortex* 2015;25:2929–38 CrossRef Medline

First-Line Use of Core Needle Biopsy for High-Yield Preliminary Diagnosis of Thyroid Nodules

H.C. Kim, Y.J. Kim, H.Y. Han, J.M. Yi, J.H. Baek, S.Y. Park, J.Y. Seo, and K.W. Kim

ABSTRACT

BACKGROUND AND PURPOSE: Although core needle biopsy was introduced as a diagnostic alternative to fine-needle aspiration, the utility and safety of core needle biopsy for thyroid nodules in a large population has yet to be studied comprehensively. We evaluate core needle biopsy yields on a large-scale basis to investigate its potential in the preliminary diagnosis of thyroid nodules.

MATERIALS AND METHODS: Between March 2005 and December 2013, 2448 initially detected thyroid nodules from 2120 consecutive patients who underwent core needle biopsy were retrospectively evaluated. Of these, 72 thyroid nodules from 63 patients were excluded due to prior fine-needle aspiration attempts. The inconclusive and conclusive result rates, diagnostic accuracy, sensitivity, specificity, positive predictive value, negative predictive value, and unnecessary surgery rate of core needle biopsy were evaluated.

RESULTS: With core needle biopsy as the first-line method, the inconclusive result rate was 11.9% (283/2376) and the conclusive result rate was 88.1% (2093/2376). The diagnostic accuracy, sensitivity, specificity, positive predictive value, and negative predictive value of core needle biopsy for the diagnosis of malignancy were 96.7% (1160/1200), 89.7% (347/387), 100% (813/813), 100% (347/347), and 95.3% (813/853), respectively. There were no major complications and 12 minor complications.

CONCLUSIONS: We have demonstrated that first-line use of core needle biopsy may well improve diagnostic accuracy in thyroid nodules, reducing inconclusive or false-negative results and unnecessary operations. Such benefits underscore the promising role of core needle biopsy in managing thyroid nodules and optimizing related surgical decision-making.

ABBREVIATIONS: AUS = atypia of undetermined significance; CNB = core needle biopsy; FLUS = follicular lesion of undetermined significance; FNA = fine-needle aspiration; NPV = negative predictive value; PPV = positive predictive value; US = ultrasonography

Although ultrasonography (US)-guided fine-needle aspiration (FNA) is a safe, accurate, and cost-effective method for diagnosing malignancy in thyroid nodules, there are limitations.[1,2] A major drawback is the frequency of inconclusive results (ie, indeterminate or inadequate results), accounting for 25%–30% of FNA results.[2,3] In such instances, even repeat FNA attempts may still be nondiagnostic (9.9%–47.8% incidence).[4-6] Nodules with inconclusive FNA results are commonly referred for diagnostic surgery at reported rates of 22.2%–94.7%.[7-9] Although several studies suggest that biomarkers (molecular or genetic) and clinical or sonography parameters may serve to support FNA outcomes,[10-12] surgical confirmation is often still required.[1,2,12]

Core needle biopsy (CNB) was introduced as a diagnostic alternative to FNA or tissue diagnosis. It is well-tolerated and safe and associated with a low incidence of complications.[3,4,6,13-16] However, its role has remained second-line, largely serving as a supplement in patients with inconclusive FNA results. However, a number of studies have reported that a diagnosis was established via CNB in up to 98% of nodules with indeterminate FNA results; and by performing CNB and repeat FNA in combination, 97% of nodules with prior inadequate FNA yields are eventually diagnosed.[4-6,14-16] Most interesting, there have been few studies to date on the use of CNB as a first-line examination for the diagnosis of thyroid nodules.[17-19] Consequently, the utility and safety of

Received February 10, 2016; accepted after revision September 13.

From the Department of Radiology (H.C.K., Y.J.K., J.Y.S., K.W.K.), Konyang University Myunggok Medical Research Institute, Konyang Hospital, Konyang University College of Medicine, Daejeon, Republic of Korea; Department of Radiology (H.Y.H., J.M.Y.), Daejeon Sun Hospital, Daejeon, Republic of Korea; Department of Radiology and Research Institute of Radiology (J.H.B.), University of Ulsan College of Medicine, Asan Medical Center, Seoul, Korea; and Department of Pathology (S.Y.P.), Konyang University Hospital, Konyang University College of Medicine, Daejeon, Republic of Korea

This work was supported by the Konyang University Myunggok Research Fund of 2015.

Paper previously presented at: Annual Meeting of the European Congress of Radiology, March 2–6, 2016; Vienna, Austria.

Please address correspondence to Young Joong Kim, MD, Department of Radiology, Konyang University Myunggok Medical Research Institute, Konyang Hospital, Konyang University College of Medicine, 158 Gwanjeodong-ro, Seo-gu, Daejeon 35365, Republic of Korea; e-mail: myth0318@hanmail.net

Indicates article with supplemental on-line tables.

http://dx.doi.org/10.3174/ajnr.A5007

CNB for thyroid nodules in a large population have not yet been studied comprehensively.

This study was conducted on the premise that highly diagnostic yields are achievable via CNB, without undue or major complications. We therefore evaluated CNB yields on a large-scale basis to investigate its full potential in the preliminary diagnosis of thyroid nodules.

MATERIALS AND METHODS

Study Population

This observational study was approved by the Institutional Review Board of Konyang University Hospital and Daejeon Sun Hospital, with written informed consent for data access waived. However, all patients undergoing CNB at our facility granted prior informed consent.

Between March 2005 and December 2013, 2448 thyroid nodules detected in 2120 consecutive patients at 2 institutions, Konyang University Hospital ($n = 634$) and Daejeon Sun Hospital ($n = 1814$), were subjected to ultrasound-guided CNB. Of these, 72 thyroid nodules in 63 patients were excluded on the basis of prior FNA attempts. Finally, 2376 initially detected thyroid nodules from 2057 consecutive patients (594 men and 1463 women; mean age, 50.8 ± 12.6 years, range, 11–91 years) were enrolled in this study. These enrolled thyroid nodules underwent CNB due to suspicious US findings ($n = 1538$), heavy calcifications ($n = 296$), high vascularity ($n = 289$), and requests of a small group of referring physicians ($n = 253$). The physicians of this cohort preferred the CNB rather than FNA in an attempt to avoid inconclusive FNA results.

Final diagnoses in malignant nodules were confirmed by postsurgical histopathology or other pathologic documentation (including biopsy-proved lymphoma or metastasis). Benign nodules were also confirmed by postsurgical histopathology, by sequential benign CNB or FNA outcomes (at least twice with intervals of >6 months), or by benign CNB findings with a nodule that was stable or decreased in size of after 1 year (at minimum).

Analysis of US Findings

The US images were reviewed independently by 2 radiologists (Y.J.K., and H.Y.H). The US finding of the nodules were evaluated for following features[20,21]: the size of thyroid nodules, composition (solid, predominantly solid, predominantly cystic, or cyst), shape (ovoid to round or irregular), orientation (parallel or nonparallel), margin (smooth, spiculated, or ill-defined), echogenicity (isoechoic, hypoechoic, markedly hypoechoic, or hyperechoic), and calcifications (none, macrocalcifications, or microcalcifications). The suspicious US findings were defined as nonparallel orientation, spiculated margin, marked hypoechogenicity, and the presence of micro- or macrocalcifications.[20,21] A suspicious malignant nodule was defined if 1 of the above findings was present. If there were discrepancies in the US findings, the radiologists resolved them by consensus.

Sonography-Guided CNB Procedures

US examinations were performed by using 1 of 3 US systems: an iU22 or HDI-5000 U (Philips Healthcare, Best, the Netherlands) or a Logiq 9 ultrasound (GE Healthcare, Milwaukee, Wisconsin), each equipped with a high-frequency linear probe (7–12 MHz). All US examinations and US-guided CNBs were performed by 1 of 5 radiologists (Y.J.K., Y.S.P., D.H.O., H.Y.H., or J.M.Y.) with ≥5 years of clinical experience in performing and interpreting US images of the thyroid gland. If the nodule had a cystic portion of >50% or necrosis, the internal fluid of the nodule was aspirated at first and then US-guided CNB was performed on the remaining solid portion.

Disposable 1.1-cm excursion 18-ga double-action spring-activated needles (TSK Ace-cut; Create Medic, Yokohama, Japan) were used for CNB, following local anesthetic injection (lidocaine 1%). Before insertion, power Doppler US was used to carefully evaluate vessels along the biopsy course to avoid hemorrhage. With a freehand technique, the needle was advanced into a nodule or across its margin to obtain a tissue core, but the thyroid capsule was avoided to prevent vessel injury. Once the nodule was pierced, adjacent vessels were again evaluated to minimize injury and bleeding. We measured the distance of travel (1.1 cm) before sequential firing of the needle stylet and cutting cannula.

Tissue cores were placed in 10% buffered formalin immediately at the completion of the procedure for conventional processing. Each patient was then monitored for 10–20 minutes with firm local compression of the biopsy site.

Analysis of CNB Results

All CNB specimens were reviewed by board-certified attending staff pathologists with ≥5 years of clinical experience (S.Y.P., Y.M.K., B.K.K., and H.J.L.), though thyroid CNB diagnostic criteria were not yet standardized. For this study, the 6 categories of the Bethesda System were used to classify histopathologic CNB results.[22]

In the absence of any identifiable follicular elements or with scant normal follicular content, a CNB was considered nondiagnostic. Benign CNB readings were those demonstrating colloid or hyperplastic nodules and lymphocytic thyroiditis. CNB specimens containing nodules with some atypical cells not diagnostic of malignancy were interpreted as atypia (atypia of undetermined significance [AUS]) or follicular lesions of undetermined significance (FLUSs). These included cellular follicular nodules that were difficult to distinguish (follicular neoplasm versus hypercellular/hyperplastic nodule). Nodules with histologic features favoring follicular neoplasm were categorized as suggestive of follicular neoplasm or consistent with follicular neoplasm. "Suspicious for malignancy" included specimens that displayed atypia of a borderline nature. Unequivocal malignant features were needed for a diagnosis of malignancy.

Statistical Analysis

The statistical analysis relied on standard software (SPSS Version 18.0 for Windows: IBM, Armonk, New York). Rates of nondiagnostic results, malignancy, inconclusive and conclusive results, unnecessary surgery (considered malignant by CNB but confirmed as benign or viewed as a follicular neoplasm by CNB but proved to be adenomatous hyperplasia), and complications were determined. Major complications were defined as events that might result in admission to a hospital for therapy, an unplanned

Table 1: Core-needle biopsy results and final diagnosis for initially detected thyroid nodules[a]

		Final Diagnosis (n = 1200)			Final Diagnosis (n = 455)			Final Diagnosis (n = 745)	
	Total CNB (n = 2376)	Benign (n = 813)	Malignant (n = 387)	CNB <10 mm (n = 888)	Benign (n = 232)	Malignant (n = 223)	CNB ≥10 mm (n = 1488)	Benign (n = 581)	Malignant (n = 164)
Nondiagnostic	117 (4.9)	19 (2.3)	8 (2.1)	45 (5.1)	4 (1.7)	7 (3.1)	72 (4.8)	15 (2.6)	1 (0.6)
Benign	1549 (65.2)	734 (90.3)	8 (2.1)	483 (54.4)	218 (94.0)	6 (2.7)	1066 (71.6)	516 (88.8)	2 (1.2)
AUS or FLUS	166 (7.0)	44 (5.4)	16 (4.1)	55 (6.2)	6 (2.6)	9 (4.0)	111 (7.5)	38 (6.5)	7 (4.3)
FN or SFN	70 (2.9)	16 (2.0)	8 (2.1)	18 (2.0)	4 (1.7)	1 (0.5)	52 (3.5)	12 (2.1)	7 (4.3)
Suspicious for malignancy	25 (1.1)	0	21 (5.4)	14 (1.6)	0	12 (5.4)	11 (0.7)	0	9 (5.5)
Malignancy	449 (18.9)	0	326 (84.2)	273 (30.7)	0	188 (84.3)	176 (11.8)	0	138 (84.1)

Note:—FN indicates follicular neoplasm; SFN, suspicious for a follicular neoplasm.

[a] Data are the number of nodules with percentages in parentheses. Percentages do not add up to 100% because of rounding.

increase in the level of care, lengthened hospital stay, or events that might lead to substantial morbidity or disability. Other complications such as perithyroid hemorrhage or edema were considered minor complications.[23]

Diagnosis of malignancy included nodules with suspicious for malignancy or malignant CNB results. Inconclusive results included nondiagnostic and AUS/FLUS readings. With respect to thyroid cancer, CNB was analyzed for diagnostic accuracy, sensitivity, specificity, positive predictive value (PPV), and negative predictive value (NPV).

Subgroup analysis related to sample adequacy was performed according to the nodule size (<10 mm and ≥10 mm), location (upper/lower and mid), composition (cyst; cystic component ≥50%; and solid, cystic component <50%), and the presence and type of calcification. Subgroup analysis related to inconclusive results was also performed according to the nodule size, composition, location, and suspicious US findings. The parameters of the 2 groups were compared by using Student t tests and the χ^2 or Fisher exact test. Statistical significance was set at $P < .05$.

RESULTS

In all patients, CNB procedures were well-tolerated without immediate complications. The mean nodule size was 14.3 ± 9.6 mm (range, 4–93 mm), with nodules ≥10 mm accounting for 62.6% (1488/2376) of the sample. Among the 888 nodules of <10 mm, 634 nodules underwent CNB due to suspicious US findings. Two hundred fifty-four nodules with indeterminate US findings underwent CNB to decide the extent of the surgery for multiple thyroid nodules or to evaluate primary malignancy when cervical lymph nodes were diagnosed as metastatic. The mean follow-up was 27.5 ± 21.9 months. CNB results (n = 2376) and final diagnoses (n = 1200) are summarized in Table 1.

Final Diagnosis

Final histopathologic diagnoses were ultimately acquired in 1200 of 2376 nodules (50.5%), all included in the outcome analyses. Of 2376 nodules, 1176 (49.5%) were neither followed adequately nor surgically removed to confirm prior CNB diagnostic assessments. Malignancies (n = 387) were diagnosed following surgical resections (n = 379) or biopsy-confirmed specific pathologic results, including metastasis (n = 7) or lymphoma (n = 1). Benign nodules (n = 813) were confirmed by an operation (193/813, 23.7%), sequential benign FNA or CNB readings (twice at least) (83/813, 10.2%), or a minimum 1-year follow-up of stable or shrinking nodules considered benign by CNB (537/813, 66.1%).

Diagnostic Utility of First-Line US-Guided CNB

Study outcomes of CNB as a first-line procedure for a preliminary diagnosis of thyroid nodules are summarized in Fig 1 and Table 2. In terms of detecting malignancy, CNB displayed a diagnostic accuracy of 96.7%, a sensitivity of 89.7%, a specificity of 100%, a PPV of 100%, and an NPV of 95.3%. The false-negative rate was 1.1% (8/742), with no false-positive results in this study. The diagnostic accuracy and NPV were significantly higher for nodules of ≥10 mm than for nodules of <10 mm. The malignancy rate was significantly higher for nodules of <10 mm (32.3%) than for nodules of ≥10 mm (12.6%). Moreover, sensitivity, specificity, and PPV did not show significant differences according to nodule size. Diagnostic accuracy was not associated with the composition and location of thyroid nodules (On-line Table 1).

Sample Adequacy and Conclusiveness

For CNB readings, the nondiagnostic rate was 4.9% (117/2376). Of 117 nodules, 38 contained a mix of fibromuscular tissue or normal thyroid tissue, owing to inaccurately targeted biopsies; 59 showed little or no cellular content due to cystic change or necrosis of a nodule; and 20 showed only hemorrhage. Nodule size (10 mm and ≥10 mm) and calcification did not affect the sample adequacy. The composition and location of the nodules were associated with the nondiagnostic results (Table 3).

Inconclusive results accounted for 11.9% (283/2376), whereas 88.1% (2093/2376) generated conclusive outcomes. According to our subgroup analysis, the orientation, margin, and echogenicity of the nodules were associated with the conclusiveness of CNB results. The composition, size, and calcification of nodules were not associated with the conclusiveness of CNB results (Table 4).

Correlation of CNB Results with Surgical Findings

Of the 1200 verifiable diagnoses, 813 (67.8%) were benign and 387 (32.2%) were malignant. Five hundred seventy-two nodules (47.7%) were surgically resected; these procedures confirmed 379 as malignant and 193 as benign (On-line Table 2).

All 339 nodules considered malignant or suspicious for malignancy by CNB were confirmed as malignancies at surgery. Of the 24 nodules viewed as follicular neoplasms by CNB, 2 were adeno-

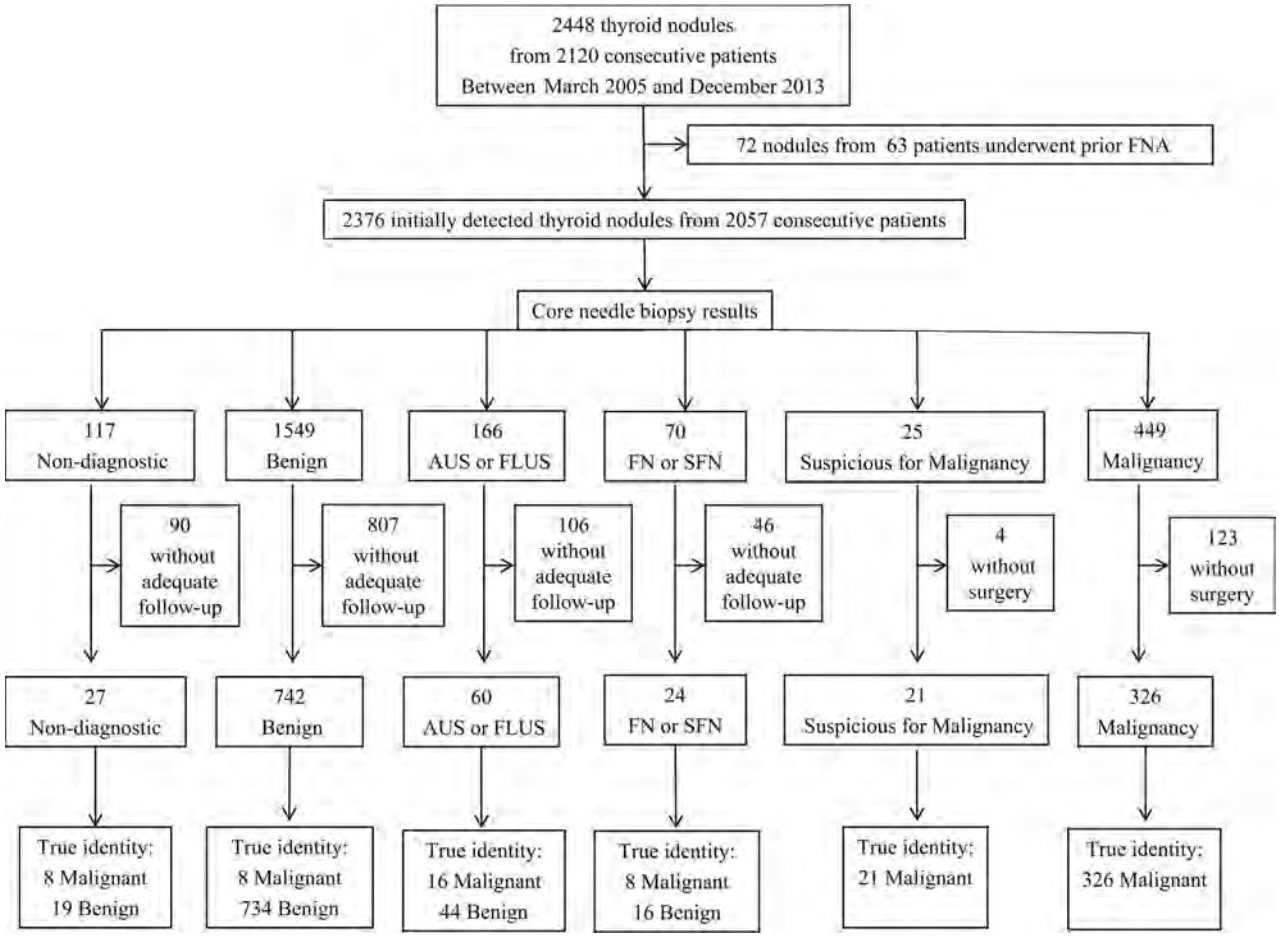

FIG 1. Flow and study outcomes in study patients. Numbers are the number of thyroid nodules. FN indicates follicular neoplasm; SFN, suspicious for a follicular neoplasm.

Table 2: Outcome of CNB for initially detected thyroid nodules

Study Outcomes	Incidence (Total)	95% CI	Incidence (<10 mm)	95% CI	Incidence (≥10 mm)	95% CI	*P* Value
Nondiagnostic	4.9% (117/2376)	(4.1–5.8)	5.1% (45/888)	(3.6–6.6)	4.8% (72/1488)	(3.8–5.9)	.803
Inconclusive	11.9% (283/2376)	(10.6–13.2)	11.3% (100/888)	(9.2–13.4)	12.3% (183/1488)	(10.6–14.0)	.450
Conclusive	88.1% (2093/2376)	(86.8–89.4)	88.7% (788/888)	(86.6–90.8)	87.7% (1305/1488)	(86.0–89.4)	.450
Malignancy	19.9% (474/2376)	(18.3–21.6)	32.3% (287/888)	(29.1–35.6)	12.6% (187/1488)	(10.9–14.3)	<.001
Diagnostic accuracy	96.7% (1160/1200)	(95.7–97.7)	94.9% (432/455)	(92.8–96.9)	97.7% (728/745)	(96.6–98.8)	.012
Sensitivity	89.7% (347/387)	(86.6–92.7)	89.7% (200/223)	(85.3–93.4)	89.6% (147/164)	(84.9–94.1)	1.000
Specificity	100% (813/813)	(100.0–100.0)	100% (232/232)	(100.0–100.0)	100% (581/581)	(100.0–100.0)	1.000
PPV	100% (347/347)	(100.0–100.0)	100% (200/200)	(100.0–100.0)	100% (147/147)	(100.0–100.0)	1.000
NPV	95.3% (813/853)	(93.9–96.7)	91.0% (232/255)	(87.3–94.2)	97.2% (581/598)	(95.8–98.3)	<.001
Unnecessary surgery	0.6% (2/363)	(0–1.4)	0% (0/163)		1.0% (2/200)	(0–2.5)	.504
Major complication	0		0		0		
Minor complication	0.5% (12/2376)	(0.3–0.8)	0.6 (5/888)	(0.1–1.1)	0.5% (7/1488)	(0.1–0.9)	.758

matous hyperplasia. Thus, unnecessary surgery was performed for only 2 nodules (2/363, 0.6%).

Motives for resecting nodules with benign CNB results were image-pathology discordance (benign by CNB but suspicious US features) ($n = 21$), malignancy on follow-up FNA or CNB ($n = 5$), coexistent nodules with a resected nodule ($n = 40$), and patient preference or aesthetic concerns. Of the 21 nodules with image-pathology discordance, 3 proved to be papillary carcinomas. Nodules ($n = 48$) interpreted as AUS/FLUS by CNB were resected to exclude papillary carcinoma. Among them, 12 (63.2%) were confirmed as malignant (11 papillary carcinomas, 1 follicular variant of papillary carcinoma) in the AUS group ($n = 19$) and 4 nodules (13.8%) were confirmed malignant (2 papillary carcinomas, 1 follicular carcinoma, and 1 follicular variant of papillary carcinoma) in the FLUS group ($n = 29$).

Complications

There were no major complications or hospitalizations associated with interventions in our patient cohort. Twelve patients developed minor complications. There was no difference according to

Table 3: Univariate analysis for factors associated with nondiagnostic result on CNB

Study Outcomes	Nondiagnostic Results	Diagnostic Results	*P* Value
Nodule size (mm)	13.3 ± 8.0	14.4 ± 9.7	.220
<10 mm	45 (5.1%)	843 (94.9%)	.803
≥10 mm	72 (4.8%)	1416 (95.2%)	
Composition (No.) (%)			
Solid (cystic component <50%)	98 (4.4%)	2135 (95.6%)	<.001
Cyst (cystic component ≥50%)	19 (13.3%)	124 (86.7%)	
Calcification (No.) (%)			
None	82 (4.9%)	1576 (95.1%)	.941
Macrocalcification	15 (4.1%)	349 (95.9%)	.441
Microcalcification	20 (5.6%)	334 (94.4%)	.494
Location (No.) (%)			
Upper/lower	61 (6.4%)	896 (93.6%)	.007
Mid	56 (3.9%)	1363 (96.1%)	

Table 4: Univariate analysis for factors associated with conclusive and inconclusive results on CNB

Study Outcomes	Conclusive	Inconclusive	*P* Value
Age (mean) (yr)	51.2 ± 12.6	48.5 ± 12.2	<.001
Sex (M/F)	440:1653	44:293	.032
Nodule size (mm)	14.2 ± 9.4	15.4 ± 10.3	.064
<10 mm	788 (88.7%)	100 (11.3%)	.450
≥10 mm	1305 (87.7%)	183 (12.3%)	
Composition (No.) (%)			
Solid	1336 (87.4%)	192 (12.6%)	.186
Predominantly solid	95 (84.8%)	17 (15.2%)	.274
Predominantly cystic	99 (84.6%)	18 (15.4%)	.234
Cystic	4 (66.7%)	2 (33.3%)	.154
Shape (No.) (%)			
Ovoid to round	2033 (87.9%)	279 (12.1%)	.156
Irregular	60 (93.8%)	4 (6.3%)	
Orientation (No.) (%)			
Parallel	1728 (87.5%)	247 (12.5%)	.047
Nonparallel	365 (91.0%)	36 (9.0%)	
Margin (No.) (%)			
Smooth	1360 (85.6%)	228 (14.4%)	<.001
Spiculated	366 (94.6%)	21 (5.4%)	<.001
Ill-defined	367 (91.5%)	34 (8.5%)	.020
Echogenicity (No.) (%)			
Isoechoic	767 (88.5%)	100 (11.5%)	.667
Hypoechoic	913 (86.0%)	149 (14.0%)	.004
Markedly hypoechoic	402 (92.6%)	32 (7.4%)	.001
Hyperechoic	11 (84.6%)	2 (15.4%)	.662
Calcification (No.) (%)			
None	1456 (87.8%)	202 (12.2%)	.533
Macrocalcification	321 (88.2%)	43 (11.8%)	.950
Microcalcification	316 (89.3%)	38 (10.7%)	.459
Location (No.) (%)			
Upper/lower	1100 (87.6%)	156 (12.4%)	.417
Mid	993 (88.7%)	127 (11.3%)	

nodule size. All minor complications were successfully managed by manual compression. No needle-tract seeding occurred in association with CNB.

DISCUSSION

This present study validates the usefulness of CNB as a first-line option for assessing thyroid nodules, accruing a higher rate of conclusive results (88.1%) with low inconclusive (11.9%) and nondiagnostic (4.9%) rates compared with conventional FNA. The diagnostic accuracy of CNB was high (96.7%), with a PPV of 100% and no false-positive results. Moreover, the diagnostic performance of this study was consistent with that in previous studies (On-line Table 3).[15,17-19,24,25] The unnecessary surgery (0.6%) rate was also compatible with that in a previous study (0.5%).[19] There were low rates of minor complications (0.5%) without any major complication in the course of biopsy procedures. These findings indicate that CNB is a safe and reliable method and that repeated biopsies or unnecessary operations are likely to be avoided through this approach.

For small nodules (<10 mm), the diagnostic performance and the inconclusive or nondiagnostic rate showed no significant difference compared with nodules of >10 mm in this study. These findings are similar to the results reported in previous studies,[15,19] and they suggest that CNB is a reliable and effective method for evaluating small and large thyroid nodules.

US-guided FNA is safe, relatively accurate, and cost-effective, but inconclusive or false-negative results of FNA are problematic. The inconclusive results of up to 25%–30% (nondiagnostic, 5%–17%; AUS/FLUS readings, 3%–18%) and false-negative results (17%–21%) of FNA are the major drawback of this technique.[2,3,26-28] Recently, several studies have suggested that CNB is more useful than repeat FNA for nodules with prior nondiagnostic FNA results, especially if CNB and FNA are combined.[4,5,15,24] Some sources have also indicated that CNB could be more useful for management decisions than repeat FNA in nodules with prior AUS/FLUS.[4,29,30]

Several studies have reported factors associated with nondiagnostic FNA results. The following factors were associated with nondiagnostic results of FNA: errors during tissue sampling (experience or skill of the operator, processing errors); interpretation errors; and the nature of the lesions, including cyst dominancy, small size, type of calcification, vascularity, and benign pathology.[31-33] Performing repeat FNA for a nodule with a previously nondiagnostic FNA was significantly associated with a repeat nondiagnostic result.[34] Distinct from FNA, the size of nodules and the presence or type of calcification did not affect the nondiagnostic and inconclusive results of CNB. However, nodules with cystic components, which represented >50% of the nodules, showed significantly higher nondiagnostic CNB results. It is important to aspirate the internal fluid of any cystic lesion before the CNB procedure. The location of the nodule was associated with nondiagnostic results in our study. This association

might be caused by the level of the operator's skill or experience. Most of the CNB procedures were performed via a craniocaudal approach, which could restrict accurate targeting when obstructed by the clavicle or mandible. Although it has been previously reported that the operator's experience does not affect the conclusive results on CNB,[19] the operator's experience or skill might be a factor.

In our study, there were 8 false-negative cases (1.1%) with benign CNB results consistent with previous studies (0%–1%).[4,15,24,29] This rate remains superior to the false-negative results of FNA, reported up to 17%–21%.[35,36] A recent study reported that one-third of sonographically suspicious nodules with initially benign cytology were upgraded after CNB, and among them, about 32% were proved malignant.[37] False-negative FNA diagnoses may be explained by the nature of the lesions, intrinsic procedural limitations, levels of operator skill/experience,[38,39] and interpretation errors.[40] Unlike false-negative findings on FNA, the false-negative results of CNB in our study may reflect inaccurate targeting (6 nodules confirmed malignant at follow-up CNB or FNA, 1 nodule at the posterior margin of lower isthmus, and 1 nodule in a case of lymphocytic thyroiditis) due to procedural inexperience. An advantage of CNB is less operator dependency if the biopsy device successfully penetrates the nodule.[15] Our study suggested that the ability of accurate targeting of the nodule might be important to reduce false-negative and nondiagnostic results on CNB. Awareness and expertise in several approach methods (transisthmic, craniocaudal, and lateral approaches) might be necessary.[41]

According to the Bethesda system for reporting thyroid cytopathology, the category of AUS/FLUS is related to a FNA specimen that manifests as scenarios of nuclear atypia, architectural atypia, and an oncocytic pattern in paucicellular aspirates.[42] Although this category is regarded as having inconclusive results, nodules with AUS on FNA showed a significantly higher risk of malignancy than nodules with FLUS on FNA.[29] Repeat FNA has been recommended for this subcategory, but inconclusive results, including nondiagnostic and AUS/FLUS readings, occur in 20%–49.1% of nodules with prior AUS/FLUS FNA results.[4,6,27] Recently, several studies have shown that CNB is more useful than repeat FNA in cases with previous AUS/FLUS results.[4,29,30] Although it is possible to get larger tissue samples through CNB procedures, there was still a low rate of AUS/FLUS on CNB for thyroid nodules in this study. It might be caused by the variable heterogeneity of this group and the lack of standardized diagnostic CNB categorization. In our study, malignancy was diagnosed significantly higher in nodules with AUS on CNB (63.2%) than nodules with FLUS (13.8%). Further investigations are needed to manage AUS/FLUS on CNB.

Although CNB conducted by experienced radiologists is safe and well-tolerated, there are still safety concerns.[6,13,14,43] However, we encountered no major complications. To minimize the potential for complications and patient discomfort, technical provisions are in place, including strict color Doppler US monitoring and immediate compression of biopsy sites after CNB procedures. Compared with FNA, CNB may be technically unfeasible or difficult at times (typically in small nodules at the posterior thyroid margin).[15] Furthermore, CNB can be uncomfortable for the patient, requiring local anesthesia and greater experience in image-guided thyroid interventions.

Our study has several limitations. First, it was a retrospective study performed during a relatively long period. This feature may cause selection bias. This study involved multiple radiologists and pathologists performing US-guided CNB and histopathologic interpretation. Second, up to 50% of total enrolled cases do not have final results. This lack of results might be due to loss of follow-up or lack of final surgery in 1 (general hospital) of 2 participating hospitals. Finally, we did not apply the standardized diagnostic CNB categorization of a recent publication.[22]

CONCLUSIONS

We have demonstrated that the first-line use of CNB may improve the diagnostic accuracy in thyroid nodules, reducing nondiagnostic or inconclusive results. The high PPV and NPV of CNB for a diagnosis of malignancy could prevent repeat biopsy or unnecessary surgery. Such benefits underscore the promising role of CNB in managing thyroid nodules and optimizing related surgical decision-making.

REFERENCES

1. Gharib H, Papini E, Paschke R, et al. **American Association of Clinical Endocrinologists, Associazione Medici Endocrinologi, and European Thyroid Association medical guidelines for clinical practice for the diagnosis and management of thyroid nodules.** *J Endocrinol Invest* 2010;33(5 suppl):51–56 CrossRef Medline
2. Cooper DS, Doherty GM, Haugen BR, et al; American Thyroid Association (ATA) Guidelines Taskforce on Thyroid Nodules and Differentiated Thyroid Cancer. **Revised American Thyroid Association management guidelines for patients with thyroid nodules and differentiated thyroid cancer.** *Thyroid* 2009;19:1167–214 CrossRef Medline
3. Baloch ZW, Cibas ES, Clark DP, et al. **The National Cancer Institute thyroid fine needle aspiration state of the science conference: a summation.** *Cytojournal* 2008;5:6 CrossRef Medline
4. Na DG, Kim JH, Sung JY, et al. **Core-needle biopsy is more useful than repeat fine-needle aspiration in thyroid nodules read as nondiagnostic or atypia of undetermined significance by the Bethesda system for reporting thyroid cytopathology.** *Thyroid* 2012;22:468–75 CrossRef Medline
5. Samir AE, Vij A, Seale MK, et al. **Ultrasound-guided percutaneous thyroid nodule core biopsy: clinical utility in patients with prior nondiagnostic fine-needle aspirate.** *Thyroid* 2012;22:461–67 CrossRef Medline
6. Park KT, Ahn SH, Mo JH, et al. **Role of core needle biopsy and ultrasonographic finding in management of indeterminate thyroid nodules.** *Head Neck* 2011;33:160–65 CrossRef Medline
7. Hryhorczuk AL, Stephens T, Bude RO, et al. **Prevalence of malignancy in thyroid nodules with an initial nondiagnostic result after ultrasound-guided fine needle aspiration.** *Ultrasound Med Biol* 2012;38:561–67 CrossRef Medline
8. Lubitz CC, Nagarkatti SS, Faquin WC, et al. **Diagnostic yield of nondiagnostic thyroid nodules is not altered by timing of repeat biopsy.** *Thyroid* 2012;22:590–94 CrossRef Medline
9. Jo VY, Vanderlaan PA, Marqusee E, et al. **Repeatedly nondiagnostic thyroid fine-needle aspirations do not modify malignancy risk.** *Acta Cytol* 2011;55:539–43 CrossRef Medline
10. Bartolazzi A, Orlandi F, Saggiorato E, et al. **Galectin-3-expression analysis in the surgical selection of follicular thyroid nodules with indeterminate fine-needle aspiration cytology: a prospective multicentre study.** *Lancet Oncol* 2008;9:543–49 CrossRef Medline
11. Mathur A, Weng J, Moses W, et al. **A prospective study evaluating**

the accuracy of using combined clinical factors and candidate diagnostic markers to refine the accuracy of thyroid fine-needle aspiration biopsy. *Surgery* 2010;148:1170–77 CrossRef Medline
12. Cibas ES, Ali SZ; NCI Thyroid FNA. **The Bethesda system for reporting thyroid cytopathology.** *Am J Clin Pathol* 2009;132:658–65 CrossRef Medline
13. Renshaw AA, Pinnar N. **Comparison of thyroid fine-needle aspiration and core needle biopsy.** *Am J Clin Pathol* 2007;128:370–74 CrossRef Medline
14. Screaton NJ, Berman LH, Grant JW. **US-guided core-needle biopsy of the thyroid gland.** *Radiology* 2003;226:827–32 CrossRef Medline
15. Sung JY, Na DG, Kim KS, et al. **Diagnostic accuracy of fine-needle aspiration versus core-needle biopsy for the diagnosis of thyroid malignancy in a clinical cohort.** *Eur Radiol* 2012;22:1564–72 CrossRef Medline
16. Nasrollah N, Trimboli P, Guidobaldi L, et al. **Thin core biopsy should help to discriminate thyroid nodules cytologically classified as indeterminate: a new sampling technique.** *Endocrine* 2013;43:659–65 CrossRef Medline
17. Trimboli P, Nasrollah N, Guidobaldi L, et al. **The use of core needle biopsy as first-line in diagnosis of thyroid nodules reduces false negative and inconclusive data reported by fine-needle aspiration.** *World J Surg Oncol* 2014;12:61 CrossRef Medline
18. Paja M, del Cura JL, Zabala R, et al. **Ultrasound-guided core-needle biopsy in thyroid nodules: a study of 676 consecutive cases with surgical correlation.** *Eur Radiol* 2016;26:1–8 CrossRef Medline
19. Suh CH, Baek JH, Lee JH, et al. **The role of core-needle biopsy as a first-line diagnostic tool for initially detected thyroid nodules.** *Thyroid* 2016;26:395–403 CrossRef Medline
20. Kwak JY, Jung I, Baek JH, et al; Korean Society of Thyroid Radiology (KSThR), Korean Society of Radiology. **Image reporting and characterization system for ultrasound features of thyroid nodules: multicentric Korean retrospective study.** *Korean J Radiol* 2013;14:110–17 CrossRef Medline
21. Moon W, Baek JH, Jung SL, et al; Korean Society of Thyroid Radiology (KSThR), Korean Society of Radiology. **Ultrasonography and the ultrasound-based management of thyroid nodules: consensus statement and recommendations.** *Korean J Radiol* 2011;12:1–14 CrossRef Medline
22. Jung CK, Min HS, Park HJ, et al; Korean Endocrine Pathology Thyroid Core Needle Biopsy Study Group. **Pathology reporting of thyroid core needle biopsy: a proposal of the Korean Endocrine Pathology Thyroid Core Needle Biopsy Study Group.** *J Pathol Transl Med* 2015;49:288–99 CrossRef Medline
23. Burke DR, Lewis CA, Cardella JF, et al; Society of Interventional Radiology Standards of Practice Committee. **Quality improvement guidelines for percutaneous transhepatic cholangiography and biliary drainage.** *J Vasc Interv Radiol* 2003;14:S243–46 Medline
24. Yeon JS, Baek JH, Lim HK, et al. **Thyroid nodules with initially nondiagnostic cytologic results: the role of core-needle biopsy.** *Radiology* 2013;268:274–80 CrossRef Medline
25. Ha EJ, Baek JH, Lee JH, et al. **Core needle biopsy can minimise the non-diagnostic results and need for diagnostic surgery in patients with calcified thyroid nodules.** *Eur Radiol* 2014;24:1403–09 CrossRef Medline
26. Nayar R, Ivanovic M. **The indeterminate thyroid fine-needle aspiration: experience from an academic center using terminology similar to that proposed in the 2007 National Cancer Institute Thyroid Fine Needle Aspiration State of the Science Conference.** *Cancer* 2009;117:195–202 CrossRef Medline
27. Yassa L, Cibas ES, Benson CB, et al. **Long-term assessment of a multidisciplinary approach to thyroid nodule diagnostic evaluation.** *Cancer Cytopathol* 2007;111:508–16 CrossRef
28. Yang J, Schnadig V, Logrono R, et al. **Fine-needle aspiration of thyroid nodules: a study of 4703 patients with histologic and clinical correlations.** *Cancer Cytopathol* 2007;111:306–15 CrossRef
29. Choi YJ, Baek JH, Ha EJ, et al. **Differences in risk of malignancy and management recommendations in subcategories of thyroid nodules with atypia of undetermined significance or follicular lesion of undetermined significance: the role of ultrasound-guided core-needle biopsy.** *Thyroid* 2014;24:494–501 CrossRef Medline
30. Na DG, Min HS, Lee H, et al. **Role of core needle biopsy in the management of atypia/follicular lesion of undetermined significance thyroid nodules: comparison with repeat fine-needle aspiration in subcategory nodules.** *Eur Thyroid J* 2015;4:189–96 CrossRef Medline
31. Degirmenci B, Haktanir A, Albayrak R, et al. **Sonographically guided fine-needle biopsy of thyroid nodules: the effects of nodule characteristics, sampling technique, and needle size on the adequacy of cytological material.** *Clin Radiol* 2007;62:798–803 CrossRef Medline
32. Choi SH, Han KH, Yoon JH, et al. **Factors affecting inadequate sampling of ultrasound-guided fine-needle aspiration biopsy of thyroid nodules.** *Clin Endocrinol (Oxf)* 2011;74:776–82 CrossRef
33. Moon HJ, Kwak JY, Kim EK, et al. **Ultrasonographic characteristics predictive of nondiagnostic results for fine-needle aspiration biopsies of thyroid nodules.** *Ultrasound Med Biol* 2011;37:549–55 CrossRef Medline
34. Choi SH, Baek JH, Lee JH, et al. **Thyroid nodules with initially nondiagnostic, fine-needle aspiration results: comparison of core-needle biopsy and repeated fine-needle aspiration.** *Eur Radiol* 2014;24:2819–26 CrossRef Medline
35. Raab SS, Vrbin CM, Grzybicki DM, et al. **Errors in thyroid gland fine-needle aspiration.** *Am J Clin Pathol* 2006;125:873–82 CrossRef Medline
36. Yeh MW, Demircan O, Ituarte P, et al. **False-negative fine-needle aspiration cytology results delay treatment and adversely affect outcome in patients with thyroid carcinoma.** *Thyroid* 2004;14:207–15 CrossRef Medline
37. Ha EJ, Baek JH, Lee JH, et al. **Sonographically suspicious thyroid nodules with initially benign cytologic results: the role of a core needle biopsy.** *Thyroid* 2013;23:703–08 CrossRef Medline
38. Ylagan LR, Farkas T, Dehner LP. **Fine needle aspiration of the thyroid: a cytohistologic correlation and study of discrepant cases.** *Thyroid* 2004;14:35–41 CrossRef Medline
39. Wu HH, Jones JN, Osman J. **Fine-needle aspiration cytology of the thyroid: ten years experience in a community teaching hospital.** *Diagn Cytopathol* 2006;34:93–96 CrossRef Medline
40. Baloch ZW, Sack MJ, Yu GH, et al. **Fine-needle aspiration of thyroid: an institutional experience.** *Thyroid* 1998;8:565–69 CrossRef Medline
41. Baek JH, Lee JH, Valcavi R, et al. **Thermal ablation for benign thyroid nodules: radiofrequency and laser.** *Korean J Radiol* 2011;12:525–40 CrossRef Medline
42. Bongiovanni M, Krane JF, Cibas ES, et al. **The atypical thyroid fine-needle aspiration: past, present, and future.** *Cancer Cytopathol* 2012;120:73–86 CrossRef Medline
43. Harvey JN, Parker D, De P, et al. **Sonographically guided core biopsy in the assessment of thyroid nodules.** *J Clin Ultrasound* 2005;33:57–62 CrossRef Medline

CT Accuracy of Extrinsic Tongue Muscle Invasion in Oral Cavity Cancer

J.C. Junn, K.L. Baugnon, E.A. Lacayo, P.A. Hudgins, M.R. Patel, K.R. Magliocca, A.S. Corey, M. El-Deiry, J.T. Wadsworth, J.J. Beitler, N.F. Saba, Y. Liu, and A.H. Aiken

ABSTRACT

BACKGROUND AND PURPOSE: Extrinsic tongue muscle invasion in oral cavity cancer upstages the primary tumor to a T4a. Despite this American Joint Committee on Cancer staging criterion, no studies have investigated the accuracy or prognostic importance of radiologic extrinsic tongue muscle invasion, the feasibility of standardizing extrinsic tongue muscle invasion reporting, or the degree of agreement across different disciplines: radiology, surgery, and pathology. The purpose of this study was to assess the agreement among radiology, surgery, and pathology for extrinsic tongue muscle invasion and to determine the imaging features most predictive of extrinsic tongue muscle invasion with surgical/pathologic confirmation.

MATERIALS AND METHODS: Thirty-three patients with untreated primary oral cavity cancer were included. Two head and neck radiologists, 3 otolaryngologists, and 1 pathologist prospectively evaluated extrinsic tongue muscle invasion.

RESULTS: Fourteen of 33 patients had radiologic extrinsic tongue muscle invasion; however, only 8 extrinsic tongue muscle invasions were confirmed intraoperatively. Pathologists were unable to determine extrinsic tongue muscle invasion in post-formalin-fixed samples. Radiologic extrinsic tongue muscle invasion had 100% sensitivity, 76% specificity, 57% positive predictive value, and 100% negative predictive value with concurrent surgical-pathologic evaluation of extrinsic tongue muscle invasion as the criterion standard. On further evaluation, the imaging characteristic most consistent with surgical-pathologic evaluation positive for extrinsic tongue muscle invasion was masslike enhancement.

CONCLUSIONS: Evaluation of extrinsic tongue muscle invasion is a subjective finding for all 3 disciplines. For radiology, masslike enhancement of extrinsic tongue muscle invasion most consistently corresponded to concurrent surgery/pathology evaluation positive for extrinsic tongue muscle invasion. Intraoperative surgical and pathologic evaluation should be encouraged to verify radiologic extrinsic tongue muscle invasion to minimize unnecessary upstaging. Because this process is not routine, imaging can add value by identifying those cases most suspicious for extrinsic tongue muscle invasion, thereby prompting this more detailed evaluation by surgeons and pathologists.

ABBREVIATIONS: AJCC = American Joint Committee on Cancer; CECT = contrast-enhanced CT; ETM = extrinsic tongue muscle; ETMI = extrinsic tongue muscle invasion; FOM = floor of the mouth; OCC = oral cavity cancer; SCC = squamous cell carcinoma

Oral cavity cancer accounts for nearly 30% of all head and neck malignancies. The diagnosis is often made at a more advanced stage, resulting in low 5-year survival rates: 50%–60% overall and as low as 22% for advanced-stage disease.[1,2] Preoperative imaging provides the basis for staging and surgical planning for advanced oral cavity cancer (OCC). While the T1–T3 classification is based on tumor size, the T4 classification is based on identification of locally advanced disease with invasion of surrounding structures.

In the seventh edition of the American Joint Committee on Cancer (AJCC) staging, extrinsic tongue muscle invasion (ETMI) or bone involvement upstages the primary tumor to a T4a classification.[3] Although all extrinsic tongue muscles (genioglossus, hyoglossus, palatoglossus, and styloglossus) are currently included in the AJCC staging system, only genioglossus and hyoglossus muscles are easily and routinely identified on cross-sectional imaging. The definitive determination of ETMI is often more difficult than bone invasion, but its presence also upstages

Received June 21, 2016; accepted after revision August 30.

From the Departments of Imaging Sciences (J.C.J., K.L.B., P.A.H., A.S.C., A.H.A.), Otolaryngology (M.R.P., M.E.-D., J.T.W.), Pathology (K.R.M.), Radiation Oncology (J.J.B.), Hematology Oncology (N.F.S.), and Statistics (Y.L.), Emory University School of Medicine, Atlanta, Georgia; and Department of Radiology (E.A.L.), Georgetown University, Washington, DC.

Paper previously presented at: Annual Meeting of the Radiological Society of North America, November 29 to December, 2015; Chicago, Illinois.

Please address correspondence to Ashley H. Aiken, MD, 1364 Clifton Rd, Atlanta, GA 30322; e-mail: Ashley.aiken@emoryhealthcare.org

http://dx.doi.org/10.3174/ajnr.A4993

to T4a. ETMI and upstaging a tumor may not only necessitate adjuvant radiation therapy but may also change the eligibility for enrollment in certain therapy clinical trials.

The current American College of Radiology guidelines advocate postoperative radiation therapy "in patients with higher-risk features for locoregional recurrence after surgery. These include advanced T stage (T3/T4), the presence of lymphovascular invasion, the presence of perineural invasion, positive surgical margins, lymph node involvement, extracapsular nodal extension, and bone involvement."[4] For instance, postoperative radiation therapy would not be indicated for a patient with a T2N0 tumor with negative margins at surgery, no perineural invasion, or other high-risk factors. However, a size-matched OCC with similar characteristics staged T4a due to ETMI would require adjuvant radiation treatment or could influence the enrollment in current clinical trials that examine the role of adding systemic agents to radiation.

In current practice, head and neck radiologists evaluate invasion of at least the genioglossus muscle and, in many cases, the hyoglossus muscle.[5-7] The styloglossus and palatoglossus muscles are more difficult to evaluate on imaging, though deep extension to involve the anterior tonsillar pillar would imply palatoglossus muscle invasion. Contrast-enhanced CT (CECT), MR imaging, and ultrasound can be used in OCC staging.[8,9] MR imaging is usually reserved for questions of perineural tumor or when extensive dental artifacts obscure oral cavity anatomy on CECT. While some authors favor MR imaging for T staging because of its soft-tissue resolution, recent studies have demonstrated the accuracy of CECT in the oral cavity.[10-15] Proponents of CECT prefer this technique because of its accuracy in staging the primary tumor of the head and neck and its ability to combine with PET imaging for additional metabolic information regarding regional and distant metastases.

One of the shortcomings in evaluating the accuracy of radiologic ETMI is that there is no definite surgical or pathologic criterion standard to confirm invasion. Intraoperative evaluation and documentation of ETMI remains inconsistent without a set of guidelines. ETMI has not been consistently recorded within pathology reports at our institution; this inconsistency has created opportunities for inaccurate final pathologic staging and/or dependence on the radiologic stage. Currently, clinical and prognostic implications of ETMI in OCC remain elusive.[16] Since the introduction of ETMI as a determinant for T4a disease in 1998 (3rd edition of the AJCC *Manual for Staging of Cancer*), no prospective radiologic-surgical-pathologic correlative studies have been performed to confirm the accuracy or prognostic importance of radiologic identification of ETMI. Boland et al[17] questioned the prognostic implications and rationale behind automatic upstaging when only superficial extrinsic tongue muscles such as the hyoglossus and styloglossus are involved. Despite the lack of literature supporting the prognostic value and accuracy of radiologic ETMI, current practice often relies on radiologic staging for ETMI.

Although radiologic staging and determination of ETMI does not affect surgical eligibility, it can affect the postoperative treatment course, specifically the radiation treatment plan and eligibility for certain clinical trials. Because surgeons and pathologists do not routinely assess or report ETMI, the radiologic staging can "unofficially" persist despite the lack of data on CT accuracy. Therefore, our study investigates the feasibility of routine evaluation and reporting of ETMI across all 3 disciplines, in addition to the degree of agreement among radiology, surgery, and pathology to determine the accuracy of CECT for determining ETMI in cases of OCC.

MATERIALS AND METHODS

Inclusion Criteria

This institutional review board–approved prospective study accrued patients during a 12-month period. Before the initiation of this study, members of head and neck radiology, head and neck surgery, and head and neck subspecialty–designated pathology faculty agreed on consistent reporting of ETMI in radiology, operative, and pathology reports, respectively. After 1 year of prospectively recording ETMI, we searched the institutional radiology data base for untreated primary OCCs with preoperative CECT available for review and surgical resection at our institution. This search yielded 50 patients.

The inclusion criteria were the following:

1) Untreated OCC, accrued during the 12-month period
2) Preoperative CECT available for review
3) Surgical resection at our institution with operative and pathologic ETMI documentation.

Patients who did not undergo an operation at our institution and those who did not have intraoperative ETMI documentation were excluded from the study. Thirty-three patients met the inclusion criteria.

Imaging Methods

Patients underwent CECT on 1 of several commercially available CT systems with multidetector capability ranging from 16 to 64 channels. Onsite imaging CT studies were performed on LightSpeed VCT 64-section, Discovery HD 750, Discovery 16-section, and BrightSpeed 16-section scanners (GE Healthcare, Milwaukee, Wisconsin) or 16- to 64-channel scanners (Somatom Definition, Somatom Definition Flash; Siemens, Erlangen, Germany). Our split-bolus technique used 110 mL of intravenous iopamidol (Isovue-370; Bracco, Princeton, New Jersey), with 55 mL injected first at a rate of 2.5 mL/s, followed by a 40-second delay, then another 55 mL at the same rate, with a total scan delay of 90 seconds, including a pre- and postcontrast saline bolus. We acquired contiguous axial images from the skull base through the mediastinum with the following settings: 1.25-mm section thickness; pitch, 0.984:1; 0.7-second gantry rotation time; 25-cm FOV; 120 kV(peak); and automatic exposure control with a noise index of 13.78. Reformatted images at 2.5-mm section thickness in the axial planes and 3-mm sagittal and coronal reformations were sent to the PACS.

Image Review

Members of all 3 disciplines used a 4-point "Likert-type" scale to record an assessment of ETMI: "no" (definitely no ETMI), "probably no," "probably yes," and "yes" (definite ETMI). For radiology, 2 dedicated head and neck radiologists with Certificates of Added Qualification (10 years and 9 years of experience, respectively) blindly and independently reviewed these images. Discrepant cases were resolved by a consensus read. For each case, they recorded their overall impression regarding the presence of ETMI

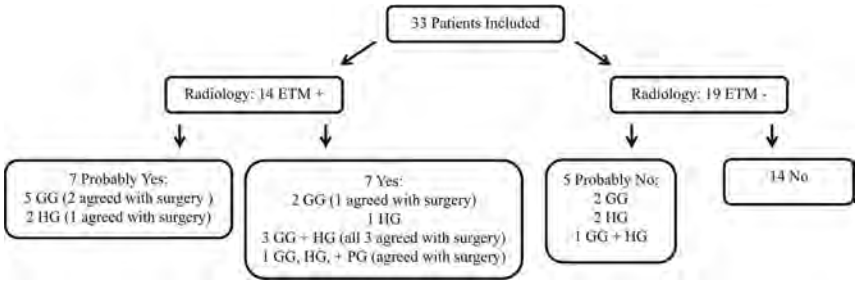

FIG 1. Schematic illustration of radiologic ETMI. Of the 33 included patients, 14 patients have radiologic ETMI. Of the 14 radiologic ETMI cases, 3 of 7 "probably yes" cases were concordant with surgery and 5 of 7 "yes" cases were concordant with surgery. GG indicates genioglossus; HG, hyoglossus; PG, palatoglossus.

Table 1: Radiologic and surgical assessment of ETMI[a]

Parameters	Radiologist 1	Radiologist 2	Surgery
Yes	6	7	7
Probably yes	7	7	1
Probably no	6	4	1
No	14	15	24

[a] Individual ETMI responses by each radiologist and collective responses by head and neck surgeons.

but also evaluated each individual muscle: genioglossus, hyoglossus, styloglossus, and palatoglossus.

After the initial review, there were 5 imaging patterns: no contact, narrow contact, broad contact, linear enhancement within the muscle, and masslike enhancement within the muscle. "Narrow contact" was defined as <50% of tumor contacting the extrinsic tongue muscle (ETM), and "broad contact" was defined as >50% of the tumor contacting the ETM. After establishing these imaging features, the radiologists re-evaluated the cases and put each case into 1 of the 5 categories.

Surgery Review

One of 3 head and neck surgeons was always present during each operation, and an otolaryngology resident was routinely present to accurately record surgical ETMI prospectively. Before and during resection, the operating head and neck surgeon palpated the tumor en bloc for muscle tension anywhere between the proximal and distal insertion site to subjectively evaluate muscle invasion. Three of the muscles (genioglossus, styloglossus, and hyoglossus) originate from bone attachments, while the palatoglossus originates from the buccopharyngeal fascia. On completion of the resection, the operating surgeon carefully oriented the en bloc fresh specimen and evaluated the frozen section specimen in consultation with the pathologist performing gross examination. Any consensus evaluation during this intraoperative consultation was recorded under "surgery" for the purposes of this study.

Pathology Review

On completion of the intraoperative evaluation, the residual specimen was completely immersed in 10% buffered formalin. The formal pathology gross examination of the surgical specimen occurred on a formalin-fixed specimen within 1–2 days of receiving the specimen. During examination of the formalin-fixed specimen, a single head and neck pathology faculty member evaluated ETMI by macroscopic examination in cases lacking the interdisciplinary intraoperative notation of ETMI. The same pathologist retrospectively reviewed all finalized pathology reports and the corresponding hematoxylin-eosin–stained slides to ensure pathologic staging accuracy.

For statistical purposes, "probably yes" cases were included as "yes" and "probably no" cases were included as "no." Statistical analysis included calculation of the frequency of findings and the sensitivity, specificity, positive predictive value, and negative predictive value of radiologic assessment of ETMI by using surgery as the criterion standard. κ statistics were used to assess interobserver reliability of radiologic ETMI determination.

RESULTS

This study recruited 50 consecutive patients with primary OCC during a 12-month period. Thirty-three patients met the inclusion criteria, with 9 women (27%) and 24 men (73%). Patient ages ranged from 31 to 88 years. Most of the subsites were the floor of the mouth (FOM) and oral tongue ($n = 29$), with only 5 cases from the alveolar ridge or buccal mucosa. The time from imaging to surgery ranged from 4 to 112 days, with an average imaging-to-surgery time lapse of 36.3 days.

Of the 33 cases, 14 had radiologic findings of ETMI (7 yes and 7 probably yes). The 14 no and 5 probably no cases were all concordant with surgical findings.

Of the 7 yes cases, 2/7 involved the genioglossus; 1/7, the hyoglossus; 3/7, the genioglossus and hyoglossus; and 1/7 the genioglossus, hyoglossus, and palatoglossus muscles. Of the 7 probably yes cases, there were 5 genioglossus and 2 hyoglossus involvements (Fig 1).

There were 8 surgical/gross pathologic ETMI cases during the routine intraoperative consultation for margin analysis (7 yes cases and 1 probably yes). Of the 7 radiologic yes cases, 5 agreed with surgery, and of the 7 radiologic probably yes cases, 3 were concordant with surgery (Fig 1). Due to tissue distortion and lack of orientation, it was not possible to evaluate ETMI in the delayed, post-formalin-fixed specimen in the postoperative setting.

The results of individual radiologist and surgical/gross pathologic determination of ETMI are represented in Table 1. These findings underscore the degree of uncertainty by radiologists when evaluating ETMI, as 40% of radiologist 1 and 33% of radiologist 2 findings fell under either the probably yes or probably no category. Despite the number of questionable cases, there was high interobserver agreement between the 2 radiologists: 0.937. When cases with the original radiologic ETMI assessment were compared with surgical ETMI as the criterion standard, radiologic findings were 100% sensitive but specificity was only 76%. The positive predictive value was 57.1%, whereas the negative predictive value was 100%. If surgery/pathology intraoperative evaluation was assumed to be the criterion standard, our study suggests that radiologic ETMI results in too many false-positives, especially if this finding leads to additional treatment and is not confirmed at the time of the operation.

Subsequently, the radiologists re-reviewed, without knowledge of surgical or pathologic findings with respect to ETMI, all

Table 2: Detailed review of specific imaging features[a]

Initial Radiologic Assessment	Radiologic Features on Reassessment	Surgical Finding
7 Probably yes		
GG[b]	Masslike enhancement	GG
GG[b]	Broad contact (some borders not visualized due to amalgam)	ETMI without specification
GG	Narrow contact	None
GG	Narrow contact	None
GG	Narrow contact	None
HG	Linear enhancement	None
HG[b]	Linear enhancement, also not definitive intraoperatively	HG (probably yes)
7 Yes		
GG[b]	Masslike enhancement	GG HG
GG	Broad contact	None
HG	Narrow contact	None
GG HG[b]	Masslike enhancement	GG HG
GG HG[b]	Masslike enhancement	GG HG
GG HG[b]	Masslike enhancement	GG HG
GG HG PG[b]	Masslike enhancement	GG HG PG
5 Probably no		
GG[b]	Narrow contact	None
GG[b]	Broad contact (partially obscured by amalgam)	None
HG[b]	Linear enhancement	None
HG[b]	Linear enhancement	None
GG HG[b]	Narrow contact	None

Note:—GG indicates genioglossus; HG, hyoglossus; PG, palatoglossus.
[a] Detailed list of the imaging features in the 19 cases with initial "probably yes," "yes," and "probably no" classifications.
[b] Agree with operational findings.

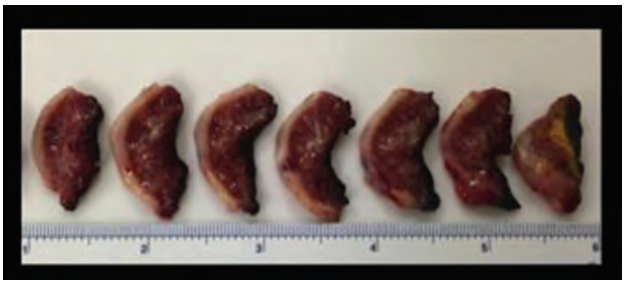

FIG 2. Partial glossectomy specimen entirely sectioned. Once formalin-fixed, ETMI or subtle tongue muscle anatomy are nearly impossible to precisely identify.

cases to determine radiologic features most predictive of ETMI to establish whether more specific imaging features could improve accuracy. For all cases scored "no" for ETMI, the tumor had no contact with any extrinsic tongue muscle. For cases scored probably no, probably yes, or yes, there were 4 imaging patterns: masslike enhancement, linear enhancement, broad contact, or narrow contact (Table 2). Masslike enhancement was the only imaging feature that accurately predicted surgical/gross pathologic ETMI (100% specificity, 75% sensitivity, 100% positive predictive value, and 93% negative predictive value). Narrow contact alone never predicted (100% negative predictive value) surgical/gross pathologic ETMI. Broad contact and linear enhancement were less reliable with 33% and 25% positive predictive values, respectively.

DISCUSSION

As we continue to advance the role of imaging in the staging of head and neck cancer, it is important to review and understand the implications and accuracy in a multidisciplinary setting. On our multidisciplinary tumor board, the oncologists and radiation oncologists often request that head and neck radiologists prospectively determine ETMI on imaging, regardless of pathologic and surgical confirmation. After discussing ETMI as a group, we learned that not only are pathologists not trained to routinely look for ETMI but it is also not possible to accurately determine ETMI retrospectively on a formalin-fixed specimen. Furthermore, surgeons also did not routinely record ETMI. Representatives from radiology, surgery, and pathology decided to prospectively look closely for ETMI for this study.

Multidisciplinary ETMI Evaluation

This prospective study proposes a more standardized approach for multidisciplinary evaluation and documentation of ETMI. Our findings highlight the importance of a true multidisciplinary team to coordinate the effort of radiologists, surgeons, and pathologists. We have initiated a sequence of events for the most accurate and optimal OCC staging based on ETMI. First, the radiologist evaluates and documents ETMI on the preoperative imaging examination. Then the surgeon performs a primary resection in most cases. At the time of the operation, the surgeon subjectively evaluates ETMI by palpating the tumor and observing tension on the muscle insertions. After the en bloc resection, the specimen is simultaneously evaluated in the frozen section suite by the surgeon and the pathology team. The suspicion or presence of ETMI or both are documented on the fresh specimen, before formalin fixation.

We have found that collaborative intraoperative evaluation by the surgeons and pathologists is the best opportunity to identify ETMI. The ETMs are identified when the specimen is fresh; then, serial cuts are made through the tumor to evaluate specific muscle invasion grossly, which is subsequently confirmed by microscopic examination. On completion of the intraoperative pathology evaluation, fresh resection specimens immersed in formalin will then be macrodissected to capture key relationships between tumor and resected normal anatomic structures and to evaluate any remaining surgical margins. Microscopic examination of these selected sections provides the basis of the final pathology report. However, retrospective determination of ETMI after formalin fixation alone is challenging or, in most cases, impossible due to tissue fixation/distortion, muscle retraction, and inability to identify a small portion of the ETM on a completely sectioned specimen (Fig 2).

ETMI Imaging Features

When we reassessed all of the probably yes, yes, and probably no cases, we discovered 4 different imaging patterns: masslike enhancement, narrow contact, broad contact, and linear enhance-

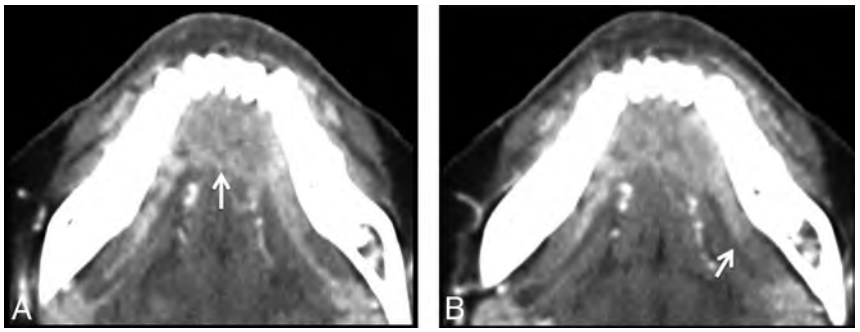

FIG 3. A 70-year-old woman with anterior FOM squamous cell carcinoma (SCC), pT4aN0M0. Concordant: Radiology and surgery positive for ETMI (genioglossus). *A*, Anterior floor of the mouth tumor with masslike invasion into the genioglossus muscle at its insertion site (*arrow*). *B*, Dilated left submandibular duct lateral to the hyoglossus muscle (*arrow*).

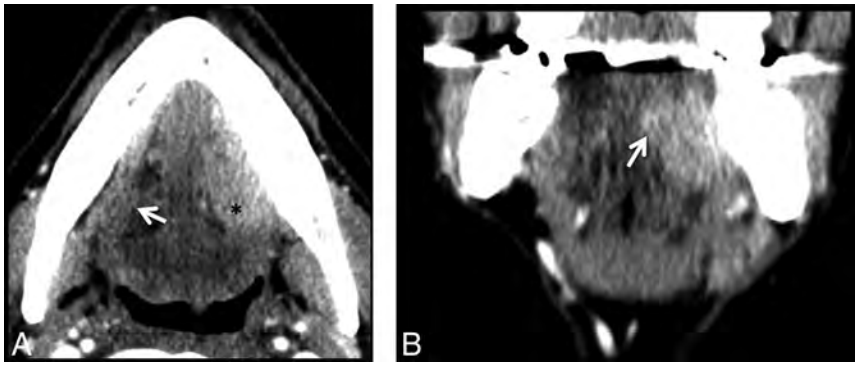

FIG 4. A 53-year-old man with left FOM SCC, pT4aN2cM0. Concordant: Radiology and surgery positive for ETMI (genioglossus and hyoglossus muscles). *A*, Axial image shows broad contact along the genioglossus muscle with obliteration and masslike enhancement in the expected location of the hyoglossus muscle (*asterisk*). Note the uninvolved hyoglossus muscle on the contralateral side (*arrow*). *B*, Coronal image shows complete replacement of the hyoglossus muscle with tumor and masslike invasion into the genioglossus muscle (*arrow*).

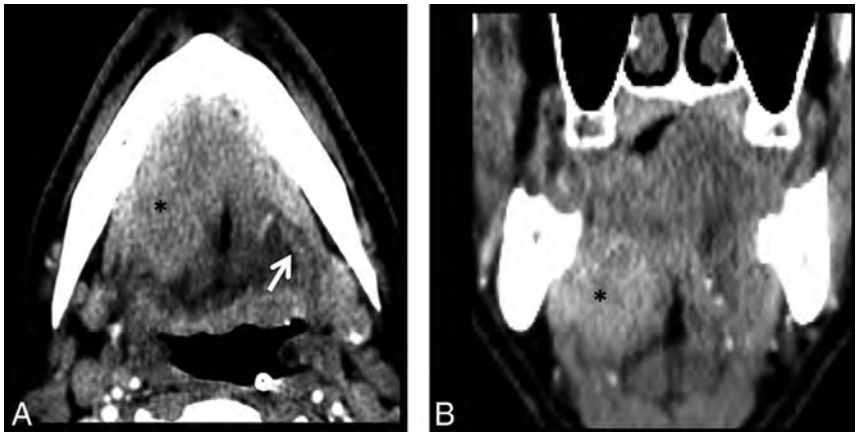

FIG 5. A 56-year-old man with right FOM SCC, pT4aN2bM0. Concordant: Radiology and surgery positive for ETMI (genioglossus and hyoglossus muscles). *A*, Axial image shows masslike enhancement involving the entire genioglossus and hyoglossus muscles (*asterisk*). A normal hyoglossus muscle is seen on the contralateral side *(arrow*). *B*, The coronal image confirms masslike tumor enhancement involving the genioglossus and hyoglossus muscles (*asterisk*).

ment. All 6 patients with masslike enhancement also had ETMI on surgical/pathologic intraoperative evaluation. None of the 6 patients with narrow contact had surgical/pathologic ETMI. Only 1 of 3 patients with radiologic broad contact had surgical/gross pathologic ETMI. Similarly, only 1 of 4 patients with linear enhancement had surgical/pathologic ETMI.

Therefore, masslike enhancement indistinguishable from the ETM is the most specific finding that leads to an agreement among radiology, surgery, and gross pathology (Figs 3–5). Linear enhancement (Fig 6) and broad contact are less reliable imaging signs with variable intraoperative findings. On the basis of our results, narrow contact (Figs 7 and 8) does not predict surgical/pathologic ETMI and should not be used to determine ETMI. Of the 6 radiologic ETMI cases without surgical ETMI, 1 patient had linear enhancement, 4 patients had anterior floor of the mouth tumor near the genioglossus genial tubercle insertion site with only narrow contact, and 1 patient had a large oral tumor mass above the genioglossus muscle with broad contact.

Limitations in Other Disciplines

Surgical evaluation is imprecise for determining ETMI. Intraoperative assessment by surgical palpation alone is a subjective evaluation and, in our experience, is not consistently documented in the operative report. Additionally, there is often not a definitive answer regarding invasion of the small, thin hyoglossus muscle because it may not be readily visible to the surgeons intraoperatively. In turn, hyoglossus invasion is not discernible by the pathologist. Therefore, to optimize evaluation of ETM, a careful and deliberate "consensus" examination and analysis of the fresh resection specimen by the surgeon and pathology team at the time of intraoperative consultation, and before formalin fixation, appear to result in the highest level of confidence among the surgeons and pathologists and should be the criterion standard.

Although documentation of pathologic ETMI is important,[18] a review of the current pathology dissection texts and literature reveals no systematic approach to ETMI determination in the fresh or formalin-fixed state.[19,20] While this study highlights a mechanism to facilitate identification of ETMI, particularly in collaboration with surgical colleagues, variations in intraoperative and interdisciplinary work flow and resources may preclude replication at some institutions. In cases in which portions of the oral tongue are resected from their bony attachments, the surrounding anatomic context and relationships can be difficult to discern in a formalin-fixed specimen because they may have been multiply-sectioned or key por-

tions of the specimen may have been removed for frozen section analysis intraoperatively. We believe this scenario represents a hurdle in providing microscopic confirmation of ETMI. Other obstacles to pathologic confirmation of ETMI include the following: the relatively nonspecific microscopic appearance of intrinsic tongue skeletal muscle in comparison with extrinsic tongue muscle, the procedures performed to evaluate tumor margin status intraoperatively, piecemeal submission of subsequent portions of tissue/margins (which may or may not include ETM), distortion induced by formalin fixation, the range of expertise or familiarity of the person performing gross examination with an oral resection specimen, and the appreciation of the importance of ETMI by the pathologist performing gross examination. Furthermore, it seems impossible to expect pathologic confirmation of hyoglossus invasion once the muscle is detached from insertions because it is too small for routine identification.

All specialties need to be aware, therefore, that hyoglossus muscle invasion appears, on the basis of our results, to be an observation that might be best made on cross-sectional imaging when there is masslike enhancement in the muscle.

Importance of Multidisciplinary ETMI Confirmation

Upstaging a tumor from T1 or T2 to T4a based on ETMI may have treatment implications and/or may impact eligibility for therapy trials. Currently, postoperative radiation therapy is indicated in patients with higher risk features for locoregional recurrence postoperatively: advanced T stage (T3/4), lymphovascular invasion, perineural invasion, positive surgical margins, lymph node involvement, nodal extracapsular spread, and bone invasion.[4] In addition, the radiation fields themselves may be influenced by the determination of ETMI, because the coverage at our institution is extended caudally to include the hyoid bone. Because the surgeon and pathologist closely collaborating and orienting the specimen is not routine practice and may not be feasible in all settings, radiology can best add value by identifying those cases most suspicious for ETMI, thereby prompting more careful evaluation by the surgeons and pathologists. Furthermore, now that we have established imaging features that are more predictive of ETMI, it will be important to look at patient outcomes to determine whether radiologic ETMI is indeed prognostic. It is crucial to determine whether invasion of certain ETMs is more important than invasion of others (eg, deeper genioglossus versus more superficial hyoglossus muscle). If radiologic ETMI is prognostic and a routine consensus read between surgeons and pathologists is not practical, then imaging can serve as a biomarker for more aggressive disease.

These preliminary radiologic data combined with surgical and pathologic limitations suggest that the AJCC staging of OCC based on ETMI should be carefully re-evaluated, especially since ETMI involving 2 of the 4 muscles is not routinely evaluated by any of the disciplines (only genioglossus and hyoglossus muscles are routinely described). If surgical and pathologic documentation of ETMI does not become the criterion standard and if the upcoming revisions to the AJCC *Manual* maintain ETMI for upstaging to T4a, then MR imaging may

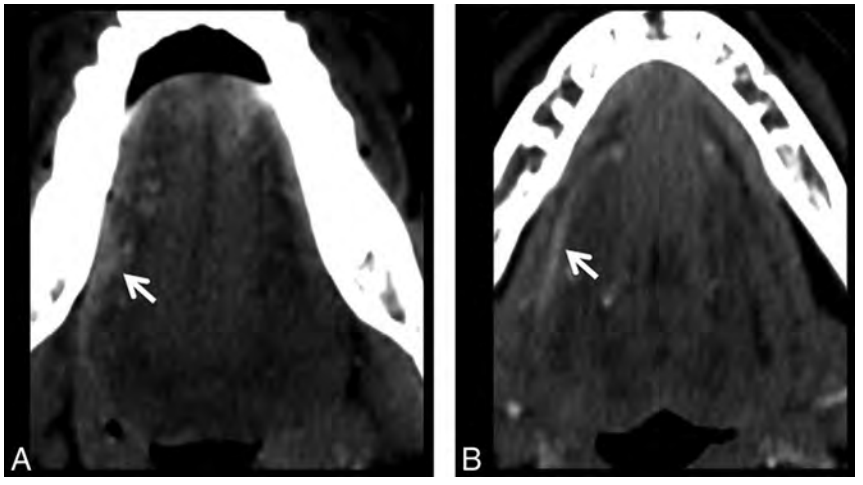

FIG 6. A 33-year-old woman with right lateral tongue SCC, pT1N0M0. Discordant: Radiology positive for ETMI (hyoglossus muscle) and surgery negative. Initial radiologic evaluation was probably yes due to linear enhancement along the hyoglossus muscle. *A*, Small right lateral tongue mass (*arrow*). *B*, Linear enhancement of the hyoglossus muscle (*arrow*).

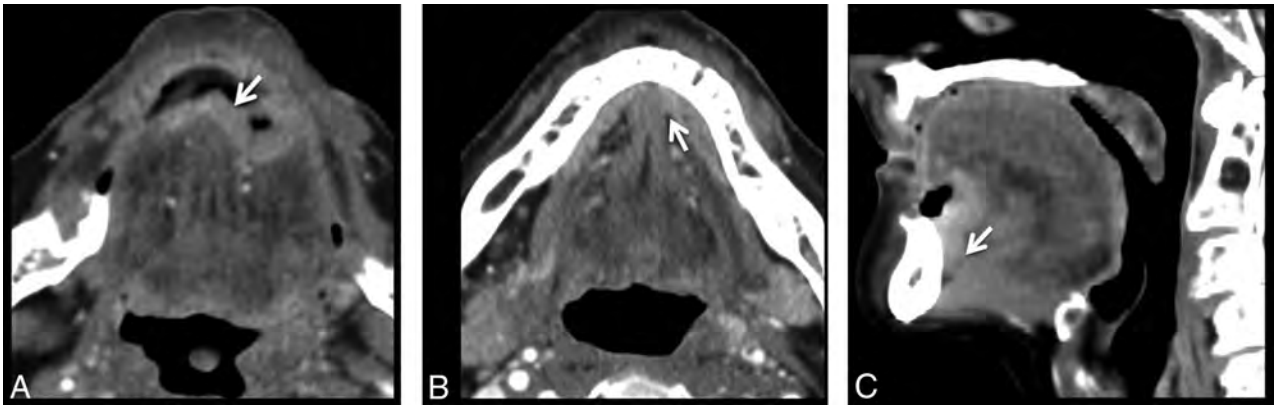

FIG 7. A 55-year-old woman with anterior FOM SCC, pT2N0M0. Discordant: Radiology positive (genioglossus muscle) and surgery negative for ETMI. *A* and *B*, Axial images show an anterior FOM tumor with apparent broad contact at the genioglossus insertion site (*arrow*). *C*, A closer look at the axial and sagittal images shows the tumor just above the insertion site with only narrow contact at the superior margin of the genioglossus insertion (*arrow*). This finding highlights a possible pitfall of the axial acquisition because volume averaging could depict the tumor with more masslike involvement of the ETM.

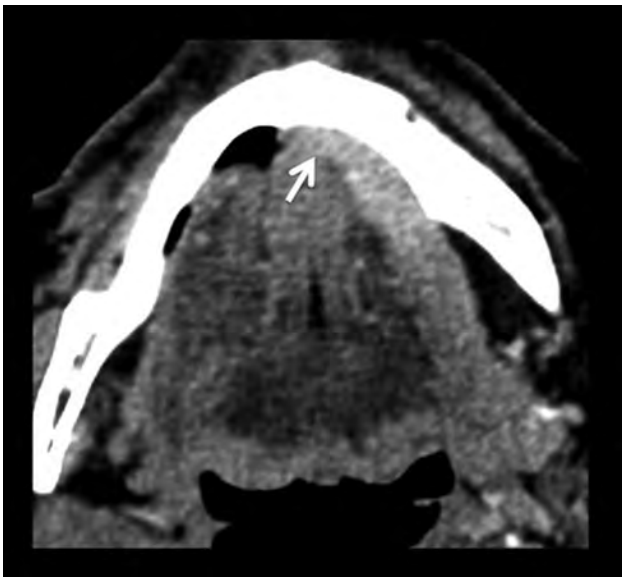

FIG 8. A 78-year-old man with left FOM SCC, pT4aN0M0. Note that T4a is for pathologic bone invasion only. Discordant: Radiology positive (genioglossus muscle) and surgery negative for ETMI. This was initially scored as probably yes due to broad contact, but in retrospect, there appears to be only focal contact at the insertion point of the left genioglossus muscle (*arrow*).

play a role in evaluating equivocal cases, given its greater soft-tissue detail.

The limitations of this study include the small sample size and multiple different surgeons and pathologists involved in the surgical determination of ETMI, though we attempted to minimize this limitation by meeting prospectively to standardize our approach. The high interobserver agreement regarding radiologic ETMI determination is likely because both readers are subspecialty trained neuroradiologists with a focus on head and neck imaging.

CONCLUSIONS

CECT is sensitive for ETMI but has reduced specificity (76%) compared with intraoperative surgical and pathology consensus evaluation. Masslike enhancement is the most specific imaging feature for predicting ETMI. Broad contact and linear enhancement of ETM are equivocal and often lead to false-positives; and narrow contact is not predictive.

A careful but perhaps time-intensive consensus read between the operating surgeon and the pathologist performing gross examination (in which the surgeon properly orients the fresh specimen for the pathologist) should be the criterion standard for ETMI. Because this process is currently not standard practice, imaging can best add value by identifying those cases most suspicious for ETMI, thereby prompting a more detailed evaluation by the surgeons and pathologists in these cases. This preliminary study has established imaging features that are more predictive of ETMI and will facilitate future correlation with patient outcomes to determine whether radiologic ETMI is indeed prognostic.

Disclosures: Mihir R. Patel—*UNRELATED*: *Consultancy*: AstraZeneca, *Comments*: served on a panel discussing potential genes and markers of immunotherapy, specifically as it relates to Programmed Death Ligand-1. Amanda S. Corey—*UNRELATED*: *Consultancy*: Radiology in Medical Development, *Comments*: Reviewer; *Employment*: Emory University Hospital and Clinics; *Payment for Lectures including Service on Speakers Bureaus*: Osler Institute, *Comments*: lecturer. Nabil F. Saba—*UNRELATED*: *Consultancy*: Bristol-Myers Squibb, Merck, Pfizer, *Comments*: consultation fees; *Royalties*: PubMed publications. Yuan Liu—*UNRELATED*: *Grant*: National Institutes of Health/National Cancer Institute, *Comments*: award No. P30CA138292.* *Money paid to the institution.

REFERENCES

1. Jemal A, Thun MJ, Ries LA, et al. **Annual report to the nation on the status of cancer, 1975–2005, featuring trends in lung cancer, tobacco use, and tobacco control.** *J Natl Cancer Inst* 2008;100:1672–94 CrossRef Medline
2. Steele TO, Meyers A. **Early detection of premalignant lesions and oral cancer.** *Otolaryngol Clin North Am* 2011;44:221–29, vii CrossRef Medline
3. Edge SB, Compton CC. **The American Joint Committee on Cancer: the 7th edition of the AJCC cancer staging manual and the future of TNM.** *Ann Surg Oncol* 2010;17:1471–74 CrossRef Medline
4. Salama JK, Saba N, Quon H, et al; Expert Panel on Radiation Oncology-Head and Neck. **ACR appropriateness criteria® adjuvant therapy for resected squamous cell carcinoma of the head and neck.** *Oral Oncol* 2011;47:554–59 CrossRef Medline
5. Aiken AH. **Pitfalls in the staging of cancer of oral cavity cancer.** *Neuroimaging Clin N Am* 2013;23:27–45 CrossRef Medline
6. Kirsch C. **Oral cavity cancer.** *Top Magn Reson Imaging* 2007;18:269–80 CrossRef Medline
7. Chong V. **Oral cavity cancer.** *Cancer Imaging* 2005;5(Spec No A):S49–52 CrossRef Medline
8. Law CP, Chandra RV, Hoang JK, et al. **Imaging the oral cavity: key concepts for the radiologist.** *Br J Radiol* 2011;84:944–57 CrossRef Medline
9. Yuen AP, Ng RW, Lam PK, et al. **Preoperative measurement of tumor thickness of oral tongue carcinoma with intraoral ultrasonography.** *Head Neck* 2008;30:230–34 CrossRef Medline
10. Arya S, Rane P, Deshmukh A. **Oral cavity squamous cell carcinoma: role of pretreatment imaging and its influence on management.** *Clin Radiol* 2014;69:916–30 CrossRef Medline
11. Dammann F, Horger M, Mueller-Berg M, et al. **Rational diagnosis of squamous cell carcinoma of the head and neck region: comparative evaluation of CT, MRI, and 18FDG PET.** *AJR Am J Roentgenol* 2005;184:1326–31 CrossRef Medline
12. Park JO, Jung SL, Joo YH, et al. **Diagnostic accuracy of magnetic resonance imaging (MRI) in the assessment of tumor invasion depth in oral/oropharyngeal cancer.** *Oral Oncol* 2011;47:381–86 CrossRef Medline
13. Lam P, Au-Yeung KM, Cheng PW, et al. **Correlating MRI and histologic tumor thickness in the assessment of oral tongue cancer.** *AJR Am J Roentgenol* 2004;182:803–08 CrossRef Medline
14. Gődény M. **Prognostic factors in advanced pharyngeal and oral cavity cancer; significance of multimodality imaging in terms of 7th edition of TNM.** *Cancer Imaging* 2014;14:1 CrossRef Medline
15. Madana J, Laliberté F, Morand GB, et al. **Computerized tomography based tumor-thickness measurement is useful to predict postoperative pathological tumor thickness in oral tongue squamous cell carcinoma.** *J Otolaryngol Head Neck Surg* 2015;44:49 CrossRef Medline
16. Boland PW, Pataridis K, Eley KA, et al. **A detailed anatomical assessment of the lateral tongue extrinsic musculature, and proximity to the tongue mucosal surface: does this confirm the current TNM T4a muscular subclassification?** *Surg Radiol Anat* 2013;35:559–64 CrossRef Medline
17. Boland PW, Pataridis K, Eley KA, et al. **Automatic upstaging of tongue squamous cell carcinoma with lateral extrinsic muscle involvement is not justified.** *Int J Oral Maxillofac Surg* 2013;42:1397–402 CrossRef Medline
18. Zarbo RJ, Barnes L, Crissman JD, et al. **Recommendations for the reporting of specimens containing oral cavity and oropharynx neoplasms: Association of Directors of Anatomic and Surgical Pathology.** *Hum Pathol* 2000;31:1191–93 CrossRef Medline
19. Lester S. *Manual of Surgical Pathology: Expert Consult.* Philadelphia: Elsevier; 2010:473–86
20. Westra H, Hruban RH, Phelps TH, et al. *Surgical Pathology Dissection: An Illustrated Guide.* New York: Springer; 2003:44–47

Fetal Brain Anomalies Associated with Ventriculomegaly or Asymmetry: An MRI-Based Study

E. Barzilay, O. Bar-Yosef, S. Dorembus, R. Achiron, and E. Katorza

ABSTRACT

BACKGROUND AND PURPOSE: Fetal lateral ventriculomegaly is a relatively common finding with much debate over its clinical significance. The purpose of this study was to examine the association between ventriculomegaly and asymmetry and concomitant CNS findings as seen in fetal brain MR imaging.

MATERIALS AND METHODS: Fetal brain MR imaging performed for various indications, including ventriculomegaly, with or without additional ultrasound findings, was assessed for possible inclusion. Two hundred seventy-eight cases found to have at least 1 lateral ventricle with a width of ≥10 mm were included in the study. Ventriculomegaly was considered mild if the measurement was 10–11.9 mm; moderate if, 12–14.9 mm; and severe if, ≥15 mm. Asymmetry was defined as a difference of ≥2 mm between the 2 lateral ventricles. Fetal brain MR imaging findings were classified according to severity by predefined categories.

RESULTS: The risk of CNS findings appears to be strongly related to the width of the ventricle (OR, 1.38; 95% CI, 1.08–1.76; $P = .009$). The prevalence of associated CNS abnormalities was significantly higher ($P = .005$) in symmetric ventriculomegaly compared with asymmetric ventriculomegaly (38.8% versus 24.2%, respectively, for all CNS abnormalities and 20% versus 7.1%, respectively, for major CNS abnormalities).

CONCLUSIONS: In this study, we demonstrate that the rate of minor and major findings increased with each millimeter increase in ventricle width and that the presence of symmetric ventricles in mild and moderate ventriculomegaly was a prognostic indicator for CNS abnormalities.

Fetal lateral ventriculomegaly is a relatively common finding. Some have estimated the incidence of ventriculomegaly identified on sonography to be about 1%.[1] Fetal ventriculomegaly is defined as a dilation of the lateral ventricle atrium to a width of ≥10 mm.[2,3] A measurement of 10–12 mm is commonly referred to as mild ventriculomegaly, while measurements of 12–15 and >15 mm are defined as moderate and severe ventriculomegaly, respectively.[4] Severe ventriculomegaly has been associated with poorer neurodevelopmental outcome compared with mild ventriculomegaly[5,6]; however, it has been previously suggested that the neurodevelopmental outcome in cases of moderate ventriculomegaly is similar to that observed in mild ventriculomegaly.[7]

Many studies have focused on the neurodevelopmental outcome of children who were diagnosed in utero with lateral ventriculomegaly.[6,8-16] One of the most important factors determining outcome is the presence and severity of additional CNS anomalies. Although most anomalies can be identified by using sonography, MR imaging was shown to be superior in identifying CNS anomalies. A recent study found that MR imaging could detect additional findings in 15.3% of the seemingly isolated ventriculomegaly/ventricle asymmetry cases.[17] In this study, we aimed to establish the proportion of MR imaging–detected CNS anomalies associated with ventriculomegaly in correlation with the severity of ventriculomegaly and ventricle asymmetry. To prevent underestimation of associated anomalies, we did not exclude cases with CNS anomalies previously identified on sonography. To the best of our knowledge, this is the first large-scale MR imaging study that has examined the association between lateral ventricle width and asymmetry and CNS anomalies.

MATERIALS AND METHODS

We conducted a cross-sectional study of all brain MR imaging scans performed in a single tertiary center (Sheba Medical Center, Tel-Hashomer, Israel) between January 2011 and December 2014.

Received July 9, 2016; accepted after revision September 19.

From the Department of Obstetrics and Gynecology (E.B., R.A., E.K.) and Pediatric Neurology Unit (O.B.-Y.), Sheba Medical Center, Tel-Hashomer, Ramat-Gan, Israel; and Sackler School of Medicine (E.B., O.B.-Y., S.D., R.A., E.K.), Tel Aviv University, Tel Aviv, Israel.

E. Barzilay and O. Bar-Yosef contributed equally to this work.

Please address correspondence to Eran Barzilay, MD, PhD, Department of Obstetrics and Gynecology, Sheba Medical Center, Tel-Hashomer, Ramat-Gan, 52621, Israel; e-mail: eran.barzilay@gmail.com

http://dx.doi.org/10.3174/ajnr.A5009

Classification of MRI findings according to severity

Malformation Type	Severity		
	Normal Variant	Minor Findings	Major Findings
NTD		Meningocele	Acrania/anencephaly encephalocele Myelocele
Cystic lesions	CPC Cavum verge CVI	Isolated PVPC Arachnoid cyst	Nonisolated PVPC PVL Porencephalic cyst
Bleeding		IVH grade 1	IVH grade 2–4
Ischemia			Parenchymatic damage
Cortical disorders	Delayed sulcation (up to 2 weeks)		Lissencephaly Schizencephaly Heterotopia Microcephaly
White matter	Isolated T2 hypersignal		Nonisolated T2 hypersignal
Midline CC	Lipoma	Short intact CC thick/thin	Complete/partial CC agenesis
Midline CSP		Isolated septal agenesis	SOD
Posterior fossa	MCM	Blake pouch cyst	Chiari 2 DWS Primary disruption of cerebellum/vermis/brain stem Secondary disruption of cerebellum/vermis/brain stem
Vascular			Vein of Galen aneurysm

Note:—NTD indicates neural tube defect; CPC, choroid plexus cyst; CVI, cavum vellum interpositum; PVPC, periventricular pseudocyst; PVL, periventricular leukomalacia; IVH, intraventricular hemorrhage; CMV, cytomegalovirus; CC, corpus callosum; CSP, cavum septum pellucidum; SOD, septo-optic dysplasia; MCM, mega cysterna magna; DWS, Dandy-Walker syndrome; CSVT, cerebral sinovenous thrombosis.

"Ventriculomegaly" was defined as a lateral ventricle width of ≥10 mm.[2-4] Lateral ventricle asymmetry was defined as a difference of ≥2 mm between the 2 lateral ventricles. All MR imaging scans during the study period were assessed for possible eligibility, regardless of the reason for the referral. Inclusion criteria for this study were singleton pregnancy and ventriculomegaly (at least 1 lateral ventricle with a width of ≥10 mm). Exclusion criteria were fetal cytomegalovirus or toxoplasma infection and cases with abnormal genetic tests (karyotype or microarray). Two hundred seventy-eight cases met the inclusion/exclusion criteria.

Fetal MR imaging was performed with a 1.5T system (Optima 1.5T; GE Healthcare, Milwaukee, Wisconsin) as previously published.[17] Single-shot fast spin-echo T2-weighted sequences in 3 orthogonal planes were performed by using the following parameters: section thickness, 3–4 mm; no gap; flexible coil (8-channel cardiac coil); matrix, 320 × 224; TE, 90 ms; and TR, 1298 ms. The FOV was determined by the size of the fetal head: 24 cm for the smaller fetuses and 30 cm for the larger fetuses. T1 fast-spoiled gradient-echo sequences were performed only in the axial plane with a larger FOV (400 mm), with section thickness, 4 mm; gap, 0.5 mm; TR, 160 ms; and TE, 2.3 ms. Measurements of the lateral ventricle widths were obtained on the coronal plane at the level of the ventricles (with good visibility of the choroid plexuses). For this study, ventriculomegaly was considered mild if the measurement was 10–11.9 mm; moderate if, 12–14.9 mm; and severe if, ≥15 mm. Asymmetry was defined as a difference of ≥2 mm between the 2 lateral ventricles.

Fetal brain MR imaging findings were classified according to severity by predefined categories as shown in the Table. Classification of findings into minor or major was determined on the basis of previously published data.[18-27]

Statistical analyses were conducted by using the Statistical Package for the Social Sciences (SPSS, Version 23; IBM, Armonk, New York). Q-Q plots were used to assess normality. Continuous variables were described as mean (SD) or median (interquartile range) as appropriate. Continuous variables were compared by using an unpaired *t* test and a 1-way ANOVA test as appropriate or by using the Mann-Whitney *U* test and Kruskal Wallis test for nonparametric continuous variables as appropriate. The χ^2 test was used for comparison of categoric variables. Logistic regression analysis was used to examine the relationship among ventricle width, width difference, and CNS findings. Significance was $P < .05$.

The study was approved by the local institutional review board of the Sheba Medical Center.

RESULTS

Two hundred seventy-eight pregnancies were included in the study. The average maternal age was 31.8 ± 5.2 years. Maternal age did not differ significantly between cases with or without ventricle asymmetry (32 versus 31.4 years, respectively; $P = .693$) or among cases of mild, moderate, and severe ventriculomegaly (32, 31.5, and 29.5 years of age, respectively; $P = .235$). The median gestational age at MR imaging acquisition was 32 weeks (interquartile range, 31–34 weeks). There was no difference in median gestational age between cases with or without ventricle asymmetry (32 versus 32 weeks, respectively; $P = .079$) or among cases of mild, moderate, and severe ventriculomegaly (32, 32, and 31.5 weeks, respectively, $P = .785$).

Median ventricle width for the widest ventricle was 11 mm (interquartile range, 11–13 mm), and for the contralateral ventricle, it was 9 mm (interquartile range, 7–11 mm). Median ventricle width difference was 3 mm (interquartile range, 1–4 mm).

Figure 1 depicts the distribution of ventriculomegaly cases according to severity and the presence or absence of asymmetry.

Most cases were defined as mild ventriculomegaly (73%), while moderate and severe ventriculomegaly comprised 22.7% and 4.3% of the cases, respectively. Most cases of ventriculomegaly were asymmetric (71.2%).

Figure 2 depicts the distribution of CNS findings according to the width of the ventricle (the larger of the 2 ventricles). The risk of CNS findings appears to be strongly related to the width of the ventricle. The association between CNS findings and ventricle width was particularly evident in moderate ventriculomegaly, in which each 1-mm increase in ventricle width increases the risk for both minor and major CNS findings. Logistic regression analysis, with each ventricle width along with maternal age, gestational age at the time of MR imaging, and fetal sex as variables, demonstrated that the widths of both ventricles were positively associated with an increased risk for CNS anomalies (OR, 1.38; 95% CI, 1.08–1.76; $P = .009$, for the maximal ventricle; and OR, 1.21; 95% CI, 1.03–1.44; $P = .025$, for the contralateral ventricle). Gestational age at the time of MR imaging was found to be negatively associated with CNS anomalies (OR, 0.86; 95% CI, 0.77–0.95; $P = .003$), possibly indicating that the more complicated cases tended to be diagnosed earlier. Maternal age ($P = .75$) and fetal sex ($P = .304$) were not found to be associated with CNS anomalies. The correlation between ventricle width and associated anomalies appears to be strongest within the 12- to 15-mm range because the OR for CNS anomalies increased from 1.38 (95% CI, 1.08–1.76; $P = .009$) to 2.53 (95% CI, 1.48–4.34; $P = .001$) when the analysis was restricted to cases with a ventricle width of 12–15 mm.

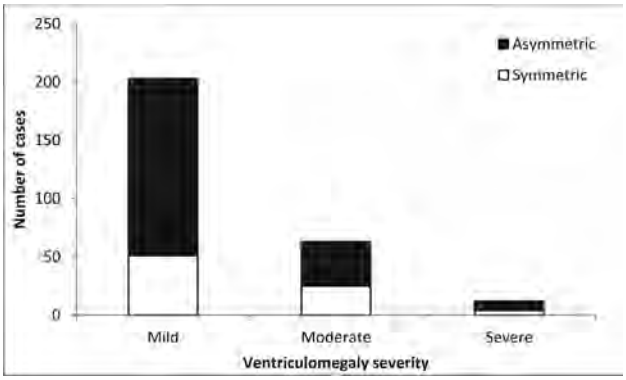

FIG 1. Distribution of ventriculomegaly cases according to severity and the presence or absence of asymmetry. *Filled bars* represent asymmetric ventriculomegaly; *empty bars* represent symmetric ventriculomegaly.

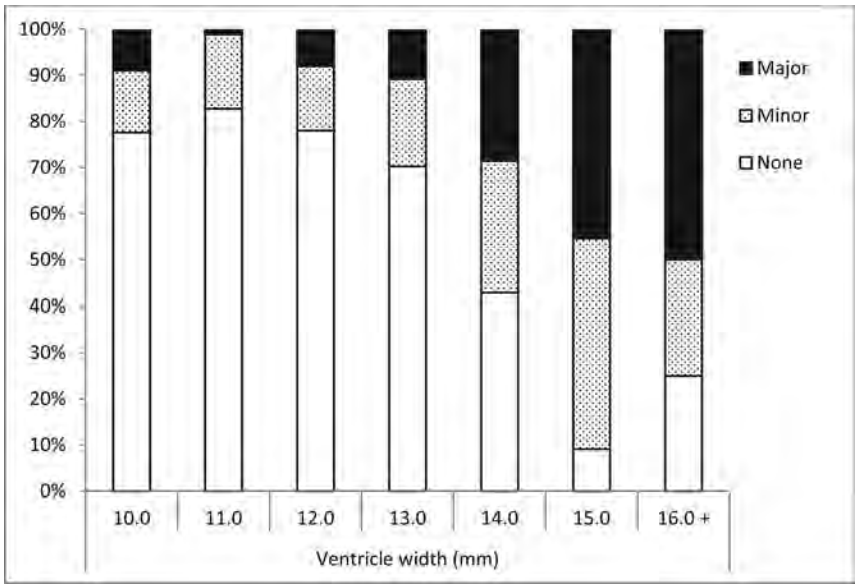

FIG 2. Distribution of additional CNS findings in cases of fetal ventriculomegaly according to maximal ventricle width. *Filled bars* represent major CNS findings, *dotted bars* represent minor CNS findings, and *empty bars* represent no additional CNS findings. Due to small numbers, cases with dilation of ≥16 mm were grouped together.

Most cases in this study were asymmetric ventriculomegaly (71%). We have found more CNS abnormalities in symmetric ventriculomegaly compared with asymmetric ventriculomegaly (38.8% versus 24.2%, respectively) and more major CNS abnormalities in symmetric ventriculomegaly compared with asymmetric ventriculomegaly (20% versus 7.1%, respectively). These differences between symmetric and asymmetric ventriculomegaly were found to be statistically significant ($P = .005$).

Figure 3 illustrates the distribution of CNS abnormalities according to ventriculomegaly severity and the presence or absence of asymmetry. We found that the differences in the risk of CNS abnormalities between symmetric and asymmetric ventriculomegaly were only apparent in the mild and moderate groups. In cases of severe ventriculomegaly, the rates of minor (25%) and major (50%) findings were identical in symmetric and asymmetric ventriculomegaly. The number of cases in the severe ventriculomegaly group ($n = 12$) was much smaller than in the moderate ($n = 63$) and mild ($n = 203$) groups.

Next, we used regression analysis to explore the individual impact of ventricle width and ventricle asymmetry on the risk of CNS findings. Using maximal ventricle width and width difference as variables, we found that ventricle width was an independent risk factor for CNS findings (OR, 1.56; 95% CI, 1.32–1.85; $P < .001$), while ventricle width difference was inversely associated with CNS findings (OR, 0.79; 95% CI, 0.68–0.92; $P = .003$). When average ventricle width was used in the regression model instead of maximal ventricle width, average ventricle width appeared to be independently associated with CNS findings (OR, 1.56; 95% CI, 1.32–1.85; $P < .001$). However, width difference lost its significant association with CNS findings (OR, 0.99; 95% CI, 0.84–1.16; $P = .896$).

DISCUSSION

In this study we analyzed a large number MR imaging scans of fetuses diagnosed with fetal ventriculomegaly. We have shown that the risk of minor and major CNS findings is closely related to the width of the lateral ventricle. The association between ventricle width and CNS findings is particularly evident in moderate ventriculomegaly. As seen in Fig 2, the rate of minor and major findings significantly increased with each millime-

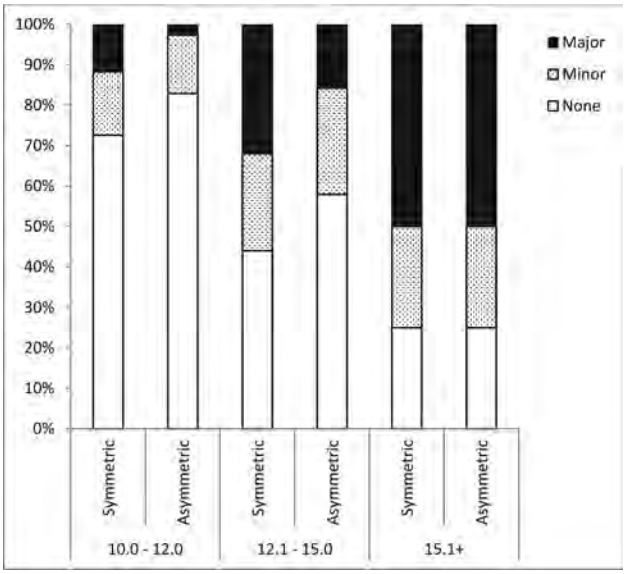

FIG 3. Distribution of additional CNS findings in cases of fetal ventriculomegaly according to ventriculomegaly severity and the presence or absence of asymmetry. *Filled bars* represent major CNS findings, *dotted bars* represent minor CNS findings, and *empty bars* represent no additional CNS findings.

ter increase in ventricle width. Thus, while the prevalent categorization of mild, moderate, and severe ventriculomegaly appears to adequately portray the risk of CNS anomalies, taking into account the ventricle width greatly improves the risk estimation. Moreover, these findings are contrary to those in previous studies that defined mild ventriculomegaly at an atrial width of 10–15 mm.[7,16]

Another intriguing result of this study is the correlation between ventricle asymmetry and CNS findings in fetal MR imaging. We have found that symmetric ventriculomegaly was associated with more CNS findings than asymmetric ventriculomegaly. This difference was apparent in mild and moderate ventriculomegaly, while the rates of minor and major CNS findings were similar between symmetric and asymmetric severe ventriculomegaly. The apparent advantage of asymmetric ventriculomegaly might be somewhat counterintuitive. However, the presence of asymmetry for a case with a given ventricle width translates to a smaller contralateral ventricle. Thus, in asymmetric mild ventriculomegaly, the contralateral ventricle will be in the normal range, while in moderate ventriculomegaly, most cases will have a contralateral ventricle width in the normal-to-mild ventriculomegaly range. This hypothesis gains support from our regression analysis that demonstrated that the association between width difference and CNS findings was eliminated when average ventricle width was used as a variable in the analysis instead of maximal ventricle width, thereby encompassing data on both ventricles.

The relatively low incidence of major anomalies in cases of mild symmetric ventriculomegaly (2.6%) may merit re-evaluation of the cost-effectiveness of fetal MR imaging in these cases. Nevertheless, we believe that given the clinical implications of major CNS anomalies and in light of the prevalence of minor findings in mild asymmetric ventriculomegaly (14.5%), fetal brain MR imaging still plays an important role in the work-up of these cases.

The data portrayed in this study aid in establishing the correlation between lateral ventricle width and CNS anomalies. The high rate of CNS anomalies observed in this study stresses the need for a thorough investigation of fetal ventriculomegaly and especially for meticulous examination in cases of moderate-to-severe ventriculomegaly and bilateral ventriculomegaly.

This study is in accordance with previous studies that found more CNS anomalies in moderate and severe ventriculomegaly compared with mild ventriculomegaly.[10,11] However, in most of these studies, imaging was based almost exclusively on ultrasound,[9-11] despite the known advantages of fetal brain MR imaging.[17] Moreover, none of these studies, including those with fetal MR imaging as an imaging technique,[15,17] have analyzed the impact of ventricle width on the risk of CNS anomalies.

One of the advantages of this study is that it included a large number of fetal MR imaging scans, enabling us to examine in depth the association between ventriculomegaly and CNS findings. Thus, we could identify differences in the rate of CNS findings not only among mild, moderate, and severe ventriculomegaly but also due to minute increases in ventricle width. Another major advantage is that the study is MR imaging–based, thereby increasing the ability to identify CNS abnormalities compared with neurosonography.[17,28-31]

This study is limited by the lack of data on neurodevelopmental outcome. Here we examined the association between ventriculomegaly and CNS anomalies in the fetus without assessing the outcome of the child. Nevertheless, because the presence of CNS abnormalities has been shown to be closely related to the neurodevelopmental outcome of the child,[6] findings in fetal MR imaging can be used as an indication of the outcome. Moreover, to improve the clinical significance of the association between ventriculomegaly and CNS anomalies, we classified CNS anomalies according to severity (Table).

CONCLUSIONS

In this study, we demonstrate that the rate of minor and major findings increases with each millimeter increase in ventricle width and that the presence of symmetric ventricles in mild and moderate ventriculomegaly is a prognostic indicator for CNS anomalies in MR imaging examinations.

REFERENCES

1. Salomon LJ, Bernard JP, Ville Y. **Reference ranges for fetal ventricular width: a non-normal approach.** *Ultrasound Obstet Gynecol* 2007;30:61–66 CrossRef Medline
2. Cardoza JD, Goldstein RB, Filly RA. **Exclusion of fetal ventriculomegaly with a single measurement: the width of the lateral ventricular atrium.** *Radiology* 1988;169:711–14 CrossRef Medline
3. Almog B, Gamzu R, Achiron R, et al. **Fetal lateral ventricular width: what should be its upper limit? A prospective cohort study and reanalysis of the current and previous data.** *J Ultrasound Med* 2003;22:39–43 Medline
4. International Society of Ultrasound in Obstetrics and Gynecology Education Committee. **Sonographic examination of the fetal central nervous system: guidelines for performing the 'basic examination' and the 'fetal neurosonogram.'** *Ultrasound Obstet Gynecol* 2007;29:109–16 CrossRef Medline
5. Gaglioti P, Oberto M, Todros T. **The significance of fetal ventriculomegaly: etiology, short- and long-term outcomes.** *Prenat Diagn* 2009;29:381–88 CrossRef Medline
6. Weichert J, Hartge D, Krapp M, et al. **Prevalence, characteristics and perinatal outcome of fetal ventriculomegaly in 29,000 pregnancies followed at a single institution.** *Fetal Diagn Ther* 2010;27:142–48 CrossRef Medline
7. Melchiorre K, Bhide A, Gika AD, et al. **Counseling in isolated mild**

fetal ventriculomegaly. *Ultrasound Obstet Gynecol* 2009;34:212–24 CrossRef Medline
8. Mehta TS, Levine D. **Imaging of fetal cerebral ventriculomegaly: a guide to management and outcome.** *Semin Fetal Neonatal Med* 2005; 10:421–28 CrossRef Medline
9. Chu N, Zhang Y, Yan Y, et al. **Fetal ventriculomegaly: pregnancy outcomes and follow-ups in ten years.** *Biosci Trends* 2016;10:125–32 CrossRef Medline
10. Breeze AC, Alexander PM, Murdoch EM, et al **Obstetric and neonatal outcomes in severe fetal ventriculomegaly.** *Prenat Diagn* 2007;27: 124–29 CrossRef Medline
11. Gaglioti P, Danelon D, Bontempo S, et al. **Fetal cerebral ventriculomegaly: outcome in 176 cases.** *Ultrasound Obstet Gynecol* 2005;25:372–77 CrossRef Medline
12. Kelly EN, Allen VM, Seaward G, et al. **Mild ventriculomegaly in the fetus, natural history, associated findings and outcome of isolated mild ventriculomegaly: a literature review.** *Prenat Diagn* 2001;21: 697–700 CrossRef Medline
13. Laskin MD, Kingdom J, Toi A, et al. **Perinatal and neurodevelopmental outcome with isolated fetal ventriculomegaly: a systematic review.** *J Matern Fetal Neonatal Med* 2005;18:289–98 CrossRef Medline
14. Scala C, Familiari A, Pinas A, et al. **Perinatal and long-term outcome in fetuses diagnosed with isolated unilateral ventriculomegaly: systematic review and meta-analysis.** *Ultrasound Obstet Gynecol* 2016 Apr 19. [Epub ahead of print] CrossRef Medline
15. Ouahba J, Luton D, Vuillard E, et al. **Prenatal isolated mild ventriculomegaly: outcome in 167 cases.** *BJOG* 2006;113:1072–79 CrossRef Medline
16. Pagani G, Thilaganathan B, Prefumo F. **Neurodevelopmental outcome in isolated mild fetal ventriculomegaly: systematic review and meta-analysis.** *Ultrasound Obstet Gynecol* 2014;44:254–60 CrossRef Medline
17. Gat I, Hoffmann C, Shashar D, et al. **Fetal brain MRI: novel classification and contribution to sonography.** *Ultraschall Med* 2016;37: 176–84 CrossRef Medline
18. Toi A, Chitayat D, Blaser S. **Abnormalities of the foetal cerebral cortex.** *Prenat Diagn* 2009;29:355–71 CrossRef Medline
19. Santo S, D'Antonio F, Homfray T, et al. **Counseling in fetal medicine: agenesis of the corpus callosum.** *Ultrasound Obstet Gynecol* 2012;40: 513–21 CrossRef Medline
20. Vasudevan C, McKechnie L, Levene M. **Long-term outcome of antenatally diagnosed agenesis of corpus callosum and cerebellar malformations.** *Semin Fetal Neonatal Med* 2012;17:295–300 CrossRef Medline
21. Malinger G, Lev D, Ben Sira L, et al. **Congenital periventricular pseudocysts: prenatal sonographic appearance and clinical implications.** *Ultrasound Obstet Gynecol* 2002;20:447–51 CrossRef Medline
22. Epelman M, Daneman A, Blaser SI, et al. **Differential diagnosis of intracranial cystic lesions at head US: correlation with CT and MR imaging.** *Radiographics* 2006;26:173–96 CrossRef Medline
23. Volpe P, Campobasso G, De Robertis V, et al. **Disorders of prosencephalic development.** *Prenat Diagn* 2009;29:340–54 CrossRef Medline
24. Hayward R. **Postnatal management and outcome for fetal-diagnosed intra-cerebral cystic masses and tumours.** *Prenat Diagn* 2009; 29:396–401 CrossRef Medline
25. Carletti A, Colleoni GG, Perolo A, et al. **Prenatal diagnosis of cerebral lesions acquired in utero and with a late appearance.** *Prenat Diagn* 2009;29:389–95 CrossRef Medline
26. Garel C, Fallet-Bianco C, Guibaud L. **The fetal cerebellum: development and common malformations.** *J Child Neurol* 2011;26:1483–92 CrossRef Medline
27. Malinger G, Lev D, Lerman-Sagie T. **The fetal cerebellum: pitfalls in diagnosis and management.** *Prenat Diagn* 2009;29:372–80 CrossRef Medline
28. Morris JE, Rickard S, Paley MN, et al. **The value of in-utero magnetic resonance imaging in ultrasound diagnosed foetal isolated cerebral ventriculomegaly.** *Clin Radiol* 2007;62:140–44 CrossRef Medline
29. Benacerraf BR, Shipp TD, Bromley B, et al. **What does magnetic resonance imaging add to the prenatal sonographic diagnosis of ventriculomegaly?** *J Ultrasound Med* 2007;26:1513–22 Medline
30. Kandula T, Fahey M, Chalmers R, et al. **Isolated ventriculomegaly on prenatal ultrasound: what does fetal MRI add?** *J Med Imaging Radiat Oncol* 2015;59:154–62 CrossRef Medline
31. Salomon LJ, Ouahba J, Delezoide AL, et al. **Third-trimester fetal MRI in isolated 10- to 12-mm ventriculomegaly: is it worth it?** *BJOG* 2006;113:942–47 CrossRef Medline

MRI Brain Volume Measurements in Infantile Neuronal Ceroid Lipofuscinosis

E.H. Baker, S.W. Levin, Z. Zhang, and A.B. Mukherjee

ABSTRACT

BACKGROUND AND PURPOSE: Infantile neuronal ceroid lipofuscinosis is a devastating neurodegenerative storage disease caused by palmitoyl-protein thioesterase 1 deficiency, which impairs degradation of palmitoylated proteins (constituents of ceroid) by lysosomal hydrolases. Consequent lysosomal ceroid accumulation leads to neuronal injury, resulting in rapid neurodegeneration and childhood death. As part of a project studying the treatment benefits of a combination of cysteamine bitartrate and *N*-acetyl cysteine, we made serial measurements of patients' brain volumes with MR imaging.

MATERIALS AND METHODS: Ten patients with infantile neuronal ceroid lipofuscinosis participating in a treatment/follow-up study underwent brain MR imaging that included high-resolution T1-weighted images. After manual placement of a mask delineating the surface of the brain, a maximum-likelihood classifier was applied to determine total brain volume, further subdivided as cerebrum, cerebellum, brain stem, and thalamus. Patients' brain volumes were compared with those of a healthy population.

RESULTS: Major subdivisions of the brain followed similar trajectories with different timing. The cerebrum demonstrated early, rapid volume loss and may never have been normal postnatally. The thalamus dropped out of the normal range around 6 months of age; the cerebellum, around 2 years of age; and the brain stem, around 3 years of age.

CONCLUSIONS: Rapid cerebral volume loss was expected on the basis of previous qualitative reports. Because our study did not include a nontreatment arm and because progression of brain volumes in infantile neuronal ceroid lipofuscinosis has not been previously quantified, we could not determine whether our intervention had a beneficial effect on brain volumes. However, the level of quantitative detail in this study allows it to serve as a reference for evaluation of future therapeutic interventions.

ABBREVIATIONS: *CLN* = ceroid-lipofuscinosis, neuronal; EEG = electroencephalogram; ERG = electroretinogram; INCL = infantile neuronal ceroid lipofuscinosis

Neurodegeneration is a devastating manifestation in most of the >50 known lysosomal storage disorders. Among the neurodegenerative lysosomal storage disorders, neuronal ceroid lipofuscinoses,[1-3] also known as Batten disease,[4,5] are the most common. Mutations in at least 13 different genes (ceroid-lipofuscinosis, neuronal [*CLN*]) cause various types of neuronal ceroid lipofuscinoses.[6] Among these genes, *CLN1*, *CLN2*, *CLN10*, and *CLN13* encode lysosomal enzymes; *CLN4* and *CLN14* encode peripherally associated cytoplasmic proteins; *CLN5* encodes a soluble lysosomal protein; *CLN11* encodes a protein in the secretory pathway; and several transmembrane proteins with varying subcellular localizations are encoded by *CLN3*, *CLN6*, *CLN7*, *CLN8*, and *CLN12*.[7] The infantile type, infantile neuronal ceroid lipofuscinosis (INCL),[8] has an early age of onset and rapid progression to death. INCL is caused by mutations in the *CLN1* gene,[9] which encodes palmitoyl-protein thioesterase 1. Patients with INCL appear healthy at birth, but by 11–18 months of age, they exhibit developmental delay, followed by loss of developmental milestones. Many develop seizures. By 2 years of age, they are blind due to retinal degeneration, and they reach a persistent vegetative

Received June 3, 2016; accepted after revision August 29.

From the Department of Radiology and Imaging Sciences (E.H.B.), Clinical Center, National Institutes of Health, Bethesda, Maryland; and Program on Endocrinology and Molecular Genetics (S.W.L., Z.Z., A.B.M.), Eunice Kennedy Shriver National Institute of Child Health and Human Development, National Institutes of Health, Bethesda, Maryland.

This research was supported in full by the intramural research program of the Eunice Kennedy Shriver National Institute of Child Health and Human Development, National Institutes of Health (protocol 01-CH-0086). Healthy volunteers were studied under protocols 89-M-0006 and 11-M-0144.

The authors report no conflicts of interest.

The views herein are those of the authors and are not necessarily those of the National Institutes of Health.

Please address correspondence to Eva H. Baker, MD, PhD, Clinical Center, Department of Radiology and Imaging Sciences, National Institutes of Health, 10 Center Dr, MSC 1074, Bethesda, MD 20892-1074; e-mail: bakere@mail.nih.gov

Indicates open access to non-subscribers at www.ajnr.org

Indicates article with supplemental on-line photos.

http://dx.doi.org/10.3174/ajnr.A4978

state at around 4 years of age, manifested by an isoelectric electroencephalogram (EEG) (including visual-evoked potentials).[10] This grim trajectory highlights the desirability of developing an effective therapy for this disease.

The pathologic findings include intralysosomal accumulation of autofluorescent material (ceroid), rapidly progressing brain atrophy resulting predominantly from loss of neurons in the cerebral cortex, and neuroinflammatory findings[11] in the early stages. The accumulation of ceroid results in the formation of granular osmiophilic deposits,[12,13] which can be visualized in the brain and other tissues by using electron microscopy.

Previous in vitro studies demonstrated that phosphocysteamine had a beneficial effect on INCL-derived cell cultures, resulting in depletion of ceroid deposits and suppression of apoptosis.[14] The antioxidant *N*-acetyl cysteine has been reported to be beneficial in other neurogenerative diseases.[15] These 2 observations led us to conceive a study of a combination therapy with these 2 drugs. Because INCL is a rare disease (1 in >100,000 births) with a short life expectancy, recruitment of a large study group is impractical; this issue led to a "compassionate use" type of experimental design in which all patients received treatment, without a control group. The intention was to compare with the natural history and future treatment interventions by using behavioral and developmental assessments and quantifiable measures such as electroencephalography, electroretinography, MR imaging–derived brain volume measurements, MR spectroscopy, and quantification of intralysosomal ceroid deposits. An overview of the study results has been published recently[16]; the current report details the MR imaging–derived brain volume measurements.

MATERIALS AND METHODS

Study Participants

Recruitment and inclusion criteria for this study have been described in detail elsewhere (ClinicalTrials.gov number NCT00028262).[16] Ten patients were recruited for the study, 9 of whom had treatment initiated after the baseline study and returned for follow-up; the other patient dropped out of the study after the baseline evaluation and did not undergo treatment. The *CLN1* gene mutations represented in our patient sample were C451T, T29A, A364T, A169i, and 798+2T>C. The patients were all younger than 3 years of age on entry to the study.

Treatment

Following initial evaluation, the 9 patients who continued in the study began oral treatment with cysteamine bitartrate (Cystagon) at 10 mg/kg per day, escalated weekly to a target of 60 mg/kg per day. After achieving this target dose, oral treatment with *N*-acetyl cysteine (Mucomyst) was added at 10 mg/kg per day and escalated weekly to a target of 60 mg/kg per day. Treatment was discontinued after demonstration of an isoelectric electroencephalogram or when the patient was too sick to travel for follow-up appointments; this was an interval of 8–75 months after initiation of treatment, at which time follow-up also stopped.

MR Imaging

Patients. Eight patients were studied by using a 1.5T Signa scanner (GE Healthcare, Milwaukee, Wisconsin) with a quadrature transmit-receive head coil. Two patients were studied by using a 3T Achieva scanner (Philips Healthcare, Best, the Netherlands) with an 8-channel SENSE head coil. A standard noncontrast clinical MR imaging examination was performed in all patients; this included either axial or sagittal 3D-SPGR images or axial 3D-MPRAGE images. Axial or sagittal 3D-SPGR images were acquired with the following parameters: FOV = 200 × 200 mm or 240 × 240 mm, acquisition matrix = 256 × 256, reconstruction matrix = 256 × 256, section thickness = 1–2 mm, NEX = 1, TE = 2.2–5.5 ms, TR = 9.5–12.8 ms. Axial 3D-MPRAGE images were acquired with the following parameters: FOV = 220 × 220 mm, acquisition matrix = 256 × 131, reconstruction matrix = 256 × 256, section thickness = 1 mm, NEX = 2, TE = 6.6 ms, TR = 11.5 ms, echo-train length = 131.

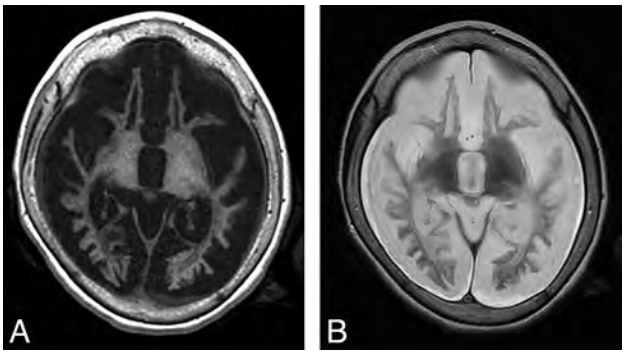

FIG 1. MR imaging findings in end-stage INCL. T1-weighted (*A*) and T2-weighted (*B*) images in the plane defined by the anterior and posterior commissures. These images demonstrate findings that include extreme atrophy, near-complete lack of gray matter, extensive abnormal signal in the white matter, loss of internal landmarks separating the basal ganglia, and subdural effusions.

Sedation

Because all patients were young children, most examinations were performed with the patient under sedation with propofol.[17] Some late-stage patients did not require sedation for the MR imaging examinations.

Brain Volume Measurement

Brain volumes were calculated by using the 3D-SPGR or 3D-MPRAGE images. Medical Image Processing, Analysis, and Visualization software[18] (MIPAV; http://mipav.cit.nih.gov/) was used to manually generate a mask that stripped the skull, meninges, and other tissues away from the brain; a shading correction was applied to compensate for radiofrequency transmission nonuniformity; and finally, a single-channel 3-tissue maximum likelihood classifier was applied to the area within the mask to estimate the volume of the brain parenchyma. The mask was manually subdivided into cerebrum, cerebellum, and brain stem to separately measure these volumes. For healthy controls, we used images from 23 healthy volunteers (12 girls, 11 boys; 1.1–9.6 years of age) participating in other research studies at our institution who had been scanned using imaging parameters similar to ours; control brain volumes were measured in the same manner as the brains of patients with INCL.

Measurement of the thalamus volumes was challenging due to the abnormal intrinsic tissue contrast that obscures the boundaries between the deep nuclei and adjacent structures (Fig 1); this

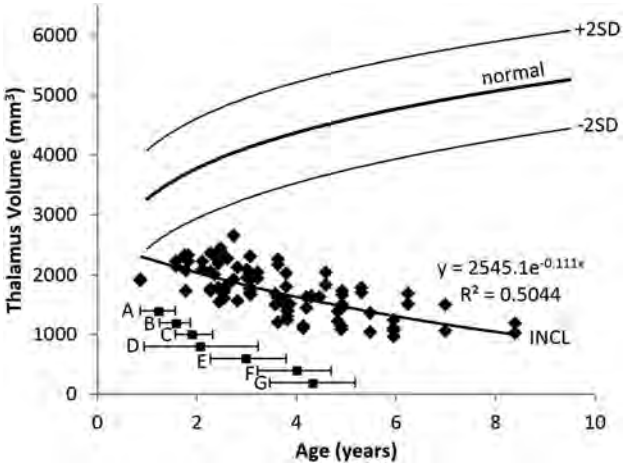

FIG 2. Thalamus volume measurements in patients with INCL. Due to lack of visible boundaries of the thalamus (secondary to disease-related alterations in intrinsic contrast), an ellipsoidal approximation to the volume was made on the basis of brain surface landmarks. Thalamus volumes were out of the normal range by the time of our earliest measurements and further decreased with time. The equation for the best curve fit is shown. We did not detect a difference between INCL in boys and girls ($P = .98$). The normal curve reflects thalamus volumes measured on 23 healthy volunteers 1.1–9.6 years of age participating in other studies at our institution; for the healthy volunteers, we did not find a statistical difference between boys and girls ($P = .89$) or between right and left ($P = .86$) (*dark line* = mean, *light lines* = ±2 SDs). For comparison, the onset ages of major clinical findings (mean and 95% CI) observed in our patients are plotted below the volume curve. A indicates developmental regression; B, cerebral atrophy noted in clinical MR imaging report; C, myoclonic jerks and seizures; D, loss of vision; E, deceleration of head growth; F, isoelectric visual-evoked potentials; and G, isoelectric EEG or electroretinogram.

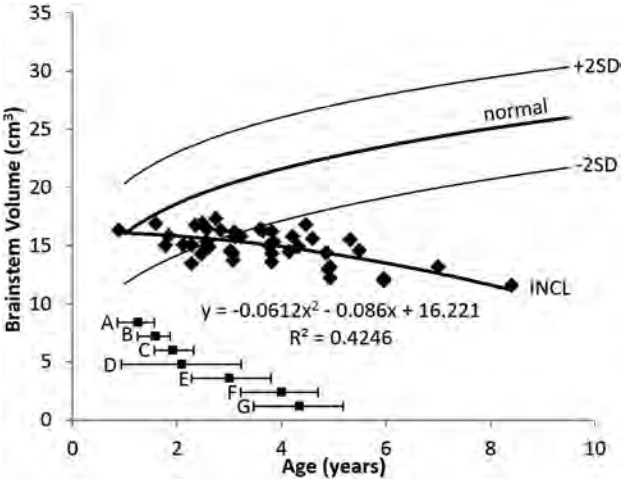

FIG 3. Brain stem volume measurements in patients with INCL. Brain stem volumes decreased with time, dropping below the 2.5th percentile before 3 years of age. The equation for the best curve fit is shown. We did not detect a difference between INCL in boys and girls ($P = .88$). We defined the brain stem as including the cerebral peduncles, midbrain, pons, and medulla. The normal curve reflects brain stem volumes measured on 23 healthy volunteers 1.1–9.6 years of age participating in other studies at our institution; for the healthy volunteers, we did not find a statistical difference between boys and girls ($P = .94$) (*dark line* = mean, *light lines* = ±2 SDs). For comparison, the onset ages of major symptoms (mean and 95% CI) observed in our patients are plotted below the volume curve. A indicates developmental regression; B, cerebral atrophy noted in clinical MR imaging report; C, myoclonic jerks and seizures; D, loss of vision; E, deceleration of head growth; F, isoelectric visual-evoked potentials; and G, isoelectric EEG or electroretinogram.

issue becomes worse as the disease advances. Therefore, we devised a scheme based on using surface landmarks to draw 3 perpendicular diameters of an ellipsoid to approximate the volume of the thalamus (On-line Fig 1). The same measurements were performed on our images of healthy volunteers.

Statistical Tests

We applied the Student *t* test to our total and segmental brain volumes to check for sexual dimorphism in our patients and healthy volunteers. The SD of the healthy volunteers (difference from the fitted curve) was also calculated.

Curve Fitting

For both patients and healthy volunteers, linear, quadratic, power, and logarithmic curves were fitted to the volume measurements as a function of age. For each measurement, the curve with the highest *r* value (Pearson correlation coefficient) is shown in the relevant figure.

RESULTS

Demographics

Forty-five scans were obtained in 10 patients; 43 of these scans could be used for volume calculations, while the other 2 had motion artifacts severe enough to exclude them from the analysis. Of the 43 useable scans, 25 were obtained in girls, and 18, in boys; the number of volume calculations performed for each patient ranged from 1 to 8. The overall age range of the patients at the time of the examination was 0.88–8.40 years. Applying the Student *t* test to the total brain volume and to the segmental brain volumes did not reveal sexual dimorphism in our sample; therefore, further analysis combined the results for boys and girls. Plotting segmental volumes for each mutation separately revealed overlapping curves with similar slopes (On-line Fig 2), confirming previous observations that these genotypes produce a uniform phenotype[19]; therefore, further analysis combined the results of all genotypes.

Thalamus Volume

The evolution of thalamus volumes is shown in Fig 2. The plot shows that the measurements on even the youngest patients were out of the normal range; the curve extrapolates into the normal range, suggesting that thalamus volume could have been normal (or near-normal) for a few months after birth. The initial decline in thalamus volume was gradual, and the rate of decline decreased with age. The pattern was best described by an exponential equation.

Brain Stem Volume

The evolution of brain stem volumes is shown in Fig 3. The plot shows that the measurements on the youngest patients fell within the normal range; therefore, we presume that the evolution before our measurements was normal. The initial decline in the brain stem volume was gradual, but the rate of decline increased with age. The pattern was best described by a quadratic equation. The patients' average fell out of the normal range (below the 2.5th percentile) by 3 years of age.

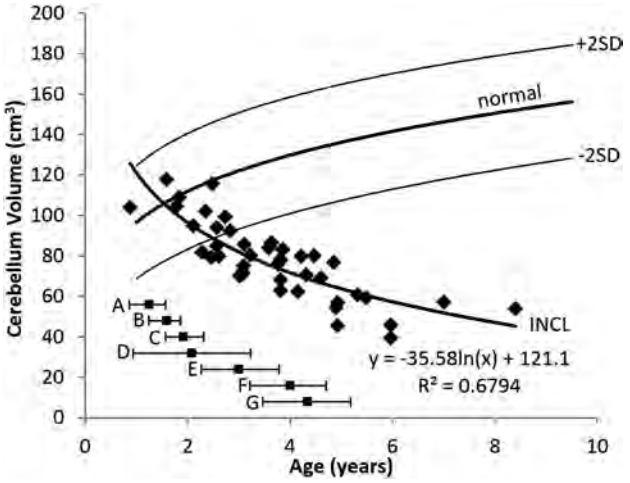

FIG 4. Cerebellum volume measurements in patients with INCL. Cerebellar volumes were initially near normal but decreased with time and dropped below the 2.5th percentile by about 2.5 years of age. The equation for the best curve fit is shown. We did not detect a difference between INCL in boys and girls ($P = .94$). We included the cerebellar peduncles in our measurement of cerebellar volume. The normal curve reflects cerebellum volumes measured on 23 healthy volunteers 1.1–9.6 years of age participating in other studies at our institution; for the healthy volunteers, we did not find a statistical difference between boys and girls ($P = .91$) (*dark line* = mean, light lines = ±2 SDs). For comparison, the onset ages of major symptoms (mean and 95% CI) observed in our patients are plotted below the volume curve. A indicates developmental regression; B, cerebral atrophy noted in clinical MR imaging report; C, myoclonic jerks and seizures; D, loss of vision; E, deceleration of head growth; F, isoelectric visual-evoked potentials; and G, isoelectric EEG or electroretinogram.

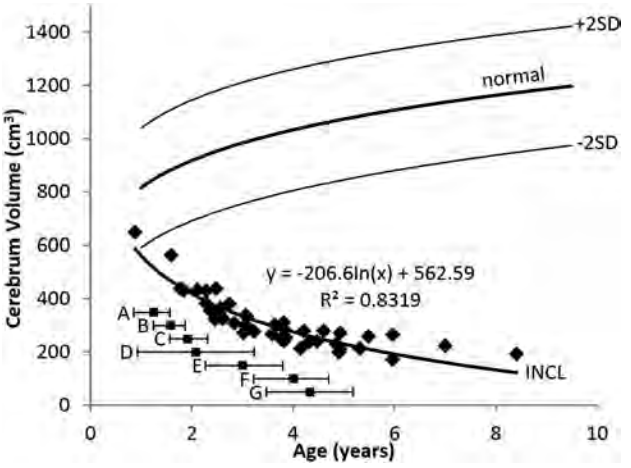

FIG 5. Cerebrum volume measurements in patients with INCL. Even our earliest measurements of cerebral volumes were lower than normal, and volumes decreased dramatically with time. The equation for the best curve fit is shown. We did not detect a difference between INCL in boys and girls ($P = .94$). We defined the cerebrum as including the deep nuclei but not the cerebral peduncles. The normal curve reflects cerebrum volumes measured on 23 healthy volunteers 1.1–9.6 years of age participating in other studies at our institution; for the healthy volunteers, we did not find a statistical difference between boys and girls ($P = .78$) (*dark line* = mean, *light lines* = ±2 SDs). For comparison, the onset ages of major symptoms (mean and 95% CI) observed in our patients are plotted below the volume curve. A indicates developmental regression; B, cerebral atrophy noted in clinical MR imaging report; C, myoclonic jerks and seizures; D, loss of vision; E, deceleration of head growth; F, isoelectric visual-evoked potentials; and G, isoelectric EEG or electroretinogram.

Cerebellum Volume

The evolution of the cerebellum volumes is shown in Fig 4. Our measurements of the youngest patients were in the normal range; therefore, we presume that the evolution before our measurements was normal. The decline in cerebellum volume was initially rapid (the patients' average dropped out of the normal range just after age 2 years) and slowed later. The pattern was best described by a logarithmic equation.

Cerebrum Volume

The evolution of the cerebrum volumes is shown in Fig 5. Only the baseline measurement of our youngest patient (at 10 months of age) was above the 2.5th percentile; all other measurements of cerebral volume were far below normal, and extrapolation of the curve to intersect the normal curve suggests that if the cerebral volumes were ever normal in the patients with INCL, it would have been only in the first few months after birth. The initial decline in cerebral volume was rapid, slowing later (possibly becoming asymptotic). The pattern was best described by a logarithmic equation.

Total Brain Volume

Because the total brain volume is thoroughly dominated by the cerebral volume, the pattern for the total brain volume closely followed that of the cerebral volume, with a rapid initial decline and slower decline later. However, because the decline of the cerebellum started later and did not proceed as rapidly, we did not observe asymptotic behavior in the total brain volume within the timeframe of the study. The pattern was best described by a logarithmic equation. The evolution of the total brain volume is shown in Fig 6.

Ratio of Segmental Volumes to Cerebrum Volume

In the healthy children, the cerebellum/cerebrum ratio and thalamus/cerebrum ratio changed very gradually with age, following a pattern best described by a quadratic equation; for the cerebellum, the peak ratio was at 5.8 years of age, and for the thalamus, the peak ratio was at 7.0 years of age. The normal brain stem/cerebrum ratio rose gradually throughout the age range we measured.

In the patients with INCL, the cerebellum/cerebrum ratio was more than twice the normal mean in nearly all of our baseline measurements. The ratio in the patients with INCL rose until about 5 years of age (the maximum of the fitted curve occurred at 4.97 years) and then fell off somewhat. This rising and falling pattern reflects the earlier involvement of the cerebrum relative to the cerebellum. The pattern was best described by a quadratic equation. Extrapolation of the fitted curve to earlier ages does not intersect with the normal curve; this finding suggests that the ratio may never have been normal in these patients. Because the initial measurements of cerebellum volumes were within the normal range, this suggests that the cerebral volume may never be really normal in these patients, not even in neonates or fetuses. The evolution of the ratio of cerebellum volume to cerebral volume is shown in Fig 7*A*.

The evolution of thalamus/cerebrum and brain stem/cerebrum volume ratios followed a pattern similar to that of the evolution of the cerebellum/cerebrum ratio, all best described by a

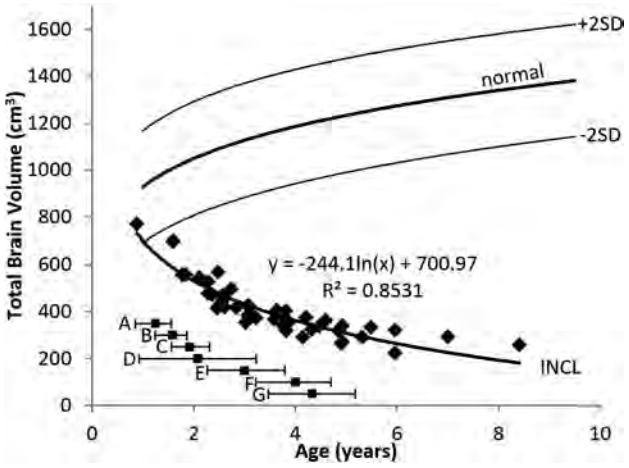

FIG 6. Total brain volume measurements in patients with INCL. Total brain volumes (dominated by the cerebral volume) were initially lower than normal and decreased dramatically with time. The equation for the best curve fit is shown. We did not detect a difference between INCL in boys and girls ($P = .96$). The normal curve reflects total brain volumes measured on 23 healthy volunteers 1.1–9.6 years of age participating in other studies at our institution; for the healthy volunteers, we did not find a statistical difference between boys and girls ($P = .80$) (*dark line* = mean, *light lines* = ±2SD). For comparison, the onset ages of major symptoms (mean and 95% CI) observed in our patients are plotted below the volume curve. A indicates developmental regression; B, cerebral atrophy noted in clinical MR imaging report; C, myoclonic jerks and seizures; D, loss of vision; E, deceleration of head growth; F, isoelectric visual-evoked potentials; and G, isoelectric EEG or electroretinogram.

quadratic equation. The thalamus/cerebrum volume ratio (Fig 7*B*) peaked at 4.96 years of age, and the brain stem/cerebrum volume ratio (Fig 7*C*) peaked at 5.89 years of age. The thalamus/cerebrum ratio started in the upper part of the normal range, rose out of the normal range (to about 50% more than the normal mean), and later returned to the upper part of the normal range. The brain stem/cerebrum ratio started at the upper extreme of the normal range and peaked at 3 times the normal mean. The later and higher peak of the brain stem/cerebrum ratio relative to the cerebellum/cerebrum ratio and thalamus/cerebrum ratio suggests later and less severe involvement of the brain stem relative to the cerebrum, thalamus, and cerebellum.

DISCUSSION

In this analysis, we have made detailed, quantitative serial measurements of brain volumes in a group of patients with INCL followed for up to 7 years. We have demonstrated that among the regions that we measured separately, atrophy begins earliest and proceeds fastest in the cerebrum, with the thalamus lagging slightly behind; there is later involvement of the cerebellum and then the brain stem. Although our patients had a variety of different gene mutations, the pattern and rate of atrophy that we observed did not appear to vary by genotype, in agreement with previous reports that these particular gene mutations are clinically indistinguishable.[16,19]

In the palmitoyl-protein thioesterase ($Ppt1^{-/-}$) mouse model of INCL, a previous microscopy study demonstrated that neuron loss starts in the sensory relay nuclei of the thalamus, first involving the visual system, then the auditory and somatosensory relay nuclei, and then the inhibitory reticular thalamic nucleus.[20] Loss of thalamic relay neurons was followed by loss of other neurons in the interconnected chains, with cortical interneurons preceding cortical granule neurons. Segmental atrophy of the cortex proceeded in the same order as the related thalamic nuclei; and within each segment, the interneuron layer was involved before the granule layer. The much coarser resolution of our MR imaging measurements could not resolve individual thalamic nuclei or reliably measure the thickness of the atrophied cerebral cortex, so we were unable to observe these processes in our patients. In contrast to the results in $Ppt1^{-/-}$ mice,[20] we observed that measurable cerebral atrophy preceded measurable thalamus atrophy. An earlier study of the mouse model[21] found that fractional volume loss in the thalamus was greater than that in the cerebrum, also opposite to our findings; these discrepancies are consistent with previously reported differences between the mouse model and human disease.[21] Our results are in agreement with the mouse model in demonstrating that atrophy of the cerebrum precedes atrophy of the cerebellum.[21]

Extrapolation of our cerebral volume curve to ages younger than those included in our study suggests that if the cerebral volume was ever normal, it would have been in the normal range for, at most, a few months after birth. Extrapolation of the cerebellum-to-cerebrum volume ratio suggests that the cerebral volume may never have been normal, not even in the fetus. A previous MR spectroscopy study[22] found low NAA in the cerebral white matter of a patient at 4 months of age. In the separately reported MR spectroscopy component of the current study,[11] we found that extrapolation of cerebral NAA levels beyond the age of our youngest patient does not appear to intersect the normal curve. NAA is produced mainly (or perhaps exclusively) by healthy neurons,[23,24] and a decline in the level of NAA indicates loss or injury of neurons. Logically, loss or injury of neurons should precede atrophy; therefore, the timing of our cerebral atrophy observations is consistent with the timing of NAA decline observed in the previous MR spectroscopy reports.

Extrapolation of our thalamus volume curve suggests that the thalamus volume may have been in the normal range before 6 months of age. Extrapolation of our previously published measurements of NAA in the thalamus[11] suggests that NAA in the thalamus may be in the normal range for a few months after birth; previous measurements[22] on very young children with INCL have demonstrated normal NAA in the thalamus of a 2-month-old child and a slight deficit of NAA in the thalamus of a 4-month-old child. Thus, the relative order of volume loss (cerebrum before thalamus) that we report in this study is concordant with the order of previously reported MR spectroscopy changes in humans.

Both cerebellum and brain stem volumes measured on our youngest patients fell into the normal range, with the curve for the cerebellum volume dropping below the 2.5th percentile at about 2.5 years of age and the curve for the brain stem volume dropping below the 2.5th percentile by about 3 years of age. Extrapolation of the MR spectroscopy results that we previously reported measuring NAA in the cerebellum and brain stem[11] suggests that NAA levels are probably normal at these locations for up to a year after birth. As with NAA in the cerebrum, it would be expected that neuron injury or loss would precede the observation of atrophy,

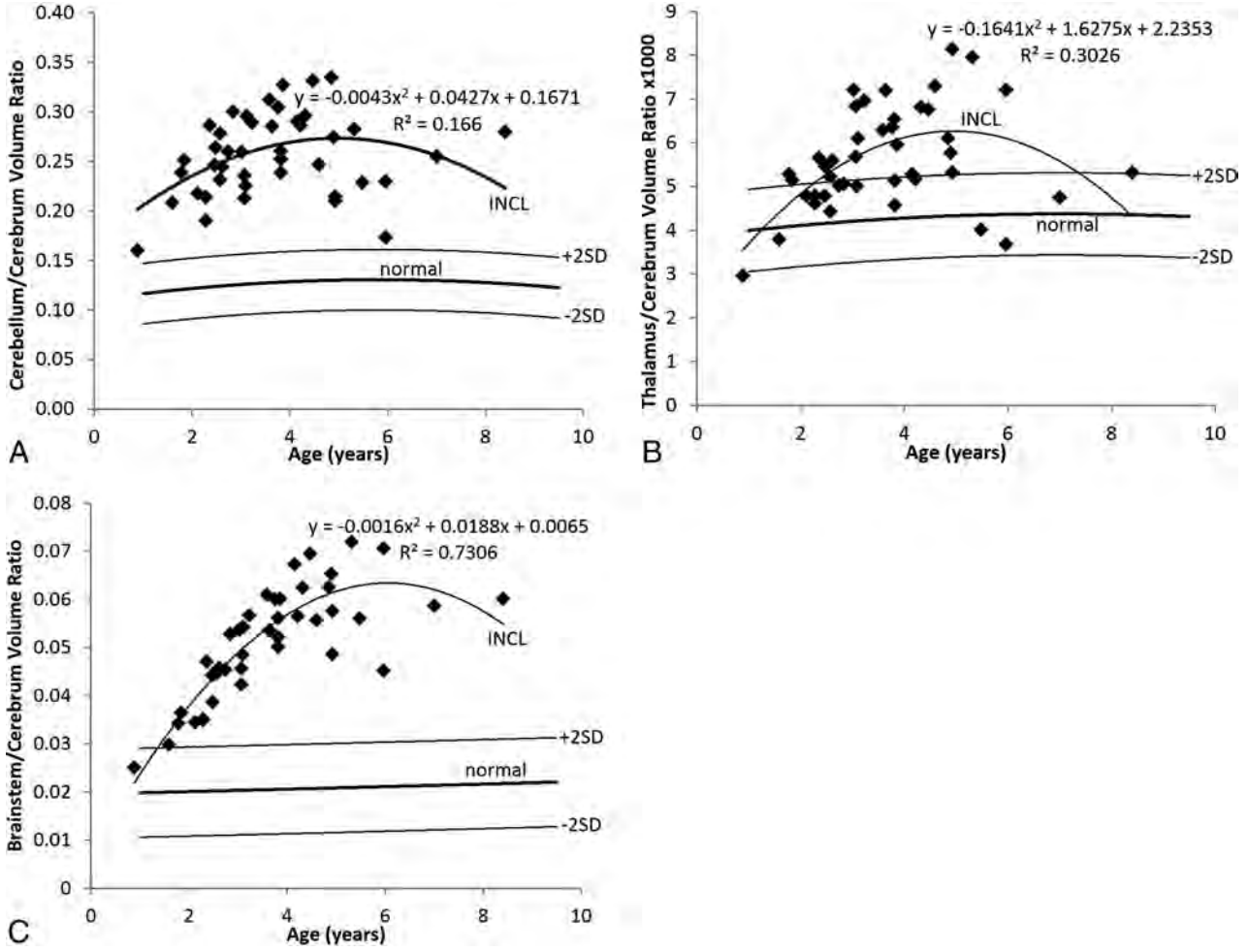

FIG 7. Relative segmental volumes in patients with INCL. *A*, In INCL, the cerebellum is large relative to the cerebrum, reflecting the observation that volume loss begins earlier and progresses faster in the cerebrum than elsewhere in the brain. The ratio initially rises as cerebral loss outpaces cerebellar loss and decreases later because the cerebrum reaches asymptotic volume earlier than the cerebellum. *B*, In INCL, the thalamus becomes somewhat large relative to the cerebrum for a while, reflecting the tight linkage between the volumes of these structures with a bit of a delay in involvement of the thalamus relative to the cerebrum. *C*, In INCL, the brain stem is also large relative to the cerebrum, with a later peak relative to both the thalamus/cerebrum ratio and cerebellum/cerebrum ratio, indicating that the brain stem is involved last among the structures that we measured. In all plots, the equation describes the best curve fit to the INCL results. We did not detect a difference between boys and girls for either patients with INCL or healthy volunteers. The normal curves reflect volume ratios measured on 23 healthy volunteers 1.1–9.6 years of age participating in other studies at our institution (*dark line* = mean, *light lines* = ±2 SDs).

so the patterns we observed in the cerebellum and brain stem volume measurements are consistent with the pattern observed in our MR spectroscopy measurements.

We would have liked to have compared our quantitative atrophy measurements with previous reports on the natural history of volume loss in INCL,[16,25] to evaluate the treatment benefits of cysteamine bitartrate and *N*-acetyl cysteine; in particular, we would have liked to determine whether the treatment resulted in any delay in atrophy onset or any slowing of the rate of atrophy. However, because all previous studies evaluating atrophy in INCL used qualitative scoring without correspondence to any particular absolute or fractional volume loss, we could not determine the effect of the treatment on brain atrophy. The sequence of brain involvement we observed agreed with that in the previous qualitative reports.

The measurements we present here are quantitative and should be reproducible. Although we were not able to compare our results directly with the previous qualitative studies of brain atrophy in INCL, the detailed quantitative measurements we have made of the temporal progression of atrophy in INCL in the patients under treatment with cysteamine bitartrate and *N*-acetyl cysteine will be useful as a reference for comparative evaluation of future treatment trials.

CONCLUSIONS

We made quantitative measurements of brain volumes in treated patients with INCL. The pattern of volume loss suggests that the order of involvement was cerebrum, thalamus, cerebellum, and brain stem, in agreement with other previously published studies of this disease in humans. In contrast to other previously published reports, we have made quantitative measurements of the volume of the brain (and several major divisions). As a reproducible quantitative measure, these volumes can be used as a surrogate outcome measure in future treatment trials to compare proposed treatments with one another and potentially detect small

differences that may not be apparent if coarser outcome measures (such as qualitative evaluation of symptoms) are used.

ACKNOWLEDGMENTS

We thank the patients (and their families) who participated in this study, and the MR imaging technologists (Bonita Damaska, Mastaneh Owhadi, and Betty Wise) who scanned them. We also thank Armin Raznahan and Audrey Thurm for the use of their images of healthy volunteers.

REFERENCES

1. Anderson GW, Goebel HH, Simonati A. **Human pathology in NCL.** *Biochim Biophys Acta 2* 2013;1832:1807–26 CrossRef Medline
2. Mole SE, Williams RE, Goebel HH. *The Neuronal Ceroid Lipofuscinoses (Batten Disease).* Oxford: Oxford University Press; 2011
3. Haltia M. **The neuronal ceroid-lipofuscinoses: from past to present.** *Biochim Biophys Acta* 2006;1762:850–56 CrossRef Medline
4. Platt FM, Boland B, van der Spoel AC. **The cell biology of disease: lysosomal storage disorders: the cellular impact of lysosomal dysfunction.** *J Cell Boil* 2012;199:723–34 CrossRef Medline
5. Rider JA, Rider DL. **Batten disease: past, present, and future.** *Am J Med Genet Suppl* 1988;5:21–26 Medline
6. Warrier V, Vieira M, Mole SE. **Genetic basis and phenotypic correlations of the neuronal ceroid lipofusinoses.** *Biochi Biochim Biophys Acta* 2013;1832:1827–30 CrossRef Medline
7. Mole SE, Cotman SL. **Genetics of the neuronal ceroid lipofuscinoses (Batten disease).** *Biochim Biophys Acta* 2015;1852:2237–41 CrossRef Medline
8. Haltia M, Rapola J, Santavuori P. **Infantile type of so-called neuronal ceroid-lipofuscinosis: histological and electron microscopic studies.** *Acta Neuropathol* 1973;26:157–70 CrossRef Medline
9. Vesa J, Hellsten E, Verkruyse LA, et al. **Mutations in the palmitoyl protein thioesterase gene causing infantile neuronal ceroid lipofuscinosis.** *Nature* 1995;376:584–87 CrossRef Medline
10. Vanhanen SL, Sainio K, Lappi M, et al. **EEG and evoked potentials in infantile neuronal ceroid-lipofuscinosis.** *Dev Med Child Neurol* 1997;39:456–63 Medline
11. Baker EH, Levin SW, Zhang Z, et al. **Evaluation of disease progression in INCL by MR spectroscopy.** *Ann Clin Transl Neurol* 2015;2:797–809 CrossRef Medline
12. Goebel HH, Wisniewski KE. **Current state of clinical and morphological features in human NCL.** *Brain Pathol* 2004;14:61–69 CrossRef Medline
13. Santavuori P, Vanhanen SL, Sainio K, et al. **Infantile neuronal ceroid-lipofuscinosis (INCL): diagnostic criteria.** *J Inherit Metab Dis* 1993;16:227–29 CrossRef Medline
14. Zhang Z, Butler JD, Levin SW, et al. **Lysosomal ceroid depletion by drugs: therapeutic implications for a hereditary neurodegenerative disease of childhood.** *Nat Med* 2001;7:478–84 CrossRef Medline
15. Bavarsad Shahripour R, Harrigan MR, Alexandrov AV. **N-acetylcysteine (NAC) in neurological disorders: mechanisms of action and therapeutic opportunities.** *Brain Behav* 2014;4:108–22 CrossRef Medline
16. Levin SW, Baker EH, Zein WM, et al. **Oral cysteamine bitartrate and N-acetylcysteine for patients with infantile neuronal ceroid lipofuscinosis: a pilot study.** *Lancet Neurol* 2014;13:777–87 CrossRef Medline
17. Miao N, Levin SW, Baker EH, et al. **Children with infantile neuronal ceroid lipofuscinosis have an increased risk of hypothermia and bradycardia during anesthesia.** *Anesth Analg* 2009;109:372–78 CrossRef Medline
18. McAuliffe MJ, Lalonde FM, McGarry D, et al. **Medical image processing, analysis and visualization in clinical research.** In: *Proceedings of the 14th IEEE Symposium on Computer-Based Medical Systems,* Washington, DC. July 26–27, 2001:381–86 CrossRef
19. Das AK, Becerra CH, Yi W, et al. **Molecular genetics of palmitoyl-protein thioesterase deficiency in the U.S.** *J Clin Invest* 1998;102:361–70 CrossRef Medline
20. Kielar C, Maddox L, Bible E, et al. **Successive neuron loss in the thalamus and cortex in a mouse model of infantile neuronal ceroid lipofuscinosis.** *Neurobiol Dis* 2007;25:150–62 CrossRef Medline
21. Bible E, Gupta P, Hofmann SL, et al. **Regional and cellular neuropathology in the palmitoyl protein thioesterase-1 null mutant mouse model of infantile neuronal ceroid lipofuscinosis.** *Neurobiol Dis* 2004;16:346–59 CrossRef Medline
22. Vanhanen SL, Puranen J, Autti T, et al. **Neuroradiological findings (MRS, MRI, SPECT) in infantile neuronal ceroid-lipofuscinosis (infantile CLN1) at different stages of the disease.** *Neuropediatrics* 2004;35:27–35 CrossRef Medline
23. Miller BL. **A review of chemical issues in 1H NMR spectroscopy: N-acetyl-L-aspartate, creatine and choline.** *NMR Biomed* 1991;4:47–52 CrossRef Medline
24. Simmons ML, Frondoza CG, Coyle JT. **Immunocytochemical localization of N-acetyl-aspartate with monoclonal antibodies.** *Neuroscience* 1991;45:37–45 CrossRef Medline
25. Vanhanen SL, Raininko R, Autti T, et al. **MRI evaluation of the brain in infantile neuronal ceroid-lipofuscinosis, part 2: MRI findings in 21 patients.** *J Child Neurol* 1995;10:444–50 CrossRef Medline

The Prevalence of Malformations of Cortical Development in a Pediatric Hereditary Hemorrhagic Telangiectasia Population

G.J. Palagallo, S.R. McWilliams, L.A. Sekarski, A. Sharma, M.S. Goyal, and A.J. White

ABSTRACT

BACKGROUND AND PURPOSE: Brain AVM, cerebral abscess, and ischemic stroke are among the well known neurologic manifestations of hereditary hemorrhagic telangiectasia. However, recently reported data suggest an additional association with malformations of cortical development. The purpose of this study was to determine the prevalence of malformations of cortical development in a population of pediatric patients with hereditary hemorrhagic telangiectasia.

MATERIALS AND METHODS: A retrospective review of brain MRIs from 116 pediatric patients was performed. Each patient was referred from our institution's Hereditary Hemorrhagic Telangiectasia Clinic. Each MRI included a 3D sequence, most frequently MPRAGE. The 3D sequence was evaluated by a neuroradiology fellow, with specific attention to the presence or absence of malformations of cortical development. Positive studies were subsequently reviewed by 2 attending neuroradiologists, who rendered a final diagnosis.

RESULTS: Fourteen of 116 (12.1%) patients were found to have a malformation of cortical development. Among these 14, there were 12 cases of polymicrogyria and 2 cases of bifrontal periventricular nodular heterotopia.

CONCLUSIONS: Pediatric patients with hereditary hemorrhagic telangiectasia have a relatively high prevalence of malformations of cortical development, typically perisylvian polymicrogyria.

ABBREVIATIONS: HHT = hereditary hemorrhagic telangiectasia; MCD = malformation of cortical development; PMG = polymicrogyria

Hereditary hemorrhagic telangiectasia (HHT) is an autosomal dominant disorder with a geography-dependent prevalence that ranges from approximately 1/5000 to 1/8000 in Japan to 1/10,000 in the United Kingdom.[1,2] HHT is diagnosed clinically based on the Curacao criteria, which include: 1) spontaneous and recurrent epistaxis, 2) mucocutaneous telangiectasias, 3) visceral AVMs, and 4) a first-degree relative who has the disease. If 3 or 4 of the criteria are present, a patient is considered to have "definite" HHT. "Possible" HHT requires that 2 criteria be present, whereas patients with fewer than 2 positive criteria are considered "unlikely" to have the disease. HHT results from various mutations in genes involved in signaling in the transcription growth factor–β pathway in vascular endothelial cells. Known mutations include *endoglin* (*ENG*), *activin receptor-like kinase* (*ALK1*), and *SMAD4*.[3-6] Cerebral manifestations of HHT include brain AVMs, which are estimated to occur in 10%–20% of patients.[7] In addition, pulmonary AVMs are present in approximately 30% of patients with HHT. The presence of a right-to-left pulmonary shunt predisposes patients with HHT to cerebral abscess and embolic stroke.[8,9]

Malformations of cortical development (MCDs) encompass a broad array of disorders seen in patients with developmental delay and epilepsy. Included in this category is polymicrogyria (PMG), a term that refers to cerebral cortex that contains unusually small convolutions.[10] MRI features of PMG include small gyri separated by thin, shallow sulci. This often results in the appearance of a thickened cortex with irregularity of the cortical surface and gray-white junction.[11] Heterotopia is another MCD, resulting from abnormal neuronal migration and most commonly manifesting in a nodular periventricular form.[12] A variety of syndromes and genetic mutations have been shown to be associated with PMG.[10,12] Data reported at the 10th International Scientific HHT Conference in 2013 suggested an 8% prevalence of MCDs in the HHT population.[13] However, to date, there have been no publications in the scientific literature describing an association be-

Received June 22, 2016; accepted after revision August 29.

From the Mallinckrodt Institute of Radiology (G.J.P., S.R.M., A.S., M.S.G.) and Department of Pediatrics (L.A.S., A.J.W.), Washington University in St. Louis School of Medicine, St. Louis, Missouri.

M.S. Goyal and A.J. White are senior authors who contributed equally to this work.

Paper previously presented at: American Society of Neuroradiology Annual Meeting 2016, May 21–26, 2016; Washington, D.C.

Please address correspondence to Gerald J. Palagallo, MD, 366 West Point Ct, St. Louis, MO 63130; e-mail: gerald.palagallo@gmail.com

http://dx.doi.org/10.3174/ajnr.A4980

tween MCDs and HHT. Our study aims to determine the prevalence of PMG and other MCDs in pediatric patients with HHT.

MATERIALS AND METHODS

We identified 116 pediatric patients—referred to our institution's HHT clinic between 2005 and 2015—who underwent a brain MRI that included at least 1 high-resolution 3D sequence. At our institution, children being evaluated for HHT are routinely screened with brain MRI. In most cases, the 3D sequence was T1 MPRAGE, which is routinely performed at our institution for pediatric brain MRI. All MRI examinations were performed at either 1.5T or 3T. Each MRI was retrospectively evaluated with specific attention to the presence or absence of MCDs by a neuroradiology fellow (G.J.P.). For each case, the radiology report was consulted with attention to documentation of MCDs. Potentially positive cases were then confirmed by 2 board-certified attending neuroradiologists (M.S.G., A.S.), with 2 and 10 years of experience, respectively. For each of the 116 patients, the following information was acquired from the electronic medical record and a pediatric HHT data base: sex, age, diagnosis by Curacao criteria, genetic testing (if available), and the presence or absence of pulmonary and brain AVMs. For each patient who screened positive, the medical record was reviewed to document history of neurologic symptoms with particular attention to the presence or absence of epilepsy. Descriptive statistics were computed, and associations were tested with the Fisher exact test. The criterion for statistical significance was $P < .05$.

Table 1: Summary of 116 patients

Characteristic	Summary
Demographics, no. (%)	
Female sex	63/116 (54.3)
Age (yr)	9.2 ± 4.4
HHT-causing mutation, no. (%)	
Endoglin	31/46 (67.4)
ALK1	10/46 (21.7)
SMAD4	1/46 (2.2)
All tests negative	4/46 (8.7)
Vascular malformations, no. (%)	
Brain AVM	18/116 (15.5)
Pulmonary AVM	38/113 (33.6)
Curacao criteria, no. (%)	
Definite	78/116 (67.2)
Possible or suspected	34/116 (29.3)
Unlikely	4/116 (3.4)

RESULTS

Demographic information, genetic mutation status, and other clinical data for the 116 patients are detailed in Table 1. Because our institution is an HHT Center of Excellence for adults and children, most patients included in our pediatric HHT data base are the children of adults with known HHT, thus accounting for the higher proportion of children meeting Curacao criteria for definite HHT. Fourteen of 116 (12.1%) patients were found to have an MCD (Table 2). The positive studies included 12 cases of PMG (12/116, 10.3%) and 2 cases of bifrontal periventricular nodular heterotopia (2/116, 1.7%). Two sets of siblings were positive for MCD. This included a set of 3 boys, 2 of whom had perisylvian PMG, with the other sibling having periventricular nodular heterotopia (Fig 1). An additional set of 2 sisters each had perisylvian PMG, but in opposite cerebral hemispheres. The siblings of 2 other positive cases were negative for MCD.

PMG was seen unilaterally in all 12 instances. Multifocal PMG was seen in 4/12 cases. In 1 case, PMG was seen adjacent to a previously resected AVM. In 2 patients, focal PMG was seen immediately adjacent to a small AVM (Fig 2). In another case, PMG was noted to line a large porencephalic cyst. Clinically, this patient had both epilepsy and hemiplegia and was the only patient to exhibit either of those manifestations among the cases of MCD. Additional neurologic symptoms included 6 patients with headaches, 1 with a gait disorder, and 1 with a prior stroke (Table 2).

AVMs were seen more frequently in patients with MCD compared with those without MCD. Eight of 13 (61.5%) patients with MCD who underwent testing had a pulmonary AVM; 30/100 (30.0%) of patients without MCD who underwent testing had a pulmonary AVM ($P = .029$). Five of 14 (35.7%) patients with MCD also had a brain AVM, compared with 13/102 (12.7%) patients without MCD ($P = .042$).

Table 2: Description of 14 patients with MCD

Patient	Age	Sex	Curacao	Genetics	Family Genetics	Pulmonary AVM	Brain AVM	Neurologic History	MCD
A	8 yr	F	4	*ENG*	*ENG*	Y	Y	Headache	L perisylvian PMG
B	3 yr	M	3		*ENG*	Y	N		1) L perisylvian PMG, 2) L inferior temporal PMG
C	3 yr	F	4		Ind	Y	Y	Headache	L perisylvian PMG
D	7 yr	F	4			Y	N	Headache	1) R perisylvian PMG, 2) R parietal PMG
E	8 yr	F	4			Y	N	Headache	L temporal PMG
F	3 mo	F	2	*ENG*	*ENG*	N	N	Gait disorder	R perisylvian PMG
G	5 yr	F	4	*ENG*	*ENG*	Y	Y	Stroke	L perisylvian PMG along margin of AVM resection cavity
H	9 yr	M	3			N	N	Headache	Bifrontal periventricular nodular heterotopia
I	11 yr	M	3			N	N		L parietal PMG
J	12 yr	M	4			Ind	N		L perisylvian PMG
K	11 yr	M	2		*ENG*	N	Y	Headache	1) R parietotemporal PMG, 2) R frontal PMG adjacent to AVM
L	15 yr	F	2		*SMAD4*	N	N		Bifrontal periventricular nodular heterotopia
M	8 yr	M	4			Y	Y		1) R frontal PMG adjacent to small AVM, 2) R mesial temporal PMG
N	7 yr	F	4			Y	N	Hemiplegia, epilepsy	L frontal PMG adjacent to large porencephalic cyst

Note:—Ind indicates indeterminate; L, left; R, right.

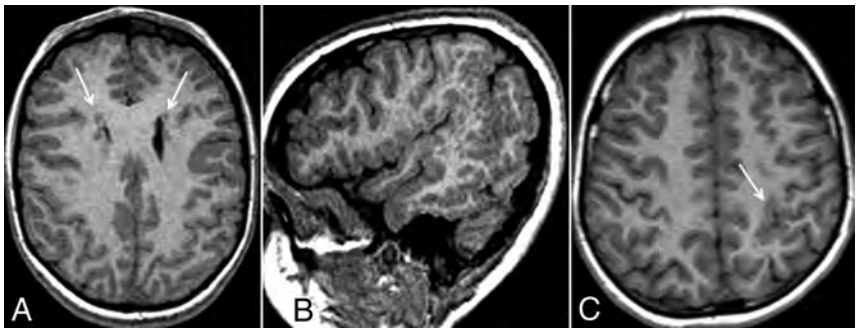

FIG 1. Three siblings with HHT and malformations of cortical development. Axial T1 MPRAGE demonstrates bilateral periventricular nodular heterotopia (*A*, *arrows*) in a 9-year-old boy. Sagittal T1 MPRAGE demonstrates extensive perisylvian PMG (*B*) in a 12-year-old boy. Axial T1 MPRAGE demonstrates thickened and excessively convoluted cortex in the left posterior frontoparietal region (*C*, *arrow*), consistent with PMG.

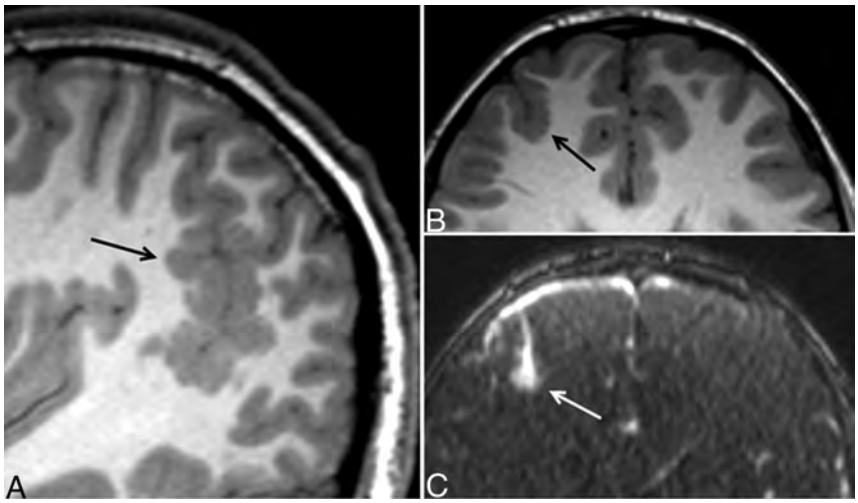

FIG 2. Eleven-year-old boy with unilateral, multifocal PMG and an AVM. Sagittal T1 MPRAGE shows extensive PMG in the right parietotemporal region (*A*, *arrow*). An additional, smaller focus of PMG is seen in the right frontal lobe (*B*, *arrow*). Immediately adjacent to the right frontal PMG, postcontrast MRA demonstrates a small enhancing nidus (*C*, *arrow*) with cortical venous drainage, consistent with an AVM.

DISCUSSION

This study demonstrated a relatively high prevalence (12.1%) of MCD within a pediatric HHT population, consistent with the results reported in the conference abstract by Bergerot et al[13] in 2013. Most cases of MCD were PMG, seen predominantly in a perisylvian distribution, which is the most common location for PMG in general.[14] The prevalence of PMG in the general population is unknown, but is likely quite rare. Large series of brain MRIs of healthy, asymptomatic patients reported no cases of PMG.[15,16] A study looking at incidental brain MRI findings in 120 healthy Japanese children, which included MPRAGE sequences, also reported no cases of PMG.[17] Many possible causes for PMG have been identified, including various in utero neurologic insults. Prenatal infection with cytomegalovirus has been associated with the development of PMG.[18] In utero ischemic insults have also been implicated as a cause of both layered and unlayered PMG.[19] PMG has been described in association with several genetic mutations and metabolic diseases.[10,12]

Although the cause for MCD in HHT is unclear, the distribution of PMG in our cases supports a regional rather than global pathogenesis. Twelve of 12 cases were unilateral, which is notable for the fact that a prior series of 71 cases of PMG showed unilaterality in only 42% of cases.[14] In another series of 328 patients with PMG, the unilateral perisylvian pattern was seen only 9% of the time.[20] The genetic basis for HHT is abnormal vascular development related to various mutations in the transcription growth factor-β pathway. Three of our cases provide circumstantial support of abnormal vascular development being associated with PMG by virtue of spatial proximity. This includes 2 cases of a small AVM directly adjacent to focal PMG and another case with PMG lining an AVM resection cavity.

Notably, the prevalence of both brain AVMs and pulmonary AVMs was significantly higher in our patients with MCD compared with those without MCD. In 1 of our cases, PMG was seen adjacent to a porencephalic cyst, an association that has been described previously and attributed to prenatal ischemia.[21] The pathogenesis of brain AVMs and vascular dysplasia has been recently investigated in mouse models of HHT. Given the results of our study, it would be informative to investigate for cortical malformations in these mouse models.

Genetic testing was not available for most of our cases, but at least 5 of 12 cases with PMG were very likely in patients with *ENG* mutations. *Endoglin* mRNA expression peaks throughout the brain during the latter half of gestation and the perinatal period and, in the brain, spatiotemporally correlates with the expression of other genes involved with transcription growth factor-β–mediated angiogenesis, such as *ALK1*, another gene implicated in HHT.[22]

The clinical manifestations of PMG are widely variable, including developmental delay, cognitive abnormalities, and epilepsy. The incidence of epilepsy in the setting of PMG has been reported to be as high as 78%.[20] However, in our study, only 1 patient, who had a large porencephalic cyst in the left cerebral hemisphere, had documented epilepsy. A review of 87 patients with PMG and epilepsy found that a more extensive distribution of PMG correlated with an earlier age of seizure onset.[23] More favorable clinical outcomes are seen when PMG is unilateral, localized, and not associated with other structural malformations.[10] Our findings suggest that PMG in the HHT population may be subclinical, possibly because of its unilaterality and lack of association with other major structural abnormalities. Nevertheless, it is likely prudent to consider the possibility of PMG as a cause for seizures in patients with HHT and

epilepsy, in addition to the more well-known causes such as brain AVM, abscess, and infarct.

Our study is limited by its retrospective nature and variability in MR imaging protocols that may alter the sensitivity for cortical malformations or brain AVMs. At present, PMG is likely underdiagnosed in the HHT population, as evidenced by the fact that several of the cases with PMG were only identified in this retrospective review. Our results suggest that a high spatial resolution sequence in brain MRIs performed for HHT evaluation may be useful.

CONCLUSIONS

In summary, our study confirms a high prevalence of MCDs in the pediatric HHT population, particularly perisylvian PMG. Our data suggest that PMG in this setting is typically subclinical, but can be associated with epilepsy and often coexists with other manifestations of HHT. Moreover, though the underlying pathogenesis of MCDs in HHT remains unknown, our findings suggest an association between vascular anomalies and PMG.

Disclosures: Manu Goyal—*UNRELATED*: *Grants/Grants Pending*: ASNR/RSNA Scholar Grant,* McDonnell Center for Systems Neuroscience,* *Comments*: Scholar Grant 2015–2017, McDonnell Center Grant to obtain lifespan MRA data. *Money paid to the institution.

REFERENCES

1. Dakeishi M, Shioya T, Wada Y, et al. **Genetic epidemiology of hereditary hemorrhagic telangiectasia in a local community in the northern part of Japan.** *Hum Mutat* 2002;19:140–48 CrossRef Medline
2. Donaldson JW, McKeever TM, Hall IP, et al. **The UK prevalence of hereditary haemorrhagic telangiectasia and its association with sex, socioeconomic status and region of residence: a population-based study.** *Thorax* 2014;69:161–67 CrossRef Medline
3. McAllister KA, Grogg KM, Johnson DW, et al. **Endoglin, a TGF-beta binding protein of endothelial cells, is the gene for hereditary haemorrhagic telangiectasia type 1.** *Nat Genet* 1994;8:345–51 CrossRef Medline
4. Johnson DW, Berg JN, Baldwin MA, et al. **Mutations in the activin receptor-like kinase 1 gene in hereditary haemorrhagic telangiectasia type 2.** *Nat Genet* 1996;13:189–95 CrossRef Medline
5. Gallione CJ, Repetto GM, Legius E, et al. **A combined syndrome of juvenile polyposis and hereditary haemorrhagic telangiectasia associated with mutations in MADH4 (SMAD4).** *Lancet* 2004;363:852–59 CrossRef Medline
6. Govani FS, Shovlin CL. **Hereditary haemorrhagic telangiectasia: a clinical and scientific review.** *Eur J Hum Genet* 2009;17:860–71 CrossRef Medline
7. Fulbright RK, Chaloupka JC, Putman CM, et al. **MR of hereditary hemorrhagic telangiectasia: prevalence and spectrum of cerebrovascular malformations.** *AJNR Am J Neuroradiol* 1998;19:477–84 Medline
8. Kjeldsen AD, Tørring PM, Nissen H, et al. **Cerebral abscesses among Danish patients with hereditary haemorrhagic telangiectasia.** *Acta Neurol Scand* 2014;129:192–97 CrossRef Medline
9. Angriman F, Ferreyro BL, Wainstein EJ, et al. **Pulmonary arteriovenous malformations and embolic complications in patients with hereditary hemorrhagic telangiectasia.** *Arch Bronconeumol* 2014;50:301–04 CrossRef Medline
10. Guerrini R, Dobyns WB. **Malformations of cortical development: clinical features and genetic causes.** *Lancet Neurol* 2014;13:710–26 CrossRef Medline
11. Barkovich AJ. **MRI analysis of sulcation morphology in polymicrogyria.** *Epilepsia* 2010;51:17–22 CrossRef Medline
12. Barkovich AJ, Guerrini R, Kuzniecky RI, et al. **A developmental and genetic classification for malformations of cortical development: update 2012.** *Brain* 2012;135:1348–69 CrossRef Medline
13. Bergerot JF, Dupuis-Girod S, Berthezene Y, et al. Malformations of cortical development and brain vessels in patients with hereditary haemorrhagic telangiectasia. In: *10th International Hereditary Hemorrhagic Telangiectasia Scientific Conference*, Cork, Ireland. June 12–15, 2013
14. Hayashi N, Tsutsumi Y, Barkovich AJ. **Polymicrogyria without porencephaly/schizencephaly. MRI analysis of the spectrum and the prevalence of macroscopic findings in the clinical population.** *Neuroradiology* 2002;44:647–55 CrossRef Medline
15. Katzman GL, Dagher AP, Patronas NJ. **Incidental findings on brain magnetic resonance imaging from 1000 asymptomatic volunteers.** *JAMA* 1999;282:36–39 CrossRef Medline
16. Weber F, Knopf H. **Incidental findings in magnetic resonance imaging of the brains of healthy young men.** *J Neurol Sci* 2006;240:81–84 CrossRef Medline
17. Seki A, Uchiyama H, Fukushi T, et al. **Incidental findings of brain magnetic resonance imaging study in a pediatric cohort in Japan and recommendation for a model management protocol.** *J Epidemiol* 2010;20(suppl 2):S498–504 CrossRef Medline
18. Barkovich AJ, Lindan CE. **Congenital cytomegalovirus infection of the brain: imaging analysis and embryologic considerations.** *AJNR Am J Neuroradiol* 1994;15:703–15 Medline
19. Barkovich AJ, Rowley H, Bollen A. **Correlation of prenatal events with the development of polymicrogyria.** *AJNR Am J Neuroradiol* 1995;16:822–27 Medline
20. Leventer RJ, Jansen A, Pilz DT, et al. **Clinical and imaging heterogeneity of polymicrogyria: a study of 328 patients.** *Brain* 2010;133:1415–27 CrossRef Medline
21. Levine DN, Fisher MA, Caviness VS Jr. **Porencephaly with microgyria: a pathologic study.** *Acta Neuropathol* 1974;29:99–113 CrossRef Medline
22. © 2015 Allen Institute for Brain Science. BrainSpan Atlas of the Developing Human Brain [Internet]. Available from: http://brainspan.org. Accessed April 1, 2016
23. Shain C, Ramgopal S, Fallil Z, et al. **Polymicrogyria-associated epilepsy: a multicenter phenotypic study from the Epilepsy Phenome/Genome Project.** *Epilepsia* 2013;54:1368–75 CrossRef Medline

Palliative CT-Guided Cordotomy for Medically Intractable Pain in Patients with Cancer

T.M. Shepherd, M.J. Hoch, B.A. Cohen, M.T. Bruno, E. Fieremans, G. Rosen, D. Pacione, and A.Y. Mogilner

ABSTRACT

SUMMARY: Palliative cervical cordotomy can be performed via percutaneous radiofrequency ablation of the lateral C1–2 spinothalamic tract. This rare procedure can be safe, effective, and advantageous in mitigating medically intractable unilateral extremity pain for selected patients with end-stage cancer. This report reviews the indications, techniques, risks, and potential benefits of cordotomy. We describe our recent experience treating 3 patients with CT-guided C1–2 cordotomy and provide the first characterization of spinal cord diffusion MR imaging changes associated with successful cordotomy.

Up to 50% of patients with cancer have undertreated pain[1] and continue to experience pain even after oral and intrathecal therapy are maximized.[2,3] Intrathecal opioid administration can provide potent anesthesia but requires an operation with general anesthesia, regular medical follow-up, restricts patient mobility, and increases infection risks. These requirements may be detrimental to quality of life for patients with end-stage cancer. In such patients, percutaneous CT-guided C1–2 cordotomy can provide immediate pain relief by selective ablation of the lateral spinothalamic tract that transmits pain, temperature, and deep touch sensation. This procedure is inexpensive and does not require an operating room, hospitalization, or outpatient follow-up. Cordotomy can reduce oversedation and memory disturbance associated with high-dose opioid therapy, thus enabling patients better interpersonal interactions at the end of their lives. Two recent series outside North America reported that patients with end-stage cancer with extremity pain experienced 40%–83% increases in Karnofsky Performance Status and 83%–86% reductions in pain immediately after cordotomy.[4,5] Pain relief was sustained for 6 months in most patients.[5,6] Furthermore, there is a GRADE 1c recommendation[7] for cordotomy to treat patients with cancer with poorly controlled pain.[8]

The CT-guided cordotomy procedure was previously described in the neurosurgery literature.[4,9-11] Fig 1 and On-line Table 1 characterize the key relevant cervical spinal cord anatomy for understanding the procedure. The Table provides a summary of the ideal patient, absolute and relative contraindications for the procedure. The risk/benefit ratio[6] of the procedure has improved with CT myelography image guidance, dynamic real-time electrode impedance measurements, and confirmation of electrode position via stimulation. In a recent series, <3% of patients experienced temporary paresis, ataxia, dysesthesia, hypotension, or urinary retention.[4] Cordotomy also has been performed safely in a child.[12]

Recent improvements in pain management have reduced the need for cordotomy to the point that the neurosurgery community is concerned that expertise in this procedure is disappearing.[8-10,13] Only 3 medical centers in the United States have reported performing cordotomy during the past decade.[12,14-17] Yet, a subset of patients with end-stage cancer with persistent incapacitating extremity pain not relieved by medical and intrathecal therapy could benefit from cordotomy if it were offered. Most interventional neuroradiologists have more experience than neurosurgeons in performing CT-guided ablative procedures and thus can help with these procedures as part of a multidisciplinary team. Here, we provide a summary of the procedure based on our recent experiences.

CT-Guided Cordotomy

The procedure first requires a cervical myelogram. For C1–2 puncture, the needle is directed toward the lateral cervical spinal

Received June 16, 2016; accepted after revision August 28.

From the Department of Radiology (T.M.S., M.J.H., B.A.C., M.T.B., E.F.), Center for Advanced Imaging Innovation and Research (T.M.S., E.F.), and Departments of Medicine (G.R.) and Neurosurgery (D.P., A.Y.M.), New York University, New York, New York.

Timothy Shepherd received research support from the National Institute of Aging (NIH 1K23 AG048622-01). This work was supported, in part, by the Center for Advanced Imaging Innovation and Research and the National Institutes of Health National Institute of Biomedical Imaging and Bioengineering Biomedical Technology Resource Center (grant P41EB017183).

Please address correspondence to Timothy Shepherd, MD, PhD, Department of Radiology, New York University, 660 First Ave, Room 226, New York, NY 10016; e-mail: timothy.shepherd@nyumc.org

Indicates open access to non-subscribers at www.ajnr.org
Indicates article with supplemental on-line tables.
Indicates article with supplemental on-line photos.
http://dx.doi.org/10.3174/ajnr.A4981

cord anterior to the dentate ligament (On-line Fig 1). The spinothalamic tract has a ventromedial-to-dorsolateral axis of somatotopy. For intractable lower extremity pain, the needle is directed 1–2 mm anterior to the ligament to target the dorsolateral portion, whereas for upper extremity pain, the needle is directed 2–3 mm anterior to the ligament to target the ventromedial portion (Fig 1). After the outer needle has penetrated the tented dura,[18] the stylet is exchanged for the inner electrode (Cosman Medical, Burlington, Massachusetts), which has demarcations to precisely control electrode extension beyond the needle. Electrical impedance measurements from the electrode tip provide real-time feedback of anatomic location. Impedance is $<200\ \Omega$ for CSF, $<400\ \Omega$ for pial surface, and $>700\ \Omega$ for cord parenchyma. Once the electrode appears correctly positioned by CT, sedation is removed and the functional position is confirmed with stimulation. With high-frequency sensory stimulation (50–100 Hz, 0.2–1.5 V), patients should report warmth that increases to a burning sensation in the symptomatic contralateral extremity.[9] Voltage is slowly increased because 0.2 V is often sufficient for confirming the correct electrode position. Next, the patient is observed during low-frequency motor stimulation (2–5 Hz, 0.2–1.5 V), which ideally does not provoke a motor response. Trapezius contractions suggest that the electrode tip is too deep and stimulating the ventral horn neurons, whereas ipsilateral lower extremity movements indicate that the electrode is too posterior in the corticospinal tract. Once the electrode position appears acceptable, a test ablation is obtained with the tip heated to 80°C for 60 seconds, then the patient is reassessed. Assuming that patient-reported sensory changes are acceptable, 2 additional radiofrequency ablations are performed. The patient must be sedated throughout the ablations. The procedure requires 2–3 hours for completion; if available, CT fluoroscopy could reduce this time, but the dominant time factor is alternating patient sedation. The procedure-related CT radiation dose was not a primary concern for terminally ill patients, but should be within normal limits. Afterward, we monitored patients overnight for changes in pain control, limb strength or ataxia, respiratory status, bowel or bladder function. Patients then were followed as outpatients by their oncologist.

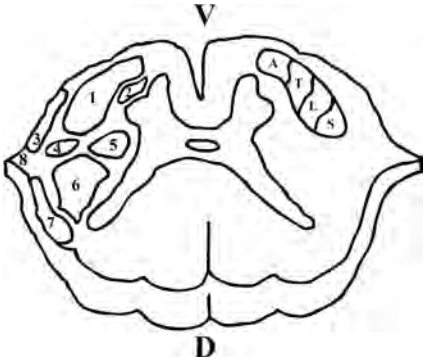

FIG 1. Schematic for the relevant functional anatomy of the axial cervical spinal cord when performing C1–2 cordotomy (V indicates ventral; and D, dorsal). Important ventral and lateral white matter pathways include the lateral spinothalamic tract (1), ventral reticulospinal tract (2), ventral spinocerebellar tract (3), lateral reticulospinal tract (4), rubrospinal tract (5), lateral corticospinal tract (6), dorsal spinocerebellar tract (7), and dentate ligament (8). Furthermore, it is important to understand the somatopic organization of the lateral spinothalamic tract delineated on the opposite side. A indicates arm; T, trunk; L, leg; and S, sacrum. Please also see the Table.

Individual Cases

Case 1. A 52-year-old man with right pelvic osteosarcoma presented with severe lancinating hip pain not relieved by high doses of methadone and hydromorphone. Intrathecal narcotics and bupivacaine did not relieve his pain. A myelogram was obtained via direct injection into the intrathecal pump reservoir. Electrode placement was challenging because the patient rotated his head to the left during the procedure, but after confirmation of the correct electrode position with stimulation, left C1–2 dorsolateral spinothalamic tract radiofrequency ablation was performed without complications. The patient immediately noticed pain relief and was now comfortable moving himself independently onto the hospital bed from the scanner. Marked improved function and pain relief were sustained until the patient died from complications of pulmonary metastases 2 months later.

Case 2. A 59-year-old woman with right pelvic leiomyosarcoma presented with burning, aching pain in the right buttock, hip, and thigh not relieved by high doses of gabapentin, methadone, fentanyl, or hydromorphone. Intravenous fentanyl was effective, but "knocked her out completely." The intrathecal pump was deferred because of her infection risk from chemotherapy immunosuppression. A myelogram was obtained by lumbar puncture. Initial electrode placement resulted in unintended right upper extremity sensory stimulation, but after we repositioned the electrode, left C1–2 dorsolateral spinothalamic tract radiofrequency ablation was performed without complications (Fig 2). The patient no longer experienced right lower extremity pain but remained concerned about her persistent right lower extremity numbness, an expected result of the procedure. The patient died from systemic disease 5 months later.

Case 3. A 67-year-old woman with C7–T2 vertebral body metastases from esophageal cancer presented with severe right upper ex-

Summary of ideal patient for cordotomy, contraindications, and specific additional material risks to the procedure

Ideal Patient	Contraindications	Additional Risk
Unilateral nociceptive pain from extremity	Bilateral upper extremity pathology	Ondine's curse (apnea during sleep) if bilateral ablation
$pO_2 > 80\%$ on room air	Severe pulmonary dysfunction	Insufficient reserve to tolerate decreased function
Life expectancy between 3 and 12 mo	Survival <3 mo[a] or >12 mo	Deafferentation pain ≥6 mo after procedure
Normal ICP	Intracranial metastasis and/or mass effect	Brain herniation during procedure
Absence of psychiatric comorbidities	Opiate dependence or emotional problems	Persistent pain control problems after cordotomy
Intact autonomic system	Sympathetic dysfunction[a]	Hypotension, Horner syndrome, bladder dysfunction
Comfortable in supine position	Orthopnea[a]	Inability to be supine long enough to complete procedure

Note:—pO_2 indicates partial pressure of oxygen; ICP, intracranial pressure.
[a] Relative contraindication.

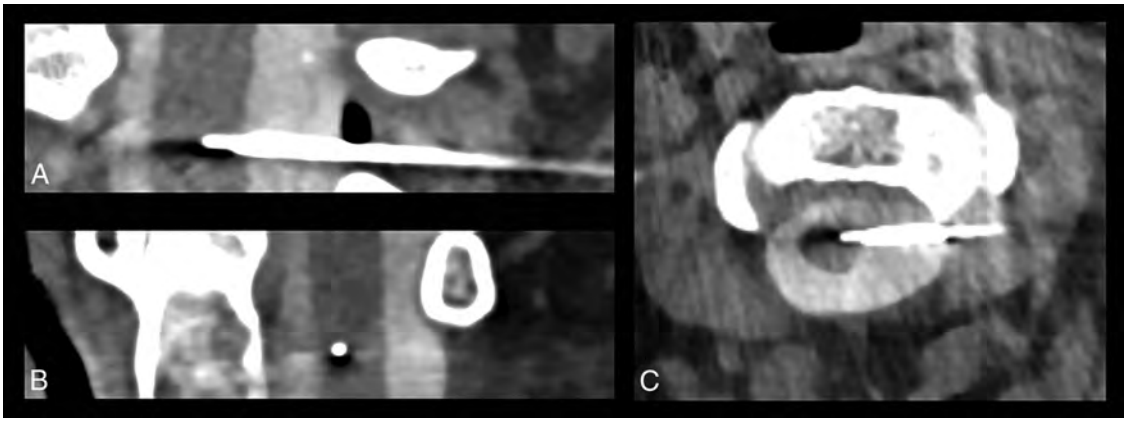

FIG 2. Coronal (*A*), sagittal (*B*), and axial (*C*) reformats of the CT myelogram demonstrate outer needle and inner electrode placement immediately before completion of a left lateral C1–2 cordotomy via radiofrequency ablation. The outer needle was placed into the thecal space near the pial surface of the cord approximately 2 mm ventral to the dentate ligament. The electrode was then advanced into the CSF, pia mater, and spinal cord with real-time monitoring of dynamic electrical impedance changes. Multimodal data, including the CT images, confirmed that the electrode was in the left spinothalamic tract. Note that the upper cervical cord is displaced to the right (we observed this in all 3 cases).

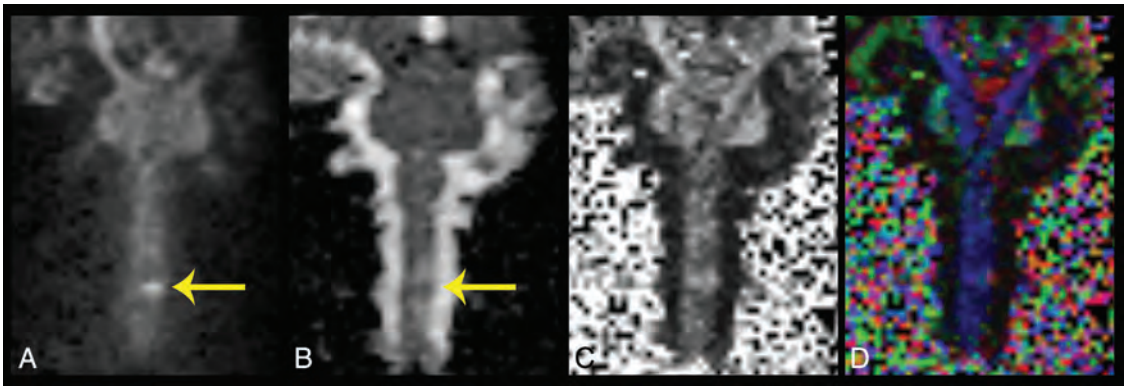

FIG 3. Coronal diffusion trace (*A*), apparent diffusion coefficient (*B*), fractional anisotropy (*C*), and color-encoded fractional anisotropy maps (*D*) of the cervical cord 48 hours after technically successful CT-guided left C1–2 cordotomy. There is a small focus of hyperintensity on the diffusion trace image with corresponding reduced diffusion indicative of focal cytotoxic edema (*arrow*) and more extensive surrounding vasogenic edema. Manual ROI quantitation of these diffusion changes is summarized in On-line Table 2.

tremity stabbing pain not controlled by high doses of gabapentin, methadone, and morphine. A myelogram was obtained by CT-guided cisternal puncture. Initial electrode placement resulted in visible trapezius contractions during motor stimulation. After the electrode penetration was reduced 1 mm, muscle contractions were not observed during repeat stimulation, and left C1–2 ventromedial spinothalamic tract radiofrequency ablation was performed without complications. A contrast MRI with diffusion (20 directions, $b=1000$ s/mm^2) was performed 2 days later to characterize the ablation (Fig 3 and On-line Fig 2). Five months later, the patient's right upper extremity pain remains well-controlled by using a methadone regimen that had been ineffective before cordotomy.

DISCUSSION

We successfully performed 3 CT-guided palliative C1–2 spinal cordotomies without complications. Our subjects all experienced meaningful postcordotomy improvement in pain control. Our series is limited in size, but the results and safety corroborate 2 larger cohorts reported from outside North America[4,5] and case reports from 3 institutions in the United States documenting CT-guided cordotomies during the past decade.[12,14-17] Needle placement by using CT myelography with dynamic real-time impedance feedback during electrode penetration increases the safety of modern cordotomy. Radiofrequency ablation also enabled us to physiologically confirm the target with patient-reported feedback during motor and sensory stimulation. Another key factor for success is selecting the correct patient—ideally this is a patient with end-stage cancer with medically refractory nociceptive pain from a single extremity (other major sources of pain should be excluded).

Several groups have performed myelography during the C1–2 puncture, but published images[4,12,14,15] suggested limited redistribution of viscous contrast because the patient cannot be moved.[5] We preferred a separate myelogram injection to plan the trajectory to the spinothalamic tract relative to the skin entry, lateral C1–2 window, and intrathecal spinal cord position. Furthermore, we found that a CT-guided cisternal myelography has practical advantages once contrast is instilled and the needle is removed; alternating the patient between supine, right and left decubitus positions gave excellent myelographic contrast in <5 minutes (Fig 2)[18] without moving the patient off the table or removing monitoring equipment for sedation.

We also used volumetric 3D T2 MR imaging multiplanar re-

constructions to plan the procedure. A previous study reported precordotomy cervical spine MR imaging for frameless intraoperative stereotaxy.[19] MR imaging may be contraindicated in some patients but helped us identify individual-specific anatomic corridors to reach the desired part of the spinothalamic tract before the procedure (On-line Fig 1). A previous study found that vertebral arteries overlaid the C1–2 spinal canal in 31% of cases.[20] In case 3, preprocedural 3D T2-weighted structural MR imaging identified the left vertebral artery lateral to the canal just anterosuperior to the planned trajectory.

For all 3 cases, we observed lateral displacements of the spinal cord away from the electrode (Fig 2). Cord displacement up to 0.5 cm has been reported historically[21] and also can be observed in recent CT-guided cordotomies.[5,11,12,15] We observed no problems in our subjects due to spinal cord displacement, and the cord in subject 3 had returned to a normal position on MR imaging 2 days later (On-line Fig 2).

Postprocedural MR imaging demonstrated focal enhancement at the electrode ablation zone in the anteromedial spinothalamic tract. More extensive surrounding edema (On-line Fig 2) was similar to observations in a previous report.[14] We characterized diffusion changes associated with cordotomy (Fig 3 and On-line Table 2). Compared with the contralateral homolog, diffusivity and fractional anisotropy for the ablative lesion decreased 12% and 30%, respectively. A 13% increase in radial diffusivity was attributed to electrode penetration trauma in the transverse plane, while a 33% reduction in axial diffusivity was attributed to axonal injury from the ablation. It would be informative to study the evolution of diffusion changes after a precise cord injury at a specific time, but it is challenging to obtain MR imaging in these patients. A previous study demonstrated focal spinal cord atrophy in a patient 41 years after cordotomy.[15]

A subset of patients with end-stage cancer who continue to experience extremity pain even with maximal medical and/or intrathecal therapy[1-3] could benefit from CT-guided cordotomy, but only 3 medical centers in North America have reported performing this procedure during the past decade.[12,14-17] Our small series corroborates that this relatively precise, ablative procedure can be safe and effective in reducing both oversedation and the need for medical follow-up for carefully selected patients with end-stage cancer.[4,5] Underuse of cordotomy may be due to unfamiliarity, reluctance, and/or insufficient experience to perform palliative ablative procedures safely and effectively, even in the neurosurgery community.[8-10,13] Many neuroradiologists frequently perform similar CT-guided spine procedures and ablations. These neuroradiologists can provide the missing expertise to safely perform this procedure as part of a multidisciplinary team for improved patient care.

Disclosures: Timothy M. Shepherd—*UNRELATED*: *Grants/Grants Pending*: industry-sponsored study unrelated to this article, *Comments*: Principal Investigator, integration of advanced MRI into planning and monitoring for patients with intracranial metastases undergoing radiosurgery; BrainLab AG (academic-industry partnership through New York University Office of Industrial Liaison) (June 1, 2015, to May 31, 2017)*; *Patents (Planned, Pending, or Issued)*: 3 patents filed for medical devices not discussed in the article, *Comments*: Patent Cooperation Treaty Patent Application No. PCT/US2015/020426, filed March 13, 2015, entitled "Position Guidance Device with Bubble Level"; US Provisional Patent Application No. 62/243,478, filed October 19, 2015, entitled "Electronic Position Guidance Device with Real-Time Auditory and Visual Feedback"; US Provisional Patent Application No. 62/307,257, filed March 11, 2016, entitled "Pseudo-Tissue for Securing, Protecting and Adjusting the Position of Percutaneous Medical Devices."* Donato Pacione—*UNRELATED*: *Consultancy*: Medtronic, *Comments*: paid an honorarium for a discussion group on anterior cervical discectomy and fusion. *Money paid to the institution.

REFERENCES

1. Deandrea S, Montanari M, Moja L, et al. **Prevalence of undertreatment in cancer pain: a review of published literature.** *Ann Oncol* 2008;19:1985–91 CrossRef Medline
2. Newsome S, Frawley BK, Argoff CE. **Intrathecal analgesia for refractory cancer pain.** *Curr Pain Headache Rep* 2008;12:249–56 CrossRef Medline
3. Grossman SA, Staats PS. **Current management of pain in patients with cancer.** *Oncology (Williston Park)* 1994;8:93–107; discussion 107, 110, 115 Medline
4. Kanpolat Y, Ugur HC, Ayten M, et al. **Computed tomography-guided percutaneous cordotomy for intractable pain in malignancy.** *Neurosurgery* 2009;64(3 suppl):ons187–93; discussion ons193–94 Medline
5. Raslan AM. **Percutaneous computed tomography-guided radiofrequency ablation of upper spinal cord pain pathways for cancer-related pain.** *Neurosurgery* 2008;62(3 suppl 1):ons226–33; discussion ons233–34 Medline
6. Sindou M, Jeanmonod D, Mertens P. **Ablative neurosurgical procedures for the treatment of chronic pain.** *Neurophysiol Clin* 1990;20:399–423 CrossRef Medline
7. Atkins D, Best D, Briss PA, et al; GRADE Working Group. **Grading quality of evidence and strength of recommendations.** *BMJ* 2004;328:1490 CrossRef Medline
8. Raslan AM, Cetas JS, McCartney S, et al. **Destructive procedures for control of cancer pain: the case for cordotomy.** *J Neurosurg* 2011;114:155–70 CrossRef Medline
9. Binder DK, Barbaro NM. **Cordotomy.** In: Follett K, ed. *Neurosurgical Pain Management.* Philadelphia: Saunders; 2004:165–71
10. Konrad P. **Dorsal root entry zone lesion, midline myelotomy and anterolateral cordotomy.** *Neurosurg Clin N Am* 2014;25:697–22 CrossRef Medline
11. Rosenberg WS. **Cordotomy for intractable malignant pain.** In: Narang S, Ross EL, Weisheipl A, eds. *Surgical Pain Management: A Complete Guide to Implantable and Interventional Pain Therapies.* Oxford: Oxford University Press 2016:375–79
12. Reddy GD, Okhuysen-Cawley R, Harsh V, et al. **Percutaneous CT-guided cordotomy for the treatment of pediatric cancer pain.** *J Neurosurg Pediatr* 2013;12:93–96 CrossRef Medline
13. Fitzgibbon DR. **Percutaneous CT-guided C1–2 cordotomy for intractable cancer pain.** *Curr Pain Headache Rep* 2009;13:253–55 CrossRef Medline
14. Collins KL, Patil PG. **Flat-panel fluoroscopy O-arm-guided percutaneous radiofrequency cordotomy: a new technique for the treatment of unilateral cancer pain.** *Neurosurgery* 2013;72(1 suppl operative):27–34; discussion 34 CrossRef Medline
15. Collins KL, Taren JA, Patil PG. **Four-decade maintenance of analgesia with percutaneous cordotomy.** *Stereotact Funct Neurosurg* 2012;90:226–72 CrossRef Medline
16. Viswanathan A, Bruera E. **Cordotomy for treatment of cancer-related pain: patient selection and intervention timing.** *Neurosurg Focus* 2013;35:1–4 CrossRef Medline
17. Bentley JN, Viswanathan A, Rosenberg WS, et al. **Treatment of medically refractory cancer pain with a combination of intrathecal neuromodulation and neurosurgical ablation: case series and literature review.** *Pain Med* 2014;15:1488–95 CrossRef Medline
18. Orrison WW, Eldevik OP, Sackett JF. **Lateral C1–2 puncture for cervical myelopathy, part III: historical, anatomic, and technical considerations.** *Radiology* 1983;146:401–08 CrossRef Medline
19. McGirt MJ, Villavicencio AT, Bulsara KR, et al. **MRI-guided frameless stereotactic percutaneous cordotomy.** *Stereotact Funct Neurosurg* 2002;78:53–63 Medline
20. Katoh Y, Itoh T, Tsuji H, et al. **Complications of lateral C1–2 puncture myelography.** *Spine* 1990;15:1085–87 CrossRef Medline
21. Taren JA, Davis R, Crosby EC. **Target physiologic corroboration in sterotaxic cervical cordotomy.** *J Neurosurg* 1969;30:569–84 CrossRef Medline

Doing More with Less: Diagnostic Accuracy of CT in Suspected Cauda Equina Syndrome

J.G. Peacock and V.M. Timpone

ABSTRACT

BACKGROUND AND PURPOSE: Cauda equina syndrome typically requires emergent MR imaging to detect compressive lesions on the cauda equina, which may require surgical decompression. While CT is sometimes performed as a complementary imaging technique to evaluate osseous integrity in patients with cauda equina syndrome, the accuracy of CT in detecting significant spinal stenosis and cauda equina impingement is not well-defined in the literature. We hypothesized that percentage thecal sac effacement on CT of the lumbar spine would have high sensitivity and high negative predictive value in evaluating significant spinal stenosis and cauda equina impingement.

MATERIALS AND METHODS: We analyzed imaging studies for 151 consecutive patients with clinically suspected cauda equina syndrome. The percentage thecal sac effacement (<50%, ≥50%) was determined on CT and MR imaging. The presence or absence of cauda equina impingement was determined on MR imaging. Using MR imaging as the reference standard, we performed statistical analysis to determine the accuracy of CT in predicting significant spinal stenosis (percentage thecal sac effacement, ≥50%) and cauda equina impingement.

RESULTS: Forty of 151 patients had a percentage thecal sac effacement of ≥50% on MR imaging. Nineteen of 40 had cauda equina impingement. Readers determined that there was a CT percentage thecal sac effacement of <50% in 97/151 cases, and CT percentage thecal sac effacement of ≥50% in 54/151 cases. Reader sensitivity for the detection of significant spinal stenosis (MR percentage thecal sac effacement of ≥50%) was 0.98; specificity, 0.86; positive predictive value, 0.72; and negative predictive value, 0.99. No cases read as CT percentage thecal sac effacement of <50% were found to have cauda equina impingement.

CONCLUSIONS: CT percentage thecal sac effacement of ≥50% predicts significant spinal stenosis on MR imaging in patients with clinically suspected cauda equina syndrome. CT percentage thecal sac effacement of <50% appears to reliably rule out cauda equina impingement. This imaging marker may serve as an additional tool for the clinician in deciding whether MR imaging can be deferred.

ABBREVIATIONS: CEI = cauda equina impingement; CES = cauda equina syndrome; PTSE = percentage thecal sac effacement

Cauda equina syndrome (CES) requires emergent imaging to rule out compressive lesions on the cauda equina, which could necessitate emergent surgical decompression. Failure of the timely recognition and treatment of CES can result in debilitating long-term neurologic complications such loss of bowel, bladder, and sexual function. MR imaging is the established imaging criterion standard to screen for the various etiologies accounting for CES, including degenerative disc disease, trauma, neoplasm, infection, and hematoma.[1-5]

The clinical presentation of CES is defined by a broad range of symptoms and physical examination findings including severe low back pain, bilateral sciatica, lower extremity weakness, bladder/bowel dysfunction, saddle numbness, or reduced rectal tone. Some of these symptoms are common and nonspecific to CES, presenting the clinician with the diagnostic challenge of deciding which patients warrant further evaluation with MR imaging.[4,6-9]

The prevalence of cauda equina syndrome among the general population is estimated between 1 in 33,000 to 1 in 100,000 and is diagnosed in approximately 0.04% of patients presenting to the emergency department with low back pain.[10-13] Friedman et al[13] reviewed data for the 2.63 million annual emergency department visits in the United States for low back pain and found imaging performed in 45% of cases, with 2.8% of all patients scanned with MR imaging and 5.5% scanned with CT, resulting in an overall cost of >$819 million to US payers.[11,13] Studies have demonstrated that most MR images obtained to evaluate CES do not demonstrate concordant pathology; however, these scans are

Received May 28, 2016; accepted after revision August 23.

From the Department of Radiology, San Antonio Military Medical Center, San Antonio, Texas.

Please address correspondence to Vincent M. Timpone, MD, Department of Radiology, Division of Neuroradiology, San Antonio Military Medical Center, 551 Roger Brooke Dr, San Antonio, TX 78219; e-mail: vincent.timpone@us.af.mil

http://dx.doi.org/10.3174/ajnr.A4974

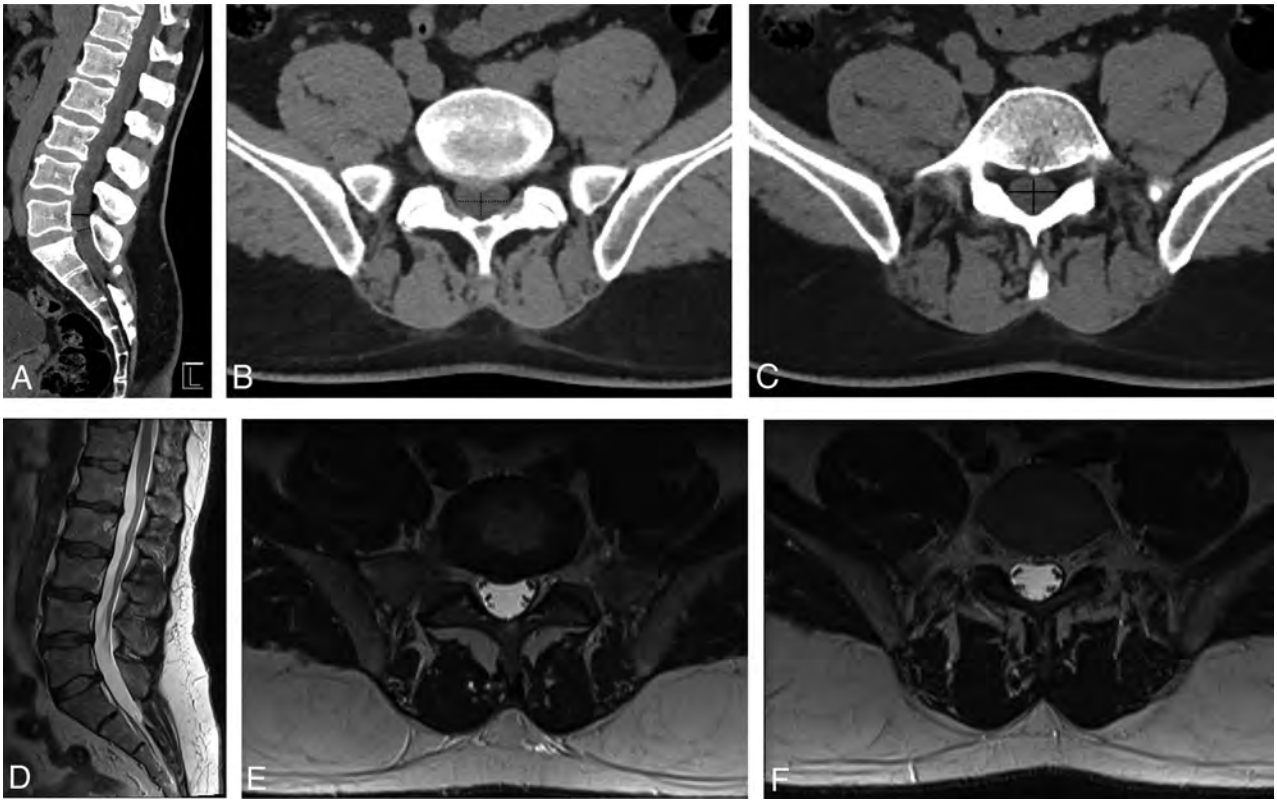

FIG 1. A 50-year-old man with acute-onset bilateral lower extremity numbness and severe low back pain. Application of the CT-PTSE imaging marker is demonstrated. Spinal stenosis from a disc protrusion at the L5/S1 level is assessed by delineating the estimated area of the thecal sac at this level (*dashed black line*, *A* and *B*). A normal reference level is identified just cranial to the stenosis (*solid black line*, *A* and *C*). The readers determined that CT-PTSE for this stenosis and others throughout the lumbar spine was <50%. MR imaging of the lumbar spine performed on the same day (*D–F*), with axial images through the L5–S1 stenosis (*E*) and the reference level (*F*), demonstrates concordant results with <50% thecal sac effacement and no evidence of cauda equina impingement.

Demographic and clinical characteristics of the study population[a]

Characteristics	
Patients (No.)	151
Female (No.)	46 (30.5%)
Age (mean) (yr)	54.5 ± 19.5
MR-PTSE ≥50% (No.)	40 (26.5%)
MR-PTSE <50% (No.)	111 (73.5%)
CEI (No.)	19 (12.6%)
MR-PTSE ≥50%, degenerative changes (No.)	23 (15.2%)
MR-PTSE ≥50%, traumatic osseous retropulsion (No.)	12 (8%)
MR-PTSE ≥50%, neoplastic (No.)	3 (1.9%)
MR-PTSE ≥50%, hematoma (No.)	1 (0.7%)
MR-PTSE ≥50%, infection (No.)	1 (0.7%)

[a] Results are expressed as absolute numbers (%) and mean.

nonetheless frequently ordered, given the impact of missing or delaying a diagnosis of CES.[1,4-6,9,11,14]

While CT is sometimes performed as a complementary imaging technique to evaluate osseous integrity in patients with CES, the diagnostic accuracy of CT in detecting significant spinal stenosis and cauda equina impingement (CEI) compared with MR imaging is not well-defined in the literature.

The purpose of this study was to evaluate whether CT could reliably identify significant spinal stenosis and rule out cauda equina impingement in patients presenting with clinically suspected cauda equina syndrome.

MATERIALS AND METHODS

Patient Selection

This study was Health Insurance Portability and Accountability Act–compliant and was approved by our institutional review board. During a 12-month period, we reviewed the clinical and imaging data of 4691 consecutive lumbar spine MR imaging examinations performed at our institution. One hundred fifty-one patients met the following inclusion criteria: 1) acute neurologic symptoms (new onset or worsening of symptoms within the past 48 hours) with clinical suspicion of cauda equina syndrome (symptoms include severe low back pain, bilateral sciatica, lower extremity weakness, bladder/bowel dysfunction, saddle numbness, or reduced rectal tone); 2) CT of the lumbar spine performed within 48 hours of MR imaging; and 3) no interval operation or change in symptoms between CT or MR imaging.

Image Acquisition

All imaging was performed in accordance with standard institutional spine imaging protocols. Noncontrast lumbar spine CT was acquired in the helical mode (5-mm thickness, 100 kV, auto-mAs) and reformatted at 2-mm intervals. Lumbar spine CTs obtained in conjunction with CT abdomen/pelvic examinations were reconstructed from the CT abdomen/pelvis source data and had the same scanning parameters following administration of 80–90 mL of nonionic contrast (iopamidol, Isovue Multipack-370; Bracco, Princeton, New Jersey). All axial CT acquisitions were recon-

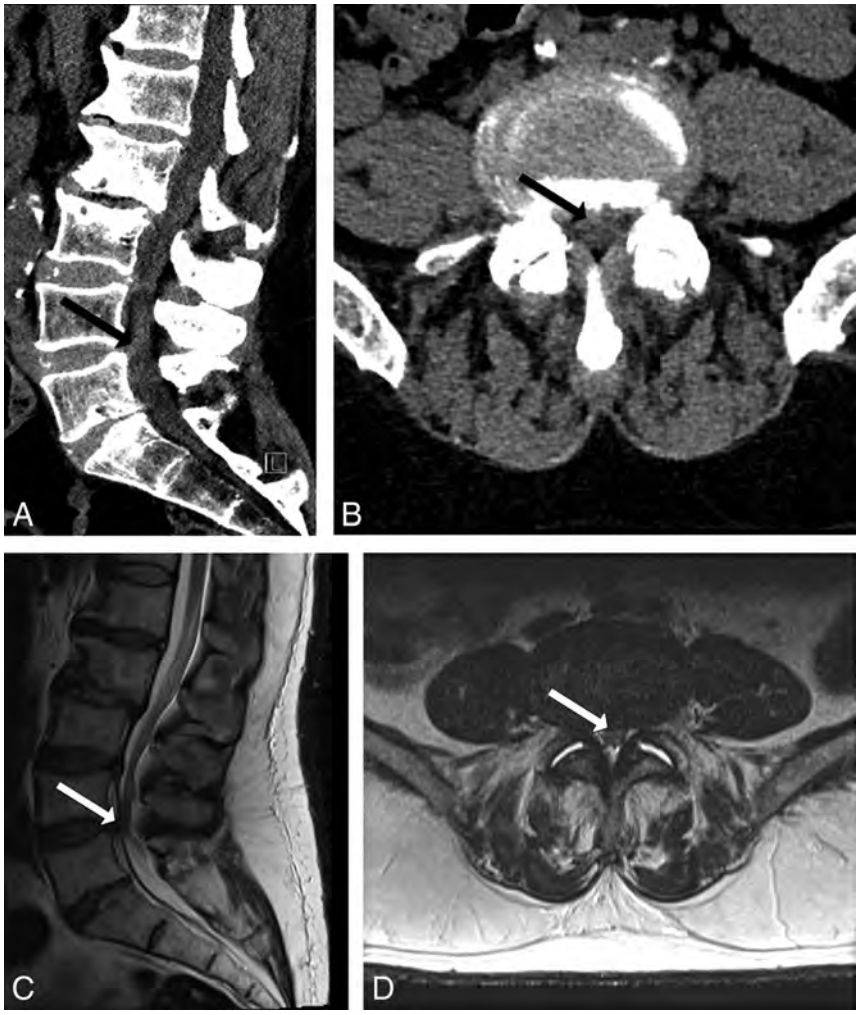

FIG 2. A 61-year-old man with acute bilateral increased lower extremity paresthesias. CT (*A* and *B*) demonstrates degenerative spinal stenoses, most severe at L3/4 and L4/5 (*solid arrow*). Readers determined that CT-PTSE was ≥50%. MR imaging (*C* and *D*) confirms PTSE of ≥50% and demonstrates early impingement of the cauda equina.

structed in the sagittal and coronal planes, in both soft-tissue and bone algorithms.

MR imaging was performed on multiple different 1.5T and 3T scanners across our institution. Sagittal T2WI parameters were the following: TR/TE = 3600/100 ms, matrix = 290 × 230, NEX = 2, section thickness = 3 mm, gap = 0 mm. Axial T2WI parameters were the following: TR/TE = 5500/100 ms, matrix = 290 × 230, NEX = 1.5, section thickness = 3 mm, gap = 0 mm.

Image Analysis

We analyzed by visual inspection the percentage thecal sac effacement (≥50%, <50%) on lumbar spine CT and the percentage thecal sac effacement (≥50%, <50%) on lumbar spine MR imaging. The percentage thecal sac effacement was determined by visually inspecting the area of the thecal sac at the most stenotic level by using the axial and sagittal planes and comparing it with a normal level above or below the stenosis (Fig 1). A threshold of 50% thecal sac effacement was used because this was easily reproducible and, on the basis of preliminary analysis, was a threshold below which the cauda equina and conus medullaris would not be impinged.

Images were reviewed independently by 2 radiologists: a Certificate of Added Qualification–certified neuroradiologist with 9 years of radiology experience and a radiology resident with 1 year of radiology experience. The presence or absence of cauda equina impingement on MR imaging was also recorded. Cauda equina impingement was defined as complete effacement of CSF within the thecal sac secondary to an extrinsically compressing lesion. The underlying dominant cause of spinal stenosis on MR imaging was recorded (traumatic osseous retropulsion, degenerative changes, tumor, hematoma, infection). Levels analyzed spanned T12/L1 through L5/S1. Early tapering of the thecal sac secondary to prominent epidural fat was not considered positive for cauda equina impingement unless associated with a superimposed compressive lesion. Interpreting radiologists were blinded to all clinical and imaging report information. MR images were reviewed 2 weeks following review of CT images with readers blinded to the CT interpretation. Any disagreements were resolved by consensus.

Statistical Analysis

Using lumbar spine MR imaging as the reference standard, we performed statistical analysis to determine the sensitivity, specificity, positive predictive value, and negative predictive value of lumbar spine CT in detecting percentage thecal sac effacement of

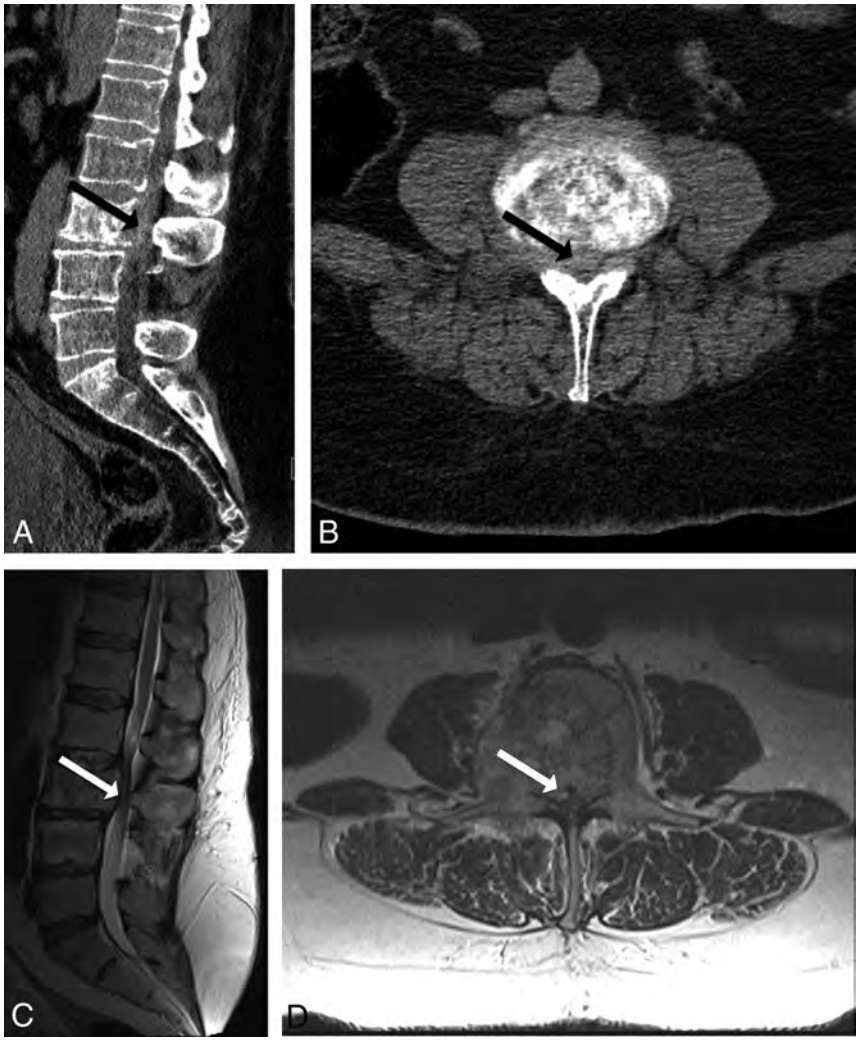

FIG 3. A 59-year-old man with metastatic renal cell carcinoma with worsening left lower extremity pain and difficulty ambulating. CT (*A* and *B*) demonstrates sclerotic osseous metastasis at L3, with a hyperdense soft-tissue component bowing and extending through the posterior vertebral body wall (*solid arrow*). Readers determined that CT-PTSE was ≥50%. MR imaging (*C* and *D*) confirms PTSE of ≥50 and demonstrates impingement of the cauda equina by tumor.

≥50% and cauda equina impingement on MR imaging. MedCalc 11.5.1.0 software (MedCalc Software, Mariakerke, Belgium) was used to perform statistical analysis. Statistical significance was $P < .05$. Interrater agreement for imaging markers was determined by using the κ statistic.

RESULTS

Patient demographics and clinical characteristics of the study population are listed in the Table. Of 151 patients, 40 had MR imaging percentage thecal sac effacement (MR-PTSE) of ≥50% (23 degenerative, 12 traumatic, 3 neoplastic, 1 hematoma, 1 infection). Of 40 patients with MR-PTSE of ≥50%, 19 had cauda equina impingement (10 degenerative, 6 traumatic, 2 neoplastic, 1 hematoma). One hundred eleven patients had MR-PTSE of <50%. No patients with MR-PTSE of <50% had cauda equina impingement.

On the basis of the evaluation of lumbar spine CT, the readers determined that there was CT-PTSE of <50% in 97/151 cases and CT-PTSE of ≥50% in 54/151 cases. Reader sensitivity for the detection of significant spinal stenosis (MR-PTSE of ≥50%) was 98% (95% CI, 87%–100%), specificity was 86% (95% CI, 79%–92%), positive predictive value was 72% (95% CI, 58%–84%), and negative predictive value was 99% (95% CI, 94%–100%).

No cases read as CT-PTSE of <50% were found to have cauda equina impingement. One false-negative case of CT-PTSE of <50% underestimated the stenosis in a patient with MR-PTSE of ≥50% without cauda equina impingement. All cases of CT-PTSE of ≥50% corresponded to the concordant level of maximum lumbar spinal stenosis on MR imaging.

Of 151 cases, 86 CTs were performed with contrast and 65 CTs were performed without contrast. There was no significant difference in sensitivity ($P = .37$) or specificity ($P = .06$) for predicting MR-PTSE of ≥50% between the 2 groups. Interreader agreement for determination of CT-PTSE was good ($\kappa = 0.62$).

Soft-tissue resolution of lumbar spine CT with the application of the CT-PTSE marker to rule out degenerative CEI (Fig 1), identify patients at risk for degenerative CEI (Fig 2) and neoplastic CEI (Fig 3) is demonstrated. Figure 4 shows how, in the setting of trauma, CT can readily identify a patient at risk for traumatic CEI by delineating osseous effacement of the thecal sac. In certain

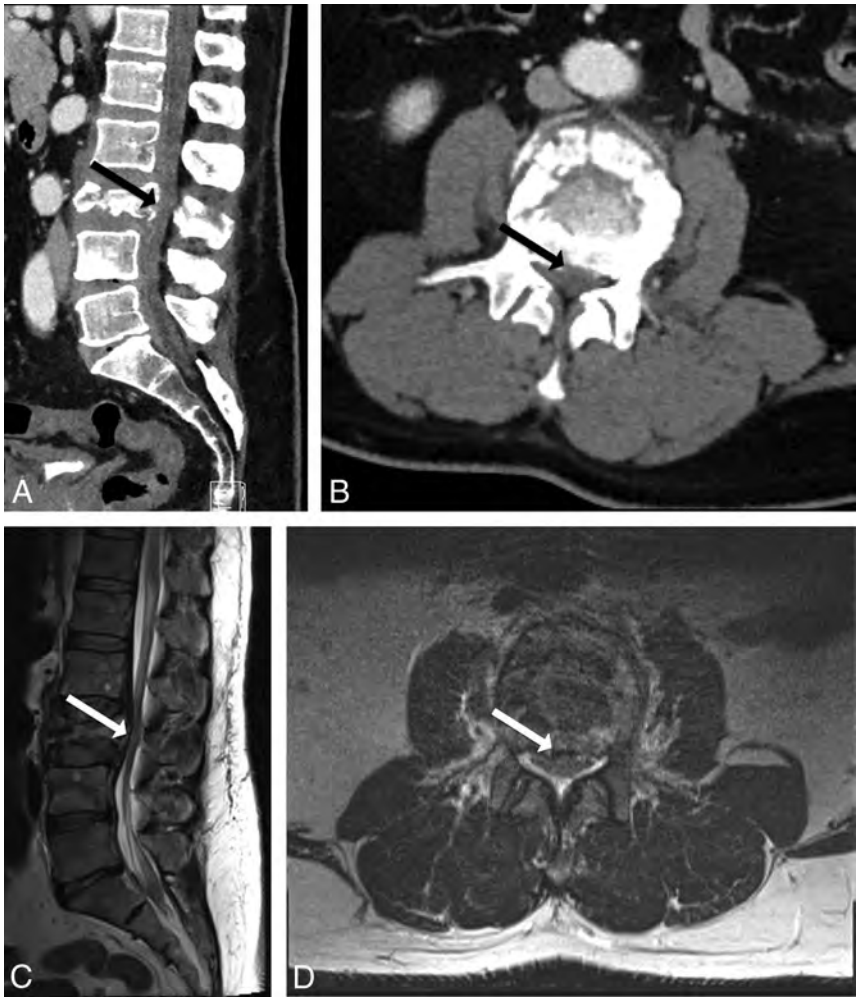

FIG 4. A 55-year-old man with severe low back pain following a fall from a roof. CT (*A* and *B*) demonstrates an L3 burst fracture with osseous retropulsion into the spinal canal (*solid arrow*). Readers determined that CT-PTSE was ≥50%. MR imaging (*C* and *D*) confirms PTSE of ≥50% and demonstrates impingement of the cauda equina.

cases, streak artifacts from hardware or surrounding bone limited the diagnostic accuracy of the CT-PTSE marker (Fig 5).

DISCUSSION

The purpose of this study was to determine whether CT could reliably and safely identify patients with significant spinal stenosis and cauda equina impingement. Our results demonstrate that CT-PTSE has a high sensitivity and high negative predictive value for detecting significant spinal stenosis on MR imaging. On the basis of careful analysis of CT alone, the readers missed no cases of cauda equina impingement.

The American College of Radiology Appropriateness Criteria for the evaluation of cauda equina syndrome lists MR imaging of the lumbar spine as a level 9 rating ("usually appropriate"), with CT of the lumbar spine listed as a level 5 rating ("may be appropriate").[2] This determination is based on the superior soft-tissue contrast resolution of MR imaging in evaluating lumbar spine pathology, particularly for visualizing nerve roots within the thecal sac, anatomy not readily visible on CT. We found that with careful adjustment of the CT window-level settings, in addition to bone, CT can distinguish the margins of the thecal sac by identifying various levels of soft-tissue attenuation within and around the spinal canal, including intervertebral discs, epidural fat, and CSF within the thecal sac. This limited soft-tissue resolution of CT allows one to reliably determine the PTSE, a marker that we hypothesized could infer the presence or absence of underlying cauda equina impingement when applied with a threshold of 50%. We found CT-PTSE a useful imaging marker in predicting significant spinal stenosis on MR imaging and one that excluded cauda equina impingement in our patient population.

While CT cannot replicate the superior soft-tissue contrast resolution of MR imaging in evaluating lumbar spine pathology, careful analysis of CT-PTSE can help radiologists communicate to the clinician their suspicion of significant spinal stenosis and cauda equina impingement. This imaging marker may be particularly useful in the community setting where some centers may have limited access to MR imaging in the emergency department. On the basis of our observations, a clinician could potentially decide to defer MR imaging in cases with a low clinical suspicion and CT-PTSE of <50% or to expedite MR imaging in cases of CT-PTSE of ≥50%.

As a screening tool, application of the CT-PTSE imaging marker could potentially lower associated health care costs by

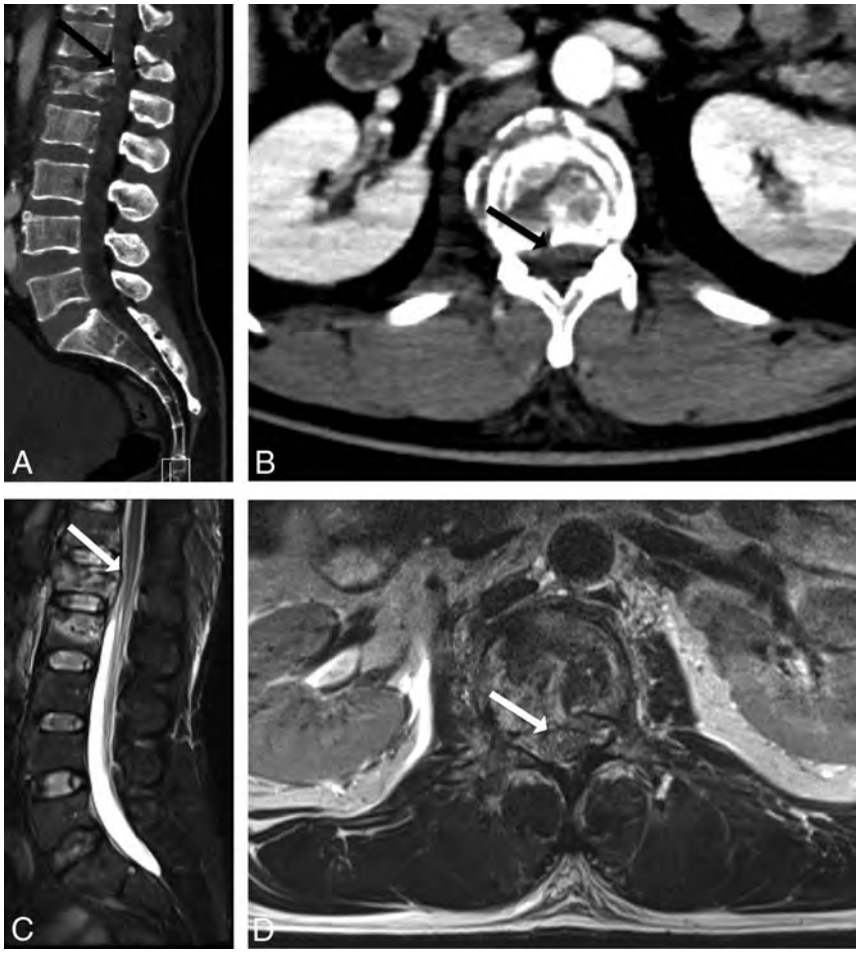

FIG 5. A 42-year-old woman with lumbar back pain following trauma. CT (*A* and *B*) demonstrates a burst fracture of L1 with retropulsion of bone into the spinal canal (*solid arrow*). Streak artifacts from bone and the patient's upper extremities obscure the margins of the thecal sac, and readers determined that CT-PTSE may be ≥50%. This case proved to represent a false-positive because MR imaging (*C* and *D*) demonstrates a PTSE of <50% and no evidence of cauda equina impingement.

decreasing the number of low-diagnostic-yield MR imaging examinations or shifting visits to primary care settings, where costs and the propensity for imaging may be less.[15] In our study, we identified 97/151 (64%) patients with CT-PTSE of <50%, none of whom had cauda equina impingement on MR imaging. Provided that there is a corresponding low clinical suspicion for CES, this represents nearly two-thirds of our patient population where MR imaging could have been deferred on the basis of CT results. Using the national average of combined technical and professional component 2016 Medicare payment rates for MRI and CT of the lumbar spine without contrast of $245.26 and $180.81 respectively, we determined that the estimated cost savings per 1000 patients imaged with CT would be approximately $41,248. We recognize that this is likely a low estimate considering the higher costs paid by private commercial insurers and potential additional expenditures associated with hospital admissions or transferring patients to other facilities for MR imaging.[13]

There were several limitations to our study. We used a retrospective design and included both contrast and noncontrast CT examinations of the lumbar spine; however, there was no significant difference in our results when adjusting for the presence of contrast. Most of our cases were degenerative and traumatic in etiology, and we had few cases of tumor, infection, or hemorrhage. The level of reader experience was also relatively low (9 years and 1 year, respectively); however, neither reader missed any case of cauda equina impingement, and increased reader experience might have improved the specificity and positive predictive value of results obtained in this study. Additionally, there are limitations related to the 50% PTSE threshold. While we did not encounter patients with a low-lying conus medullaris, it is possible that those patients could experience distal thoracic cord or conus impingement at a PTSE of <50%. It is also possible that in patients with congenital spinal stenosis, a PTSE of <50% could result in cauda equina impingement.

Considering the aforementioned limitations of this study, the CT-PTSE marker to exclude cauda equina impingement may be best-suited for those with a low pretest clinical suspicion. Clinicians may choose to lower their threshold for obtaining MR imaging in cases of suspected infection, hemorrhage, tumor, congenital spinal stenosis, when symptoms or findings are localized to the thoracolumbar junction or in cases in which CT is degraded by artifacts.

These results should be validated in a larger prospective study.

Areas for additional future investigation may include optimizing CT scanning parameters to reduce artifacts and further improve the accuracy of the CT-PTSE imaging marker.

CONCLUSIONS

CT-PTSE of ≥50% predicts significant spinal stenosis on MR imaging in patients with clinically suspected cauda equina syndrome. CT-PTSE <50% appears to reliably rule out cauda equina impingement. This imaging marker may serve as an additional tool for the clinician in helping to decide whether MR imaging can be deferred, and it has the potential to lower associated health care costs.

REFERENCES

1. Fairbank J, Hashimoto R, Dailey A, et al. **Does patient history and physical examination predict MRI proven cauda equina syndrome?** *Evid Based Spine Care J* 2011;2:27–33 CrossRef Medline
2. American College of Radiology ACR Appropriateness Criteria 2015; www.acr.org/ac. Accessed August 10, 2016
3. Fraser S, Roberts L, Murphy E. **Cauda equina syndrome: a literature review of its definition and clinical presentation.** *Arch Phys Med Rehabil* 2009;90:1964–68 CrossRef Medline
4. Bell DA, Collie D, Statham PF. **Cauda equina syndrome: what is the correlation between clinical assessment and MRI scanning?** *Br J Neurosurg* 2007;21:201–03 CrossRef Medline
5. Chou R, Qaseem A, Owens DK, et al; Clinical Guidelines Committee of the American College of Physicians. **Diagnostic imaging for low back pain: advice for high-value health care from the American College of Physicians.** *Ann Intern Med* 2011;154:181–89 CrossRef Medline
6. Modic MT, Obuchowski NA, Ross JS, et al. **Acute low back pain and radiculopathy: MR imaging findings and their prognostic role and effect on outcome.** *Radiology* 2005;237:597–604 CrossRef Medline
7. Murray CJ, Lopez AD. **Measuring the global burden of disease.** *N Engl J Med* 2013;369:448–57 CrossRef Medline
8. Gitelman A, Hishmeh S, Morelli BN, et al. **Cauda equina syndrome: a comprehensive review.** *Am J Orthop (Belle Mead NJ)* 2008;37:556–62 Medline
9. Ahad A, Elsayed M, Tohid H. **The accuracy of clinical symptoms in detecting cauda equina syndrome in patients undergoing acute MRI of the spine.** *Neuroradiol J* 2015;28:438–42 CrossRef Medline
10. Lavy C, James A, Wilson-MacDonald J, et al. **Cauda equina syndrome.** *BMJ* 2009;338:b936 CrossRef Medline
11. Shah LM, Long D, Sanone D, et al. **Application of ACR appropriateness guidelines for spine MRI in the emergency department.** *J Am Coll Radiol* 2014;11:1002–04 CrossRef Medline
12. Mukherjee S, Thakur B, Crocker M. **Cauda equina syndrome: a clinical review for the frontline clinician.** *Br J Hosp Med (Lond)* 2013;74:460–64 CrossRef Medline
13. Friedman BW, Chilstrom M, Bijur PE, et al. **Diagnostic testing and treatment of low back pain in United States emergency departments: a national perspective.** *Spine (Phila Pa 1976)* 2010;35:E1406–11 CrossRef Medline
14. Henschke N, Maher CG, Ostelo RW, et al. **Red flags to screen for malignancy in patients with low-back pain.** *Cochrane Database Syst Rev* 2013;2:CD008686 CrossRef Medline
15. Mehrotra A, Liu H, Adams JL, et al. **Comparing costs and quality of care at retail clinics with that of other medical settings for 3 common illnesses.** *Ann Intern Med* 2009;151:321–28 CrossRef Medline

Inadvertent Intrafacet Injection during Lumbar Interlaminar Epidural Steroid Injection: A Comparison of CT Fluoroscopic and Conventional Fluoroscopic Guidance

P.G. Kranz, A.B. Joshi, L.A. Roy, K.R. Choudhury, and T.J. Amrhein

ABSTRACT

BACKGROUND AND PURPOSE: Inadvertent intrafacet injection can occur during interlaminar epidural steroid injection, resulting in a false-positive loss of resistance and nontarget injection of medication. The purpose of this investigation was to compare the observed rates of this phenomenon during lumbar interlaminar epidural steroid injection performed by using conventional fluoroscopic and CT fluoroscopic guidance.

MATERIALS AND METHODS: We retrospectively reviewed 349 lumbar interlaminar epidural steroid injections performed by using conventional fluoroscopy or CT fluoroscopic guidance to determine the observed rates of inadvertent intrafacet injection with each technique. Cases of inadvertent intrafacet injection were classified as either recognized or unrecognized by the proceduralist at the time of the procedure. Multivariate logistic regression was used to determine the independent effect of imaging guidance technique, age, and sex.

RESULTS: The rate of inadvertent intrafacet injection was observed to be 7.5% in the CT fluoroscopic group and 0.75% in the conventional fluoroscopy group. All 16 cases identified from CT fluoroscopic procedures were recognized during the procedure; the single case identified from conventional fluoroscopy procedures was not recognized prospectively. The type of imaging guidance showed a statistically significant effect on the detection of the phenomenon (OR for conventional fluoroscopy versus CT fluoroscopy = 0.10, $P = .03$) that was independent of differences in age or sex.

CONCLUSIONS: Inadvertent intrafacet injection is identified during CT fluoroscopic–guided interlaminar epidural steroid injection at a rate that is 10-fold greater than the same procedure performed under conventional fluoroscopy guidance.

ABBREVIATIONS: CF = conventional fluoroscopy; CTF = CT fluoroscopy; ILESI = interlaminar epidural steroid injection

Inadvertent intrafacet injection during interlaminar epidural steroid injection (ILESI) can result in nontarget injection outside the epidural space.[1] It is thought to be due to unintentional needle entry into the retrodural space of Okada, a space located dorsal to the ligamentum flavum that allows communication between the bilateral facet joints and interspinous bursa.[2,3] Needle placement into this space causes a false-positive loss of resistance, which can mimic the loss of resistance normally felt during entrance into the epidural space.

The observed incidence of inadvertent intrafacet injection during attempted ILESI by using fluoroscopic guidance has been previously reported to be 1.2%.[4] However, most cases (63%) are not recognized by the operator at the time of the injection.[4] Thus, most instances of this type of injection result in nontarget delivery of medication and, as a result, do not successfully treat the intended pathology. Although the observed incidence of this phenomenon has been studied by using fluoroscopic guidance, the rate of occurrence during CT fluoroscopy (CTF)–guided injections, which may be more sensitive to detection of small amounts of intrafacet contrast, has not yet been studied, to our knowledge.

The purpose of this investigation was to determine the observed rate of inadvertent intrafacet injection resulting in false-positive loss of resistance during CTF-guided ILESI and to compare that with the rate observed during conventional fluoroscopy (CF)–guided ILESI at a single institution.

MATERIALS AND METHODS

This study is a retrospective investigation of lumbar ILESIs performed under CTF or CF guidance at a single institution. Cases

Received May 27, 2016; accepted after revision September 2.

From the Departments of Radiology (P.G.K., K.R.C., T.J.A.), Orthopedic Surgery (A.B.J.), and Anesthesiology (L.A.R.), Duke University Medical Center, Durham, North Carolina.

Please address correspondence to Peter G. Kranz, MD, Department of Radiology, Duke University Medical Center, Box 3808, Durham, NC 27710; e-mail: peter.kranz@duke.edu; @PeterGKranz

http://dx.doi.org/10.3174/ajnr.A5000

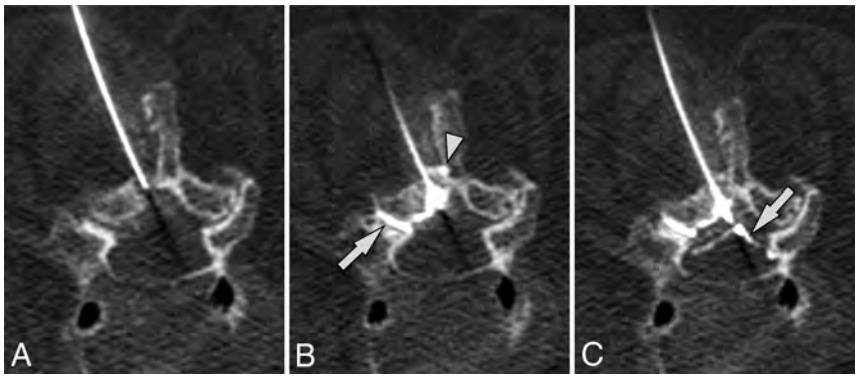

FIG 1. Inadvertent intrafacet injection in an 84-year-old woman with back pain who underwent ILESI with CTF. *A*, Preinjection axial CTF image before needle placement into the ligamentum flavum. *B*, Initial CTF image obtained after loss of resistance shows contrast in the facet joint ipsilateral to the injection (*arrow*). Contrast also pools around the needle tip in the retrodural space of Okada and extends into the interspinous bursa (*arrowhead*). *C*, The needle was subsequently advanced through the ligamentum flavum. Contrast is now seen in the epidural space (*arrow*).

were identified by using the institutional electronic medical record to review procedure schedules. For the CTF-guided cases, all consecutive outpatient lumbar ILESIs performed by a single proceduralist during an 18-month period were included. For the CF-guided cases, all consecutive outpatient lumbar ILESIs performed by 7 proceduralists during an 18-month period were included. The start time for collection of CF-guided cases was 17 months later than that for CTF-guided cases because of differences in when CF-guided cases were archived in a unified institutional PACS. The exclusion criteria were technically inadequate intraprocedural images or images that were missing from the institutional PACS.

The proceduralist performing the CTF-guided ILESIs was a board-certified radiologist with a Certificate of Added Qualification in neuroradiology with 8 years' experience performing spine interventions under CTF guidance. The CF-guided injections were performed by 7 proceduralists (1 board-certified physiatrist and 6 board-certified anesthesiologists) with 2–29 years' experience performing spine interventions under fluoroscopic guidance. The average number of years of proceduralist experience per injection in the CF cohort was 7.7 years.

Demographic data and procedural reports were obtained from the electronic medical record. The study was approved by our local institutional review board and was compliant with Health Insurance Portability and Accountability Act regulations.

Injection Technique

CTF-guided procedures were performed by using a posterior oblique interlaminar approach, as previously described.[5] Briefly, a 22-ga Quincke-Point Needle (Becton-Dickinson, Washington, DC) was placed into the ligamentum flavum by using intermittent CTF, a syringe containing contrast (iopamidol, Isovue-M 200; Bracco, Princeton, New Jersey) was attached, and the needle was then advanced until loss of resistance was obtained. The volume of contrast injected was typically approximately 0.5 mL. Immediately on loss of resistance, an additional image was obtained to evaluate the location of the injected contrast. All images from the procedure were archived in the PACS.

CF-guided injections were performed by using a method similar to that of injections performed under CTF.[6] However, an 18- or 20-gauge Tuohy needle was used, and the epidurogram was obtained under either live or spot fluoroscopy, according to operator preference. Some proceduralists in the CF group used saline to judge loss of resistance; location was subsequently confirmed by all proceduralists with approximately 2 mL of contrast (Isovue-M 300). All proceduralists used at least 2 views, an anteroposterior view and either a lateral or 55° contralateral oblique view. The fluoroscopic images documenting the injected contrast and final needle position were archived in the PACS.

Image Analysis

Intraprocedural images from both CTF- and CF-guided procedures were retrospectively reviewed on the PACS to determine whether inadvertent contrast injection into the facet joints occurred. A false-positive loss of resistance was determined to have occurred if contrast medium was documented in the facet joint before injection of contrast into the epidural space (Fig 1). Cases of inadvertent facet injection were classified as either recognized or unrecognized. Cases were considered recognized if images confirmed subsequent advancement of the needle with resultant contrast injection into the epidural space. Cases were considered unrecognized if no further needle adjustment was made.

Initial image review was performed by one of the study proceduralists who performed injections with the same type of imaging technique. For the CTF-guided procedures, cases were reviewed by the performing neuroradiologist. For the CF-guided procedures, cases were reviewed by the study physiatrist. All cases considered either equivocal or positive for inadvertent facet injection were then independently reviewed by a second board-certified radiologist with a Certificate of Added Qualification in neuroradiology who has 5 years' experience performing injections by using both CTF and CF guidance. Cases of disagreement between readers were resolved by consensus.

Statistical Analysis

Initial univariate analysis compared differences in patient ages between groups by using the Mann-Whitney *U* test, and sex, by using the Fisher exact test. This analysis revealed an unequal age distribution between the CTF and CF groups; multivariate logistic regression was therefore used to examine the independent effect of 3 variables on intrafacet injection: imaging technique (ie, CTF or CF), age, and sex.

Statistical analyses were performed by using commercially available software (univariate analysis was performed with GraphPad Prism 6 software, Version 6.0b; GraphPad Software, San Diego, California; multivariate analysis was performed with R statistical and computing software, Version 3.0.2; http://www.r-project.org/). *P* values $< .05$ were considered statistically significant.

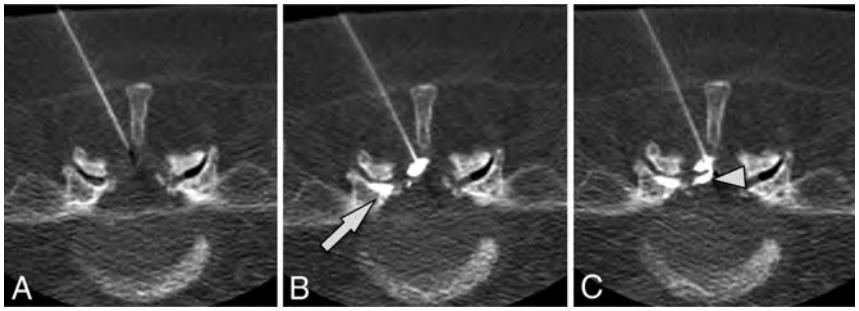

FIG 2. Inadvertent intrafacet injection in a 67-year-old man with spinal stenosis and back pain who underwent ILESI with CTF. *A*, Preinjection axial CTF image before needle placement into the ligamentum flavum. *B*, Initial CTF image obtained after loss of resistance shows contrast in the facet joint (*white arrow*). *C*, Image obtained after needle advancement shows contrast in the epidural space (*arrowhead*).

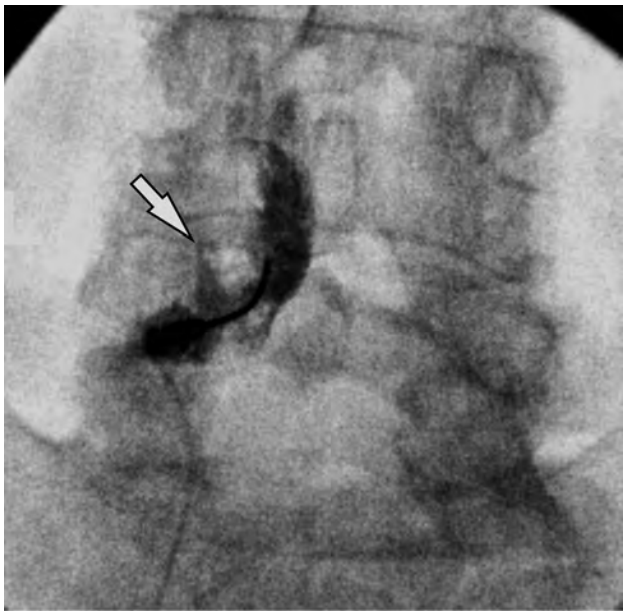

FIG 3. Inadvertent intrafacet injection in a 63-year-old man with a painful L4–5 central disc protrusion who underwent ILESI by using conventional fluoroscopic guidance. The final procedural image shows a triangular configuration of contrast overlying the inferior aspect of the left L4–5 facet joint, consistent with intrafacet injection.

RESULTS

A total of 349 lumbar ILESIs were identified. Of these, 214 were performed under CTF-guidance and 135 were performed under CF guidance. No cases were excluded.

The mean subject age for the CTF group was slightly older than the CF group (65.6 ± 14.4 versus 60.6 ± 13.7 years), a difference that was statistically significant ($P = .002$). Female patients composed 56% of the CTF group and 59% of the CF group, a difference that was not significant ($P = .51$).

Sixteen cases of inadvertent intrafacet injection were identified in the CTF cohort, resulting in a rate of 7.5% (16/214). All 16 cases (100%) were identified during the procedure, and the needle was repositioned into the epidural space with subsequent technically successful completion of the procedure (Fig 2). All 16 cases identified as positive for inadvertent intrafacet injection by the first reader were also considered positive by the second reader.

In the CF cohort, 1 case of inadvertent facet injection was identified (Fig 3), resulting in an overall rate of 0.75% (1/135). In this case, the proceduralist did not recognize the inadvertent injection during the procedure. This case was considered equivocal by the first reader, positive for inadvertent intrafacet injection by the second reader, and positive on consensus read. No disagreement between readers occurred in the remaining CTF or CF cases.

Because of the unequal age distribution between the CTF and CF groups, multivariate logistic regression was used to determine the independent effect of 3 variables on the rate of recognition of intrafacet injection: type of image guidance, age, and sex. Of these 3 factors, the only variable that showed a statistically significant effect was the type of image guidance: The CF group showed a significantly lower rate of recognized intrafacet injections compared with the CTF group (OR for CF versus CTF = 0.10; 95% CI, 0.01–0.80; $P = .03$). Increasing age was associated with a nonsignificant trend toward a small increase in risk (OR = 1.04, $P = .06$). Sex was not significantly associated with the risk of intrafacet injection ($P = .09$).

Of the 17 cases in which intrafacet injection was identified, all (100%) had contrast flow into the facet ipsilateral to the injection. Additional contrast flow into the contralateral facet joint was seen in 2 cases (12%) and into the interspinous bursa in 3 cases (18%). Injections were distributed along the entire lumbar spine, with cases positive for intrafacet injection seen at L1–2 ($n = 1$), L3–4 ($n = 7$), L4–5 ($n = 8$), and L5–S1 ($n = 1$). Of the cases performed under CTF guidance, a widened facet joint (>2 mm), with or without gas in the joint, was noted at the injected level in 5 cases (31%).

DISCUSSION

Identification of inadvertent intrafacet injection during attempted lumbar ILESI is important because it results in the false-positive loss of resistance and, if not recognized, may decrease the effectiveness of the procedure due to nontarget delivery of medication. Previous studies of CF-guided ILESI have demonstrated that these injections are often overlooked at the time of the procedure and that the contrast pattern associated with such injections may mimic a true epidural injection.[1,4] Our investigation showed that inadvertent intrafacet injection was identified during 7.5% of CTF-guided lumbar ILESIs, a rate 10-fold higher than the rate observed during CF-guided injections. The rate of 0.75% we observed for CF-guided injections is generally comparable with the rate of 1.2% previously reported in the literature for CF-guided procedures.[4]

Previous anatomic investigations have identified mechanisms for the communication between the interlaminar space and the facet joint. In 1981, Okada[7] described an anatomic space located dorsal to the ligamentum flavum that allows communication between the bilateral facet joints and the interspinous region at a single spinal level. This space has become known as the "retrodural space of Okada" and may be identified on imaging during

spinal procedures in which contrast is injected or in cases in which infection spreads along this space.[2,8] Spread of contrast in the retrodural space of Okada specifically during lumbar ILESI, resulting in intrafacet injection, has been previously documented in the literature.[3] In a postmortem anatomic study, Xu et al[9] showed that in some patients, the facet joint capsule extends not only dorsal to the ligamentum flavum but also into the ligamentum flavum itself. This relationship would provide a pathway for intrafacet spread of contrast (and resultant loss of resistance) while a needle passes through the ligamentum flavum before entry into the epidural space.

There are 2 possible explanations for the difference in rates of identified inadvertent intrafacet injections between CTF and CF: The phenomenon may be more common during CTF-guided procedures or it may be more readily recognized during CTF-guided procedures.

For the first explanation to be true, there would need to be procedural differences between CTF- and CF-guided ILESI that could account for this difference. The techniques for performing the ILESI under fluoroscopic guidance and CTF-guidance are generally the same; however, in our investigation, the proceduralists used different needle types (Tuohy for CF versus Quincke-Point Needle for CTF). This difference might have had an effect on the observed rates of intrafacet injection. Other procedural variables such as the spinal level of injection and relative laterality of needle placement within the interlaminar space would not be likely to account for the difference because they have been previously investigated and shown not to affect the likelihood of inadvertent intrafacet injection.[1,4]

An alternate explanation is that the cross-sectional nature of the imaging used with CTF is more sensitive for the detection of this type of injection. Fluoroscopic imaging would be expected to be less likely to detect inadvertent facet injection, and indeed previous evidence shows that most cases occurring during CF-guided procedures go unrecognized. In a study examining inadvertent intrafacet injections during 686 lumbar ILESIs performed under CF guidance, only 37.5% of inadvertent intrafacet injections were prospectively identified by the proceduralist at the time of the original procedure.[4] The same investigators, in a separate report describing the appearance of the phenomenon by using CF, indicated that the imaging appearance of an intrafacet injection might mimic the appearance of a successful epidural injection. They noted that differentiation of intrafacet injection from epidural injection may require injection of a larger volume of contrast sufficient to distend the facet joint capsule, producing more clearly visible contrast in the joint on lateral projection.[1] This increase in the volume of contrast injection is not commonly performed in routine practice, however. Furthermore, the best projection for recognizing intrafacet injection under fluoroscopy would be an oblique image oriented in the same plane as the facet joint; this view is not routinely obtained during most CF-guided lumbar ILESIs. Given the difficulty in recognizing this injection type, it is certainly plausible that previous estimates of an incidence of 1.2% during CF-guided procedures may be underestimations.

If the true incidence of intrafacet injection is indeed closer to our estimate of 7.5% as seen with CTF-guided cases, the clinical impact of this phenomenon would not be trivial. Based on 2011 use data from Medicare alone, more than 914,000 lumbar ILESIs are performed per year in the United States.[10] Assuming a true rate of 7.5% for intrafacet injections, the number of attempted ILESIs that resulted in inappropriate intrafacet injection would be in excess of 68,500 per year, with most of those cases likely going unrecognized. These cases represent patients for whom the intended epidural injection of steroid would not occur; thus, the target pathology would go untreated.

Elimination of these cases should have the effect of increasing clinical success rates for ILESIs. Of note, all instances of inadvertent intrafacet injection during CTF-guided procedures were prospectively recognized, which would markedly decrease the risk of nontarget injection when this method of imaging guidance is used. Further investigation into how to more reliably detect these injection types during CF-guided ILESI, including the possibility of additional fluoroscopic views to optimize the chances of its visualization, is necessary.

When performing ILESI, one must also remember that intrafacet injection may not be the only potential source of false-positive loss of resistance. False-positive rates of loss of resistance of up to 25%–30% have been reported when using air-filled syringes to enter the epidural space.[11,12] It is possible that some of these previously reported cases may have been due to unrecognized entry into the retrodural space of Okada. The use of iodinated contrast markedly decreases the rate of incorrect needle-tip placement,[13] but as mentioned previously, it does not completely protect against error because the appearance of contrast injected into the facet may closely resemble an epidural injection on lateral views.[1] Proceduralists must take care to confirm that the suspected epidural entry, whether judged by loss of resistance or contrast injection, is confidently confirmed before medication delivery.

Our study has limitations. First, and perhaps most important, this investigation does not definitely establish the reason for the observed difference in rates on intrafacet injection performed under CF and CTF guidance. Although CTF may recognize cases missed under CF, we cannot preclude the possibility that unrecognized differences in the CTF and CF techniques predispose CTF-guided procedures to a higher likelihood of this type of injection. The implementation of conventional fluoroscopic techniques or views that more reliably identify intrafacet injection would help resolve this question by providing a better estimate of the true incidence. Second, the small number of total cases of intrafacet injections could result in failure to detect a statistically significant influence of age and/or sex (ie, a type II error). Age, the closest variable to achieving statistical significance, showed only a very small effect size, however, suggesting that even if there was a statistically significant effect, it would not explain the 10-fold increase in the rate of intrafacet injection we observed under CTF. Sex was equal between the CF and CTF groups ($P = .51$) and would therefore not result in the observed difference in rates either.

CONCLUSIONS

We detected inadvertent intrafacet injection resulting in a false-positive loss of resistance during CTF-guided lumbar ILESI in

7.5% of procedures, a 10-fold increase in the rate we observed when the same procedure was performed under conventional fluoroscopy. Because this type of injection can result in nontarget injection of medication if not recognized, further investigation is needed to determine how to optimize detection during CF-guided procedures and whether this observed difference in intrafacet injection rates is attributable to differences in technique or whether it is the result of the increased sensitivity of CTF imaging to this type of phenomenon.

Disclosures: Lance A. Roy—*UNRELATED*: *Consultancy*: Medtronic, *Comments*: neuromodulation; *Grants/Grants Pending*: Pfizer, *Comments*: drug study; *Payment for Lectures including Service on Speakers Bureaus*: Medtronic, *Comments*: neuromodulation.

REFERENCES

1. Huang AJ, Rosenthal DI, Palmer WE. **Inadvertent intra-articular lumbar facet joint injection during fluoroscopically guided interlaminar epidural steroid injection.** *Skeletal Radiol* 2011;40:33–45 CrossRef Medline
2. Lehman VT, Murthy NS, Diehn FE, et al. **The posterior ligamentous complex inflammatory syndrome: spread of fluid and inflammation in the retrodural space of Okada.** *Clin Radiol* 2015;70:528–35 CrossRef Medline
3. Murthy NS, Maus TP, Aprill C. **The retrodural space of Okada.** *AJR Am J Roentgenol* 2011;196:W784–89 CrossRef Medline
4. Huang AJ, Palmer WE. **Incidence of inadvertent intra-articular lumbar facet joint injection during fluoroscopically guided interlaminar epidural steroid injection.** *Skeletal Radiol* 2012;41:157–62 CrossRef Medline
5. Wagner AL. **CT fluoroscopy-guided epidural injections: technique and results.** *AJNR Am J Neuroradiol* 2004;25:1821–23 Medline
6. Bogduk N. *International Spine Intervention Society Practice Guidelines for Spinal Diagnostic and Treatment Procedures.* San Francisco: International Spine Intervention Society; 2013:409
7. Okada K. **Studies on the cervical facet joints using arthrography of the cervical facet joint (author's transl)** [Japanese]. *Nihon Seikeigeka Gakkai Zasshi* 1981;55:563–80 Medline
8. Sarazin L, Chevrot A, Pessis E, et al. **Lumbar facet joint arthrography with the posterior approach.** *Radiographics* 1999;19:93–104 CrossRef Medline
9. Xu GL, Haughton VM, Carrera GF. **Lumbar facet joint capsule: appearance at MR imaging and CT.** *Radiology* 1990;177:415–20 CrossRef Medline
10. Manchikanti L, Benyamin RM, Hansen H, et al. **Reversal of epidural cuts in 2015 physician payment schedule: two steps forward, one step back.** *Pain Physician* 2014;17:E565–73 Medline
11. White AH, Derby R, Wynne G. **Epidural injections for the diagnosis and treatment of low-back pain.** *Spine (Phila Pa 1976)* 1980;5:78–86 CrossRef Medline
12. Bartynski WS, Grahovac SZ, Rothfus WE. **Incorrect needle position during lumbar epidural steroid administration: inaccuracy of loss of air pressure resistance and requirement of fluoroscopy and epidurography during needle insertion.** *AJNR Am J Neuroradiol* 2005;26:502–05 Medline
13. Johnson BA, Schellhas KP, Pollei SR. **Epidurography and therapeutic epidural injections: technical considerations and experience with 5334 cases.** *AJNR Am J Neuroradiol* 1999;20:697–705 Medline

Comparison of 3 Different Types of Spinal Arteriovenous Shunts below the Conus in Clinical Presentation, Radiologic Findings, and Outcomes

T. Hong, J.E. Park, F. Ling, K.G. terBrugge, M. Tymianski, H.Q. Zhang, and T. Krings

ABSTRACT

BACKGROUND AND PURPOSE: Spinal arteriovenous shunts below the conus constitute 3 types of lesions, which have previously been mainly described in case reports, given their rarity, and are sometimes misdiagnosed. The purpose of this study was to describe the features of each type and compare these types as to epidemiologic features, clinical and radiologic presentations, treatment, and outcomes in a consecutive series of 48 cases.

MATERIALS AND METHODS: The prospectively collected data bases of 2 referral centers for spinal vascular lesions were retrospectively reviewed. Spinal arteriovenous shunts below the conus were defined as all dural and intradural shunts below the conus medullaris. Clinical features, radiologic findings, treatment results, and clinical outcomes were assessed.

RESULTS: There were filum terminale arteriovenous fistulas in 11 patients (22.9%), radicular arteriovenous shunts in 7 patients (14.6%), and spinal dural arteriovenous fistulas in 30 patients (62.5%). Radicular arteriovenous shunts presented at a younger age ($P = .017$) and with a higher incidence of back pain symptoms ($P = .037$). A tethered spinal cord was found in 54.5% of patients with filum terminale arteriovenous fistulas and 23.3% of patients with spinal dural arteriovenous fistulas. After treatment, the angiographic complete obliteration rate was 89.4% and spinal function was improved significantly ($P < .001$).

CONCLUSIONS: Three groups of spinal arteriovenous shunts below the conus can be differentiated according to clinical and radiologic features. Filum terminale arteriovenous fistulas are frequently associated with dysraphic malformations, which may suggest a particular embryologic origin.

ABBREVIATIONS: ALS = Aminoff-Logue scale; FTAVF = filum terminale arteriovenous fistula; rAVS = radicular arteriovenous shunt; SDAVF = spinal dural arteriovenous fistula

Spinal arteriovenous lesions are rare and complex neurovascular diseases that can be categorized according to embryologic considerations,[1] anatomic and imaging features,[2] or their locations.[3] Among the spinal vascular malformations, arteriovenous shunts below the conus medullaris include some particular groups of lesions and are sometimes misdiagnosed due to similar clinical and radiologic presentations, which are worth addressing and differentiating separately.[4] This group of lesions is distant from the spinal cord,[5,6] presents mainly with progressive myelopathy rather than hemorrhage, and may be associated with dysraphic malformations, which suggest a unique embryologic origin. If diagnosis and angioarchitecture are correctly identified, treatment is relatively simple compared with spinal vascular lesions in other locations.[7,8]

According to their feeding arteries, we can classify 3 different types of spinal arteriovenous shunts below the conus: shunts fed by the artery of the filum terminale (filum terminale arteriovenous fistulas [FTAVFs]), shunts fed by dural branches (spinal dural arteriovenous fistulas [SDAVFs]), and shunts fed by radic-

Received June 8, 2016; accepted after revision September 6.

From the Department of Neurosurgery (T.H., F.L., H.Q.Z.), Xuanwu Hospital, Capital Medical University, Beijing, China; Department of Radiology and Research Institute of Radiology (J.E.P.), Asan Medical Center, University of Ulsan College of Medicine, Seoul, Korea; and Department of Medical Imaging (K.G.T., T.K.) and Division of Neurosurgery (M.T.), Toronto Western Hospital, University of Toronto, Ontario, Canada.

Drs Krings and Zhang contributed equally to this work.

This work was supported by the National Natural Science Foundation of China (81171165, 81671202), the Beijing Municipal Administration of Hospital Clinical Medicine Development Project (ZY201309), and the Beijing Municipal Science and Technology Commission (D161100003816001).

Please address correspondence to Timo Krings, MD, PhD, Division of Neurosurgery, Department of Medical Imaging, Toronto Western Hospital, 399 Bathurst St, 3 McLaughling Wing, Toronto, Ontario M5T 2S8, Canada; e-mail Timo.Krings@uhn.ca

Indicates open access to non-subscribers at www.ajnr.org

Indicates article with supplemental on-line table.

Indicates article with supplemental on-line photos.

http://dx.doi.org/10.3174/ajnr.A5001

ular arteries (radicular arteriovenous shunts [rAVSs]). Previously, these types of vascular malformations have been described mainly in smaller case series or case reports. Since Djindjian et al[9] reported the first case of FTAVF, several case reports[10-13] and 2 patient series studies[14,15] have been published. rAVSs that are located on a nerve root of the cauda equina have been reported in 2 cases to date.[16] SDAVFs in this region can have lumbar or sacral segmental artery supply and constitute approximately 23% of the dural AVFs in larger series.[17] Clinical and epidemiologic features, their relative proportion to each other, and the associated malformations of these 3 different shunts below the conus have not been described however, and the differential diagnoses of the 3 groups have not been investigated in greater detail, presumably given their rarity.

In this study, we review a series of 48 spinal arteriovenous shunts below the conus derived from the combined prospectively maintained data bases of 2 referral centers (Xuanwu Hospital, Beijing, China and Toronto Western Hospital, Toronto, Canada) and thus aim to compare epidemiologic features, clinical presentations, MR imaging and angiographic findings, treatment, and outcomes of 3 types of lesion at this location.

MATERIALS AND METHODS

Patient Population and Clinical Evaluation

We retrospectively reviewed patients from the combined prospectively maintained spinal vascular disease data bases (from January 2000 to August 2015) of 2 tertiary hospitals after having obtained local ethics board approval. Both institutions are referral centers for treating spinal vascular lesions and share similar protocols on diagnosis, treatment, and data base maintenance. We defined spinal arteriovenous shunts below the conus as all dural and intradural vascular lesions with the shunt occurring below the conus medullaris. For the SDAVF lesions, we selected those with fistula points on DSA located lower than the vertebral level of the conus, the latter was assessed by MR imaging in all screened patients. The clinical follow-up plan was 3, 12, 24, and 60 months after treatment, and angiographic follow-up was performed at 2–4 months after embolization or within 1 week after the surgical procedure to verify obliteration. Pretreatment and follow-up spinal functions were evaluated for gait, micturition, and defecation status according to the Aminoff-Logue scale (ALS)[18]; these evaluations were performed on the basis of the medical record by a clinician (T.H.) not directly involved in the care of these patients. We added a defecation subscale (On-line Table) due to frequent anal sphincter disturbance of lesions at the sacrum.

Radiologic Evaluation

Multisequence spinal MR images were available in all patients and were reviewed by an independent diagnostic neuroradiologist (J.E.P.), who was blinded to the clinical information of the patient. The evaluation included the presence of congestive edema, engorged veins, hemorrhage, and associated MR imaging findings (tethered spinal cord, lipoma, sacral cysts, or spina bifida). The radiologic definition of the tethered cord was the tip of the conus medullaris below the lower border of the L2 vertebral body.[19]

Standardized spinal DSA was performed, with evaluation of all segmental arteries including the bilateral internal iliac arteries and median sacral artery. Location of the shunt (dural, filum terminale, or along a nerve root of the cauda equina), angioarchitecture, and other associated vascular lesions were assessed. The angioarchitecture was evaluated regarding the number and type of the feeding arteries, the type of lesion (direct fistula versus intervening network or nidus), location of the lesion, and direction of venous drainage. Consensus diagnosis was made by the 2 senior authors (H.Q.Z. and T.K.).

Treatment

Treatment options included endovascular embolization, open surgery, or a combined approach. The decision to choose an open surgical versus an endovascular route was mainly based on the vascular anatomy and was done in a multidisciplinary conference. In general, the features of a tortuous course of the parent artery, a small caliber of the distal feeding artery, or a glomus-like architecture were considered unfavorable for an endovascular approach. Embolization was the first choice when the endovascular operator predicted that the arterial approach was available and an adequate safety margin to normal spinal feeding arteries was ensured. Only liquid embolic agents were used. Surgery was indicated when the embolization was not feasible or failed to achieve complete obliteration. The surgical approach varied according to lesion location and involved identification of the distal feeding artery and the proximal arterialized vein that was surgically disconnected to cure the shunt. Motor- and sphincter-evoked potential monitoring and indocyanine green video-angiography facilitated identification and safety during the surgical procedure.

Statistical Analysis

We performed mean age comparison with the ANOVA test and incidence comparison among different groups with the Fisher exact test. For the duration time data that deviated from a normal distribution, the Kruskal-Wallis test was applied. The Wilcoxon signed rank test was used to analyze the pre- and posttreatment ALS scores. Statistical significance was set at $P < .05$. All analyses were performed with SPSS software, Version 19.0.0 (IBM, Armonk, New York).

RESULTS

Forty-eight patients with spinal arteriovenous shunts below the conus were identified from the combined data bases that comprised a total of 359 spinal arteriovenous shunts (13.3%). There were 36 males (75%) and 12 (25%) females with a mean age of 52.4 years (range, 5–81 years). Mean clinical follow-up duration was 25.7 months (range, 3–77 months). Ten patients (20.8%) were lost to follow-up after treatment.

Angioarchitecture

In our series, there were 11 patients (22.9%) with FTAVFs, 7 patients (14.6%) with rAVSs, and 30 patients (62.5%) with SDAVFs (Table 1).

The FTAVFs ($n = 11$) were shown on angiograms as a direct communication of the filum terminale artery (distal continuation of the anterior spinal artery) and the filum terminale vein, which

drained upward to the perimedullary veins (Fig 1 and On-line Fig 1). The origin of the anterior spinal artery feeding the artery of the filum terminale included the intercostal arteries ($n = 4$), lumbar arteries ($n = 4$), iliac arteries ($n = 2$), and the median sacral artery ($n = 1$). The fistula location ranged between the level of L2 and S2. FTAVFs with extra supply were found in 3 of the 11 patients (Fig 1*B*), and in 1 patient, an FTAVF was present together with a separate conus AVM (On-line Fig 1).

The rAVSs ($n = 7$) were located on an intradural nerve root of the cauda equina between the radicular artery and a radicular vein draining to the perimedullary vein (Fig 2 and On-line Fig 2). The origin of the feeding artery was from the lateral sacral artery of the iliac artery in all 7 patients. The shunt presented as a direct fistula without an intervening network of abnormal arteries ($n = 4$) or as a micronidus-like structure with venous outpouching ($n = 3$). The shunt was located between L4 and S1 off the midline but intradurally (ie, on a nerve root). An rAVS was concomitant with a conus AVM in 3 of the 7 patients (Fig 2).

Table 1: Proportion of 3 types of spinal arteriovenous shunts below the conus

Classification	No. of Patients (%)	Feeding Artery
FTAVF	11 (22.9%)	Artery of the filum terminale
FTAVF with extra supply	3 (6.2%)	
FTAVF with conus AVM	1 (2.1%)	
rAVS	7 (14.6%)	Radicular artery of the segmental artery
rAVS with conus AVM	3 (6.3%)	
SDAVF	30 (62.5%)	Dural branch from the lumbar artery or lateral sacral artery

SDAVFs ($n = 30$, 62.5%) constituted the largest group in our case series and were defined as fistulous communications between a radiculomeningeal artery and an intradural vein within the dura mater with retrograde drainage toward the perimedullary veins (Fig 3 and On-line Fig 3). The origin of the feeding artery included lumbar arteries in 9 patients and the lateral sacral artery of the iliac arteries in 21 patients. A single feeding artery was present in most patients ($n = 27$); in 2 patients, the shunt was fed by bilateral iliac arteries (On-line Fig 3); and in 1 patient, the shunt was fed by 2 adjacent lumbar segmental arteries. The location of the fistulas was between L2 and S2.

Demographics, Clinical Presentation, and MR Imaging Findings

Comparison of demographics, pretreatment clinical data, and MR imaging findings according to 3 different types of the lesions are summarized in Table 2. The mean ages among patients with FTAVFs, rAVSs, and SDAVFs were significantly different ($P = .017$). The post hoc analysis demonstrated that the patients with rAVSs were younger at presentation compared with those with FTAVFs (37.4 versus 52.9 years, $P = .032$) or SDAVFs (37.4 versus 55.6 years, $P = .005$). All 3 groups showed a male predominance, though there was a nonsignificantly higher proportion of female (42.9%) patients in the rAVS group compared with 27.3% in the FTAVF group and 20% in SDAVF group.

At the time of diagnosis, the symptoms of arteriovenous shunts below the conus were progressive paraparesis in 44 patients (91.7%), bowel/bladder dysfunction in 38 patients (79.2%), progressive hypesthesia in 33 patients (68.8%), sensory numbness

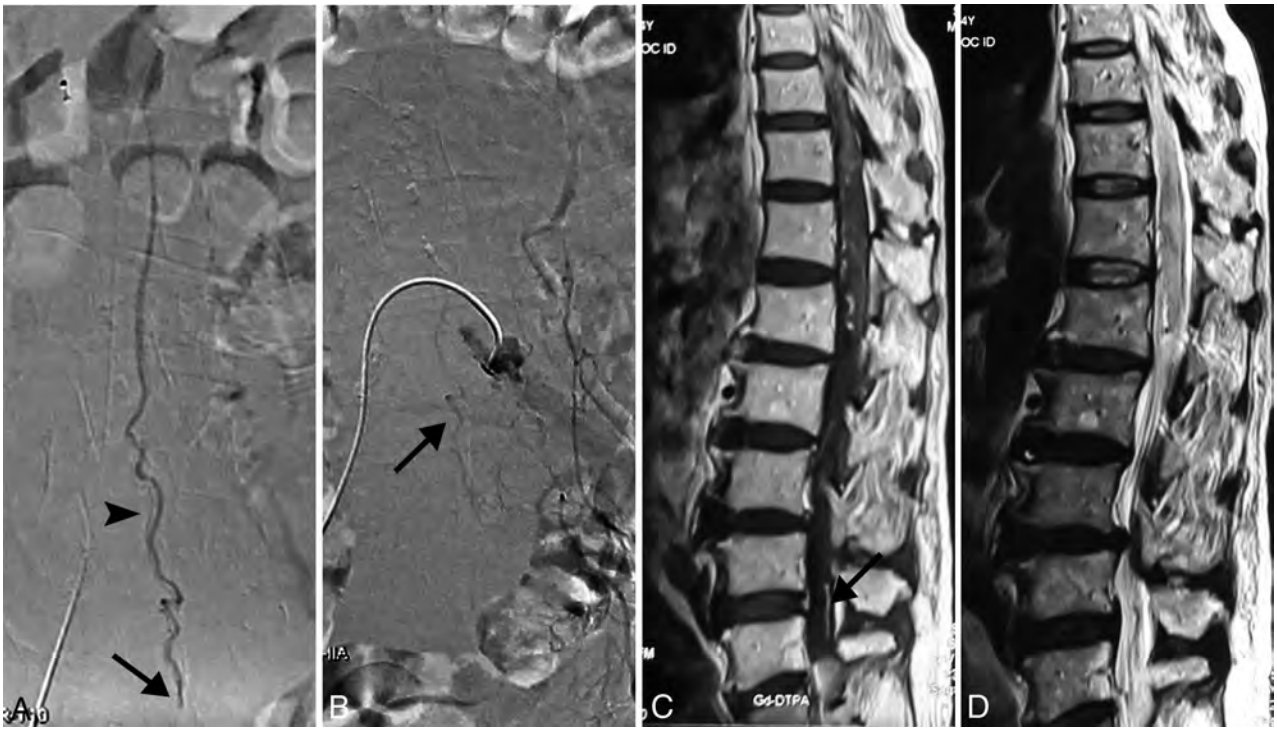

FIG 1. The radiologic presentation of a 64-year-old man with a FTAVF. *A*, Spinal angiogram shows the FTAVF at the level of S2 (*arrow*). Note the faint filum terminale artery (*arrowhead*) from the T10 intercostal artery, converging with the draining vein upwardly. *B*, Internal iliac artery angiogram demonstrates the extra supply of the FTAVF lesion in *A*. Note the same appearance of the drainage vein (*arrow*) as in *A*. *C*, The T1 contrast-enhanced image demonstrates the abnormally dilated and tortuous vessels situated on the surface of the spinal cord (*arrow*). *D*, T2-weighted image of the thoracic spine shows cord edema extending to the upper thoracic spinal cord.

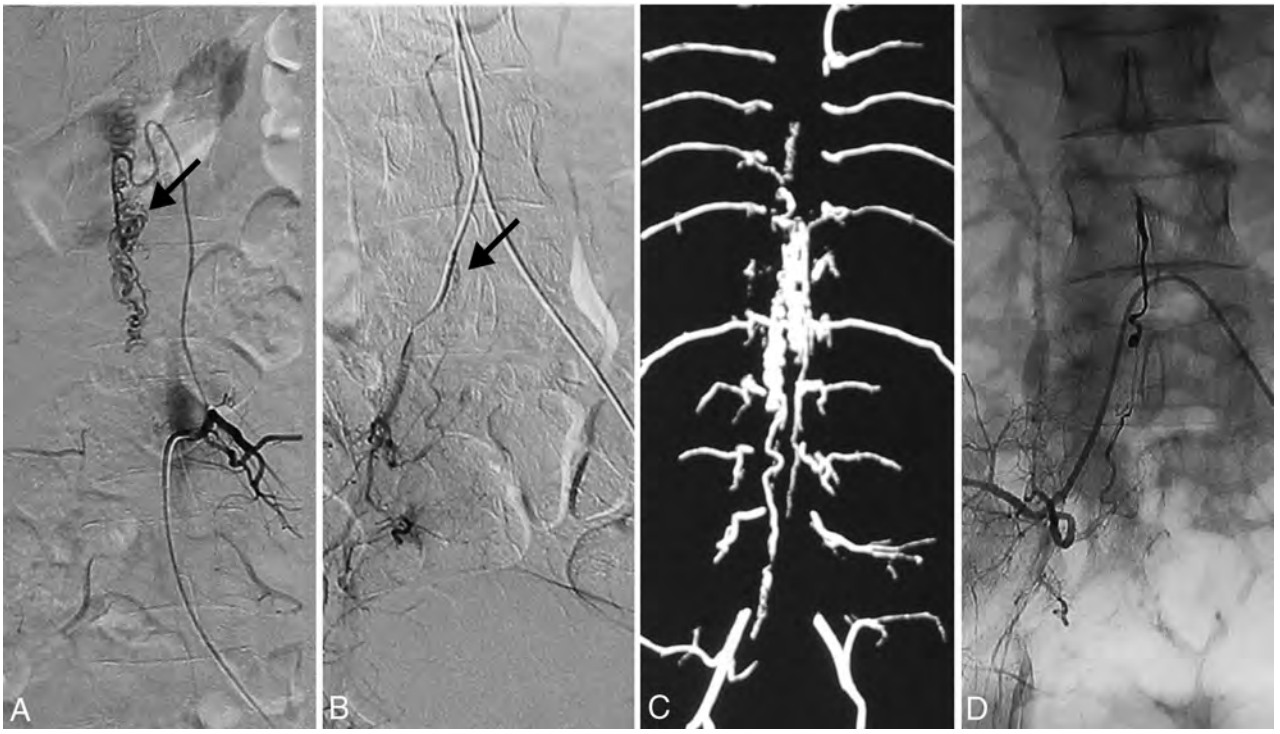

FIG 2. The radiologic presentation of a 34-year-old man with concomitant rAVS and conus AVM. *A*, Left L3 lumbar artery angiogram shows the nidus-type conus AVM at the level of L1 (*arrow*). *B*, Right internal iliac artery angiogram demonstrates an rAVS (*arrow*), which shares the draining vein of the AVM. *C*, Spinal CT angiography shows the draining vein of the rAVS and its connection to the conus AVM. *D*, Cast of liquid embolic agent with complete occlusion of the rAVS from the right internal iliac artery.

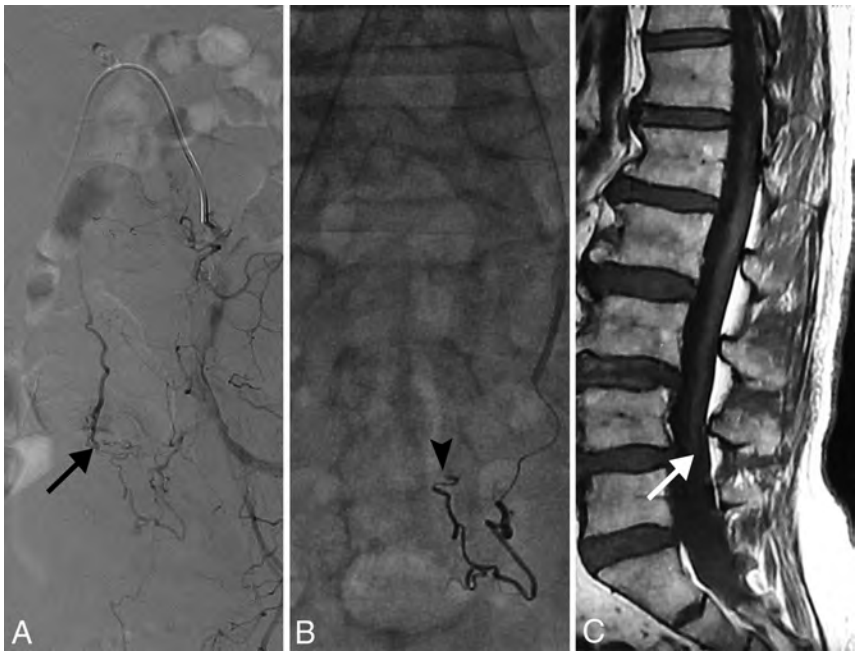

FIG 3. The radiologic presentation of a 64-year-old man with an SDAVF below the conus associated with a tethered cord. *A*, Left internal iliac artery angiogram shows the SDAVF at the level of S2 (*arrow*). *B*, Embolic material cast reveals that the embolic agent is approaching the proximal venous end (*arrowhead*). *C*, The patient also has a tethered cord (*white arrow*) on the T1-weighted MR image.

in 24 patients (50%), and back pain in 8 patients (17.0%). The incidence of the symptoms among 3 different groups showed no statistical significance except for back pain. Three of 7 patients (42.9%) had arteriovenous shunts with back pain, which was higher compared with those with SDAVFs ($P = .037$, multiple comparison analysis). The mean duration between the initial symptoms and diagnosis was 12.4 months (range, 10 days to 13.1 years). One patient with an rAVS presented with subarachnoid hemorrhage as verified by cranial CT and spinal MR imaging. None of the other lesions presented with hemorrhage. Delay of diagnosis due to initial misdiagnosis was recorded before admission and included lumbar degenerative diseases in 6 patients (12.5%) and hypokalemia in 1 patient (2.0%). Two patients had symptom deterioration after pulsed high-dose corticosteroid treatment.

On the MR imaging findings, 45 patients (93.8%) had engorged perimedullary veins on T2-weighted or T1-weighted gadolinium-enhanced MR images and 44 patients (91.7%) had spinal cord edema on the lower thoracic cord or conus medullaris. Both findings showed no obvious differences among the 3 groups. A tethered spinal cord was found in 6 (54.5%) patients with FTAVF, in 7 (23.3%) patients with SDAVF (Fig 3*C*), and in none of the patients with rAVS ($P = .032$). Ten patients had sacral lipomas on MR imaging, which included 7 lipomas of the filum terminale and 3 lipomeningoceles. Patients with FTAVF showed a higher inci-

Table 2: Comparison of demographics, clinical presentation, and MRI findings of 3 types of spinal arteriovenous shunts below the conus[a]

Characteristics	FTAVF (*n* = 11)	rAVS (*n* = 7)	SDAVF (*n* = 30)	All (*n* = 48)	*P* Value[b]
Demographic					
Age (mean) (yr)	52.9 ± 12.6	37.4 ± 15.7	55.6 ± 14.9	52.4 ± 15.5	.017[c]
Female sex	3 (27.3%)	3 (42.9%)	6 (20%)	12 (25%)	.443
Clinical symptoms					
Duration of symptoms (mean) (mo)	12.1 ± 7.8	9.9 ± 9.8	13.1 ± 28.0	12.4 ± 22.6	.396
Back pain	3 (27.3%)	3 (42.9%)	2 (6.7%)	8 (17.0%)	.028[c]
Progressive paraparesis	11 (100.0%)	6 (85.7%)	27 (90.0%)	44 (91.7%)	.598
Progressive hypesthesia	7 (63.6%)	6 (85.7%)	20 (66.7%)	33 (68.8%)	.739
Numbness	5 (45.5%)	3 (42.9%)	16 (53.3%)	24 (50%)	.844
Bowel/bladder dysfunction	8 (72.7%)	4 (57.1%)	26 (86.7%)	38 (79.2%)	.167
MRI findings					
Spinal cord edema	11 (100%)	5 (71.4%)	28 (93.3%)	44 (91.7%)	.129
Engorged vein	10 (90.9%)	6 (85.7%)	29 (96.7%)	45 (93.8%)	.313
Spinal cord tethering	6 (54.5%)	0 (0.0%)	7 (23.3%)	13 (27.1%)	.032[c]
Sacral lipoma	5 (45.5%)	0 (0.0%)	5 (16.7%)	10 (20.8%)	.061

[a] Data are number and percentage unless otherwise indicated.
[b] Comparison among FTAVF, rAVS, and SDAVF.
[c] Statistically significant values.

Table 3: Comparison of treatment and clinical outcomes of spinal arteriovenous shunts below the conus

	FTAVF	rAVS	SDAVF	All	*P* Value[a]
Treatment option (No.)					
Embolization	0	5	16	21	.002[b]
Surgery	9	1	8	18	
E+S	2	1	6	9	
Mean FU[c]	24.0 ± 26.1	21.3 ± 5.3	27.6 ± 20.6	25.7 ± 20.2	.54
Complete obliteration (No.) (%)	9 (100%)	6 (100%)	19 (82.6%)	34 (89.4%)	.476
Median ALS grade pretreatment[c]	9	7.5	7	7.5	.273
Median ALS grade at last FU[c]	5	4	5	4.5	
P value[d]	.023[b]	.063	<.001[b]	<.001[b]	

Note:—E+S indicates combined embolization-surgery; FU, follow-up.
[a] Comparison among FTAVF, rAVS, and SDAVF.
[b] Statistically significant values.
[c] Ten patients lost to follow-up after the treatments were excluded.
[d] Comparison between pretreatment and last FU ALS grades.

dence of sacral lipoma (5 in 11, 45.5%) compared with those with SDAVF (5 in 30, 16.7%) and rAVS (0%). Four patients with sacral cysts were noted, and 1 patient with an SDAVF had spina bifida.

Treatment and Outcomes

According to the therapeutic strategies, 21 (43.8%) patients underwent embolization; 18 (37.5%), surgery; and 9 (18.8%), combined embolization and surgery due to failure to achieve complete obliteration by embolization (Table 3). The treatment patterns were different among the 3 groups ($P = .002$). Of 11 patients with FTAVF, 9 (81.8%) underwent surgery and 2 (18.2%) underwent surgery after embolization failure, whereas patients with rAVS and SDAVF primarily underwent embolization (71.4% and 53.3%, respectively).

Of 38 patients with long-term clinical and angiographic follow-up data, angiographic complete obliteration was achieved in 34 patients (89.4%). Embolization resulted in a complete obliteration rate of 56.0% (14 of 25), while surgery achieved a 100% (21 of 21) cure. The median pretreatment ALS grade was 9 (range, 4–11) in patients with FTAVF, 7.5 (range, 0–10) in those with rAVS, and 7 (range, 0–11) in those with SDAVF, which showed a nonsignificant worse pretreatment function in patients with FTAVF. After treatment, the ALS grade showed significant improvement ($P < .001$). According to the subgroups, the median ALS grade of patients with FTAVF at last follow-up was 5 compared with 9 before treatment ($P = .023$), 4 versus 7.5 in patients with rAVS ($P = .063$), and 5 versus 7 in those with SDAVF ($P < .001$).

DISCUSSION

To our knowledge, this is the first reported patient series focusing solely on spinal arteriovenous shunts below the conus. Given the consecutive inclusion and large series size, we were able to reveal the profile of each type and compare the clinical presentations, radiologic findings, and outcomes among FTAVF, rAVS, and SDAVF with statistical analysis.

Comparison of Angioarchitecture

The angioarchitecture of the 3 types of spinal arteriovenous lesions below the conus share some common features. Our study showed that most[20] of these shunts were fistulous in nature, with nidus-type shunts being very rare and indicating rAVS if present. In addition, most shunts had a relatively slow flow and thus only mildly dilated arteries and veins. Furthermore, the venous drainage pattern was similar because in all shunts, the veins of the shunts drained upward to the perimedullary veins and thus caused venous congestion of the spinal cord. This drainage pattern explains that progressive myelopathy was the main symptom of all 3 types and hemorrhage occurred only rarely. In our series,

it only occurred in 1 patient with an rAVS. Despite the above similarities, the 3 types of lesions have distinctive features to differentiate.

The filum terminale extends downward from the apex of the conus medullaris to the cul de sac of the dura at S2, so the FTAVF should be fed mainly by the filum terminale artery as the caudal continuation of the anterior spinal artery below the arcade of the cone. Whether the filum can have other blood supplies besides the filum terminale artery is still debatable[13,14]; as Djindjian et al[5] reported, the coccygeal nerve with a radicular artery supply was adherent to the filum in its proximal portion. Thus, an explanation for FTAVFs localizing in the distal portion of the filum having an additional blood supply could be a radicular artery or dural artery, as shown in our series and in 1 previous case report.[10] In some circumstances, a radicular artery may adhere to the distal portion of the filum and provide an extra vascular supply. The other possibility is a dural supply because the fistula localizes to the dural attachment point of the filum at around the S2 level, which then may include the dural arterial supply.

In our series, rAVSs were the type least often encountered, which is reflected by the literature because previously only 2 cases were reported.[16] The arterial vascularization of the cauda equina nerve roots includes both distal and proximal radicular arteries with an anastomosis at the proximal one-third of the root.[6] Ohtonari et al[16] reported 2 cases of rAVSs fed by proximal radicular arteries, while in our study, all 7 rAVSs were fed by distal radicular arteries from segmental arteries. We believe that at least some of our cases may have also had proximal radicular artery feeders, which are suppressed by the main flow from their distal counterpart.

SDAVFs below the conus usually present with a single segmental feeding artery, which implies that the fistula is located within the dura directly adjacent to the nerve root (ie, where the radiculomeningeal artery pierces the dura). In cases in which the fistula is located between 2 adjacent nerve roots, dual segmental arterial supply from adjacent segmental arteries may be seen. This configuration was present in 3 patients in our series with SDAVFs supplied by 2 lumbar arteries or bilateral iliac arteries. During embolization, embolic agents should always approach the proximal venous end of the fistula to achieve complete obliteration, which may be more difficult to achieve with *N*-butyl-cyanoacrylate (glue) in cases of dual supply because the glue will harden on contact with blood from the second feeder.

Embryologic Consideration

Development of the human spinal cord involves both primary and secondary neurulation. Unlike the primary neurulation, which establishes the brain and spinal cord and is derived from the ectoderm, all neural elements of secondary neurulation are developed from pluripotent mesodermal cells. These cells, termed the "caudal cell mass," coalesce and then epithelialize to form a separate neural tube that will connect with the neural tube formed by the primary neurulation.[21,22] The exact level where the 2 neural tubes meet is still debatable, ranging from the upper conus[23] to the lowest sacral level of the conus[21]; however, it is agreed that the caudal cell mass will give rise to the filum terminale and the cauda equina. Thus, the embryologic origin of FTAVFs and rAVSs below the conus is associated with secondary neurulation, differing from the remainder of intradural spinal vascular shunt origins that are associated with the primary neurulation. This may explain the interesting finding in our study that FTAVFs below the conus were often associated with spinal dysraphisms such as tethered cord, spinal lipoma, and spina bifida; this association was also shown in a previous case report.[24] One may hypothesize that patients with abnormal secondary neurulation are more prone to develop abnormal vascular shunts: If during embryologic development, pluripotent cells at the caudal end of the human embryo were abnormally triggered to form a lipoma that will cause tethering, these abnormal pluripotent cells may also be prone to develop abnormal vascular shunts.[25] The reason why SDAVFs were associated with dysraphisms may also be due to the abnormal pluripotent cells, which have a propensity to develop this acquired vascular lesion. However, why rAVSs were not associated with spinal dysraphisms in this series remains unclear.

The interesting finding that some patients demonstrated coexistence of rAVS with a conus AVM is presumably related to a low spinal arteriovenous metameric syndrome. We hypothesize that similar to thoracic, cervical, and cerebral metameric syndromes, abnormal cells that are prone to form arteriovenous shunts migrated along their segment and seeded daughter cells along their migrational path as previously described in cerebral arteriovenous metameric syndromes (Wyburn-Mason syndrome).[26]

Differential Diagnosis and Treatment

Spinal arteriovenous shunts below the conus may not be as rare as was previously thought because they represented 13.3% of all spinal shunts in our data base. However, misdiagnosis is not uncommon according to the similar clinical manifestation and nonspecific radiologic findings among the different groups. Our study suggests some differential diagnostic clues. rAVSs show a younger age at first presentation, a larger female proportion, and a higher incidence of pain symptoms and hemorrhage. FTAVFs and SDAVFs share a similar age at onset, which may be related to the same pathophysiology of venous hypertension. However, FTAVFs present with a different feeding artery derived from the anterior spinal artery and they are more commonly associated with dysraphic malformations. A standard spinal angiography, including the bilateral internal iliac arteries and median sacral artery, is the criterion standard to diagnose a lesion in this region. Treatment outcomes are better compared with spinal vascular lesions in other regions. Although embolization resulted in only a 56.0% complete obliteration rate in our series (given the often tortuous vascular anatomy and small caliber of the feeding arteries), surgical resection achieved 100% cure because disconnection of the venous outflow could be easily achieved after accurate intraoperative identification of the draining vein.

Limitations

Our study has some limitations pertaining to its retrospective design and sample volume. Due to the rarity of the disease and the potential of referral basis, our data may not represent the situation in the general population. Because some statistical comparisons are based on small numbers, there is the possibility of spurious statistically significant associations. Additionally, some cases were

associated with additional abnormalities (ie, conus AVMs or spinal dysraphic disorders); thus, patient symptomatology may be related to various sources.

CONCLUSIONS

Our study reveals the differences in 3 types of spinal arteriovenous shunts below the conus. rAVSs have a younger age of onset and a higher incidence of pain symptoms and hemorrhage. FTAVFs are more commonly associated with dysraphic malformations. If diagnosed correctly, the treatment outcomes are better compared with spinal vascular lesions in other regions.

Disclosures: Tao Hong—*RELATED*: *Grant*: government granting agencies, *Comments*: National Natural Science Foundation of China (81171165, 81671202), Beijing Municipal Administration of Hospital Clinical Medicine Development Project (ZY201309), and Beijing Municipal Science and Technology Commission (D161100003816001).* *Money paid to the institution.

REFERENCES

1. Rodesch G, Hurth M, Alvarez H, et al. **Angio-architecture of spinal cord arteriovenous shunts at presentation: clinical correlations in adults and children—the Bicêtre experience on 155 consecutive patients seen between 1981–1999.** *Acta Neurochir (Wien)* 2004;146:217–26; discussion 217–226 CrossRef Medline
2. Krings T. **Vascular malformations of the spine and spinal cord*: anatomy, classification, treatment.** *Clin Neuroradiol* 2010;20:5–24 CrossRef Medline
3. Spetzler RF, Detwiler PW, Riina HA, et al. **Modified classification of spinal cord vascular lesions.** *J Neurosurg* 2002;96:145–56 Medline
4. Lasjaunias P. **Spinal cord vascular lesions.** *J Neurosurg* 2003;98(1 suppl):117–19; author reply 119–20
5. Djindjian M, Ribeiro A, Ortega E, et al. **The normal vascularization of the intradural filum terminale in man.** *Surg Radiol Anat* 1988;10:201–09 CrossRef Medline
6. Parke WW, Gammell K, Rothman RH. **Arterial vascularization of the cauda equina.** *J Bone Joint Surg Am* 1981;63:53–62 Medline
7. Trinh VT, Duckworth EA. **Surgical excision of filum terminale arteriovenous fistulae after lumbar fusion: value of indocyanine green and theory on origins (a technical note and report of two cases).** *Surg Neurol Int* 2011;2:63 CrossRef Medline
8. Takami T, Yamagata T, Mitsuhashi Y, et al. **Direct surgery for spinal arteriovenous fistulas of the filum terminale with intraoperative image guidance.** *Spine (Phila Pa 1976)* 2012;37:E1524–28 CrossRef Medline
9. Djindjian M, Djindjian R, Rey A, et al. **Intradural extramedullary spinal arterio-venous malformations fed by the anterior spinal artery.** *Surg Neurol* 1977;8:85–93 Medline
10. Jin YJ, Kim KJ, Kwon OK, et al. **Perimedullary arteriovenous fistula of the filum terminale: case report.** *Neurosurgery* 2010;66:E219–20; discussion E220 CrossRef Medline
11. Djindjian M, Ayache P, Brugieres P, et al. **Sacral lipoma of the filum terminale with dural arteriovenous fistula: case report.** *J Neurosurg* 1989;71:768–71 CrossRef Medline
12. Fischer S, Aguilar Perez M, Bassiouni H, et al. **Arteriovenous fistula of the filum terminale: diagnosis, treatment, and literature review.** *Clin Neuroradiol* 2013;23:309–14 CrossRef Medline
13. Hsu SW, Rodesch G, Luo CB, et al. **Concomitant conus medullaris arteriovenous malformation and sacral dural arteriovenous fistula of the filum terminale.** *Interv Neuroradiol* 2002;8:47–53 Medline
14. Lim SM, Choi IS, David CA. **Spinal arteriovenous fistulas of the filum terminale.** *AJNR Am J Neuroradiol* 2011;32:1846–50 CrossRef Medline
15. Chanthanaphak E, Pongpech S, Jiarakongmun P, et al. **Filum terminale arteriovenous fistulas: the role of endovascular treatment.** *J Neurosurg Spine* 2013;19:49–56 CrossRef Medline
16. Ohtonari T, Ota S, Nishihara N, et al. **Arteriovenous fistula in a nerve root of the cauda equina fed by a proximal radiculo-medullary artery: a report of two cases.** *Interv Neuroradiol* 2011;17:217–23 Medline
17. Saladino A, Atkinson JL, Rabinstein AA, et al. **Surgical treatment of spinal dural arteriovenous fistulae: a consecutive series of 154 patients.** *Neurosurgery* 2010;67:1350–57; discussion 1357–1358 CrossRef Medline
18. Aminoff MJ, Logue V. **The prognosis of patients with spinal vascular malformations.** *Brain* 1974;97:211–18 CrossRef Medline
19. Pang D, Wilberger JE Jr. **Tethered cord syndrome in adults.** *J Neurosurg* 1982;57:32–47 CrossRef Medline
20. Troude L Jr, Melot A, Brunel H, et al. **Arteriovenous malformation of the filum terminale: an exceptional case.** *J Neurosurg* 2016;124:1712–15 CrossRef Medline
21. Sadler TW. **Embryology of neural tube development.** *Am J Med Genet C Semin Med Genet* 2005;135C:2–8 CrossRef Medline
22. Saitsu H, Yamada S, Uwabe C, et al. **Development of the posterior neural tube in human embryos.** *Anat Embryol (Berl)* 2004;209:107–17 Medline
23. Hertzler DA 2nd, DePowell JJ, Stevenson CB, et al. **Tethered cord syndrome: a review of the literature from embryology to adult presentation.** *Neurosurg Focus* 2010;29:E1 CrossRef Medline
24. Krisht KM, Karsy M, Ray WZ, et al. **Extraspinal type I dural arteriovenous fistula with a lumbosacral lipomyelomeningocele: a case report and review of the literature.** *Case Rep Neurol Med* 2015;2015:526321 CrossRef Medline
25. Lew SM, Kothbauer KF. **Tethered cord syndrome: an updated review.** *Pediatr Neurosurg* 2007;43:236–48 CrossRef Medline
26. Krings T, Geibprasert S, Luo CB, et al. **Segmental neurovascular syndromes in children.** *Neuroimaging Clin N Am* 2007;17:245–58 CrossRef Medline

MRI Atlas-Based Measurement of Spinal Cord Injury Predicts Outcome in Acute Flaccid Myelitis

D.B. McCoy, J.F. Talbott, Michael Wilson, M.D. Mamlouk, J. Cohen-Adad, Mark Wilson, and J. Narvid

ABSTRACT

BACKGROUND AND PURPOSE: Recent advances in spinal cord imaging analysis have led to the development of a robust anatomic template and atlas incorporated into an open-source platform referred to as the Spinal Cord Toolbox. Using the Spinal Cord Toolbox, we sought to correlate measures of GM, WM, and cross-sectional area pathology on T2 MR imaging with motor disability in patients with acute flaccid myelitis.

MATERIALS AND METHODS: Spinal cord imaging for 9 patients with acute flaccid myelitis was analyzed by using the Spinal Cord Toolbox. A semiautomated pipeline using the Spinal Cord Toolbox measured lesion involvement in GM, WM, and total spinal cord cross-sectional area. Proportions of GM, WM, and cross-sectional area affected by T2 hyperintensity were calculated across 3 ROIs: 1) center axial section of lesion; 2) full lesion segment; and 3) full cord atlas volume. Spearman rank order correlation was calculated to compare MR metrics with clinical measures of disability.

RESULTS: Proportion of GM metrics at the center axial section significantly correlated with measures of motor impairment upon admission (r [9] = −0.78; P = .014) and at 3-month follow-up (r [9] = −0.66; P = .05). Further, proportion of GM extracted across the full lesion segment significantly correlated with initial motor impairment (r [9] = −0.74, P = .024). No significant correlation was found for proportion of WM or proportion of cross-sectional area with clinical disability.

CONCLUSIONS: Atlas-based measures of proportion of GM T2 signal abnormality measured on a single axial MR imaging section and across the full lesion segment correlate with motor impairment and outcome in patients with acute flaccid myelitis. This is the first atlas-based study to correlate clinical outcomes with segmented measures of T2 signal abnormality in the spinal cord.

ABBREVIATIONS: %CSA = proportion of cross-sectional area; %GM = proportion of gray matter; %WM = proportion of white matter; AFM = acute flaccid myelitis; EV = enterovirus; MRC = Medical Research Council; SC = spinal cord; SCT = Spinal Cord Toolbox

After the eradication of wild poliovirus, the clinical syndrome of spinal motor neuron injury called acute flaccid myelitis (AFM) nearly disappeared from North America. The reemergence of this syndrome has coincided with the appearance of West Nile virus in Europe and North America, enterovirus (EV) A71 in Southeast Asia, and EV-D68 in North America.[1,2] In fact, at the same time that EV-D68 caused widespread outbreaks of respiratory illness in the United States in 2014, the number of patients with AFM spiked.[3] The Centers for Disease Control and Prevention noted this association, describing the incidence of AFM in a subset of patients with acute flaccid paralysis with evidence of spinal cord (SC) injury.[4]

More recently, longitudinally extensive SC lesions predominantly affecting the central GM have been described in children with AFM during the 2014 EV outbreak.[5] These patients reported acute limb weakness, cranial nerve dysfunction, or both. The prognosis in such patients is variable, with few predictors of recovery aside from the severity of initial paralysis. However, in a variety of SC pathologies, defining the pattern and extent of signal abnormality on MR imaging can aid in diagnosis and prognosis.[6]

The recent development of a standard SC template[7]—as part of the Spinal Cord Toolbox (SCT)[8]—that includes probabilistic maps of GM and WM[9] now makes it possible to quantify the severity of SC

Received May 17, 2016; accepted after revision September 21.

From the Department of Radiology and Biomedical Imaging (D.B.M., J.F.T., M.D.M., Mark Wilson, J.N.), University of California, San Francisco, Zuckerberg San Francisco General Hospital and Trauma Center, San Francisco, California; Brain and Spinal Injury Center (J.F.T.), Zuckerberg San Francisco General Hospital and Trauma Center, San Francisco, California; Institute of Biomedical Engineering (J.C.-A.), Ecole Polytechnique Montreal, Montreal, Quebec, Canada; Functional Neuroimaging Unit (J.C.-A.), CRIUGM, University of Montreal, Montreal, Quebec, Canada; and Department of Neurology (Michael Wilson), University of California, San Francisco.

Please address correspondence to Jared A. Narvid, MD, University of California, San Francisco, Zuckerberg San Francisco General Hospital and Trauma Center, 1001 Potrero Ave, Room 1x57, SFGH Box 1325, San Francisco, CA 94110; e-mail: jared.narvid@ucsf.edu

Indicates open access to non-subscribers at www.ajnr.org

http://dx.doi.org/10.3174/ajnr.A5044

injury.[10-12] We aimed to measure the proportion of GM and WM damage in patients with AFM occurring in association with the EV-D68 outbreak. We hypothesized that the degree of GM and WM signal abnormality in these patients would both correlate with severity of initial symptoms and symptoms at follow-up after hospitalization. Although several studies have investigated the association between GM and WM signal abnormality on MR imaging and disease severity,[13-18] to date, this is first study using this analysis method to register SCs with abnormal signal to an unbiased average anatomic template; quantify proportions of GM (%GM), WM (%WM), and CSA (%CSA) occupied by lesion in the probabilistic template; and correlate data with clinical outcomes.

MATERIALS AND METHODS

Case Definition

All patients (9 total) admitted to the Benioff Children's Hospital at the University of Califronia, San Francisco with AFM were included in the study. Dates of hospital admission ranged from February 12, 2012, to February 2, 2015. All patients included in the study met the clinical case definition of AFM as described by the Centers for Disease Control and Prevention. Patients were defined as having acute limb weakness with MR imaging SC abnormality. Other infectious causes of AFM were excluded, such as Guillain-Barré syndrome, West Nile virus, poliovirus, stroke, transverse myelitis, myasthenia gravis, and botulism. Nasopharyngeal swab, oropharyngeal swab, serum, stool, or CSF samples were tested for EV RNA by using polymerase chain reaction for all patients. EV polymerase chain reaction was conducted at ViraCor for 3 patients, California Department of Public Health—Neurologic Testing and Surveillance Viral & Rickettsial Disease Laboratory for 2 patients, Kaiser Permanente Medical Group for 2 patients, Lucile Packard Children's Hospital for 1 patient, and Stanford University Hospitals for 1 patient.

During initial hospitalization, all patients underwent complete neurologic testing. Strength testing was formalized with the composite Medical Research Council (MRC) Scale for Muscle Strength scores, using 3 proximal muscles and 2 distal muscles in the affected limb for a score ranging from 0–25.[19] At follow-up, MRC strength testing was repeated and recorded. Improvement in strength was recorded as the numeric difference in MRC score.

Local institutional review board approval was obtained through the University of California, San Francisco Committee on Human Research for retrospective review and analysis of patient clinical information and MR images.

MR Imaging Acquisition Parameters

All MR imaging studies were performed on a 1.5T Genesis HDxt Signa scanner with software version 15 (GE Healthcare, Milwaukee, Wisconsin). Axial and sagittal T2 FSE imaging was performed with the following parameters (presented as mean ± SD from all 9 examinations): TR, 3398.78 ms ± 1430.99 ms; TE, 99.04 ms ± 12.93 ms; section thickness, 3.33 mm; echo-train length, 18.56 ± 3.28. Average native plane resolution after interpolation of images is (2D to 3D): X, 0.40; Y, 0.40; Z, 4.17. Additional sequences performed as part of our routine spine and brain MR imaging protocol were not evaluated for the purposes of this study.

Image Processing

T2-weighted images for 9 patients with AFM were analyzed with SCT. The FMRIB Software Library v5.0 (FSL; http://fsl.fmrib.ox.ac.uk/)[20] viewer module was used to manually mark the seed points for analysis. These locations flag the beginning and end regions for the propagation deformation model to segment the SC.[21] During automatic segmentation, detection of the SC is done in the axial plane by using the Hough transform. This is followed by propagation of an elliptical triangular tubular mesh built inside the SC. The tubular mesh is then deformed toward the edges of the SC.[21] Results of segmentation accuracy were unsatisfactory because of the large signal hyperintensity in this cluster of patients. Because of this, segmentation of normal tissue was done using the SCT segmentation algorithm. Areas where segmentation deviated from the SC as a result of hyperintensity were manually adjusted by creating images of SC voxel locations by using FSL and 2 centerline points to mark the beginning and end axial sections for registration. Registration to the template took roughly 540 seconds per patient. The SCT automatic pipeline to register, warp, and extract WM and GM metrics for each SC consisted of (Fig 1):

1) A 3D labels file was created based on the coordinates of the first (C2–C3) and last (through T6) vertebral level landmarks to be analyzed by using the SC labeling utility;
2) A 3D mask file was created manually in FSL to identify voxels within the SC. SC masks were confirmed by 2 radiologists as identifying only areas within the SC;
3) A combination of affine and nonlinear registrations was done of the T2-weighted image to the corresponding MNI-Poly-AMU template. The MNI-Poly-AMU template is an image of the SC averaged across multiple patients and is used as a reference point for registration of patient SCs and atlas-based MR signal quantification.[7] Registration was done in 4 steps. In step 1, a nonlinear transformation was estimated to straighten the SC (to match the MNI-Poly-AMU straight template). In step 2, an affine transformation was found based on the input labels to match the vertebral levels between the subject and the template. In step 3, a 2D section-wise registration was done to bring the subject closer to the template, while ensuring robustness toward pathology by using the cord segmentation instead of the image, by using the mean-square metric and smoothing factor of 2. In step 4, local registration adjustment was made using the B-Spline SyN algorithm with the mean-square metric, gradient step of 0.5, and smoothing factor of 0, with 5 iterations. The outputs were a T2-weighted image warped to the template and a template warped to the T2-weighted image, along with a pair of forward and reverse deformation fields;
4) The reverse deformation field (template to subject) was then applied to the WM and GM atlases, projecting them in the subject space. These warping fields were used to register multiparametric data to a common space for quantification of image-derived metrics;
5) Raw images were thresholded to provide binary ROI of lesion area for analysis with the WM/GM and SC probabilistic atlases. Thresholding of images was performed in ImageJ (National Institutes of Health, Bethesda, Maryland),[22] with manual percentile adjustment to segment the lesions from surrounding normal-appearing SC. Thresholded T2 images were confirmed by 2 neu-

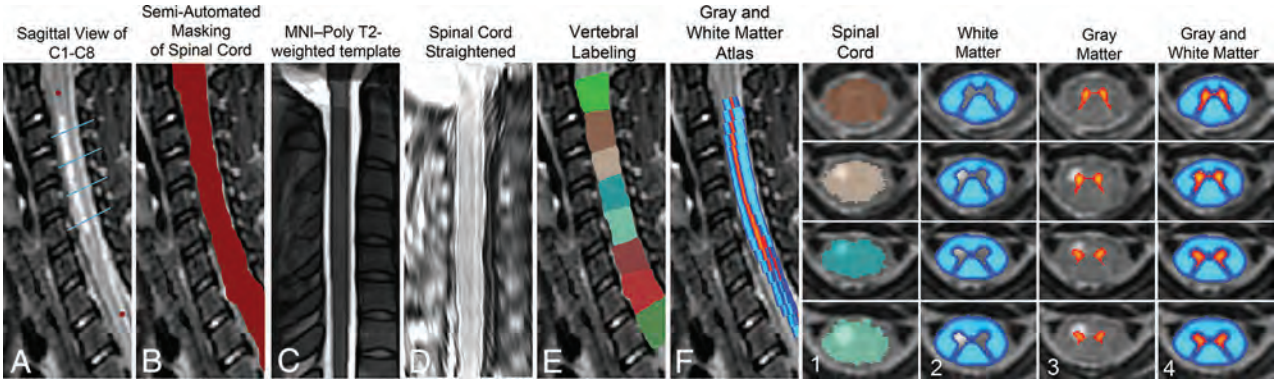

FIG 1. Steps for registering patient 5 (acute flaccid paralysis) to template. *A*, *Red circles* indicate manual marking of anatomic features C1 and C8. *Blue lines* indicate axial sections illustrated in far right grid. *B*, Manual masking of SC centerline was done at each axial section because of signal hyperintensity interfering with automatic reconstruction of centerline. *C*, MNI-Poly-AMU T2-weighted template. *D*, SC straightening using thin-plate spline interpolation. *E*, Labeling of vertebral levels after registering to template and warping back to native space. *F*, Sagittal view of GM and WM probabilistic atlas after registering to template and warping back to native space. *Far right grid*, Output of template-based atlas. *Column 1*, Automatic vertebral body labeling and SC space. *Column 2*, Probabilistic masks of WM. *Column 3*, Probabilistic masks of GM. *Column 4*, Probabilistic masks of GM and WM overlaid.

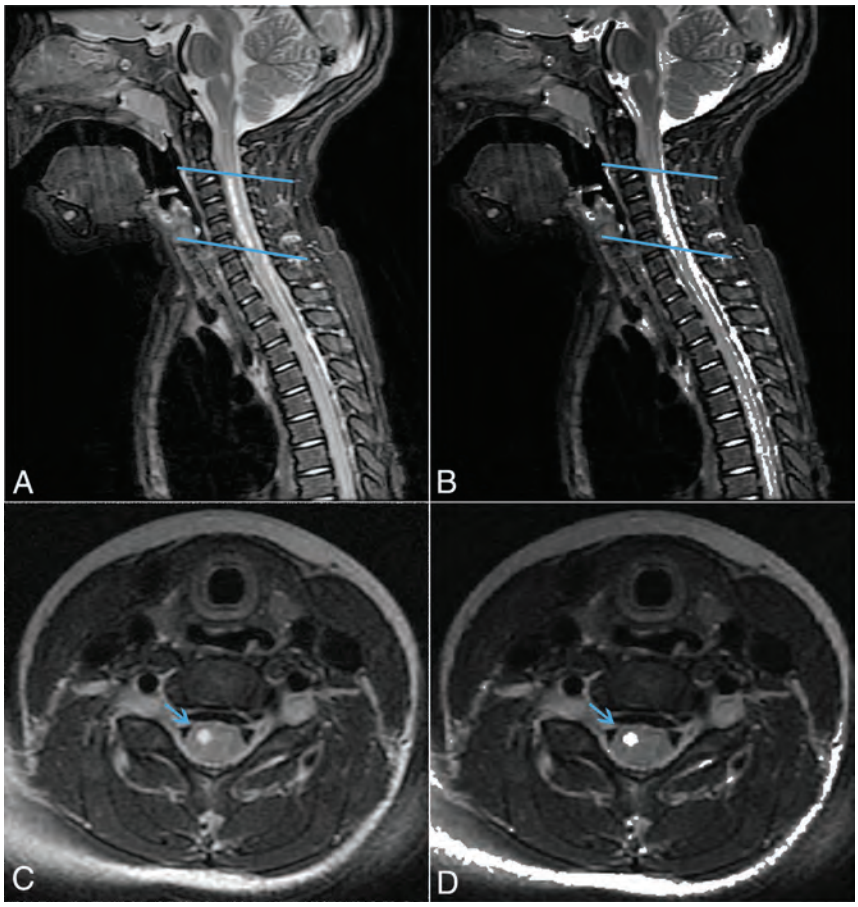

FIG 2. MR imaging of patient 1. *A*, Sagittal plane T2-weighted image centered on lesion. *B*, Overlay of binary thresholded image for lesion and T2-weighted sagittal image. *C*, Axial T2-weighted image at lesion center. *D*, Overlay of binary thresholded image for lesion and T2-weighted axial image.

roradiologists (J.N., J.F.T.) who were blinded to clinical data, segmenting only areas affected by lesions. Metrics were extracted by using the SCT extract metric function. The percentage of lesion within GM/WM and SC probabilistic atlas voxel space was extracted as a cumulative partial volume by using the thresholded MR images;

6) Cumulative partial volume metrics for GM and WM were extracted from the lesion axial center, lesion segment, and full cord atlas volume. A binary image of lesion area in this analysis is used to summate the voxel-wise probabilities occupied by the lesion per axial section;
7) Spearman rho (r), P values, linear regression slopes, and intercepts were calculated by NumPy and matplotlib in Python. Regression plots and bar charts were also plotted using matplotlib; and,
8) To quantify differences in thresholding, binary images, which were thresholded by each neuroradiologist, were overlaid by using ImageJ. Pixels identifying areas of the images that were different between the reviewers were summed and divided by total pixels of the axial section image. These metrics are reported as the percentile average, SD, and range of pixel differences.

Atlas-Based Spinal Cord Injury Assessment

Probabilistic maps containing all cervical levels and extending to T6 were created for all 9 patients. For analysis at the lesion center, 2 neuroradiologists (J.N., J.F.T.) reviewed each SC image and identified the axial section showing the most significant T2 hyperintensity, the so-called "lesion center." In 1 patient, the lesion center showing the most extensive hyperintensity could not be analyzed because it was below T6. In this case (patient 1), the second-most severely affected region was analyzed. For analysis of the full lesion segment, sagittal T2 images

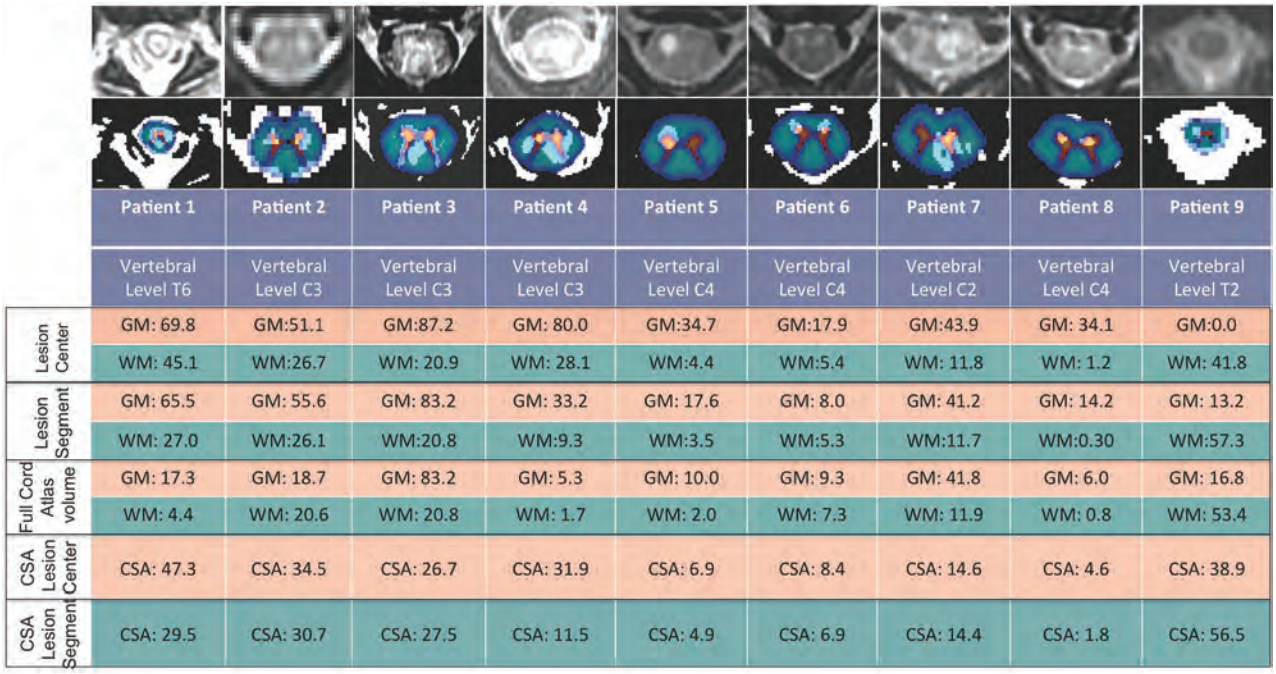

FIG 3. *First row*, Axial T2 image from center of lesion. *Second row*: Probabilistic GM (*orange*) and WM (*blue*) map overlaid on thresholded axial T2 image from lesion center. Lesion Center indicates %WM and %GM weighted average metrics at axial lesion center. Lesion Segment indicates %WM and %GM weighted average metrics for lesion segment. Full Cord Atlas Volume indicates %WM and %GM weighted average metrics for full cord atlas volume. CSA Lesion Center indicates %CSA weighted average metrics at axial lesion center. CSA Lesion Segment indicates %CSA weighted average metrics at lesion segment.

Clinical description of 9 patients with AFM used in analysis

Patient No.	Age, yr	Sex	Limb Weakness	MRC Composite Score	Enterovirus Detected	MRC Score at Follow-Up	Discharge Diagnosis	Days to MRI
1	3	M	Right UE	11	NP swab	2	Disease due to EV	9
2	7	M	Bilateral LE	20	None	3	Encephalomyelitis, paraesthesia/hyperestheia	14
3	4	F	Bilateral LE	9	None	1	Flaccid paralysis, unspecified	2
4	8	M	Right UE	9	NP swab	0	Acute flaccid paralysis	13
5	27	M	Bilateral LE	1	Serum	3	Virus-related myelitis	6
6	8	F	Left UE	16	None	2	Viral meningitis	11
7	24	M	Bilateral LE	24	None	3	Meningomyelitis	5
8	10	M	Left UE	18	None	2	Postinfectious mycoplasma transverse myelitis	3
9	2	F	Left UE	3	None	1	Hopkins syndrome	1

Note:—LE, lower extremities; NP, nasophyryngeal; UE, upper extremities.

were used to identify the starting and ending axial section where the lesion was involved (Fig 2). In the full cord atlas volume analysis, the entire length of thresholded SC within the probabilistic atlases was used. Cumulative partial volumes for GM, WM, and SC affected by lesion at the center axial section, full lesion segment, and full cord atlas volume for each patient are described in Fig 3. A Spearman rank order correlation was used to determine whether metrics from each lesion analysis significantly correlated with MRC strength scores or clinical outcome scores.

Statistical Analysis

Composite MRC for Muscle Strength scores, clinical outcomes scores, and cumulative partial volumes of the binary thresholded image in probabilistic GM and WM voxel space were used in a Spearman rank order correlation. *P* values comparing patients testing as EV positive and EV negative were calculated by the Mann-Whitney *U* test. Furthermore, Mann-Whitney *U* tests for medians were used to determine whether GM and WM cumulative partial volumes were significantly different between outcome and MRC groups. An independent-samples Kruskal-Wallis test on GM metrics was used to compare groups. Spearman rank order correlations were also used to determine the correlation between the neuroradiologists' evaluation of the center axial section showing the most hyperintensity, the vertebral body with the most hyperintensity, and the thresholding level necessary to successfully segment the lesion from surrounding SC space. The Student *t* test was used to determine whether the pixel percent differences from thresholding were significantly different from 0. An α of .05 was considered statistically significant for all tests of association. No mathematic correction was made to adjust the α level for multiple corrections because the comparisons were planned before data inspection.

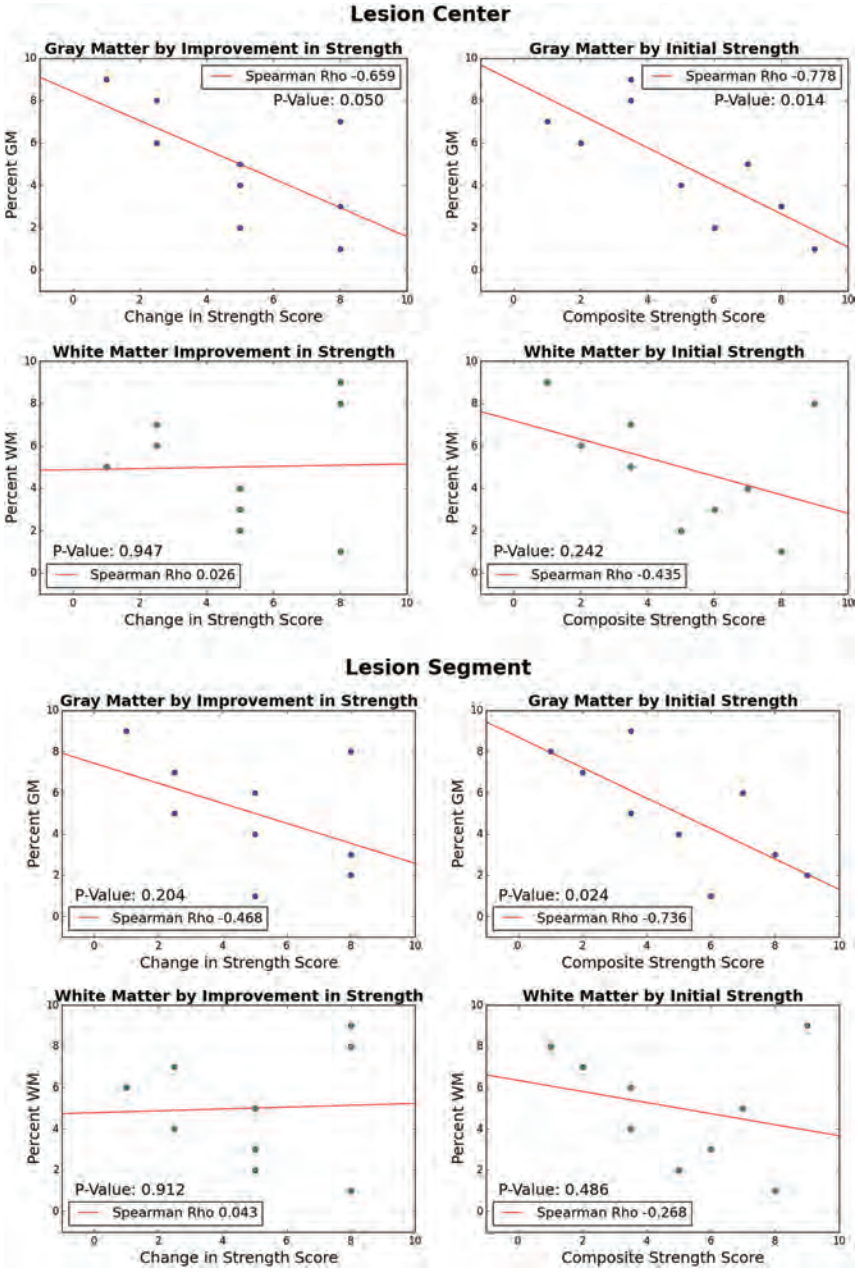

FIG 4. Scatterplots of numeric outcome of initial strength or improvement in strength MRC score by %GM or %WM injury (weighted average metric ranking) separated by analysis types (lesion center and lesion segment).

RESULTS

Clinical Findings

Patients were of age 2–27 years at the time of study, with most patients being younger than 10 years old (6 male, 3 female). The patient demographics, discharge diagnosis, MRC composite score, and clinical outcome rating are detailed in the Table. Additional presenting symptoms included fever (8 patients), upper respiratory infection (4 patients), body pain/pruritus/allodynia/abnormal sensation (5 patients), nausea/food intolerance/emesis (3 patients), urinary retention (2 patients), and ataxia (1 patient). EV polymerase chain reaction of the CSF was negative in all patients. Nasopharyngeal swabs tested positive for EV RNA in 2 patients and serum samples for 1 patient tested positive for EV. One nasopharyngeal swab sample was positively subtyped as EV-D68. Mean time between clinical symptoms and MR imaging was 6.89 days (interquartile range, 3–11 days) (Table). Mean clinical follow-up time was 396.33 days (interquartile range, 262–362 days).

MR Imaging Findings

All patients had SC lesions involving the central cord GM and some degree of surrounding WM. Lesions consisted of well-defined T2 hyperintensity predominantly within anterior horn cells for 6 patients (2, 3, 4, 5, 6, 8) and ill-defined lesions affecting the entire central SC GM for 3 patients (1, 7, 9) (Fig 3). In 1 case, ill-defined T2 hyperintensity extended the entire length of the SC. Patients with the most longitudinally extensive hyperintensity throughout both cervical and thoracic areas had bilateral flaccid lower extremities. On MR T2 images, brain lesions were identified in 2 patients. One patient showed hyperintensity in the right frontal lobe. The second patient showed brain stem and thalamic edema.

Spinal Cord Analysis

MR SC injury metrics were calculated for each patient (Fig 3). Measuring at the center of the lesion (lesion center section), clinical outcome significantly worsened as %GM increased (r [9] = −0.66, P = .05) (Fig 4). Similarly, the %GM injured showed significant correlation with weakness at initial examination for both lesion center measurement (r [9] = −.78, P = .014) and full lesion segment volume measurements (r [9] = −0.74, P = .024). There was no significant association between %WM injured and clinical outcome or MRC strength scores at lesion center or full lesion segment volume. In full cord atlas volume analysis, neither GM nor WM significantly correlated with either improvement or initial weakness. No significant correlation was found between %CSA at lesion center and clinical outcome (r [9] = 0.03, P = .95) or initial MRC score (r [9] = −.46, P = .213). Furthermore, cumulative partial volumes extracted for %CSA at lesion segment did not significantly correlate with clinical outcome (r [9] = −0.05, P = .89) or initial MRC score (r [9] = −.25, P = .52). No significant differences were found between the EV-positive and EV-negative groups or among clinical outcome groups in the degree of initial weakness (strength score), extent of GM or WM injury in either lesion center, or full lesion segment volume.

Selection of the axial section showing the most hyperintensity had good concordance between the 2 neuroradiologists (J.N., J.F.T.) (r [9] = 0.60, P = .088). Differences in axial section selection were mostly caused by several regions showing the same degree of hyperintensity. A strong degree of correlation was found between the neuroradiologists with regard to the vertebral body of the most hyperintensity (r [9] = 0.92, $P < .001$) and with regard to level of thresholding (r [9] = 0.98, $P < .001$). Average pixel differences as a result of thresholding variation between the neuroradiologists was 0.86% (SD, 1.87%; range, 0%–5.8%). A 2-tailed t test comparing the percentage difference to 0 showed no significant difference (P = .19).

DISCUSSION

In the present study, we have used a semiautomated analysis pipeline to quantify T2 signal abnormality in the SC of patients diagnosed with AFM. More specifically, T2-weighted MR imaging sequences from 9 patients with AFM were successfully registered to the recently developed MNI-Poly-AMU SCT. Using SCT, measures of %GM, %WM, and %CSA pathologic T2 signal hyperintensity were derived after thresholded T2 images segmented relative to pathologic signal were compared with probabilistic GM, WM, and SC maps from SCT. The primary aim of this study was to determine the feasibility and prognostic validity of implementing an atlas-based approach for MR imaging analysis in a population of patients with AFM. To this end, the positive correlations observed between SCT-derived MR imaging metrics of GM pathology and clinical outcome validate this approach. Although atlas-based analysis techniques have been applied to a variety of brain pathologies,[23,24] this is the first study to implement an atlas-based approach for study of WM- and GM-specific pathology in the SC.

Patients with AFM occurring in association with a recent EV-D68 outbreak were studied because this type of myelopathy distinctively targets central GM, primarily the anterior horn cells.[25] Accordingly, an atlas that allows specific evaluation of GM signal abnormality would improve our ability to assess degree of injury and prognosis. In precisely this way, %GM signal abnormality on a single axial section at the injury center most strongly correlated with neurologic impairment, whereas statistically insignificant correlations were seen with measures of %WM and %CSA injury. This is despite the presence of T2 signal abnormality involving WM to a varying degree in all patients. These findings are consistent with the presumed underlying pathophysiology of disease in this cohort of patients, wherein anterior horn cells of SC GM are particularly vulnerable to enteroviral toxicity and manifestations of their injury would be expected to best predict outcome.[26] Other acute myelopathies, such as autoimmune demyelinating disease and traumatic contusion injury, often involve some component of direct myelin and axonal injury in WM with associated disruption of functionally significant ascending and descending WM tracts.[23] The relative prognostic significance of GM pathology on MR imaging in this cohort of patients with AFM reflects the primary injury mechanism of AFM and highlights the value of segmented evaluation of the SC with distinct GM and WM maps.

The %GM T2 signal hyperintensity on a single axial section at the most affected level of the injury center (referred to as "lesion center") provided the strongest correlation with clinical measures of motor impairment and recovery. The value of assessing the transverse extent of T2 abnormality on a single axial section at the injury center has been similarly demonstrated in the setting of acute traumatic SC injury and compressive myelopathy,[18,27] suggesting that the transverse extent of injury in the SC on MR imaging carries significant diagnostic and prognostic information in a variety of pathologies. This result is significant because it allows for a more focused, rapid evaluation of the MR imaging findings centered at the injury center. The full lesion segment volume of %GM signal abnormality also significantly correlated with initial motor scores and, to a lesser extent, with improvement. One potential advantage of full lesion segment volume calculation is that it does not rely upon the subjective determination of the most severely affected axial section, thus potentially reducing variability and making analysis more conducive to a fully automated process. When the %GM involvement is calculated relative to the entire interrogated SC GM volume, the significance of this measure with motor scores is lost, likely as a result of the dilution of the pathologic signal within significantly larger volumes of normal GM when lesions are not longitudinally extensive.

Potential applications for SCT in quantifying SC pathology on MR imaging are vast and may greatly advance data-driven, unbiased approaches for assessing injury severity and guiding and monitoring therapy.[7,9,11,21,23,28] This proof-of-concept study demonstrates the prognostic validity of this approach and how segmented analysis of SC subregions (ie, %GM and %WM) may reflect the underlying pathophysiology of disease.

Limitations

The intramedullary T2 hyperintensity observed in our patients often resulted in obscuration of margins between SC and hyperintense CSF, thereby precluding completely automated SC segmentation and necessitating manual adjustment for this step. An algorithm that can robustly and accurately segment the SC in patient populations with intramedullary T2 hyperintensity would reduce time and any bias associated with manual segmentation of the SC. Furthermore, 3T imaging would improve this delineation, thereby improving automated segmentation. In the current study, the segmentation and thresholding process were both reviewed by fellowship-trained neuroradiologists; however, in order for large throughput analysis of patient SCs with minimal manual image postprocessing, the propagated segmentation algorithm will need the capacity to propagate through axial sections with abnormal signal intensity. In addition, nonautomated thresholding introduces the possibility of error and/or bias during the image processing. Another limitation in the current study is that signal abnormality below T6 cannot be analyzed because the MNI-Poly-AMU template only covers C1–T6 vertebral levels. This limitation resulted in 1 patient's most severe axial section being excluded from analysis and the second-most severe section being used. This limitation will be overcome with the future release of the new PAM50 template, which includes the brain stem and full SC.[29] In addition, the existing template was created from healthy young control patients similar in age to our older patients, but did not include young children. Finally, power analysis for this study by using an α of .05, and 9 patients indicates that an r

value of 0.75 is required to detect a significant difference with a power of 80%. Because of this, the current study is underpowered in determining significance for weaker correlations between atlas-derived quantitative metrics of tissue damage and clinical outcomes.

CONCLUSIONS

This proof-of-concept study used a recently developed open-source Spinal Cord Toolbox for atlas-based analysis of T2 signal abnormality in the SCs of 9 patients with AFM occurring during the EV-D68 outbreak in the western United States. This cluster of patients showed distinctive SC lesions of the anterior central GM, characteristic of EV myelopathy, with variable WM involvement. An image processing and analysis pipeline was developed to register thresholded T2 MR images to the MNI-Poly-AMU template, enabling calculation of %WM, %GM, and %CSA pathology. Quantitative measures of %GM signal abnormality on a single axial section at the most severely affected level of the injury epicenter were significantly associated with clinical outcome scores and MRC muscle strength scores, reflecting the underlying pathophysiology for these patients with AFM. In addition, cumulative partial volumes of %GM involved in whole lesion segment were significantly correlated with MRC Muscle Strength scores. %GM-segmented calculations outperformed %WM and %CSA for predicting motor outcome. To date, this is the first study to use an atlas-based approach to quantify T2 measures of pathology in the SC and correlate extracted metrics with clinical outcomes.

Disclosures: Jason Talbott—*UNRELATED*: *Consultancy*: StemCells, Inc, *Comments*: member of data monitoring committee for clinical trial. Michael Wilson—*UNRELATED*: *Grant*: National Center for Advancing Translational Sciences of the National Institutes of Health, *Comments*: award number KL2TR000143. Julien Cohen-Adad—*UNRELATED*: *Consultancy*: Sanofi, Biospective, Massachusetts General Hospital; *Employment*: Ecole Polytechnique Montreal, Functional Neuroimaging Unit (University of Montreal); *Grants/Grants Pending*: Canadian Institutes of Health Research, Natural Sciences and Engineering Research Council, Fonds de Recherche du Québec – Nature et Technologies (FQRNT), Fonds de Recherche du Québec – Santé (FRQS), Canada Research Chair*; *Royalties*: Elsevier. *Money paid to the institution.

REFERENCES

1. Pons-Salort M, Parker EP, Grassly NC. **The epidemiology of non-polio enteroviruses: recent advances and outstanding questions.** *Curr Opin Infect Dis* 2015;28:479–87 CrossRef Medline
2. Greninger AL, Naccache SN, Messacar K, et al. **A novel outbreak enterovirus D68 strain associated with acute flaccid myelitis cases in the USA (2012–14): a retrospective cohort study.** *Lancet Infect Dis* 2015;15:671–82 CrossRef Medline
3. Messacar K, Schreiner TL, Maloney JA, et al. **A cluster of acute flaccid paralysis and cranial nerve dysfunction temporally associated with an outbreak of enterovirus D68 in children in Colorado, USA.** *Lancet* 2015;385:1662–71 CrossRef Medline
4. Division of Viral Diseases, National Centers for Immunization and Respiratory Diseases, CDC; Division of Vector-Borne Diseases, Division of High-Consequence Pathogens and Pathology, National Center for Emerging and Zoonotic Infectious Diseases, CDC; Children's Hospital Colorado; Council of State and Territorial Epidemiologists. **Notes from the field: acute flaccid myelitis among persons aged ≤21 years—United States, August 1-November 13, 2014.** *MMWR Morb Mortal Wkly Rep* 2015:63:1243–44 Medline
5. Maloney JA, Mirsky DM, Messacar K, et al. **MRI findings in children with acute flaccid paralysis and cranial nerve dysfunction occurring during the 2014 enterovirus D68 outbreak.** *AJNR Am J Neuroradiol* 2015;36:245–50 CrossRef Medline
6. Baruah D, Chandra T, Bajaj M, et al. **A simplified algorithm for diagnosis of spinal cord lesions.** *Curr Probl Diagn Radiol* 2015;44:256–66 CrossRef Medline
7. Fonov VS, Le Troter A, Taso M, et al. **Framework for integrated MRI average of the spinal cord white and gray matter: the MNI-Poly-AMU template.** *Neuroimage* 2014;102(Pt 2):817–27 CrossRef Medline
8. Cohen-Adad J, De Leener B, Benhamou M, et al. **Spinal Cord Toolbox: an open-source framework for processing spinal cord MRI data.** In: *Proceedings of the 20th Annual Meeting of Organization for Human Brain Mapping,* Hamburg, Germany. June 8–14, 2014
9. Lévy S, Benhamou M, Naaman C, et al. **White matter atlas of the human spinal cord with estimation of partial volume effect.** *Neuroimage* 2015;119:262–71 CrossRef Medline
10. Ullmann E, Pelletier Paquette JF, Thong WE, et al. **Automatic labeling of vertebral levels using a robust template-based approach.** *Int J Biomed Imaging* 2014;2014:719520 CrossRef Medline
11. Yiannakas MC, Mustafa AM, De Leener B, et al. **Fully automated segmentation of the cervical cord from T1-weighted MRI using PropSeg: application to multiple sclerosis.** *Neuroimage Clin* 2016;10:71–77 CrossRef Medline
12. Martin AR, De Leener B, Aleksanderek I, et al. **A prospective longitudinal study in degenerative cervical myelopathy using quantitative microstructural MRI with tract-specific metrics.** In: *Proceedings of the 24th Annual Meeting of International Society for Magnetic Resonance in Medicine*, Suntec City, Singapore. May 7–13, 2016
13. Okuda DT, Mowry EM, Cree BA, et al. **Asymptomatic spinal cord lesions predict disease progression in radiologically isolated syndrome.** *Neurology* 2011;76:686–92 CrossRef Medline
14. Schlaeger R, Papinutto N, Zhu AH, et al. **Association between thoracic spinal cord gray matter atrophy and disability in multiple sclerosis.** *JAMA Neurol* 2015;72:897–904 CrossRef Medline
15. Kearney H, Miller DH, Ciccarelli O. **Spinal cord MRI in multiple sclerosis–diagnostic, prognostic and clinical value.** *Nat Rev Neurol* 2015;11:327–38 CrossRef Medline
16. Bede P, Bokde AL, Byrne S, et al. **Spinal cord markers in ALS: diagnostic and biomarker considerations.** *Amyotroph Lateral Scler* 2012;13:407–15 CrossRef Medline
17. Mabray MC, Talbott JF, Whetstone WD, et al. **Multidimensional analysis of magnetic resonance imaging predicts early impairment in thoracic and thoracolumbar spinal cord injury.** *J Neurotrauma* 2016;33:954–62 CrossRef Medline
18. Talbott JF, Whetstone WD, Readdy WJ, et al. **The Brain and Spinal Injury Center score: a novel, simple, and reproducible method for assessing the severity of acute cervical spinal cord injury with axial T2-weighted MRI findings.** *J Neurosurg Spine* 2015;23:495–504 CrossRef Medline
19. Dyck PJ, Boes CJ, Mulder D, et al. **History of standard scoring, notation, and summation of neuromuscular signs. A current survey and recommendation.** *J Peripher Nerv Syst* 2005;10:158–73 CrossRef Medline
20. Jenkinson M, Beckmann CF, Behrens TE, et al. **FSL.** *Neuroimage* 2012;62:782–90 CrossRef Medline
21. De Leener B, Kadoury S, Cohen-Adad J. **Robust, accurate and fast automatic segmentation of the spinal cord.** *Neuroimage* 2014;98:528–36 CrossRef Medline
22. Schneider CA, Rasband WS, Eliceiri KW. **NIH Image to ImageJ: 25 years of image analysis.** *Nat Methods* 2012;9:671–75 CrossRef Medline
23. Martin AR, Aleksanderek I, Cohen-Adad J, et al. **Translating state-of-the-art spinal cord MRI techniques to clinical use: a systematic review of clinical studies utilizing DTI, MT, MWF, MRS, and fMRI.** *Neuroimage Clin* 2016;10:192–238 CrossRef Medline
24. Evans AC, Janke AL, Collins DL, et al. **Brain templates and atlases.** *Neuroimage* 2012;62:911–22 CrossRef Medline
25. Tihan T. **Pathologic approach to spinal cord infections.** *Neuroimaging Clin N Am* 2015;25:163–72 CrossRef Medline

26. Jubelt B, Lipton HL**. Enterovirus/picornavirus infections.** *Handb Clin Neurol* 2014;123:379–416 CrossRef Medline
27. You JY, Lee JW, Lee E, et al. **MR classification system based on axial images for cervical compressive myelopathy.** *Radiology* 2015;276: 553–61 CrossRef Medline
28. Hendrix P, Griessenauer CJ, Cohen-Adad J, et al. **Spinal diffusion tensor imaging: a comprehensive review with emphasis on spinal cord anatomy and clinical applications.** *Clinical Anat* 2015;28:88–95 CrossRef Medline
29. De Leener B, Taso M, Fonov V, et al. **Fully-integrated T1, T2, T2*, white and gray matter atlases of the spinal cord.** In: *Proceedings of the 24th Annual Meeting of International Society for Magnetic Resonance in Medicine*, Suntec City, Singapore. May 7–13, 2016

Impact of MR Neurography in Patients with Chronic Cauda Equina Syndrome Presenting as Chronic Pelvic Pain and Dysfunction

J.R. Petrasic, A. Chhabra, and K.M. Scott

ABSTRACT

BACKGROUND AND PURPOSE: Chronic cauda equina syndrome, defined as persistent damage of the cauda equina nerve roots within the spinal canal can be a challenging diagnosis with varied presentations. MR neurography imaging is more commonly being used to evaluate the lumbosacral spine of patients suspected of having subacute or chronic cauda equina syndrome. Our aim was to evaluate the impact of lumbosacral plexus MR neurography in the diagnostic thinking and therapeutic management of patients presenting with chronic pelvic pain and dysfunction and suspected chronic cauda equina syndrome.

MATERIALS AND METHODS: Consecutive MR neurography lumbosacral plexus examinations at our institution were reviewed retrospectively. Relevant data collected included the following: patient demographics, clinical history, pertinent physical examination findings, preimaging diagnostic impression, prior MR imaging lumbar spine findings, MR neurography findings, postimaging diagnosis, and postimaging treatment plan. The impact of imaging on the preimaging clinical diagnosis and therapeutic management was evaluated.

RESULTS: Of 185 studies of patients who presented with chronic pelvic pain and/or dysfunction, 23 with clinically suspected chronic cauda equina syndrome and imaging findings were included in the study (2 subjects were lost to follow-up). The mean ages were 53 ± 12 years and 53 ± 16 years for men and women, respectively. The common etiologies included arachnoiditis ($n = 8$), tethered cord ($n = 2$), and simple/Tarlov cysts ($n = 3$). Eighteen of 23 (78%) subjects had a change in diagnosis resulting from MR neurography findings, and 5/23 (22%) had no change. Seventeen of 21 (81%) subjects had a change in management, and 4/21 (19%) had no change.

CONCLUSIONS: MR neurography impacts the diagnosis and therapeutic management of patients with suspected chronic cauda equina syndrome.

ABBREVIATIONS: CES = cauda equina syndrome; LS = lumbosacral; MRN = MR neurography; SHINKEI = nerve-SHeath signal increased with INKed rest-tissue rarE Imaging; SPAIR = spectral-attenuated inversion recovery

Cauda equina syndrome (CES) is a rare condition with an annual incidence rate of approximately 3.4 per million and a period prevalence of approximately 8.9 per 100,000 in developed countries.[1] Acute presentations are considered a true emergency; however, chronic and/or incomplete presentations can occur much more indolently and can produce major morbidity and impact on the quality of life. Rapid recognition combined with prompt neurosurgical intervention provide the best opportunity for recovery.[2] However, if symptoms are not recognized and/or treated within a reasonable amount of time or if the initial damage is quite significant, it can lead to permanent and severe neurologic deficits. Chronic CES, defined as persistent damage of the cauda equina nerve roots within the spinal canal, can be a challenging diagnosis with varied presentations of lower spinal symptoms, pelvic pain, gastrointestinal symptoms, urologic issues, and other chronic neurologic problems.[3]

MR imaging is commonly used to evaluate the lumbosacral spine of patients suspected of having acute or subacute CES; however, conventional MR imaging may not identify an attributable cause of the patient's symptoms.[4,5] Electrodiagnostic studies are not always useful in this setting, are technically difficult to perform, and are often not practical in identifying more proximal lesions or lesions involving predominantly sacral and pelvic nerves and musculature. CT myelography has somewhat fallen out of favor due to its invasive nature, involved radiation, and limited interrogation of extraforaminal nerves. MR neurography (MRN) of the lumbosacral (LS) plexus offers a comprehensive evaluation of the lumbar spine,

Received July 6, 2016; accepted after revision September 2.

From the Departments of Physical Medicine and Rehabilitation (J.R.P., K.M.S.) and Radiology (A.C.), University of Texas Southwestern Medical Center, Dallas, Texas; and Department of Radiology (A.C.), Johns Hopkins University, Baltimore, Maryland.

Please address correspondence to Avneesh Chhabra, MD, UT Southwestern Medical Center, 5323 Harry Hines Blvd, Dallas, TX 75390-9178; e-mail: avneesh.chhabra@utsouthwestern.edu

Indicates article with supplemental on-line table.

http://dx.doi.org/10.3174/ajnr.A4994

conus and cauda equina, extraforaminal plexus nerves, and their peripheral branches due to inherent superior soft-tissue contrast and excellent multiplanar spatial resolution.[6-10]

The aim of this study was to find the prevalence of chronic CES in subjects with chronic pelvic pain and dysfunction, assess the MRN findings in these patients, and identify how MRN findings impacted the diagnosis and clinical management of such patients.

MATERIALS AND METHODS

Institutional review board approval was obtained for this Health Insurance Portability and Accountability Act–compliant retrospective study, and informed consent was waived.

Subjects

All consecutive MRN LS plexus examinations (185 total) referred by a board-certified physical medicine and rehabilitation pelvic pain specialist (K.M.S.) during 2 years from July 2013 to September 2015 were screened for inclusion in this study. Twenty-three of these patients presented with a chief symptom of chronic pelvic pain and/or dysfunction and had clinical suspicion for chronic CES (Table 1). One subject who deferred MRN imaging was excluded from this study. Of the final 23 subjects, 2 patients were lost to follow-up after MRN results. All the remaining 21 patients who presented with a chief symptom of chronic pelvic pain and/or dysfunction had clinical suspicion for chronic CES (Table 1). Examinations were performed on either a 1.5T MR imaging scanner (Avanto; Siemens, Erlangen, Germany) or a 3T MR imaging scanner (Achieva/Ingenia; Philips Healthcare, Best, the Netherlands) by using standard MRN protocol[8,11] and an XL torso coil (Philips Healthcare) combined with posterior spine elements. All the interpretations were performed as part of the regular care in light of clinical findings by an experienced radiologist at our institution. Respective subject charts were reviewed to retrieve pertinent clinical data, including the following: clinical presentation (pertinent history and physical findings), patient demographics, preimaging diagnostic impression, prior MR imaging lumbar spine findings (if any), pertinent MRN findings, postimaging diagnosis, and postimaging treatment plan.

Table 1: Patient demographics

Demographics	
No. of male patients	7
No. of female patients	16
Mean male age (SD) (yr)	53 (12)
Mean female age (SD) (yr)	53 (16)
Age range (yr)	28–80
Pelvic pain (No.)	18
Urinary symptoms (No.)	21
Defecatory symptoms (No.)	17
Sensory deficit (No.)	9
Motor weakness (No.)	3

MRN LS Plexus Protocol

Our institutional MRN LS plexus protocol includes the lumbosacral spine and peripheral nerve evaluation in the abdomen and pelvis. The protocol is outlined in Table 2. All examinations were performed on a 3T scanner except for 1 subject due to known metal in the lumbar spine, for whom a 1.5T scanner was used. All examinations were reported by an experienced MRN reader (A.C., 7 years of experience in reading MRN) using a structured template as part of the clinical care. The template included pathologic findings of the spine (canal or neural foramina stenosis), any bone lesions, cord or cauda equina lesions, muscle lesions, peripheral nerve lesions, masses, or other visceral findings. The MRN findings confirming the clinical suspicion of CES included thickening or clumping of cauda equina nerve roots, tethered cord, lumbosacral perineural mass lesion, and increased signal and/or thickening of sacral nerve roots with or without the presence of a focal lesion, such as a Tarlov cyst. Subject charts were reviewed by a physiotherapy resident (J.R.P.) for pre- and post-MRN clinical impressions and whether the diagnosis and clinical management changed on the basis of the post-MRN clinical impression. The impact on diagnosis and clinical management was assessed as "no" (no change in diagnosis or pre-MRN treatment strategy) or "yes" (change in diagnosis or change in proposed treatment, such as ordering immediate follow-up/surgical consultation, or transitioning from surgical to nonsurgical management). Descriptive statistics were performed, and all data were stored on Numbers software, Version 3.6.1 (Apple, Palo Alto, California).

RESULTS

Prevalence of Cauda Equina Syndrome

Twenty-three of 185 (12.4%) subjects with chronic pelvic dysfunction presented with symptoms suggesting CES. There were 7 men and 16 women with a mean age of 53 years and a mean duration of symptoms of 4.5 ± 5.7 years. The subjects presented with a chief symptom of pelvic dysfunction with varied histories of pelvic pain, pelvic paresthesias, urinary/defecatory dysfunction, and sacral nerve deficits (Table 1).

MRN Findings

MRN findings and the impact on management are summarized in the On-line Table. Eleven of 23 (48%) studies identified at least mild lumbosacral spinal canal and/or neuroforaminal stenosis. Thirteen of 23 (57%) subjects had MRN findings confirming the diagnosis of chronic CES. Thirteen of 23 (57%) subjects had prior conventional MR imaging studies of the LS spine (only 10 of those

Table 2: Imaging protocol and parameters of MRN LS plexus

Sequence	TR (ms)	TE (ms)	Gap	Turbo Factor	Acquisition Time	Voxel (mm)
Axial T1	500	8	10%	8	4 min 39sec	4 × 0.6 × 0.6
Axial T2 SPAIR	4000	60	10%	7	6 min 13sec	1 × 1 × 4
SHINKEI	2000	78	0	100	8 min	1.5 × 15 × 1.5
Sagittal T2 spine	3500	120	10%	19	4 min 18sec	0.9 × 1.1 × 4.0
Axial T2 spine	3000	120	10%	27	4 min 19sec	1 × 1 × 5
Axial DTI	16,000	54	0		5 min	3.5 × 3.5 × 5

Note:—SPAIR indicates spectral-attenuated inversion recovery; SHINKEI, nerve-SHeath signal increased with INKed rest-tissue rarE Imaging.

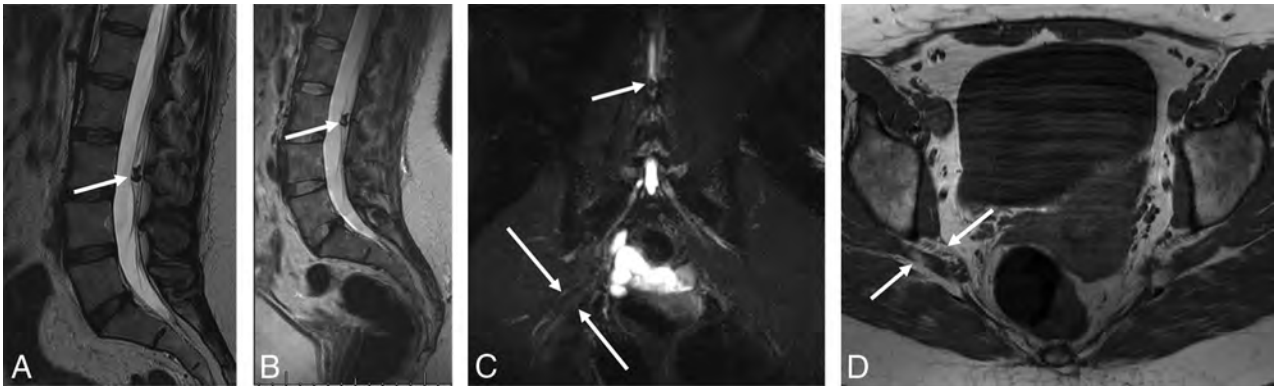

FIG 1. A 43-year-old woman with an intradural calcified lesion and piriformis syndrome (patient 11, On-line Table). Sagittal T2-weighted (*A*) image from an outside scan showed the intradural calcified lesion (*arrow*) at the L3 level, likely an ependymoma. 3T MRN images (*B–D*) obtained 6 months later. Sagittal LS spine (*B*) T2-weighted image again shows the lesion with an unchanged appearance (*arrow*). Coronal MIP 3D SHINKEI image (*C*) shows the lesion displacing the cauda equina nerve roots (*small arrow*) and, in addition, a split and mildly hyperintense right sciatic nerve (*large arrows*). Axial T1-weighted (*D*) image shows the split components of right sciatic nerve (*arrows*). The patient did well on physiotherapy.

FIG 2. MRN followed by MR imaging in a 61-year-old woman with chronic cauda equina syndrome (patient 5, On-line Table). Sagittal T2-weighted (*A*) image and axial T2 SPAIR image obtained on a 1.5T scanner (*B*) show thickened and clumped nondependent cauda equina nerve roots (*arrows*), consistent with arachnoiditis. MR image obtained 3 days later was read by a neuroradiologist as showing no arachnoiditis. However, sagittal T2-weighted from that MRI shows (*C*) similar clumping of nerve roots (*arrow*). This case reflects the importance of increased sensitivity of the reader, which is enhanced while reading MR neurography studies.

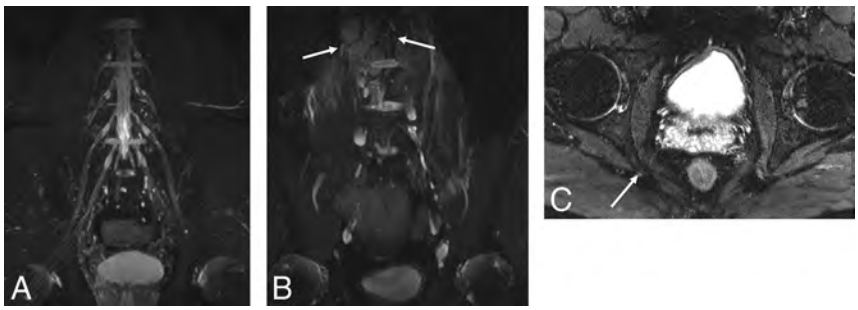

FIG 3. Incidental detection of lymphoma in a 44-year-old man with suspected cauda equina syndrome (patient 8, On-line Table). Coronal MIP SHINKEI images obtained on a 3T scanner (*A* and *B*) show a normal LS plexus and numerous incidentally found lymph nodes (*arrows*, biopsy-proved lymphoma). Axial T2 SPAIR image (*C*) shows a prominent and hyperintense right pudendal nerve at the ischial spine, suggesting pudendal neuropathy (*arrow*).

were available for review within the image-viewing system of our institution), and 4/10 of these studies identified pertinent positive findings (Fig 1). One patient had their conventional MR imaging LS spine study completed after MRN, which notably did not reveal the notable findings seen on MRN (Fig 2). These positive conventional MR imaging findings included 2 studies demonstrating sacral Tarlov cysts, one showing calcified intradural lesions, and an other showing arachnoiditis (Fig 3). Etiologies of CES identified on MRN included arachnoiditis (8/13), sacral/Tarlov cysts (3/13), and tethered cord (2/13).

Impact of MRN on Diagnostic Thinking

Eighteen of 23 (78%) subjects had a change in diagnosis resulting from MRN findings, and 5/23 (22%) had no change in diagnosis. One patient underwent MR imaging after MRN, but MR imaging failed to detect arachnoiditis. MRN also had incremental value in patients who had positive MR imaging findings (eg, in an MR imaging study with positive findings, MRN further added thickening and increased signal of the sacral nerves, suggesting neuropathy; Fig 4). In another case, additional findings of increased signal of the bilateral pudendal nerves added an additional potential etiology to the differential and prompted consideration of nerve blocks.

Impact of MRN on Clinical Management

Seventeen of 21 (81%) patients benefited from a change in management due to notable MRN findings. Four of 21 (19%) patients had no change in clinical management. These changes included neurosurgical referral, peripheral nerve blocks, epidural injections, and discontinuation of physical therapy, and so forth, as detailed in the On-line Table.

DISCUSSION

This retrospective analysis of a series of subjects with clinically suspected chronic cauda equina syndrome presenting with chronic pelvic pain or dysfunction in a tertiary care setting confirms the ability of lumbosacral MRN to impact their diagnoses

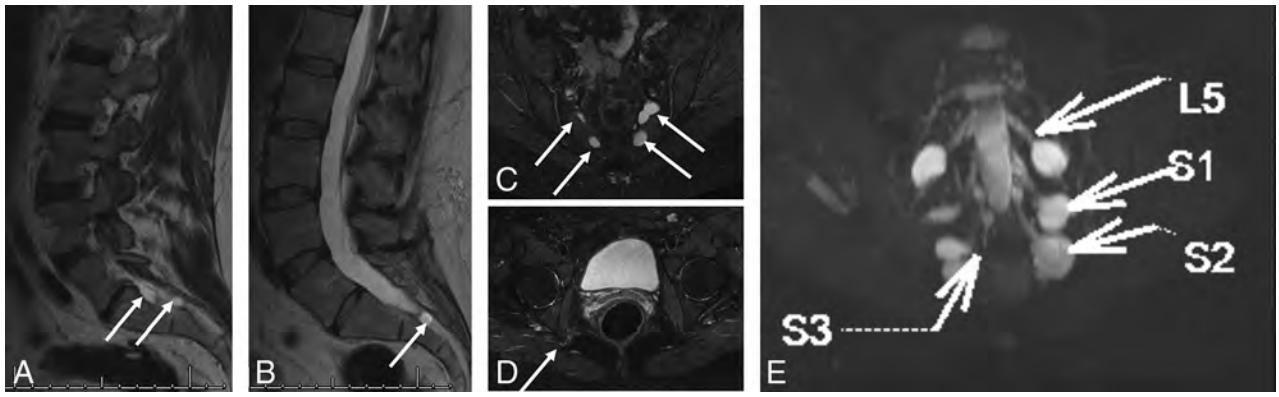

FIG 4. Tarlov cysts and lumbosacral neuropathies (patient 16, On-line Table). Sagittal T2-weighted MR images from outside MR imaging (*A* and *B*) show multiple Tarlov cysts (*arrows*). MRN obtained 4 months later on a 3T scanner (*C–E*). Axial T2 SPAIR images (*C* and *D*) again show multiple Tarlov cysts (*arrows* in *C*) and right pudendal neuropathy change (*arrow* in *D*). 3D MIP SHINKEI image shows multiple bright lumbosacral nerves in association with these cysts. Pudendal neuropathy change could be incidental to and/or exacerbated by sacral neuropathy.

and therapeutic strategies. No longer considered "experimental," this imaging technique has the potential of quick transition into the community setting. Although CES is a challenging diagnosis, our analysis suggests that this examination can add considerable value to the evaluation of these patients because the clinical presentation, findings, and examination are often confounded with vague chronic and stable neurologic dysfunction and/or pelvic pain symptoms.[12] Lumbar spinal and lumbosacral nerve root analysis on MRN is more consistently able to distinguish arachnoiditis or clumping of nerve roots and tethered cord in regard to the effect on the neural components within the spinal canal. MRN was also able to help determine whether cysts within the spinal cord were creating an objective pathologic effect on the nerve roots (edema, inflammation, and so forth) or were merely seen in association with the nerve roots. Some other specific peripheral nerve findings on MRN, as noted by a trained radiologist, included peripheral nerve size and signal intensity (and associated symmetry), nerve discontinuity, mechanical distortion, relations of nerves to masses, image features revealing distortion of nerves at entrapment points, fibrosis, inflammation, and edema.[13-15] These findings should be clinically correlated.

When performed appropriately, this examination can provide an accurate and timely diagnosis for patients with an often confusing clinical picture and complex differential diagnosis. Notably, one of the patients who demonstrated a change was diagnosed with extensive lymphadenopathy on MRN (no prior MR imaging), prompting admission to the hospital for malignancy workup, later revealing Hodgkin lymphoma, though a simple MR imaging with contrast, had it been ordered earlier, would have been enough to identify this condition. Subsequent management changes that may not have occurred without the information obtained from MRN included neurosurgical referral, peripheral nerve blocks, epidural steroid injections, and discontinuation of pelvic physical therapy (treatment for lower motor neuron dysfunction via referral to spinal cord injury clinic). One large retrospective case series that looked at the role of MRN in the diagnosis of spinal and peripheral nerve lesions also concluded that a significant indication for MRN is in patients in whom electromyography/nerve conduction study and MR imaging findings are inconclusive.[14] More accurate and timely diagnosis helps prevent further expensive and potentially invasive work-ups, providing some clarity to an otherwise confusing clinical picture. Although there were no cost-effectiveness analyses performed, the results of our study suggest that a more resolute diagnosis helps the patient focus more on symptom treatment and management rather than continuing further work-ups and misdirected treatments.

One potential point of contention that should be addressed is the appropriateness of the term "chronic" CES. Although CES is an acutely presenting syndrome with a classic presentation of red flag symptoms, it may also be a chronic condition as a result of delayed treatment of the acute syndrome. The chronic and progressive form is more commonly seen in inflammatory or demyelinating conditions. Giving reference to these more indolent etiologies of their neurologic compromise also gives patients more clarity in understanding their diagnosis.

A search of the literature did not reveal any other reports of using MRN to look for lumbosacral intraspinal lesions, and in particular chronic CES. Additionally, lumbosacral plexus MR neurography studies not only help identify lesions within the spinal cord but also aid in finding peripheral neuropathies and plexopathies elsewhere in the pelvis.[8,13,14]

There are several limitations in our study. The analysis, including the retrospective methodology and, to some degree, the categorization of "no" or "yes" with regard to change in management, is somewhat subjective, leaving it open to bias. A few patients were lost to follow-up; thus, we do not have complete imaging or clinical management data for these subjects. Due to the retrospective nature of this study, no interobserver performance in repeat readings of the MRN examinations was obtained (all studies were ultimately interpreted by one of the authors), stressing the need for an increase in the number of radiologists qualified to read these studies. Figure 2 illustrates the increased sensitivity of the radiologist reading the MRN examinations. However, we were attempting to uncover the impact of routine reads of these examinations in a tertiary care setting.

Future directions include performance of a larger, prospective randomized clinical trial looking at the clinical impact of MR neurography on this and other neurologic diseases. A multicenter trial would be ideal to decrease potential bias, given the relative paucity of specialized radiologists qualified to read these studies. Performing a cost-effectiveness analysis on the impact of MRN

results would also be helpful in identifying how these studies impact standard practice economy.[16]

CONCLUSIONS

MRN impacts the diagnostic and therapeutic management of patients with chronic CES when the diagnosis is suspected but unclear.

Disclosures: Avneesh Chhabra—*UNRELATED*: *Consultancy*: Icon Medical, Siemens, *Comments*: for the MSK computer-aided diagnosis group (now finished); *Royalties*: Jaypee, Wolters Kluwer. Kelly M. Scott—*UNRELATED: Payment for Lectures including Service on Speakers Bureaus*: SUFU, UAPA, and SGA national and regional conferences; invited speaker.

REFERENCES

1. Podnar S. **Epidemiology of cauda equina and conus medullaris lesions.** *Muscle Nerve* 2007;35:529–31 CrossRef Medline
2. Fraser S, Roberts L, Murphy E. **Cauda equina syndrome: a literature review of its definition and clinical presentation.** *Arch Phys Med Rehabil* 2009;90:1964–68 CrossRef Medline
3. Ahad A, Elsayed M, Tohid H. **The accuracy of clinical symptoms in detecting cauda equina syndrome in patients undergoing acute MRI of the spine.** *Neuroradiol J* 2015;28:438–42 CrossRef Medline
4. Bell DA, Collie D, Statham PF. **Cauda equina syndrome: what is the correlation between clinical assessment and MRI scanning?** *Br J Neurosurg* 2007;21:201–03 CrossRef Medline
5. Chhabra A, Farahani SJ, Thawait GK, et al**. Incremental value of magnetic resonance neurography of lumbosacral plexus over noncontributory lumbar spine magnetic resonance imaging in radiculopathy: a prospective study.** *World J Radiol* 2016;8:109–16 CrossRef Medline
6. Neufeld EA, Shen PY, Nidecker AE, et al. **MR imaging of the lumbosacral plexus: a review of techniques and pathologies.** *J Neuroimaging* 2015;25:691–703 CrossRef Medline
7. Chhabra A, Rozen S, Scott K. **Three-dimensional MR neurography of the lumbosacral plexus.** *Semin Musculoskelet Radiol* 2015;19:149–59 CrossRef Medline
8. Delaney H, Bencardino J, Rosenberg ZS. **Magnetic resonance neurography of the pelvis and lumbosacral plexus.** *Neuroimaging Clin N Am* 2014;24:127–50 CrossRef Medline
9. Pham M, Bäumer T, Bendszus M. **Peripheral nerves and plexus: imaging by MR-neurography and high-resolution ultrasound.** *Curr Opin Neurol* 2014;27:370–79 CrossRef Medline
10. Bäumer P, Pham M, Ruetters M, et al. **Peripheral neuropathy: detection with diffusion-tensor imaging.** *Radiology* 2014;273:185–93 CrossRef Medline
11. Soldatos T, Andreisek G, Thawait GK, et al. **High-resolution 3-T MR neurography of the lumbosacral plexus.** *Radiographics* 2013;33:967–87 CrossRef Medline
12. Arunkalaivanan A, do Nascimento VC, Needham M**. Cauda equina syndrome: an uncommon cause of urinary retention in a young woman.** *Int Urogynecol J* 2016;27:1121–23 CrossRef Medline
13. Chhabra A. **Peripheral MR neurography: approach to interpretation.** *Neuroimaging Clin N Am* 2014;24:79–89 CrossRef Medline
14. Du R, Auguste KI, Chin CT, et al. **Magnetic resonance neurography for the evaluation of peripheral nerve, brachial plexus, and nerve root disorders.** *J Neurosurg* 2010;112:362–71 CrossRef Medline
15. Filler A. **Magnetic resonance neurography and diffusion tensor imaging: origins, history, and clinical impact of the first 50,000 cases with an assessment of efficacy and utility in a prospective 5000-patient study group.** *Neurosurgery* 2009;65(4 suppl):A29–43 CrossRef Medline
16. Chhabra A, Belzberg AJ, Rosson GD, et al. **Impact of high resolution 3 Tesla MR neurography (MRN) on diagnostic thinking and therapeutic patient management.** *Eur Radiol* 2016;26:1235–44 CrossRef Medline

The "Vexata Quaestio" on Lacunar Stroke: The Role of CT Perfusion Imaging

We read with great interest the study of Benson et al,[1] which demonstrates that CT perfusion has low sensitivity and high specificity in identifying lacunar infarcts. However, we believe that some clarification on the topic might be useful. Lacunar infarcts are defined as small subcortical infarcts (<15–20 mm) normally located in the basal ganglia, thalamus, internal capsule, corona radiata, and brain stem, which result (usually presumed rather than demonstrated) from the occlusion of a single penetrating artery of the brain.[2] The etymology of the word "lacune" dates back as early as 1838,[3] and since then, many different definitions have been proposed. Unfortunately, there is currently still considerable confusion about the real pathogenesis of these lesions.[2] It is striking that the concepts attached to lacunes have only recently aroused interest.

The precise diagnosis of lacunar infarction due to small-vessel disease is tricky in clinical practice because the nature of the vascular lesion itself can only be determined by neuropathologic examination. In clinical practice, the diagnosis relies on the following: 1) probability assumptions based on the clinical features, 2) neuroimaging of the brain parenchyma, and 3) ancillary investigations such as ultrasonography (cardiac and carotid) to rule out other potential causes of ischemia. The term "lacune" or "lacunar lesion" should be used only for small infarcted areas (largest diameter, <15–20 mm) limited to the deep perforator territory likely to be due to in situ disease (small-vessel disease). When embolism or larger artery disease is more likely presumed on a clinical basis, the term "lacune" should be avoided and the lesion should be described as a small deep infarct associated with another presumed etiology rather than defined as a small-vessel disease. Defining a lesion as "lacunar" by relying on only infarct size is rather reductive.

Diffusion-weighted MR imaging is much more sensitive to acute ischemia within the first few hours after stroke onset, while CT and conventional MR imaging are both relatively insensitive. Studies have shown that most patients with lacunar syndromes do indeed have DWI findings suggestive of lacunar infarcts, such as infarct in the territory of a single penetrating artery. However, a pattern of multiple ischemic areas in the cortex or subcortex is demonstrated with DWI in no less than one-third of patients with a lacunar syndrome, suggesting that embolism (from the heart or extracranial arteries) might be the real cause instead of cerebral small-vessel disease.[4]

In this respect Figs 2 and 3 in the article of Benson et al[1] may raise some concerns that the lesions described are actually lacunar rather than embolic. If the lesions are located in the subcortical white matter, it does not necessarily mean that they are lacunar. Diffusion restriction areas shown in the figures appear to be mostly localized in the subcortex region rather than in the territory of the penetrating artery of the brain usually affected in small-vessel disease.

Nevertheless, it is known that imaging physics teaches us that the most important factor for distinguishing a pathology is the relative imaging signal given by the pathology compared with the normal appearance in the presence of background noise. This is the signal-to-noise ratio or, more precisely, the contrast-to-noise ratio (CNR), which is the difference between the SNR of the pathology and the SNR of normal tissue.[5] The inherently poor SNR of CTP-derived images is the fundamental flaw in the technique (meaning low signal and high noise) so that many of the small lesions may be missed. Moreover, as reported in the "Materials and Methods" section, if the section thickness is equal to 10 mm, the image interpretation may be susceptible to partial volume artifacts, further reducing the sensitivity of the method for detecting lacunar ischemic lesions, which may be smaller than the section thickness.

Because the technologic advancement and reconstruction algorithms will not be able to exceed the low CNR limitations inherent to the method, CTP cannot compete with the sensitivity of DWI in detecting ischemic lacunar infarcts. Also, software applications from different vendors do not generate equivalent quantitative perfusion results. Caution should thus be exercised when interpreting quantitative CTP measures because these values may vary considerably depending on the postprocessing software used.

http://dx.doi.org/10.3174/ajnr.A4983

REFERENCES

1. Benson JC, Payabvash S, Mortazavi S, et al. **CT perfusion in acute lacunar stroke: detection capabilities based on infarct location.** *AJNR Am J Neuroradiol* 2016 Aug 18. [Epub ahead of print] CrossRef Medline
2. Norrving B. **Lacunar infarcts: no black holes in the brain are benign.** *Pract Neurol* 2008;8:222–28 CrossRef Medline

3. Chambre A. **Mémoire sur la durabilité du ramollissement cérébral.** *Gaz Méd Paris* 1838;6:305–14
4. Caso V, Budak K, Georgiadis D, et al. **Clinical significance of detection of multiple acute brain infarcts on diffusion weighted magnetic resonance imaging.** *J Neurol Neurosurg Psychiatry* 2005;76:514–18 CrossRef Medline
5. González RG. **Low signal, high noise and large uncertainty make CT perfusion unsuitable for acute ischemic stroke patient selection for endovascular therapy.** *J Neurointerv Surg* 2012;4:242–45 CrossRef Medline

N. Morelli
Neurology Unit
Radiology Unit
E. Rota
Neurology Unit
E. Michieletti
Radiology Unit
D. Guidetti
Neurology Unit
Guglielmo da Saliceto Hospital
Piacenza, Italy

REPLY:

We thank Morelli et al for their comments regarding our article "CT Perfusion in Acute Lacunar Stroke: Detection Capabilities Based on Infarct Location." We acknowledge the important points our colleagues raised concerning lacunar infarcts and have responded to those comments below.

To begin, we agree that the size of lacunae should be defined as <15–20 mm. Although both 15 and 20 mm have been suggested as the uppermost diameter limit for lacunar infarcts, we chose to use 20 mm to be consistent with other recent publications on the topic.[1]

However, we disagree with our colleagues' conclusion that the definition of lacunae should only be used for infarcts within the deep perforator territory. Such restrictive use of the term "lacunae" ignores the variability in vascular supply throughout the brain. For example, supply to the caudate head from the artery of Heubner may arise either as a medial lenticulostriatal perforator or as a direct artery. Thus, the necessity that lacunar infarcts be located in the "deep" perforator territory prevents the inclusion of subcortical infarcts, which were shown in a study of 3660 participants to represent 11.9% of lacunae.[2]

Nevertheless, the distinction should be made between periventricular white matter (PVWM) contiguous with the ventricle, deep white matter (DWM), and subcortical white matter (SCWM) immediately subjacent to the cortex. According to this classification system used by Fazekas et al[3] and Kim et al,[4] the infarcts in Figs 2 and 3 of our article would be better classified as DWM, rather than SCWM as our colleagues stated, because they are located several millimeters deep to the unaffected overlying cortex.[3,4] Even if our colleagues' presumption that only "deep" infarcts may be classified as lacunae is correct, it is speculative to conclude that these infarcts must be within the PVWM rather than the DWM.

Next, we agree with our colleagues that the contrast-to-noise (CNR) ratio and 10-mm sections are limitations of CTP imaging; both the CNR and section thickness may lead to partial volume artifacts, affect the absolute infarct size on CBV, and cause smaller infarcts to be missed. However, one aim of our study was to assess whether an abnormal perfusion or delay (ie, CBF and MTT) is present in the setting of lacunar infarcts, which theoretically could affect a larger area than a lacune (an example of this is seen in Fig 2). Hence, the sensitivity of CTP may be higher than first suspected because it may be used to arouse suspicion of lacunar infarcts when a severely elevated MTT or TTP region is observed. This is an area that deserves further study.

Finally, it is important to address our colleagues' presumption that DWI is the criterion standard in the setting of lacunar infarcts. A recent study showed that up to 29% of patients with nondisabling ischemic stroke have negative findings on DWI, and the prognosis in patients with negative findings on DWI was no better than those with positive findings on DWI.[5] Furthermore, DWI positive for lesions in the setting of acute stroke sometimes demonstrates reversal of restricted diffusion.[6] Our study compared CTP imaging with DWI—not with the clinical presence or absence of lacunar syndrome. The diagnostic capability of DWI would, therefore, naturally be superior to that of CTP because DWI was used as the criterion standard in our study. A direct comparison of both CTP and DWI with the presence or absence of clinically apparent lacunae would be needed to determine the relative sensitivity of both modalities, which was not performed in this study. This, too, is an area of potential future research.

http://dx.doi.org/10.3174/ajnr.A4991

REFERENCES

1. Das T, Settecase F, Boulos M, et al. **Multimodal CT provides improved performance for lacunar infarct detection.** *AJNR Am J Neuroradiol* 2015;36:1069–75 CrossRef Medline
2. Longstreth WT, Bernick C, Manolio TA, et al. **Lacunar infarcts defined by magnetic resonance imaging of 3660 elderly people: the Cardiovascular Health Study.** *Arch Neurol* 1998;55:1217–25 Medline
3. Fazekas F, Chawluk JB, Alavi A, et al. **MR signal abnormalities at 1.5 T in Alzheimer's dementia and normal aging.** *AJR Am J Roentgenol* 1987;149:351–56 CrossRef Medline
4. Kim KW, MacFall JR, Payne ME. **Classification of white matter lesions on magnetic resonance imaging in elderly persons.** *Biol Psychiatry* 2008;64:273–80 CrossRef Medline
5. Makin SD, Doubal FN, Dennis MS, et al. **Clinically confirmed stroke with negative diffusion-weighted imaging magnetic resonance imaging: longitudinal study of clinical outcomes, stroke recurrence, and systematic review.** Stroke 2015;46:3142–48 CrossRef Medline
6. Olivot JM, Mlynash M, Thijs VN, et al. **Relationships between cerebral perfusion and reversibility of acute diffusion lesions in DEFUSE: insights from RADAR.** *Stroke* 2009;40:1692–97 CrossRef Medline

J.C. Benson
Department of Radiology
University of Minnesota Medical Center
Minneapolis, Minnesota
S. Payabvash
Department of Radiology
University of California San Francisco
San Francisco, California
B. Hoffman
M. Oswood
Department of Radiology
Hennepin County Medical Center
Minneapolis, Minnesota
A.M. McKinney
Department of Radiology
University of Minnesota Medical Center
Minneapolis, Minnesota

Concerning "Nonaneurysmal Perimesencephalic Hemorrhage Is Associated with Deep Cerebral Venous Drainage Anomalies: A Systematic Literature Review and Meta-Analysis"

We would like to thank Rouchaud et al[1] for their study entitled "Nonaneurysmal Perimesencephalic Hemorrhage Is Associated with Deep Cerebral Venous Drainage Anomalies: A Systematic Literature Review and Meta-Analysis." This is a timely effort to investigate the underlying mechanisms of bleeding in nonaneurysmal perimesencephalic subarachnoid hemorrhage (pSAH) because no known causes for this condition have been established yet. However, we raise a few concerns regarding this article.

Deep cerebral venous anomalies may be more common in patients with pSAH, but the meta-analysis does not prove their guilt beyond association. Higher rates of a primitive venous system may be seen in patients with pSAH, but it is not clear how the authors concluded that it has the potential to facilitate the diagnosis of pSAH. Are the authors advocating performing digital subtraction angiography to assess the venous anatomy in patients with SAH in the distribution typical for SAH? As per the literature, patients with nonaneurysmal SAH may have a normal bilateral basal vein of Rosenthal (BVR) drainage pattern (18.3%), and an abnormal venous drainage pattern can be seen in patients with aneurysmal SAH (15.3%).[1] It is unclear how detecting the venous anatomy would change management or prognosis in patients with nonaneurysmal pSAH. The available current literature indicates that negative findings on CT angiography are conclusive in most cases in excluding an aneurysm as the source of SAH in patients with a typical distribution pattern of pSAH, and these patients generally have good outcomes.[2] Recurrent pSAH is rarely reported, and primitive venous drainage has been noted in recurrent pSAH as well. However, even the few reported cases of recurrent pSAH have been reported to have a good outcome with no clear explanation for the etiology of the bleed.[3]

Not all studies have found an association between variant venous anatomy and pSAH.[4] Variants in venous anatomy are also much more common than the incidence of pSAH. Although intracranial venous congestion caused by straining in patients with anomalous venous drainage has been hypothesized to cause a tear in the vein fixed to a dural sinus, Song et al[5] found physical actions, including breath-holding during coughing, shouting, and ejaculation, in only 30% of instances of nonaneurysmal SAH in their series.

Performing conventional angiography after negative findings on CTA may not be cost-effective and is not without risks.[6] We request that the authors elaborate on how a primitive BVR pattern might affirm the diagnosis of nonaneurysmal perimesencephalic hemorrhage and the utility of looking for it, in the absence of better evidence and based solely on association.

http://dx.doi.org/10.3174/ajnr.A4984

REFERENCES

1. Rouchaud A, Lehman VT, Murad MH, et al. **Nonaneurysmal perimesencephalic hemorrhage is associated with deep cerebral venous drainage anomalies: a systematic literature review and meta-analysis.** *AJNR Am J Neuroradiol* 2016;37:1657–63 CrossRef Medline
2. Kalra VB, Wu X, Matouk CC, et al. **Use of follow-up imaging in isolated perimesencephalic subarachnoid hemorrhage: a meta-analysis.** *Stroke* 2015;46:401–06 CrossRef Medline
3. Malhotra A, Wu X, Borse R, et al. **Should patients be counseled about possible recurrence of perimesencephalic subarachnoid hemorrhage?** *World Neurosurg* 2016 Aug 10. [Epub ahead of print] CrossRef Medline
4. Daenekindt T, Wilms G, Thijs V, et al. **Variants of the basal vein of Rosenthal and perimesencephalic nonaneurysmal hemorrhage.** *Surg Neurol* 2008;69:526–29; discussion 529 CrossRef Medline
5. Song JH, Yeon JY, Kim KH, et al. **Angiographic analysis of venous drainage and a variant basal vein of Rosenthal in spontaneous idiopathic subarachnoid hemorrhage.** *J Clin Neurosci* 2010;17:1386–90 CrossRef Medline
6. Kalra VB, Wu X, Forman HP, et al. **Cost-effectiveness of angiographic imaging in isolated perimesencephalic subarachnoid hemorrhage.** *Stroke* 2014;45:3576–82 CrossRef Medline

X. Wu
R. Liu
A. Malhotra
Department of Radiology and Biomedical Imaging
Yale School of Medicine
New Haven, Connecticut

REPLY:

We would like to thank Wu and colleagues for their critical analysis of our recently published study. As the authors point out, our meta-analysis found a strong association between deep cerebral venous anomalies and nonaneurysmal perimesencephalic SAH.[1] As demonstrated in our meta-analysis, patients with aneurysmal SAH might also have deep cerebral venous drainage anomalies, thus making the presence of this imaging finding, especially in the case of a subarachnoid hemorrhage extending beyond the perimesencephalic cisterns, nonspecific. However, in case of a typical perimesencephalic hemorrhage with negative DSA findings for aneurysm, the identification of deep cerebral venous drainage is an additional imaging finding in favor of nonaneurysmal perimesencephalic SAH.

Contrary the suggestion of Wu et al, the literature does not recommend abandonment of DSA in the initial phase of perimesencephalic hemorrhage.[2] In a recently published study of 230 patients with CTA negative for hemorrhage, Heit et al[3] found that DSA identified vascular pathology in 13% of patients. Among patients with perimesencephalic hemorrhage, an aneurysm was found in 3% of cases and vasculitis was found in 1.5% of cases. While admittedly the diagnostic yield of angiography was low (4.5%), the risks of DSA are even lower and the importance of establishing the correct diagnosis is high.[4,5] We do agree, however, that second-look DSA does not appear to have a sufficient diagnostic yield for the detection of a causative aneurysm in case of negative findings on 6-vessel DSA with 3D rotational angiography.[6] If some authors maintain the futility of DSA in cases of typical perimesencephalic hemorrhage, the drainage venous pattern may still be evaluated with cross-sectional imaging (ie, CTV or MRV).[7]

One of the most interesting aspects of studying venous anomalies and disease in perimesencephalic hemorrhage is that we may be slowly arriving at a better understanding of the nature of the disease. The association between venous anomalies and nonaneurysmal perimesencephalic hemorrhage suggests that this could be secondary to a venous rupture/leak. In case of primitive venous drainage, the direct connection of the thin-walled perimesencephalic veins with the dural sinuses may predispose to sudden increases in venous pressure with engorgement and rupture of the veins as a result.[8-10] However, because the anatomic venous drainage pattern is not likely to change after bleeding, it is surprising that the incidence of rebleeding is very low in patients after the initial perimesencephalic SAH.[11] Matsumaru et al[12] speculated that the spontaneous healing of the venous rupture by fibrous tissue reaction would reinforce the wall of the vein, decreasing the risk of rupture.[9]

http://dx.doi.org/10.3174/ajnr.A4990

REFERENCES

1. Rouchaud A, Lehman VT, Murad MH, et al. **Nonaneurysmal perimesencephalic hemorrhage is associated with deep cerebral venous drainage anomalies: a systematic literature review and meta-analysis.** *AJNR Am J Neuroradiol* 2016;37:1657–63 CrossRef Medline
2. Kalra VB, Wu X, Matouk CC, et al. **Use of follow-up imaging in isolated perimesencephalic subarachnoid hemorrhage: a meta-analysis.** *Stroke* 2015;46:401–06 CrossRef Medline
3. Heit JJ, Pastena GT, Nogueira RG, et al. **Cerebral angiography for evaluation of patients with CT angiogram-negative subarachnoid hemorrhage: an 11-year experience.** *AJNR Am J Neuroradiol* 2016; 37:297–304 CrossRef Medline
4. Fifi JT, Meyers PM, Lavine SD, et al. **Complications of modern diagnostic cerebral angiography in an academic medical center.** *J Vasc Interv Radiol* 2009;20:442–47 CrossRef Medline
5. Kaufmann TJ, Huston J 3rd, Mandrekar JN, et al. **Complications of diagnostic cerebral angiography: evaluation of 19,826 consecutive patients.** *Radiology* 2007;243:812–19 CrossRef Medline
6. Potter CA, Fink KR, Ginn AL, et al. **Perimesencephalic hemorrhage: yield of single versus multiple DSA examination: a single-center study and meta-analysis.** *Radiology* 2016 May 27:152402. [Epub ahead of print] CrossRef Medline
7. van der Schaaf IC, Velthuis BK, Gouw A, et al. **Venous drainage in perimesencephalic hemorrhage.** *Stroke* 2004;35:1614–18 CrossRef Medline
8. Song JH, Yeon JY, Kim KH, et al. **Angiographic analysis of venous drainage and a variant basal vein of Rosenthal in spontaneous idiopathic subarachnoid hemorrhage.** *J Clin Neurosci* 2010;17:1386–90 CrossRef Medline
9. Watanabe A, Hirano K, Kamada M, et al. **Perimesencephalic nonaneurysmal subarachnoid haemorrhage and variations in the veins.** *Neuroradiology* 2002;44:319–25 CrossRef Medline
10. Yamakawa H, Ohe N, Yano H, et al. **Venous drainage patterns in perimesencephalic nonaneurysmal subarachnoid hemorrhage.** *Clin Neurol Neurosurg* 2008;110:587–91 CrossRef Medline
11. Malhotra A, Wu X, Borse R, et al. **Should patients be counseled about possible recurrence of perimesencephalic subarachnoid hemorrhage?** *World Neurosurg* 2016 Aug 10. [Epub ahead of print] CrossRef Medline
12. Matsumaru Y, Yanaka K, Matsumura A. **Is perimesencephalic nonaneurysmal hemorrhage of venous origin?** *Stroke* 2004;35:2753–54; author reply 2754 CrossRef Medline

A. Rouchaud
Interventional Neuroradiology NEURI Center
Hôpital Bicêtre
Le Kremlin Bicêtre, France
W. Brinjikji
Department of Radiology
Mayo Clinic
Rochester, Minnesota

Regarding "Neurovascular Manifestations of Hereditary Hemorrhagic Telangiectasia: A Consecutive Series of 376 Patients during 15 Years"

We would like to thank the authors Brinjikji et al[1] for their study titled "Neurovascular Manifestations of Hereditary Hemorrhagic Telangiectasia: A Consecutive Series of 376 Patients during 15 Years." The authors have nicely described the spectrum of cerebrovascular lesions in a large series of patients with hereditary hemorrhagic telangiectasia (HHT).

The authors included only patients with definite HHT (met ≥3 of 4 Curacao criteria) and had a group of 376 patients over a 15-year period. Could the authors tell us how many patients in total were imaged for screening for HHT during this time period at their institution? Did these patients have any neurologic symptoms, or was neuroimaging performed to screen for brain vascular malformations? The authors stated that screening MR imaging may be warranted for both adults and children. However, the group formulating the guidelines found only Level 3 evidence for this recommendation (opinions of respected authorities, based on clinical experience, descriptive studies, or reports of expert committees).[2] To better understand the utility of screening, answers to a few questions would be helpful.

Five patients in this study with single nidal brain AVMs presented with hemorrhage. Could the authors describe how many other patients included in the study had hemorrhage over the course of the study (assuming follow-up was available) and how many patients were treated? It would also help if the authors could mention the criteria used for treatment of nidal AVMs in these patients. Did any of the treated patients develop complications from treatment or have hemorrhage on follow-up?

We would also appreciate if the authors could comment on the utility of vascular imaging in this patient subset. CTA/MRA was performed in 140 patients (37.2%), and DSA performed in 46 patients. The authors acknowledged absence of cerebral angiography in all patients as a limitation of the study because angiography is more sensitive for detection of smaller AVMs. Do the authors advocate angiography in all patients? Other than finding additional small AVMs, could the authors elaborate on the added utility of performing angiography? Did any patients receive repeat imaging?

Of the spectrum of vascular lesions described in patients with HHT, the nidus-type AVMs may not have a completely benign natural history. The rationale for screening patients with HHT for brain vascular malformations has been stated to be to detect a vascular malformation before the development of a debilitating hemorrhage.[2] However, there is absence of literature proving that screening or preemptive treatment are effective strategies in HHT. It would be very helpful if the authors, through their large series, can answer these questions.

Disclosures: Kimberly Seifert—*UNRELATED*: *Employment*: Virginia Commonwealth University, Yale, *Comments*: residency training compensation.

REFERENCES

1. Brinjikji W, Iyer VN, Yamaki V, et al. **Neurovascular manifestations of hereditary hemorrhagic telangiectasia: a consecutive series of 376 patients during 15 years.** *AJNR Am J Neuroradiol* 2016;37:1479–86 CrossRef Medline
2. Faughnan ME, Palda VA, Garcia-Tsao G, et al. **International guidelines for the diagnosis and management of hereditary haemorrhagic telangiectasia.** *J Med Genet* 2011;48:73–87 CrossRef Medline

A. Malhotra
X. Wu
K. Seifert
Department of Radiology and Biomedical Imaging
Yale School of Medicine
New Haven, Connecticut

http://dx.doi.org/10.3174/ajnr.A4986

REPLY:

Malhotra and colleagues have brought up a number of interesting questions regarding our recently published article on the neurovascular manifestations of hereditary hemorrhagic telangiectasia (HHT).[1] A number of the questions raised by the authors would require completely new studies; however, we will do our best to answer their questions in general terms.

Regarding the use of screening MR imaging for patients with HHT, a vast majority of the patients included in our study received brain MRIs as part of a standard screening protocol. As an HHT Center of Excellence, our preference is to adhere to the international guidelines for diagnosis and management of HHT.[2] We fully understand that there is no level 1 evidence to support the use of screening; however, screening is part of the standard of care for management of these patients.

A total of 23 patients with HHT who presented with ruptured or unruptured AVMs underwent treatment of their AVMs during this time period. A vast majority of these patients had surgery or radiosurgery. In general, outcomes related to treatment of these lesions were good, with low complication rates and no rehemorrhage. We recently published a study on the natural history of capillary vascular malformations and reported that the risk of hemorrhage from these lesions is zero.[3] It is likely that the inclusion of capillary vascular malformations in natural history studies of brain AVMs in HHT is responsible for the deceivingly benign natural history of these lesions compared with sporadic AVMs.[4-6]

Regarding the utility of vascular imaging in this patient subset, we certainly do not advocate the use of screening with conventional cerebral angiography for AVM diagnosis. Although cerebral angiography is a very safe procedure at our institution, it would not be cost-effective. We advocate the use of cerebral angiography if there is an equivocal finding on MR imaging or in preparation for treatment of a known brain AVM. MRA and CTA are also useful as problem-solving tools; however, based on our experience, contrast-enhanced MR imaging is generally sufficient as a screening modality for clinically significant brain AVMs. The recent addition of SWI to our HHT brain MR imaging protocol has proved useful.

A number of patients included in our study received repeat imaging. However, this was not part of a screening protocol. In general, patients who received repeat imaging had a neurologic symptom that warranted further investigation. In general, studies have found no utility in the use of repeat screening for the presence of brain AVMs, even in children.[7]

Ultimately, Maholtra and colleagues are correct that there is no literature proving that screening or preemptive treatment of AVMs are effective strategies in HHT. It is unlikely that a definitive answer to this question will be borne from a single large institution's experience. This is a rare disease that remains poorly understood. Large, multi-institutional collaborations such as the Brain Vascular Malformation Consortium HHT Investigator Group will be needed to better answer these questions.

http://dx.doi.org/10.3174/ajnr.A5006

REFERENCES

1. Brinjikji W, Iyer VN, Yamaki V, et al. **Neurovascular manifestations of hereditary hemorrhagic telangiectasia: a consecutive series of 376 patients during 15 years.** *AJNR Am J Neuroradiol* 2016;37:1479–86 CrossRef Medline
2. Faughnan ME, Palda VA, Garcia-Tsao G, et al. **International guidelines for the diagnosis and management of hereditary haemorrhagic telangiectasia.** *J Med Genet* 2011;48:73–87 CrossRef Medline
3. Brinjikji W, Iyer VN, Lanzino G, et al. **Natural history of brain capillary vascular malformations in hereditary hemorrhagic telangiectasia patients.** *J Neurointerv Surg* 2016 Feb 26. [Epub ahead of print] CrossRef Medline
4. Kim H, Nelson J, Krings T, et al. **Hemorrhage rates from brain arteriovenous malformation in patients with hereditary hemorrhagic telangiectasia.** *Stroke* 2015;46:1362–64 CrossRef Medline
5. Brinjikji W, Iyer VN, Sorenson T, et al. **Cerebrovascular manifestations of hereditary hemorrhagic telangiectasia.** *Stroke* 2015;46:3329–37 CrossRef Medline
6. Brinjikji W, Lanzino G. **Lower risk of intracranial arteriovenous malformation hemorrhage in patients with hereditary hemorrhagic telangiectasia.** *Neurosurgery* 2016 Jul 27. [Epub ahead of print] CrossRef Medline
7. Latino GA, Al-Saleh S, Carpenter S, et al. **The diagnostic yield of rescreening for arteriovenous malformations in children with hereditary hemorrhagic telangiectasia.** *J Pediatr* 2014;165:197–99 CrossRef Medline

W. Brinjikji
V. Yamaki
G. Lanzino
Department of Neurosurgery and Radiology
Mayo Clinic
Rochester, Minnesota